

SECOND EDITION

Grain
Boundary
Migration
in
Metals

*Thermodynamics,
Kinetics,
Applications*

CRC Series in **Materials Science and Technology**

Series Editor

Brian Ralph

**Grain Boundary Migration in Metals: Thermodynamics, Kinetics, Applications,
Second Edition**

Günter Gottstein and Lasar S. Shvindlerman

Corrosion Science and Technology, Second Edition

David E. J. Talbot and James D. R. Talbot

Surface Engineering of Metals: Principles, Equipment, Technologies

Tadeusz Burakowski and Tadeusz Wierzchon'

Image Analysis Applications in Materials Engineering

Leszek Wojnar

The Quantitative Description of the Microstructure of Materials

K J. Kurzydowski and Brian Ralph

The Extraction and Refining of Metals

Colin Bodsworth

Control of Microstructures and Properties in Steel Arc Welds

Lars-Erik Svensson

Grain Growth and Control of Microstructure and Texture in Polycrystalline Materials

Vladimir Novikov

SECOND EDITION

Grain Boundary Migration *in* Metals

*Thermodynamics,
Kinetics,
Applications*

*Günter Gottstein
Lasar S. Shvindlerman*



CRC Press

Taylor & Francis Group

Boca Raton London New York

CRC Press is an imprint of the
Taylor & Francis Group, an **informa** business

CRC Press
Taylor & Francis Group
6000 Broken Sound Parkway NW, Suite 300
Boca Raton, FL 33487-2742

© 2010 by Taylor and Francis Group, LLC
CRC Press is an imprint of Taylor & Francis Group, an Informa business

No claim to original U.S. Government works

Printed in the United States of America on acid-free paper
10 9 8 7 6 5 4 3 2 1

International Standard Book Number: 978-1-4200-5435-4 (Hardback)

This book contains information obtained from authentic and highly regarded sources. Reasonable efforts have been made to publish reliable data and information, but the author and publisher cannot assume responsibility for the validity of all materials or the consequences of their use. The authors and publishers have attempted to trace the copyright holders of all material reproduced in this publication and apologize to copyright holders if permission to publish in this form has not been obtained. If any copyright material has not been acknowledged please write and let us know so we may rectify in any future reprint.

Except as permitted under U.S. Copyright Law, no part of this book may be reprinted, reproduced, transmitted, or utilized in any form by any electronic, mechanical, or other means, now known or hereafter invented, including photocopying, microfilming, and recording, or in any information storage or retrieval system, without written permission from the publishers.

For permission to photocopy or use material electronically from this work, please access www.copyright.com (<http://www.copyright.com/>) or contact the Copyright Clearance Center, Inc. (CCC), 222 Rosewood Drive, Danvers, MA 01923, 978-750-8400. CCC is a not-for-profit organization that provides licenses and registration for a variety of users. For organizations that have been granted a photocopy license by the CCC, a separate system of payment has been arranged.

Trademark Notice: Product or corporate names may be trademarks or registered trademarks, and are used only for identification and explanation without intent to infringe.

Library of Congress Cataloging-in-Publication Data

Gottstein, G., 1944-

Grain boundary migration in metals : thermodynamics, kinetics, applications, /
authors, Günter Gottstein, Lasar S. Shvindlerman. -- 2nd ed.

p. cm.

"A CRC title."

Includes bibliographical references and index.

ISBN 978-1-4200-5435-4 (hardcover : alk. paper)

1. Kirkendall effect. 2. Metals--Thermomechanical properties. 3. Metal crystals. I.
Shvindlerman, L. S. (Lazar' Simkhovich) II. Title.

QC176.8.D5G68 2010

620.1'699--dc22

2009038935

Visit the Taylor & Francis Web site at
<http://www.taylorandfrancis.com>

and the CRC Press Web site at
<http://www.crcpress.com>

“That we find out the cause of this effect
Or rather say the cause of this defect
For this effect defective comes with cause”
— *W. Shakespeare, “Hamlet”*

Contents

The Authors

Preface to the Second Edition

Acknowledgments

Introduction

List of Symbols

1	Thermodynamics of Grain Boundaries	1
1.1	Introductory Remarks	1
1.2	Thermodynamics of Surfaces	2
1.2.1	Introduction	2
1.2.2	Is Equilibrium Thermodynamics Applicable to Grain Boundaries?	4
1.2.3	Gibbs Thermodynamics of Surface Phenomena	7
1.2.4	Gibbs Thermodynamic Method Applied to Grain Boundaries	14
1.2.5	Grain Boundary Solutions	24
1.2.6	Statistical Analysis of the Adsorption on Internal Interfaces in Solids	34
1.3	Experiments	44
1.3.1	Adsorption	44
1.3.2	Grain Boundary Surface Tension	52
1.3.3	Examples	59
1.3.4	Adsorption of Vacancies at Grain Boundaries	66
1.4	Applications of Grain Boundary Thermodynamics	69
1.4.1	Grain Boundary Phase Transitions	69
1.5	The Equilibrium Shape of Grain Boundaries	102
1.6	Problems	108
2	Structure of Grain Boundaries	111
2.1	Terminology and Definitions	111
2.2	Atomic Structure of Grain Boundaries	115
2.2.1	Low-Angle Grain Boundaries	115
2.2.2	High-Angle Grain Boundaries	118

2.3	Problems	131
3	Grain Boundary Motion	135
3.1	Fundamentals	135
3.2	Driving Forces for Grain Boundary Migration	140
3.3	Drag Effects During Grain Boundary Motion	144
3.3.1	Origin of Drag Effects	144
3.3.2	Impurity Drag in Ideal Solute Solutions	144
3.3.3	Impurity Drag in Regular Solutions	150
3.3.4	Vacancy Drag	158
3.3.5	Drag Effects by Second-Phase Particles	163
3.3.6	Groove Dragging	171
3.4	Measurement of Grain Boundary Mobility	181
3.4.1	Polycrystal Methods	181
3.4.2	Bicrystal Methods	181
3.4.3	Shape of a Moving Grain Boundary	197
3.5	Experimental Results	217
3.5.1	Relation between Driving Force and Migration Rate	217
3.5.2	Kinetic Parameters of Grain Boundary Mobility	222
3.5.3	Misorientation Dependence of Grain Boundary Mobility	223
3.5.4	Correlation of Grain Boundary Migration and Diffusion	231
3.5.5	Segregation Effects Other Than Misorientation	233
3.5.6	Impurity Drag and Breakaway	236
3.5.7	Athermal Motion of Grain Boundaries	248
3.5.8	Effect of Pressure on Grain Boundary Migration: Activation Volume	259
3.5.9	Effect of Grain Boundary Orientation	267
3.6	Effect of Wetting Phase Transitions on Grain Boundary Migration	285
3.7	Compensation Effect in Grain Boundary Motion	294
3.7.1	The Fundamental Rate Equation	294
3.7.2	Examples	295
3.7.3	Thermodynamics of the Activated State	295
3.7.4	Applications	305
3.8	Mechanisms of Grain Boundary Migration	311
3.9	Problems	324
4	Thermodynamics and Kinetics of Connected Grain Boundaries	329
4.1	Microstructural Elements of Polycrystals	329
4.2	Thermodynamics of Triple Junctions	331
4.2.1	Grain Boundary Triple Line Tension — Experimental Approach	335

4.3	Motion of a Grain Boundary System with Triple Junctions . .	337
4.4	Triple Junctions Motion in the Presence of Impurities	341
4.5	Experimental Investigations of Triple Junction Motion	344
4.5.1	Motion of a Grain Boundary System with Triple Junction in a Material with Impurities	366
4.6	Triple Junction Drag and Grain Growth in 2D Polycrystals .	374
4.6.1	Introduction	374
4.6.2	Topology of Grain Structures	376
4.6.3	Elementary Topological Rearrangements	377
4.6.4	Grain Growth Kinetics	378
4.6.5	Uniform Grain Boundary Model and the Von Neumann-Mullins Relation	380
4.6.6	Effect of Triple Junction Drag on the Von Neumann-Mullins Relation	383
4.7	Grain Growth in 3D Systems	412
4.7.1	Analytical Approaches	412
4.7.2	Computer Simulations of 3D Grain Growth	416
4.8	Kinetics of Grain Growth Inhibited by Vacancy Generation .	429
4.8.1	Diffusion-Controlled Creep in Nanocrystalline Materials under Grain Growth	443
4.9	Problems	447
5	Computer Simulation of Grain Boundary Motion	451
5.1	Introduction	451
5.1.1	Classical Molecular Dynamics	452
5.1.2	Parrinello-Rahman Method	453
5.1.3	Time Integration Schemes	455
5.1.4	Boundary Concepts	457
5.1.5	Finite Temperature MD Simulations	457
5.2	Driving Force Concepts	460
5.2.1	Introduction	460
5.2.2	Elastic Driving Force	460
5.2.3	Peach-Koehler Driving Force	462
5.2.4	Orientation-Correlated Driving Force	464
5.3	Migration of [001] Twist Grain Boundaries	466
5.3.1	Procedure	466
5.3.2	Atomistic Structure of the Relaxed [001] Twist GBs .	466
5.3.3	GB Migration Due to an Elastic Driving Force	470
5.3.4	Data Analysis with Respect to GB Migration	471
5.3.5	Mobility of [001] Twist GBs	472
5.4	Motion of Tilt Boundaries	476
5.5	Compensation Effect	483
5.6	Comparison with Experiments	484
5.7	Grain Boundary Diffusion	485
5.7.1	Computational Procedure	485

5.7.2	Activation Energies	487
5.7.3	Temperature Effects	490
5.8	Atomic Mechanisms	495
5.8.1	GB Migration of [001] Twist Boundaries	495
5.8.2	Grain Boundary Diffusion of [001] Twist Boundaries	496
5.9	Simulation of Triple Junction Motion	497
5.9.1	Theoretical Background	497
5.9.2	Simulation Method	499
5.9.3	Simulation Results	501
6	Applications	509
6.1	Characterization of Microstructure and Texture	509
6.1.1	Introductory Remarks	509
6.1.2	Microstructure	510
6.1.3	Crystallographic Texture	513
6.2	Recrystallization and Grain Growth	535
6.2.1	Phenomenology and Terminology of Recrystallization and Grain Growth	535
6.2.2	Nucleation of Recrystallization	539
6.2.3	Kinetics of Primary Recrystallization	543
6.2.4	Recrystallization Texture	544
6.2.5	Grain Growth	558
6.3	On Precipitation-Controlled Grain Size	563
6.4	Mechanisms on Retardation of Grain Growth	573
6.5	Grain Boundary Junction Engineering	577
7	Appendices	585
7.1	Appendix A	585
7.1.1	Mass Transport in Solids in Terms of Osmotic Pres- sure	585
7.2	Appendix B	588
7.2.1	Calculation of the Rotation Matrix	588
7.3	Appendix C	592
7.3.1	Indexing of Pole Figures	592
8	Solutions	597
9	References	645

The Authors

Since 1989, **Prof. Dr. Günter Gottstein**, has been director of the Institute of Physical Metallurgy and Metal Physics of the RWTH Aachen University, Germany. He obtained his doctoral degree in metal physics from RWTH and, following his habilitation at the faculty of mining and metallurgy of RWTH, he spent about 10 years in the U.S. at Argonne National Laboratory, MIT, and Michigan State University. He was promoted to the rank of full professor at Michigan State University in 1985. Prof. Gottstein has published over 400 scientific papers, primarily in refereed journals, on topics such as interfaces, recrystallization, textures, and high-temperature crystal plasticity. He is the author, coauthor, or coeditor of 12 books on material science, including a textbook which has been translated into several languages. Since 1991 he has worked closely with his co-author, Prof. Shvindlerman, on topics of grain boundary migration.

Prof. Dr. Lasar S. Shvindlerman, is a leading scientific researcher at the Institute of Solid State Physics (ISSP), Russian Academy of Sciences (Cherno-golovka, Russia) and professor of metal physics at the Moscow Institute of Steel and Alloys. He studied materials science at the Kiev Polytechnic Institute, and obtained his doctoral degree in 1968 and his Dr. Sci. degree in metal physics in 1980. Since 1967, he has been associated with the Institute of Solid State Physics in Chernogolovka. Prof. Shvindlerman has published over 250 scientific papers and 3 books, primarily on topics of surface phenomena in solids, diffusion in metals, and phase transitions of grain boundaries in metals. *Grain Boundary Migration in Metals: Thermodynamics, Kinetics, Applications, Second Edition* is the result of his 1991 research collaboration with Prof. Gottstein.

Preface to the Second Edition

In this second edition we tried to augment the first edition, reflecting the progress achieved in grain boundary physics and related phenomena during the past decade. This includes the motion of connected grain boundaries, i.e. the motion of grain boundary systems with triple and quadruple junctions; the effect of grain boundary faceting on grain boundary motion; grain growth in 2D and 3D systems; and the influence of grain boundary junctions on grain growth kinetics, on grain microstructure evolution, and on the stability of fine grained and nanocrystalline materials. Recently, computer simulations have been employed to study the motion of individual grain boundaries and of grain boundary systems with junctions. Therefore, we added a chapter on computer simulation of grain boundary motion. The chapter on grain boundary thermodynamics and the paragraph dedicated to triple junction thermodynamics were supplemented by the latest experimental data of grain boundary free volume measurements and the first measurements of grain boundary junction line tension. Finally, we complied with the request of the readers of the first edition and added problems with solutions to almost all chapters of the book. We trust that with these amendments the book reflects our current state of knowledge of the fascinating phenomena associated with grain boundary migration.

Günter Gottstein
Lasar S. Shvindlerman

Acknowledgments

The authors are indebted to Mrs. Irene Zeferer for her dedication to this second edition and for production of the pages. We want to thank Mrs. Barbara Eigelshoven for the graphic arts and Mrs. Sijia Mu for her careful proofreading of the manuscript. Finally, we are grateful to members of the interface dynamics group at the Institute of Physical Metallurgy and Metal Physics, particularly Prof. Dr. Dmitri Molodov and Dr. Bernd Schönfelder, for helpful comments and valuable discussions.

Introduction

“I know very well, how little Reputation is to be got by Writings which require neither Genius nor Learning, nor indeed any other Talent, except a good memory, or an exact Journal.”

— *Jonathan Swift*

... Piglet said, “But, on the other hand, Pooh, we must remember,” and Pooh said, “Quite true, Piglet, although I had forgotten it for the moment.”

— *A.A. Milne*

Although the fabrication of metallic materials has long been known — early periods in the history of the earth actually were named according to the capability of producing metals, like the Bronze Age or the Iron Age — it was only recognized today that the properties of a metallic material are not primarily controlled by the overall chemistry, i.e. its macroscopic chemical composition, but rather by the distribution of chemical elements and crystal defects, i.e. by its microstructure. The major goal of modern materials science and engineering is the optimization of material microstructure for low cost but optimum performance of a fabricated part under service conditions. The discrepancy between the tremendous manpower efforts of natural scientists and engineers both past and present on the one hand and our lingering inability to comprehensively characterize microstructure and to accurately predict properties of a material or model material behavior on the basis of fundamental concepts on the other hand is evidence of the difficulty of characterizing microstructure, of predicting its evolution and finally, of yielding unambiguous microstructure-property relationships.

The reason for this discrepancy is the extreme complexity of microstructure and the nonlinear interaction of its elements to yield a particular property. One important step of microstructure evolution is the development of the grain structure of a material, i.e. grain size, morphology and topology. The crystallographic volume property of a grain in a single phase material is its orientation, i.e. the atomic arrangement with regard to an external reference coordinate system. Neighboring grains share a common grain boundary, across which the orientation changes discontinuously.

Grain boundaries are the longest known crystal defects. Although they were discovered in the mid-eighteenth century, until quite recently, our understand-

ing of grain boundaries was very poor. Essentially they were associated with an undercooled liquid or quasi-liquid.

An essential feature of grain boundaries is the strong dependence of their thermodynamic and, especially, kinetic properties on crystallography, first of all, on the misorientation between next neighbor grains, but also on the inclination, i.e. the orientation of the grain boundary plane with respect to the adjoining crystalline lattices. Polycrystals are commonly represented as an assembly of grains which are equal in their physical and chemical properties but which vary in size and shape. These grains, however, are surrounded by boundaries which are substantially different in structure and properties. That is the reason why the characteristics of grain boundaries along with their behavior, if extracted from the properties and behavior of polycrystals, are only very general in nature, e.g. in the course of grain growth the total area of grain boundaries decreases; Bi in copper polycrystals causes embrittlement, etc.

The most important property of grain boundaries with regard to microstructure evolution and microstructure control is their ability to move, if exposed to a force. The motion of grain boundaries is the dominant process of microstructural evolution during recrystallization and grain growth, which are liable to occur during heat treatment of a material, except if grain boundary motion is suppressed by special measures.

The objective of this book is to give a state-of-the-art overview of our current knowledge of the process of grain boundary migration and how it affects microstructure evolution. The distinguishing feature of this book is that it focuses exclusively on the properties and behavior of grain boundaries with well-defined geometry and crystallography. Moreover, these parameters can be chosen deliberately during the fabrication of the bi- or tricrystals to be investigated.

The book is intended to serve as a source of information and reference for scientists working in related fields comprising interface physics and materials science of microstructure evolution and property control. We tried to give both the physics and materials science community easy access to the complementary issues by providing auxiliary chapters on an introductory level on grain boundary physics and microstructure evolution in terms of recrystallization, grain growth and textures. Being aware of the need to read textures we provide a worked example in the appendix to acquaint the inexperienced reader with this important application of grain boundary migration. These auxiliary chapters are meant to provide a concise basis of understanding for the topic of concern, namely grain boundary motion. For a more fundamental and comprehensive treatment of grain boundary structure the reader is referred to other books like A. Sutton and R.W. Balluffi's, *Interfaces in Crystalline Materials*; on the topics of recrystallization and grain growth to books like J. Humphreys and M. Hatherly's *Recrystallization and Related Phenomena*; and on textures to books like A.R. Wenk's (editor) *Preferred Orientation in Deformed Metals and Rocks: An Introduction to Modern Texture Analysis*.

We also hope that this book will be a useful textbook for graduate students in solid state physics and materials science, especially for those concerned with problems of recrystallization, grain growth and textures, and also as a textbook for advanced level solid state physics and materials science courses. This book is dedicated to everybody who wants to understand more about the fascinating phenomenon of grain boundary motion.

With the restrictions mentioned, we believe that this text represents our current knowledge of grain boundary motion. But the need for better microstructural design provides permanent impetus for research in this field so we expect rapid progress in the coming years. In particular, computer simulation and advanced analytical and imaging methods may help us gain a deeper insight into this phenomenon. So, exciting times are ahead and we hope this book contributes to a broader recognition of this important field and stimulates new and genuine research on grain boundary motion and its effect on microstructure evolution.

List of Symbols

We tried to use the same symbols for the same quantity throughout the text, but sometimes the same symbol is a standard designation for different quantities in a different context. Below we list all the meanings of the symbols used. There is no possibility of confusion, however, about different meanings of a symbol, since within a particular context the meaning of a symbol is unambiguous.

I	LATIN SYMBOLS
A_b	reduced grain boundary mobility
A_V	surface area per unit volume
\tilde{A}	surface area
\bar{A}_i	partial atomic (molar) area, occupied by its component in a surface
a_i	activity of i -th component
B	adsorption constant (the parameter of an adsorption isotherm equation which determines the intensity of adsorption as a function of temperature and specific characteristics of a surface (boundary))
b	Burgers vector; as index, designates that the quantity relates to a grain boundary
c	concentration; c_i — concentration of i -th component; c_v — concentration of vacancies; c_{vb} — concentration of vacancies at the boundary
D	diffusion coefficient; D_b — grain boundary diffusion coefficient; D_v — diffusion coefficient of vacancies; also diameter of a grain
d	distance between dislocations in a small angle grain boundary; as index, designates that the quantity relates to dislocations
E	internal energy; E_i — elastic modulus; E_v — dislocation energy per unit length; E^V — energy of bulk phase
e	as index, designates that quantity considered relates to an equilibrium state
F	Helmholtz free energy: $F = E - TS$
G	Gibbs potential: $G = E - TS + pV = F + pV$
g	g_i — number of sites for atoms of i -th component at the grain boundary
\mathbf{g}	orientation; rotation matrix
H	enthalpy: $H = E + pV$; H_m — enthalpy of activation of grain boundary migration; H_D — activation enthalpy of self-diffusion
h	depth of a groove

I	LATIN SYMBOLS (continued)
J	flux
K	curvature
k	Boltzmann constant; also number of components
L	length; as index, designates that the quantity relates to a liquid state
l	as index, designates that the quantity relates to a triple junction line
M	an extensive characteristic of the system (energy, entropy, volume, etc.)
M^S	a surface excess of an extensive characteristic
m	bulk density of the extensive characteristic; as index, designates that the quantity relates to a liquid state
m_i	mobility of i -th subject; for instance, m_b — grain boundary mobility
N	number of particles
P	driving force
p	pressure
Q	activation energy
q	specific heat
R	radius, also gas constant
r	radius
S	entropy; as index, denotes that the quantity relates to a surface
s	entropy per atom
T	temperature; T_m — melting temperature
U	interaction energy; U_0 — energy of interaction between an adsorbed atom and a surface (grain boundary)
V	volume of the system; V^S — volume of a surface layer; also velocity of a system; as index, denotes that the quantity relates to the volume
v	velocity; usually the normal velocity of grain boundary of a surface; as index, denotes that the quantity relates to vacancies
W	work; also configuration (permutation) probabilities
w	as index; designates that the quantity relates to grain boundary wetting
X	coordinate
Y	coordinate
Z	coordinate; also coordination number, \tilde{Z} — partition function
z	adsorption capacity

II GREEK SYMBOLS

α	as index of a phase or a part (fraction) of a system
β	as index of a phase or a part of a system; also adsorption enrichment coefficient
Γ	adsorption; Γ_i — adsorption of i-th component
γ	parameter of Frumkin-Fowler isotherm; grain boundary surface tension; γ^S — surface tension of a free surface of a crystal; γ^ℓ — grain boundary triple junction line tension
Δ	distance; also heat of mixing
δ	an infinitely small change; also grain boundary width
ε	energies (enthalpies), associated with different types of bonds; also torque terms in the orientation dependence of grain boundary surface tension
ζ	mobility anisotropy
Θ	degree of coverage of an adsorption layer; also dihedral angle at the root of a grain boundary groove; also inclination of a boundary; also angle at the tip of a triple junction
Λ	dimensionless criterion, which reflects the influence of the triple junction mobility on grain boundary motion
λ	thickness; thickness of a surface (interface) layer
μ	chemical potential; also shear modulus; μ_i — chemical potential of the i-th component; μ_{ist} — chemical potential of a standard state
ξ	parameter, determines the position of the grain boundary
ρ	density of a material or a phase
Σ	inverse density of coincidence sites
σ	width of the grain size distribution
τ	stress
Φ	thermodynamic potential $\Phi = G - \gamma\tilde{A}$; also Euler angle
φ	misorientation (rotation) angle
Ω	Gibbs grand potential; Ω_a — atomic volume
ω	bulk density of a potential Ω ; ω_i — partial area of an atom of i-th component

Thermodynamics of Grain Boundaries

“Sometimes he thought sadly to himself, ‘Why?’ and sometimes he thought, ‘Wherefore?’ and sometimes he thought, ‘Inasmuch as which?’”
“...because it is a thing which you can easily explain twice before anybody knows what you are talking about.”

— *A.A. Milne*

1.1 Introductory Remarks

Thermodynamics is one of the most general methods of investigation; it is free from model assumptions concerning the internal design of the object studied or its behavior.

The thermodynamics of interfaces is a classical division of thermodynamics with well-developed methodology, terminology and numerous startling applications to dissimilar systems and processes.

While an interface is conceived to be represented by a 2D surface, the interface in a solid also will affect the volume adjacent to the interface. Therefore, we introduce the term interphase which comprises the interface as well as its affected volume. In other words, the interphase consists of a layer of finite thicknesses adjacent to the interface. In the following we will discuss the thermodynamics of this volume, i.e. the thermodynamics of the interphase. It is sufficient at least to discuss the properties and behavior of grain boundaries on the basis of the methods and concepts of the equilibrium thermodynamics of interphases. Nevertheless, the direct application of those concepts to grain boundaries involves some problems caused by the actual distinctions between grain boundaries and interphases.

The present chapter is designed on the basis of a consistent application of the thermodynamical methods of equilibrium surface investigations to grain boundaries in crystals. The feasibility of this concept is confirmed by the analysis of grain boundaries as an object of equilibrium thermodynamics.

1.2 Thermodynamics of Surfaces

1.2.1 Introduction

The fundamental thermodynamic characteristic of a surface is the surface tension γ . The work performed by a reversible increase of the surface area \tilde{A} by $\delta\tilde{A}$ is

$$\delta W = \gamma \delta \tilde{A} \quad (1.1)$$

If this process takes place at constant temperature T , constant volume V of the system and invariant chemical potentials μ_i of the components ($i = 1, 2, \dots, k$, where k is the number of components)

$$\delta W = d\Omega_{T,V,\mu_i} \quad (1.2)$$

where

$$\Omega = F - \sum \mu_i N_i \quad (1.3)$$

is the so-called Gibbs grand potential. (F is the Helmholtz free energy and N_i is the number of atoms of the i th component.)

From Eqs. (1.1) and (1.2) follows that in a system with a surface

$$d\Omega = -pdV - SdT - \sum_{i=1}^k N_i d\mu_i + \gamma d\tilde{A} \quad (1.4)$$

(p is the pressure in the system, S is the entropy).

Since the Gibbs potential G is

$$G = E - TS + pV = \sum_{i=1}^k \mu_i N_i \quad (1.5)$$

(E is the internal energy of the system), the potential Ω is equal to

$$\Omega = -pV + \gamma \tilde{A} \quad (1.6)$$

In accordance with the theorem of small variations of the thermodynamic potential we get

$$\begin{aligned} \gamma &= \left(\frac{\partial E}{\partial \tilde{A}} \right)_{V,S,N_i} = \left(\frac{\partial H}{\partial \tilde{A}} \right)_{p,S,N_i} = \left(\frac{\partial F}{\partial \tilde{A}} \right)_{V,T,N_i} \\ &= \left(\frac{\partial G}{\partial \tilde{A}} \right)_{p,T,N_i} = \left(\frac{\partial \Omega}{\partial \tilde{A}} \right)_{V,T,\mu_i} \end{aligned} \quad (1.7)$$

(H is the enthalpy of the system, G is the Gibbs potential).

Correspondingly:

$$E = TS - pV + \sum_i \mu_i N_i + \gamma \tilde{A} \quad (1.8)$$

$$dE = TdS - pdV + \sum \mu_i dN_i + \gamma d\tilde{A} \quad (1.9)$$

$$H = TS + \sum_i \mu_i N_i + \gamma \tilde{A} \quad (1.10)$$

$$dH = TdS + Vdp + \sum_i \mu_i dN_i + \gamma d\tilde{A} \quad (1.11)$$

$$F = -pV + \sum_i \mu_i N_i + \gamma \tilde{A} \quad (1.12)$$

$$dF = -SdT - pdV + \sum_i \mu_i dN_i + \gamma d\tilde{A} \quad (1.13)$$

$$G = \sum \mu_i N_i + \gamma \tilde{A} \quad (1.14)$$

$$dG = -SdT + Vdp + \sum \mu_i dN_i + \gamma d\tilde{A} \quad (1.15)$$

$$\Omega = -pV + \gamma \tilde{A} \quad (1.16)$$

$$d\Omega = -SdT - pdV - \sum_i N_i d\mu_i + \gamma d\tilde{A} \quad (1.17)$$

The thermodynamic potential G for systems without surface is equal to $G = \sum_i \mu_i N_i$. For systems with a surface the Gibbs thermodynamic potential G is no longer the product of the chemical potentials with the number of particles.

Let us introduce the potential with the desired property:

$$\Phi = G - \gamma \tilde{A} \quad (1.18)$$

$$d\Phi = -SdT + Vdp + \sum_i \mu_i dN_i - \tilde{A}d\gamma \quad (1.19)$$

Since

$$G = \sum_i \mu_i N_i + \gamma \tilde{A} \quad (1.20)$$

$$\Phi = \sum_i \mu_i N_i \quad (1.21)$$

Consequently, the chemical potential in a single component system with a surface is the potential Φ which is related to one particle.

As can be seen from Eq. (1.17) the equilibrium, i.e. the minimum of the thermodynamic potential of the system with a surface at constant volume, temperature and chemical potentials of the components, corresponds to the extremum of the surface area \tilde{A} : that is, to the minimum if $\gamma > 0$. Usually, the value \tilde{A} is not restricted upward since the surface area can increase until the system becomes homogeneous. Consequently, if restrictions on the surface shape are not imposed, the equilibrium surface tension γ cannot be negative, and the equilibrium state of the system fits the minimal surface area \tilde{A} . Of course, if the concept of the surface tension is extended to unstable interfaces, e.g. those liable to chemical reactions, the surface tension can be negative as well.

1.2.2 Is Equilibrium Thermodynamics Applicable to Grain Boundaries?

It is well known that grain boundaries are non-equilibrium defects of crystals, contrary to vacancies, for example.

This is because the energy of a grain boundary cannot be compensated by the configuration entropy, which is small for grain boundaries. Therefore, grain boundaries could only be produced by fluctuations, which is, however, very unlikely. In this case the potential grain boundary unit area per unit volume reads

$$\bar{M} = \int_0^\infty \tilde{A} \frac{\gamma}{kT \cdot \Omega_a} \exp\left(-\frac{\gamma \tilde{A}}{kT}\right) d\tilde{A} = \frac{kT}{\gamma \Omega_a} \sim 10^{-15} \text{cm}^{-3} \quad (1.22)$$

(Ω_a is the atomic volume).

To analyze the applicability of the methods of equilibrium thermodynamics to grain boundaries it is first of all necessary to provide the exact meaning of the statement that the grain boundary is a non-equilibrium object in a finite system. The equilibrium of the system with interfaces, in particular, with grain boundaries, fits the minimum of the corresponding thermodynamic potential of the system with regard to the restrictions applied to the system. Inasmuch as the surface tension of the equilibrium surface is positive, a minimum of the thermodynamic potential can be achieved if the area of the surface is equal to zero. Consequently, a definite number of restrictions is required for the existence of any equilibrium surface.

The restrictions may be of thermodynamic character if parameters of the system like volume, energy and so on are fixed, or geometrical ones if the points or lines through which the surface must pass are determined. If, for example, in two-phase systems the temperature, volume and the quantity of material are fixed in such a way that the minimum of the free energy corresponds to the existence of the two-phase state, there will be no net atom transfer from phase to phase because the specific volumes of atoms in different phases are different. That is why such a system cannot become a single-phase one, and the minimum area of the interphase cannot vanish. Therefore, there are plenty of thermodynamic restrictions only for the existence of an equilibrium surface.

The main difference between grain boundaries and interphases in thermodynamic terms is determined by the properties of the volumes divided by them. Namely, each side of the grain boundary consists of the same phase; the regions divided by it differ by the orientation in space only ("phase" means a part of a system which can be characterized by a definite functional relationship between the state parameters, e.g. by a certain dependence of the chemical potential on the basic intensive variables: temperature, pressure, concentrations, etc.). If there is no specific direction — the space is isotropic — the thermodynamic properties of these regions are the same. From the

thermodynamic point of view it can be said that the grain boundary represents a “degenerated” case of the interphase — in the sense that there are differences in the regions divided by the boundary. If there are no anisotropic external thermodynamic forces like electric, magnetic or elastic fields, there is the same phase on each side of the grain boundary. Hence, the transfer of material across the grain boundary, in other words, the grain boundary migration, is not connected with a change of the volume of the system. So the existence of a grain boundary in a crystal cannot be achieved by thermodynamic boundary conditions only. Therefore, if only thermodynamic and no other conditions are imposed on the system, equilibrium interphases may exist, but there are no conditions for equilibrium grain boundaries.

Due to the “degeneracy” of grain boundaries the existence of thermodynamic boundary conditions alone is inadequate for them to be in equilibrium — in this sense they are less equilibrium objects than interphases. But the existence of grain boundaries in a crystal can be forced by geometrical restrictions. For example, the grain boundary can be fixed to the surface by thermal grooves. Under these conditions grain boundaries are in equilibrium with the adjacent bulk regions by them and can be studied using the approaches of equilibrium thermodynamics.

If the crystal is under the action of an anisotropic thermodynamic force the situation changes drastically, and the indicated “degeneracy” will not take place. If, for example, a magnetoanisotropic polycrystal is placed into a magnetic field, the specific free energy of different grains will be different and the grain boundaries will have the thermodynamic properties of interphases. Actually, the chemical potential of the atoms of different grains will depend, apart from the usual scalar parameters, on the grain orientation in relation to the magnetic field. Consequently, two grains divided by the grain boundary and oriented differently with respect to the magnetic field direction represent, with our definition, two different thermodynamic phases. So, in this case the grain boundary is, from the thermodynamic point of view, an interphase — the “degeneracy” is lifted. The isolated equilibrium grain may exist in such a crystal.

The classical thermodynamics of surface phenomena describes surfaces between the liquid and gas or between two liquids. The grain boundary divides two crystalline bulk regions, and this problem should be analyzed. The surface tension γ is a surface excess of the thermodynamic potential $\Omega = -pV + \gamma\hat{A}$. But what is the pressure when it comes to solids?

As mentioned by Gibbs [1], the thermodynamic properties of a surface in solids should be described not only by the single value γ like in a liquid, but also by two distinct ones. The first one, which Gibbs denoted also by γ , is the work required to create the unit of area of a surface. This is a scalar value γ , which depends on the orientation of the surface with respect to the crystallographic axes of the crystal.

The second characteristic of a surface is consistent with the work required to stretch the existing surface and represents a 2D tensor of second order $\beta_{\mu\nu}$,

inasmuch as the work of stretching the surface depends on the orientation in which the surface is stretched. The tensor $\beta_{\mu\nu}$ is designated as the tensor of surface tension [2]. It means that the dependence of the surface energy on deformations can be given as [2]

$$G^S = \int (\gamma + \beta_{\mu\nu} \mu_{\mu\nu}) d\tilde{A} \quad (1.23)$$

where $u_{\mu\nu}$ are the tangential components of the tensor of deformation. The surface free energy γ and the components are functions of two angles which specify the orientation with respect to the crystallographic axes. Consequently, the crystal has to undergo a deformation. Inasmuch as the values of this deformation are determined by minimization of the sum of the surface energy which depends linearly on the deformation tensor and the bulk energy which changes with the square of the strain, the total energy of these deformations is necessarily negative.

To show more clearly the sense of these characteristics let us consider a “Gedankenexperiment” to measure the values mentioned above.

The first experiment of measuring γ is the idealization of the well-known method of zero creep. A thin crystalline sheet is compressed elastically by surface forces. If we heat the sheet to the temperature of the beginning of a pronounced diffusivity of atoms, the area of the sheet will begin to decrease. These forces can be balanced if the corresponding forces will be applied to the edges of the sheet, so that the velocity of the decrease in size of the sheet becomes zero, which explains the name of the method. By measuring these forces we determine the value of γ .

The second “Gedankenexperiment” was considered by Gibbs. Let us apply forces to the edges of the sheet so that all internal tensions are reduced to zero. These forces balance the surface tensions of the sheet and make it possible to measure them. The tensions, measured in such a manner, are obviously different for different directions and generally permit us to determine the tensor $\beta_{\mu\nu}$.

“As in the case of two fluid masses ...” we may regard γ as expressing the work spent in forming a unit of the surface of discontinuity — under certain conditions, which we need not specify here — but it cannot properly be regarded as expressing the tension of the surface. The latter quantity depends upon the work spent in stretching the surface, while the quantity γ depends upon the work spent in forming the surface. With respect to perfectly fluid masses, these processes are not distinguishable, unless the surface of discontinuity has components which are not found in the contiguous masses, and even in this case (since the surface must be supposed to be formed out of matter supplied are the same potentials which belong to the matter in the surface) the work spent in increasing the surface infinitesimally by stretching is identical with that which must be spent in forming an equal infinitesimal amount of new surface. But when one of the masses is solid, and its states of strain are to be distinguished, there is no such equivalence between the stretching of the

surface and the forming of new surface. This will appear more distinctly if we consider a particular case. Let us consider a thin plane sheet of a crystal in a vacuum (which may be regarded as a limiting case of a very attenuated fluid), and let us suppose that the two surfaces of the sheet are alike. By applying the proper forces to the edges of the sheet, we can make all stress vanish in its interior. The tensions of the two surfaces are in equilibrium with these forces, and are measured by them. But the tensions of the surfaces, thus determined, may evidently have different values in different directions, and are entirely different from the quantity which we denote by γ which represents the work required to form a unit to the surface by any reversible process, and is not connected with any idea of direction.

In certain cases, however, it appears probable that the values of γ and of the superficial tension will not greatly differ. This is especially true of the numerous bodies which, although generally (and for many purposes properly) regarded as solids, are really very viscous fluids [1].

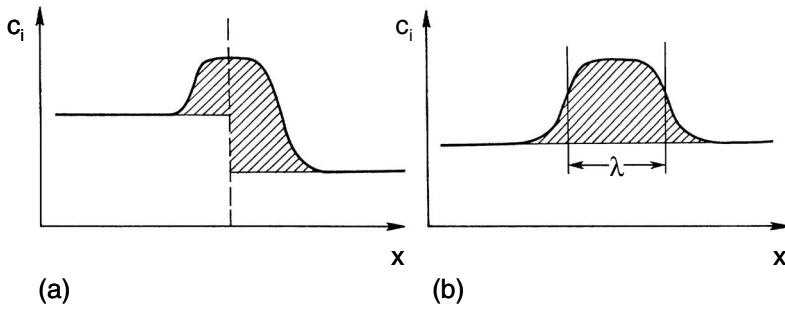
These two procedures, described above, differ essentially, inasmuch as it is impossible to create a new bit of crystal surface with a size less than the lattice constant in the given direction, whereas it is possible to stretch the surface in such a manner. Hence, it follows that the effects are of the order of the ratio of the lattice constant to the crystal size. But, nevertheless, taking these effects into account in some cases is important even for macroscopic crystals [3, 4]. Anyhow, the existence of two independent characteristics of the surface tension imposes limitations, e.g. for 2D phases of the surface of a crystal [4].

The thermodynamic relations and geometrical restrictions discussed above determine the conditions under which the grain boundaries are equilibrium objects, and it is absolutely correct to implement the concepts and methods of equilibrium thermodynamics and statistical physics.

1.2.3 Gibbs Thermodynamics of Surface Phenomena

The method of the thermodynamic description of surfaces in equilibrium systems was proposed by Gibbs in 1876–1878. The properties of the surface in terms of a surface layer can be determined by the Gibbs method as differences between a real system, in which the surface is a certain transition layer between two phases, and an ideal system, in which the phases are considered to be homogeneous up to the plane of their contact (Fig. 1.1). So, according to Gibbs the surface is the transition layer between two homogeneous regions α and β , the thickness of which is much smaller than the other dimensions of the system.

If M is a certain extensive characteristic of the system (energy, entropy, volume, mass, etc.), then its surface part (the surface excess) M^s can be determined as a difference (excess) between the total value of M and its bulk

**FIGURE 1.1**

Schematic diagram illustrating the application of Gibbs method to interphases (a) and grain boundaries (b). The area of the hatched regions corresponds to the surface excess.

part (sometimes the Gibbs method is called a method of excesses):

$$M^S = M - (M^\alpha + M^\beta) \quad (1.24)$$

where M^α , M^β are the constituents of M , relating to the volumes α and β , accordingly.

If m^α and m^β are the bulk densities of the quantity M in the regions α and β divided by the surface, then

$$M^S = M - (m^\alpha V^\alpha + m^\beta V^\beta) \quad (1.25)$$

where V^α and V^β are the volumes ascribed to the regions α and β . This definition is not complete, since it does not contain any indication of the method by which the volumes V^α and V^β were determined. Consequently, it will be sufficient to make an assumption which part of the volume of the system is occupied by each of the regions, and the separation of all other parameters of the bulk and surface constituents will be completely determined. Defining the quantities V^α and V^β in a variety of ways (of course, under the condition $V^\alpha + V^\beta + V^s = V = \text{const.}$), we will get different, though equivalent forms of the thermodynamic description of surface phenomena. Since for an equilibrium system with a flat interface the above definition has the property of linearity, its application to the main thermodynamic equations will give the same relationships between the excess surface quantities irrespective of the method used, though the excess surface values themselves do depend on the method. This is the idea of the method of surface excesses. Gibbs divided the quantities into surface and bulk parts in the following way. First, he assumed the excess surface volume to be zero ($V^s = 0$) or $V^\alpha + V^\beta = V$, where V is the complete volume of the system. In geometric terms it means that the transition surface layer is replaced by a two-dimensional dividing surface.

The scheme of change of the bulk density m of an extensive property (the coordinate x is directed normally to the dividing surface) is given in Fig. 1.1. Far from the surface the values of the quantity m coincide with the bulk density of it in the phases α and β : m^α and m^β , while in the transition layer m differs from them. The dividing surface is indicated by a dotted line. If the properties of the phases were on the level of the bulk values, then $m(x)$ would change in accordance with parallel lines, and the total quantity M would be determined as

$$M = m^\alpha V^\alpha + m^\beta V^\beta \quad (1.26)$$

Because the system properties in the transition layer differ from the bulk ones, the additional term $M^s = m^s \tilde{A}$ is required — the surface excess of the property in question, where m^s is the surface excess density (the excess per unit area of the surface), and \tilde{A} is the area of the surface. Thus,

$$M = m^\alpha V^\alpha + m^\beta V^\beta + m^s \tilde{A} \quad (1.27)$$

In such a manner the surface excesses and the densities of the surface excesses of the different thermodynamic parameters can be introduced. The excess of material in the equilibrium system is referred to by a special term, the adsorption Γ . For the component i -th we get

$$N_i = n_i^\alpha V^\alpha + n_i^\beta V^\beta + \Gamma_i \tilde{A} \quad (1.28)$$

(N_i is the number of atoms of the component i -th, n_i indicates the respective atomic density.)

Geometrically m^s is equal to the shaded area in Fig. 1.1. As mentioned above, Eq. (1.25) is not complete, so the method of determination of the volumes V^α and V^β should be given, in other words, the exact position of the dividing surface should be set. The surface location can be preset by the parameter

$$\xi = V^\alpha / V \quad (1.29)$$

For a given ξ , the quantities V^α and V^β , and, consequently, all the excess surface quantities, are determined uniquely and can be presented in the following form:

$$M^S = M - V m^\beta + \xi V (m^\beta - m^\alpha) \quad (1.30)$$

In the case of interphases $m^\alpha \neq m^\beta$ and the values of the surface excesses depend on the choice of the position of the dividing surface, i.e. on ξ .

Thus, it is seen that the dependence of excess surface quantities on the position of the dividing surface [$\partial M^S / \partial \xi = V \cdot (m^\beta - m^\alpha)$] is due to the difference in the intensive characteristics of the bulk divided by this surface. Physically, the position of the dividing surface is determined with an accuracy up to the thickness of a real transition layer. It could look as if such a small ambiguity could not affect substantially the values of physical quantities under consideration. However, if the dividing surface is displaced by a distance equal to the

thickness of the transition layer, the changes in the excess surface values can be of the same order of magnitude as the excess surface values themselves [5]. Thus, for interfaces the ambiguity of surface quantities is essential.

There is, however, a quantity with an excess surface value, which does not depend on the position of the dividing surface. This is the potential Ω . Actually, $\Omega^\alpha = -pV^\alpha$, $\Omega^\beta = -pV^\beta$, so the bulk densities of the potential Ω are equal to

$$\omega^\alpha = \omega^\beta = -p \quad (1.31)$$

For the surface excess of Ω , as for any extensive function, we have, in accordance with Eq.(1.24)

$$\Omega^S = \Omega + pV \quad (1.32)$$

In other words, the surface excess Ω^S does not depend on the position of the dividing surface.

Comparing Eqs.(1.32) and (1.16) we get

$$\Omega^S = \gamma \tilde{A} \quad (1.33)$$

Consequently, in the Gibbs method the surface tension is equal to the density of the surface excess of the potential Ω .

The excesses and the densities of other thermodynamic functions can be expressed in terms of γ and Γ_i . Taking into account that the expression for the surface excess of extensive parameters (Eq.(1.24)) offers the property of linearity, we have

$$(a_1 M_1 + a_2 M_2)^S = a_1 M_1^S + a_2 M_2^S \quad (1.34)$$

where a_1 and a_2 are the intensive parameters common in both phases.

For the Helmholtz free energy F we get

$$F^S = \left(\Omega + \sum_i \mu_i N_i \right)^S = \Omega^S + \sum_i \mu_i N_i^S \quad (1.35)$$

The surface density of the Helmholtz free energy is

$$F^S / \tilde{A} = f^S = \gamma + \sum_i \Gamma_i \mu_i \quad (1.36)$$

The surface density of the Gibbs free energy is

$$\frac{G^S}{\tilde{A}} = \frac{\sum_i \mu_i N_i^S}{\tilde{A}} = \sum_i \Gamma_i \mu_i \quad (1.37)$$

The surface density of the entropy can be represented as

$$S^S = - \left(\frac{\partial \Omega^S}{\partial T} \right)_{V, \mu_i, \tilde{A}}; \quad \frac{S^S}{\tilde{A}} = - \frac{1}{\tilde{A}} \left(\frac{\partial \Omega^S}{\partial T} \right) = - \left(\frac{\partial \gamma}{\partial T} \right)_{\mu_i} \quad (1.38)$$

and the surface density of the internal energy is equal to

$$\frac{E^S}{\tilde{A}} = \frac{F^S + TS^S}{\tilde{A}} = \gamma + \sum_i \Gamma_i \mu_i - T \frac{\partial \gamma}{\partial T} \quad (1.39)$$

It should be pointed out that the definition of the surface tension γ through the work performed by a reversible increase of the surface area by $\delta \tilde{A}$ — the relation (1.1) — is the most general at fixed values of the corresponding thermodynamic parameters. Which parameters should be fixed depends on the analyzed situation. Sometimes it can be found that the definition of γ as the surface density of some thermodynamic potential is most commonly the Helmholtz free energy

$$\gamma = F^S / \tilde{A} \quad (1.40)$$

One can see that for fixed T , V , μ_i the relation is obeyed with an accuracy of the terms $\sum_i \Gamma_i \mu_i$.

If we fix volume, number of the particles of each component, and temperature, Eq. (1.40) will be an exact one. But it should be remembered that in this case the change of surface area means a bulk concentration change.

The Gibbs method is most familiar and used most often, although, as we have emphasized, it is not the only one. Let us consider two examples [6].

Assume that the additional condition, imposed on the system, is $\Omega^S = 0$. Then the surface excess of the volume does not vanish. Actually, in accordance with Eq. (1.34)

$$\Omega^S = \left(-pV + \gamma \tilde{A} \right)^S = pV^S + \gamma \tilde{A} \quad (1.41)$$

and

$$V^S = \frac{\gamma}{p} \tilde{A} \quad (1.42)$$

Introducing the parameter η

$$\eta = V^\alpha / (V - V^S) \quad (1.43)$$

we get

$$M^S = M - m^\beta (V - V^S) + \eta (V - V^S) (m^\beta - m^\alpha) \quad (1.44)$$

The relation between the values, obtained by the Gibbs method M_G^S and by the given one, can be found if we compare Eqs. (1.30) and (1.44):

$$M^S = M_G^S + \frac{\gamma}{p} \tilde{A} [m^\beta (1 - \eta) + \eta m^\alpha] \quad (1.45)$$

Hart [7] studied phase transformations in a one-component system with a method determined by the condition $N^S = 0$. Correspondingly, for the k -component system $\sum_i^k N_i^S = 0$, and the surface excess of the volume is

$$V^S = V - \frac{\sum_i^k N_i}{\sum_i^k n_i} \quad (1.46)$$

where n_i is the atomic density of the i -th component. The correlation between the surface excesses according to Hart (M_H^S) and according to Gibbs (M_G^S) is given by

$$M_H^S = M_G^S + m^V \left(V - \sum_i^k N_i / \sum_i^k n_i \right) \quad (1.47)$$

We would like to remind the reader once again that on the one hand, the choice of a particular method is governed by the specific conditions of the problem and, on the other hand, it is also a matter of convenience.

Let us return to Eq.(1.17). For the surface parameters it reads

$$d\Omega^S = -pdV^S - S^S dT - \sum_i^k N_i^S d\mu_i + \gamma d\tilde{A} \quad (1.48)$$

Then, comparing Eqs. (1.41) and (1.48) one can get

$$\tilde{A} d\gamma = -S^S dT - \sum_i^k N_i^S d\mu_i + V^S dp \quad (1.49)$$

For the specific values $s^s = S^s / \tilde{A}$, $\Gamma_i = N_i^S / \tilde{A}$, $v^s = V^s / \tilde{A}$, Eq. (1.49) acquires the form

$$d\gamma = -s^S dT - \sum_i^k \Gamma_i d\mu_i + v^S dp \quad (1.50)$$

This is the well-known Gibbs equation, which connects the change in surface tension with the variations in temperature, pressure and chemical potentials of the bulk phases. The relation (1.50) holds for any surface which is in equilibrium with the volumes, divided by it.

The Gibbs equation is equally applicable to adsorption at interphases and to adsorption at grain boundaries, but the grain boundary degeneracy results in several important distinctions between adsorption at grain boundaries and at interphases.

A system with an interphase has, at least, two phases, and the number f of thermodynamic degrees of freedom in such a system, according to the Gibbs rule of phases, is

$$f = k + 2 - p \quad (1.51)$$

where p is the number of coexisting phases and k the number of components. The number of differentials on the right-hand side of the adsorption Eq. (1.50) is $k + 2 > k$; therefore, not all of them are independent, so it is not possible to calculate excess surface quantities by direct differentiation of the surface tension with respect to a corresponding variable. In order to represent surface excesses in the form of a partial derivative of the surface tension with respect to one of the variables two additional links are required. One of them can be the method of calculation of the surface excesses. So, in the Gibbs method, in

a local sense, $V^s = 0$, and the number of differentials on the right-hand side of Eq. (1.50) decreases to $k + 1$. Then Eq. (1.50) assumes the form

$$d\gamma = -s^S dT - \sum_{i=1}^k \Gamma_i d\mu_i \quad (1.52)$$

and for $T = \text{const.}$

$$d\gamma = - \sum_i \Gamma_i d\mu_i \quad (1.53)$$

This is the most frequently used form of the Gibbs adsorption equation.

As mentioned before, the differential relations between the surface excesses should be insensitive to the position of dividing surface; nevertheless, the values of surface excess quantities depend on it. Let us illustrate this by means of Eq.(1.53). Assume there are two dividing surfaces A_1 and A_2 , and the adsorption by them is Γ_i and Γ'_i , respectively. Obviously,

$$\Gamma_i = \Gamma'_i - \left(c_i^\alpha - c_i^\beta \right) \Delta \quad (1.54)$$

where c_i^α, c_i^β are the bulk concentrations of the i -th component in the bulk phases, and Δ is the distance between the dividing surfaces. The sign of Δ depends on the position with respect to the phases α and β : if A_2 is nearer to the phase α than A_1 then Δ is positive ($\Delta > 0$). If the temperature of the system is constant, the Gibbs-Duhem equation is valid for each of the phases:

$$dp = \sum c_i^\alpha d\mu_i; \quad dp = \sum c_i^\beta d\mu_i \quad (1.55)$$

and the equation for the phase equilibrium acquires the form

$$\sum_i \left(c_i^\alpha - c_i^\beta \right) d\mu_i = 0 \quad (1.56)$$

Rewriting Eqs. (1.53) and (1.54) in terms of Eq. (1.56) we get

$$d\gamma = - \sum_i \Gamma'_i d\mu_i \quad (1.57)$$

As can be seen, Eq. (1.52) does not depend on the position of an arbitrary dividing surface, as we intended to prove.

A further relation can be found by choosing the position of the dividing surface. This is usually done in such a way that the adsorption of one of the components (as a rule, of the solvent) will be equal to zero.

Guggenheim and Adam [8] suggested placing the dividing surface between the transition layer and the bulk of the condensed phase. There is an important advantage to such approach. If the second phase is liquid, in the case mentioned above, the calculated values of the surface excesses coincide with

the real concentrations, densities and so on in the surface layer. Let us express the differential of the chemical potential of one of the components, say the first one, and the differential of the surface tension as a function of the differentials of the other components (Eqs. (1.56) and (1.53)):

$$d\mu_1 = - \frac{\sum_{i=2}^k (c_i^\alpha - c_i^\beta) d\mu_i}{c_1^\alpha - c_1^\beta} \quad (1.58)$$

$$d\gamma = - \sum_{i=2} \left(\Gamma_i - \Gamma_1 \frac{c_i^\alpha - c_i^\beta}{c_1^\alpha - c_1^\beta} \right) d\mu_i \quad (1.59)$$

The parameters $\Gamma_{(1)} = \Gamma_i - \Gamma_1 \left(\frac{c_i^\alpha - c_i^\beta}{c_1^\alpha - c_1^\beta} \right)$ are called the relative Gibbs adsorptions. Contrary to the adsorptions Γ_i , the relative adsorptions are independent of the position of the dividing surface. $\Gamma_{(1)}$ is the adsorption of the i -th component attributed to the dividing surface, where $\Gamma_1 = 0$ (Fig. 1.1).

For binary systems with an interphase such an approach makes it possible to express conveniently the adsorption (of the second component) Γ

$$\Gamma = - \frac{d\gamma}{d\mu} = - \frac{a}{kT} \frac{d\gamma}{da} \quad (1.60)$$

where a is the activity.

The relationship (1.60) is used very often for adsorption at the grain boundaries, neglecting that this is a different situation.

1.2.4 Gibbs Thermodynamic Method Applied to Grain Boundaries

The title of this chapter reflects the essential thermodynamic distinctions between grain boundaries and interphases. In turn these distinctions are connected with the above-mentioned property of grain boundaries — they divide similar phases. The first distinction consists of the fact that the surface excesses of any extensive value for the grain boundary are independent of the choice of the Gibbs dividing surface. Actually, inasmuch as the regions α and β , divided by the grain boundary, are occupied by the common phase, the bulk densities m^α and m^β of the extensive quantity M have the same value $m^\alpha = m^\beta = m^v$. In accordance with Eq. (1.30), the surface excesses M^S are equal:

$$M^S = M - Vm^v \quad (1.61)$$

and do not depend on the position of the dividing surface, i.e. on the parameter ξ . Naturally, this is a physical result, and it is connected with the alternative version of the Gibbs approach. For example, for the approach, which is defined

by the condition $\Omega^S = 0$ (Eq. (1.44)), we obtain for grain boundaries

$$M^S = M - m^v \left(V - \frac{\gamma}{p} \hat{A} \right) \quad (1.62)$$

i.e. a value that does not depend on the parameter η , which is the analogue of the parameter ξ . This is clearly demonstrated in Fig. 1.1.

The second peculiarity of grain boundary thermodynamics consists of the fact that for a system with a grain boundary the number of degrees of freedom by one is greater than for the interphase (see Eq. (1.51)).

Therefore, for a system with a grain boundary all differentials on the right-hand side of the Gibbs equation (1.52) are independent; for a grain boundary the Gibbs-Duhem equation does not impose any restrictions on the system, due to $c_i^\alpha = c_i^\beta$ for all i (compare with the results of [9]). The surface excesses of the grain boundaries are independent of the position of the dividing surface and depend on the properties of the grain boundary only. The same can be described more rigidly in terms of the method mentioned above. The surface excesses can be determined by the Gibbs method as differences between a real system, in which the surface is a certain transition layer between two phases, and an ideal system, in which the phases are considered to be homogeneous up to the plane of contact (Fig. 1.1a). For an interphase the excesses are obviously determined by the position of the imaginary surface, which divides two homogeneous planes. In the case of the grain boundary (Fig. 1.1b), precisely because the properties of the bulk on both sides of the boundary are the same, the excess quantities are independent of the imaginary surface position and have themselves an objective significance.

Due to the availability of the additional degree of freedom a number of unique possibilities arise. In particular, one can consider adsorption at grain boundaries in a one-component system, which we shall call autoadsorption. (There is no sense in considering such a problem for an interphase, inasmuch as at constant temperature such a system is completely determined.) In this case Eq. (1.52) takes the form [9]:

$$d\gamma = -s^S dT - \Gamma_0 d\mu \quad (1.63)$$

The parameter Γ_0 has the meaning of an autoadsorption at grain boundaries in pure material. Expressing μ through the thermodynamic characteristics of the volume and taking into account that $s^S = \Gamma_0 s_a^S$, where s_a^S is the surface excess of the entropy per atom at the surface, we get [9]:

$$d\gamma = -\Gamma_0 (s_a^S - s_a^v) dT - \Gamma_0 \Omega_a dp \quad (1.64)$$

where s_a^v is the entropy of one atom inside the crystal, Ω_a is the atomic volume.

Hence

$$\left(\frac{\partial \gamma}{\partial p} \right)_T = -\Gamma_0 \Omega_a \quad (1.65)$$

$$\left(\frac{\partial \gamma}{\partial T}\right)_p = -\Gamma_0 (s_a^S - s_a^V) = -\frac{q}{T} \quad (1.66)$$

where q is the specific heat of grain boundary formation and $-q/T$ is the specific surface excess of entropy.

From Eqs. (1.65) and (1.66) it is evident that it is in principle possible to measure the autoadsorption and the surface excess of entropy.

For our evaluation we shall take $\Gamma_0 = 5 \cdot 10^{-14}$ mol/m³, which approximately corresponds to the concept of the grain boundary as an undercooled liquid layer of a width of 3 atomic rows, $\Omega_a(10^{-5}$ m³/mol). Assuming that $\gamma(p)$ is linear, a variation of pressure from 0 to ~ 2.5 GPa gives a change of 0.1 J/m², which is comparable with the absolute value of γ (0.3–0.5 J/m²).

1.2.4.1 Grain Boundary Excess Free Volume — Direct Thermodynamic measurement

Eqs. (1.63)–(1.66) form the theoretical basis of the direct experimental measurements of grain boundary excess free volume (BFV).

BFV along with surface tension belongs to the major thermodynamic properties of grain boundaries. It controls to a large extent the grain boundary diffusivity, grain boundary mobility, vacancy generation during grain growth and the behavior of the system with grain boundaries under mechanical loading. The value of the BFV defines the force which would like to “squeeze” grain boundary out of a polycrystal. This effect is especially pronounced in fine grained and nanocrystalline materials, in this films on substrate [11]–[15]. Unfortunately, until quite recently we were forced to contend with results of computer simulation, which, in its turn, is strictly limited by grain boundaries in the vicinity of special misorientation.

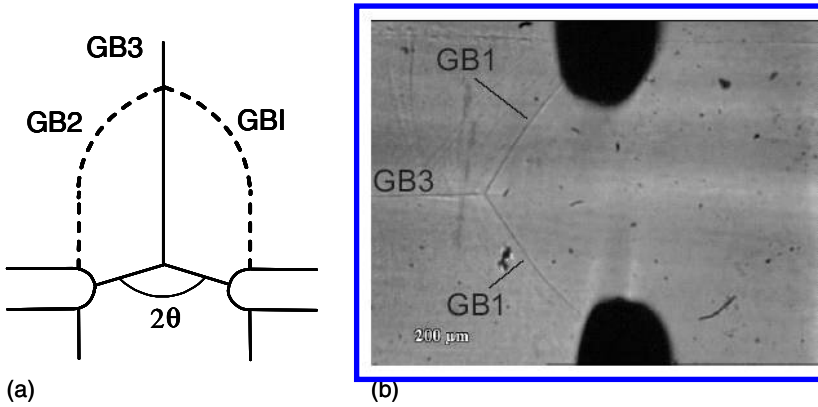
Some experimental attempts were undertaken to determine the BFV [16, 17]. Meiser and Gleiter [16] measured the change of misorientation for grain boundary energy cusps by applying a hydrostatic pressure of $7 \cdot 10^8$ Pa.

Merkle et al. [17] measured the BFV by HRTEM observations of the lattice parameter change in the vicinity of the grain boundary. The value of BFV averaged over all measurements carried out is in the range of $1^{-12} - 10^{-10}$ m³/m².

It should be stressed, however, that all estimates are based on models since they have to rely on assumptions of the grain boundary width, which is unknown.

As shown above, Eqs. (1.63)–(1.66) make it possible, in principle, to measure correctly the grain boundary excess free volume. To “realize” these equations the pressure dependence of the grain boundary surface tension should be known.

The major idea of the method put forward in [18] can be understood from Fig. 1.2. The tricrystal with grain boundaries GB1, GB2, GB3 is annealing under high hydrostatic pressure. The change in grain boundary surface tension has to be reflected in the change in the angles at the tip of the triple

**FIGURE 1.2**

(a) Grain boundary geometry to determine the BFV: the grain boundary system with triple junction attains an equilibrium configuration at the notches introduced from the lateral surfaces of the tricrystal. (b) SEM image of investigated grain boundary system after annealing [18].

junction.

The proposed method was realized in specially grown tricrystals where the triple junction is formed by two high-angle grain boundaries GB1 and GB2 with equal grain boundary surface energy $\gamma_1 = \gamma_2 = \gamma$ (Fig. 1.2). The third grain boundary has to be a low-angle grain boundary whose surface energy γ_3 can be calculated according to the Read and Shockley approach [19]. The system in Fig. 1.2 is homogeneous through the thickness of the tricrystal, i.e. the triple junction line is rectilinear and runs perpendicular to the diagram plane. Since through the thickness all three grain boundaries extend perpendicular to the diagram plane, the configuration of the grain boundary system in Fig. 1.2 is quasi-two-dimensional. So, the motion of the grain boundary system is similar to the motion of a grain boundary system with a triple junction (see Chapter 4), until GB1 and GB2 arrive at the notches (Fig. 1.2). Boundary motion will cease, and force equilibrium at the triple junction will be established. In this equilibrium the contact angle 2θ reflects the balance between the energy of boundaries GB1, GB2 and GB3 at the given temperature and pressure

$$2\gamma \cos \theta = \gamma_3 \quad (1.67)$$

Eqs. (1.65) and (1.67) gives us the relationship between the contact angle and the hydrostatic pressure

$$\frac{\partial \gamma}{\partial p} = \frac{2\gamma \frac{\partial \theta}{\partial p} \sin \theta + \frac{\partial \gamma_3}{\partial p}}{2 \cos \theta} \quad (1.68)$$

In Eq. (1.68) θ , $\frac{\partial\theta}{\partial p}$ and γ are experimentally measured quantities. (The grain boundary surface tension γ can be found from Eq. (1.67), if the surface tension of the low angle boundary is measured or calculated.) In our consideration we neglect the influence of the torque terms. To define the derivative $\left(\frac{\partial\gamma_3}{\partial p}\right)_r$ the following approach was used. According to Read and Shockley [19] a low-angle grain boundary can be represented by a periodic arrangement of lattice dislocations. In particular, a low-angle twist grain boundary is represented by at least two sets of screw dislocations. The elastic energy of a screw dislocation (apart from the dislocation core energy) is not affected by the hydrostatic pressure since a screw dislocation represents a state of pure shear. The energy of the dislocation core does not exceed 10% of the total energy of the dislocation. The effect of the hydrostatic pressure on the lattice constant and, therefore, on the dislocation and low-angle boundary energy is less than 10%. It can, therefore, be assumed that the energy of a low-angle twist grain boundary does not change with an increase of hydrostatic pressure.

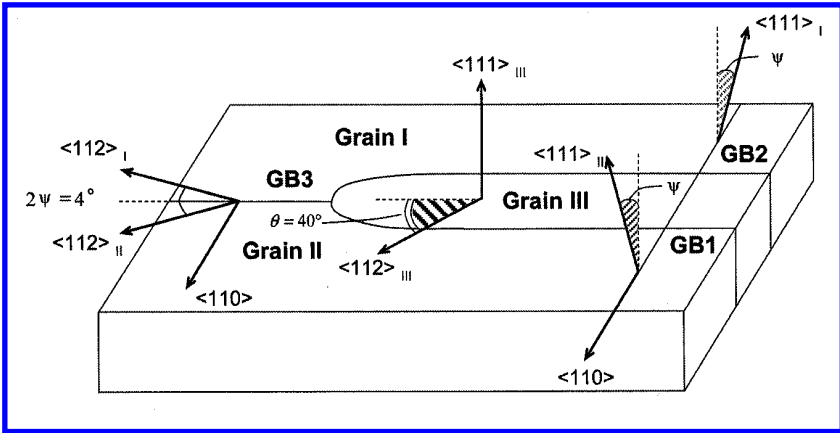
If the grain boundary GB3 in Fig. 1.2 is a low-angle twist boundary and $\left(\frac{\partial\gamma_3}{\partial p}\right)_T \cong 0$, Eq. (1.68) can be rewritten as

$$\left(\frac{\partial\gamma}{\partial p}\right)_T = \gamma \left(\frac{\partial\theta}{\partial p}\right)_T \cdot \tan \theta \quad (1.69)$$

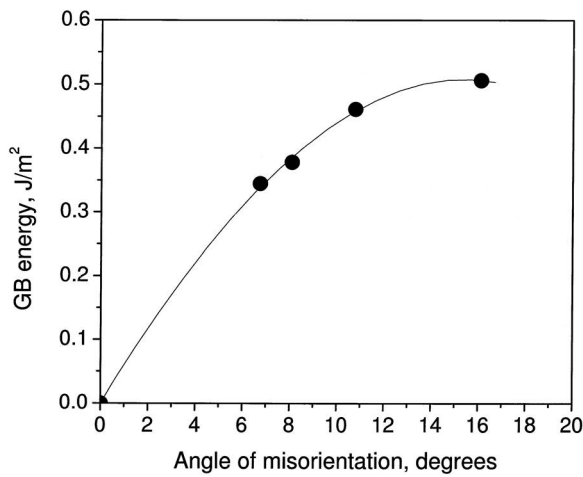
and BFV can be expressed as

$$V_{gb}^{\text{ex}} = \gamma_3 \frac{\sin \theta}{2 \cos^2 \theta} \frac{\partial\theta}{\partial p} \quad (1.70)$$

BFV was measured for two 40° asymmetrical grain boundaries: $\langle 111 \rangle$ and $\langle 110 \rangle$. The experiments were carried out on high purity aluminum (99.999%) [18]. Fig. 1.3 shows the geometrical configuration of the investigated tricrystals for $\langle 111 \rangle$ and $\langle 110 \rangle$ tilt boundaries. The two asymmetrical 40° $\langle 111 \rangle$ of 39° $\langle 110 \rangle$ tilt grain boundaries (GB1 and GB2) were superimposed by a rotation around the axis perpendicular to the grain boundary plane by an angle Ψ of 2°. The third grain boundary (GB3) was, therefore, a low-angle twist boundary with rotation angle of 4° and the rotation axis $\langle 110 \rangle$. The samples were annealed at 630°C for 60 min under a hydrostatic pressure up to 12.7 kbar (grain boundary system $\langle 111 \rangle$) and 10 kbar grain boundary system $\langle 110 \rangle$) [18, 20]. The surface tension of 4° $\langle 110 \rangle$ twist grain boundary was determined by molecular dynamic simulation [20] (Fig. 1.4). This small deviation does not change perceptibly the properties of high-angle grain boundaries; however, for the energy of the low-angle grain boundary is might be essential. The relation γ vs. angle (Fig. 1.4) of misorientation allows us to determine the energy of the low-angle twist boundary for each specific sample. That is why in Figs. 1.5 and 1.6 the measured pressure dependence of the surface tension γ is presented. To check the results obtained the pressure dependence of the equilibrium vertex angle θ was measured for a grain boundary system of two

**FIGURE 1.3**

Geometry of tricrystals used in experiment [18].

**FIGURE 1.4**

Misorientation dependence of low-angle $\langle 110 \rangle$ twist grain boundary computer simulation [20].

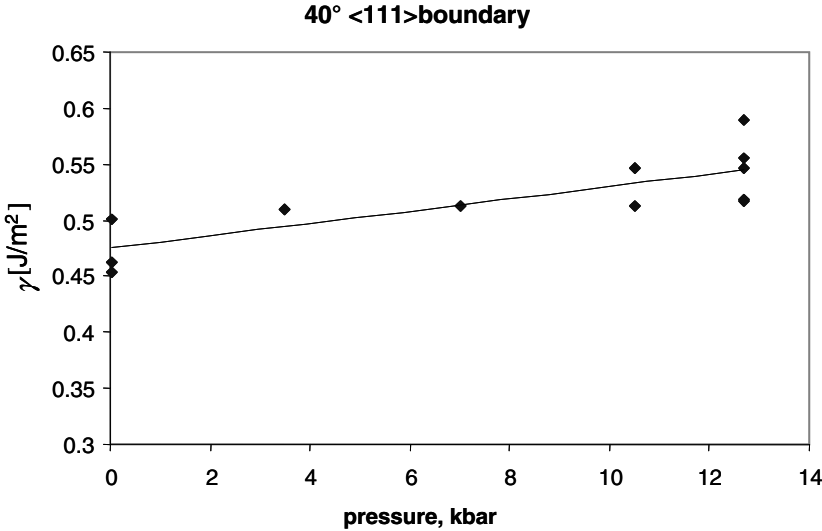


FIGURE 1.5
Pressure dependence of grain boundary surface tension γ for 40°<111> tilt boundary [18, 20].

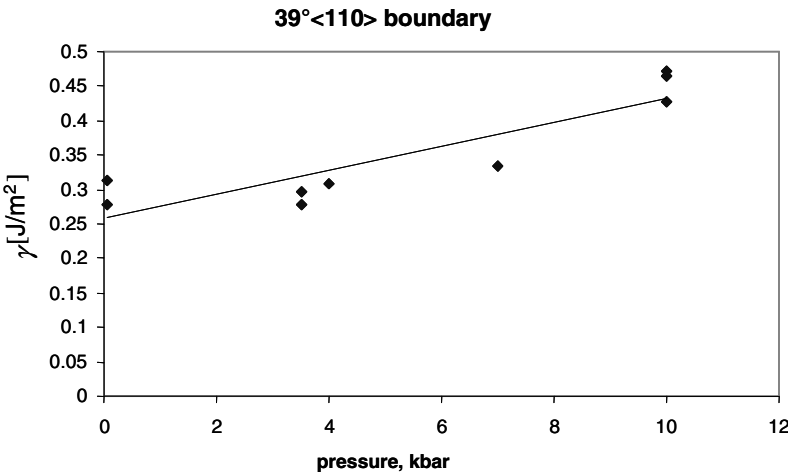
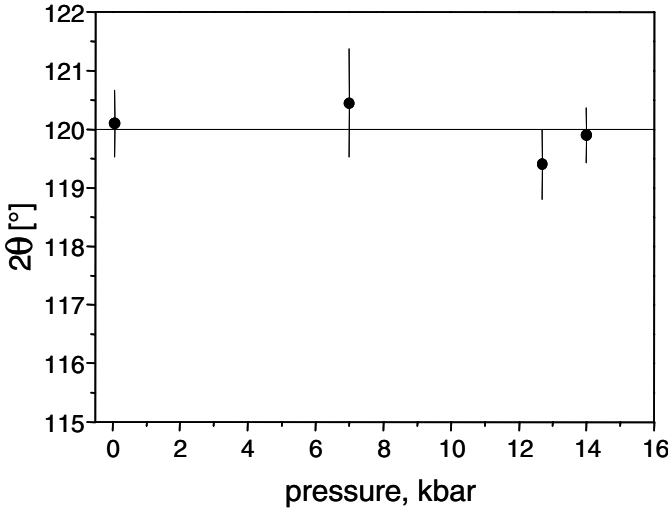


FIGURE 1.6
Pressure dependence of grain boundary surface tension γ for 39°<110> tilt boundary [18, 20].

**FIGURE 1.7**

Pressure dependence of grain boundary surface tension γ of high-angle boundaries: two $40^\circ\langle 111 \rangle$ grain boundaries and $80^\circ\langle 111 \rangle$ tilt boundaries [18].

$40^\circ\langle 111 \rangle$ tilt grain boundaries as GB1 and GB2 and an $80^\circ\langle 111 \rangle$ tilt boundary as GB3. Due to crystal symmetry $80^\circ\langle 111 \rangle$ corresponds to $-40^\circ\langle 111 \rangle$, and the grain boundary energy of GB3 should be the same as the energy of GB1 and GB2. The results of the measurements are shown in Fig. 1.7. The measured angle was about 120° in the whole pressure range and, what is of importance, $\left(\frac{\partial\theta}{\partial p}\right)_r = 0$. Below are given the value of the BFV for $40^\circ\langle 111 \rangle$ tilt grain boundary and $39^\circ\langle 110 \rangle$ tilt grain boundary extracted from the experimental data (Figs. 1.5 and 1.6) in accordance with Eqs. (1.65) and (1.68) [18, 20]

$$\begin{aligned} \langle 110 \rangle : \Gamma_0 &= -\Omega_s^{-1} \left(\frac{\partial\gamma}{\partial p} \right) = -1.35 \cdot 10^{-5} \text{ mol/m}^2 & (1.71) \\ V^{\text{ex}} &= -\Gamma_0 \Omega_a = 1.35 \cdot 10^{-10} \pm 0.6 \cdot 10^{-10} \text{ m}^3/\text{m}^2 \end{aligned}$$

$$\begin{aligned} \langle 111 \rangle : \Gamma_0 &= -\Omega_a^{-1} \left(\frac{\partial\gamma}{\partial p} \right) = 0.55 \cdot 10^{-5} \text{ mol/m}^2 & (1.72) \\ V^{\text{ex}} &= -\Gamma_0 \Omega_a = 0.55 \cdot 10^{-10} \pm 0.13 \cdot 10^{-10} \text{ m}^3/\text{m}^2 \end{aligned}$$

$$\frac{V_{\langle 110 \rangle}^{\text{ex}}}{V_{\langle 111 \rangle}^{\text{ex}}} = 2.5 \quad (1.73)$$

The corresponding expression for grain boundary surface tension is given by the relationship

$$\gamma = \gamma_0 + \left(\frac{\partial \gamma}{\partial p} \right)_T p \quad (1.74)$$

It should be noted that the excess grain boundary volume $V_{gb}^{ex} = -\Gamma_0 \Omega_0$ measured in the approach discussed defines the absolute value of BFV, for instance on the grain boundary width.

One can see from Eqs. (1.72) and (1.74) that the value of BFV differs for grain boundaries with different misorientation. The difference is essential, in spite of not so high experimental accuracy. We believe that such a difference can play an important role in grain microstructure evolution in the course of grain growth, in particular in thin films on the substrate [11, 12].

In modern theories of grain boundary structure autoadsorption is closely related to the concept of a free volume. Autoadsorption determines how much the substance density in the boundary differs from the substance density in the crystal bulk.

Contrary to the interphases, in the case of a multicomponent system at the grain boundaries, there is also, in principle, the possibility of determining adsorption values for all components from the Gibbs equation. Let us consider this by means of the example of a binary system. As originally shown by Speiser and Spetnak [10] the Gibbs equation (1.53) can be recast due to the relation of Gibbs and Duhem (1.56) in the form:

$$d\gamma = - \left(\Gamma_2 - \frac{c}{1-c} \Gamma_1 \right) d\mu_2, \quad p, T = \text{const.} \quad (1.75)$$

where c is the concentration of the second component. On this basis Stout [21], Cahn and Hillard [22] and McLean [23] assumed that Γ_1 and Γ_2 cannot be obtained by measurement separately, but only in the combination $(\Gamma_2 - c\Gamma_1 / (1-c))$. This is true if the pressure in the system remains constant. The relation (1.75) has been derived on the basis of the Gibbs equation (1.53) and the Gibbs-Duhem relation (1.56): $(1-c)d\mu_1 + cd\mu_2 = 0$ for constant pressure and temperature. But if the pressure (or, aside from pressure, any generalized thermodynamic force such as electric field or magnetic field strength and so on) can be varied, then [9]:

$$(1-c)d\mu_1 + cd\mu_2 = \Omega_a dp \quad (1.76)$$

and from Eqs. (1.53) and (1.76) we get:

$$d\gamma = - \left(\Gamma_2 - \frac{c}{1-c} \Gamma_1 \right) d\mu_2 - \frac{\Gamma_1}{1-c} \cdot \Omega_a dp, \quad T = \text{const.} \quad (1.77)$$

Hence

$$\left(\frac{\partial \gamma}{\partial \mu_2} \right)_{p,T} = - \left(\Gamma_2 - \frac{c}{1-c} \Gamma_1 \right) \quad (1.78)$$

$$\left(\frac{\partial\gamma}{\partial p}\right)_{\mu_2,T} = -\frac{\Omega_a\Gamma_1}{(1-c)} \quad (1.79)$$

Now we can move on to the more convenient variables T, p, c :

$$\left(\frac{\partial\gamma}{\partial c}\right)_{p,T} = -\left(\Gamma_2 - \frac{c}{1-c}\Gamma_1\right)\left(\frac{\partial\mu_2}{\partial c}\right)_{p,T} \quad (1.80)$$

$$\left(\frac{\partial\gamma}{\partial p}\right)_{c,T} = -\frac{\Gamma_1\Omega_a}{(1-c)} - \left(\Gamma_2 - \frac{c}{1-c}\Gamma_1\right)\left(\frac{\partial\mu_2}{\partial p}\right)_{c,T} \quad (1.81)$$

The relations (1.78)–(1.81) show that the separate determination of the adsorption of the different components at the grain boundary basically is possible. But for that purpose it is still necessary to know the dependence of the surface tension on composition and pressure in the system. Measurement of grain boundary surface tension is a very complicated problem, and no appropriate high-pressure experiments ever have been carried out. At the same time, important information can be obtained from the dependence of the surface tension on concentration.

Adsorption values depend, firstly, on how much the composition of the boundary differs from that of the bulk, and, secondly, on how much the atomic packing density in the boundary differs from the bulk one. The enrichment of the boundary with an impurity is in many cases a much more important and interesting effect than the change in density. It turns out that the total adsorption Γ_i can be subdivided into two components: the concentration component, Γ'_i , and the density component, Γ_0 , related only to the difference in densities [24].

Let us direct our attention to a model, where we consider the grain boundary as a homogeneous layer of the width λ and of the density ρ^s ; then the adsorption of the i -th component will be

$$\Gamma_i = \lambda(c_i^S p^S - c_i \rho) \quad (1.82)$$

where c_i^S , c_i are the concentrations (the atomic fractions) of the i -th component in the grain boundary and in the bulk of the grain, respectively, and ρ is the density in the bulk of the grain.

The result to emerge from such a model is:

$$\sum_i^k \Gamma_i = \lambda \rho^S \sum_i^k c_i^S - \lambda \rho \sum_1^k c_i = \lambda(\rho^S - \rho) \equiv \Gamma_0 \quad (1.83)$$

Inasmuch as the bulk and the boundary densities are different, $\sum_i^k \Gamma_i \neq 0$. Γ_0 is an important characteristic of grain boundaries; for pure materials it coincides with the autoadsorption [9]:

$$\Gamma_0 = -\Omega_a \left(\frac{\partial\gamma}{\partial p}\right)_T$$

Eq. (1.82) can be represented in the form:

$$\Gamma_i = \lambda \rho^S (c_i^S - c_i) + \lambda c_i (\rho^S - \rho) \quad (1.84)$$

or

$$\Gamma_i = \Gamma'_i + c_i \Gamma_0 \quad (1.85)$$

Consequently, the adsorption of the i -th component can be represented as a sum of two components: the concentration Γ'_i and the density component $c_i \Gamma_0$. Γ'_i is the number of atoms of i -th kind, which should be added to the equilibrium system at an isothermal increase of the surface area of the system by one unit, so that the total number of the particles and the bulk concentrations in the phases remain constant (the volume of the system should be changed):

$$\Gamma'_i = \left(\frac{\partial N_i}{\partial \tilde{A}} \right)_{T, c_i} \quad (1.86)$$

From Eqs. (1.83) and (1.85) it follows that

$$\sum_i^k \Gamma'_i = 0 \quad (1.87)$$

The second property of the concentration components of grain boundary adsorption is that at constant pressure and temperature in the system they satisfy the same Gibbs equation as the total adsorption. These two advantages of the concentration components of grain boundary adsorption enable us to determine them from the concentration dependence of the surface tension alone.

As an example, for the binary system from Eq. (1.63), the Gibbs-Duhem equation (1.56) and the relation (1.87) we get:

$$d\gamma = -\Gamma'_1 d\mu_1 - \Gamma'_2 d\mu_2 = -\frac{\Gamma'_2 d\mu_2}{1 - c} \quad (1.88)$$

This is the maximum we can get in the framework of Gibbs theory, namely, to determine the concentration components of grain boundary adsorption, using the concentration dependence of the grain boundary surface tension, which gives us the surface excesses of the atoms of the components. To determine the grain boundary solution characteristics this is essential but not sufficient. The peculiarities of the behavior of the atoms of each component and their activity should be found. In other words, the chemical potentials of the atoms of the grain boundary solution remain to be determined.

1.2.5 Grain Boundary Solutions

The equations of the thermodynamics of surfaces and the thermodynamics of the “bulk” system are similar in a definite sense: the relations between

the surface excesses of different thermodynamics parameters have the same appearance as the relations for the bulk ones. In this case the role of the bulk is “played” by the area of the surface and the role of pressure by the surface tension (with opposite sign), respectively.

So, if the energy of the bulk phase is

$$E^v = TS^v - pV + \sum_i^k \mu_i N_i^v \quad (1.89)$$

then the surface excess of the energy is

$$E^s = TS^S + \gamma \tilde{A} + \sum_i^k \mu_i^S N_i^S \quad (1.90)$$

This allows us to consider the surface formally as a two-dimensional phase with its own dependence of the chemical potentials μ^S on the intensive parameters: temperature, surface tension, concentration. The values of the chemical potentials of the surface atoms in equilibrium are identical to those in the bulk (otherwise the atoms would leave their positions at the surface for those ones in the bulk or vice versa):

$$\mu_i^s(T, \gamma, c_i^s) = \mu_i(T, p, c_i) \quad (1.91)$$

“Introducing” the new surface phase is not inconsistent with the Gibbs rule of phases, inasmuch as, together with a new phase, a new intensive parameter — the surface tension — will be brought into play. The introduction of this parameter compensates the reduction of the number of degrees of freedom, associated with the appearance of the new phase.

Eq. (1.91) permits us to derive some general relations for the surface phase, if, instead of the bulk ones, the differentials of the surface chemical potentials in terms of the temperature, content and the surface tension are used in the adsorption equation (1.52):

$$-\sum_i^k \Gamma_i \frac{\partial \mu_i^s}{\partial \gamma} = 1; \quad \sum_i^k \Gamma_i \frac{\partial \mu_i^s}{\partial T} = -s^s; \quad \sum_i^k \Gamma_i \frac{\partial \mu_i^s}{\partial c_i^s} = 0 \quad (1.92)$$

The physical meaning of the values $[-\partial \mu_i^s / (\partial \gamma) |_{c_i}]$ can be determined in analogy with “bulk” thermodynamics: $-\gamma$ is the analogue of the pressure p . So, $[-\partial \mu_i^s / (\partial \gamma) |_{c_i}]$ are the partial molar areas $(\bar{\tilde{A}}_i)$, occupied by the i -th component in the surface. They obey the relation

$$\sum_i^k \Gamma_i \bar{\tilde{A}}_i = 1 \quad (1.93)$$

The last in the row of relations (1.92) is the surface analogue of the Gibbs-Duhem equation

$$\sum_i^k \Gamma_i \frac{\partial \mu_i^s}{\partial c_i^s} = 0$$

The thermodynamic theory, which considers the interphase as a phase, was put forward for binary systems by Zhuchovitskii in 1944 [25].

The transition layer between the phases is considered to be homogeneous. For the interphase “condensed phase-gas” the irregularity is concentrated in a monolayer.

For grain boundaries the situation is more complicated, although there is, in principle, no distinction between them and the interface “condensed phase-gas.” The data of microscopic observations indicate that the crystallographic width of the grain boundary is not more than 2–3 lattice constants. The equilibrium between surface and bulk phases leads for the binary solution to the system of equations:

$$\mu_1^s(\gamma, T, c_1^s) = \mu_1(p, T, c_1) \quad (1.94)$$

$$\mu_2^s(\gamma, T, c_2^s) = \mu_2(p, T, c_2) \quad (1.95)$$

where μ_1^s, μ_2^s are the values of surface chemical potentials, and μ_1, μ_2 are the bulk ones for the first and the second component, respectively. The system of Eqs. (1.94) and (1.95) permits us to find the dependence of the surface tension and the surface composition on temperature, pressure and bulk composition, if the functional dependencies of the chemical potentials are known, or, in other words, the types of solution are known. Let us transform Eqs. (1.94) and (1.95) to a more convenient form by introducing the activities both in the bulk (a_1, a_2) and in the boundary phases (a_1^s, a_2^s):

$$\mu_1 = \mu_{1st}(T, p) + kT \ln a_1(T, p, c_1) \quad (1.96)$$

$$\mu_1^s = \mu_{1st}^s(T, \gamma) + kT \ln a_1^s(T, \gamma, c_1^s) \quad (1.97)$$

and, by analogy, for the second component. At constant temperature and pressure we get:

$$\mu_1 = \mu_{1st} + kT \ln a_1(c_1) \quad (1.98)$$

$$\mu_1^s = \mu_{1st}^s + kT \ln a_1^s(\gamma, c_1^s) \quad (1.99)$$

The standard states both in the bulk and in the boundary (denoted by st in Eqs. (1.96)–(1.99)) are chosen in such a manner that the activities of the pure components have to be equal to unity.

Substituting Eqs. (1.98) and (1.99) into (1.93) we obtain for $c_1 \rightarrow 1$

$$\mu_{1st} = \mu_{1st}^s(\gamma_1) \quad (1.100)$$

where γ_1 is the grain boundary surface tension in the pure first component.

Then, from Eq. (1.93) we arrive at:

$$\mu_{1st}^s(\gamma_1) - \mu_{1st}^s(\gamma) = kT \ln \frac{a_1^s}{a_1} \quad (1.101)$$

Considering that $(\gamma - \gamma_1)$ is a small value in the whole concentration interval, let us expand $\mu_{1st}^s(\gamma)$ in series and neglect high-order terms:

$$\mu_{1st}^s(\gamma) \cong \mu_{1st}^s(\gamma_1) + \left(\frac{\partial \mu_{1st}^s}{\partial \gamma} \right)_{p,T,\gamma_1} \cdot (\gamma - \gamma_1) \quad (1.102)$$

Let us denote $(\partial \mu_{1st}^s / \partial \gamma)_{p,T,\gamma_1} = -\bar{A}_1$. By definition, this value does not depend on concentration.

Then

$$\gamma = \gamma_1 + \frac{kT}{\bar{A}_1} \ln \frac{a_1^s}{a_1} \quad (1.103)$$

and

$$\gamma = \gamma_2 + \frac{kT}{\bar{A}_2} \ln \frac{a_2^s}{a_2} \quad (1.104)$$

where γ_2 is the grain boundary surface tension in the second pure component, and $\bar{A} = -(\partial \mu_2^s / \partial \gamma)_{p,T,\gamma_2}$ is the partial area of the second component in the boundary. Eliminating the variable γ from Eqs. (1.103) and (1.104) we arrive at

$$\frac{a_1^s}{a_1} = \left(\frac{a_2^s}{a_2} \right)^{\bar{A}_1 / \bar{A}_2} \cdot e^{\frac{\bar{A}_1(\gamma_2 - \gamma_1)}{kT}} \quad (1.105)$$

Eqs. (1.103)–(1.105) were obtained by Zhuchovitskii [25]. The Zhuchovitskii derivation was based on the same idea of equilibrium between surface and bulk phases. Then, taking into account that the surface solution is elastically stretched and the force per unit length is the value of the surface tension γ , we get

$$\mu_i = \mu_i^s - \gamma \bar{A}_i \quad (1.106)$$

where A_i is the partial area of the i -th component in the surface (boundary).

For the binary solution

$$\mu_1 = \mu_1^s - \gamma \bar{A}_1 \quad (1.107a)$$

$$\mu_2 = \mu_2^s - \gamma \bar{A}_2 \quad (1.107b)$$

Then, from Eqs. (1.94) and (1.95) we obtain Eq.(1.105). Eqs. (1.103)–(1.105) enable us to determine the activity of the atoms of a specific kind in the surface (boundary) solution as a function of the bulk concentration, if the concentration dependence $\gamma(c)$ and the thermodynamic characteristics of the bulk solution are known. The knowledge of the behavior of the atoms in the

surface solution can indicate their activity, which, naturally, should be related to their surface concentration, i.e. to the fraction of the atoms of a particular kind in the surface. However, the values of the chemical potentials are assigned to surface atoms, which are the surface excesses but not the real atoms of the surface (boundary) solution. The surface activities and the surface concentrations are activities and concentrations not of the atoms making up the interface, but of the excess atoms in the Gibbs method. Compatibility between the thermodynamic approach, given above, and the model theories is possible only when the number of “excess thermodynamic” atoms coincides with the number of the real or model atoms.

For interphases this can be achieved if the dividing surface is placed at a certain position. So, for the system gas-condensed phase the imaginary dividing surface will be placed between the monolayer and the bulk of the condensed phase. Then, due to the fact that the gas density is negligible compared to the density of the condensed phase, the adsorption quantities are simply the numbers of atoms of a certain kind per unit area of the surface layer, and the surface concentration is (Fig. 1.8)

$$c_i^s = \Gamma_i / \sum_i \Gamma_i \quad (1.108)$$

Therefore, if the surface activity is known as a function of the surface concentration, we get a comprehensive description of the thermodynamic properties of the surface.

There is an essentially different situation for grain boundaries. As mentioned, the surface excesses are independent of the position of the dividing surface, and the values of the grain boundary adsorptions will always differ significantly from the number of atoms in the grain boundary. Consequently, the Gibbs method, where the surface excess of volume is zero, is not applicable. The alternative approach is known as the method of the surface layer of finite thickness. We still consider the phases as homogeneous, but now they do not come into contact along the two-dimensional dividing surface to which, in the Gibbs method, surface excess quantities belong, but instead are divided by a surface layer of a finite thickness. As a result the net volume of the phase V^s (the volume of the transition layer) is less than the total volume of the system. Accordingly the expressions for the other surface excesses will be changed as well; for example, the number of the particles is

$$N^s = \tilde{N} - n^v (V^\alpha + V^\beta) = \tilde{N} - n^v V + n^v V^s \quad (1.109)$$

where \tilde{N} is the number of all particles in the system.

Inasmuch as the surface excess of the volume differs from zero, the right-hand side of the Gibbs equation will contain an additional term that includes the pressure differential

$$d\gamma = -s^s dT - \sum_i^k \Gamma_i d\mu_i + V^s dp \quad (1.110)$$

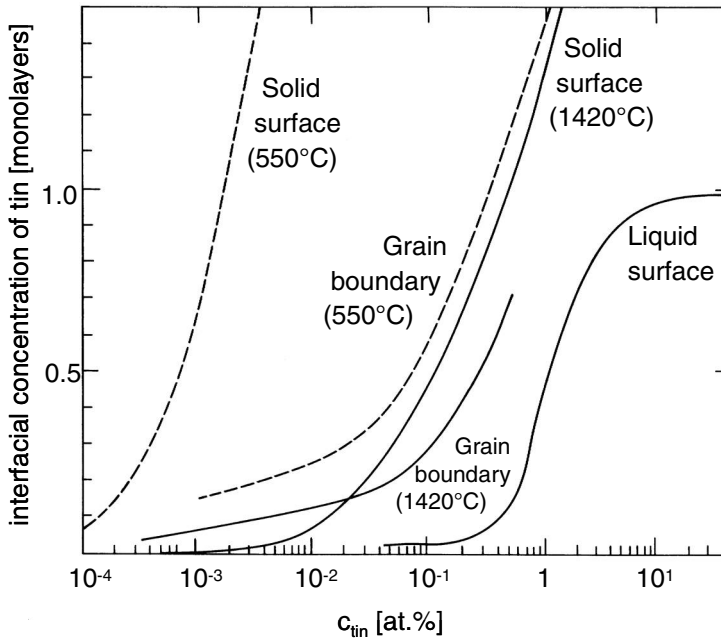


FIGURE 1.8

Adsorption isotherms for tin at iron interfaces: the low temperature isotherms (dashed) are measured directly by AES; the others are derived from the interfacial energy data [31].

where V^s is the specific surface excess of the volume.

Now the number of differentials on the right-hand side of the Gibbs equation exceeds by one the system variance, and the choice of the conditional parameter provides the freedom which, in the case of interphases, was ensured by the dependence of surface excess quantities on the position of the dividing surface. It is precisely the choice of V^s which permits us to obtain agreement between the excess surface parameters and the model ones.

This parameter should be chosen in such a way that the number of atoms in the grain boundary equals the respective surface excesses. Consider the simplest model of a grain boundary — a layer of thickness λ and density ρ^s . If $V^s = \lambda$ (per unit area) the correspondence between the thermodynamic quantities and those of the model is achieved.

We would like to emphasize that in the method of a surface layer of finite thickness all above-mentioned advantages of the Gibbs method are conserved. Each method has its own field of application, which best suits it. It is appropriate to use the Gibbs method for the description of surfaces that divide

two different phases. The method of a layer of finite thickness is suitable to analyze boundaries with the same phase on each side: i.e. grain boundaries, domain walls, thin films.

The introduction of a new parameter V^s requires an explicit dependence of the surface chemical potentials on the pressure in the system

$$\mu_i^s = \mu_i^s(T, c_i^s, p) \quad (1.111)$$

Accordingly, the grain boundary thermodynamic identities will be changed:

$$\begin{aligned} -\Sigma \Gamma_i (\partial \mu_i^s / \partial \gamma) &\equiv \Sigma \Gamma_i \bar{A}_i = 1 \\ \Sigma \Gamma_i (\partial \mu_i^s / \partial p) &= V^s \\ \Sigma \Gamma_i (\partial \mu_i^s / \partial c_i^s) &= 0 \end{aligned} \quad (1.112)$$

The derivation and the final form of the Zhuchovitskii equations are the same as for interphases, but the parameter \bar{A}_i now depends on V^s . This quantity should be chosen in such a way that the number of atoms in the grain boundary coincides with the corresponding surface excess values.

The adsorption values in our model are expressed by Eq. (1.82), and the numbers of parameters can be reduced by relating to the concentration components of the adsorption. The important property of these concentration components is their independence of the value V^s . Actually

$$\Gamma_i = \Gamma_i^G + V^s \rho^v c_i \quad (1.113)$$

where the parameter, determined by the Gibbs method, is marked off by using the index “G”

$$\begin{aligned} \Gamma'_i &= \Gamma_i - c_i \Sigma \Gamma_i = \Gamma_i - c_i \Sigma \Gamma_i^G - c_i \Sigma V^s \rho^v c_i = \\ &= \Gamma_i - c_i \Sigma \Gamma_i^G - c_i V^s \rho^v = \Gamma_i^G - c_i \Sigma \Gamma_i^G = \Gamma_i'^G \end{aligned} \quad (1.114)$$

which proves the independence of the adsorption components on V^s .

The concentration components can be expressed in terms of a parameter z :

$$\Gamma'_i = z (c_i^s - c_i) \quad (1.115)$$

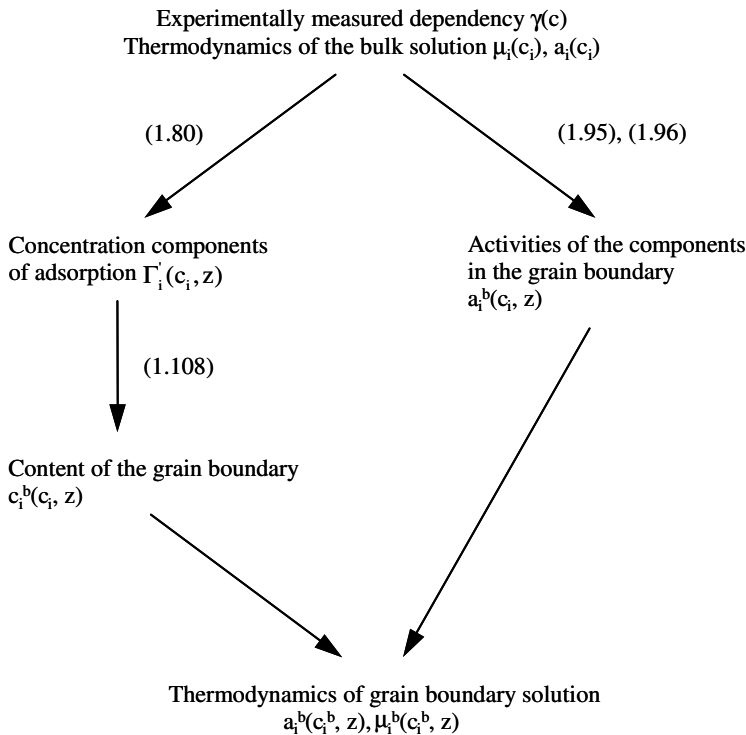
where $z = \lambda \rho^s$.

The content of the grain boundary can be determined as

$$c_i^s = c_i \frac{\Gamma'_i}{z} \quad (1.116)$$

The Zhuchovitskii equations contain the same parameter z

$$\bar{A}_i = \left(\frac{1}{\Gamma_i} \right)_{c_i=1} = \left(\frac{1}{z} \right)_{c_i=1}$$



So the scheme of determination of the thermodynamic characteristics of the grain boundary solution takes the form shown in the diagram above. In such a way the thermodynamic characteristics of the grain boundary solution can be defined using the experimentally measured dependency of the grain boundary surface tension on the content ($\gamma(c_i)$) and the thermodynamic properties of the bulk solution. The parameter z — the adsorption capacity of the grain boundary — cannot be defined by thermodynamic measurements.

Up to now we have presented the scheme of a purely thermodynamic analysis: the main thermodynamic properties of the system were reconstructed from the boundary surface tension data. Another method is widely used: the change in the grain boundary properties depending on the impurity concentration is considered on the basis of a model of adsorption isotherms, i.e. of the functional dependence of the quantity in connection with an impurity in the boundary on the concentration of this impurity in the bulk.

Let us return to Eq. (1.105). It constitutes the general adsorption isotherm, expressed in terms of the activity of the components. In order to connect the variables of the isotherm with the concentrations of the components at the surface and in the bulk let us now take into account the relation between the

activity and the chemical potentials of real and ideal solutions:

$$a_i = c_i \exp \left(\frac{\mu_i - \mu_{i \text{ ideal}}}{kT} \right) = c_i \exp \left(\frac{\bar{H}_i - H_i^0}{kT} \right) \cdot \exp \left(-\frac{\bar{S}_i - S_{i \text{ ideal}}}{k} \right) \quad (1.117)$$

where c_i is the molar fraction of the i -th component; \bar{H}_i , S_i are the partial characteristics (enthalpy and entropy, respectively) of the real solution; H_i is the enthalpy of the i -th pure component; $S_{i \text{ ideal}}$ is the partial entropy of the ideal solution.

We obtain the general adsorption isotherm, expressed in terms of the concentrations of components at the surface and in the bulk and the thermodynamic functions of real and ideal solutions in a binary system [26]:

$$\begin{aligned} & \frac{c_1^s \exp \left(\frac{\bar{H}_1^s - H_1^0}{kT} \right) \exp \left(-\frac{\bar{S}_1^s - S_{1 \text{ ideal}}}{k} \right)}{c_1 \exp \left(\frac{\bar{H}_1 - H_1^0}{kT} \right) \exp \left(-\frac{\bar{S}_1 - S_{1 \text{ ideal}}}{k} \right)} = \\ & = \left[\frac{c_2^s \exp \left(\frac{\bar{H}_2^s - H_2^0}{kT} \right) \exp \left(-\frac{\bar{S}_2^s - S_{2 \text{ ideal}}}{k} \right)}{c_2 \exp \left(\frac{\bar{H}_2 - H_2^0}{kT} \right) \exp \left(-\frac{\bar{S}_2 - S_{2 \text{ ideal}}}{k} \right)} \right]^{\bar{A}_1 / \bar{A}_2} \cdot \\ & \quad \cdot \exp \left[\frac{\bar{A}_1 (\gamma_2 - \gamma_1)}{kT} \right] \end{aligned} \quad (1.118)$$

The further development of isotherm Eq. (1.118) can be done in terms of a more specific, detailed consideration of the thermodynamic functions and some additional, statistical assumptions, adopted for the sake of simplicity. We would like to stress that all adsorption isotherms can be derived from Eq. (1.118), if the corresponding thermodynamic functions are described in suitable variables.

Then, in the simplest case, the bulk and grain boundary (surface) solutions are ideal, and the partial areas of the components are equal

$$\bar{A}_i = \bar{A}_2 = \bar{A} \quad (1.119)$$

Eq. (1.118) transforms to

$$c_1^s = \frac{B c_1}{1 - c_1 + B c_1} \quad (1.120)$$

where $B = \exp \left(\bar{A} (\gamma_2 - \gamma) / (kT) \right) = b_0 \exp (U_0 / kT)$, and U_0 is the energy of interaction between the boundary (surface) and the adsorbed atom. The relationship (Eq. (1.120)) is known as the Zhuchovitskii-McLean isotherm [25].

More complicated is the adsorption for atoms which interact both in the surface and in the bulk solution. Let us consider this interaction in the Bragg-Williams approximation — the approximation of a regular solution. For a

regular solution the third factor on the right-hand side of Eq. (1.117) is equal to one, and all deviations from an ideal solution are determined by the second factor. The enthalpy H of the regular solution can be expressed as

$$H = n_1 H_1^0 + n_2 H_2^0 + Z \Delta \frac{n_1 n_2}{n_1 + n_2} \quad (1.121)$$

where n_i is the number of atoms of the i -th component, Z is the coordination number, $\Delta = \varepsilon_{12} - (\varepsilon_{11} + \varepsilon_{22})^2$ is the heat of mixing with ε_{i-i} , ε_{i-j} and ε_{j-j} the enthalpies associated with the different type of bonds.

The partial enthalpy of the regular solution is

$$\overline{H}_1 = \frac{\partial H}{\partial n_1} = H_1^0 + Z \Delta \frac{n_2^2}{(n_1 + n_2)^2} \quad (1.122)$$

or

$$\overline{H}_1 - H_1^0 = Z \Delta c_2^2 \quad (1.123)$$

Hence, the activity of the components in a regular solution can be represented by

$$a_1 = c_1 \exp \left(\frac{Z \Delta c_2^2}{kT} \right) \quad (1.124)$$

and, respectively,

$$a_2 = c_2 \exp \left(\frac{Z \Delta c_1^2}{kT} \right) \quad (1.125)$$

Then from Eqs. (1.118), (1.124) and (1.125) we arrive at the relation between the surface (boundary) concentration of the component and that of the bulk, if both the bulk and the surface solutions are regular solutions:

$$\frac{c_1^s}{c_1} = \frac{\exp \left(\frac{Z \Delta c_2^2}{kT} \right)}{\exp \left(\frac{Z^s \Delta^s c_2^{s2}}{kT} \right)} e^{\frac{\overline{A}_1 (\gamma_2 - \gamma_1)}{kT}} \left[\frac{c_2^s \exp \left(\frac{Z^s \Delta^s c_1^{s2}}{kT} \right)}{c_2 \exp \left(\frac{Z \Delta c_1^2}{kT} \right)} \right]^{\overline{A}_1 / \overline{A}_2} \quad (1.126)$$

where Δ^s , Z^s are the heat of mixing and the coordination number, respectively, at the grain boundary.

Let us apply this result to some special situations.

1. No difference between the bulk and boundary solution with regard to the heat of mixing and the coordination number; the partial areas of the different species are equal as well:

$$\begin{aligned} \Delta^s &= \Delta \\ Z^s &= Z \\ \overline{A}_1 &= \overline{A}_2 = \overline{A} \end{aligned} \quad (1.127)$$

Then

$$c_1^s = \frac{B c_1 \exp \left[\frac{2Z\Delta}{kT} (c_1^s + c_1 - 1) \right]}{1 - c_1 + B c_1 \exp \left[\frac{2Z\Delta}{kT} (c_1^s + c_1 - 1) \right]} \quad (1.128)$$

Obviously, the relationship (1.128) is valid over the whole concentration range.

2. Ideal bulk solution but regular boundary solution

$$\begin{aligned}\Delta &= 0 \\ \Delta^s &\neq 0 \\ \bar{A}_1 &= \bar{A}_2\end{aligned}\tag{1.129}$$

Then

$$c_1^s = \frac{Bc_1 \exp \left[\frac{Z^s \Delta^s}{kT} (2c_1^s - 1) \right]}{1 - c_1 + Bc_1 \exp \left[\frac{Z^s \Delta^s}{kT} (2c_1^s - 1) \right]}\tag{1.130}$$

In the form

$$c_1^s = \frac{Bc_1 \exp \left[\frac{Z^s \Delta^s}{kT} (2c_1^s - 1) \right]}{1 + Bc_1 \exp \left[\frac{Z^s \Delta^s}{kT} (2c_1^s - 1) \right]}\tag{1.131}$$

it is known as the Fowler-Guggenheim isotherm.

3. Ideal bulk solution and regular surface (boundary) solution; the areas of the species at the boundary are different:

$$\begin{aligned}\Delta &= 0 \\ \Delta^s &\neq 0 \\ \bar{A}_1 &\neq \bar{A}_2\end{aligned}\tag{1.132}$$

In this case

$$c_1^s = c_1 \exp \left(-\frac{Z^s \Delta^s c_2^{s2}}{kT} \right) \exp \left[\frac{\bar{A}_1 (\gamma_2 - \gamma_1)}{kT} \right] \cdot \left[\frac{c_2^s}{c_2} \exp \left(\frac{Z^s \Delta^s c_1^{s2}}{kT} \right) \right]^{\bar{A}_1 / \bar{A}_2}\tag{1.133}$$

1.2.6 Statistical Analysis of the Adsorption on Internal Interfaces in Solids

As mentioned above, the thermodynamic description of grain boundaries is based on the experiment, on the analysis of the experimentally obtained dependencies of the surface tension on pressure and concentration of the components. By contrast, for the statistical analysis of the problem model concepts must be invoked. A detailed statistical analysis of the adsorption at internal interfaces in solids, including grain boundaries, is given in [27].

Let us consider the equilibrium in the system: bulk solution - interface solution (more specifically, the interface is the grain boundary). We shall restrict our consideration to binary systems. To describe equilibrium in the bulk solution - grain boundary solution system, the isobaric-isothermal potential G was calculated via the Gibbs canonical distribution:

$$G = -kT \ln \tilde{Z}\tag{1.134}$$

Since for the system under consideration the partition function $\tilde{Z} = \tilde{Z}$ (of the bulk solution) $\cdot \tilde{Z}$ (of the grain boundary solution), then

$$\tilde{Z} = w \tilde{Z}_1^{N_1} \cdot \tilde{Z}_2^{N_2} \cdot w_x \cdot (\tilde{Z}'_x)^{N'_x} \cdot (\tilde{Z}''_x)^{N''_x} \left(-\frac{N'_x U_1}{kT} \right) \exp \left(-\frac{N''_x U_2}{kT} \right) \quad (1.135)$$

Here \tilde{Z}_1 and \tilde{Z}_2 are the partition functions for one atom of the first and second components of the bulk solution; \tilde{Z}'_x and \tilde{Z}''_x are the same quantities for the grain boundary solution; N_1 and N_2 and N'_x and N''_x are the numbers of atoms of the first and second kind in the bulk and the grain boundary solution; w and w_x are the corresponding configurational (permutation) probabilities; U_1 and U_2 are the heats of transfer of atoms of the first and second kind from the bulk solution into the grain boundary solution. The equilibrium distribution of the impurities between the bulk and the grain boundary corresponds to a minimum of the thermodynamic potential G of the system, that is to say either the corresponding partial derivatives is equal to zero, in other words the chemical potentials of the impurity atoms in both solutions are the same. This minimum is usually found from the constancy condition either for the number of solvent atoms or for the number of sites.

One can see that the statistical approach allows considerable freedom. Firstly, it is associated with the choice of the constants for the determination of a chemical potential. Let us discuss this problem in greater detail. Assume that g_1 and g_2 are the number of sites for the atoms of the first and second kind in the bulk solution. If the atoms form a disordered substitutional solid solution the values of g_1 and g_2 are indistinguishable; the total number of sites in such a solution is $g = g_1 + g_2$ and it is just this quantity that appears in the statistical calculations for both atoms of the first and the second kind. However, if the atoms form an interstitial solid solution (or an ordered substitutional solid solution) the values g_1 and g_2 appear separately.

Let g'_x and g''_x be the number of sites for the atoms of the first and second kind in the boundary solution. For the disordered substitutional solid solution the sum $g'_x + g''_x = g_x = \text{const.}$ appears as before in the calculations.

Let us postulate that the number of sites in the boundary solution is constant, in other words

$$g'_x + g''_x = g_x = \text{const.} \quad (1.136)$$

Notice that for the bulk solution this condition need not be satisfied. As an example, if the components form a substitutional solution in the grain (in the bulk), whereas at the grain boundary there is an interstitial one, a non-compensated transfer of impurity atoms from the bulk to the grain boundary is possible. Vacant lattice points should appear in this instance. Let us consider, however, an equilibrium concentration of vacancies in the bulk ($N_v = N_v^e$). Then the vacant lattice points will disappear and $g \neq \text{const.}$ (We assume, also, that the value of N_v^e does not depend on the content of the impurities in the solution.)

Finally, we assume that the following conditions are always met:

$$\begin{aligned} N_1 + N'_x &= \text{const.} \\ N_2 + N''_x &= \text{const.} \end{aligned} \quad (1.137)$$

With regard to the conditions mentioned above, the thermodynamic situation is defined by the type of bulk and boundary solution: substitutional or interstitial.

If the bulk and boundary solutions are disordered substitutional solid solutions, the following conditions will be true:

$$\begin{aligned} N_1 + N_2 &= N = \text{const.} \\ N'_x + N''_x &= N_x = \text{const.} \end{aligned} \quad (1.138)$$

This means that there is no uncompensated transfer of atoms from the bulk solution to the boundary: if the impurity atoms transfer to the boundary the solvent atoms come back to the bulk.

Note also that in this case $g = N_1 + N_2 + N_v$. It should be stressed that there are no conditions $N_1 = \text{const.}$ or $N'_x = \text{const.}$ which are commonly employed in the course of the determination of the chemical potential.

If there is a substitutional solid solution in the bulk and an interstitial one at the boundary, then, as already noted, the non-compensated transfer of impurity atoms is possible and the following conditions will be valid:

$$\begin{aligned} N_1 &= \text{const.} \\ N'_x &= \text{const.} \end{aligned} \quad (1.139)$$

i.e. the solvent atoms occupy the lattice points of corresponding lattices and they (the atoms) can change only the sites between themselves.

Finally, if both solutions are interstitial solutions, the number of the sites is constant only if:

$$\begin{aligned} g_1 &= \text{const.} \\ g_2 &= \text{const.} \\ g'_x &= \text{const.} \\ g''_x &= \text{const.} \end{aligned} \quad (1.140)$$

So, the following four situations can be considered:

1. Both bulk and boundary solutions are disordered substitutional solid solutions:

$$\begin{aligned} g &= \text{const.} \\ g_x &= \text{const.} \end{aligned} \quad (1.141)$$

The sites of the solvent and the impurity atoms in the bulk and grain boundary solutions (g_1 and g_2 and g'_x and g''_x , respectively) are indistinguishable. Moreover,

$$N_1 + N_2 = N = \text{const. and } N'_x + N''_x = N_x = \text{const.} \quad (1.142)$$

2. There is a substitutional solid inside the grain body and an interstitial solid solution at the boundary:

$$N_1 = \text{const.}; g_2 = \text{const.}; g'_x = \text{const.}; g''_x = \text{const.} \quad (1.143)$$

3. Both solutions are interstitial solid solutions:

$$g_1 = \text{const.}; g_2 = \text{const.}; g'_x = \text{const.}; g''_x = \text{const.} \quad (1.144)$$

4. There is an interstitial solid solution in the bulk, whereas at the grain boundary a substitutional solid solution is formed.

We will restrict our consideration to the first and second situation but even under this limitation the variety of possibilities is much larger than in the case of adsorption at the solid-gas interface.

While the adsorption at free surfaces which occurs from gas and bulk solution is obviously ideal, in the case of adsorption at grain boundaries new possibilities arise since the solid solution is nonideal. It is nonideal not only thermodynamically, because of the usual force interaction, but also because of an “exchange” interaction caused by the crystalline order. Thus, one site can be occupied by only one atom, etc. In principle, three situations are possible for each of the subsystems under consideration (the bulk solution, the boundary solution).

The first is realized when the number of particles is much smaller than the number of sites, i.e. $N \ll g$; consequently, either the bulk solution (concentration $c \ll 1$) or the grain boundary solution (the degree of boundary filling $\Theta \ll 1$) is dilute.

Then the permutation probability in this case is determined by the Boltzmann distribution

$$W = \frac{g^N}{N!} \quad (1.145)$$

The second possible situation is realized when each site of both the bulk and the grain boundary solution can be occupied by not more than one particle ($n \leq g$) (in analogy to the Fermi-Dirac distribution)

$$W = \frac{g!}{N!(g-N)!} \quad (1.146)$$

then $c, \Theta \leq 1$.

Finally, we come to the third possibility: each site can be occupied by an infinite number of particles (an analogue of the Bose-Einstein distribution)

$$W = \frac{(g + N)!}{g!N!} \quad (1.147)$$

As a result of possible situations for adsorption at internal interfaces in solids, in particular at grain boundaries, largely exceeds the diversity of situations for adsorption at solid-gas interfaces.

Let us comment on the derivation of the adsorption isotherm. We are looking for the minimum of the isobaric-isothermic potential by setting the partial derivative $\partial G/\partial N_2$ equal to zero under the boundary conditions given in [Table 1.1](#). Since $N_2 + N_x'' = \text{const.}$, it follows that $\partial/\partial N_2 = -\partial/\partial N_x''$ etc. We assume also that $U_1 = 0$ and $U_2 = U$, in other words, the adsorption heat of the matrix component is zero: it means that only the solute atoms segregate at the grain boundary.

If the phase has different types of sites — which is typical for ordered solutions, and consequently, which is particularly important for grain boundaries — it is necessary to take into account not only the kinds of atoms but also their number and sites of each type. For example, if there are two distinguishable kinds of sites α and β , the number of matrix atoms at the sites of the first kind is n_1^α and so on. Then the permutation probability should be written as

$$\frac{(N_1^\alpha + N_2^\alpha)! (N_1^\beta + N_2^\beta)!}{N_1^\alpha! N_2^\alpha! N_1^\beta! N_2^\beta!} \quad \text{instead of} \quad \frac{(N_1 + N_2)!}{N_1! N_2!}$$

For the substitutional solid solution the concentration of solute atoms in the bulk solution c and the part of occupied sites in the boundary solution Θ can be defined in the natural way: $c = N_2/g$, $\Theta = N_x''/g_x$. For the interstitial boundary solution $\Theta = N_x''/g_x$.

Let us consider, as an example, the isotherm in a system, where both bulk and boundary solutions are concentrated and in the boundary solution each site can be occupied by one particle

$$Z = \frac{g!}{(g - N_2)! N_2!} \cdot (Z_1)^{N_1} \cdot (Z_2)^{N_2} \frac{g_x!}{(g_x - N_x'')! N_x''!} \cdot (Z'_x)^{N'_x} (Z''_x)^{N''_x} \cdot \exp\left(\frac{N''_x U}{kT}\right) \quad (1.148)$$

Since $N_2 + N_x'' = \text{const.}$, $N_1 + N'_x = \text{const.}$, $N_1 + N_2 = g = \text{const.}$

$$Z = \frac{g!}{N_1! N_2!} (Z_1)^{N_1} (Z_2)^{N_2} \frac{g_x!}{N'_x! N''_x!} \cdot (Z'_x)^{N'_x} \cdot (Z''_x)^{N''_x} \exp\left(\frac{N''_x U}{kT}\right) \quad (1.149)$$

TABLE 1.1

Different Variants of the Isotherms

No.	Bulk solution Conditions	W	Surface solution Conditions	W_x
1				
2		$g^{N_2}/N_2!$		
3				
4	substitutional $g = \text{const.}$	$g!/N_1!/N_2!$	substitutional $g_x = \text{const.}$	$g_x^{N''}/N_x''!$ $g_x!/N_x'!N_x''!$ $(g_x + N_x'')!/g_x!N_x''!$
5				
6				
7		$(g + N_2)!/g!N_2!$		
8				
9	substitutional	$g^{N_2}/N_2!$	substitutional	
10				
11	$g = N_1 + N_2 + N_v$	$g!/N_1!N_2!$	$g'_x = \text{const.}$	$(g'_x)^{N''_x}/N''_x!$
12	$N_1 = \text{const.}$		$g''_x = \text{const.}$	$g''_x!/N''_x'!(g''_x - N''_x)!$
13	$N_v = \text{const.}$		$N'_x = \text{const.}$	$(g'_x + N'_x)!/g'_x!N''_x!$
14				
15				
16		$(g + N_2)!/g!N_2!$		
17				
18				

Therefore, taking Stirling's approximation, and the obvious relations

$$\frac{\partial}{\partial N_2} = -\frac{\partial}{\partial N_x''} = -\frac{\partial}{\partial N_1} = \frac{\partial}{\partial N'_x} \quad (1.150)$$

we get

$$\begin{aligned} \left(\frac{\partial \ln Z}{\partial N_2} \right)_{g, g_x = \text{const.}} &= \ln N_1 - \ln N_2 - \ln Z_1 + \ln Z_2 + \\ &+ \ln N''_x - \ln N'_x + \ln Z'_x - \ln Z''_x - \frac{U}{kT} = 0 \end{aligned} \quad (1.151)$$

With the notations

$$c = N_2/g, \quad \Theta = N''_x/g_x$$

and

$$B = (Z_1 Z''_x/Z_2 Z'_x) \exp(U/kT)$$

we have

$$\ln \frac{g - N_2}{N_2} - \ln \frac{g_x - N''_x}{N''_x} = \ln \left[\frac{Z_1 Z''_x}{Z_2 Z'_x} \exp(U/kT) \right]$$

and thus

$$\ln \left(\frac{1}{c} - 1 \right) - \ln \left(\frac{1}{\Theta} - 1 \right) = \ln B$$

and finally

$$\Theta = \frac{Bc}{1 - c + Bc} \quad (1.152)$$

This result coincides with the Zhuchovitskii-McLean isotherm [23, 25]. Neglecting the term “ c ” in the denominator, we obtain the Langmuir isotherm:

$$\Theta = \frac{Bc}{1 + Bc} \quad (1.153)$$

For $c \ll 1$ and $bc \ll 1$ both equations give the Henry isotherm.

The coefficient b , which is proportional to $\exp(U/kT)$, consists in fact of the solubility, more correctly, the ratio, of the impurity solubilities at the grain boundary and the bulk (c'_0/c_0). Actually, the heat of adsorption, or the heat of transfer of the impurity atom from the bulk to the grain boundary U , is equal to the difference between the heat for dissolving it in the bulk q and that for dissolving it at the grain boundary q_x (if as zero energy level is taken the energy of the atom in a phase, which is in equilibrium with both our solutions, for example, in the gas phase). So, $c'_0/c_0 \sim \exp[(q - q_x)/kT] \sim \exp[U/kT] \sim B$. Conceptually, the same result was obtained by McLean, since in his derivation $U = E - e$, where E is the energy of dissolution in the bulk, and e is the energy of dissolution in the grain boundary.

The last group of isotherms describes the situation when each site in the interface (grain boundary) can be occupied by a number of particles.

For concentrated substitutional bulk and boundary solutions, in accordance with the procedure elaborated above, we get:

$$Z = \frac{g!}{N_1!N_2!} (Z_1)^{N_1} (Z_2)^{N_2} \cdot \frac{(g_x + N''_x)!}{g_x!N''_x!} \cdot (Z'_x)^{N'_x} (Z''_x)^{N''_x} \exp\left(\frac{N''_x U}{kT}\right) \quad (1.154)$$

$$\begin{aligned} N_2 + N''_x &= \text{const.}; \quad g = \text{const.} \\ N_1 + N'_x &= \text{const.}; \quad g_x = \text{const.} \\ N_1 + N_2 &= g = \text{const.} \end{aligned} \quad (1.155)$$

and

$$\Theta = \frac{Bc}{1 - c - Bc} \quad (1.156)$$

As mentioned above $\Theta = \Gamma/\Gamma_f$, where Γ is the adsorption and Γ_f is the number of sites. In the example considered, it is possible that $\Gamma > \Gamma_f$, and, consequently, $\Theta > 1$ and even, under certain conditions, it is possible that $\Theta \rightarrow \infty$ (Table 1.2).

The expression (1.156) is an analogue of the multilayer adsorption, other

TABLE 1.2

Adsorption isotherms

No.	Isotherms	Restrictions
1	Bc	$c \ll 1$
2	$Bc/(1 + Bc)$	$c \ll 1$
3	$Bc/(1 - Bc)$	$c \ll 1$
4	$Bc/(1 - c)$	$\Theta \ll 1$ or $c \ll (1 + B)^{-1}$
5	$Bc/(1 - c + Bc)$	$c \leq 1$ or $\Theta \leq 1$
6	$Bc/(1 - c - Bc)$	$c \leq (1 + B)^{-1}$ or $c_0 + c'_0 \leq 1$
10	$B'c \exp(-c)$	$c \ll 1$
11	$B'c/[\exp(c) + Bc]$	$c \ll 1$
12	$B'c/[\exp(c) - Bc]$	$c \ll 1$
13	$B'c$	$\Theta \ll 1$ or $c \ll B^{-1}$
14	$B'c/(1 + B'c)$	$c \leq 1$ or $\Theta \leq 1$
15	$B'c/(1 - B'c)$	$c \leq B^{-1}$ or $c'_0 \leq 1$

Notes:

The numbering of isotherms in Table 1.1 is consistent with Table 1.2.

$$B = Z_1 Z''_x \exp(U/kT) / Z_2 Z'_x = B_0 \exp(U/kT)$$

$$B' = Z''_x \exp(U/kT) / Z_2 = B'_0 \exp(U/kT)$$

c_0 and c'_0 are the solubility of impurity atoms in the bulk (grain) and at the boundary

$$B = c'_0 / c_0$$

than in the BET (Brunauer, Emmet, Teller) version, where two types of sites with two different heats of adsorption were introduced. There is one heat of adsorption for each adsorption layer in the example considered (Eq. (1.156)). Such a situation was considered by Langmuir in 1918

$$\Theta = \frac{Bp}{1 - Bp} \quad (1.157)$$

It is obvious that $B = p_0^{-1}$, where p_0 is the pressure of the saturated vapor. When $p \rightarrow p_0$, Θ and $\Gamma \rightarrow \infty$, then condensation occurs.

Thus far we have taken into account the degrees of freedom associated with the type of the bulk and boundary solutions. We also assumed that the grain boundary is homogeneous, with regard to the adsorption sites, and that there is an interaction between the adsorbed atoms. The further development of adsorption theory should consider the effects mentioned. Some of the adsorption isotherms with interaction (both in the bulk and the boundary solution) were considered above (Eqs. (1.126)–(1.133)). Now we would like to show how this problem can be solved in the statistical approach. The consideration will be given in the Bragg-Williams approximation.

The expression for the statistical sum of the system can be obtained by multiplying the right-hand side of Eq. (1.127) by $\exp[-Z\Delta(N''_x)H^2/(2g_x kT)]$.

Following the procedure given above we get instead of the isotherm $\Theta = Bc/(1 + Bc)$ the isotherm

$$\Theta = \frac{Bc \exp(-\tilde{\gamma}\Theta)}{1 + Bc \exp(-\tilde{\gamma}\Theta)} \quad (1.158)$$

The expression (1.158) is the Frumkin isotherm, with $\tilde{\gamma} = Z\Delta/kT$. Obviously, under the condition $|\varepsilon_{12}| > |(\varepsilon_{11} + \varepsilon_{22})/2|$ the heat of mixing $\Delta < 0$ and $\tilde{\gamma} < 0$. Then for large $|\Delta| \gg kT$ we have $\Theta \rightarrow 1$: interaction leads to saturation. In contrast, for $\Delta > 0$ and $\tilde{\gamma} > 0$ saturation cannot be reached.

An analysis of the isotherms (1.126)-(1.135), (1.158) shows that at a temperature lower than the critical temperature T_{cr} there is a “jump” on the isotherm — a segregational phase transition, which disappears at $\Theta_{cr} = 1/2$ or $T_{cr} = Z\Delta/2k$ (for the isotherm (1.158)).

In order to derive the expressions for a multilayer isotherm, i.e. the adsorption at a non-homogeneous surface (grain boundary), it is rational to consider the transfer process of particles between the boundary solution and the bulk solution by using the Gibbs grand canonical distribution. In such an approach the number of impurity particles in the solution is

$$N_x = \lambda \left(\frac{\partial \ln \tilde{Z}}{\partial \lambda} \right)_{T,V} \quad (1.159)$$

where $\tilde{Z} = \Sigma \lambda^N Z_{N_x}$ is the grand canonical sum; the summation is taken over all possible states, which differ in the number of particles; Z_{N_x} is the statistical sum for N particles in the boundary solution and a is the thermodynamic activity: $a = \exp(\mu/kT)$.

The calculation reduces, consequently, to the determination of the grand statistical sum for the different situations [28, 29]

1. There are states in the boundary solution at the common Langmuir adsorption which do or do not contain one particle. Then for the first particle the grand sum is equal to $1 + \lambda Z_{1x}$ and for g_x adsorbed particles

$$\tilde{Z} = (1 + aZ_x)^{g_x} \quad (1.160)$$

Using Eqs. (1.159) and (1.160) we obtain the Langmuir equation $\Theta = Bc/(1 + Bc)$ or, over the range of concentrations, $\Theta = Bc/(1 - c + Bc)$. For a solution with a limited solubility

$$\Theta = \frac{Bc}{c_0 - c + Bc} \quad (1.161)$$

where c_0 is the limit of the bulk solubility.

In the description of the adsorption at a non-homogeneous surface the dependence of the heat of adsorption on the “number of sites” $dU/d\Gamma$

should be given. If the adsorption heat takes the discontinuous values $U_1, U_2, U_3, \dots U_i$, then with $B_i \cong \exp(U_i/kT)$ we obtain

$$\Theta = \sum_i \alpha_i \frac{B_i c}{1 + B_i c} \quad (1.162)$$

where α_i is the fraction of sites with the heat U_i . (Obviously, $\sum \alpha_i = 1$.) If $dU/d\Gamma = \text{const.}$ (Temkin isotherm):

$$\Theta = \frac{1}{\gamma} \ln \frac{1 + B_{\max} c}{1 + B_{\min} c} \quad (1.163)$$

where $B_{\max} \sim \exp(U_{\max}/kT)$; $B_{\min} \sim \exp(U_{\min}/kT)$; $\gamma = (U_{\max} - U_{\min}/kT)$; U_{\max}, U_{\min} are the maximum and the minimum value of the heat of adsorption, respectively.

2. In the case of multilayer adsorption it should be assumed that there are states with 0, 1, 2, ..., N particles. In accordance with concepts of multilayer adsorption (BET) let us distinguish the states when the particle is in the first layer (Z_{1x}), or in the second (Z_{2x}), third (Z_{3x}) and so on. In this case all states succeeding the first are indistinguishable from one another, i.e. $Z_{1x} = \alpha Z_{2x}$, $\alpha = \exp(U_1/kT)$, and $Z_{2x} = Z_{3x} = \dots = Z_{Nx}$. Then:

$$\tilde{Z} = (1 + \lambda Z_{1x} + \lambda^2 Z_{1x} Z_{2x} + \lambda^3 Z_{1x} Z_{2x} Z_{3x} + \dots)^{g_x}$$

or, at specified conditions

$$\begin{aligned} \tilde{Z} &= (1 + \lambda \alpha Z_{2x} + \lambda^2 \alpha Z_{2x}^2 + \lambda^3 \alpha Z_{2x}^3 + \dots)^{g_x} = \\ &= \left\{ 1 + \lambda \alpha Z_{2x} \frac{(\lambda Z_{2x})^{N-1} - 1}{\lambda Z_{2x} - 1} \right\}^{g_x} \end{aligned} \quad (1.164)$$

Here, like in the previous case, $\lambda Z_{1x} = \lambda \alpha Z_x = Bc$, $\lambda Z_{2x} = B'c$, where

$$B = \exp(U/kT) = c'_0/c_0 \text{ and } B' = c_0^{-1}$$

Finally

$$\frac{N_x}{g_x} = Bc \frac{N (B'c)^{N-1} + (N-1) (B'c)^{N-2} + \dots + 2B'c + 1}{1 + Bc [(B'c)^{N-1} + (B'c)^{N-2} + \dots + B'c + 1]} \quad (1.165)$$

We can also introduce the fraction $Bc/(1-c)$ or $Bc/(c_0-c)$ instead of Bc to describe Θ over the whole range of concentrations.

In the special case $n = 1$ Eq. (1.165) coincides with the Langmuir isotherm. In the special case $N = 2$

$$\frac{N_x}{g_x} = Bc \frac{2B'c + 1}{1 + Bc(B'c + 1)} \quad (1.166)$$

At last, in the special case $N \rightarrow \infty$ we get the BET isotherm:

$$\frac{N_x}{g_x} = \frac{Bc}{(1 - B'c)(1 + Bc - B'c)} \quad (1.167)$$

Consequently, the given analysis shows that there are many situations that can be realized for the adsorption from a solid solution to internal surfaces.

1.3 Experiments

1.3.1 Adsorption

All experimental methods of studying grain boundary adsorption, or, as it is more customary to say, “segregation,” can be subdivided into two groups.

The methods of the first group are associated with the direct analysis of the composition of the surface (grain boundary) layer and subsequent calculation of the value of adsorption from the formula: $\Gamma'_i = \tilde{z}(c_i^s - c_i)$. The quantity \tilde{z} determines the thickness of the grain boundary. The adsorption (segregation) calculated in this way is the concentration part of the total adsorption (segregation); this part is the excess adsorption in Gibbs' sense, i.e. specific boundary excess of the particles of the i -th kind. The adsorption quantities of different components are connected by the apparent relationship

$$\Gamma'_1 + \Gamma'_2 = 0 \quad (1.168)$$

The methods of direct measurement of the grain boundary adsorption (segregation) were actively developed in recent years [30]–[34]. Comprehensive reviews give an idea of the present state of the art of grain boundary adsorption and, in particular, how the segregation experiments fit the modern concepts of grain boundary structure [34, 35].

The following problems are most interesting for the physicist and materials scientist:

- (a) how wide is the zone of grain boundary segregation;
- (b) which way is the segregation associated with the grain boundary structure;

- (c) which isotherms can describe the grain boundary segregation, which is the magnitude of the adsorption (segregation) heat, number of adsorption sites, and the enrichment of grain boundaries;
- (d) finally, what are the activities of atoms in the grain boundary solution.

The first three problems can be treated equally by the direct and indirect methods of investigating grain boundary segregation, whereas the last problem (d) is best studied by analysis on the basis of the Gibbs adsorption equation (1.150). All investigations give an unambiguous answer to the first question: the zone of grain boundary segregation, or, in other words, the enriched zone is narrow, not more than some monolayers. Usually, the enrichment does not exceed the capacity of one monolayer, but for grain boundary adsorption of Sn in bcc Fe polycrystals the capacity of 1.5 monolayers was achieved [31]. It is of significance that the result mentioned above was obtained using the Gibbs adsorption equation as well as Auger electron spectroscopy measurements (Fig. 1.8).

The direct criterion for the surface activity is the derivative $\partial\gamma/\partial\mu_i$; for dilute or ideal solutions $\partial\gamma/\partial c$, respectively. (It should be taken into account that even if the bulk solution is dilute the grain boundary solution can be saturated.) However, the dependence $\gamma(c)$ as a rule is unknown. That is why a number of criteria were proposed to estimate the grain boundary activity of different impurities including the difference of the melting temperature of the solvent and the solute, the difference of the generalized moments, the atomic volumes, etc. All correlations were qualitative; only the coincidence of the sign was checked.

The development of new direct experimental methods enables us to obtain quantitative correlations. Hondros and Seah [36] introduced the enrichment coefficient $\beta = \Theta/c$, where Θ is the fraction of the packed area of the grain boundary, which can be determined as $\Theta = \Gamma/\Gamma_f$. Γ_f fits the situation that all adsorption sites are occupied. It is of importance that the linear dependence between the coefficient β and the bulk solubility c_0^{-1} has been observed (Fig. 1.9) [36]. The coefficient β determined in [36] ranges from 10^0 to $10^3 - 10^4$. The linear dependence between β and c_0^{-1} is satisfactorily met over a wide range: from the system with complete solid solubility (Cu-Au, Fe-Ni; for such systems $\beta \cong 1$) to systems with $c_0 \cong 10^{-2}\%$ (α -Fe-S, Ni-S, Cu-Bi; for them $\beta \cong 10^3 - 10^4$). It should be mentioned, however, that for systems with extremely low solubility in the solid state some side effects can interfere with the segregation process.

A new point of view of this problem was recently suggested [37]. In this work, the segregation of Bi at grain boundaries in polycrystalline Cu was studied by the AES technique. The grain boundary segregation in Cu-Bi has been treated previously in a number of experimental studies and by computer simulation techniques [38]. The transition from intercrystalline to intracrystalline fracture, induced by an increase in temperature was associated with the abrupt decrease of the grain boundary segregation of Bi, which can be de-

rived from an isotherm similar to the isotherms or (1.128), (1.130), (1.131) — the Fowler-Guggenheim isotherm, (1.158) — the Frumkin isotherm. However, in all previous works the question has been ignored whether the samples are in a single- or in a two-phase region of the binary Cu-Bi phase diagram. Due to this fact it is conceivable that the exact values of the solubility of Bi in the bulk of solid Cu were unknown. Chang et al. [37] determined the solidus line at the Cu-rich side of the Cu-Bi phase diagram precisely. Simultaneous AES measurements showed that the abrupt decrease of grain boundary segregation of Bi during the increase of temperature occurred approximately at the solidus temperature. Therefore, at low temperatures the Cu-Bi alloys were in a two-phase state and the high grain boundary segregation of Bi can be explained by the precipitation of the Bi-rich phase at the grain boundaries. Such precipitates can have the form of continuous planar layers, if the conditions for complete wetting of the grain boundaries by the Bi-rich phase are fulfilled. The thickness of the layer should be proportional to the supersaturation of Bi. Extending this behavior to other binary systems one can state that in systems with a low solubility of segregating impurities in the solid matrix the degree of the supersaturation impurities is high, which leads to thick precipitation layers at the grain boundaries. This is an alternative approach to the correlation of Hondros and Seah [36] (Fig. 1.9). It should be noted that the thickness of the layer could be stabilized by an attractive interaction of two interphase boundaries (see Sec. 1.3).

In which way is the segregation at grain boundaries associated with the grain boundary structure? The experimental results obtained by direct methods of grain boundary segregation, essentially by AES and atom probe-field ion microscopy, show that the segregation at grain boundaries is determined by their structure. So, the data of segregation of Po at symmetrical $\langle 100 \rangle$ tilt grain boundaries in alloys of Pb-5%Bi are shown in Fig. 1.10 [39]. The abrupt increase of segregation in the vicinity of misorientation angles of $\sim 15^\circ$ corresponds to the transition from low-angle to high-angle grain boundaries. In Fig. 1.11 the dependence on misorientation of the enthalpy of segregation of carbon (C), phosphorus (P) and silicon (Si) at symmetrical $\langle 100 \rangle$ tilt grain boundaries in bicrystals of Fe-3.5%Si is shown [40]. It is easy to see that the observed minima of the curves relates to special misorientations. Fig. 1.12 gives the misorientation dependence of the segregation of Re at $\langle 011 \rangle$ twist grain boundaries in a W-25%Re alloy [41].

The sharp minima of the segregation of Re were discovered at a grain boundary of the special misorientation $\Sigma 3$. It should be stressed that other special misorientations do not show particular minima of segregation [42, 43]. This can be explained by the assumption that the adsorption capacity of twist grain boundaries is lower than that of tilt grain boundaries. It was shown experimentally that the zone of adsorption is narrow enough [43, 44], so most of the adsorbed material is disposed in the “core” of the grain boundary; nevertheless, a small part of it is located outside the enriched layer [43]. Recent results of computer simulations suggest that segregation is determined

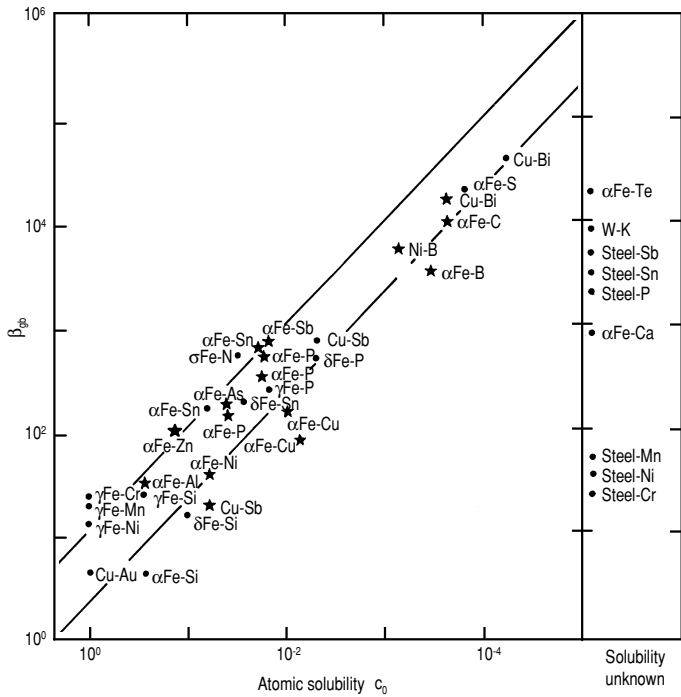
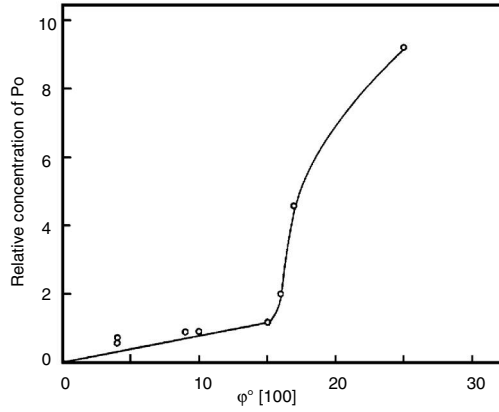
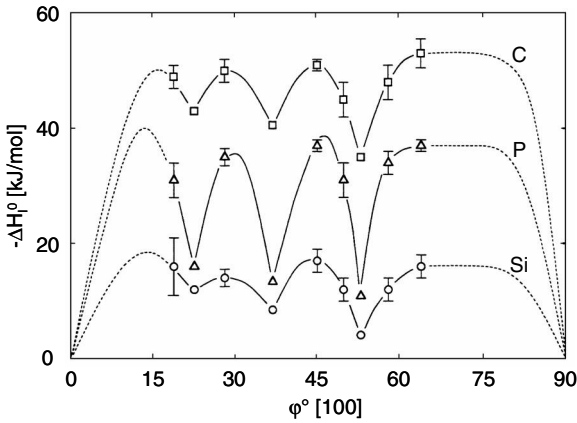


FIGURE 1.9
Correlation of measured grain boundary enrichment ratios with the atomic solid solubility. The points denoted by stars represent measurements published since the first correlation was made [36].

**FIGURE 1.10**

Orientation dependence of Po segregation at $\langle 100 \rangle$ symmetrical tilt grain boundaries in bicrystals of a Pb-5%Bi alloy [39].

**FIGURE 1.11**

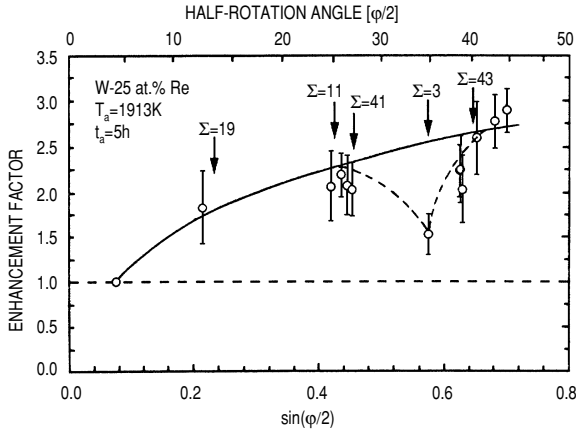
Dependences of segregation enthalpies ΔH_i ($i = C, P, Si$) on the misorientation angle φ of both adjacent crystals in $\langle 100 \rangle$ symmetrical tilt bicrystals of an Fe-3.5 at % Si alloy [40].

by the grain boundary structure [38], [45]–[48]. Monte-Carlo simulations revealed that in Pt-3%N alloys the segregation at the $\Sigma 5$ boundary can be described successfully [42]. Further Monte-Carlo simulations indicate the magnitude of how impurity atoms fill the grain boundary. So, first the cores of grain boundary dislocations are filled and then the remaining grain boundary sites. Monte-Carlo simulations make clear the segregation behavior of twist grain boundaries and predict an increase of segregation with an increase of the angle of misorientation [47, 48].

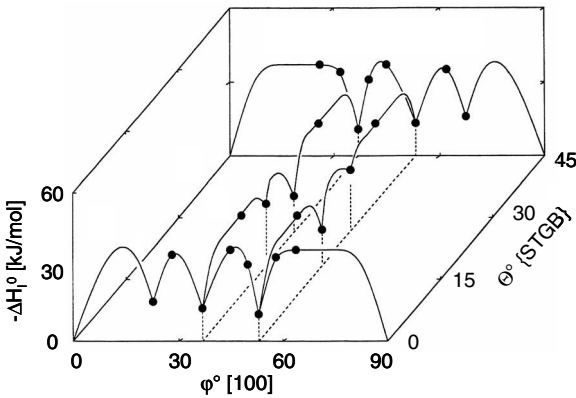
Beyond any doubt, the construction of a grain boundary segregation diagram constitutes a real success of theory and experiment [49]. Fig. 1.13 demonstrates the 3D diagram of the enthalpy of grain boundary segregation of P in α -Fe as a function of the angles of misorientation and inclination (with respect to the symmetrical position) [50].

It should be pointed out that the comparison of theory and experiment of grain boundary segregation has been a problem. The crucial point is that the success of such a reference depends on whether there is a sole parameter with respect to which the reference can be accomplished. As noted in [34], such a reference can be constructed on the basis of the theory of the structural units. There are two essential objections to this method. First, the structural units are known for only a small number of grain boundaries. Second, there is not a sole parameter which can be compared by experiment and theoretical calculations. Therefore, the relationship between structure and segregation can be judged by the special misorientation (Σ), the correlation with the average interplanar spacing of the lattice planes running parallel to the boundary [i.e. $d = 1/2d \{d_1(hkl) + d_2(hkl)\}$]. The first well-known attempt to perform a direct comparison between the experiment and the computer-simulated segregation picture for the grain boundary $\Sigma 3$ (111) in the system Cu-Bi belongs to Luzzi et al. [51, 52] (Fig. 1.14). The HREM image of segregated Bi at a specific grain boundary in Cu was compared with the computer simulated structure, and good agreement between experiment and computer model was found. Taking into account the circumstances, mentioned above, associated with the wetting of grain boundaries in Cu by Bi, the comparison of Bi segregation at grain boundaries in Cu seems to be not as ambiguous as it was represented in [52].

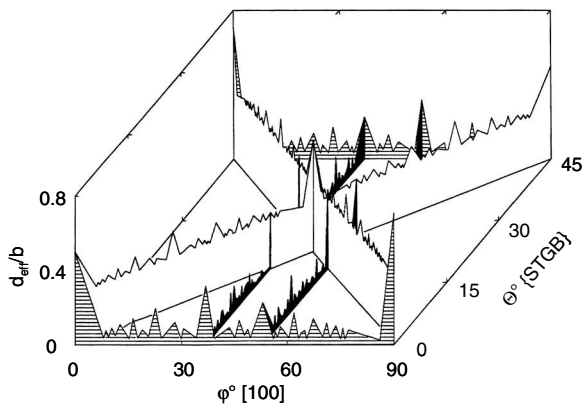
Next we would like to stress that there is a crucial discrepancy between the experimental and the theoretical approach. As mentioned in [34] the theoretical modeling is most commonly based on the study of simple (from the theoretical point of view) systems and simple grain boundaries. For instance, the solution of two metallic elements of a similar electronic structure such as Au-Ag, Cu-Ag was considered. As is well known, such similarity leads to a continuous solubility in the solid. Contrary to the theoretical approach, experimentators choose systems with high segregation of one of the components and with embrittlement of grain boundaries, which is of vital importance. These conditions fit systems with an extremely small solubility of one of the components. That is why the good agreement is so encouraging between the

**FIGURE 1.12**

Enrichment factor vs. misorientation angle [41].

**FIGURE 1.13**

Dependence of segregation enthalpy of phosphorus in $\delta\text{-Fe}$, ΔH_i^0 , on boundary misorientation angle φ and inclination Θ with respect to symmetrical tilt boundary (STGB) [50].

**FIGURE 1.14**

Dependence of the effective interplanar spacing d_{eff}/b for $\langle 100 \rangle$ tilt grain boundaries on the misorientation angle φ and inclination Θ with respect to symmetrical boundary (STGB) (Cu-Bi) [51, 52].

experimental and theoretical values of the segregation energy for phosphorus (0.138 eV and 0.15 eV, respectively) and for silicon (0.09 eV and 0.10 eV, respectively), at the special $\Sigma 5 \langle 100 \rangle$ (36.9°) symmetrical tilt grain boundary [34, 53, 54]. This success should not be overestimated: for P in α -iron the predicted values of segregation energy vary within wide limits: from 0.8 to 2.25 eV as compared to experiments: $\sim 0.22 - 0.4$ eV [34, 55, 56].

The last question we promised to consider in this chapter is how the grain boundary structure is determined by impurity segregation. Actually, the description of grain boundary (generally, interface) segregation as a distribution of impurity atoms between a certain number of active segregation sites is a model. In reality, the structure of the interface is a function of the nature and amount of impurity atoms in it; in other words, the segregated atoms should change the structure of the interface, and in turn the structure of the interface should determine the number of possible adsorbed atoms and their adsorption characteristics. In spite of the first steps in this direction were made almost 15 years ago by Sutton, Lundberg and Srolovitz [35], [57]–[59], it is too early to talk about the definite results.

The next problem we would like to consider is which types of isotherms of segregation discussed above apply to grain boundary segregation. The first who pointed out that grain boundary segregation can be described on the basis of the classical theory of interface phenomena were supposedly Mehl [60] and Stout [21]. The term “intercrystalline adsorption” was introduced by Arharov [61].

The Gibbs equation (1.50), which connects the change of the surface tension with the variations in temperature, pressure and chemical potentials of the

bulk phases, is true for any surface which is in equilibrium with the volumes subdivided by it. At constant T and V , Eq. (1.50) can be transformed into the relation (1.53):

$$\Gamma_i = - \left(\frac{\partial \gamma}{\partial \mu_i} \right)_{T,V,S} \quad (1.169)$$

The Gibbs equation in the form of Eq. (1.169) and in its simplest form (Eq. (1.60)) may be used to determine the grain boundary adsorption (segregation). It was implemented for the grain boundary segregation by Hondros and Seah [36, 62, 63]: P in γ -Fe, Sn, Si and S in δ -iron. Even for a binary solution this is not a very easy measurement. But actually the crucial point is not the difficulty of experiment and calculation, but rather to understand which law governs grain boundary segregation.

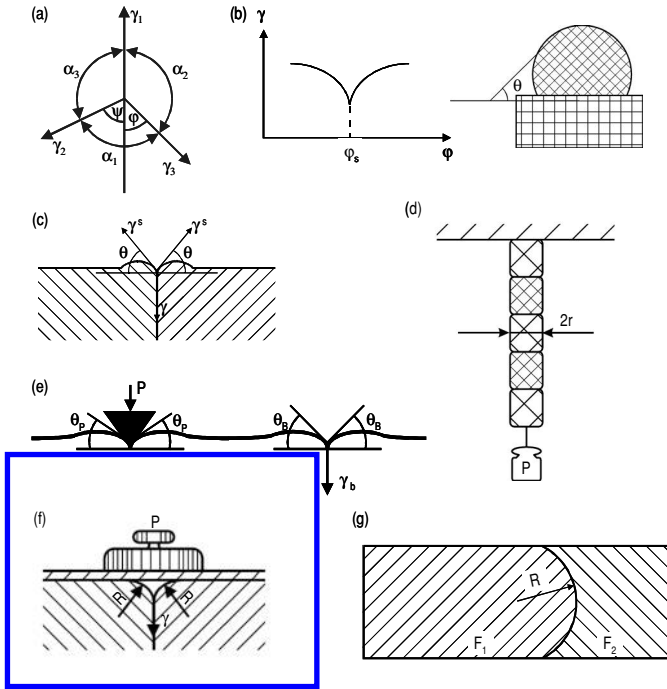
The Langmuir-Zhuchovitskii-McLean isotherm (Eqs. (1.152),(1.153)) [23] was historically the first isotherm of surface adsorption which was applied to explain the concentration dependence of grain boundary segregation. Examples of systems described successfully by this isotherm are: P in α -Fe [64], In in Ni [65].

The isotherm of multilayer adsorption (Eqs. (1.165)–(1.167)) was also used to describe experimental data [36, 66]. This isotherm was first put forward by Brunauer, Emmet and Teller (BET) [67] to explain the gas adsorption at a free surface in a close vicinity of the condensation point: $C \rightarrow C_0$; $\Gamma \rightarrow \infty$. The “infinite” adsorption in this case physically means condensation, i.e. the formation of a liquid film. Similarly, an “infinite” segregation at grain boundaries indicates the formation of a new phase or at least the pre-precipitate stage. The grain boundary segregation of tin, sulfur, phosphorus and antimony in iron and nickel [36, 63, 66] was explained on a basis of a multilayer grain boundary segregation.

An important feature of the adsorption isotherms, mentioned above, is that the physical act of adsorption is independent of the degree of filling of the adsorbed layer (of the number of atoms, which have been adsorbed before); in other words, these isotherms do not take into account the interaction between the adsorbed atoms. This type of isotherm was considered above (Eqs. (1.128)–(1.133)). One of the “isotherms with interaction,” the Fowler-Guggenheim isotherm (Eq. (1.131)), was repeatedly applied to different systems to explain the peculiarities of adsorption (segregation) behavior (selenium and tellurium in α -iron [66], Bi in Cu [68], and antimony in α -iron [69]).

1.3.2 Grain Boundary Surface Tension

Unfortunately, direct experimental investigation of boundary adsorption is only possible in a very few systems. In this case the only way to calculate the equilibrium grain boundary segregation Γ_i is to use the Gibbs equation (1.57)

**FIGURE 1.15**

Methods of grain boundary surface tension measurement: (a) equilibrium angles at triple junction; (b) rotating ball method: sintering of small signal crystal balls to single crystal substrate; (c) thermal groove method; (d) zero-creep method; (e) method of a “floating” wedge; (f) hypothetical method of an “equilibrium” grain boundary thermal groove; (g) balance of grain boundary surface tension and volume driving force.

and to relate it to macroscopic parameters such as the grain boundary surface tension γ and the chemical potentials μ_i of the components in the grain. In this case the surface tension of the grain boundary should be measured for a number of alloys and preferably at different temperatures. Let us consider the — unfortunately few — experimental methods, which give us an opportunity to measure the grain boundary surface tension. A brief summary of different schemes of the measurement of grain boundary surface tension is shown in Fig. 1.15 [70].

The first method can be called the triple junction method [71, 72] (Fig. 1.15a). If there is a mechanical equilibrium at the triple junction and the grain boundary surface tensions do not depend on the orientation of the boundaries, the relation between the surface tension of different boundaries can be found

from Young's theorem:

$$\frac{\gamma_l}{\sin \alpha_1} = \frac{\gamma_2}{\sin \alpha_2} = \frac{\gamma_3}{\sin \alpha_3} \quad (1.170)$$

where α_i indicates the contact angles opposite to γ_i . If the surface tensions of the grain boundaries depend on their orientation, the dependency $\partial\gamma_i/\partial\Theta_i$ should be taken into account where Θ is the inclination of the boundary with regard to a reference plane [73]. These terms are associated with the forces which tend to rotate the boundary into the position with minimum energy; according to Herring [73]

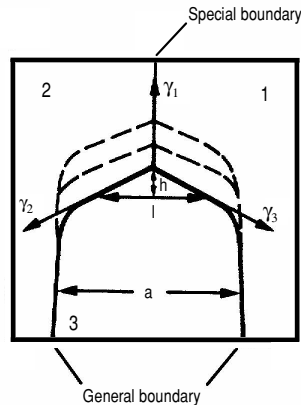
$$\begin{aligned} & \frac{\gamma_1}{(1 + \varepsilon_2 - \varepsilon_3) \sin \alpha_1 + (\varepsilon_3 - \varepsilon_1) \cos \alpha_1} = \\ & = \frac{\gamma_2}{(1 + \varepsilon_1 - \varepsilon_3) \sin \alpha_2 + (\varepsilon_1 - \varepsilon_3) \cos \alpha_2} = \\ & = \frac{\gamma_3}{(1 + \varepsilon_1 - \varepsilon_2) \sin \alpha_3 + (\varepsilon_2 - \varepsilon_3) \cos \alpha_3} \end{aligned} \quad (1.171)$$

where $\varepsilon_i = \frac{\partial \ln \gamma}{\partial \Theta_i}$ denotes the dependence of the grain boundary surface tension on grain boundary orientation. These ε_i are referred to as torque terms.

The influence of the torque terms is important in the vicinity of special misorientations (see Chapter 2). For random grain boundaries and far from special misorientations the values of $(\partial\gamma_i/\partial\Theta_i)$ are small enough and Eq. (1.170) gives a reasonable approximation.

This method was used in many experimental investigations [74]–[76]. It is especially suitable for grown tricrystals, where two grain boundaries have the same misorientation and the surface tension of the third can be calculated, or when the observation of the change of the surface tension of the third grain boundary is the main purpose of investigation (Fig. 1.16). Such experiments make it possible to compare the surface tensions of different grain boundaries, or grain boundaries with different orientation in the same material. It was shown, in particular, that the minima of the misorientation dependence of the grain boundary surface tension correlate with special misorientations in the coincidence site lattice theory (see Chapter 2).

Another relative method of investigation of the grain boundary surface tension was proposed by Wilson and Shewmon [77] and was applied in many experimental studies [78]–[80]. If a number of small single-crystal balls would be put on a single-crystal substrate of the same material at diffusion temperature, they then would rotate during sintering to the substrate to decrease the surface tension of the newly formed grain boundary. The main condition for the proper conduct of the experiment is: the misorientation dependence of the grain boundary surface tension must have singularities, sharp minima with a discontinuity of the derivative of the surface tension with respect to misorientation angle α , but not a usual minimum as mentioned in [35] (Fig. 1.15b). As the driving force of the rotation of the balls is proportional to the

**FIGURE 1.16**

Sequential junction position during measurement of temperature dependence of γ_1/γ_2 .

derivative ($\partial\gamma/\partial\Theta$), the driving force is kept up in the case of a singular discontinuity until the balls reach the minimum energy position, whereas for a usual minimum the derivative — the driving force for rotation — tends to zero with the misorientation angle tending to the special misorientation. Fig. 1.17 [81] gives an example of the positions at special misorientations as estimated by the method (Fig. 1.15b) discussed in [77].

To determine the absolute value of the grain boundary surface tension, the tension of the reference surface must be known. For a known tension of the free surface we can determine the grain boundary surface tension from the equilibrium of the surface tensions at the root of a thermal groove (Fig. 1.15c). Unfortunately, there are only few methods to determine the tension of a free surface of the crystal.

One of them is the method of zero creep [82] (Fig. 1.15d). Let us imagine a wire of small diameter D or a thin foil with perimeter $\pi \cdot D$ which is loaded with a weight P at diffusional creep temperatures. The free energy of the wire (or foil) can be defined as

$$F = P_x + \gamma^s \pi DL \quad (1.172)$$

where x is the coordinate of the weight P relative to the arbitrary point on the normal to the earth surface, L is the length of the wire, γ^s is the surface tension of the free surface of the wire. The equilibrium ($\delta F = 0$) corresponds to such changes of x and length which compensate each other. Taking into account that $\delta_x = -\delta L$, we get

$$\left(\frac{\partial F}{\partial x} \right)_{x=0} = P_0 - \gamma^s \pi D = 0 \quad (1.173)$$

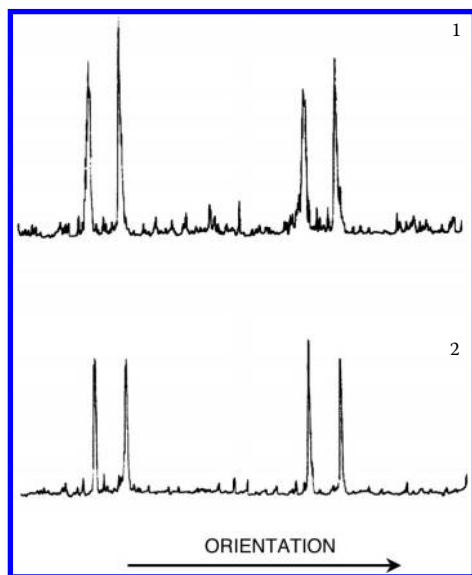


FIGURE 1.17

Corresponding sections through the pole figures of two specimen (1 and 2) of the same type, demonstrating the reproducibility of the method used to identify low energy boundaries. Both curves show similar peaks of diffracted X-ray intensity at identical orientations [81].

and $\gamma^s = P_0/\pi D$, where P_0 is the so-called zero-creep weight.

A more correct description takes into account the area of the grain boundaries and their shape [83]–[85]. Evidently, the value of the free surface tension determined in this way is averaged over a large number of crystallographic planes.

The method of “float wedge,” put forward and realized for the first (and the last) time by Shewmon, is free of the disadvantages mentioned above. The scheme is given in Fig. 1.15e. The sharp hard wedge, which is not wetted by the tested metal, is pressed to its surface by a known force P at diffusion temperature. A groove which is similar to the thermal groove of the grain boundary will form under the wedge. As we know the force acting on the tip of the groove from the side of the wedge, we can calculate the surface tension of the free surface, if the dihedral angle is measured. If, as shown in Fig. 1.15e, a grain boundary comes to the same surface, the surface tension of the grain boundary is equal to

$$\gamma = \frac{P \sin \Theta_b}{L \sin \Theta_p} \quad (1.174)$$

where L is the length of the wedge perpendicular to the plane of Fig. 1.15e.

Admittedly, the described method has not been used and developed in the 30 years since the Shewmon paper was published. Apparently, this method is extremely laborious, the main reason that it has fallen into oblivion.

The principle of another method to determine the absolute value of the surface tension of both the free surface and a grain boundary meeting this surface is given in Fig. 1.15f [70]. A plate of a material, which is not wetted by the tested metal, is placed on the smooth flat surface of the sample. (Graphite is not wetted by many metals, like Cu, Au and so on.) The grain boundary intersects the surface of the sample as well.

Under these conditions the groove will not grow unlimitedly, as would happen at the free surface. The growth of the groove will stop the sooner the larger the load, comprised by the plate on the surface, i.e. as soon as the excess chemical potential of the atoms at the curved surface of the groove, which is $\gamma^s \Omega_a / R$ (Ω_a is the atomic volume), becomes equal to the increase of the chemical potential which is caused by the pressure of the plate: $p \Omega_a / \tilde{A}$ (\tilde{A} is the contact area under the plate). Then the surface tension of the external surface of the crystal is $\gamma^s = pR / \tilde{A}$, and the grain boundary surface tension can be determined from the dihedral angle at the root of the groove. Nevertheless, this method, which may be called the method of equilibrium groove, has not yet been realized.

Let us use this opportunity to consider the question of how large the thermal groove of the grain boundary could get under terrestrial conditions. The development of the thermal groove will stop if the hydrostatic (capillary) pressure which results from the curvature of the groove equals the gravitational force:

$$\gamma^s / R = \rho gh \quad (1.175)$$

where h is the depth of the groove, and ρ is the density of the metal.

Assuming $h \cong R$, we get

$$R \cong \sqrt{\frac{\gamma^s}{\rho g}} \quad (1.176)$$

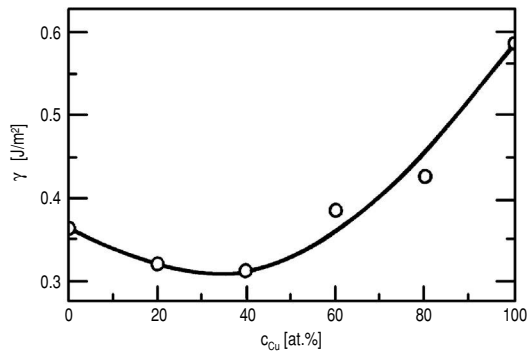
The expression under the root sign is known as the capillary constant. For values which are typical for metals, the limiting value of the radius of curvature R , i.e. for the depth of the thermal groove h , is approximately ~ 0.3 cm. Of course, it is impossible to obtain such a groove in a reasonable time. Usually, the depth of the thermal groove does not exceed some ten micrometers, and this result is important for us, less from the general point of view than for pragmatic reasons.

We discussed above that the grain boundary is a degenerate kind of interphase, and if an external tensorial field is applied to the system, the degeneration will be removed and, from the thermodynamical standpoint, the grain boundary can be described as an interphase. This provides a method to measure the absolute value of the grain boundary surface tension. If an external field is applied to a system with a grain boundary, which is locked at the surface of the sample, a difference in the specific free energies of the grains will arise ($g_2 - g_1$); due to this difference the initially flat grain boundary will bend like a membrane under the pressure. In this case the grain boundary surface tension can be estimated as (Fig. 1.15g)

$$\gamma = R(g_2 - g_1) \quad (1.177)$$

The difference in the specific free energies of the grains ($g_2 - g_1$) should be large enough, otherwise the radius of grain boundary curvature R will be too large to be measured with sufficient accuracy. Such a scheme, as can be seen, provides a unique opportunity to determine the absolute value of grain boundary surface tension. Firstly, this method was applied to the measurement in polycrystalline Bi in a magnetic field [86], and, quite recently, to the grain boundary in bicrystals of Bi in a magnetic field [87].

The modern techniques of determination of the chemical content of surface layers in solids together with the thermodynamics of surfaces suggest a new method of “experimental calculation” of the surface tension of free surfaces of solid alloys [88]. As shown in [89], modern methods like low-energy ion-ion scattering permits us to determine the content of a surface monolayer. Hence, the surface tension of a free surface can be estimated by integrating the Gibbs adsorption equation. This method, together with the determination of the dihedral angle at the root of the grain boundary groove, holds considerable promise for the study of grain boundary and interface phenomena in metals and alloys.

**FIGURE 1.18**

Dependence of grain boundary surface tension in Cu-Au on (atomic) Cu concentration [90].

1.3.3 Examples

In the following we will show how to determine grain boundary segregation and how to obtain an estimation of the activity of the atoms in the boundary solution in the event that the dependence of the grain boundary surface tension on the concentration has been measured, using the example of the binary system Cu-Au [90]. The point is that there is very little information about the isotherms of the surface tensions. Even if the dependence of the surface tension on composition is known, it is only over a very narrow range of concentrations. Moreover, the isotherms of the activities (chemical potentials) of the components usually are not known, and without sufficient evidence the conclusion is drawn that the solutions are dilute.

There appear to be only two studies in which the surface tension of grain boundaries has been measured for the entire range of concentration, namely of the systems Cu-Au and Cu-Ni [24, 91], and there are isotherms of the bulk activities of both components for these systems. For the system Cu-Au the surface tension was determined by the zero-creep technique, while for the system Cu-Ni the technique described above was applied using the measurement of the chemistry of the surface monolayer and the Gibbs adsorption equation [88, 89, 91]. Because the method of thermodynamic treatment of grain boundaries considered above (Eqs.(1.82)–(1.116)) was first applied to the system Cu-Au [24], the explanation of how this method works in detail will be given using this system as an example.

The experimentally determined dependence of the grain boundary surface tension on the atomic fraction of Cu in the system Cu-Au is depicted in Fig. 1.18. The grain boundary surface tension γ was determined at 1123 K by

measuring the equilibrium angle at the root of a thermal groove:

$$\cos \Theta/2 = \gamma/2\gamma^s \quad (1.178)$$

where γ^s is the surface tension of the free surface was determined by the zero-creep technique at the same temperature (Fig. 1.18). The isotherms for the activities a_i of Cu-Au components at 800 K were taken from reference books [92, 93] and converted to 1123 K using the equation

$$\frac{\partial \ln a_i}{\partial T} = \frac{\Delta \bar{H}_i}{RT} \quad (1.179)$$

assuming that the partial molar enthalpy of dissolution of the i -th component $\Delta \bar{H}_i$ does not depend on temperature in the range from 800 to 1123 K.

We would like to reiterate once again that the model of a homogeneous grain boundary used in Eqs.(1.82)–(1.116) and taken as a basis for the calculations in [24, 90] coincides with the model for the surface layer of Guggenheim and Adam [8]. The same model was used by Zhuchovitskii in his theory of surface solutions [25]. Zhuchovitskii treated a surface layer as a two-dimensional solution with its own thermodynamic properties and in equilibrium with a volume solution. The dependence of the surface tension on composition in such a system is defined by Eqs.(1.93)–(1.105):

$$\gamma - \gamma_i = z RT \ln a_i^s/a_i$$

where z is the total number of adsorption centers in a unit boundary area; z is assumed to be independent of composition. In our notation $z = \lambda\rho^s$. The combined solution of Eqs.(1.103)–(1.104) and the Gibbs equation in the form

$$z RT [C_1^s d \ln a_1 + (1 - C_1^s) d \ln a_2] = -d\gamma \quad (1.180)$$

provides a means for obtaining the activity isotherm of each component of a binary surface (boundary) solution: $a_i^s (C_i^s)$. But if the adsorption isotherm Γ_i' is calculated, then the composition of the surface solution N_i^s can be found from Eq. (1.115)

$$\Gamma_i' = z (C_i^s - C_i)$$

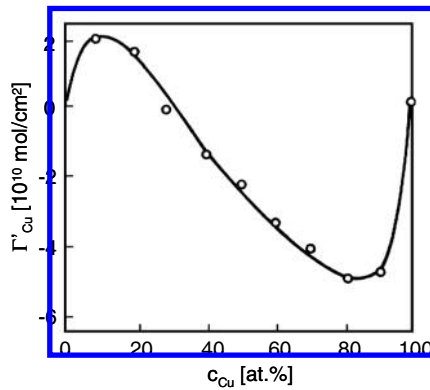
The relation between the activities of the components in surface and volume solutions according to Zhuchovitskii (Eq. (1.97)) is given by

$$\frac{a_1^s}{a_2^s} = \frac{a_1}{a_2} \exp \left(\frac{\gamma_2 - \gamma_1}{z RT} \right)$$

where, obviously, $(\gamma_2 - \gamma_1)/z$ means the heat of adsorption, which is a constant in the discussed model.

Eqs.(1.103)–(1.105) can be generalized to the case of several “types of sites” at the grain boundary [24]:

$$\gamma - \gamma_i = RT \sum_k z_k \ln \left(\frac{a_{ik}^s}{a_i} \right) \quad (1.181)$$

**FIGURE 1.19**

Isotherm of Cu adsorption on grain boundaries in Cu-Au at 850°C [24].

$$\frac{a_{1k}^s}{a_{2k}^s} = \left(\frac{a_1}{a_2} \right) \exp(q_k/kT) \quad (1.182)$$

where z_k is the number of sites of the k -th type, a_{ik}^s and q_k are the activity and heat of adsorption of the component i in a site k of the grain boundary. The adsorption of the i -th component is given by

$$\Gamma'_i = \sum_k (C_{ik}^s - C_i) \quad (1.183)$$

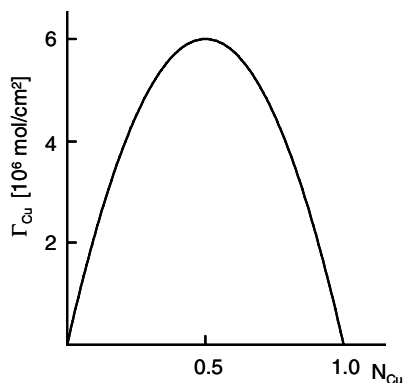
C_{ik}^s is the atomic fraction of the component i in a site k of the grain boundary ($C_{1k}^s + C_{2k}^s = 1$).

The boundary adsorption was calculated from Eq. (1.53) due to the fact that $d\mu_i = RT d \ln a_i$ and $\Gamma'_{Cu} + \Gamma'_{Au} = 0$. Using the Gibbs-Duhem equation the value of Γ'_{Cu} can be calculated from either $a_{Cu}(c_1)$ or $a_{Au}(c_1)$. The isotherm of the boundary adsorption of copper $\Gamma_{Cu}(c_1)$ is given in Fig. 1.19. The dependence $\Gamma'(c_1)$ is oscillating because of the minimum of the curve of $\gamma(c_1)$.

The experimental data, given above, were treated thermodynamically in [24], modifying the model until a reasonable agreement between experiment and calculation is reached. So, for the Langmuir adsorption and a non-ideal bulk solution ($\gamma_i = a_i/C_i$, $q' = q + RT \ln \gamma_1/\gamma_2$) we have

$$\Gamma'_1 = z c_1 (1 - c_1) \frac{e^{q'/RT} - 1}{c_1 e^{q_1/RT} - c_1 + 1} \quad (1.184)$$

It is evident from the equation that Γ'_1 has the same sign as q' . As can be seen from Eq. (1.184), the dependence $\gamma(c_1)$ must have a maximum. Since the experimentally determined dependence $\gamma(N_1)$ is quite different, this model

**FIGURE 1.20**

Isotherm of Cu adsorption on grain boundaries in system Cu-Ni at 950°C [91].

cannot explain the behavior of grain boundary surface tension.

The model of an inhomogeneous non-ideal solution for two types of sites at the boundary leads to unreasonably large values for the heat of adsorption for both types of sites:

$$q_1 \cong -4 \text{ eV}, \quad q_2 \cong 4 \text{ eV}$$

Finally, the authors of [24] came to the conclusion that the best agreement between experiment and calculations was observed for a homogeneous boundary and a non-ideal boundary solution.

The same result was obtained for grain boundary solutions in the binary system Cu-Ni [91]. Contrary to the system Cu-Au, the boundary solution is enriched by copper for all concentrations of the alloy (Fig. 1.20).

In general, systems with an unlimited solubility in the solid are exceptions. By far the majority of them are systems with a limited, and furthermore with a small, solubility. These systems have been our main interest inasmuch as all effects associated with the grain boundary adsorption clearly manifest themselves in these systems. The alloys Fe-P, Fe-S, Mo-C and others in which extremely small amounts of the second component drastically change the mechanical properties belong just to such a class of systems. The analysis of the thermodynamics of adsorption in the systems with limited solubility in the solid is given in [94]. Inasmuch as for systems with a narrow interval of solubility the thermodynamics of the bulk solution is unknown as a rule, the information regarding the properties of the grain boundary solution necessarily has to be extracted from the properties of the solvent and the dependence of the grain boundary surface tension on concentration. The expressions for the chemical potential of the solvent (μ_1) and the solute (μ_2) with regard to

the corrections to the equations for ideal solutions up to square terms are adaptable both for the bulk and the grain boundary solutions [94]:

$$\mu_1 = \mu_{10} + kT \ln (1 - c) + \varepsilon c^2 \quad (1.185)$$

$$\mu_2 = (\mu_{20} + \varepsilon) + kT \ln c + 3(1 - c)^2 \quad (1.186)$$

where ε is a parameter, which can be described as a heat of mixing, though it can include entropy terms, which are absent in the classical theory of regular solutions.

Introducing the thermodynamic activities

$$\mu_i = \mu_{i0} + kT \ln a_i \quad (1.187)$$

we can determine the thermodynamic characteristics of the boundary solution from the dependence $\gamma(c)$, Eqs. (1.85) and (1.103)–(1.104), (1.116). Actually,

$$\frac{\varepsilon^s}{kT} = \frac{1}{c^s} \ln \frac{a_1^s}{1 - c^s} \quad (1.188)$$

The boundary activity a_1^s can be found from Eq. (1.103), and the boundary concentration c_s from Eq. (1.116).

In accordance with the Gibbs adsorption equation and the Gibbs-Duhem equation the component concentration of the adsorption can be represented as

$$\Gamma_2 = -(1 - c) \frac{\partial \gamma / \partial c}{\partial \mu_2 / \partial c} = c \frac{\partial \gamma / \partial c}{\partial \mu_1 / \partial c} \quad (1.189)$$

(The adsorption capacity z enters into these equations as a parameter.)

It is reasonable for systems with a very narrow interval of solubility to consider the values of the thermodynamic characteristics of the boundary solution at $c \rightarrow 0$. In this case the “heat of mixing” ε and the heat of adsorption q take the form

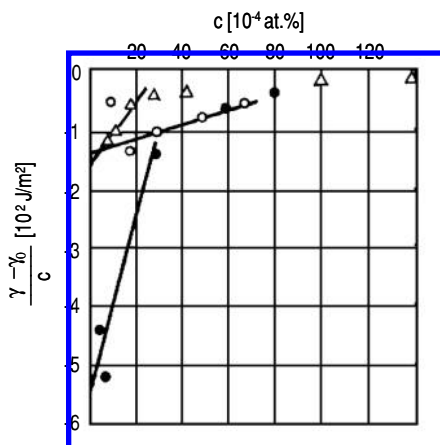
$$\frac{\varepsilon^s}{k} = \frac{\frac{\varepsilon}{kT} (1 - 2\alpha\gamma') - \frac{1}{2} [\alpha\gamma'' - \alpha^2 (\gamma')^2]}{(1 - \alpha\gamma')^2} \quad (1.190)$$

$$q = kT \ln (1 - \alpha\gamma') \quad (1.191)$$

where $\gamma' = (\partial \gamma / \partial c)_{c=0}$; $\gamma'' = (\partial^2 \gamma / \partial c^2)_{c=0}$; $\alpha = 1/(z kT)$; ε is the “heat of mixing” in the bulk solution.

So, for the determination of the main characteristics of the boundary phase it is sufficient to know, apart from the data of the bulk solution thermodynamics and the parameter z , the values of the first and second derivatives of the grain boundary surface tension with respect to the impurity concentration at $c = 0$.

In Fig. 1.21 the concentration dependencies of the grain boundary surface

**FIGURE 1.21**

Concentration dependence of surface tension in S-Fe-P (\circ); Cu-Sb (\bullet); Fe-Sn(Δ) [94].

tension for the systems δ -Fe-P, Cu-Sb and δ -Fe-Sn [95] are presented. The authors of [94] transformed the data to coordinates $(\gamma - \gamma(0))$ vs. c . The results of the calculation of the heat of adsorption and the heat of mixing in the grain boundary solution as a function of z are shown in Figs. 1.22 and 1.23. For comparison the results of the discussed calculation for the system Cu-Au [24] are shown too.

Of course, the value of the parameter z can only be determined from direct microscopic experiments. A reasonable value of z , which was discussed above, is apparently given by $2z_0 \leq z \leq 4z_0$, where z_0 is the capacity of a monolayer.

Let us sum up our experience in consideration of the data of macroscopic thermodynamic experiments. We have seen how the described scheme of thermodynamic analysis “works” in the case of grain boundaries, how it enables us to obtain quantitative data regarding the interaction of the atoms in the boundary solution from macroscopic measurements. However, the value of the adsorption capacity of grain boundaries can be obtained from direct microscopic experiments, so in this case the thermodynamic and microscopic investigations complement each other.

It would be very attractive to extract insight into the adsorption capacity from model theories of the grain boundaries, but currently there is no way to realize it. We conclude from the results that the heat of adsorption is relatively small in systems with unlimited solubility in the solid (~ 0.05 eV for Cu-Au and 0.02 eV for Cu-Ni), but the heat of mixing in the grain boundary solution is close to its magnitude in the volume value (for example, for the system Cu-Ni 0.13 and 0.11 eV, respectively) for all reasonable values of z .

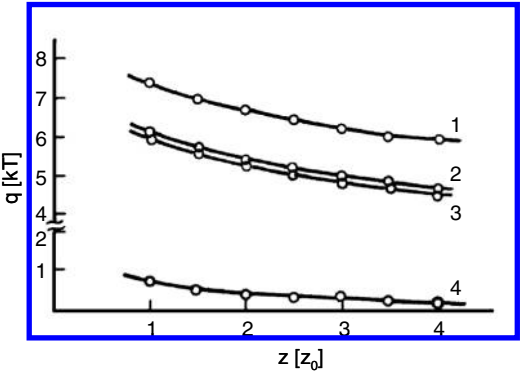


FIGURE 1.22
Calculated heat of adsorption on grain boundaries in Cu-Sb (1); δ -Fe-Sn (2); δ -Fe-P (3); Cu-Au (4) as a function of the adsorption capacity z .

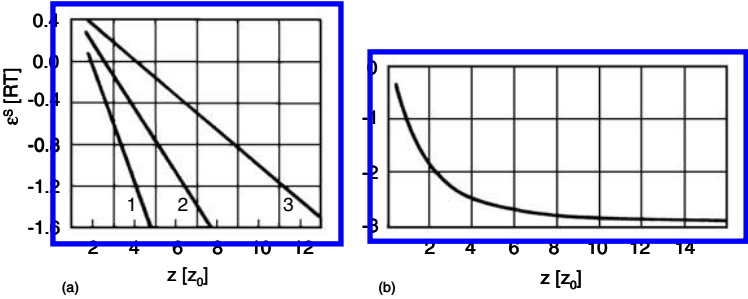


FIGURE 1.23
Calculated heat of mixing of grain boundary solution in δ -Fe-Sn (a):(1) δ -Fe-P (2); Cu-Sb (3) and Cu-Au; (b) as a function of the adsorption capacity z .

The situation is quite different in systems with a narrow solubility range. Here the heat of adsorption is high ($\sim 0.7\text{--}0.9$ eV), and thus the surface solution ceases to be dilute even if the amount of impurities in the system is so small that the bulk solution still can be considered as fully dilute. The values of the heat of mixing in the surface layer, on the other hand, are small for all reasonable values of the parameter z , even smaller than in systems with an unlimited solubility in the solid (less than 0.1 eV).

1.3.4 Adsorption of Vacancies at Grain Boundaries

A crystal of a pure material is a single component system, by definition. On the other hand, even in the ultra-pure material there is a defect, which may be considered as an impurity. The case at hand is the vacancies. Usually, the concentration of vacancies in the crystal is rather small (even at the melting point $c_v^{eq} \sim 10^{-4}$ where c_v^{eq} is the equilibrium concentration of vacancies). However, due to the adsorption, at grain boundaries the vacancy concentration and the associated thermodynamical effects can be much higher. The salient feature of vacancies as impurities should be taken into account. Contrary to ordinary impurity atoms, the number N_v of vacancies is determined by the minimum of the free energy G of the crystal. So, for vacancies $\partial G / \partial N_v = 0$ at $T, p = \text{const.}$ Since $(\partial G / \partial N_v)_{T,p} = \mu_v$, where μ_v is the chemical potential of the vacancies, the chemical potential of the vacancies in the equilibrium is zero. For dilute solutions $\mu_v = \mu_{0v} + kT \ln c_v$, since $\mu_v(T, c_v^{eq}) = 0$; $\mu_{0v} = -kT \ln c_v^{eq}$ and $\mu_v = kT \ln c_v / (c_v^{eq})$.

So, in accordance with Eq. (1.50), the adsorption of equilibrium vacancies does not change the thermodynamic properties of the grain boundary. The situation changes if the concentration of vacancies in the crystal deviates from equilibrium. Such a possibility has been discussed often in the literature. Actually, inasmuch as the formation and disappearance of vacancies do not occur at regular lattice points, but require diffusion from sources or to sinks, a non-equilibrium concentration of vacancies can be kept for a long time [96]. The redistribution of vacancies over short distances proceeds much faster. That is why a crystal can be obtained where a partial equilibrium between grain boundaries or interphases has been established whereas the concentration of vacancies in the crystal is not in equilibrium. Such a situation — high concentration of excess vacancies, regarding the equilibrium concentration of course, and their adsorption at the grain boundary — was considered in [96]. The result of such an adsorption can be a decrease of the grain boundary (generally, interface) surface tension, which is essential for recrystallization, formation of a new phase and so on. The relation between surface tension and vacancy concentration is determined by the Gibbs adsorption equation, on the one hand, and by one of the considered adsorption isotherms, on the other hand. Of course in the case of vacancy adsorption at an internal interface each adsorption site can be occupied by not more than one particle (vacancy). As a

result we obtain an equation where the left-hand side is the Gibbs equation for the dilute solution, while the right-hand side is the Langmuir isotherm [96]

$$-\frac{c_v}{kT} \frac{d\gamma}{dc_v} = \frac{z B c_v}{1 + B c_v} \quad (1.192)$$

where c_v is the vacancy concentration, $B = (c_v^e)_b / (c_v^e)_{\text{bulk}} = B_0 \exp(U/kT)$ is the adsorption constant, $(c_v^e)_b$ and $(c_v^e)_{\text{bulk}}$ are the solubility of vacancies at the boundary and in the bulk, respectively, i.e. the equilibrium concentration of vacancies in these parts of the crystal. Bearing in mind that $(c_v^e)_b$ and $(c_v^e)_{\text{bulk}}$ are the equilibrium thermal vacancy concentration for a given temperature in the grain boundary and the bulk, respectively, we obtain from Eq. (1.192) by integration

$$\gamma - \gamma_0 = -z kT \ln \left(\frac{1 + B c_v}{1 + B (c_v^e)_{\text{bulk}}} \right) \quad (1.193)$$

where γ_0 is the equilibrium grain boundary surface tension.

It is evident from Eq. (1.193) that any increase in vacancy concentration of the sample to a level above equilibrium (which is maintained for a time necessary to establish the equilibrium between grain boundary and bulk) results in a decrease of the free energy of the boundary. The estimation used in [96] shows that an oversaturation of the sample by vacancies by $c_v/c_v^e = 10^5$, which corresponds to quenching an aluminum sample from 900 K to room temperature, reduces the grain boundary surface tension by ~ 0.15 J/m². In [97] this problem was considered from a general thermodynamic viewpoint. It was shown that the equilibrium grain boundary surface tension γ_0 in a system with vacancies is given by

$$\gamma_0 = \gamma_1 - \frac{kT}{\bar{A}} \ln \left\{ 1 - (c_v^e)_{\text{bulk}} + \exp \left(\frac{\gamma_1 \bar{A}}{kT} \right) (c_v^e)_b \right\} \quad (1.194)$$

where γ_1 is the surface tension of a grain boundary in a sample without vacancies and \bar{A} is the partial area of the first component (matrix) in the boundary.

If the entropy part of the free energy of vacancy formation is small enough, then Eq. (1.194) can be simplified to

$$\gamma_0 \cong \gamma_1 - \frac{kT}{\bar{A}} \ln \left\{ 1 + \exp \left(\frac{\gamma_1 \bar{A} - H_v^b}{kT} \right) \right\} \quad (1.195)$$

where H_v^b is the enthalpy of vacancy formation in the bulk of the sample on the grain boundary.

If the exponential term is much smaller than one, the vacancy relaxation does not give any noticeable contribution to the grain boundary free energy. Certainly we are not able to estimate accurately the numerator in the exponent by thermodynamical means, but it can be shown that it is close to zero

[97]. An interesting corollary to this part of the discussion arises from further simplifying Eq. (1.194)

$$\gamma_0 \cong \gamma_1 - \frac{kT}{\bar{A}} \left\{ \frac{\gamma_1 \bar{A}}{kT} - \frac{H_v^b}{kT} \right\} \quad (1.196)$$

This means that if the vacancy concentration of the system is at equilibrium level, the grain boundary surface tension is determined by the enthalpy of vacancy formation alone. It was shown in [96, 97] also that the contribution of the vacancy concentration to the temperature dependence of the grain boundary surface tension is negligibly small.

This analysis of the influence of vacancies on the surface properties of defects in solids is fairly general and applicable to a variety of defects, such as grain boundaries, phase boundaries, dislocations, etc. Until now the studies of the influence of vacancies on the behavior of defects have mainly focused on the purely kinetic aspect of the effect, e.g. on the fact that an increase in vacancy concentration accelerates diffusion processes. We can see that there is also another aspect of this problem, and that is the reduction of the free surface energy due to the equilibrium adsorption of non-equilibrium vacancies.

The behavior of vacancies in an external stress field imposed on a system by rotary motion was considered in [97]. A practical application might be a running turbine blade. The distribution of vacancies across the sample can be expressed by

$$c_v = \exp \left(\frac{S_v}{k} \right) \exp \left(\frac{(-H_v - \frac{1}{2}m\omega^2 R^2)}{kT} \right) \quad (1.197)$$

where S_v , H_v are the entropy and enthalpy of vacancy formation, respectively, m is the mass of the atoms in the system, ω is the angular velocity and R is the radius of rotation of a given point in the sample. As can be shown, the chemical potential of the atoms must be kept constant for any part of the system during angular motion. But Eq. (1.197) indicates that N_v decreases with the radial distance R from the rotation axis. The formula (1.197), nevertheless, describes the equilibrium concentration of vacancies in an external field, created by angular motion.

Consideration of Eq. (1.53) shows that if the concentration of impurities, particularly vacancies, varies across the sample but the chemical potential is constant, then the adsorption will also be constant, even though the bulk concentration is changing. It was mentioned in [97] that although the enthalpy of vacancy formation H_v changes moderately (~ 0.01 eV) the climb rate of dislocation may be affected and, therefore, may influence the creep behavior of a material.

1.4 Applications of Grain Boundary Thermodynamics

1.4.1 Grain Boundary Phase Transitions

The problem of phase transitions at grain boundaries now attracts considerable attention from scientists in solid state physics and materials science. There are several reasons for this interest. Firstly, the progress in research in the field of free surfaces stimulates investigations of grain boundaries. Phase transformations at external surfaces of solids is a well-studied part of surface science with its own theoretical and experimental base. Secondly, successes in the theoretical description of grain boundaries, grain boundary thermodynamics and the kinetics of processes at grain boundaries have spurred their physical consideration and analysis. This is especially true with respect to the progress in experimental techniques, in particular bicrystal techniques. Further, the grain boundary phase transformations, by changing the structure of the grain boundaries, modify some of their physical properties, in particular the grain boundary mobility and the adsorption ability. Finally, the problem of grain boundary phase transformations is of great practical importance. In many cases grain boundaries determine the mechanical, chemical and electrical properties of a polycrystal. An illustration of the keen interest in grain boundary phase transitions is the number of review papers, dedicated to the problem [98]–[100].

The problem of phase transitions at the grain boundary has been dealt with for a long time. The fact that a grain boundary is a thin layer in a crystal with properties which are essentially different from the bulk ones gives cause to expect some specific transitions. On the other hand, phase transitions which are inherent in the bulk of the crystal might occur at grain boundaries at different magnitudes of the thermodynamic parameters (temperature, pressure, concentration, etc.).

Since the grain boundary symmetry is significantly lower than that of the crystal phase transitions at grain boundaries accompanied by a formation of dissolved interlayers near the boundary (or replacing) are likely to occur. Grain boundary melting is a most interesting phenomenon among many transitions and historically the first kind of grain boundary phase transition the existence of which was searched for experimentally and discussed theoretically [98, 99].

1.4.1.1 Is Grain Boundary Melting Possible?

Grain boundary melting implies that the grain boundary consists of melt, whereas the bulk of the adjacent grains is solid. It is presumed that a thermodynamic effect is responsible, inasmuch as we try to exclude kinetic factors from consideration. Sometimes, grain boundary melting is confused with a

lowering of the melting point by ΔT of a polycrystal due to the presence of grain boundaries.

As early as 1957 P. Shewmon came to recognize that the melting of a grain boundary at a temperature different from the bulk melting point is impossible [101]. If the grain boundary is in equilibrium with the bulk the chemical potentials of the atoms (both of matrix and solute) at the grain boundary μ_i^s must be equal to the chemical potentials of the atoms μ_i in the bulk.

The melting point, by definition, is the point of equality of the chemical potentials of crystal and liquid, which is why the grain boundary should melt simultaneously with the bulk of the crystal. Equilibrium effects (segregation of solute atoms, vacancies) cannot change this result.

Nevertheless, not all scientists were convinced by the thermodynamically clear conclusions of Shewmon. Li [102] proposed a thermodynamic cycle in accordance with which the grain boundary transforms into liquid at a temperature below the melting point. In accordance with Li's approach the grain boundary is considered as a strongly "deformed" layer of perfect crystal. Because of this, the melting temperature of such a "deformed" or "strained" crystal must be lower than the one of the perfect crystal. As an illustration Li considered a thermodynamic cycle 1–5, the final result of which is a liquid phase 5. The liquid phase is reached by the melting of the perfect crystal from one side, and by grain boundary melting from the other side (see the diagram on the next page). S_{solid} and S_{liquid} are the entropies of the solid with a perfect structure and the liquid, respectively.

Since

$$\Delta G_1 + \Delta G_2 + \Delta G_3 + \Delta G_4 = 0 \quad (1.198)$$

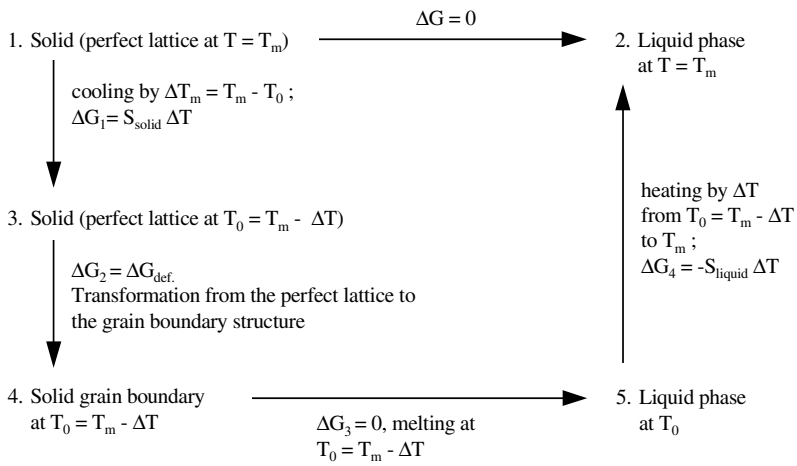
the decrease of the melting temperature ΔT in accordance with Li is equal to (1.199)

$$\Delta T = \frac{\Delta G_{\text{def}}}{S_{\text{liquid}} - S_{\text{solid}}} = \frac{\Delta G_{\text{def}}}{q} T_m \quad (1.199)$$

where q is the latent heat of fusion and T_m is the melting point of a perfect single crystal.

Nonetheless, the question put forward by Shewmon still remains unanswered: if the grain boundary is in equilibrium with the bulk of the crystal, its transformation into the liquid phase at a temperature **below** the melting point of the perfect crystal means that at this temperature (T_0) the crystal is in equilibrium with its own melt, which, in turn, signifies that at $T = T_0 < T_m$ the relation $\mu_i^{liq} > \mu_i^{solid}$ holds.

How does all of this fit into the thermodynamic scheme of Shewmon? Caution must be exercised in reducing equations from thermodynamic cycles. One of J.W. Gibbs' students recollected that Gibbs once had confused him with the derivation of the Carnot cycle. With the restrictions imposed by Li—the boundary of constant volume is formed by elastic deformation of the perfect crystal — equilibrium is possible if the chemical potentials of the atoms in



the bulk and at the grain boundary are equal:

$$\mu^s(p^s, T) = \mu(p, T) \quad (1.200)$$

As this takes place, the pressure in the bulk of the crystal differs from the pressure at the grain boundary. Actually, the deformed crystal can be “confined” only if a definite pressure is applied. The grains in a bicrystal play the role of a source of pressure with respect to the grain boundary; $p^s = p + p_0$. (The material inside the grain boundary is stretched and $p - 0$ is negative: $p_0 < 0$.) The conditions for an equilibrium will not be violated if we remove one of the grains and apply instead the corresponding pressure p :

$$p^s V^s = \mu(p, T) - \mu^s(p, T) \quad (1.201)$$

where V^s is the specific volume of the material inside the grain boundary.

The situation when two phases in equilibrium occur under different pressure is not very rare in thermodynamics. The droplet in an oversaturated vapor or small piece of solid in an oversaturated liquid can be cited as an example of a situation mentioned, when the droplet or solid particle is under higher pressure than the surrounding medium. The osmotic pressure, no doubt, is one of the most important effects in this series of similar phenomena (see Appendix A).

The difference in the chemical potentials in the right-hand side of (1.201) constitutes the work of deformation (with an opposite sign) for an isothermal transition from the perfect lattice to the grain boundary in Li's cycle as ΔG_{def} (ΔG_2 in the scheme of the cycle). At grain boundary melting ΔG_3 does not vanish, as it was reasoned by Li, but is equal to pV^s [103]

$$\Delta G_3 = p^s V^s = -\Delta G_{def} \quad (1.202)$$

Correspondingly, the temperature of melting for grain boundary is equal to:

$$T_0 = T_m + \frac{\Delta G_{def} + \Delta G_3}{S_{liquid} - S_{solid}} = T_m \quad (1.203)$$

The change of the grain boundary melting point is given by Li's expression (1.199). Let us try to derive this relationship under the repeatedly mentioned assumption of the equality of the chemical potentials at the grain boundary and in the bulk. The introduction of a grain boundary into the single crystal changes the chemical potential of its atoms by $d\mu$

$$\mu^s - \mu = d\mu \cong \frac{\Delta G_{def}}{N} \quad (1.204)$$

where N is the number of atoms in the former single crystal.

Let us consider the differences between the chemical potentials of the atoms in the perfect crystal (μ), in the “deformed” one μ^s (in the bicrystal) and in

the liquid (μ^L) (in the melt of the mentioned crystal), respectively. Expanding these differences into a series with respect to the temperature in the vicinity of the melting point of the perfect crystal (T_m) and of the crystal with a grain boundary (T_0), respectively, and restricting ourselves to the first term, we obtain:

$$\mu - \mu^L = (\mu - \mu^L)_{T_m} + \left[\frac{\partial (\mu - \mu^L)}{\partial T} \right]_{T_m} \Delta T + \dots \quad (1.205)$$

$$\mu^s - \mu^L = (\mu^s - \mu^L)_{T_0} + \left[\frac{\partial (\mu^s - \mu^L)}{\partial T} \right]_{T_0} \Delta T' + \dots \quad (1.206)$$

where ΔT and $\Delta T'$ is the temperature deviation from the melting point T_m and T_0 , respectively.

Let us consider the difference of the relationships (1.205) and (1.206) at the temperature $T = T_0$:

$$\begin{aligned} \mu^s - \mu &\equiv (\mu^s - \mu^L)_{T_0} - (\mu - \mu^L)_{T_m} + \\ &+ \left[\frac{\partial (\mu^s - \mu^L)}{\partial T} \right]_{T_0} \Delta T' - \left[\frac{\partial (\mu - \mu^L)}{\partial T} \right]_{T_m} \Delta T + \dots \end{aligned} \quad (1.207)$$

By definition, the terms $(\mu^s - \mu^L)_{T_0}$, $(\mu - \mu^L)_{T_m}$ on the right-hand side are equal to zero. The term $[\partial \mu^s - \mu^L / \partial T]_{T_0} \Delta T'$ is also equal to zero, because at $T = T_0$ we have $\Delta T' = 0$. So we come to the relationship

$$\mu^s - \mu \cong \left[\frac{\partial (\mu - \mu^L)}{\partial T} \right]_{T_m} \Delta T = (\Delta S)_{T_m} \Delta T = \frac{q}{T_m} \Delta T \quad (1.208)$$

But, on the other hand, the quantity $\mu^s - \mu$ is equal to $\Delta G_{def}/N$ (Eq. (1.204)). Consequently

$$\mu^s - \mu = d\mu = \frac{\Delta G_{def}}{N} = \frac{q}{T_m} \Delta T \quad (1.209)$$

and the decrease in the melting temperature of a bi- or polycrystal, associated with the grain boundaries, can be expressed as:

$$\Delta T = \frac{\Delta G_{def}}{NL} T_m \quad (1.210)$$

The decrease in the melting temperature of a polycrystal with grains of volume V , derived in the framework of similar assumptions, is equal to (see, for example, [70])

$$\Delta T = \frac{\Delta \gamma T_m}{qV^{1/3}} \quad (1.211)$$

where $\Delta \gamma$ is the difference of the grain boundary surface tension γ and the solid-liquid interface.

Representing ΔG_{def} as $\Delta G_{def} \cong \gamma N^{2/3}$ and taking into account that the surface tension of the solid interface wetted by its own melt is very small, we come to the conclusion that the decrease in the melting point of the grain boundaries obtained by Li:

$$\Delta T = \frac{\Delta G_{def}}{Nq} T_m = \frac{\gamma}{qN^{1/3}} T_m \quad (1.212)$$

practically fits the expression for the decrease in the melting point of a polycrystal caused by the presence of grain boundaries.

From the physical point of view this result is quite understandable: the crystal can be in equilibrium with its own melt at the temperature of melting, which is common for the whole crystal regardless of whether there are some defects in it or not. In other words, in systems of thermodynamical equilibrium the melting point is common for all parts of it. Strictly speaking, in such a system all properties reflect the property of the system, but not of a definite part of it. Unfortunately, the understanding of it has not been universally adopted. As an example, the statement that in an equilibrium crystal the energy of vacancy formation depends on the place where the vacancy was formed (dislocation, grain boundary, etc.), violates the first law of thermodynamics. Apparently, a vacancy being formed at a defect where the formation energy is smaller, for instance, than in the perfect crystal, and that vanishes in the perfect lattice gives us energetic profit, which, naturally, violates the first law.

On the other hand, the question arises whether or not the analysis given above implies that grain boundary melting is forbidden in the wide sense, in other words, whether a first-order phase transformation is possible at the grain boundaries.

A first-order phase transformation at the grain boundary means that at the point of phase transformation one bulk and two surface (grain boundary) phases, separated by the interphase line, are allowed to exist simultaneously. The possibility of such a transition follows from Gibbs' phase rule, and for the interphase in a single component system not more than two surface phases may be in equilibrium whereas for grain boundaries three surface phases may exist simultaneously. Actually, for a single component system with an interphase (two bulk phases) the number of degrees of freedom f is equal to zero when the total number of phases is equal to 4: because the number of the intensive parameters, including the surface tension, is equal to 3.

The additional degree of freedom in the system with grain boundaries is due to the fact that a grain boundary separates two regions of the same phase and distinguished by the orientation only. This permits the three grain boundary phases to be in equilibrium simultaneously [70].

Quite a number of investigations have been carried out to establish this experimentally. The most direct way is the study of the wetting of a grain boundary by the melt. In this case the boundary melting is accompanied by the angle Θ going to zero, where Θ is the dihedral angle at the root of a grain boundary groove, formed at the site of contact of a solid metal with its liquid.

This method was realized in [104]. Bismuth films were observed in the column of the electron microscope under the condition that they were melting under the electron beam. Thus, the site of contact of a solid sample containing a boundary with its own melt has been studied *in situ*. It appeared that the dihedral angle Θ was decreasing as long as the misorientation angle φ of grains increased, and at $\varphi^* \cong 7.5^\circ$ it fell abruptly from $\Theta^* = 34^\circ$ down to zero. Such behavior of Θ may be connected with the peculiarities of the orientation dependence of the surface tension σ_{sl} “crystal-melt.” Rottman [105] showed, however, that the values φ^* and Θ^* obtained from experiments, are not consistent with the symmetry conditions. Therefore, it is highly questionable if thermodynamic equilibrium was obtained in the measurements [104].

Hsieh and Balluffi tried to reveal grain boundary melting in Al bicrystals with tilt boundaries $[100]\Sigma 13(510)$, $\Sigma 17(410)$, $\Sigma 1(45^\circ)$ and the twist boundary $[100]\Sigma 1(45^\circ)$. A delocalization of the secondary grain boundary dislocation cores was not observed up to $T = 0.96T_m$. What is more, the aluminum foil was heated in the microscope column so that this portion was melted. At this point the expected amounts of a liquid phase were observed at a distance of $15\ \mu\text{m}$ from the boundary “foil-melt.” Estimates with the aid of the thermal conductivity equation demonstrated the fact that on this portion of the foil the temperature differed from the melting temperature by not more than 1° .

On this basis the authors [106] came to the conclusion that grain boundaries in aluminum do not melt up to $0.999T_m$ although the boundaries are being wetted by their own melt at $T \cong T_m$. In quite a number of works the question of high temperature behavior of grain boundaries was investigated by computer simulation techniques. The most interesting among them are those where the molecular dynamics method was utilized.

In the molecular dynamics computations the trajectory of each atom comprising the studied sample is simulated by means of an immediate solution of Newton’s equation of motion. Thus the molecular dynamics method yields a true picture of the dynamic behavior of the system.

The results of all investigations performed on the large-angle boundary $\Sigma 5$ show that, approaching the temperature of crystal melting, the degree of disorder contributed by thermal vibrations grows faster in the boundary region than in the bulk. For the quantitative characteristic of thermal disorder the order parameter is usually employed [107]:

$$\rho_J(K) = \frac{1}{N_J} \sum_{\ell=1}^{N_J} \langle \text{Re} \{ \exp(iKr_\ell) \} \rangle$$

where r_ℓ is the coordinate of the atom ℓ , K is the fixed vector of the reciprocal lattice, the brackets denote averaging over all generated trajectories and N_J is the total number of atoms in a selected part of the sample. Vanishing of ρ_J means that a corresponding part of the crystal is melted and a long-range order in the atom disposition is absent. Structure and self-diffusion along the boundary $[100](310)\Sigma 5$ in fcc material were studied. The thermal dependence

of ρ_J suggests that a phase transition in the boundary occurs. It means that ρ_J decreases faster with the increase of temperature than the corresponding value for atomic planes far from the boundary. Although the extrapolation of the value ρ_J to the melting point of the crystal, T_m , yields zero (liquid), at lower temperatures ρ_J remains finite. It indicates conservation of long-range order at the boundary. At $T = T_m$ the grain boundary self-diffusion coefficient D' is the same as for the liquid; however, at $T < T_m$ it is less than for the corresponding supercooled liquid. Based on these data the authors [107] confirm the fact that the boundary retains some order up to the crystal melting temperature. J.Q. Broughton and G.H. Gilmer chose another, “thermodynamic” approach to analyze the problem [108]. The criterion of grain boundary melting is: the grain boundary melts when twice the surface tension of a “crystal-melt” interface becomes less than that of the boundary. By determining the frequencies of normal oscillations of atoms at the boundary at $T = 0$, its entropy and the thermal dependence of the surface tension may be found. Then comparing it to the surface tension of a “crystal-melt” interface one may distinctly conclude whether this boundary is capable of melting or not. The authors performed such an analysis for three boundaries ([100] Σ 5(310), $\varphi = 36.9^\circ$; [011] Σ 11(332), $\varphi = 20.05^\circ$; [011] Σ 123(443), $\varphi = 14.65^\circ$). It appeared that the tendency of the boundaries to melt diminishes as the misorientation φ decreases. It should be noted that such a conclusion is a qualitative one, because a temperature dependence of the boundary surface tension (the boundary entropy) has not been taken into account.

Wolf was the first to use embedded atom potentials for molecular dynamics simulation of the high-temperature behavior of grain boundaries. For the twist boundary [001] Σ 29 in Cu up to $T = 0.94T_m$ the order parameter had a non-zero value in all atomic planes adjacent to the boundary [109], and the authors confirmed that grain boundary melting did not take place.

It should be noted that in a number of theoretical studies the high temperature behavior of various simplified grain boundary models (the lattice-gas model [110, 111], q -state Potts model [112]) was investigated. It was observed that a liquid layer occurs at the grain boundary significantly below the bulk melting point T_m . The thickness of the layer grows logarithmically when approaching T_m . It is not clear, however, whether these models describe the high-temperature behavior of grain boundaries adequately.

In summary, the authors [100] came to the conclusion that grain boundary melting in pure metals is rather doubtful.

1.4.1.2 Grain Boundary Wetting

We have discussed above the problem of grain boundary melting and arrived at the conclusion that it does not occur below the bulk melting point, while complete wetting of the grain boundary by the melt at the melting point does occur. Wetting of grain boundaries by the melt was repeatedly observed in two-component systems (Zn-Sn [113], Al-Sn [114], Al-Pb [115]). On the

two-phase coexisting line and below the wetting temperature T_w , the contact angle at the intersection of a grain boundary and the interface “solid-melt” is constant and roughly equals 180° . When $T \rightarrow T_w$, this angle decreases rapidly, and at $T > T_w$ a melt layer appears on the grain boundaries. So in a two-component material a liquid (or quasi-liquid) layer can occur on a grain boundary beyond the solid liquid coexisting line.

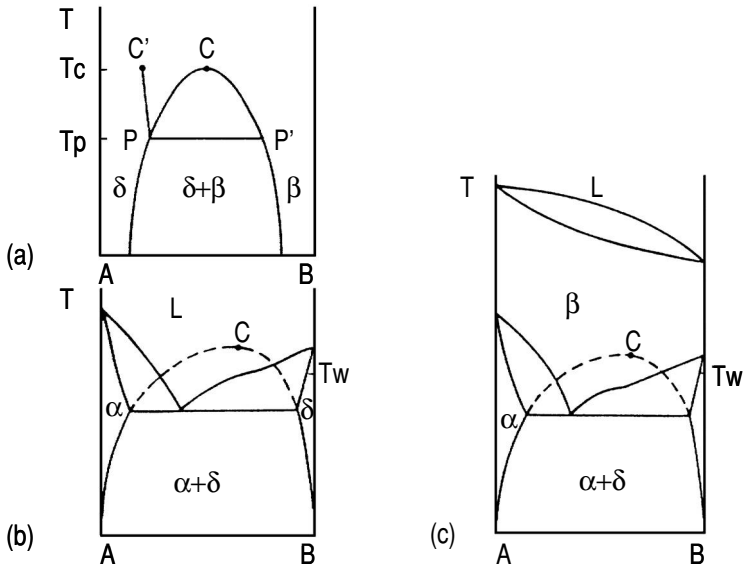
It was Cahn [116] who first understood that in a two-component solution the transition from incomplete to complete wetting must always occur at a temperature close to the critical point of immiscibility, and such a transition may have a “satellite” in a single-phase region prewetting or premelting phase transition. Consider a two-component liquid with miscibility gap $\delta + \beta$ which is in contact with a solid phase α (Fig. 1.24). The two-phase region is bounded by an arc-like curve with the critical point c . It has been shown by Cahn that when $T \rightarrow T_c$ the surface tension $\gamma_{\beta\delta}$ of the interphase boundary between β and δ decreases faster than the difference between the surface tensions $\gamma_{\alpha\delta} - \gamma_{\alpha\beta}$. This means that there should be a temperature T_w above which there must be a layer of phase β between the container wall α and the phase δ . At the temperature T_w a wetting transition occurs on the tie line PP' . Cahn showed also that a thin thermodynamical equilibrium layer of phase β at the α/γ boundary may exist even beyond the two-phase region of the phase diagram: when the line PC' is crossed, the prewetting transition occurs along the interphase boundary α/δ : a layer of phase β of finite thickness appears abruptly.

As shown in [100], Cahn’s speculations are of rather universal character, and they allow one to make some fruitful generalizations:

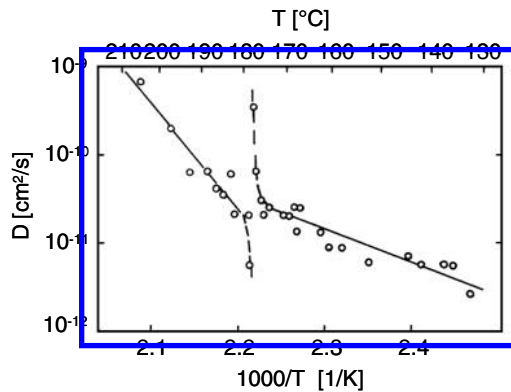
- (1) Wetting transformation may occur even if the phases β and δ are solid. It is only important that $\gamma_{\beta\gamma} \rightarrow 0$ when $T - T_c \rightarrow 0$.
- (2) For these phase transformations the third phase α is unnecessary. The layer of β may appear at grain boundaries of phase δ if $\gamma_{\delta\delta} > 2\gamma_{\beta\delta}$.
- (3) If the value of mixing enthalpy of the components A and B is positive and large enough then the critical point “C” may be “virtual.” In other words, it may be situated, for example, above the liquidus line (Fig. 1.24b).

Important for the wetting transition is only that in the vicinity of such a virtual point C the surface tension $\gamma_{\beta\delta}$ should decrease rapidly. Then we could observe, for example, the transition to complete wetting of a grain boundary by the melt.

In principle, the wetting phase may be solid. Actually, all the speculations which are true for the virtual decomposition curve (Fig. 1.24b) are true not only for the eutectic diagram, but also for a eutectoid system (Fig. 1.24c). Some data show indirectly that solid-phase wetting does exist. Such a phase transition can explain the stability of the grains of the α -phase in the β -phase

**FIGURE 1.24**

(a) Phase diagram for two-component liquid with miscibility gap. The wetting transition exists at T_p (by $T > T_p$ the phase β wets the boundary between liquid phase δ and solid container α). Between PC' and PC lines a thin layer of phase β exists on the interphase boundary δ/α . (b) Eutectic phase diagram with virtual critical point C. The wetting transition on the δ/δ boundaries exists at T_w , near the temperature of the small slope of the liquidus line. (c) Same situation as in (b), but for the eutectic diagram. In this case by $T > T_w$ the solid phase β must wet the grain boundaries δ/δ .

**FIGURE 1.25**

The temperature dependence of indium bulk interdiffusion coefficient D in tin. The discontinuity on the temperature at T_c corresponds to the critical point of the $\beta - \gamma'$ transition. Note the deviation from the Arrhenius law near T_c .

matrix in the two-phase ($\gamma + \beta$) region for different superplastic alloys [117] as well as the existence of a temperature threshold of grain boundary plasticity enhancement [118].

Two different situations of wetting near the critical point can be distinguished: the first one, when a layer of new phase is formed on the grain boundary (prewetting phase transition) and, secondly, when a grain boundary is replaced by a layer of the new phase (premelting phase transition). At prewetting transition the difference between the two phases must be small, while at a premelting transition the wetting phase may differ drastically from that of the bulk.

There is strong evidence for the occurrence of a prewetting phase transition at grain boundaries in the Sn-In system [119, 120]. In these works bulk and grain boundary diffusion of indium in tin was studied, and it was shown that there is a discontinuity in the temperature dependence of the bulk interdiffusion coefficient at the temperature of the critical point of the $\beta - \gamma'$ bulk phase transition. Analogously, but at lower temperature, discontinuities were also observed in the temperature dependence of grain boundary diffusivity, while at the bulk critical temperature these dependencies exhibited no singularities (Figs. 1.25–1.26). Such behavior may be understood according to the model of the prewetting transition given in Fig. 1.27. Suppose that an interlayer of high temperature β phase is formed at the temperature T_c^b at the grain boundaries. As the temperature is increased further, the thickness of this interlayer grows also, the structure of the grain boundary itself becoming analogous to the β -phase grain boundary structure rather than to that of the

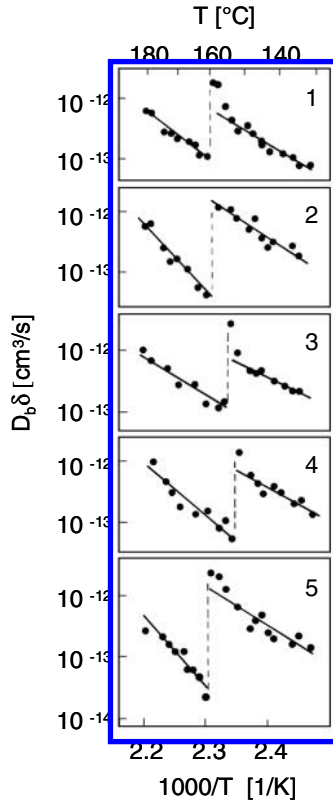
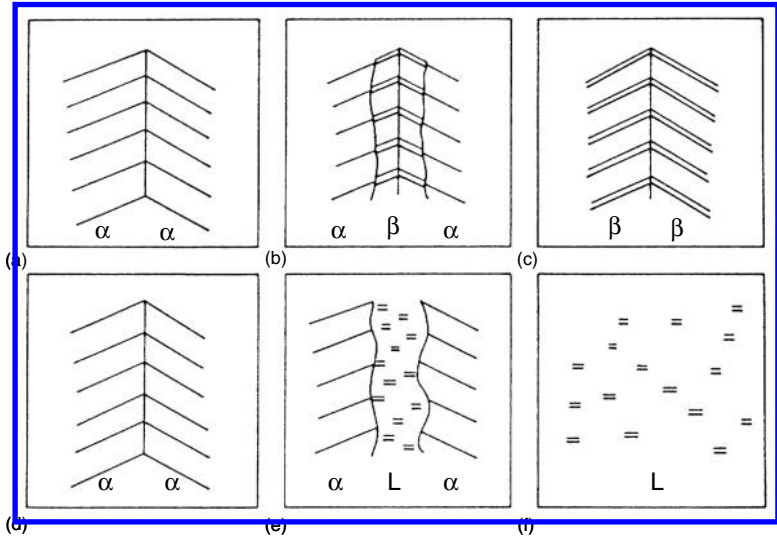


FIGURE 1.26

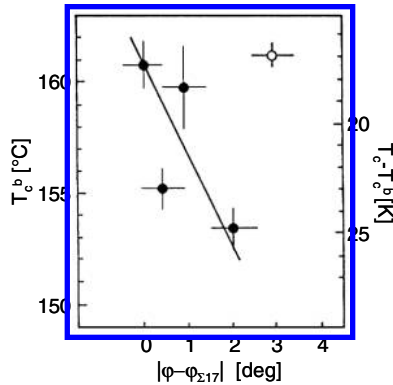
The temperature dependency of $D_b \cdot \delta$ for indium in $\langle 100 \rangle$ twist boundaries of tin for boundaries with different misorientation angles α : 1—28.1°; 2—29°; 3—27.5°; 4—30°; 5—31°.

γ' -phase. The thickness of this layer approaches infinity at the temperature of the bulk transition T_c , but this, indeed, does not affect the structure of the grain boundary. This is why the temperature dependencies of grain boundary diffusion coefficients have no singularities at T_c . The temperature T_c^b can be seen to decrease with increasing deviation of the misorientation angle from the coincidence misorientation $\varphi_{\Sigma 17} = 28^\circ$ (Fig. 1.28).

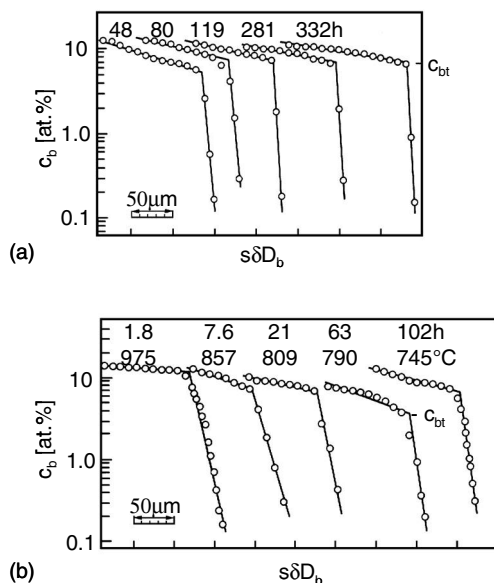
The premelting phase transition was discovered in grain boundaries of the quasi-binary system Fe(Si)-Zn in the course of a study of Zn diffusion along tilt grain boundaries in Fe-Si alloys [121]–[125]. It was found that the penetration profiles of Zn along grain boundaries in Fisher coordinates consist of two sections, one with a small slope at high Zn concentration and one with a

**FIGURE 1.27**

(a–c) Prewetting transition. Three interfaces are forming in place of the single GB, a new GB and two crystal-wetting-phase interfaces: (a) GB in the $\alpha - \beta$ -transition, and (c) GB in the β -phase. (d–f) Premelting transition. The GB is completely replaced by the wetting phase interlayer; (d) GB in the α -phase; (e) thin liquid layer between two α -crystals near the solid-liquid transition and (f) liquid phase for $T > T_m$.

**FIGURE 1.28**

Dependence of the $\beta - \gamma'$ -transition temperature T_c^b on grain boundaries in tin on the misorientation angle φ . T_c is the temperature of the critical point of the $\beta - \gamma'$ -transition in the bulk. (●) boundaries close to $\Sigma 17$, (○) general boundary, $\varphi_{\Sigma} = 28.1^\circ$ (17).

**FIGURE 1.29**

The dependencies of GB zinc concentration c_b on depth δ in a Fe-5at.%Si alloy. (a) At concentration c_{bt} the value of GB diffusivity $s\delta D_b$ changes abruptly at a constant temperature of 735°C and various annealing times t . Note that c_{bt} does not depend on t . (b) At concentration c_{bt} the value of diffusivity $s\delta D_b$ changes abruptly. The concentration c_{bt} depends on temperature.

large slope at low Zn concentrations (Fig. 1.29). The transition from one type of behavior to the other was found to occur at a definite Zn concentration c_{bt} at the GB. As shown, c_{bt} is independent of the annealing time. Consequently, this concentration is an equilibrium characteristic of a grain boundary (Fig. 1.29). It is an equilibrium characteristic of a grain boundary and depends on temperature. The ratio of the grain boundary diffusivities in the two regions was approximately 10^2 , which is an indication of the quasi-liquid nature of the layer present in the grain boundary at high Zn concentration. The dependence of c_{bt} on temperature (grain boundary phase diagrams) has been determined for alloys with different Si contents. Let us summarize the main features of the diagrams.

1. For all Si contents sharp peaks directed toward low Zn concentrations were observed in the grain boundary phase diagrams at the peritectic temperature of the Fe-Zn systems (782°C) (Fig. 1.30a,b). The nature of the peaks is connected with the fact that in the Fe-Zn system the virtual point of solid solution decomposition lies only slightly above the

peritectic temperature. It was shown [121] that the concentration c_{bt} at which a grain boundary phase transition occurs depends on the grain boundary surface tension γ and the surface tension γ_{SL} of the solid-liquid interface according to the expression

$$c_{bt} = c_0 - \frac{(\gamma - 2\gamma_{SL})^{\frac{n+1}{n}}}{b(Wn)^{1/n} (1 + n^{-1})^{\frac{n+1}{n}}} \quad (1.213)$$

where c_0 is the solubility limit of Zn in the alloy, W and n are the constants describing the repulsive interaction between two solid-liquid interfaces and b is a constant which may be determined from the thermodynamic data describing the alloy. Actually, all the miscellany of wetting phenomena may be obtained from an analysis of the free energy Ω^s of the wetting layer:

$$\Omega^s = 2\gamma_{SL} + \lambda\Delta g + V(\lambda) \quad (1.214)$$

where λ is the thickness of the wetting layer, Δg is the excess free energy of the wetting phase. The latter term describes the interaction of the “crystal-wetting phase” interfaces. The situation that the thickness of the wetting layer gets infinitely large when the line of phase coexistence is approached ($\Delta g \rightarrow 0$) is called complete wetting. Because the equilibrium thickness of the wetting layer is determined by minimization of Eq. (1.214) with respect to λ , complete wetting can be observed only in the case when the two following conditions are satisfied:

- (1) $2\gamma_{SL} < \gamma$
- (2) $V(\lambda)$ must have a global minimum for $\ell \rightarrow \infty$, in other words, the interfaces “crystal-wetting phase” must repel one another. In [100] it was assumed that $V(\lambda)$ depends on λ by a power law

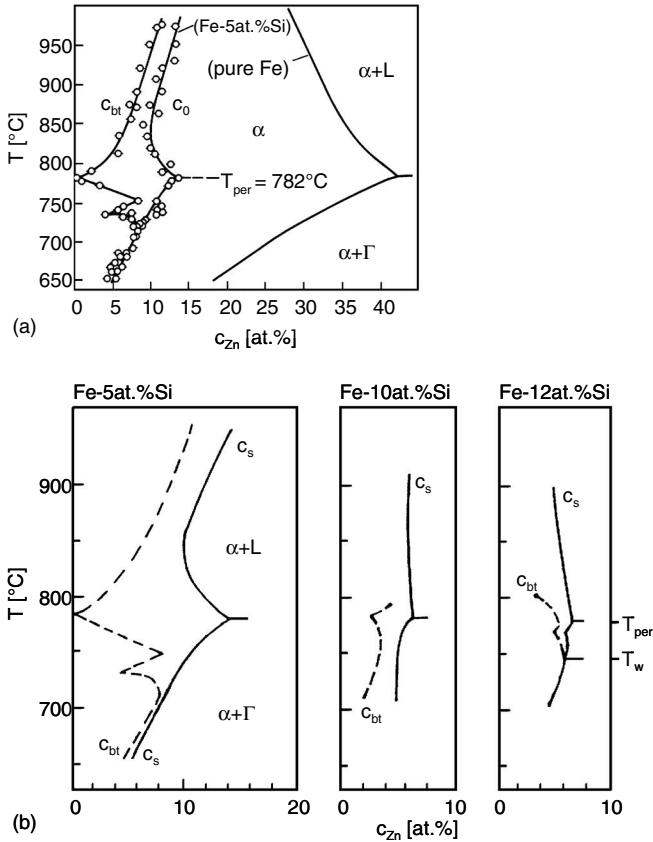
$$V(\lambda) = W/\lambda^n \quad (1.215)$$

Expanding Δg into a power series in $(c_0 - c_b)$, where c_0 is the bulk solubility limit (solvus or solidus) and restricting ourselves to the first term we obtain

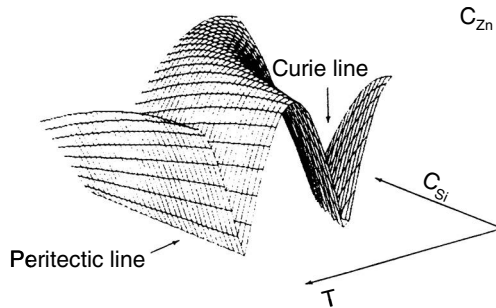
$$\Delta g = b(b_0 - c_b) \quad (1.216)$$

The function $\Omega^s(\lambda)$, determined by means of Eqs. (1.214)–(1.216), has a minimum at $\lambda_0 = \left[b(c_0 - c_b/nW)^{-1/n+1} \right]$, where at $\Omega^s(\lambda_0) = \Omega_0 = \gamma$ the premelting transition occurs. Under this condition the relationship (1.213) was obtained. In the vicinity of the critical point, γ_{SL} decreases drastically, and, according to Eq. (1.213), c_{bt} also decreases.

2. In the alloy containing 5at%Si a peak in the grain boundary phase diagram directed toward low Zn content was observed in the temperature vicinity of the Curie point (Fig. 1.30). Such effects are often observed at the intersection of a line of a second order phase transition with a line

**FIGURE 1.30**

(a) The temperature dependencies of c_{bt} and c_o vs. Zn concentration. The solubility limit of zinc in pure iron is also displaced (solidus and solvus). Γ is an intermetallic compound and L is the liquid. (b) Section of Fe-Si-Zn phase diagrams for alloys with different silicon contents. The dotted lines show the temperature dependencies of the concentration c_{bt} at which the GB diffusivity changes drastically (premelting phase transition). c_s is the bulk solubility limit of Zn in the Fe-Si alloys. T_{per} is the peritectic temperature of the binary Fe-Zn system.

**FIGURE 1.31**

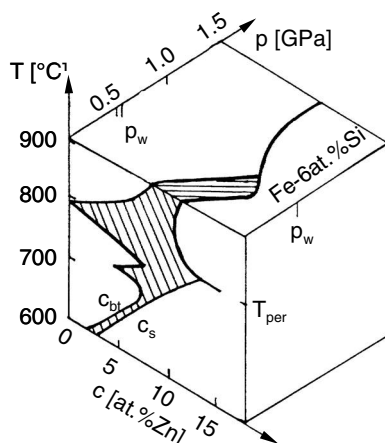
Three-dimensional grain boundary premelting surface in “Zn concentration-Si concentration-temperature” space.

of a first-order phase transition [126, 127]. Here, a transition from complete to incomplete wetting may occur. The transition of the alloy into a ferromagnetic state creates a force of attraction between the grains. Accurate calculations show that the “magnetic” part of the function $V(\lambda)$ is comparable with the “non-magnetic” part [128, 129]. All of the above may be illustrated by a three-dimensional grain boundary phase diagram with the coordinates “temperature-concentration-concentration” (Fig. 1.31). Such a diagram looks like a two-dimensional surface below which (at low Zn concentrations) grain boundaries with low Zn adsorption are stable and above which grain boundaries exist in a premelting state.

3. Below the Curie point the premelting line is very close to the line of the bulk solubility limit, and below the temperature of atomic ordering A2-B2 in an alloy containing 12at%Si the complete wetting disappears simultaneously with the grain boundary premelting phase transition. So it can be concluded that atomic and spin ordering shorten the region of stability of a grain boundary in a premelted state. In the case of a ferromagnetic transition it is connected with the long-range attractive contribution to the free energy of the premelting layer, the origin of which was discussed above.

In the case of atomic ordering A2B2 in the bulk, an additional contribution to the free energy of both the grain boundary and the premelting layer arises due to the disorder in the interface core. Since the premelting layer with a liquid-like structure is more disordered than the grain boundary, such a contribution should be greater for a premelting layer, and it loses its stability in the ordered state of the bulk.

4. It was shown [130] that when the hydrostatic pressure is increased the re-

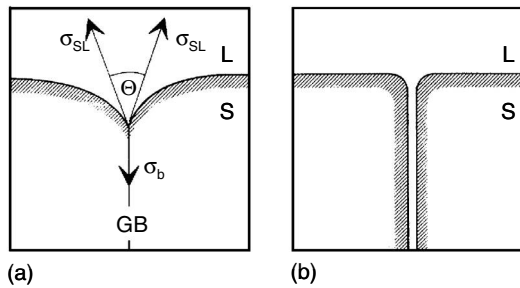
**FIGURE 1.32**

Three-dimensional phase diagram with the locations of the bulk solubility limit of Zn (c_s) and the concentration of the premelting transition on grain boundaries, c_{bt} .

gion of stability of the premelting layer at the grain boundary decreases, and at some critical pressure p_w one can observe the transition from complete to incomplete wetting of the grain boundary by the Zn-rich melt with the simultaneous disappearance of the grain boundary premelting transition. In Fig. 1.32a schematic three-dimensional grain boundary phase diagram in coordinates “temperature - Zn concentration - pressure” is shown in two sections, at $p = 0$ (isobaric) and at $T = 905^\circ\text{C}$ for different pressures (isothermal). The disappearance of grain boundary wetting and premelting is connected with a higher excess volume of the premelting layer as compared with that of an “ordinary” grain boundary.

As mentioned at the beginning of the discussion of this item, wetting of grain boundaries by the melt was repeatedly observed [100, 113, 114]. Cahn’s paper [116] gave a new impetus to research in this area [131]–[134]. Unfortunately, the exploration of wetting phenomena at solid/solid interfaces is much more poorly developed than, in part, that for planar solid substrates and fluid mixtures. From our point of view this is due to the considerable experimental difficulties connected with measurements of the boundary which is “hidden” inside the sample.

There is a good reason to believe that the experimental technique developed in [135]–[137] permits us to improve our understanding of this phenomenon. What is a wetting transition? Let us consider a system in which a solid bicrystal is in contact with a melt. The equilibrium of a bicrystal in contact with a liquid metal can be characterized by the dihedral angle Θ at the site of

**FIGURE 1.33**

Partial (a) and complete (b) wetting of a grain boundary by a melt (schematically); γ and γ_{SL} are the excess free energies of the grain boundary and solid/liquid interface, respectively. L and S denote the solid and liquid phases, respectively.

intersection of the grain boundary and the solid/liquid interface (Fig. 1.33). The angle Θ is defined by the condition of equilibrium

$$\cos\left(\frac{\Theta}{2}\right) = \frac{\gamma}{2\gamma_{SL}} \quad (1.217)$$

The two situations $\Theta > 0$ and $\Theta = 0$ correspond to a partial and complete wetting, respectively. If some intensive thermodynamic parameters like temperature, composition, pressure or the grain boundary misorientation angle are altered, a transition from partial to complete wetting can occur. This is a wetting phase transition, which can be of first or second order (Fig. 1.33b). When the situation is reversed and the temperature is decreased or the pressure is increased the angle Θ changes from zero to non-zero values. This is called the dewetting phase transition (Fig. 1.34).

First of all we would like to discuss the effect of grain boundary misorientation on the wetting parameters, then the influence of high pressure on the grain boundary wetting. Finally, the important physical problem will be discussed — to which order of phase transition the grain boundary wetting relates. There are few experimental data concerning the effect of the grain boundary misorientation on the wetting parameters. In the Cu-In system the value of the wetting temperature (T_w) for a symmetrical $\langle 011 \rangle$ tilt grain boundary close to the symmetrical coherent twin boundary was only about 30°C higher than for the general $141^\circ \langle 011 \rangle$ grain boundary, though the excess free energy difference for these grain boundaries was about 50% in pure Cu [135]. In the Al-Sn system the value of T_w for a symmetrical $38.5^\circ \langle 011 \rangle$ grain boundary close to the $\Sigma 9$ coincidence misorientation was about 13°C higher than for the general $32^\circ \langle 011 \rangle$ grain boundary [136].

One can see that there is an influence of the grain boundary misorientation

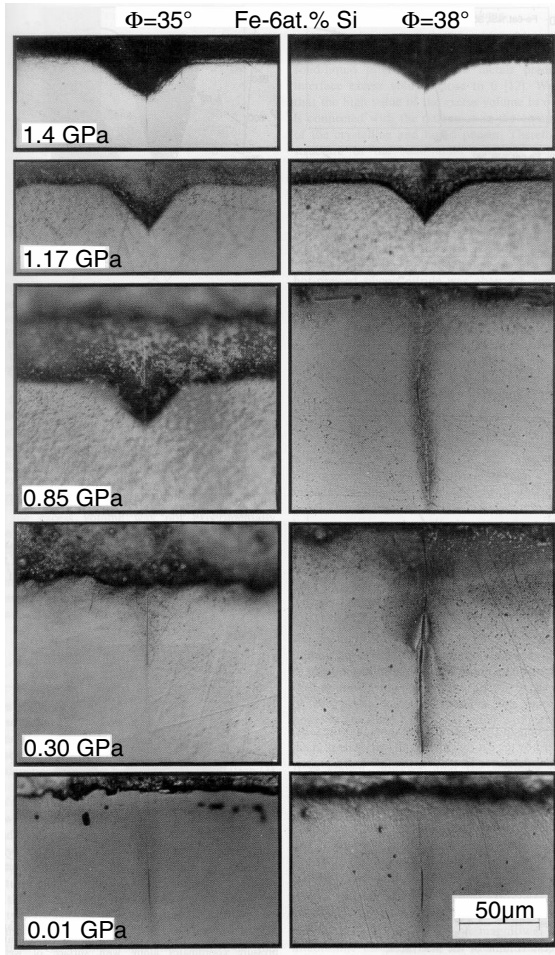
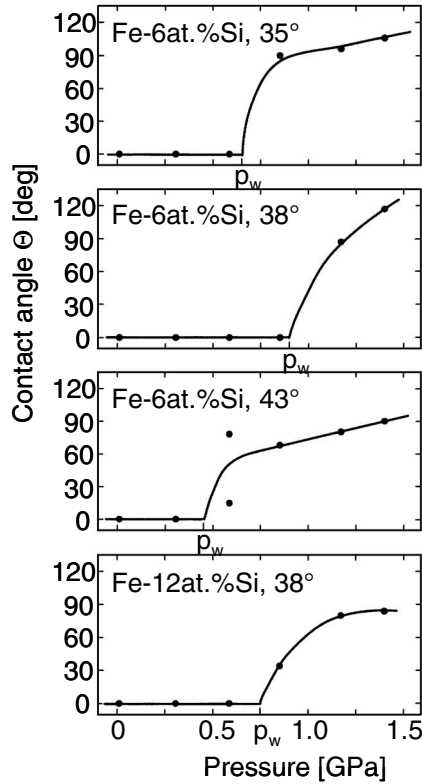


FIGURE 1.34

Optical micrographs of contact areas between Fe-Si bicrystals (bottom, bright) and Zn-rich melts (top, dark) after annealing at 950°C under different hydrostatic pressure.

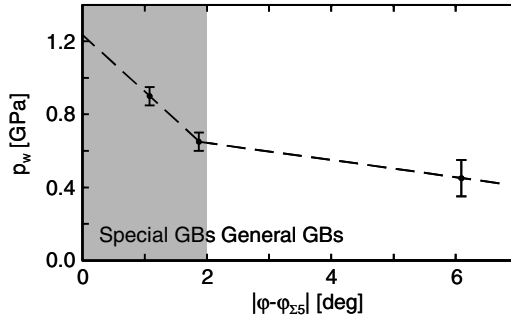
**FIGURE 1.35**

Pressure dependence of contact angle Θ for various grain boundaries. As the pressure increases, the dewetting transition from complete to partial (incomplete) wetting occurs at p_w .

and energy on the value of T_w . However, the magnitude of the temperature change cannot be predicted in a straightforward manner.

In [137] the influence of pressure on the wetting of grain boundaries in bicrystals of Fe-Si by a Zn-rich melt was studied. The transition from complete ($\Theta = 0$) to partial ($\Theta > 0$) wetting was found to occur as the pressure increased (Fig. 1.35). The dewetting transition pressure is higher for special boundaries than for general ones (Fig. 1.36). The investigation of the dewetting under a high hydrostatic pressure enables us to estimate the resulting excess volume of grain boundary and solid-liquid interfaces. Actually, from Eq.(1.217) it follows that

$$\Theta = 2 \arccos \left\{ \frac{\gamma^0 + p\Delta V_b}{2(\gamma_{SL}^0) + p\Delta V_{SL}} \right\} \quad (1.218)$$

**FIGURE 1.36**

Dependence of grain boundary phase transition pressure p_w on deviation from $\Sigma 5$ coincidence misorientation. The region of existence of the special $\Sigma 5$ grain boundary is shaded.

where γ^0 , γ_{SL}^0 are the excess energies of the grain boundary and solid-liquid interfaces at fixed constant Zn concentration; ΔV_b and ΔV_{SL} are the excess volumes of these interfaces, respectively. It was found that the excess volume ΔV_{SL} for all four boundaries studied is $\Delta V_{SL} = 2.5 \pm 1.4 \text{ \AA}$.

The problem of the order of the grain boundary wetting phase transition was discussed in [136]. If the grain boundary wetting transition is of first-order a discontinuity in the grain boundary and surface entropies should be observed, which in our case leads to a discontinuity of the temperature derivative of the grain boundary energy at T_w : $[\partial\gamma/\partial T - \partial(2\gamma_{SL})/\partial T]_{T=T_w} \neq 0$ [116, 134]. If the grain boundary wetting follows the second order, $[\partial\gamma/\partial T]_{T=T_w} = [\partial(2\gamma_{SL})/\partial T]_{T=T_w}$. The theory [131] predicts the law of the temperature dependence $\Theta(T)$ in the vicinity of the wetting point: for the first-order phase transition

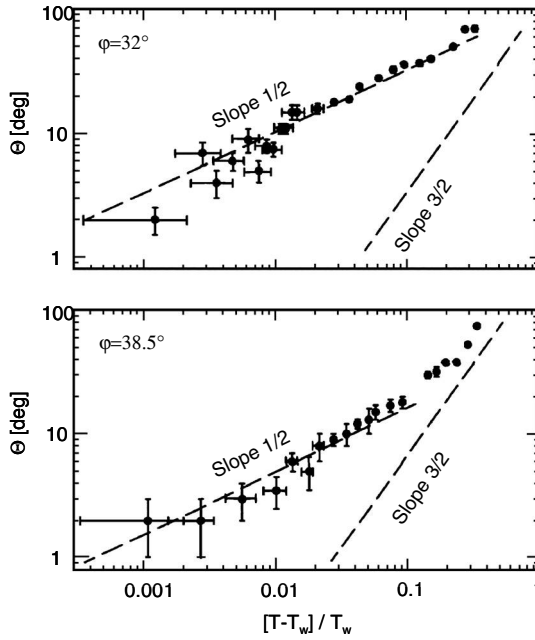
$$\Theta \sim \left(\frac{T_w - T}{T_w} \right)^{1/2};$$

for the second order

$$\Theta \sim \left(\frac{T_w - T}{T_w} \right)^{3/2}$$

Grain boundary wetting in the system Al-Sn was studied with bicrystals with symmetric tilt $\langle 011 \rangle \langle 001 \rangle$ grain boundaries with the misorientation angles 32° (random grain boundary) and 38.5° (near $\Sigma 9$). The observed hysteresis is consistent with the assumption that the wetting transition is of first-order.

An additional reason for grain boundary wetting phase transition to be of first-order is the temperature dependence of the contact angle in the vicinity of the wetting point (Fig. 1.37). As mentioned above, the theory predicts a

**FIGURE 1.37**

The dependence of the contact angle Θ on $(T - T_w) / T_w$. Curves with slope 1/2 and 3/2 (dashed lines) correspond to wetting phase transition of first and second order, respectively [136].

$\Theta \sim (T_w - T)^{1/2} / (T_w)^{1/2}$ behavior for a wetting transition of first-order and $\Theta \sim (T_w - T)^{3/2} / (T_w)^{3/2}$ for a transition of second order. As is easy to see, for both investigated grain boundaries the experiments count in favor of the first-order phase transition [136].

1.4.1.3 Structural Phase Transitions

Another type of grain boundary phase transitions which is very important both for theory and applications is the structural phase transitions¹. By using the method of thin film bicrystals Sickafus and Sass found a change in the dislocation structure of small-angle $\langle 101 \rangle$ twist boundaries in bicrystals of a Fe-Au alloy when the content of gold was increased [138], a change of the dislocation structure both of low- and high-angle boundaries, in iron bicrystals with antimony and sulphur [139, 140]. Although the authors postulated the change in the structure was a sign of a grain boundary phase transition, it needs to be analyzed in more detail. A first-order phase transformation represents itself in a large, abrupt change in the structure and properties. So, only the changes in the grain boundary structure associated with the increased content of impurities cannot be taken as proof of the grain boundary phase transition.

It is known that special grain boundaries of arbitrary orientation are faceted, which is connected with the anisotropy of the surface tension. The facets are located in those planes where the surface tension is minimal. A similar phenomenon is observed also at the surface of solids: many single crystals are of a faceted shape with flat faces corresponding to low-index crystalline faces which manifest extremely low surface tension. At a small deviation of a face orientation from a low-index one, steps occur on the surface and the energetically favorable orientation is practically conserved. With increasing temperature the contribution of the steps to the entropy increases and at a definite temperature the formation of steps may become energetically favorable.

In principle, the same phenomenon can be observed also at grain boundaries. At a definite temperature the boundary may become unstable with respect to the concentration of steps and transform into an atomically rough interface. The surface tension of such a boundary must be isotropic, the boundary becomes flat (if this shape corresponds to the minimal energy) but somewhat diffuse. It is noted that the vanishing of faceted boundaries was observed in experiments with polycrystals, but it was doubtful whether this effect was connected with the roughening transition or was of kinetic nature. A special experiment with a defined single grain boundary was performed by Balluffi et al. [141]. In his experiments $\Sigma 3 \langle 111 \rangle$ asymmetric tilt boundaries in Au and Al

¹The reader is referred to Chapter 2 for an overview and the terminology of grain boundary structure.

and an asymmetric $\Sigma 11$ boundary in Al manifested clearly defined facet structure at room temperature. In situ observation during heating of the samples with grain boundaries demonstrated that with increase in the temperature the facets gradually diffused and at high temperatures the boundaries flattened. What is of importance is that it was shown that this effect was reversible. Similar effects of reversible faceting/defaceting of grain boundaries in a Cu film was observed under deposition/evaporation of Bi [142].

Structural changes of grain boundaries must be accompanied by a change in their properties such as surface tension, mobility, diffusion permeability, sliding rate along the boundaries and so on. Therefore, one can study a grain boundary phase transition by observing the change of these and other properties. Watanabe [143] investigated the temperature dependence of the grain boundary sliding rate for seven different symmetric tilt boundaries in zinc. For six of the seven investigated boundaries distinct changes of slope were observed at various temperatures T_p . The maximal value of T_p was observed for the special misorientation $\Sigma 9\langle 10\bar{1}0 \rangle$ and for the boundary with a misorientation angle of 16.5° — the smallest of all the investigated misorientation angles — a change of slope was not observed at all. The authors reasoned that a grain boundary phase transition at temperature T_c had been observed in the studied boundaries.

The surface tension and the mobility of the special boundary $\Sigma 17$ and in the vicinity of the special boundary $\Sigma 17$ in tin at different temperatures were studied in [144]. The ratio of the surface tension γ_1 of the special boundary to that of the non-special boundary γ was measured at a triple junction, where one special and two non-special (random) boundaries were in contact (Fig. 1.38). In the investigated temperature range ($0.85\text{--}1.0T_m$) the temperature dependence of the ratio γ_1/γ showed a change of slope (Fig. 1.38) which is a characteristic feature of a first-order phase transition. In this work the mobility of the same special boundaries was studied in the same temperature interval. For the same boundaries an abrupt decrease in the mobility with increasing temperature was observed. The temperatures T_c at which an abrupt change of the mobility occurred were in good agreement with the temperatures of the change of slope of the temperature dependence of the grain boundary surface tension. It is believed that the phase transition “special grain boundary-random grain boundary” was observed in the discussed work [144]. The equilibrium phase diagram “special grain boundary random grain boundary,” based on the mentioned results, is presented in Fig. 1.39. The “special boundaries,” strictly speaking, the boundaries with the properties of special boundaries, are located under the curved part of the diagram. It was also demonstrated that with an increasing content of surface-active impurities in tin the temperature T_c decreases proportionally to the logarithm of impurity concentration. To understand the dependence of the temperature of the grain boundary phase transition on misorientation of the grains and the impurity concentration, a surface analogy of the Clausius-Clapeyron equation is required. This relation connects the change in the phase equilibrium tem-

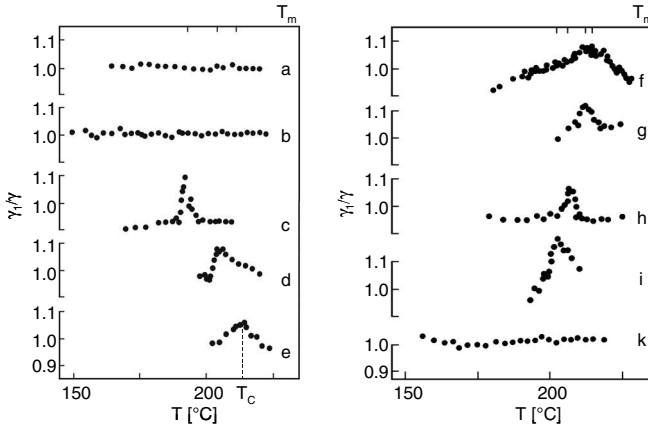


FIGURE 1.38

Temperature dependence of the surface tension of special grain boundaries (γ) and of general boundaries ($\gamma_2 = \gamma_3 = \gamma$). Misorientation angles: (a) 25.5° ; (b) 26.0° ; (c) 26.5° ; (d) 27.0° ; (e) 27.7° ; (f) 28.2° ; (g) 28.5° ; (h) 29.0° ; (i) 29.5° ; (k) 30.0° [144].

perature with the change in other intensive variables.

Let us consider the Gibbs adsorption equation written for both of the grain boundary phases [144, 145]:

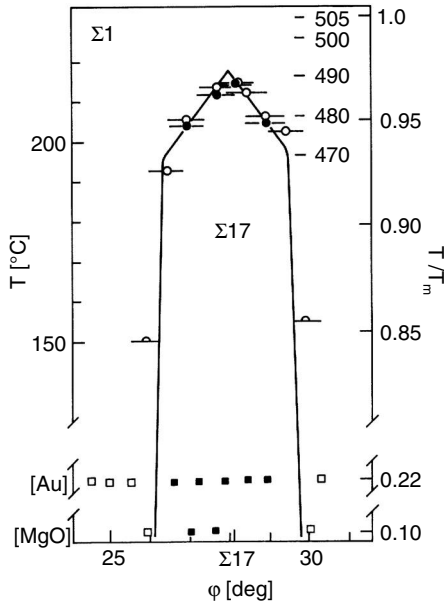
$$d\gamma = -S^p dT - \sum_i \Gamma_i d\mu_i + \hat{\xi} d\hat{n} \quad (1.219)$$

where γ is the surface tension of a boundary, S^p is the surface excess of the boundary entropy (in a solution), Γ_i is the adsorption of the i th component at a boundary, $d\hat{n}$ means a small change in the macroscopic geometric parameter of a boundary. The role of the geometric parameter can be played by angle of misorientation, the angle of inclination, the deviation of the tilt (twist) axis from a given value and so on. For instance, if the angle of misorientation is φ , then $\hat{\xi} = \partial\gamma/\partial\varphi_{T,\mu_i}$. At the point of grain boundary phase transition the surface tension of both grain boundary phases must be equal (in accordance with the condition of mechanical equilibrium). Then for a binary alloy

$$(S_A^p - S_B^p) dT + (\Gamma_A - \Gamma_B) d\mu + (\Gamma_A' - \Gamma_B') d\mu' + (\hat{\xi}_B - \hat{\xi}_A) d\hat{n} = 0 \quad (1.220)$$

where A and B are the indices denoting the two different grain boundary phases; the values with the primes refer to the atoms of a dissolved substance and those with the superscript p to the solution in general. Furthermore, we shall consider the bulk solution to be ideal. Then

$$d\mu' = RT d(\ln c) + (R \cdot \ln c - S_v') dT \quad (1.221)$$

**FIGURE 1.39**

Range of existence (phase diagram) of $\Sigma 17$ special boundaries and $\Sigma 1$ general boundaries in tin constructed with respect to T_c — the temperature of the maximum in Fig. 1.38. Open circles — T_c values obtained from the temperature dependence of the surface tension, solid circles — T_c values obtained from the temperature dependencies of the boundary migration rate. The lower part of the figure represents published data on the structures of special $\Sigma 17$ twist boundaries in gold at $T/T_m = 0.2$ [W. Bollmann, in: *Crystal Defects and Crystalline Interfaces*, Springer, Berlin (1970), p. 316] and in magnesium oxide at $T/T_m = 0.1$ [G. Masson, S.-Y. Boos and J. Merbeuval, *Surf. Sci.*, 31 (1972) p. 115]. Solid squares — boundaries which exhibited secondary grain boundary dislocations, open squares — boundaries formed exclusively by primary grain boundary dislocations [144].

$$d\mu = -RTdc - (Rc + S_v) dt \quad (1.222)$$

where c is the bulk impurity concentration, S_v is the molar entropy in the bulk solution. From (1.220) and (1.222) we obtain the relationship between the temperature of a grain boundary phase transition and the bulk concentration of the impurity, the values of grain boundary adsorption and the macroscopic geometric parameters \hat{n} :

$$dT = RT \frac{(\Gamma'_A - \Gamma'_B) d(\ln c) - (\Gamma_A - \Gamma_B) dc + \left[\left(\hat{\xi} \right)_B^p - \left(\hat{\xi} \right)_A^p \right] \frac{d\hat{n}}{RT}}{S_B^p - S_A^p - (\Gamma'_A - \Gamma'_B) (R \ln c - S'_v) + (\Gamma_A - \Gamma_B) (Rc + S_v)} \quad (1.223)$$

Equation (1.223) is effective for an analysis of the experimental results. Following [145], let us consider the dependence of the grain boundary phase transition temperature in pure tin on the misorientation angle of grains around the tilt axis $\langle 100 \rangle$. Three phases (two grain boundary phases and the bulk one) are co-existing at the grain boundary transformation point. The chemical potentials of the atoms of these phases are equal:

$$\mu_A^s(\gamma, T, \varphi) = \mu_B^s(\gamma, T, \varphi) = \mu_v(p, T) \quad (1.224)$$

At $p = \text{const.}$

$$\begin{aligned} -\bar{A}_A d\gamma - S_A dT + \left(\frac{\partial \mu_A^s}{\partial \varphi} \right) d\varphi = \\ = -\bar{A}_B d\gamma - S_B dT + \left(\frac{\partial \mu_B^s}{\partial \varphi} \right) d\varphi = -S_v dT \end{aligned} \quad (1.225)$$

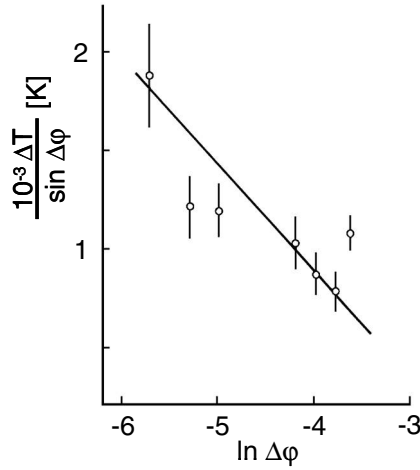
Then we come to

$$\begin{aligned} \left(\frac{dT}{d\varphi} \right)_e &= \frac{\bar{A}_A \left(\frac{\partial \mu_B^s}{\partial \varphi} \right) - \bar{A}_B \left(\frac{\partial \mu_A^s}{\partial \varphi} \right)}{\bar{A}_A (S_B - S_v) - \bar{A}_B (S_A - S_v)} = \\ &= \frac{\bar{A}_A \bar{A}_B \left\{ \left(\frac{\partial \gamma}{\partial \varphi} \right)_A - \left(\frac{\partial \gamma}{\partial \varphi} \right)_B \right\}}{S_B \cdot \bar{A}_A - S_A \cdot \bar{A}_B - S_v (\bar{A}_A - \bar{A}_B)} \end{aligned} \quad (1.226)$$

where $[\partial \mu_i^s / (\partial \mu_b)] = -\bar{A}_i$ is the specific area occupied by one mole of grain boundary substance. With the assumption $\bar{A}_A = \bar{A}_B = \bar{A}$ we come to the Clausius-Clapeyron equation:

$$\left(\frac{dT}{d\varphi} \right)_e \equiv \frac{\bar{A}}{\Delta S} \left[\left(\frac{\partial \gamma}{\partial \varphi} \right)_A - \left(\frac{\partial \gamma}{\partial \varphi} \right)_B \right] \quad (1.227)$$

The index “ e ” means that the change of the value is considered along the curve of equilibrium of two grain boundary phases; ΔS is the change in the molar entropy of the grain boundary under the phase transition: $\Delta S = q/T_{\text{trans}}$. In

**FIGURE 1.40**

Correspondence of $\Sigma 17 - \Sigma 1$ equilibrium line with dislocation model for the transition temperature T_c (solid line), φ is misorientation angle, $\Delta T = 220^\circ\text{C} - T_c$.

[140] the idea was put forward that the peculiarities observed in grain boundary behavior are conditioned by the phase transition “special grain boundary — non-special (random) grain boundary.” Taking into account that the surface tension of a random grain boundary depends weakly on the misorientation angle, it may be assumed that $(\partial\gamma/\partial\varphi)_B \cong 0$; the change of a special boundary misorientation angle by $\Delta\varphi$ gives rise to a wall of secondary grain boundary dislocations with the period of the boundary. The surface tension of tilt boundaries increases by $\Delta\gamma$:

$$\Delta\gamma = \frac{\mu b}{4\pi(1-\nu)} \sin \Delta\varphi \left(1 + \ln \frac{b}{2\pi r_0} - \ln \Delta\varphi \right) \quad (1.228)$$

Here r_0 is the cut-off radius which is approximately equal to the dislocation core width, μ and ν are the shear modulus and the Poisson ratio. From (1.227) and (1.228) one obtains

$$\Delta T = -\frac{\bar{A}}{\Delta S} \left[\frac{\mu b \sin(\Delta\varphi)}{4\pi(1-\nu)} \left(1 + \ln \frac{b}{2\pi r_0} - \ln \Delta\varphi \right) \right] \quad (1.229)$$

The linearity of (1.221) is shown in Fig. 1.40 in corresponding coordinates. The heat of grain boundary phase transition L estimated in [144] from experimental data using Eq.(1.229), appeared to be close to the heat of melting of pure tin, and the value r_0 equals approximately $5b$, which confirms the ideas

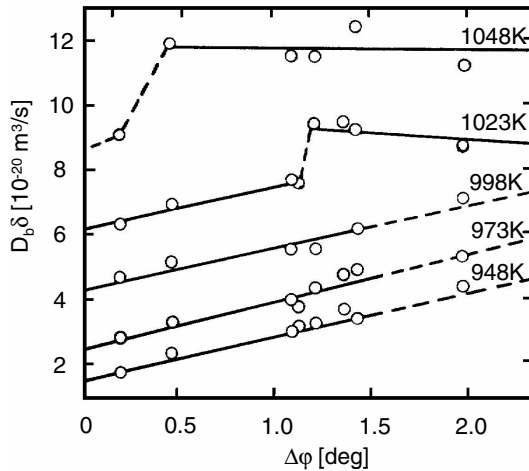
of the large width of grain boundary dislocations [146].

The influence of impurities on the grain boundary phase transition temperature was quantitatively analyzed by [147] on the basis of Eq. (1.226), assuming that the grain boundary was completely saturated by the impurities, i.e. all adsorption sites were occupied. In this case the temperature of the grain boundary phase transition is supposed to be proportional to the logarithm of the impurity concentration, which has been observed experimentally.

As another example for the use of (1.226) we consider the question: how does a rigid-body translation \mathbf{r} of a lattice, breaking down the coincidence geometry at the boundary, affect the temperature of grain boundary melting? A high temperature grain boundary phase slides without any resistance, therefore, $\xi_B = [\partial\gamma/(\partial\mathbf{r})]_B \cong 0$ while $[\partial\gamma/(\partial\mathbf{r})]_A > 0$. Hence $dT < 0$, which means that upon the described shift the transition temperature decreases. Indeed, such a decrease was observed in [148], where the influence of the grain boundary premelting transition has been simulated on the basis of a lattice gas model. In the experiments of [139] the temperature of the grain boundary phase transition also decreased with the deviation of the misorientation angle from the special value $\Sigma 29$. This proves the fact that the energy of a high temperature grain boundary phase depends on the misorientation to a weaker extent than that of a low temperature phase. Such behavior of the physical properties in a low and high temperature phase was observed for grain boundary diffusion in Cu bicrystals [149]. A conspicuous feature of this investigation was the high accuracy of the identification of the crystallography of the samples ($0.02\text{--}0.05^\circ$), which permitted us to study grain boundaries in very close vicinity of the special misorientation $\langle 100 \rangle \Sigma 5$.

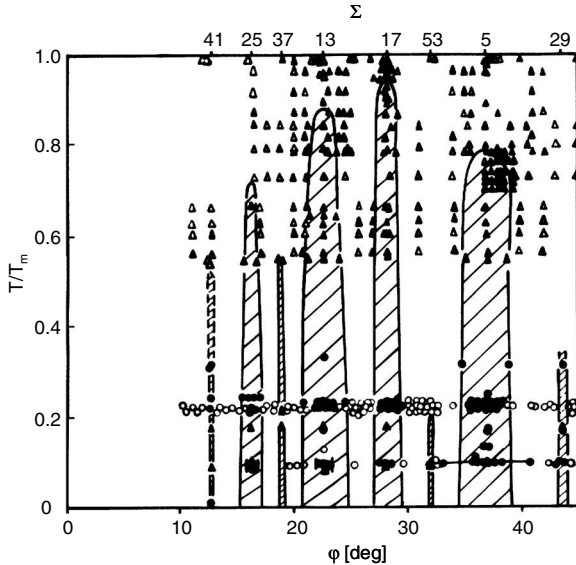
In Fig. 1.41 the misorientation dependence of the grain boundary diffusion coefficient (strictly speaking the product $D_b\delta$ where δ is a grain boundary width) is presented for different temperatures [149]. It is easy to see that at temperatures above 725° an abrupt jump of the lines $D'_b(\Delta\varphi)$ was observed. What is important is that after this the diffusion coefficient is independent of the deviation $\Delta\varphi$ from the special misorientation. Authors interpreted this jump as evidence of the phase transition special grain boundary — random one. It gives an explanation for the mentioned misorientation independence of the diffusion coefficient. Actually, the random grain boundaries, and what is more, in such narrow interval of misorientation angles, are indistinguishable in properties.

An additional reason for the presumed nature of the phenomenon is the change in the misorientation coordinate of the phase transition with the temperature, namely, the higher the temperature is, the closer is the coordinate of the boundary transformation to the special misorientation (Fig. 1.41). Traditionally, grain boundaries are divided into two broad classes, namely, special boundaries and general boundaries (non-special, see Chapter 2). The properties of special boundaries differ dramatically from those of random (general) boundaries. Orientational dependencies of thermodynamic and kinetic parameters have a sharply non-monotonic character with extrema on special “an-

**FIGURE 1.41**

Orientation and temperature dependences of $D_b\delta$ of Ni diffusion along $\langle 100 \rangle$ tilt grain boundaries in Cu in the vicinity of the special misorientation $\Sigma 5$.

gles.” The geometrical models predicting the existence of special boundaries were developed rather a long time ago. The first of these was the coincidence site lattice model (CSL), in terms of which it was shown that at particular misorientation angles a portion of sites of the interpenetrating lattices coincide. The CSL is characterized by the Σ value, that is, the reciprocal density of coincidence sites. Conventionally, this is attributed to the fact that the grain boundary occurring in a CSL with low Σ shows a periodic structure and a lower energy compared to random boundaries. Although the CSL is lost at any small departure from the exact angle, the properties of special boundaries are maintained in a certain finite interval of misorientation angles. This is attributed to the accommodation of the special boundary structure by means of grain boundary dislocations. The available geometrical models enable us, in principle, to describe the structure of any special boundary. The authors of these models realized that large Σ values and small lengths of Burgers vectors of grain boundary dislocations have no physical sense. The limits of applicability of geometrical models of the grain boundary structure have been discussed for a long time, but the question remains obscure so far. The authors of [150] embarked on an attempt to solve some problems, associated with the stability of the structure and properties of the special grain boundaries, in particular, what is the maximal value of Σ , at which special boundaries are still different in properties from random grain boundaries; whether the properties of special boundaries remain “special” in those temperature intervals; if there is Σ_{\max} then how does it depend on the temperature; what determines the width of

**FIGURE 1.42**

Range of existence (phase diagram) of special and non-special $\langle 100 \rangle$ grain boundaries: \blacktriangle — boundaries with special properties; \triangle — boundaries with non-special properties; \bullet — boundaries with special structure; \circ — boundaries with non-special structure.

the angular interval wherein a special boundary manifests its special properties. The method of attack of the problem chosen by the authors [150] can be thought of as a “statistical” one. The authors considered a large body of experimental material, which permitted them, first of all, to extract the regions of existence of special grain boundaries in the “temperature-misorientation angle” coordinates. In Fig. 1.42 the diagram for $\langle 100 \rangle$ boundaries (tilt and twist) is presented, where the ordinate shows the homologous temperature — the ratio of the temperature of the experiment to the melting point — the abscissa is the misorientation angle. The lines in Fig. 1.42 separate the region of existence of special grain boundaries with different Σ from the single region of existence of non-special (random) grain boundaries. It appears that only special boundaries with low Σ manifest themselves as special up to the melting point. The boundaries with higher Σ remain special only up to a certain finite temperature. The angular interval of existence of special boundaries narrows with increasing Σ .

One of the most important results of [150] is the conclusion that there is a threshold value of Σ , i.e. Σ_{\max} at which the properties of special boundaries are still different from those of general, random ones, the value Σ_{\max} decreases

when temperature increases (Fig. 1.43). The problem of Σ_{\max} is considered, in particular, in [151], where the authors analyzed the temperature stability of the geometric structure of special grain boundaries. The special grain boundary preserves its specific properties as long as the depth of its potential relief — the DSC-lattice period [152] — is larger than the amplitude of thermal fluctuations, in other words, kT .

Consequently, the temperature T_0 is the temperature of the phase transition “special grain boundary — random (general) grain boundary.” In the framework of the considered approach it should be a phase transition of first-order, which is corroborated by a definite temperature of the transition and the crystallographical differences of the boundary phases.

When Σ increases, the vector b_0 — the DSC lattice period — decreases. For instance, for the rotation axes with small Miller indices a good approximation for b_0 is [153]

$$b_0 \cong b/\sqrt{\Sigma} \quad (1.230)$$

where b is a Burgers vector of lattice dislocation.

On the other hand, the depth of the potential wells ΔU_0 , which corresponds to the lattice points of the DSC lattice, decreases with increasing Σ . So, if

$$\Delta U_0 \cong kT \quad (1.231)$$

the grain boundary is no more energetically favorable and, in this sense, it cannot be considered a special one. Therefore, the condition (1.231) determines Σ_{\max} . Unfortunately, the dependence $\Delta U_0(\Sigma)$ is unknown, so it is easier to estimate the value of Σ_{\max} considering the geometrical instability of the DSC lattice [151].

In accordance with Lindemans’ criterion the root-mean square amplitude \bar{u} of atomic oscillations in the vicinity of the melting point is about 10% of the lattice constant. Assuming that this criterion can be applied, at least, in a first approximation to grain boundaries and the atomic vibrations at the grain boundaries are harmonic, then \bar{u} at temperature T which is higher than the Debye temperature can be written [154]

$$\bar{u}(T) \cong 0.1b [T/T_m]^{1/2} \quad (1.232)$$

(The authors [151] took into account the possible difference between the melting temperature of the bulk and the grain boundary. As shown above, for a grain boundary which is in equilibrium with the bulk, its melting temperature coincides with the bulk melting point.)

Not every lattice point of the DSC is occupied by an atom, but all of them are “smeared out” equally on the value of $2\bar{u}$. A DSC can be considered destroyed if $2\bar{u}$ is comparable with b_0 . Consequently, the condition of existence of an energetically favorable special grain boundary is

$$0.2b [T/T_m]^{1/2} < b_0(\Sigma) \quad (1.233)$$

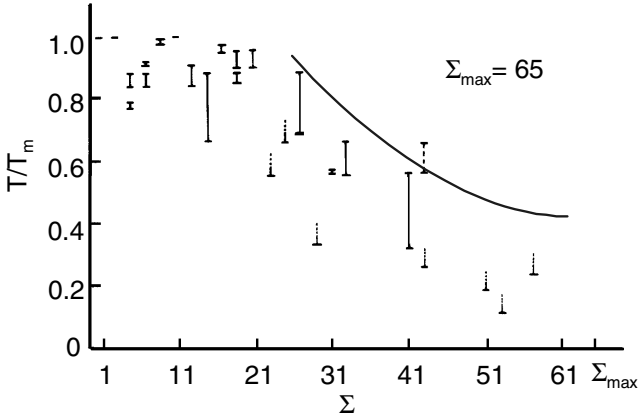


FIGURE 1.43
Temperature of transition “grain boundary with special properties-grain boundary with non-special properties” as a function of reciprocal density of coincidence sites Σ .

From (1.233) and (1.230) we come to [147]

$$\Sigma_{\max} < 25 (T_m/T) \tag{1.234}$$

In other words, a grain boundary with the reciprocal density of coincidence sites Σ exists like a special one in the definite temperature interval only

$$T < T_0 = \frac{25T_m}{\Sigma} \tag{1.235}$$

Relation (1.234) is presented in Fig. 1.43 (solid line). One can see that the agreement is reasonable. Moreover, Fig. 1.43 shows evidence that for $\Sigma < 25$ the temperature of existence of the special grain boundaries extends up to the melting temperature.

1.5 The Equilibrium Shape of Grain Boundaries

We would like to start this section with the question of whether it is possible to discuss the equilibrium shape of grain boundaries which are traditionally believed to be non-equilibrium defects of a crystal. A partial answer to this question was given when we discussed the problem of how to legitimate the applicability of equilibrium thermodynamics to grain boundaries. It was shown

that the existence of grain boundary (along with interphase) thermodynamics is a forced existence. It is a result of the external bonds imposed on the system: of the constancy of the thermodynamic conditions in the case of an interphase or the geometric conditions in the case of a grain boundary.

However, the question is which is an equilibrium shape of the crystal and whether it is possible to discuss the equilibrium shape of a grain boundary on the analogy of the equilibrium shape of a crystal! The equilibrium shape of a crystal surface is determined by the extremum of the variational isoperimetrical problem, which correlates to a minimum of the free energy of the crystal at constant volume and number of particles

$$\Omega^s = \oint \gamma dA = \int \gamma(\tilde{p}, \tilde{q}) \sqrt{1 + \tilde{p}^2 + \tilde{q}^2} dx dy = \min. \quad (1.236)$$

at isoperimetrical conditions

$$V = \int Z dx dy = \text{const.} \quad (1.237)$$

where $Z(x, y)$ is the equation of the crystal shape; $\tilde{p} = \partial Z / \partial x$, $\tilde{q} = \partial Z / \partial y$; $\gamma(\tilde{p}, \tilde{q})$ is the surface tension of the specific crystal face; γ is a function of its orientation.

The solution of the problem (1.236) and (1.237) is the interior envelope of the set of planes

$$\tilde{p}x + \tilde{q}y - Z = \frac{1}{\lambda} \gamma(\tilde{p}, \tilde{q}) \sqrt{1 + \tilde{p}^2 + \tilde{q}^2} \quad (1.238)$$

where $Z(x, y)$ is a constant which is given by the bonding equation (1.198).

The equilibrium shape of the crystal can be determined in the following way. From the origin of the coordinates draw the radius vector with the directed cosines \tilde{p} and \tilde{q} ; the length of the radius vector be proportional to the surface tension $\gamma(\tilde{p}, \tilde{q})$ of the given face. Then draw the planes perpendicular to the radius vectors through their ends. The interior envelope of these planes, i.e. Eq.(1.238), gives us the crystal shape. This construction reflects the Wulff plot.

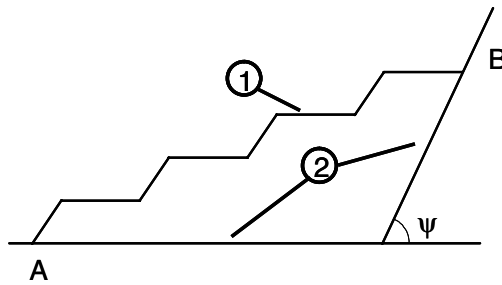
As was shown by Landau [5, 155], the function $\gamma(\tilde{p}, \tilde{q})$ has some special features. Contrary to the widespread opinion that (with regard to the orientation) closely related faces (planes) of a crystal can diverge considerably in the surface tension, γ is a continuous function, i.e. the surface tension of two faces (planes) of a crystal with infinitely small difference in orientation differs with infinitesimal quantity.

As early as 1915 Ehrenfest showed in the paper “Comments to the capillary theory of the crystalline shape” [156] that compensating steps formed on crystal faces deviating from a face with a low surface tension, which “remove” the difference in orientation and contribute to the free energy of the crystal. It is just the existence of these steps which causes the second peculiarity of

the function γ , namely the absence of a definite value of the derivative with respect to the orientation. Actually, by increasing the deviation of a crystal face from a special face with low γ , we increase the number of steps and vice versa; so, taking a deviation of the face by $d\Theta$ in different directions, we get two values of the derivative $d\gamma/d\Theta$. The difference between these values is determined by the energy of the compensating steps — for a singular face, and by the energy of interaction of the steps — for the faces with intermediate orientations. This difference $\Delta(d\gamma/d\Theta)$ decreases as fast as the orientation of the crystal face recedes from the singular orientation. As a consequence of the first special feature of the function γ , the face of a crystal which is close to special one, i.e. to a face with a small surface tension, has steps which are widely separated. As can be seen, the distance (in units of the lattice constant) between the steps is the index of the face (plane). As a result of the second peculiarity of the function γ , the area of the crystal face, constructed in the way mentioned above, is proportional to the difference $\Delta(d\gamma/d\Theta)$ between two values of the derivative of the surface tension.

Thus, the equilibrium shape of the crystal is created by the flattening of different faces (planes); in doing so, the larger the crystallographic indices of the plane are, the smaller is its area. It means that the equilibrium shape of the crystal consists of a small number of flat sections with a low energy, which are connected by curved parts, where all crystallographic planes are represented.

What prevents us from applying the given scheme to an individual grain, and to the grain boundary? For the grain boundary the variational problem is not an isoperimetrical one — there is no reason to fix the volume of the bulk while varying its shape, because on each side of the grain boundary there is the same phase. The situation changes if an external anisotropic field — magnetic field, stress field, etc. — is imposed on a system with a grain boundary. Thermodynamically different phases will be located on either side of the grain boundary, and the grain boundary itself becomes an interphase. So the results discussed above can be applied to it. If the space is isotropic, the grain boundary separates two regions with the same phase, and the role of the linkage (Eq. (1.237)) should be played by the geometrical restrictions. So, the grain boundary may be fixed to the external surface of the sample by a thermal groove, forced to extend through certain points, lines and so on. Once the grain boundary surface tension does not depend on the orientation in the crystal, a surface of zero Laplace curvature corresponds to the equilibrium shape of the grain boundaries. Just this idea is the basis of Mullins' witty analysis of the grain growth in thin sheets and foils [157]. The special feature of grain growth in thin foils is that the moving grain boundary is stabilized at the external surface of the foil or sheet by a thermal groove. The grain boundary can leave the groove only, if the angle between the boundary and the slope of the groove is larger than $\pi/2$. Consequently, the shape of an isotropic grain boundary in thin sheets and foils corresponds to the minimum of rotational geometries which are stretched on two circumferences of radius

**FIGURE 1.44**

Two possible grain boundary shapes when boundary inclination deviates from special orientation. (1) — compensating steps; (2) — macroscopic facets. A and B are the points where grain boundary is locked.

r . This is the property of a catenoid — which is the rotational figure of a chain line and the Laplace curvature of it is zero in every point. The dihedral angle between the catenoid and the plane of the sheet is $\omega = \delta/2r$, where δ is the thickness of the sheet. Grain boundaries of small grains will move until their size reaches the critical value, which is determined by the mentioned condition ($\omega = \pi/2$). Estimations yield a critical size which is approximately equal to the sheet thickness, and the experiment confirms them.

Grain boundaries, at least the special grain boundaries and those close to them, are anisotropic [35]. That is why it is of interest to consider the behavior of anisotropic grain boundaries where the shape of the grain boundary is concerned. Like in the case of the external surface of the crystal, some of the orientations of the grain boundary fit the minima of the surface tension. If the misorientation of the grains corresponds to a special one, such orientations can be called orientations of good coincidence, or good orientations.

For small deviations from the good orientation in a crystal compensating steps might appear at the grain boundary, much like the steps on the external surface of the crystal. The second possible configuration is macroscopic facets, oriented along the nearest good orientations (Fig. 1.44). The equilibrium configuration should include only one facet of such a kind, because the total length of the grain boundary along all the rectilinear sections does not depend on the number of facets and each zigzag introduces additional energy to the system. (The driving force of disappearing for the “additional” facets drops down with increasing size. So the final state with one zigzag should be observed in experiments.)

The shape of a special grain boundary having regard to the anisotropy of its surface tension was considered in [158]. The external geometrical condition, imposed on the system, is that the grain boundary is locked in the points A and B (Fig. 1.44). Let γ_1 and γ_2 be the surface tensions of two adjacent good

orientations, let the angle between these orientations be Ψ , γ_1 and γ_2 the energies of the steps related to their heights h_1 and h_2 . If the grain boundary is isotropic its equilibrium shape represents the part of the straight line, which connects the points A and B in the two-dimensional case. If the surface tension is strongly anisotropic ($\gamma_1 > \gamma_2$, $\gamma_2 > \gamma_1$), the formation of steps is energetically not favorable. The equilibrium configuration, corresponding to this case, consists of facets in the planes of good orientations. If $\gamma_1 < \gamma_2$, $\gamma_2 < \gamma_1$, the formation of steps in this case is energetically possible, the shape of the grain boundary resembles the arrangement of steps AB. There is no sole element in the described picture, i.e. the interaction of the steps. The question arises whether the appearance of qualitatively new configuration is conceivable if this factor will be taken into consideration. The calculation shows that it is possible.

The energy of a grain boundary can be written as

$$E = \gamma_1 (\ell_1 - \chi_1) + \chi_2 \tilde{\gamma}_1 + \chi_2 \varepsilon_1 \xi_1^2 + \gamma_2 (\ell_2 - \chi_2) + \chi_1 \tilde{\gamma}_2 + \chi_1 \varepsilon_2 \xi_2^2 \quad (1.239)$$

where ξ_1 , ξ_2 , are the ratios of heights h_1 , h_2 to the distances between the steps, respectively; the constants ε_1 and ε_2 describe the interaction intensity between the steps; the sense of the lengths ℓ_1 , ℓ_2 , ξ_1 and ξ_2 is clear from Fig. 1.44. The interaction between the steps was assumed to be an elastic one, its energy is inversely proportional to the square of the distance [159].

Thus, the problem is reduced to the search for values of ξ_1 and ξ_2 which, by minimizing the expression (1.239), give non-vanishing values for the angles Θ_1 and Θ_2 :

$$\xi_i = \frac{\tan \Theta_i}{\sin \psi - (\cos \psi) \cdot \tan \Theta_i} \quad (1.240)$$

In this case, in accordance with the physical sense of the values ξ , the problem is solved by the values of ξ_i which are in the range from 0 to 1.

The required conditions for aluminum are

$$\begin{aligned} \frac{\partial E}{\partial \chi_1} &= \tilde{\gamma}_2 - \gamma_1 + 3\varepsilon_2 \xi_2^2 + 2\varepsilon_1 \xi_1^2 = 0 \\ \frac{\partial E}{\partial \chi_2} &= \tilde{\gamma}_1 - \gamma_2 + 3\varepsilon_1 \xi_1^2 + 2\varepsilon_2 \xi_2^2 = 0 \end{aligned} \quad (1.241)$$

In [158] the simple situation is considered, where the “good orientation” is the crystallographic equivalence

$$\gamma_1 = \gamma_2 = \gamma, \quad \tilde{\gamma}_1 = \tilde{\gamma}_2 = \tilde{\gamma}, \quad \varepsilon_1 = \varepsilon_2 = \varepsilon \quad (1.242)$$

Then the system (1.241) degenerates into

$$\begin{cases} 3\xi_1^2 + 2\xi_2^2 = a \\ 3\xi_2^2 + 2\xi_1^2 = a \end{cases} \quad (1.243)$$

where $a = (\gamma - \tilde{\gamma}) / \varepsilon$.

For $a < 0$ the system does have positive solutions. This situation corresponds to a pure facetting — there are no steps. For $a > 5$ both positive solutions of (1.242) cannot be less than 1. This solution corresponds to the absence of facets.

For $0 < a < 5$ all solutions of Eq.(1.242) can be divided into two groups. The first group can be related to solutions, which satisfy the condition $\xi_1 = \xi_2 = \xi$; for the second group $\xi_1 \neq \xi_2 = \xi$, respectively. For $\xi_1 = \xi_2 = \xi = \xi$ the cubic equation

$$3\xi^2 + 2\xi^3 = a \quad (1.244)$$

has one positive root in the interval $0 < a < 5$. The consideration shows that in the range $0 < \xi_1, \xi_2 < 1$ the system (1.243) does not have unequal roots.

Thus, depending on the value of the parameter $a = (\gamma - \tilde{\gamma}) / \varepsilon$, three qualitatively different versions of the equilibrium shape of the grain boundary are possible.

1. $a < 0$ — the grain boundary is split into facets which are located exactly in the planes with special orientation;
2. $a > 5$ — there are no facets of the grain boundary;
3. $0 < a < 5$ — facets contributed by steps deviate from the planes of good orientation by definite angles.

The “magic” value $a = 5$ results from the assumption that the law of interaction of the steps is valid for distances, which are comparable with the interatomic ones. So, the exact value can be different, but the qualitative consequences remain valid.

The possibility of an occurrence of the last situation mentioned was confirmed by electron microscopy investigations of the geometry of 180° and 60° twin boundaries in films of Ag on mica [160]. It was found that the major part of such grain boundaries is split into facets which are located in planes close to the special orientation $\{112\}$ but with a small angle of deviation of $\pm 6^\circ$ from these planes.

1.6 Problems

PROBLEM 1.1

Use Carnot's cycle to find the temperature dependence of grain boundary surface tension.

PROBLEM 1.2

One of the disadvantages of a rivet as a structural connection element is the change in its length with temperature. Due to thermal expansion the length of the rivet increases, which weakens the connection, especially for base materials with low thermal expansion. The proposed temperature-compensation rivet is manufactured from a metal with a nanocrystalline grain microstructure. An increase in temperature leads to grain growth which, in turn, decreases the total grain boundary area in the rivet and the excess of grain boundary free volume.

Determine:

- (1) The change in the length of an Al rivet in the course of grain growth when the mean grain size increases from $D_0 = 10 \text{ nm}$ to $D = 100 \text{ nm}$.
- (2) The change in the length of the rivet due to two concurrent effects: grain growth and thermal expansion.
- (3) The stress in the rivet caused by grain growth and thermal expansion. Grain boundary excess free volume $V^{\text{ex}} = 1.35 \cdot 10^{-10} \text{ m}^3/\text{m}^2$; thermal expansion coefficient of Al $\alpha = 2 \cdot 10^{-5} \text{ K}^{-1}$; temperature increase $\Delta T = 200 \text{ K}$.

PROBLEM 1.3

Assume that the grain boundary excess free volume is the result of vacancy adsorption. Compute for grain boundaries in Al:

- (1) The adsorption constant B in the frame work of the Henry isotherm.
- (2) The heat of adsorption Q .

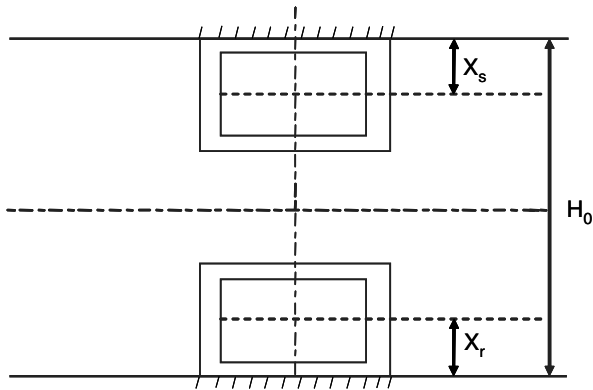
Compare the value of the enrichment coefficient $\beta = \frac{\Gamma}{z_c}$ with the diagram of Seah and Hondros (Chapter 1).

Compare the value for the quantity B , extracted from the Henry isotherm, with the value extracted from the Zhuchovitskii-McLean isotherm.

PROBLEM 1.4

Let us consider two cubic polycrystals in a furnace. One of them rests on a support (bottom plate, etc.) whereas the second is suspended on a rigid bracket (see Fig. 1.46).

- (1) Calculate the increase in size of a polycrystal by the grain boundary excess free volume; autoadsorption $\Gamma_0 = 6.4 \cdot 10^{-6} \text{ mol/m}^2$, $\Omega_0 = 10^{-5} \text{ m}^3/\text{mol}$.
- (2) Evaluate the equilibrium grain size after a long annealing time for these polycrystals. Hint: take into account the influence of gravity.
- (3) It is known that an isolated system cannot change by itself the position

**FIGURE 1.45**

Two arrangements of a polycrystal in a furnace.

of the center of mass (center of gravity). During grain growth the center of mass of a sample will shift since the specimen will expand in all directions. How can these contradictory statements be reconciled?

PROBLEM 1.5

A nanocrystalline aluminum sample is quickly heated close to the melting temperature T_m .

- (1) Determine the change of the melting temperature of a nanocrystalline Al sample with mean grain size $D = 10$ nm; $\gamma = 0.45$ J/m².
- (2) Derive the Clausius-Clapeyron equation for the sample at the melting point.
- (3) Calculate dP/dT at the melting temperature for a mean grain size:

- I* $D = 5$ nm
- II* $D = 7$ nm
- III* $D = 25$ nm

Hint: The volume change during the phase transformation solid-liquid $\Delta\Omega_{SL} = 0.066\Omega_s$.

Structure of Grain Boundaries

“... A trifling matter, and fussy of me, but we all have our little ways.”

“There must be somebody there, because somebody must have said Nobody.”

— *A.A. Milne*

2.1 Terminology and Definitions

Grain boundaries are the lattice defects that have been known for the longest time but they are also the least understood. A grain boundary separates two regions of the same crystal structure but of different orientation. In very coarse-grained materials it can be discerned by the naked eye if the surface is properly prepared (Fig. 2.1). Our deficiency of fundamental knowledge of grain boundaries is mainly due to their complex structure, which requires an extensive mathematical description for its macroscopic characterization. Already in the two-dimensional case four parameters are needed to define mathematically exactly a grain boundary (Fig. 2.2), namely an angle φ which describes the orientation difference between the adjacent crystals (orientation relationship), an angle Ψ which defines the spatial orientation of the grain boundary “plane” (grain boundary orientation) with respect to one crystal and the components t_1, t_2 of the translation vector \mathbf{t} that characterizes the displacement of the two crystals with respect to each other (translation vector). For the three-dimensional case (the real case) one even needs eight parameters to unambiguously define a grain boundary, namely three terms for the orientation relationship, for instance the Euler angles $\varphi_1, \Phi, \varphi_2$, two parameters for the spatial orientation of the grain boundary by means of the normal to the grain boundary plane $\mathbf{n} = (n_1, n_2, n_3)$, with respect to one of the adjacent crystals (keeping in mind that $|\mathbf{n}| = 1$) and finally the three components of the translation vector $\mathbf{t} = (t_1, t_2, t_3)$. The properties, in particular energy and mobility of a grain boundary, are, in principle, a function of eight parameters. Five of these eight can be influenced externally, i.e. orientation relationship and spatial orientation of the grain boundary. The translation vector will be forced by the crystals such that the total energy will be minimal; however,

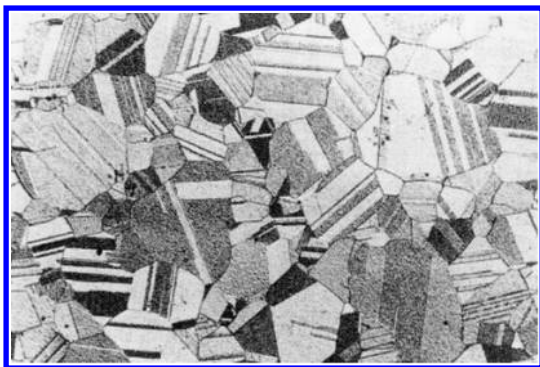
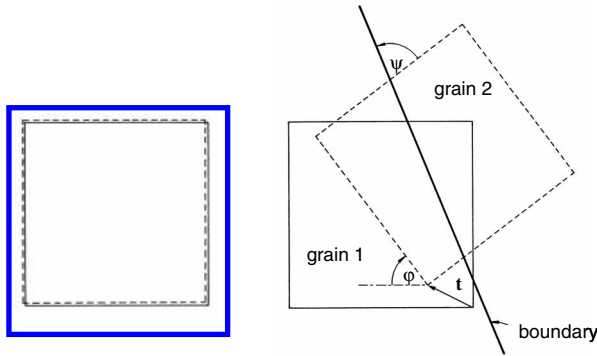


FIGURE 2.1

Microstructure of recrystallized α -brass. The grain boundaries separate areas of uniform orientation represented by a uniform shade of gray.

the vector \mathbf{t} need not be unambiguous as evident from computer simulations. To determine the dependency of grain boundary properties, for instance the mobility, on the five macroscopic parameters, it would be necessary to keep all parameters but one fixed and to systematically vary that free parameter. In real life, however, only few of the external parameters are systematically varied, and usually this is the orientation relationship in terms of a fixed rotation axis and a variable angle of rotation, and for a given rotation axis and rotation angle, the inclination of the grain boundary with regard to a reference position.

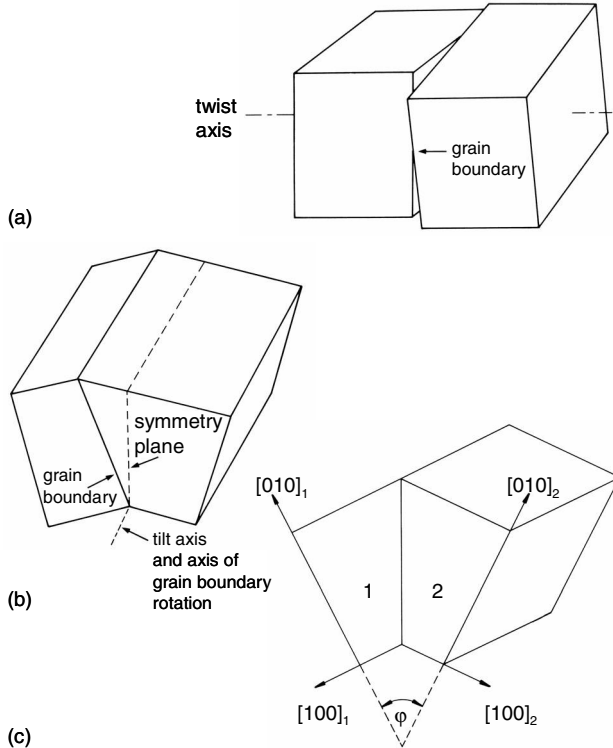
The orientation relationship between two crystal lattices is a transformation, which has to be applied to one of the crystals to make both crystal lattices coincide. If a common origin is assumed, this transformation is a pure rotation, since the relative positions of the crystal axes in both crystals are the same. We will see in Chapter 6 that there are many ways to define a rotation. Frequently the three Euler angles are used, but it is easiest to picture a grain boundary when the rotation is represented in terms of an axis and angle of rotation. In many instances it is very important to know the dependency of a property on the rotation angle for a given rotation axis. In this case it would be desirable to keep the crystallographic orientation of the grain boundary plane constant in order to obtain the dependency on the rotation angle only. If the grain boundary plane is perpendicular to the rotation axis, the boundary is referred to as a twist boundary (Fig. 2.3a). In such a case the choice of the grain boundary plane is unambiguous, no matter what the rotation angle is. In contrast, grain boundaries are called tilt boundaries, if the rotation axis is parallel to the grain boundary plane. Since there is an infinite number of possible planes parallel to a given direction, there is an infinite number of tilt boundaries for a given rotation. If the adjacent crystals are mirror images of

**FIGURE 2.2**

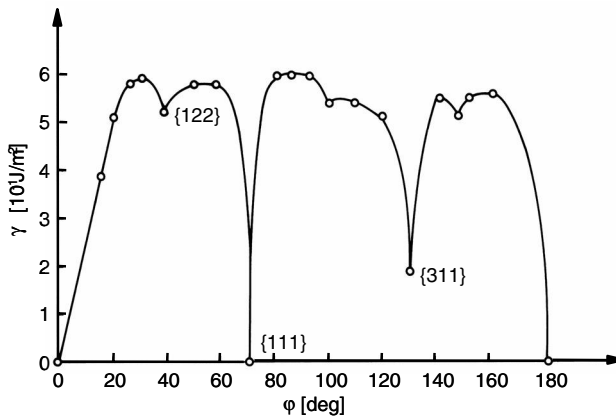
Four parameters are needed to mathematically define a two-dimensional grain boundary.

each other, then the grain boundary is referred to as a symmetric tilt boundary (Fig. 2.3c). All other tilt boundaries are called asymmetric tilt boundaries (Fig. 2.3b). In a symmetric tilt boundary the grain boundary plane has equivalent Miller indices with regard to both adjacent crystals; for instance in Fig. 2.3c the boundary normal would be $(210)_1$ and $(2\bar{1}0)_2$ for a 36.9° $[001]$ symmetric tilt boundary. By definition, the normal to the grain boundary plane must be perpendicular to the rotation axis for tilt boundaries. However, it is impossible to keep the Miller indices of the grain boundary plane constant when changing the angle of rotation. At least with regard to one of the crystals this has to change corresponding to an asymmetric tilt boundary. Therefore, to investigate boundary structure — property relationships it is sensible to first confine oneself to symmetric tilt boundaries and then treat asymmetric tilt boundaries as a deviation from the symmetric position.

As an example the dependency of grain boundary energy on the angle of rotation for a $\langle 110 \rangle$ rotation axis in aluminum is given in Fig. 2.4 for symmetrical tilt boundaries. Obviously, there are orientation relationships with particularly low energy boundaries. One example is the 70.5° $\langle 110 \rangle$ orientation relationship, which is a particularly low energy boundary, namely a coherent twin boundary. However, also when in both crystals a $\{311\}$ plane is parallel to the grain boundary, a very low grain boundary energy is observed.

**FIGURE 2.3**

Relative orientation of grain boundaries and rotation axes for different types of grain boundaries. (a) Twist boundary; (b) asymmetrical tilt boundary; (c) symmetrical tilt boundary.

**FIGURE 2.4**

Dependence of the energy of symmetrical $\langle 110 \rangle$ tilt boundaries in Al on the tilt angle φ . The indices given in the figure are Miller indices of the corresponding grain boundary planes (see text) (after [174]).

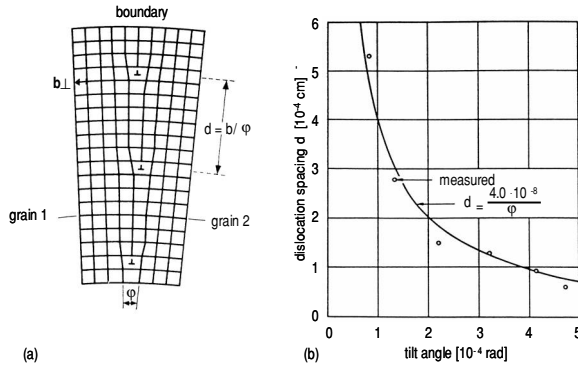
2.2 Atomic Structure of Grain Boundaries

2.2.1 Low-Angle Grain Boundaries

If the misorientation between adjacent grains is small (low-angle grain boundary), then the boundary is entirely comprised of a periodic crystal dislocation arrangement. This becomes obvious already from a simple soap froth model of a boundary, but also has been confirmed by high resolution electron microscopy. Symmetric tilt grain boundaries consist of a single set of dislocations (Burgers vector \mathbf{b}) (Fig. 2.5a), where the dislocation spacing d decreases with increasing rotation angle φ (Fig. 2.5b)

$$\frac{b}{d} = 2 \sin \frac{\varphi}{2} \approx \varphi \quad (2.1)$$

For asymmetric low-angle tilt boundaries at least two sets of edge dislocations are required, the Burgers vectors of which are perpendicular to each other (Fig. 2.6a). The fraction of dislocations of the second set increases with increasing deviation from the symmetric tilt boundary that is only comprised of the first set of dislocations. If the grain boundary is composed only of the second set of dislocations, another symmetric tilt boundary is obtained (Fig. 2.6b) which is normal to the symmetric tilt boundary that is comprised only of the first set of dislocations (Fig. 2.6a). Low-angle twist boundaries require

**FIGURE 2.5**

(a) Dislocation configuration of a symmetrical $\langle 100 \rangle$ low-angle grain boundary with tilt angle φ in a simple cubic crystal. (b) Measured and calculated dislocation spacing in a symmetrical low-angle tilt boundary in germanium.

at least two sets of screw dislocations (Fig. 2.7a). Mixed boundaries are composed of dislocation networks of three Burgers vectors. This dislocation model of low-angle grain boundaries, which is due to Read and Shockley [161], has been frequently confirmed by transmission electron microscopy (Fig. 2.7b) and is supported by measurements of grain boundary energy (Fig. 2.8).

The free energy of a low-angle grain boundary can be calculated exactly. As shown by Read and Shockley [161] the stress field of a dislocation in an infinite periodic arrangement is confined to a range in the order of the dislocation spacing d . The energy of an edge dislocation per unit length, therefore, reads

$$E_d = \frac{\mu b^2}{4\pi(1-\nu)} \ln \frac{d}{r_0} + E_c \quad (2.2)$$

μ — shear modulus, ν — Poisson ratio, $r_0 \approx b$ — radius of dislocation core, E_c — energy of dislocation core. Correspondingly, for a symmetrical tilt boundary with tilt angle φ , the number of dislocations per unit length $n = 1/d \cong \varphi/b$, and thus, the grain boundary energy per unit area

$$\gamma_{\text{STB}} = \frac{\varphi}{b} \cdot \left(\frac{\mu b^2}{4\pi(1-\nu)} \ln \frac{1}{\varphi} + E_c \right) = \varphi (A - B \cdot \ln \varphi) \quad (2.3)$$

with $A = E_c/b$ and $B = \mu b/4\pi(1-\nu)$.

The curve in Fig. 2.8 was calculated according to Eq. (2.3) for Pb and Sn and obviously agrees very well for $\varphi < 15^\circ$.

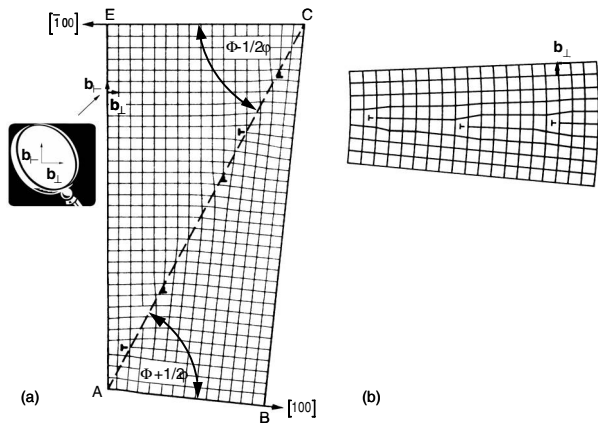


FIGURE 2.6
(a) Dislocation configuration of an asymmetrical low-angle tilt boundary with tilt angle φ and inclination Φ . (b) Symmetrical low-angle grain boundary formed exclusively from second family dislocations.

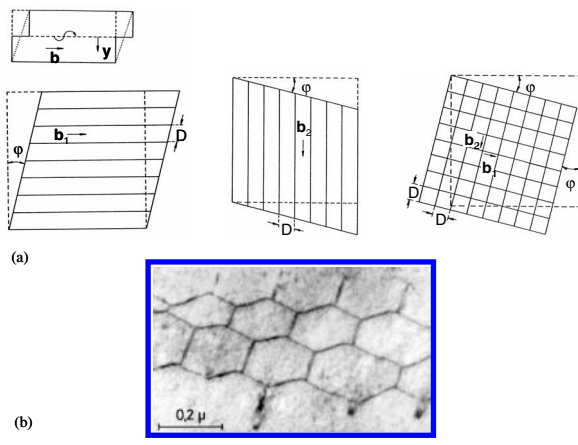
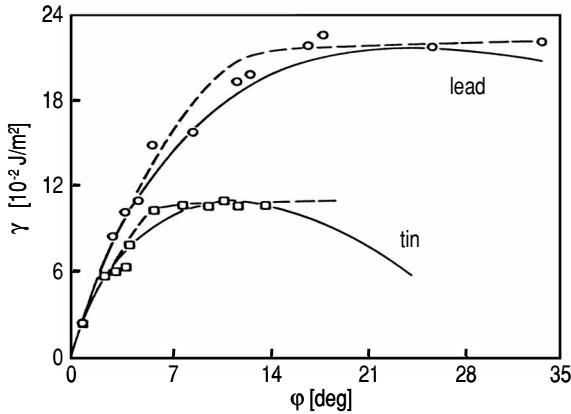


FIGURE 2.7
(a) Explanation of the basic dislocation configuration of a low-angle twist boundary. A single family of parallel screw dislocations results in a shear deformation, but two perpendicular families of dislocations result in a pure rotation. (b) TEM image of a low-angle twist boundary in α -Fe. The hexagonal dislocation configuration is composed of screw dislocations with three different Burgers vectors [165]

**FIGURE 2.8**

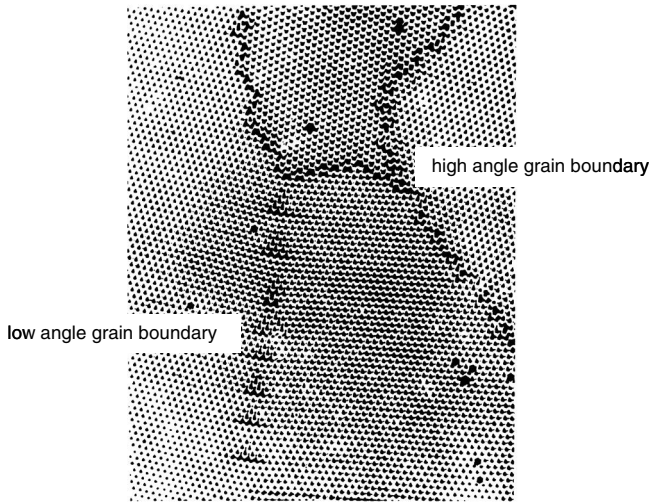
Measured (points and dashed lines) and calculated (using the dislocation model) (solid curves) energy of tilt boundaries in lead and tin (after [166]).

2.2.2 High-Angle Grain Boundaries

For low-angles of rotation the specific grain boundary energy (energy per unit area) increases exactly as predicted by the dislocation energy model. For angles of rotation in excess of 15° ; however, measurements of grain boundary energy reveal no further change with increasing rotation angle, in contrast to the dislocation model which would predict an energy decrease for high-angles of rotation (Fig. 2.8). For rotation angles larger than 15° the dislocation model fails, because the dislocation cores tend to overlap. Thus, the dislocations lose their identity as individual lattice defects so that Eq.(2.3) does not apply any more. Therefore, grain boundaries with rotation angles in excess of 15° are distinguished from the low-angle grain boundaries and are termed high-angle grain boundaries. At first glance a high-angle grain boundary appears like a zone with random atomic arrangement (Fig. 2.9). In fact, early models of grain boundary structure assumed grain boundaries to represent an under-cooled liquid. We will show below that this is a deception and that grain boundaries do have a defined atomic structure. However, this very simple model of grain boundary structure proves already that the thickness of a boundary can only be on the order of a few atomic diameters, i.e. of atomic dimensions. Since the grain boundary energy per atom γ^a corresponds to the atomic heat of melting $q_a = kT$, where k is Boltzmann constant

$$\gamma = \frac{nb}{b^3} \cdot kT \quad (2.4)$$

and b is the atomic diameter and nb is the thickness of the boundary. With the magnitude of grain boundary energy $\gamma \approx 0.5 \text{ J/m}^2$, we obtain $n \approx 1$. Although

**FIGURE 2.9**

High-angle and low-angle tilt boundaries in a soap bubble model.

this model is certainly too simple to account for any structural dependence of grain boundary properties, it is often useful for providing rough estimates of thermodynamic properties of grain boundaries.

The island model proposed by Mott [162] and refined by Gifkins [163] was a first attempt to account for grain boundary structure as observed by field ion microscopy. In this model the grain boundary consists of perfectly crystalline islands floating in a perturbed environment, e.g. in an undercooled melt. Again the model fails to properly predict grain boundary structure, but it is the first and simplest model to treat grain boundary motion differently from simple rate theory of jumps of individual atoms across the boundary as proposed by Turnbull [164]. Rather, perfect islands comprising many atoms may detach from and attach to the adjacent crystal boundaries. This departure from a single atom model to a cluster model will drastically increase activation energy and entropy of grain boundary motion, as will be discussed in Chapter 3.

Our current understanding of the structure of high-angle grain boundaries is derived from geometrical concepts, based on dislocation models of low-angle grain boundaries [35], [165]–[167]. A fundamental reason for the failure of the lattice dislocation concept for larger angles of rotation is the requirement of a strictly periodic dislocation arrangement to minimize grain boundary energy. The spacing of dislocations, however, changes discretely, namely at least by one atomic distance. What ensues is that the angle of rotation $\varphi = b/d$ also changes in steps rather than continually. For low-angles φ , $b \gg d$ so that φ

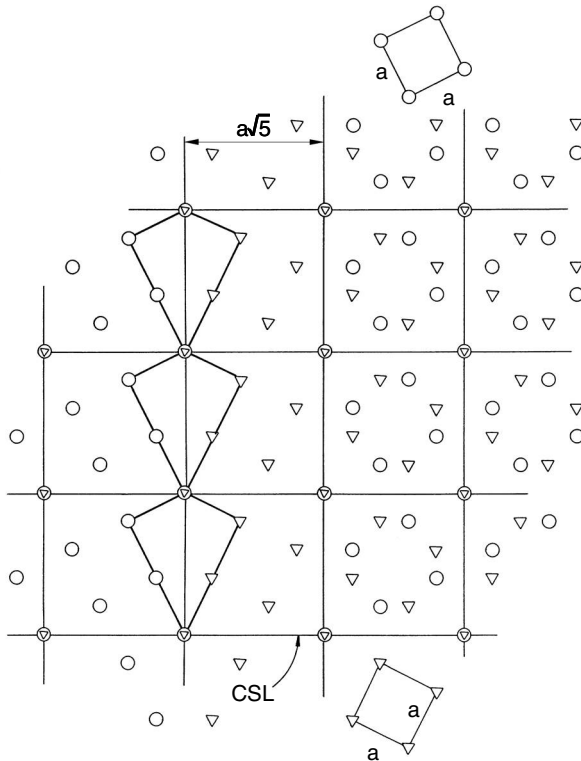
changes quasi-continually. For larger rotations the orientation difference between two consecutive periodic dislocation arrangements becomes substantial. If, for instance, there is an arrangement with dislocation spacing $d = 4b$, then $\varphi = 14.3^\circ$. Changing the dislocation spacing to three atomic spacings requires an angle of rotation of $\varphi = 19.2^\circ$. Therefore, the problem arises of what is the grain boundary structure for $14.3^\circ < \varphi < 19.2^\circ$, or, in general, between rotations that represent a periodic arrangement of (primary) crystal dislocations.

In a perfect crystal the atoms have a defined (average) position, which is determined by the minimum of the free energy. Any deviation from this position necessarily increases the free energy. Therefore, it can be assumed that the crystal will try to keep the atoms as much as possible in their ideal position, also in the grain boundary. There are orientation relationships, where crystallographic planes continue through the grain boundary from one crystal to the other, i.e. there are atomic positions in the grain boundary which coincide with ideal positions of both adjacent lattices. Such lattice points are called coincidence sites. Since the orientation relationship between the adjacent crystals is described by a rotation, it can be investigated under what conditions coincidence sites will occur. A simple example (Fig. 2.10) is a rotation of 36.87° about a $\langle 100 \rangle$ axis in a cubic lattice (respectively — 53.13° because of the $90^\circ \langle 100 \rangle$ crystal symmetry). If we consider the atomic positions of both adjacent lattices in a $\{100\}$ grain boundary plane, i.e. perpendicular to the rotation axis (right part in Fig. 2.10) then the occurrence of many coincidence sites is evident. Since both crystal lattices are periodic, the coincidence sites also must be periodic, i.e. they also define a lattice, the coincidence site lattice (CSL). The elementary cell of the CSL is larger than the elementary cell of the crystal lattice, of course. As a measure for the density of coincidence sites or for the size of the elementary cell of the CSL, we define the quantity

$$\Sigma = \frac{\text{volume elementary cell of CSL}}{\text{volume elementary cell of crystal lattice}} \quad (2.5)$$

For the rotation $36.87^\circ \langle 100 \rangle$ is $\Sigma = \frac{a(a\sqrt{5})^2}{a^3} = 5$ (Fig. 2.10).

Fig. 2.10 is only a very simple two-dimensional case. In reality the coincidence site lattice is a three-dimensional lattice, the generation of which can be imagined as follows. We take a crystal lattice, each lattice point of which carries two atoms, for instance one round and one triangular like in Fig. 2.10. Now we rotate the triangular atoms while the round atoms remain unchanged. Of course, the origin for the axis of rotation is a lattice point. After this rotation there are again lattice points where triangular and round atoms coincide. These are the coincidence sites and because of the periodicity of the crystal lattices they generate a three-dimensional lattice, the CSL. To apply this crystallographic construct to grain boundaries, we have to define the spatial orientation of the grain boundary plane. Having defined this plane, we remove on one side of the plane the round atoms, on the other side of the plane the triangular atoms. This generates a bicrystal with a boundary, and the struc-

**FIGURE 2.10**

Coincidence site lattice (CSL) and structure of a $36.9^\circ \langle 100 \rangle (\Sigma = 5)$ grain boundary in a cubic crystal lattice. Right side of figure: grain boundary plane \parallel plane of the paper (twist boundary); Left side of figure: grain boundary plane \perp plane of the paper (tilt boundary).

ture of the boundary is given by the atoms located in the boundary. If good fit of the atoms — and coincidence sites represent atoms with ideal fit — is associated with a low energy, we can expect that the grain boundary strongly favors running through coincidence sites rather than non-coincidence sites. Grain boundaries between crystallites which have an orientation relationship corresponding to a high density of coincidence sites are called CSL boundaries or special boundaries. The smaller the Σ (which is always an odd integer), the more ordered is the grain boundary. Low-angle grain boundaries can be characterized by $\Sigma = 1$, since almost all lattice points, except for the atoms of the dislocation cores, are coincidence sites. Grain boundaries between crystallites with twin orientation relationship are defined by $\Sigma = 3$, and in the coherent twin boundary all lattice sites are coincidence sites. This

TABLE 2.1
Rotation angle φ for lattice
coincidence with $\Sigma < 100$ in a cubic
lattice with $\langle 100 \rangle$ axis of rotation.

φ	Σ
8.80	85
10.39	61
12.68	41
14.25	65
16.26	25
18.92	37
22.62	13
25.06	85
25.99	89
28.07	17
30.51	65
31.89	53
36.87	5
41.11	73
42.08	97
43.60	29

is not a contradiction to $\Sigma = 3$, since the CSL is a three-dimensional lattice which also extends perpendicular to the grain boundary, and only every third plane parallel to the coherent twin boundary is in perfect coincidence. This is evident for the fcc lattice when the coherent twin boundary is a $\{111\}$ plane. Because of the stacking sequence ABC of $\{111\}$ planes, a coincidence of the 3D crystal lattices will produce coincidence sites only in every third plane parallel to the coherent twin $\{111\}$ boundary.

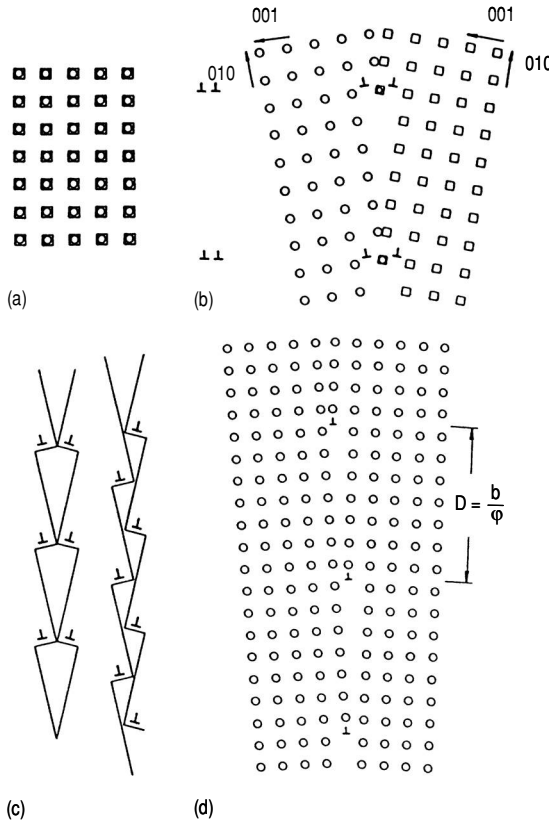
If we want to apply this crystallographic concept to real grain boundaries, there is the fundamental problem that the coincidence site lattice occurs only for very special defined rotations, and Σ does not change continually with the angle of rotation (Table 2.1). This problem is entirely complementary to the requirement of a discrete change of the angle of rotation in order to obtain a periodic crystal dislocation arrangement as described above. In essence, a strictly periodic arrangement of crystal dislocations is absolutely identical with the relaxed structure of a CSL grain boundary (Fig. 2.11). However, even for tiny deviations from the exact rotation relationship the long range coincidence gets lost. In much as the crystal tries to compensate a small misorientation by a periodic arrangement of crystal dislocations, we expect that the bicrystal will try to maintain its ideal fit and to compensate deviations from this perfect fit by localized perturbations, i.e. dislocations. These dislocations need to have a Burgers vector, which will conserve the CSL as much

as lattice dislocations conserve the crystal lattice when forming a low-angle grain boundary. As in the most trivial case the CSL will not be changed, if dislocations are introduced, the Burgers vectors of which are lattice vectors of the CSL. Equivalently, it is possible that the Burgers vector would be a vector of the crystal lattice. However, the elastic energy of dislocations increases with the square of the Burgers vector: $E_d \sim b^2$. Therefore, the energy of the grain boundary would increase dramatically if dislocations with a very large Burgers vector would be implemented into the grain boundary. However, the density of coincidence sites will determine only the energy, not their location. As a consequence we can relax the requirement that the location of the coincidence sites has to be conserved. There are very small vectors which conserve the size of the CSL if the location of the coincidence sites are allowed to change. The displacement vectors which satisfy this condition define the so-called DSC lattice. DSC is the abbreviation for displacement shift complete. This means that the CSL will displace as a whole, if one of the two adjacent crystal lattices is shifted by a translation vector of the DSC lattice. The DSC lattice is the coarsest grid, which contains all lattice points of both crystal lattices (Fig. 2.12). Of course, all translation vectors of the CSL and the crystal lattices are also vectors of the DSC lattice, but the elementary vectors of the DSC lattice are much smaller. Since the dislocation energy increases with the square of the Burgers vector, only base vectors of the DSC lattice qualify for Burgers vectors of the so-called secondary grain boundary dislocations (SGBDs). Dislocations with DSC Burgers vectors are referred to as SGBDs, in contrast to primary grain boundary dislocations, which are crystal lattice dislocations, the periodic arrangement of which generates the CSL.

SGBDs are confined to grain boundaries, since their Burgers vectors are not translation vectors of the crystal lattice and their introduction in the crystal lattice would cause a local destruction of the crystal structure. With regard to their geometry and correspondingly, to their elastic properties, secondary grain boundary dislocations can be treated like primary dislocations. As much as primary dislocations can compensate a misorientation of the perfect crystal by a low-angle grain boundary, so much can secondary grain boundary dislocations compensate an orientation difference to a CSL relationship while conserving the CSL. Since SGBDs also have an elastic strain field as does any dislocation, they can be imaged in a TEM (Fig. 2.13). The larger the orientation difference to the exact coincidence rotation, the smaller the spacing of the SGBDs according to Eq. (2.1).

SGBSs can be treated with regard to their geometrical and elastic properties like ordinary dislocations except for their much smaller Burgers vectors b_B . The orientation difference $\Delta\varphi$ to the reference CSL orientation relationships is described in complete analogy to Eq. (2.1) by their spacings d_{GB}

$$\frac{b_B}{\Delta\varphi} = d_{GB} \quad (2.6)$$

**FIGURE 2.11**

Relationship between the coincidence site lattice and the primary dislocation structure at a grain boundary. If two identical, interlocking lattices (a) are turned symmetrically toward each other about an axis perpendicular to the plane of the page (b), a coincidence site lattice forms. The coincidence points are marked by overlapping circles and squares. The associated configuration of the resulting double dislocation is relaxed along the boundary (c), and the structure of a symmetrical low-angle tilt boundary forms (d).

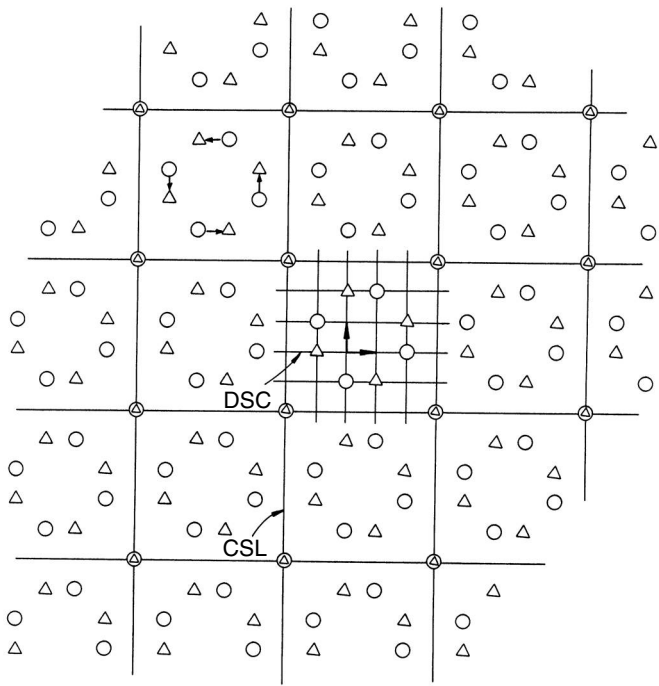
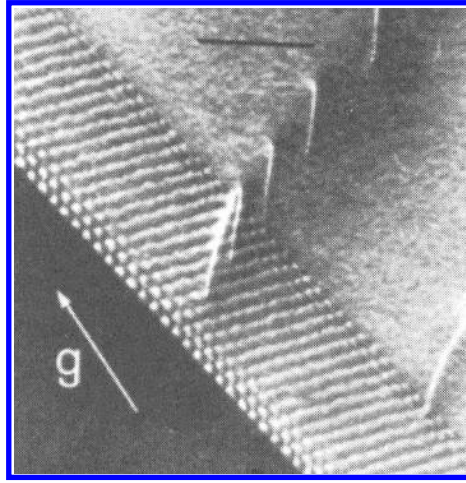


FIGURE 2.12
Coincidence site lattice (CSL) and DSC lattice at $36.9^\circ\langle 100 \rangle$ rotation in a cubic lattice.

**FIGURE 2.13**

Grain boundary dislocations in a tilt boundary in stainless steel (after [175]).

Correspondingly, the energy of a periodic SGBD arrangement $\gamma(\Delta\varphi)$ adds on to the energy of the reference CSL structure, according to Eq. (2.3)

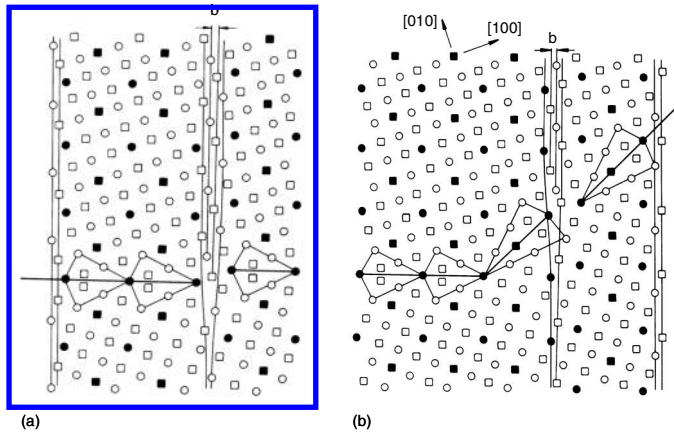
$$\gamma(\varphi) = \gamma^{\text{CSL}} + \gamma(\Delta\varphi) = \gamma^{\text{CSL}} + \Delta\varphi (A_b - B_b \ln \Delta\varphi) \quad (2.7)$$

with $A_b = E_c^b/b_B$ and $B_b = \frac{\mu b_B}{4\pi(1-\nu)}$.

The observed cusps of grain boundary energy at CSL orientation relationships (Fig. 2.4) are actually caused by the infinite slope of $\gamma(\Delta\varphi)$ for $\Delta\varphi \rightarrow 0$ owing to the logarithmic dependency.

A special property of the SGBDs is that at the location of the dislocation core the grain boundary usually has a step (Fig. 2.14). This step is a consequence of the fact that the CSL is displaced when an SGBD is introduced. If an SGBD moves along the grain boundary, the step moves along with the dislocation and thus, the grain boundary is displaced perpendicular to its plane, i.e. the grain boundary will migrate by the distance of the step height. A fundamental property of all dislocations is that they cause a shear deformation upon their motion. Therefore, the motion of a grain boundary dislocation will always cause a combination of grain boundary migration and grain boundary sliding. In the case that the Burgers vector of the SGBD is parallel to the grain boundary plane the dislocation needs only to glide to have the grain boundary displaced. This is the case, for instance, in symmetrical tilt grain boundaries (Fig. 2.14a). If the Burgers vector is inclined to the grain boundary plane, the dislocation can only move by a combination of glide and climb (Fig. 2.14b), which requires the diffusion of vacancies, and, therefore, is a thermally activated process.

The concept introduced is based on geometrical arguments only. Such a con-

**FIGURE 2.14**

Atomic configuration of a grain boundary edge dislocation at a $\Sigma = 5$ grain boundary in an fcc lattice. (a) Burgers vector parallel to the grain boundary. (b) Burgers vector inclined to the grain boundary (after [168]).

sideration cannot make predictions about the force equilibrium of the atomic arrangements considered. This problem can only be solved by computer simulations, which allow us to calculate the position of the atoms at an equilibrium of interatomic forces, i.e. by relaxation of the geometrical arrangement [35],[167]–[169] (Fig. 2.15). In contrast to the basis of the geometrical considerations, coincidence almost always gets lost upon relaxation, but the periodicity remains and that means the conceptual framework is still correct. A more detailed analysis reveals that the arrangement of atoms in the grain boundary can be described by polyhedra, and surprisingly enough, only seven different polyhedra are necessary to describe all possible arrangements of atoms in a grain boundary [170] (Fig. 2.16). These polyhedra represent characteristic structures of the grain boundary and are therefore referred to as structural units. Computer simulations prove that grain boundaries of particularly low energy consist of only one type of polyhedron. If the orientation relationship is slightly changed, other structural units (polyhedra) will be introduced into the structure, and these new structural units are identical with the cores of the SGBDs (Fig. 2.17). With increasing misorientation the density of the new structural units increases until they finally will represent the majority and therefore, on further rotation, the grain boundary structure will eventually consist of only this type of polyhedron. This structural unit concept of grain boundaries and its dependence on orientation relationship represents our current conception of grain boundary structure [171]. The computer simulations of grain boundary structure have also been confirmed by high resolution electron microscopy [172, 173] (Fig. 2.18). Of course, these are considerations

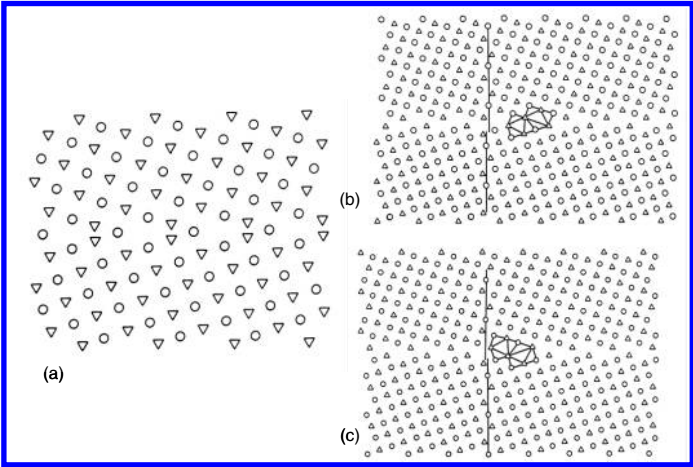


FIGURE 2.15
Structure of a symmetrical $36.9^\circ\langle 100 \rangle (\Sigma = 5)$ tilt boundary in aluminum, calculated by computer simulation: (a) Configuration after rigid rotation of the crystallites, (b) and (c) structure of grain boundaries after relaxation. The staggered vertical lines at the grain boundary indicate the shift of the crystallites. Hence, for a given misorientation there can be more than one structure (after [168]).

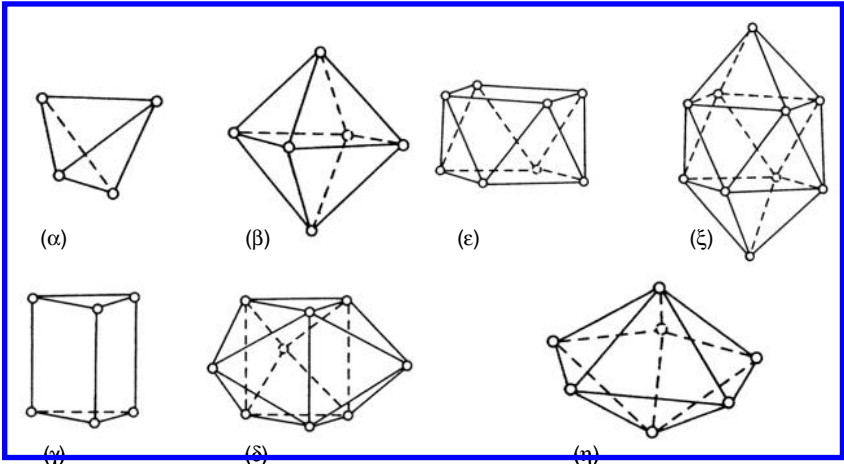


FIGURE 2.16
The seven different Bernal structures that grain boundaries (in structures formed of hard spheres) can consist of: (α) tetrahedron; (β) octahedron; (γ) trigonal prism; (δ) truncated trigonal prism; (ε) archimedean square antiprism; (ξ) truncated Archimedean square antiprism; (η) pentagonal double pyramid (after [170]).

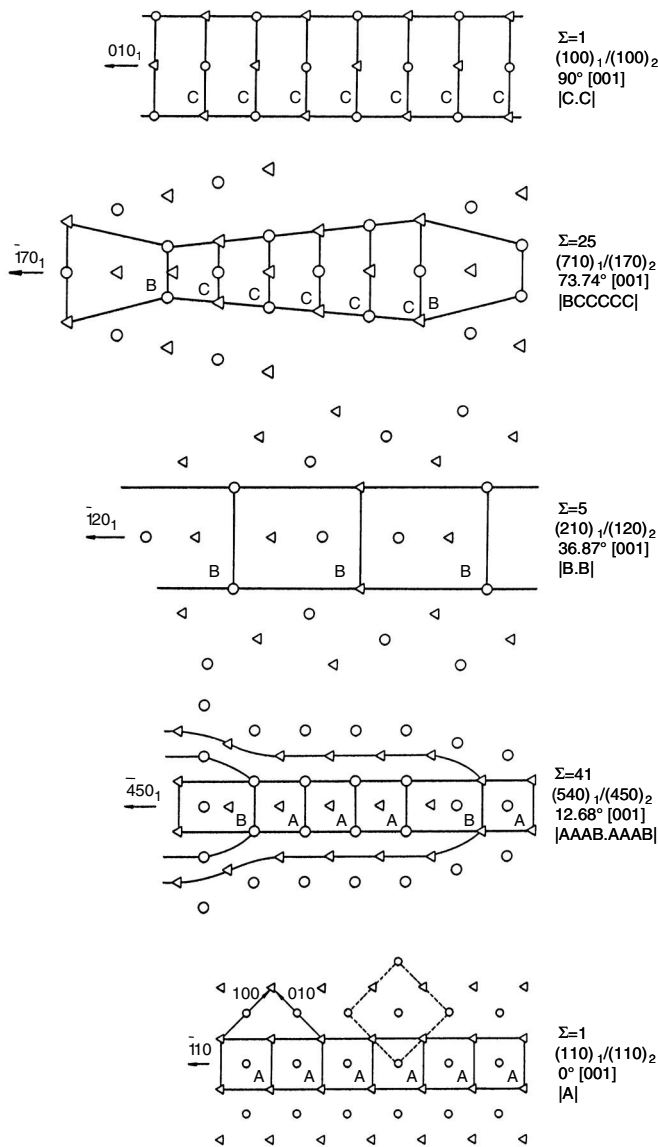
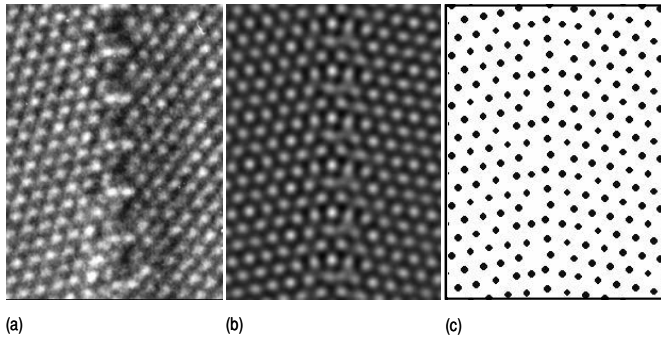


FIGURE 2.17

Calculated dependence of grain boundary structure on the tilt angle of a symmetrical $\langle 100 \rangle$ tilt boundary in aluminum for various tilt angles. For every tilt angle there is a certain arrangement of structural units (A,B,C). If this arrangement is interrupted, this forms a grain boundary dislocation (illustrated for $\Sigma = 41$) (after [171]).

**FIGURE 2.18**

Atomic structure of a $\Sigma 7$ boundary in aluminum: (a) HREM image; (b) simulated HREM image using the relaxed grain boundary structure; and (c) computed by molecular dynamics [173].

which do not include the thermal agitation of atoms. In fact, the structure may change at high homologous temperatures, when entropy becomes important, and, indeed, structural phase transformations of low Σ CSL boundaries (special boundaries) have been reported. Molecular dynamics computer simulations are now being employed to address this important issue.

2.3 Problems

PROBLEM 2.1

Compute the surface tension of a low-angle $\langle 112 \rangle$ symmetrical tilt grain boundaries in Al with following angle of misorientation φ : 0.5° ; 3° ; 5° ; 8° .

PROBLEM 2.2

Find the equilibrium angles at a triple junction with the following grain boundary energies $\gamma_1 = 0.323 \text{ J/m}^2$; $\gamma_2 = 0.620 \text{ J/m}^2$; $\gamma_3 = 0.460 \text{ J/m}^2$ (see Fig. (2.19)).

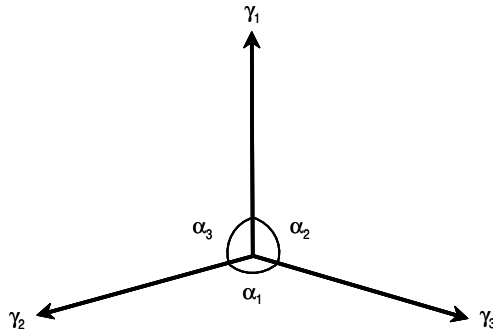


FIGURE 2.19

Equilibrium of three grain boundaries at a triple junction.

PROBLEM 2.3

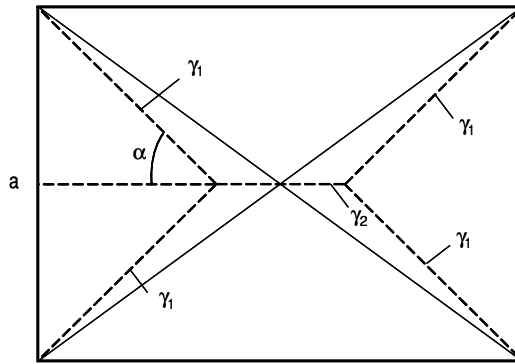
Consider a grain boundary to be a supercooled liquid. Use the Clausius-Clapeyron equation to find the pressure which should be applied to the grain boundary from the bulk to maintain the grain boundary in a liquid state for: Al (at 400°C); Pb (at 100°C); Au (at 600°C).

PROBLEM 2.4

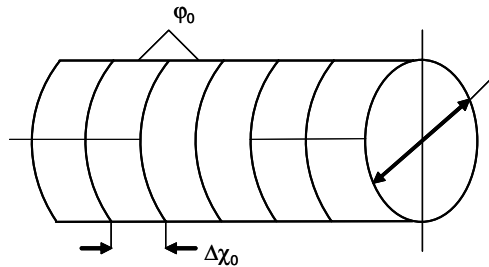
Prove that in a uniform 2D grain boundary system a quadruple junction is unstable.

PROBLEM 2.5

In problem 2.4 it was shown that for uniform grain boundaries quadruple junctions in a 2D grain boundary system are unstable.

**FIGURE 2.20**

System of grain boundaries with quadruple junction.

**FIGURE 2.21**

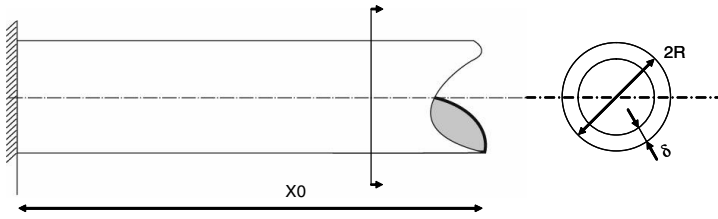
Sample with a bamboo grain boundary microstructure.

- Find the conditions under which it is possible to maintain a quadruple junction in the configuration given in Fig. 2.3.
- Assume that the Burgers vectors of the grain boundary dislocations are the same. Find the misorientation of a grain boundary with surface tension γ_2 , if the misorientation of the first grain boundary is 5° .
- Do the same as in (b) but for a misorientation of $\varphi_1 = 8^\circ$.

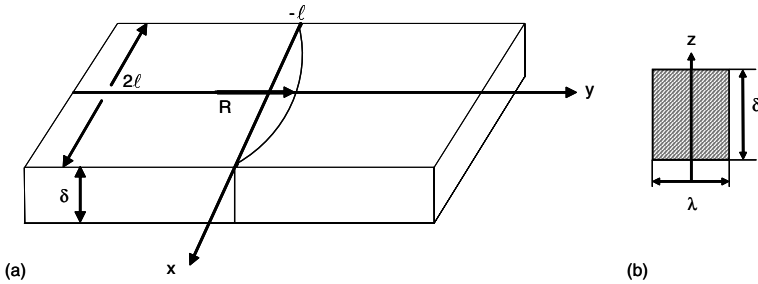
PROBLEM 2.6

Given a sample with a bamboo structure composed of equidistant low-angle grain boundaries with uniform misorientation angle φ_0 (Fig. 2.21). Grain growth is assumed to take place by unification of two neighboring grain boundaries.

- Show that such a process decreases the free energy of the system.
- Calculate the driving force for such grain growth.

**FIGURE 2.22**

Geometry of thin-walled pipe with radius r and length x_0 .

**FIGURE 2.23**

Grain boundary in a thin film which is considered as a beam.

- (c) Determine the condition when this specific grain growth will be arrested.
- (d) Find the grain size Δx_n for this condition.

PROBLEM 2.7

A thin-walled pipe of circular cross section ($R = 0.5$ cm, wall thickness δ) is twisted by the moment M_k . Find the length x_0 for a given twist angle $\Delta\varphi$ which makes it energetically advantageous to form a twist grain boundary with misorientation angle $\Delta\varphi$ (see Fig. 2.22).

PROBLEM 2.8

Consider a thin film with a grain boundary which divides two free surfaces with different surface tension. Two edges of the boundary are clamped, so that the grain boundary can be bent (see Fig. 2.23).

Consider the grain boundary as an elastic beam to define:

- (a) the free energy of the system expressed as a functional of the boundary shape;
- (b) the elastic modulus of the grain boundary.

Grain Boundary Motion

“I am not a little pleased that this Work of mine
can possibly meet with no Censures: For what
Objections can be made against a Writer who
relates only plain Facts.”

— *Jonathan Swift*

3.1 Fundamentals

Grain boundaries separate regions of the same phase and crystal structure but different orientation. A displacement of a grain boundary is entirely equivalent to the growth of one crystallite at the expense of the shrinking neighbor. In this sense the grain boundary constitutes the contact area of the internal surfaces of adjacent grains. The association of grain boundary motion with the displacement of the internal crystallite surfaces distinctly distinguishes grain boundary motion from a diffusive flux of atoms across the boundary. Of course, a non-zero atomic flux across the boundary will make one grain shrink (the emitting grain) and the other grain grow (the receiving grain), and with regard to an external reference frame opposite faces of a bicrystalline specimen would move (Fig. 3.1), but the grain boundary would remain stationary. Thus, diffusion across a grain boundary does not necessarily correspond to grain boundary motion with a displacement of crystallite surfaces. It is evident that grain boundary motion consists of the generation of lattice sites at the surface of the growing grain and conversely a destruction of lattice sites at the surface of the shrinking grain. Effectively, grain boundary motion comprises the non-zero net exchange of lattice sites across the boundary (Fig. 3.2).

In line with the definition given in Chapter 1 we shall consider the grain boundary as a layer of defined thickness comprising a phase with a specific atomic arrangement, and we associate properties like energy, entropy or mobility with this phase. However, one should keep in mind that in reality the grain boundary is only the location of a discontinuity of crystal orientation, defined by the mutually constrained adjacent internal crystallite surfaces. That the proposed simplified definition can cause problems is obvious from the fact

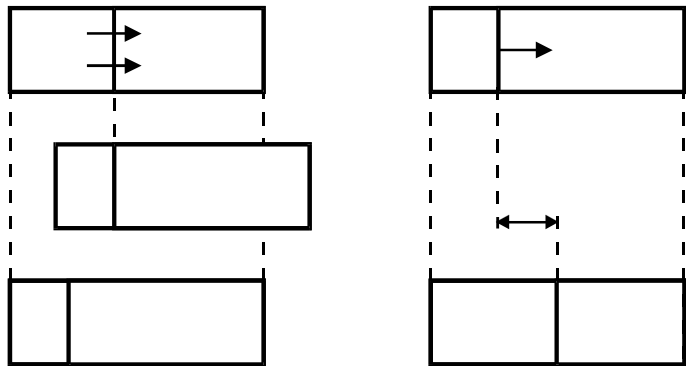


FIGURE 3.1
Diffusion across a grain boundary (left) and grain boundary motion (right) will displace a boundary with regard to an interior sample reference. Boundary motion will also displace the boundary with regard to an external reference.

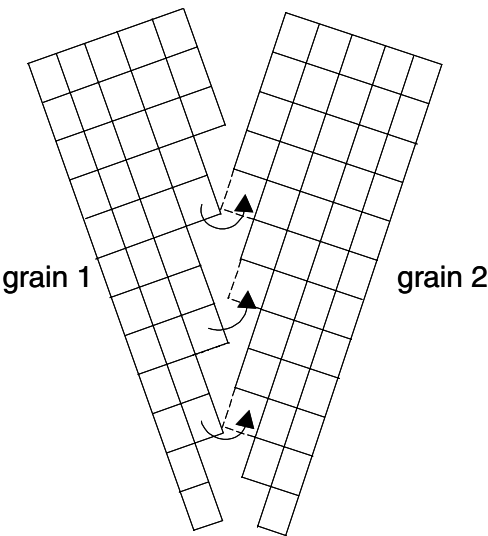


FIGURE 3.2
Grain boundary motion deletes and generates lattice sites on the surface of the shrinking and growing grain, respectively.

that grain boundary mobility can be different for motion in opposite directions, as observed recently. Nevertheless, following conventional perception we shall tacitly assume the grain boundary to have specific but unique properties, except as otherwise noted.

Despite extensive treatment in the literature, there is no real theory of grain boundary migration. Rather, virtually all theoretical attempts to describe grain boundary motion are based on simple rate theory of atoms crossing the grain boundary with net energy gain. It is tacitly assumed that the atom detaching from a crystal to join the opposite surface destroys a lattice site rather than creating a vacancy and that its attachment to the adjacent crystal surface generates a new lattice site rather than eliminating a vacancy. With these prerequisites grain boundary motion is reduced to the diffusive motion of atoms across the grain boundary. In Sec. 3.8 we shall discuss various mechanisms of grain boundary motion. In the simplest case, if the grain boundary is narrow, i.e. can be crossed by a single atomic jump, and each transferred atom displaces the boundary by the diameter of an atom, b , the grain boundary velocity reads [164, 176]

$$v = b(\Gamma_+ - \Gamma_-) \quad (3.1)$$

where Γ_+ and Γ_- are the jump frequencies in the respective directions. If there is no Gibbs free energy differential between the adjacent crystals, the net flux $\Gamma_+ - \Gamma_- = 0$, and the boundary will not move. If the Gibbs free energy of both crystals per unit volume is different, the driving force P is equal to

$$P = -\frac{dG}{dV} \quad (3.2)$$

Then each atom of volume $\Omega_a \approx b^3$ will gain the free energy Pb^3 when becoming attached to the growing grain but has to expend this free energy when moving in the opposite direction. The corresponding free energy variation across the boundary is schematically shown in Fig. 3.3. Correspondingly

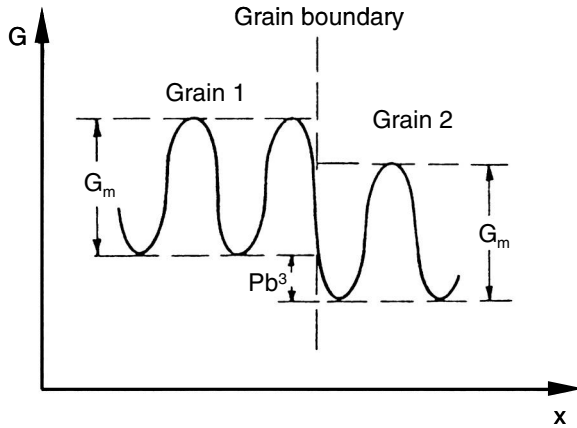
$$v = b \left(\nu_+ e^{-\frac{G_m^+}{kT}} - \nu_- e^{-\frac{G_m^- + Pb^3}{kT}} \right) \quad (3.3)$$

If the attack frequencies $\nu_+ = \nu_- = \nu \approx \nu_D$ (ν_D — Debye frequency) and the migration free energy G_m is the same in both jump directions, then

$$v = b\nu_D e^{-\frac{G_m}{kT}} \left(1 - e^{-\frac{Pb^3}{kT}} \right) \quad (3.4)$$

For all practical cases, including recrystallization in heavily cold worked metals¹, $Pb^3 \ll kT$ at temperatures where boundaries are observed to move

¹For heavily cold worked metals $P \approx 10$ MPa. For Al $kT \cong 10^{-20}$ J at $T = 0.8T_m \cong 450^\circ\text{C}$, i.e. with $b = 3 \cdot 10^{-10}\text{m}$; $Pb^3/kT = 0.01$. It is noted at this point that in molecular dynamics simulations where very high driving forces are applied to make the boundary noticeably move in the small time interval allowed, this approximation may not hold.

**FIGURE 3.3**

The free energy of a moving atom changes by the driving force Pb^3 when it crosses the boundary. G_m is the free energy barrier for bulk diffusion.

($T \geq 0.3T_m$) and, therefore,

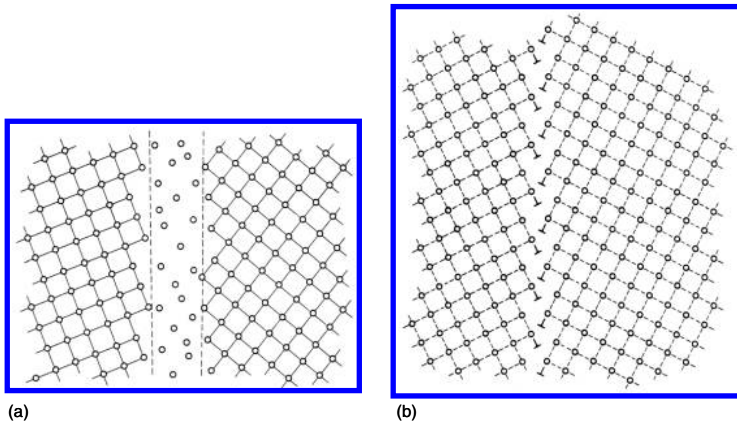
$$\exp \left\{ -\frac{Pb^3}{kT} \right\} \cong 1 - \frac{Pb^3}{kT} \quad (3.5)$$

which yields

$$v = \frac{b^4 \nu_D}{kT} e^{-\frac{G_m}{kT}} \cdot P \equiv m \cdot P \quad (3.6)$$

where m is referred to as grain boundary mobility.

This very simple model may be refined by assuming the detachments to occur in a sequence of steps or that thermal grain boundary vacancies have to assist diffusion [177]; however, these modifications will only modify the preexponential factor m_0 and the activation enthalpy H of the mobility $m = m_0 e^{-H/kT}$, but the proportionality between migration rate v and driving force P remains unaffected. Moreover, in this simple model the activation free energy for the diffusive jump across the boundary is assumed to correspond to the activation energy for volume diffusion. This will be an upper bound for the activation energy for grain boundary motion in pure metals, since the excess free volume in the grain boundary ought to facilitate diffusion and thus lower the activation energy. Frequently, the activation energy for grain boundary motion is assumed to equal the activation energy for diffusion along grain boundaries, which is on the order of half the activation energy for volume diffusion. Since diffusion along boundaries involves quite different activated

**FIGURE 3.4**

Structure of a wide (a) and narrow (b) grain boundary (schematically).

stages than diffusion across boundaries, this may be an invalid assumption².

Several theoretical approaches have assumed a wide grain boundary structure, which implies that there is a layer of undercooled melt between the crystallite surfaces [178, 179] (Fig. 3.4). Although grain boundary structures computed even for high Σ CSL boundaries (see Chapter 2) and observed in the HREM do not support this structure hypothesis, there may be special cases where this concept applies, e.g. for alloys with strongly segregating, low melting point solutes, like Ga or Pb in Al.

In such instances, grain boundary motion consists of three consecutive stages, namely detachment from the shrinking grain surface, transport through the grain boundary and attachment to the surface of the growing grain. The first and third steps have been considered above for the narrow boundary. Frequently, the transport through the boundary is considered to be a diffusive flux. This is wrong, however. There may be a random diffusive flux in the boundary, but it is irrelevant for the migration of the boundary. Since the boundary moves during the transfer of atoms, the attaching grain surface will eventually scavenge the detached atom, even if the latter does not move at all after its detachment. Therefore, the flux through the boundary is only the convection flux

$$j_c = v/\Omega_a \cong v/b^3 \quad (3.7)$$

owing to the motion of the boundary. An observer attached to the boundary would see only this convection flux, and for steady state motion of the

²Since grain boundary mobility is strongly affected by segregated impurities, and since real materials are never absolutely pure, there is no actual measurement of the grain boundary mobility in pure metals to date. This issue, therefore, remains unresolved, so far.

grain boundary this flux is constant. However, as pointed out above, real grain boundary structures in pure metals are narrow boundaries, and thus grain boundary motion is unlikely to be accounted for by evaporation and condensation of atoms on the intercrystalline surfaces.

3.2 Driving Forces for Grain Boundary Migration

The driving force for grain boundary migration P has the dimension of energy per unit volume, which is conceptually equivalent to a pressure — a force acting per unit area on a grain boundary. There are various sources of driving force (Table 3.1). In general, a driving force for grain boundary migration occurs if the boundary displacement leads to a decrease in the total free energy of the system. In principle, a gradient of any intensive thermodynamic variable offers a source of such a driving force: a gradient of temperature, pressure, density of defects, density of energy (for example, an energy of elastic deformation), contents of impurity, a magnetic field strength and so on. However, not all theoretically possible driving forces can be practically realized. To study grain boundary motion the following driving forces are relevant.

(1) An excess density of defects (e.g. dislocations) in one of the adjoining grains is a powerful source of a driving force. There are several advantages to this type of driving force: the ease of fabrication, excellent reproducibility, variation in the magnitude of driving force within a wide range up to a very large force ($P \cong \rho\mu b^2/2$, where b is the Burgers vector, μ the shear modulus, and ρ the dislocation density). For $\rho \sim 10^{15} \text{ m}^{-2}$, $\mu \cong 10^{11} \text{ J/m}^3$, $b^2 \cong 10^{-19} \text{ m}^2$, $P \cong 10^7 \text{ J/m}^3 = 10 \text{ MPa}$. These advantages as well as their relevance for recrystallization processes explain the widespread use of this kind of driving force in spite of essential drawbacks — e.g. instability of P during annealing owing to recovery, local variation of dislocation density etc.

(2) The energy of high-angle grain boundaries like in the classical experiments of [180]–[182]. The authors emphasized that their observations proved that the striation substructure provided the driving force for grain boundary migration, since migration of a grain boundary frees the crystal from the striations. Actually, these striations represented grown in low-angle grain boundaries and thus, the driving force corresponded to the energy of these low-angle boundaries. Aust and Rutter estimated the driving force to be on the order of $4 \cdot 10^{-4} \text{ MPa}$.

This kind of driving force can be considered as relatively reproducible and sufficiently stable. The magnitude of the driving force cannot be changed over a wide range, however. Furthermore, it was believed that a major advantage of this driving force was the possibility of studying the motion of a flat grain boundary, to which, strictly speaking, all microscopic theories of grain

TABLE 3.1

The driving forces for grain boundary migration

Source	Equation	Approximate value of parameters	Estimated driving force
Stored deformation energy	$P = \frac{1}{2}\rho\mu b^2$	ρ = dislocation density $\sim 10^{15}/\text{m}^{-2}$ $\frac{\mu b^2}{2}$ = dislocation energy $\sim 10^{-8}$ J/m	10 (MPa)
Grain boundary energy	$P = \frac{2\gamma}{R}$	γ = grain boundary energy ~ 0.5 J/m ² R = grain boundary radius of curvature $\sim 10^{-4}$ m	10^{-2} (MPa)
Surface energy	$P = \frac{2\Delta\gamma^s}{d}$	d = sample thickness $\sim 10^{-3}$ m $\Delta\gamma^s$ = surface energy difference of two neighboring grains ~ 0.1 J/m ²	$2 \cdot 10^{-4}$ (MPa)
Chemical driving force	$P = R(T_1 - T_0) \cdot c_0 \ln c_0$	c_0 = concentration = max. solubility at T_0 $T_1 (< T_0)$ annealing temperature (5% Ag in Cu at 300°C)	$6 \cdot 10^2$ (MPa)
Magnetic field	$P = \frac{\mu_0 H^2 \Delta\chi}{2} \cdot (\cos^2\Theta_1 - \cos^2\Theta_2)$	Material: bismuth H = magnetic field strength (10^7 A/m) $\Delta\chi$ = difference of magnetic susceptibilities $\sim 1.8 \cdot 10^{-7}$ (250°C) Θ angle between c -axis and field direction $\Theta_1 = 0^\circ$; $\Theta_2 = 90^\circ$	$3.5 \cdot 10^{-4}$ (MPa)
Elastic energy	$P = \frac{\tau^2}{2} \left(\frac{1}{E_1} - \frac{1}{E_2} \right)$	τ = elastic stress ~ 10 MPa E_1, E_2 = elastic moduli of neighboring grains $\sim 10^5$ MPa	$2.5 \cdot 10^{-4}$ (MPa)

Source	Equation	Approximate value of parameters	Estimated driving force
Temperature gradient	$P = \frac{\Delta S \cdot 2\lambda \text{grad} T}{\Omega_a}$	ΔS = entropy difference between grain boundary and crystal (approx. equivalent to melting entropy) $\sim 8 \cdot 10^3 \text{ J/K}\cdot\text{mol}$ $\text{grad } T$ = temperature gradient $\sim 10^4 \text{ K/m}$ 2λ = grain boundary thickness $\sim 5 \cdot 10^{-10} \text{ m}$ Ω_a = molar volume $\sim 10 \text{ cm}^3/\text{mol}$	$4 \cdot 10^{-5} \text{ (MPa)}$

boundary motion are related. As found recently, however, the triple junction of a moving high-angle boundary and consumed low-angle boundaries exerts a drag on the moving boundary and thus renders the interpretation of the measured results uncertain [183].

(3) It was mentioned above that the driving force for grain boundary motion can be considered as a pressure on the boundary from the grain with smaller energy density. The driving force in several methods of investigation of grain boundary motion is exerted by the pressure difference Δp on both sides of the grain boundary

$$P = \Delta p \tag{3.8}$$

Usually, the pressure difference Δp stems from the difference of capillary forces on both sides of a curved grain boundary. A capillary pressure is equal to

$$\Delta p = \gamma \left(\frac{1}{R_1} + \frac{1}{R_2} \right) \tag{3.9}$$

where γ is a surface tension [184], R_1 and R_2 are the main radii of curvature³.

Experimental procedures to study grain boundary migration by using the free energy of the grain boundary itself as a driving force offer a number of advantages, namely the possibility to control and to change the driving force, a good reproducibility, and a good stability at a given temperature. The magnitude of the driving force is on the order of $10^{-4} - 10^{-3} \text{ MPa}$.

(4) The anisotropy of any physical property, e.g. the elastic constants or the magnetic susceptibility, can be utilized as a source of driving force for grain boundary migration. The origin of the driving force for boundary migration

³Relation (3.9) is valid for an isotropic grain boundary.

in a magnetically anisotropic material was considered by Mullins [185]. If the volume density of the magnetic free energy w in a crystal induced by a uniform magnetic field is independent of crystal shape and size and the susceptibility $\xi \ll 1$ then the magnetic driving force acting on the boundary of two crystals that have different susceptibilities is given by

$$P = g_{m1} - g_{m2} = \frac{\mu_0 H^2}{2} (\chi_1 - \chi_2) \quad (3.10)$$

where ξ_1 and ξ_2 are the susceptibilities of crystals 1 and 2, respectively, parallel to the magnetic field H . In the case of Bi, which is magnetically anisotropic with $\xi \ll 1$, Eq. (3.10) reads

$$P = \mu_0 \frac{\Delta\chi}{2} H^2 (\cos^2 \Theta_1 - \cos^2 \Theta_2) \quad (3.11)$$

where Θ_1 and Θ_2 are the angles between the direction of the magnetic field and the trigonal (or c or $\langle 111 \rangle$) axes in both grains of the Bi bicrystal, $\Delta\chi$ is the difference of susceptibilities parallel and perpendicular to the trigonal axis. The pressure P is directed toward the grain with the larger value of Θ and does not depend on the sign of the magnetic field.

Bismuth is a suitable material for investigation of grain boundary migration by the magnetic method, since it is magnetically anisotropic with different susceptibilities parallel and perpendicular to the trigonal (or c or $\langle 111 \rangle$) axis (at 22°C $\chi_{||} = 1.05 \cdot 10^{-6}$ and $\chi_{\perp} = 1.48 \cdot 10^{-6}$ [186]) and, what is of importance, the susceptibilities of Bi, as shown by Kapitza [187, 188], do not depend on H up to $2 \cdot 10^7 \text{ A/m}$, and the energies associated with magnetostriction at $0.8 \cdot 10^7 \text{ A/m}$ are less than 1% of the magnetic free energies and thus can be neglected. The driving force obtained for this method is rather small: at a field strength of $H = 1.63 \cdot 10^7 \text{ A/m}$ the driving force is about $3.5 \cdot 10^{-4} \text{ MPa}$ [189].

The measurement of boundary motion under a constant magnetic driving force provides a unique opportunity to determine the absolute value of grain boundary mobility. In contrast, experiments using other driving forces, like low-angle boundaries or dislocations, need a very accurate estimate of the subboundary or dislocation energy, which is, however, uncertain. Experiments with curved grain boundaries allow us to determine grain boundary mobility to an accuracy of the surface tension γ of the grain boundary [190, 191]; the grain boundary also is not planar. The other significant advantage of a magnetic driving force is the possibility of varying it by changing the position of the sample with regard to the magnetic field. However, the main advantage of the magnetic method is that it permits us to measure the migration of planar grain boundaries [189, 192]. The major disadvantage is the restriction of this method to materials with a large magnetic anisotropy.

(5) The anisotropy of surface tensions of the free surfaces of a bicrystal represents a source for driving grain boundary migration. If the crystallographic

planes that constitute the surfaces of the adjoining grains in a bicrystal have a different surface tension $\Delta\gamma^s$, the boundary feels a driving force

$$P = 2\Delta\gamma^s/\lambda \quad (3.12)$$

where λ is the thickness of the crystals. Decreasing the thickness, e.g. by fabrication of a thin sheet, not only increases the driving force, but, as will be shown below, a drag from the free surface. It is felt that the optimal value of P in this case is about 10^{-4} MPa.

The list of potential driving forces for grain boundary migration is very long and cannot be comprehensively covered here. Other major driving forces are: a temperature gradient ($\nabla T(P = \Delta S \delta \nabla T / (\Omega_a))$), where ΔS is the entropy difference between the bulk of a grain and the grain boundary, δ is the grain boundary thickness, and Ω_a the molar volume. Under optimal conditions $\nabla T \cong 10^5$ K/m, $\Delta S \approx \Delta S_m \approx R$, $P \cong 10^{-5}$ MPa; an anisotropy of the elastic constants ($P = \tau^2 / [2 \cdot (1/(E_1) - 1/(E_2))]$), where τ is the stress, E_1 , E_2 are Young's moduli of the differently oriented crystals. For a stress on the order of 10 MPa one obtains a driving force $P \cong 10^{-5} - 10^{-4}$ MPa.

The origin of these driving forces and their approximate magnitudes are listed in [Table 3.1](#).

3.3 Drag Effects During Grain Boundary Motion

3.3.1 Origin of Drag Effects

Whenever there is an interaction between a grain boundary and other imperfections in the crystal, this interaction will affect grain boundary motion. Such imperfections can be vacancies, dislocations, interface boundaries or external crystal surfaces. Their interaction with the grain boundary is of very different nature and thus will be treated in separate sections below.

3.3.2 Impurity Drag in Ideal Solute Solutions

It is a common experience that grain boundary motion progresses much faster in pure metals than in alloys, even dilute alloys. This must be due to the effect of solute atoms on grain boundary motion [193]–[196]. If there is an interaction energy U (energy gain) between boundary and impurity atoms, these solute atoms will tend to segregate to the boundary. In fact, if thermal equilibrium could be established at all temperatures, and the boundary could adsorb an unlimited number of impurities — like in the case of the Henry isotherm — all solute atoms would end up in the boundary at $T = 0$ K. Owing to thermal agitation (entropy effect), for $T > 0$ the concentration in the boundary will

be

$$c_b = c_0 \exp\left(\frac{U}{kT}\right) \quad (3.13)$$

where c_0 is the volume impurity concentration⁴. When the grain boundary moves, the segregated atoms will attempt to remain in the boundary, i.e. the boundary has to drag its impurity load and can only migrate as fast as the slowly moving impurities.

In the simplest approximation [193] one can assume that the segregated impurities have to move along with the boundary and, therefore, exert a drag force P_v

$$P_v = n \cdot f = n_0 c_b \cdot f = n_0 f \cdot c_0 \cdot e^{U/kT} \quad (3.14)$$

where n is the number of foreign atoms per unit area of the boundary, f is the attraction force between boundary and a foreign atom (see, for instance, [193]), n_0 is the number of lattice sites per unit area of the boundary.

If boundary and foreign atoms move together the net velocity of the segregated solutes read

$$v = B \cdot f = \frac{D}{kT} f \quad (3.15)$$

where $D = D_0 \exp\left(\frac{-Q_D}{kT}\right)$ is the bulk diffusion coefficient of the solute atoms.

The boundary moves according to Eq (3.6) with the velocity

$$v = m_b \cdot (P - P_v) = m_b (P - n f) = m_b \left(P - \frac{n \cdot v \cdot kT}{D} \right) \quad (3.16)$$

and, therefore

$$v = \frac{P m_b}{1 + \frac{n \cdot m_b kT}{D}} \approx \frac{P D_0}{c_0 kT} \exp\left(-\frac{H_D + U}{kT}\right) \quad (3.17)$$

When the driving force increases it will finally reach a critical value where the segregated impurities will no longer be able to keep up with the boundary. Then the boundary will detach from the impurity cloud and move as a free boundary with the speed

$$v = m_b \cdot P \quad (3.18)$$

In this very simple model all atoms will detach from the boundary at the same time. For a more realistic approach one has to consider the diffusion of the solute atoms with the moving boundaries as proposed by Cahn and Lücke [194, 195].

Due to the motion of the grain boundary the concentration distribution of solute atoms will be altered. We are interested in the steady-state concentration ($c(x, y, z)$) of solute atoms in the presence of a boundary moving with

⁴This is only true if there is no interaction between the solutes in the boundary. If this constraint is relaxed a different isotherm has to be used, as will be addressed in Sec. 3.3.3.

constant velocity v . If we assume a planar boundary moving in x -direction, the problem can be reduced to a one-dimensional diffusion equation

$$\frac{\partial c}{\partial t} = D \frac{\partial^2 c}{\partial x^2} + \frac{\partial}{\partial x} \left(\frac{Dc}{kT} \frac{dU}{dx} \right) \quad (3.19)$$

with D the volume diffusion coefficient and $c = c_0$ for $x \rightarrow \pm\infty$. This diffusion equation is time dependent, since the grain boundary changes position with time, as does the concentration distribution attached to it. In a coordinate system affixed to a grain boundary moving with constant speed the concentration distribution remains stationary, i.e. $\partial c / \partial t = 0$. For sake of simplicity, we shall assume (Fig. 3.5a) that

$$U(x) = \begin{cases} 0 & |x| \geq a \\ -H_0 & |x| \leq a \end{cases} \quad (3.20)$$

Thus, $dU/dx = 0$ except for $x = \pm a$. Using the Galilei transformation

$$x = x' - vt \quad (3.21)$$

we obtain the diffusion equation in the coordinate system moving along with the grain boundary at its origin

$$\frac{\partial c}{\partial t} = D \frac{\partial^2 c}{\partial x'^2} + v \frac{\partial c}{\partial x'} = 0 \quad (3.22)$$

($x \neq \pm a$; $c = c_0$, $x = \pm\infty$) which yields the solution

$$c(x) = c_a + c_b e^{-\frac{vx}{D}} \quad (3.23)$$

with c_a , c_b being integration constants. For range I (behind the boundary)

$$c^I(x) = c_0 \quad (3.24a)$$

because of $c(x) = c_0$ for $x = -\infty$.

For range II (in front of the boundary)

$$c^{II}(x) = c_0 + (c_2 - c_0) e^{-\frac{vx}{D}} \quad (3.24b)$$

with $c_2 = c(+a)$.

Owing to the discontinuity of the potential U for $x = \pm a$ the constant c_2 and the concentration distribution inside the boundary cannot be calculated in closed form⁵. However, during steady-state migration the diffusive flux

⁵A closed form solution is possible, when another shape of the potential $U(x)$ is used, e.g. a triangular potential, where $|dU/dx| < \infty$. This renders the solution of the diffusion equation more difficult for the range $dU/dx \neq 0$, but the analysis yields a result very similar to the solution given here.

must be constant everywhere, i.e. equal to the convective flux $j_c = vc_0$. For a boundary comprising a single atomic layer B (Fig. 3.5c) we obtain for the flux through the interface: range II/ boundary (B) ($x = a$)

$$c_b \frac{D}{b} e^{-\frac{H_0}{kT}} - c_2 \frac{D}{b} - vc_2 = -vc_0 \quad (3.25a)$$

and the interface: boundary (B) / range I ($x = -a$)

$$c_1 \frac{D}{b} - c_b \frac{D}{b} e^{-\frac{H_0}{kT}} - vc_b = -vc_0 \quad (3.25b)$$

The first two terms of Eq. (3.20a) represent the diffusion flux through the interface B/II in terms of the difference of the number of atomic jumps from plane B to plane 2 and from plane 2 to plane B:

$$c_b \nu \exp\left(-\frac{H_0 + H_D}{kT}\right) - c_2 \nu \exp\left(-\frac{H_D}{kT}\right) \quad (3.26)$$

where H_D is the activation enthalpy of volume diffusion. The same holds for Eq. (3.25b). Eqs. (3.24b, 3.25a,b) can be solved with regard to c_2 and c_b .

We obtain, using $\Phi = bv/D$ and $\Psi = e^{-H_0/kT}$

$$c_1 = c_0 \quad (3.27a)$$

$$c_b = c_0 \frac{1 + \Phi}{\Psi + \Phi} \geq c_0 \quad (3.27b)$$

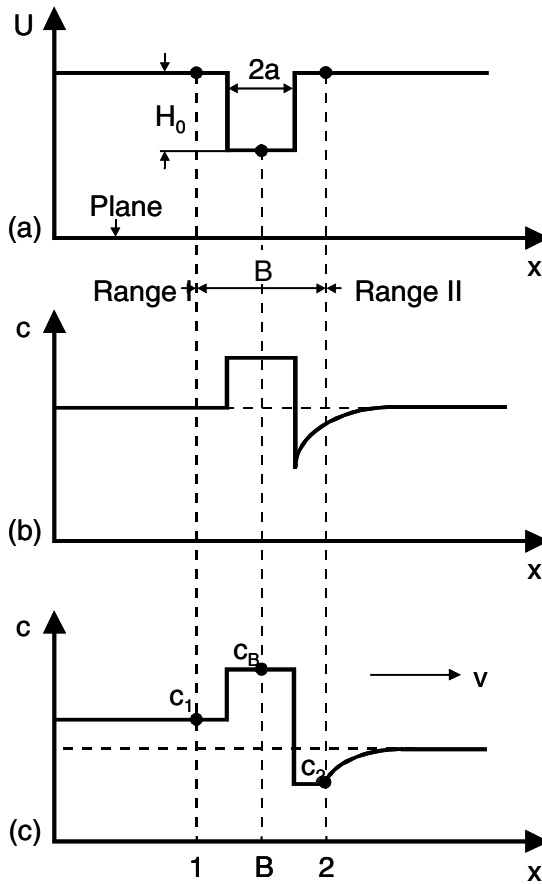
$$c_0 = \left[1 - \frac{\Phi(1 - \Psi)}{(1 + \Phi)(\Psi + \Phi)} \right] \quad (3.27c)$$

The corresponding concentration distribution is given in Fig. 3.5c.

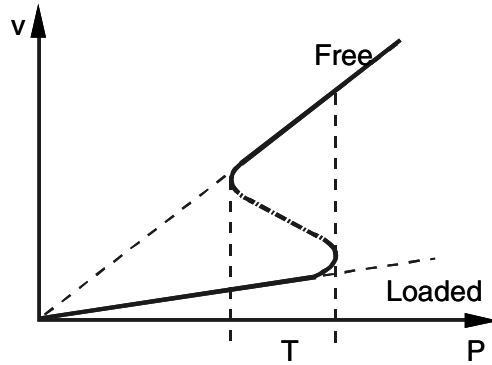
The concentration c_1 behind the boundary is here always equal to the initial concentration c_0 . Since $\Psi < 1$, the boundary concentration $c_b > c_1$. Further, $c_2 < c_0$, i.e. there is a concentration dip in front of the boundary.

As discussed above, the elementary step of grain boundary motion is assumed to consist of the jump of single atoms across the boundary from one crystal to the other. We consider boundary motion from left to right in Fig. 3.5 which corresponds to a net atom jump to the left. By such a jump the total free energy of the system may be altered for two reasons:

- (i) If there is a driving force P (free energy per cm^3) causing the boundary to move to the right, the energy is decreased by the amount $P\Omega_a \approx Pb^3$ per jump, where Ω_a is the atomic volume. Conversely, for backward jumps the energy is increased by this amount.
- (ii) If the boundary moves by one atomic step to the right, the impurities located before in plane 2 are now situated in plane B and the ones of plane B are now in plane 1. This corresponds to an energy change per atom jump $\Delta H = c_2 H_0 - c_b H_0$. A backward jump leads to an increase $\Delta H = c_b H_0 - c_1 H_0$.

**FIGURE 3.5**

One-atomic boundary (a) energy level of an impurity in bulk and boundary; (b) impurity concentration dependence across the boundary; (c) concentration dependence in atomistic model; 1,2 denote atomic positions next to boundary in the crystal, and B position in the boundary.

**FIGURE 3.6**

Dependence of grain boundary migration rate on driving force in the presence of impurity drag. In the interval denoted by T the transition from the loaded to the free boundary and vice versa occurs discontinuously.

If one supposes that the basic activation energy H_m for such a jump is decreased in the case of a forward jump and increased in the case of a backward jump by half of these energy changes, one obtains for the net velocity

$$v = b\nu \left\{ \begin{array}{l} \exp \left(-\frac{H_m - Pb^3/2 - H_0(c_2 - c_b)/2}{kT} \right) \\ -\exp \left(-\frac{H_m - Pb^3/2 + H_0(c_b - c_1)/2}{kT} \right) \end{array} \right\} \quad (3.28)$$

Assuming that $Pb^3 \ll kT$ and $H_0(c_2 - c_b) \ll kT$ the exponential function can be expanded to give

$$v = \frac{D_m}{b} \left\{ \frac{Pb^3}{kT} - \frac{H_0}{2kT} (c_1 - c_2) \right\} = m (P - P_v(v)) \quad (3.29a)$$

or

$$P = \frac{kT}{b^3} \cdot \frac{vb}{D_m} + \frac{H_0}{2b^3} (c_1 - c_2) \quad (3.29b)$$

with

$$m = \frac{D_m b^2}{kT}, \quad P_v = \frac{H_0}{2b^3} \cdot (c_1 - c_2), \quad D_m = \nu b^2 \exp \left(-\frac{H_m}{kT} \right) \quad (3.29c)$$

m is the mobility of the grain boundary without impurity atmosphere, and P_v is the retarding force due to the impurities. The important point is that c_1 and c_2 and thus also P_v depend upon the velocity v of the boundary so that the dependence $v = v(P)$ is contained only implicitly in Eq. (3.29a). Only the

inverse function $P = P(v)$ can explicitly be written (3.29b).

The introduction of the expressions for c_1 (Eq. (3.27a)) into Eq. (3.29b) leads to an equation $f(v, P) = 0$ which is of third order in v . The positive roots of this equation represent the function $v = v(P)$. In general, the solution $v(P)$ cannot be given in closed form; only for very high (v_H) and very low (v_L) velocities are approximate expressions possible. In zero order approximation one obtains

$$v_F = \frac{b^2 D_m}{kT} P; \quad (3.30a)$$

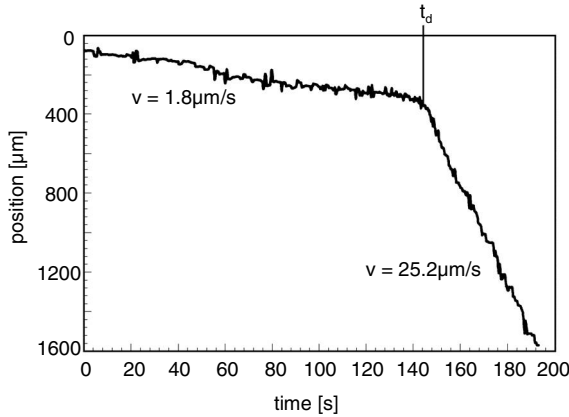
$$v_L = \frac{2b^3 D}{H_0 c_0 [\exp(H_0/kT) - 1]} \cdot P \quad (3.30b)$$

The velocity v_F describes the velocity of a free boundary, i.e. a boundary broken away from the impurity atmosphere. The velocity v_L is determined by the diffusion of the impurities together with the moving boundary. At intermediate values of v a transition from the boundary loaded with impurities to the broken away boundary occurs. This transition range (T in Fig. 3.6) is characterized by a very rapid increase in the velocity with increasing driving force P . However, it is stressed that in this transition regime the boundary also will move either as a loaded or as a free boundary or at some point can change from one state to the other, as confirmed experimentally (Fig. 3.7). This implies that the boundary cannot remain in the transition state over an extended period of time as claimed previously to explain a nonlinear relationship between grain boundary velocity and driving force.

3.3.3 Impurity Drag in Regular Solutions

Eq. (3.30) predicts that the mobility of the loaded grain boundary ought to decrease with increasing impurity concentration $m \sim 1/c_0$ and that the activation enthalpy H_m of the mobility is different for the free and loaded boundary, but in both cases H_m is independent of impurity concentration. This, however, is at variance with experimental results (Fig. 3.8). The concentration dependence of the activation energy indicates that segregated atoms in the boundary cannot be treated as a dilute solid solution, i.e. without interaction of the segregated atoms. If there is solute-solute interaction in the boundary, the impurity concentration in the boundary cannot be represented by Eq. (3.13) (the Henry isotherm) anymore. Instead, the solutes in the boundaries have to be treated as a regular solution rather than an ideal solution [197]. To simplify the mathematical treatment, we shall assume in the following that the concentration profile of solute is always given by the equilibrium concentrations in the bulk c_0 and in the boundary c^b .

When a boundary moves together with its segregated impurities, the velocity of the impurity atoms v_{im} should be equal to the boundary velocity

**FIGURE 3.7**

Recording of grain boundary position with annealing time in an Al bicrystal. At t_d the grain boundary unzips from its impurity cloud and moves freely. Note discontinuous transition without intermediate stage.

v_b . If the boundary moves under the action of an external driving force P , it imparts the same driving force to the impurities carried along

$$v_b = m_b P = v_{im} \frac{P}{\Gamma} \quad (3.31)$$

where m_b and m_{im} are the mobilities of boundary and impurity atoms, respectively. $\Gamma = c^b - c_0$ is the difference between the concentration of adsorbed impurities in the boundary c^b and the bulk concentration c_0 . With the Nernst-Einstein relation

$$m_{im} = \frac{D}{kT} \quad (3.32)$$

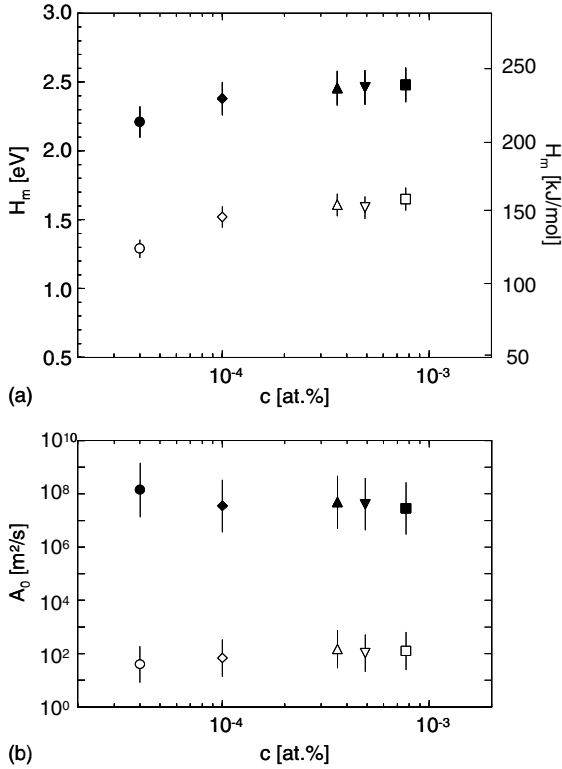
where D is the respective diffusion coefficient, Eq. (3.31) yields

$$m_b = \frac{m_{im}}{\Gamma} = \frac{D}{\Gamma \cdot kT} \quad (3.33)$$

For dilute (volume) solutions one may use the Henry isotherm

$$\Gamma = z \cdot B \cdot c_0 - c_0 = c_0 \left(z B_0 e^{\frac{H_i}{kT}} - 1 \right) \cong z B_0 e^{\frac{H_i}{kT}} c_0 \quad (3.34)$$

for $c_0 \ll c^b$. ($B = e^{G_i/kT}$, $B_0 = e^{-S_i/k}$, G_i — Gibbs free energy of adsorption, S_i — adsorption entropy, H_i — interaction enthalpy of impurity atoms with the boundary, z — number of adsorption sites in the boundary.) Eqs.

**FIGURE 3.8**

Dependence of activation enthalpy H and preexponential factor A_0 of the reduced grain boundary mobility for 38.2° (open symbols) and 40.5° (filled symbols) $\langle 111 \rangle$ tilt grain boundaries on impurity content in pure Al: \circ, \bullet — AlII; \diamond, \blacklozenge — AlIII; $\triangle, \blacktriangle$ — AlIII; $\nabla, \blacktriangledown$ — AlIV; \square, \blacksquare — AlV.

(3.31)–(3.34) render the known expression for the mobility of a boundary with impurities:

$$m_b = \frac{D_0 e^{-\frac{(H_D + H_i)}{kT}}}{zB_0 kT \cdot c_0} \quad (3.35)$$

where D_0 is the diffusion pre-exponential factor, H_D is the activation enthalpy for (volume) diffusion of the impurity atoms. According to Eq.(3.35) the activation enthalpy for grain boundary migration is the sum of two activation enthalpies, impurity diffusion and impurity adsorption. The pre-exponential mobility factor changes inversely proportionally to the impurity concentration contrary to experimental results. As evident from Fig. 3.8, even at the lowest impurity content, the activation enthalpy rises with increasing impurity concentration, whereas the pre-exponential factor remains essentially at the same level.

If there is a strong tendency toward segregation, the boundary impurity concentration may be high although the volume impurity concentration is small. For high impurity concentrations in the boundary it is necessary to take into account the mutual interaction of adsorbed atoms in the boundary. Also, grain boundaries are inhomogeneous, i.e. not every site in the grain boundary is equally favorable for impurity segregation. The essential point here is that this inhomogeneity plays an important role in the adsorption during the process of migration and thus has to be taken into account.

In the following we shall consider the interaction of impurities with grain boundaries in terms of adsorption. This allows us to express an influence of adsorption on both the activation enthalpy and the pre-exponential mobility factor. We consider a true binary system with bulk concentrations c_1 and c_2 and assume that the grain boundary chemistry is in equilibrium with the bulk, in spite of grain boundary motion

$$\mu_1^b(\gamma_1, T, c_1^b) = \mu_1^v(p, T, c_1) \quad (3.36)$$

$$\mu_2^b(\gamma_2, T, c_2^b) = \mu_2^v(p, T, c_2) \quad (3.37)$$

where μ_1^b , μ_2^b , and μ_1^v , μ_2^v are the chemical potentials of the first and second component in the bulk and in the boundary, respectively, and $c_{1,2}^b$ denote the respective boundary concentrations. The activities of atoms in both the bulk (a_1, a_2) and the boundary (a_1^b, a_2^b) are related by

$$\frac{a_1^b}{a_1} = \left(\frac{a_2^b}{a_2} \right)^{\frac{\omega_1}{\omega_2}} \cdot e^{\frac{\omega_1(\gamma_2 - \gamma_1)}{kT}} \quad (3.38)$$

where γ_1 and γ_2 are the grain boundary surface tensions of the pure first and second component, respectively, and

$$\omega_1 = - \left(\frac{\partial \mu_1^b}{\partial \gamma_1} \right)_{p, T, \gamma_2} \quad \text{and} \quad \omega_2 = - \left(\frac{\partial \mu_2^b}{\partial \gamma_2} \right)_{p, T, \gamma_1} \quad (3.39)$$

are the partial areas of the atoms of both components in the boundary⁶. Eq. (3.38) constitutes the general adsorption isotherm, expressed in terms of activities. The relation between activity and chemical potentials of components in real and ideal solutions reads

$$a_i = c_i \exp \left(\frac{\mu_i - \mu_i^{\text{ideal}}}{kT} \right) \quad (3.40)$$

For consideration of the adsorption of impurities, which interact in the boundary, and bulk solution, we can apply the Bragg-Williams approach for regular solutions, i.e. entropy changes are neglected.

With the known expressions for the enthalpy of components in a regular solution the activity in such a solution can be represented as

$$a_1 = c_1 \exp \left[\frac{z\varepsilon \cdot (c_2)^2}{kT} \right], a_2 = c_2 \exp \left[\frac{z\varepsilon \cdot (c_1)^2}{kT} \right] \quad (3.41)$$

where z is the coordination number, $\varepsilon = \varepsilon_{12} - 1/2(\varepsilon_{11} + \varepsilon_{22})$ is the heat of mixing and ε_{ij} ($i, j=1,2$) are the interaction enthalpies of the components.

Eqs. (3.38) and (3.41) yield for a regular solution in both bulk and boundary

$$\frac{c_1^b}{c_1} = \frac{\exp \left(\frac{z\varepsilon \cdot (c_2)^2}{kT} \right)}{\exp \left(\frac{z^b\varepsilon^b \cdot (c_2^b)^2}{kT} \right)} \left[\frac{c_2^b \exp \left(\frac{z^b\varepsilon^b \cdot (c_1^b)^2}{kT} \right)}{c_2 \exp \left(\frac{z\varepsilon \cdot (c_1)^2}{kT} \right)} \right]^{\frac{\omega_1}{\omega_2}} \cdot \exp \left[\frac{\omega_1(\gamma_1 - \gamma_2)}{kT} \right] \quad (3.42)$$

where ε^b, z^b are the heat of mixing and the coordination number in the grain boundary, respectively.

Some special cases are of particular interest for an analysis of experimental results.

1. Both (bulk and boundary) solutions are regular (i.e. the heat of mixing and coordination number in both solutions are the same) and the partial areas of the different species in the boundary are equal, i.e. $\varepsilon^b = \varepsilon$, $z^b = z$, $\omega_1 = \omega_2 = \omega$.

Then

$$c_1^b = \frac{Bc_1 \exp \left[\frac{2z\varepsilon}{kT} (c_1^b - c_1) \right]}{1 - c_1 + Bc_1 \exp \left[\frac{2z\varepsilon}{kT} (c_1^b - c_1) \right]} \quad (3.43)$$

where $B = e^{\omega(\gamma_2 - \gamma_1/kT)} = B_0 e^{H_i/kT}$, H_i is the enthalpy of interaction between the boundary and an adsorbed impurity atom.

⁶It should be pointed out that the partial areas as defined by Eq. (3.39) are in general not identical with the physical area fraction occupied by the respective elements in the boundary but are thermodynamical quantities exactly defined by this equation and may even assume negative values.

2. The bulk solution is ideal, whereas the boundary solution is regular, i.e. $\varepsilon = 0$, $\varepsilon^b \neq 0$, $\omega_1 = \omega_2 = \omega$. In this case

$$c_1^b = \frac{Bc_1 \exp \left[\frac{z^b \varepsilon^b}{kT} (2c_1^b - c_1) \right]}{1 - c_1 + Bc_1 \exp \left[\frac{z^b \varepsilon^b}{kT} (2c_1^b - c_1) \right]} \quad (3.44)$$

For $c_1 \ll 1$, Eq. (3.44) is known as the Fowler-Guggenheim isotherm.

3. The same as case 2, but the partial areas of the species in the boundary are different, i.e. $\varepsilon = 0$, $\varepsilon^b \neq 0$, $\omega_1 \neq \omega_2$. In this case

$$c_1^b = c_1 \exp \left(-\frac{z^b \varepsilon^b \cdot (c_2^b)^2}{kT} \right) \cdot B \left\{ \frac{c_2^b}{c_2} \exp \left[\frac{z^b \varepsilon^b \cdot (c_1^b)^2}{kT} \right] \right\}^{\frac{\omega_1}{\omega_2}} \quad (3.45)$$

The condition closest to experiments is the case of an ideal bulk and a regular boundary solution. From Eqs. (3.35) and (3.44) (denoting the impurity concentration as c and using the values for ε and z in the boundary)

$$m_b = \frac{m_{im}}{c^b - c} \cong \frac{m_{im}}{c^b} = \frac{m_0}{B_0 c} \cdot \frac{\exp \left[-\frac{H_D + H_i + z\varepsilon(2c^b - 1)}{kT} \right]}{\left\{ 1 - c + Bc \exp \left[\frac{z\varepsilon}{kT} (2c^b - 1) \right] \right\}^{-1}} \quad (3.46)$$

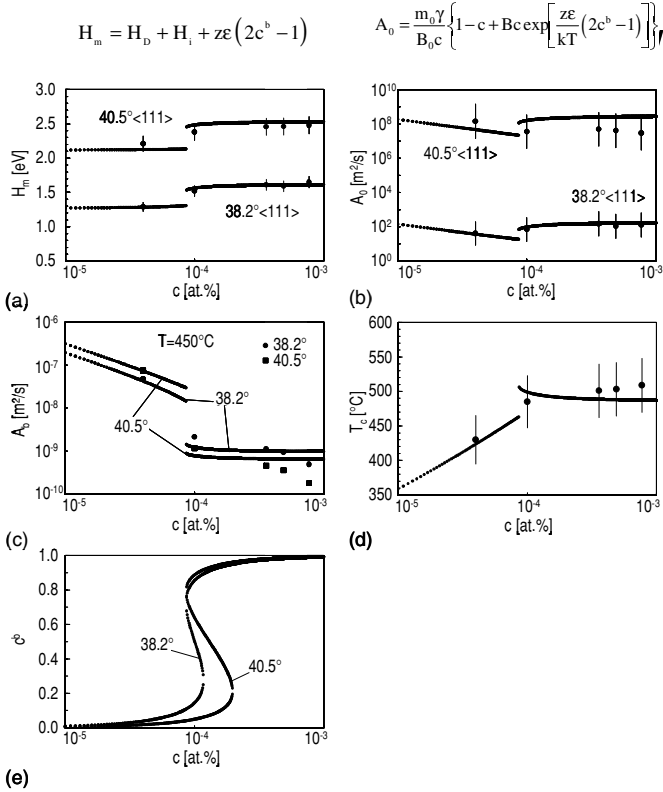
For $\omega_1 \neq \omega_2$ Eqs. (3.33) and (3.44) yield

$$m_b = \frac{m_{im}}{c^b - c} \cong \frac{m_{im}}{c^b} = \frac{m_0}{B_0 c} \cdot \frac{\exp \left[-\frac{H_D + H_i + (\beta - 1)z\varepsilon(1 - c^b)^2}{kT} \right]}{\left(\frac{1 - c^b}{1 - c} \right)^\beta} \quad (3.47)$$

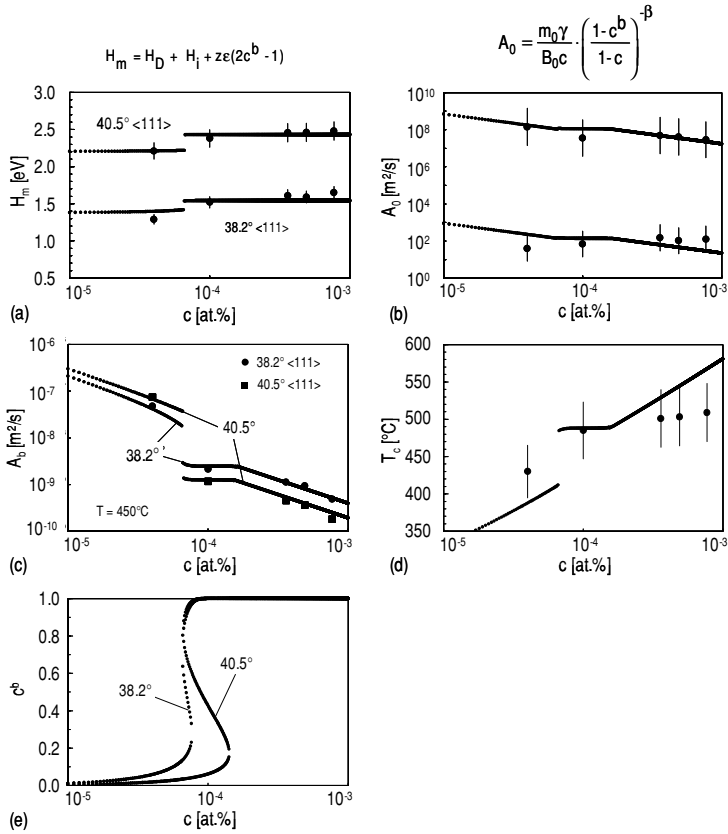
with $\beta = \omega_2/\omega_1$. An important consequence of Eqs. (3.46) and (3.47) is that the migration activation enthalpy includes the enthalpy H_D of impurity motion involved in boundary migration, the adsorption energy H_i (segregation of atoms in the pure boundary) and, in particular, the energy of interaction between adsorbed atoms. Therefore, the activation enthalpy of grain boundary migration becomes dependent on concentration, as indeed is observed in experiment (Fig. 3.8).

Figs. 3.9 and 3.10 show the dependence of boundary mobility and its parameters (A_0 , H) on impurity concentration for 38.2° and 40.5° $\langle 111 \rangle$ tilt grain boundaries as obtained by experiment and as calculated from Eqs. (3.46) and (3.47), respectively. The calculations are in a good agreement with experiment at reasonable values of H_D , H_i and $z\varepsilon$. (The magnitude of $B_0 = \exp(-S/k)$ changes in a very narrow range and was taken to be $B_0 = 5$.)

The best agreement between theory and experiment for the concentration dependence of boundary mobility was found for the isotherm, which takes into account a difference of the partial areas of the components in the boundary

**FIGURE 3.9**

Experimental data (points) and results of calculations (lines) based on Eq. (3.41) for two $\langle 111 \rangle$ tilt grain boundaries in Al. Dependence of (a) activation enthalpy H_m ; (b) preexponential factor A_0 ; (c) reduced boundary mobility A_b ; (d) compensation temperature T_c ; (e) impurity concentration in the boundary c^b on the bulk impurity content c . Parameters used for $38.2^\circ \langle 111 \rangle$ boundary: $H_D = 0.6$ eV; $H_i = 0.84$ eV; $(z\varepsilon) = 0.17$ eV; $(m_0\gamma) = 8 \cdot 10^{-5}$ m^2/s , and for $40.5^\circ \langle 111 \rangle$: $H_D = 1.5$ eV; $H_i = 0.82$ eV; $(z\varepsilon) = 0.21$ eV; $(m_0\gamma) = 90$ m^2/s .

**FIGURE 3.10**

Experimental data (points) and results of calculations (lines) based on Eq. (3.42) ($\beta = 0.05$) for two $\langle 111 \rangle$ tilt grain boundaries in Al. Dependence of (a) activation enthalpy H_m ; (b) preexponential factor A_0 ; (c) reduced boundary mobility A_b ; (d) compensation temperature T_c ; (e) impurity concentration in the boundary c^b on the bulk impurity content c . Parameters used for $38.2^\circ \langle 111 \rangle$ boundary: $H_D = 0.68$ eV; $H_i = 0.86$ eV; $(z\varepsilon) = 0.17$ eV; and for $40.5^\circ \langle 111 \rangle$: $H_D = 1.57$ eV; $H_i = 0.86$ eV; $(z\varepsilon) = 0.24$ eV.

with $\beta = 0.05$ and the fitting parameters as given in the Fig. 3.10 caption. This becomes particularly obvious from Fig. 3.10. It is interesting that the fit parameter $m_0\gamma$ for the $\Sigma 7$ boundary amounts to $m_0\gamma = 3 \cdot 10^{-4} \text{ m}^2/\text{s}$. The term $m_0\gamma$ represents the reduced mobility of the boundary in the pure matrix. If boundary migration would proceed by the transfer of individual atoms across the boundary from the shrinking to the growing grain, then m_0 ought to follow simple rate theory, i.e. $m_0\gamma \equiv 10^{-5}$ for Al. For the same reason the activation energy for a jump across the boundary ought to be comparable to the activation energy of grain boundary diffusion, i.e. for Al in the range of 0.6–0.7 eV for the $\Sigma 7$ boundary. Obviously, the motion of the special boundary $\Sigma 7$ is reasonably described in the framework of this simple theory, and the experimentally observed deviations of H_D and A_0 from rate theory can be attributed to the effect of segregated impurities according to the theory outlined above. Non-special boundaries, in this case the $40.5^\circ \langle 111 \rangle$ boundary, behave quite differently: both the activation energy for grain boundary motion ($H_D = 1.57 \text{ eV}$) and the preexponential reduced mobility factor ($m_0\gamma = 3.5 \cdot 10^2 \text{ m}^2/\text{s}$) are much higher (even orders of magnitude for $m_0\gamma$) than expected for grain boundary motion caused by the exchange of individual atoms across the boundary. This indicates that the mechanism of grain boundary motion at least in this non-special boundary is different from the migration of special boundaries. In fact, the magnitude of activation energy and preexponential factor as well as other experimental results for the non-special boundary hint at a correlated or cooperative motion of atoms during boundary migration.

3.3.4 Vacancy Drag

Not only impurities may interact with and segregate to grain boundaries. The same principle holds for intrinsic defects, like vacancies. In principle, vacancy drag can be treated completely in analogy to impurity drag. However, it is complicated by the fact that there is no conservation rule for vacancies; rather, vacancies may be produced and eliminated [198]–[200]. In fact, there is experimental evidence that grain boundaries can act as sources and sinks for vacancies [200, 201]. If there is a concentration c_s of sites which may act as sinks or sources (imagine a ledge on the crystallite surface in the boundary) then the production rate for vacancies is

$$\dot{q}_+ = c_s \nu c^* \exp \left(-\frac{H_{FB} + H_{DB}}{kT} \right) \quad (3.48)$$

where ν is a frequency factor, c^* an entropy factor, H_{FB} and H_{DB} represent the activation enthalpy for grain boundary vacancy formation and diffusion, respectively.

The annihilation rate is given by

$$\dot{q}_- = \frac{c_{vb}}{\tau} = c_{vb} \cdot c_s \nu \exp\left(-\frac{H_{DB}}{kT}\right) \quad (3.49)$$

where c_{vb} is the actual vacancy concentration and τ the lifetime of a vacancy in the boundary. The net production rate of boundary vacancies reads

$$\dot{q}_b = \dot{q}_+ - \dot{q}_- = -\frac{c_{vb} - c_{vb}^e}{\tau} \quad (3.50)$$

In equilibrium, $\dot{q} = 0$ and thus, $c_{vb} = c_{vb}^e$, i.e. the equilibrium concentration of vacancies in the boundary.

Another source of vacancy production is the annihilation of dislocations in the boundary, since each atom on a dislocation line carries an excess volume of about one atomic volume. Each atom on the dislocation line can, therefore, be considered to produce one vacancy upon absorption of the dislocation in the grain boundary, for instance during primary recrystallization. For a (uniform) dislocation density ρ and a grain boundary migration rate v , the vacancy production rate by dislocation absorption in the boundary is

$$\dot{q}_d = \alpha b \rho v \quad (3.51)$$

where the dimensionless factor $\alpha \equiv 1$ is the number of vacancies formed per dislocation site. Since the grain boundary also carries an excess volume its motion will be accompanied by a production of vacancies, e.g. during grain growth. In fact, such vacancy generation was observed in molecular dynamics computer simulations of a shrinking half-loop grain boundary [201, 202]. If the number of vacancies is not conserved, the diffusion equation (Eq.(3.19)) has to be modified to include the vacancy production term \dot{q} which is only nonzero in the grain boundary

$$\frac{\partial c}{\partial t} = D \frac{\partial^2 c}{\partial x^2} + \frac{\partial}{\partial x} \left(\frac{Dc}{kT} \frac{dU}{dx} \right) + \dot{q} \quad (3.52)$$

For a potential well as defined by Eq.(3.20) we obtain for the steady state in the reference frame of the moving boundary

$$\frac{\partial c}{\partial t} = D \frac{\partial^2 c}{\partial x^2} + v \frac{\partial c}{\partial x} + \dot{q} = 0 \quad (3.53)$$

The problem can be treated exactly as for impurities previously, except that the flux equations through the borders of the boundary now read (one atomic boundary)

$$j_{B/II} = j_{II} \quad (3.54a)$$

$$j_{I/B} = j_{B/II} - \dot{q}b = j_{II} - \dot{q}b \quad (3.54b)$$

$$j_I = j_{I/B} = j_{II} - \dot{q}b \quad (3.54c)$$

or in terms of jump frequencies

$$c_{vb} \frac{D}{b} e^{-H_0/kT} - c_2 \cdot \frac{D}{b} - v c_2 = -v c_0 \quad (3.55a)$$

$$c_1 \frac{D}{b} - c_{vb} \frac{D}{b} e^{-H_0/kT} - v c_{vb} = -v c_0 - \dot{q} b \quad (3.55b)$$

Again this can be solved for c_1 , c_2 and c_{vb} .

The migration rate is again obtained from

$$v = b\nu \left\{ \begin{array}{l} \exp \left(-\frac{H_m - Pb^3/2 - H_0(c_2 - c_{vb})/2}{kT} \right) \\ -\exp \left(-\frac{H_m - Pb^3/2 + H_0(c_{vb} - c_1)/2}{kT} \right) \end{array} \right\} \quad (3.56)$$

which cannot be solved analytically, since c_1 , c_2 and c_{vb} depend on v . In the limit of high (v_F) and low (v_L) velocities, assuming vacancy production by dislocation absorption we obtain the approximate solutions

$$v_F = \frac{b^2 D_m}{kT} \left(P - \frac{\alpha \rho H_0}{2b} \right); \quad v_L = \frac{2b^2 D}{H_0 (c_{vb}^e - c_0)} P \quad (3.57)$$

where $c_{vb}^e = c_0 \exp(H_0/kT)$. With $\Phi = bv/D$, $h = H_0/2b^3$, $\Psi = e^{-H_0/kT}$, $\gamma = b^2/\tau D$, $\lambda = \alpha \rho b^2$, and $\Theta = kT/b^3 \cdot (D/D_m)$ the following cases can be distinguished:

(a) Dislocation type sources but no sinks ($\gamma = 0$, $\lambda \neq 0$)

In this case one obtains for a one-atomic boundary the concentrations

$$c_1 = c_0 + \lambda; \quad (3.58a)$$

$$c_{vb} = \frac{1 + \Phi}{\Psi + \Phi} (c_0 + \lambda); \quad (3.58b)$$

$$c_2 = c_0 - \frac{\Phi(1 + \Psi)c_0 - \Psi(1 + \Phi)\lambda}{(1 + \Phi)(\Psi + \Phi)} \quad (3.58c)$$

Eq. (3.58a) shows that now the concentration c_1 left behind the boundary is larger than the initial concentration c_0 , it also includes the vacancies contained in the dislocations (λ). The difference $c_1 - c_2$ which is proportional to the retarding force $P_v = \alpha \cdot \rho H_0/(2b)$ (Eq.(3.57)) is zero for $\Phi = 0$ and λ for $\Phi = \infty$. For small values of Φ , P_v runs through a maximum, whereas for large Φ a continuous increase occurs.

The equation $f(\Phi, P) = 0$ is again of third order, and the approximations Φ_F and Φ_L

$$\begin{aligned} \Phi_F &= \frac{P}{\Theta} - \frac{h\lambda}{\Theta} + \frac{h}{P} \{(c_0 + \lambda)\Psi - c_0\} \rightarrow \frac{P - h\lambda}{\Theta} \\ \Phi_L &= \frac{P}{h(c_0 + \lambda - c_0\Psi)/\Psi + \Theta} \cong \frac{P}{h(c_0 + \lambda)/\Psi - hc_0} \end{aligned} \quad (3.59)$$

Of interest here is the case that the driving force P is also proportional to the dislocation density λ as in the case of primary recrystallization. Here $P = \sigma_d \lambda$ with σ_d being roughly the energy per dislocated atom divided by b^3 . Then the function $\Phi(\lambda)$ instead of $\Phi(P)$ has to be considered which contains two aspects of the dislocation density λ : the dislocations supply a driving force and thus accelerate the boundary, and they supply vacancies which retard the boundary. For $\sigma_d > h$ the accelerating influence dominates and the expressions for Φ_F and Φ_L remain valid. For $\sigma_d < h$, i.e. for dominance of the retarding effect, only Φ_L stays correct, whereas for high velocities there is no longer a proportionality between Φ and λ , but a plateau value Φ_p arises. This case, however, is improbable.

(b) Boundary sources with infinite rates ($\gamma = \infty$)

Now let us consider the opposite limiting case, where sources and sinks exist in the boundary and where the formation and annihilation frequency of vacancies is extremely high ($\gamma = \infty$). With $\Phi c_{vb}^e = c_v^e$, the equilibrium concentration in the lattice, it follows

$$c_1 = \frac{c_v^e + c_{vb}^e \Phi}{1 + \Phi}; \quad c_{vb} = c_{vb}^e; \quad c_2 = c_0 - \frac{c_1 - c_v^e}{1 + \Phi} \quad (3.60)$$

One recognizes that, due to the high source rate, the boundary layer always exhibits the (boundary) equilibrium concentration c_{vb}^e . In the neighboring plane 2 for $\Phi = 0$ the (lattice) equilibrium concentration $c_2 = c_v^e$ is found, whereas for $\Phi = \infty$ again $c_2 = c_v^e$. Depending upon whether $c_v^e < c_0$ or $c_v^e > c_0$, a concentration dip or concentration peak occurs. Most interesting, however, is the concentration of vacancies c_1 left behind the boundary. Also here for $\Phi = 0$ the lattice equilibrium value $c_1 = c_{vb}^e$, but for $\Phi = \infty$ the boundary equilibrium value c_v^e is obtained. Since c_{vb}^e and c_v^e are mostly larger than c_0 , this means that also here the boundary leaves more vacancies behind than existed in the original crystal.

The equation $f(\Phi, P) = 0$ now becomes second order in Φ and the resulting approximate solutions are

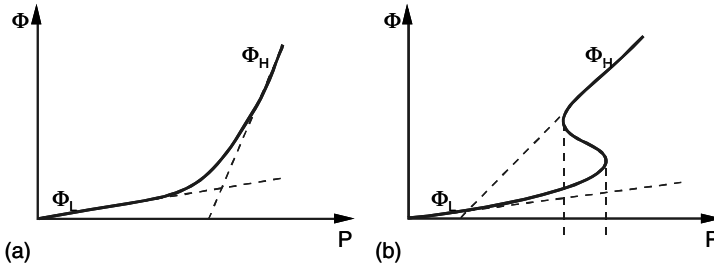
$$\Phi_h = \frac{P}{\Theta} - \frac{h}{\Theta} (c_{vB}^e - c_0) + \frac{h}{P} (c_{vb}^e - c_0) \rightarrow \frac{P - hc_{vb}^e}{\Theta} \quad (3.61a)$$

$$\Phi_L = \frac{P}{\Theta + h(c_{vb}^e - c_0)} \cong \frac{P}{hc_{vb}^e} \quad (3.61b)$$

It must be noted that Eqs. (3.60) and (3.61) do not depend upon λ and are valid for the cases $\lambda = 0$ as well as $\lambda \neq 0$. This means that, because of the infinitely high rate for establishing equilibrium, it does not matter whether a few vacancies (more or less) have to be accommodated.

(c) The general case ($\lambda \neq 0$; $0 < \gamma < \infty$)

This case is only little more complicated and contains no new features in

**FIGURE 3.11**

Normalized grain boundary migration rate Φ vs. driving force in the presence of vacancy drag. (a) Low drag force; (b) high drag force.

addition to those already discussed. One obtains for the concentrations

$$\begin{aligned}
 c_1 &= \frac{\Psi - \Phi}{1 + \Phi} c_{vb}; & c_{vb} &= \frac{c_0 \Phi + \lambda \Phi + c_{vb}^e \gamma}{\gamma + \frac{\Psi + \Phi}{1 + \Phi} \Phi} \\
 c_2 &= c_0 - \frac{c_0 - c_{vb}^e \Psi}{1 + \Phi} = \frac{c_{vb} \Psi + c_0 \Phi}{1 + \Phi}
 \end{aligned} \tag{3.62}$$

One easily recognizes that for $\Phi \rightarrow \infty$ ($c_2 = c_0$, $c_{vb} = c_1 = c_0 + \lambda$) all diffusion effects are suppressed and that for $\Phi \rightarrow 0$ ($c_{vb} = c_{vb}^e$, $c_2 = c_1 = c_{vb}^e \cdot \Psi = c_v^e$) equilibrium is approached. Since $\Psi < 1$, it is always $c_{vb} > c_1$ (due to the potential well). Mostly (except for an extremely high c_0) one also has $c_2 < c_{vb}$ and $c_1 > c_0$. Whether $c_2 < c_0$ or $c_2 > c_0$ (dip or peak in front of the moving boundary) depends upon the circumstances.

The difference $c_1 - c_2$, which is proportional to the retarding force P_v , increases from 0 at $\Phi = 0$ to λ at $\Phi = \infty$. For large values of λ this increase occurs monotonously; for small λ the function $P_v(\Phi)$ runs through a maximum. In Fig. 3.11 the function $\Phi(P)$ has schematically been derived by graphical determination of the difference $P - P_v$. One recognizes that for each value of P either one or three values of Φ exist (Fig. 3.11). In the first case one has a continuous transition from the state of a boundary loaded with vacancies to the broken away state, in the latter case a discontinuous transition. In this case the transition point (indicated by the dashed lines) cannot exactly be defined. For very high and very low velocities, however, a single solution $v = v(P)$ always exists,

$$\begin{aligned}
 \Phi_H &= \frac{P}{\Theta} - \frac{h\lambda}{\Theta} - \frac{h}{P} \{c_v^e (1 - \Psi) + \gamma (c_{vb}^e - c_0) - \lambda (\Psi + \gamma)\} \rightarrow \frac{P - h\lambda}{\Theta} \\
 \Phi_L &= \frac{P}{h(c_{vb}^e - c_0) + \Theta} \cong \frac{P}{h(c_{vb}^e - c_0)}
 \end{aligned} \tag{3.63}$$

3.3.5 Drag Effects by Second-Phase Particles

It is common knowledge that second phase particles drag grain boundary motion [203]–[207]. The physical basis of this drag effect is the attraction force between particle and grain boundary which is due to the reduction of grain boundary or interface energy upon contact of particle and grain boundary. The simplest and commonly exclusively attraction force considered is the well-known “Zener force,” which appears when a particle intersects the boundary and in doing so eliminates the area of the boundary. For a spherical particle with radius r and a planar grain boundary with specific energy γ the reduction of grain boundary energy per particle ΔG is (Fig. 3.12)

$$\Delta G = \gamma (1 - \pi r^2) \quad (3.64)$$

Correspondingly, the maximum attraction force f^* is

$$f_1^* = 2\pi r \gamma \quad (3.65)$$

A more precise calculation for a flexible boundary gives the Zener force as [203]

$$f_1^* = \pi r \gamma \quad (3.66a)$$

Actually if N is the number of particles per unit volume of the system, the volume fraction of the particles is $c = 4/3\pi r^3 N$. The particles in contact with the boundary are confined to a volume $2r \cdot 1 \text{ cm}^2$, i.e. n , the number of particles per 1 cm^2 of a grain boundary, is equal to $n = 2rN$, $n = 3c/(2\pi r^2)$. Thus the maximum pinning force

$$f_{\max} = n f_1^* = \pi r \gamma \cdot 3c/(2\pi r^2) = \frac{3}{2} c \gamma / r \quad (3.66b)$$

Eq.(3.66a) is the well-known Zener equation for the back driving force on moving grain boundaries in two phase alloys, which is utilized for the control of grain size during recrystallization and grain growth. The Zener force, however, is not the only attraction force in a particle-boundary system. For instance, if a particle has a coherent interface with the matrix and correspondingly a low free energy (surface tension), this advantage will be lost when the particle is swept by the boundary, since grain boundary migration changes the orientation of the matrix in contact with the particle and, consequently, the interface energy changes by [208]

$$\Delta G = 4\pi r^2 (\gamma_2 - \gamma_1) \quad (3.67)$$

and the maximum drag force is

$$f_2^* = 8\pi r (\gamma_2 - \gamma_1) \quad (3.68)$$

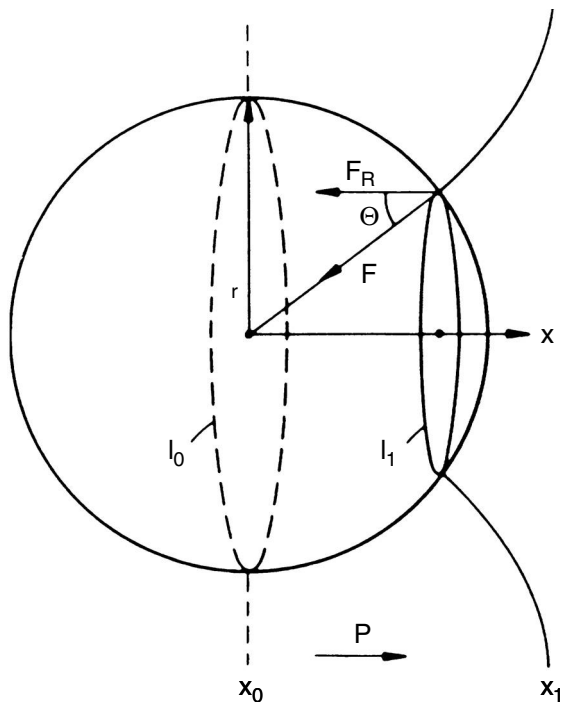


FIGURE 3.12
 Origin of Zener drag and grain boundary shape for a rigid boundary (dashed line) and a flexible boundary (solid line).

where γ_1 , γ_2 are the interface free energies of the particle in the growing and vanishing grain, respectively.

There is a third cause of attraction between particle and boundary. If the increase of interface energy, according to Eq. (3.67), exceeds a critical value, then the moving grain boundary prefers to circumvent the particle and to leave behind a spherical volume of the original grain with the particle inside [206, 208] (Fig. 3.13). In this case

$$\Delta G = 4\pi r^2 \gamma \quad (3.69)$$

and the maximum attraction force

$$f_3^* = 8\pi r \gamma \quad (3.70)$$

The maximal attraction force (see Eqs. (3.66), (3.68), (3.70)) controls the process of boundary-particle interaction, the pinning properties of the particle and the detachment of the grain boundary from the particle. Traditionally, the dragging of a moving grain boundary by particles of a second phase is considered in the approximation where the particles act as stationary pinning centers for the boundaries [203, 204]. Consequently, the smaller the size of the particles, the more pronounced the effect of particles on grain boundary motion. On the other hand, it was reported [208] that inclusions in solids are not necessarily immobile, and their mobility drastically increases with decreasing particle size. The mobilities of particles for different atomic transport mechanisms are given in Table 3.2.

For grain boundary motion in a system with mobile particles, derived from reasonings very akin to the solute drag theory, the velocity of the joint motion of grain boundary and particles reads

$$v = \frac{Pm_b}{1 + \int_0^\infty \frac{\bar{n}(r)m_b}{m_p(r)} dr} \quad (3.71)$$

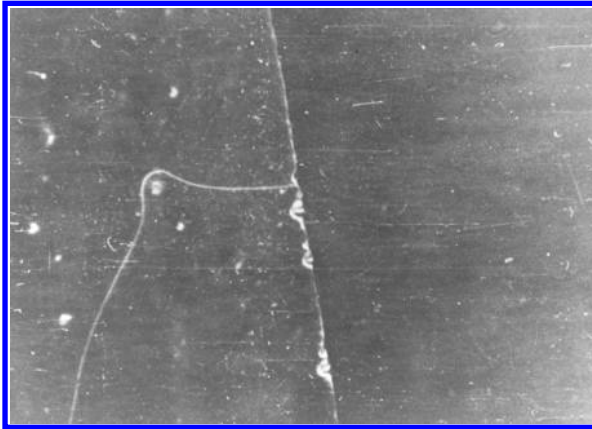
where, as usual, P is the driving force of grain boundary migration, m_b is the grain boundary mobility, $\bar{n}(r)$ is the number of particles per unit area of the boundary, $m_p(r)$ is the mobility of particles with size (radius) r . It is evident that the motion of the boundary-particle complex depends on the mobility of the boundary, the mobility of the particles, the particle distribution function and, what is particularly important, the size of the particles. There are two limiting cases where the physical nature of the phenomenon manifests itself most clearly.

(i) High particle mobility

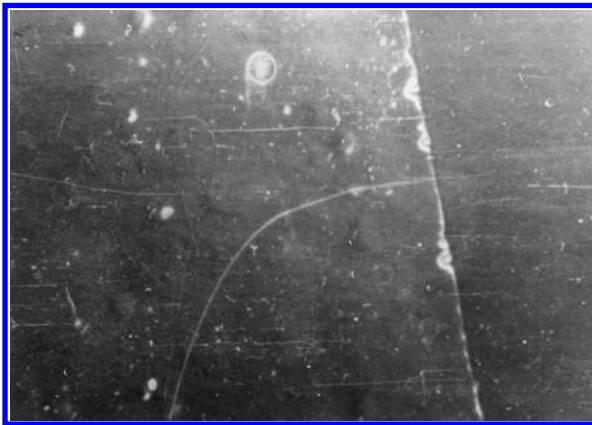
$$\int_0^\infty \frac{\bar{n}(r)m_b}{m_p(r)} dr \ll 1 \quad (3.72)$$

Then

$$v \cong m_b P \quad (3.73)$$



(a)



(b)

FIGURE 3.13

A moving grain boundary circumvents a particle in Cu (a) and leaves a spherical grain boundary behind (b).

TABLE 3.2

Mobility of Inclusions in Solids

Atomic trans- port mecha- nism	solid sphere	Type of inclusion		thermal groove*
		spherical bubble	spherical void	
Bulk diffusion in the matrix (D_{vm})	$m_p(r) \approx$ $\frac{D_{vm}\Omega_a}{kT} \frac{1}{r^3}$ [207]			$m_g(h) =$ $= \frac{3}{2} \frac{\Theta_c v_s}{h^3} \frac{\Omega_a^2 D_s}{kT}$ [210]
	$m_p(r) =$ $\frac{3}{2\pi} \frac{D_{vm}}{kT} \frac{\Omega_a^2 c_b}{r^3}$ [209]			
	$m_p(r) =$ $\frac{1}{\pi r^3} \frac{D_{vm}\Omega_a}{kT}$ [211]			
Bulk diffusion in the inclusion (D_{vi})	$m_p(r) \approx$ $\frac{D_{vi}}{10} \frac{c_i}{kT} \frac{\Omega_a^2}{\Omega'_a} \frac{1}{r^3}$ [207]		$m_p(r) =$ $\frac{\Gamma}{4\pi} \frac{\Omega_a^2 p D_{gas}}{(kT)^2 r^3}$	$m_g(h) =$ $\left(\frac{D_{gas}}{kT} \right)$ $\cdot \left(\frac{p}{kT} \right) \cdot \frac{\theta_c \Omega_a^3}{h^2}$ [210]
Interface diffusion (D_s)	$m_p(r) \approx$ $\frac{1}{10} \frac{D_s b}{kT} \frac{\Omega_a}{r^4}$ [207]	$m_p(r) =$ $0.3 \left(\frac{b}{r} \right)^4 \frac{D_s}{kT}$		
	$m_p(r) =$ $\frac{\lambda}{\pi r^4} \frac{D_s \Omega_a}{kT}$ [211]	[212]		
	$m_p(r) =$ $\frac{3}{2\pi} \cdot \frac{\Omega_a^2}{kT} \cdot \frac{v_s D_s}{r^4}$ [209]			
	$m_p(r) =$ $\frac{v_s \Omega_a^2 D_s}{\pi kT r^4}$ [208]			
Diffusion of vacancies (D_V)	$m_p(r) =$ $\frac{3\Gamma'_1 D_v \Omega_a}{2\pi f kT} \cdot \frac{1}{r^3}$ [207]			
<p>* m_g, m_p is the mobility per unit length; Θ_c is the critical angle at the vertex of the groove; h is the depth of the groove; c_b is the concentration of diffusing atoms in the bulk; c_i is the concentration of diffusing atoms in the inclusion; Ω_a is the atomic volume in the bulk; Ω'_a is the atomic volume in the inclusion; p is the pressure inside the void; D_{gas} is the diffusion coefficient for the gas inside the void; b is the lattice constant; λ is the effective thickness of the surface layer; v_s is the density of surface atoms; f is the correlation factor; $\Gamma = (1 + \nu)/3(1 - \nu)$; ν is the Poisson ratio; $\Gamma'_1 = 1$ for $\ell \gg r$; $\Gamma'_1 = \Gamma/3$ for $\ell \ll r$, ℓ is the average distance between source and sink.</p>				

In this case the grain boundary velocity is determined by the mobility of the boundary.

(ii) Low particle mobility

$$\int_0^\infty \frac{\bar{n}(r)m_b}{m_p(r)} dr \gg 1 \quad (3.74)$$

then

$$v \cong \frac{P}{\int_0^\infty \frac{\bar{n}(r)}{m_p(r)} dr} \quad (3.75)$$

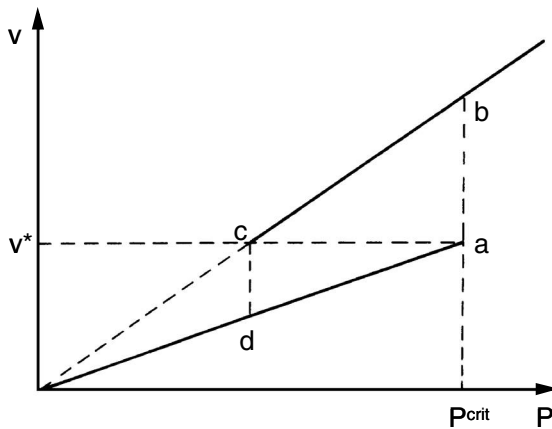
or in the simple case of a single size particle distribution: $\bar{n}(r) = n_0\delta(r - r_0)$

$$v = \frac{Pm_p(r_0)}{n_0} \quad (3.76)$$

In this limit the velocity of the grain boundary is determined by the mobility and the density of the attached particles.

$^*m_g \cdot m_p$ is mobility per length unit; Ω_c is critical angle at the vertex of the groove; h is depth of the groove c_b is concentration of diffusing atoms in the bulk; c_i is concentration of diffusion atoms in the inclusion; Ω_a is atomic volume in the bulk; Ω'_a is atomic volume in the inclusion; p is pressure inside the void; D_{gas} is diffusion coefficient for the gas inside the void; b is lattice constant; λ is effective thickness of the surface layer; v_s is density of surface atoms; f is correlation factor; $\Gamma = (1 + \nu)/3(1 - \nu)$; ν is the Poisson ratio; $\Gamma'_1 = 1$ for $\ell \gg r$; $\Gamma'_1 = \Gamma/3$ for $\ell \ll r$; ℓ is average distance between source and sink.

The collective movement of particles and grain boundary at subcritical driving forces and the detachment of particles at supercritical driving forces result in a bifurcation of the grain boundary migration rate with increasing driving force. This is schematically shown for a single size particle distribution in Fig. 3.14. At low driving forces, the boundary moves together with the particles, and the kinetics of this movement are determined by the particle mobility and density (Eq.(3.76)). When the driving force reaches the critical value $P^{crit} = f^*n$, the grain boundary will breakaway from the particles, and thus instantly increase its velocity to the migration rate of an unloaded boundary (point b in Fig. 3.14). The velocity difference between a loaded and a free boundary corresponds to the difference between the particle mobility $m_p(r)/n$ and the grain boundary mobility (m_b). On the other hand, if the driving force acting on the unloaded boundary decreases, the grain boundary velocity will decrease in proportion to the driving force until a critical value v^* (point c in Fig. 3.14) is reached. At this point the boundary velocity changes discontinuously to the velocity corresponding to the loaded boundary, since then the particles become capable of moving with the boundary and will exert a drag force. Therefore, a hysteresis exists between the points of particle detachment with increasing driving force and particle attachment at decreasing boundary velocity. In real systems the situation will be more complicated, since the

**FIGURE 3.14**

Dependence of boundary migration rate on driving force in the presence of mobile particles. At $P > P^{crit}$ the boundary is detached from the particles, for $v < v^*$ it moves together with the particles.

particles will not be of uniform size, but will have a size distribution, and the normalized particle mobility $m_p(r)/n$ and thus the hysteresis will depend on the shape of the distribution according to Eq. (3.71).

The behavior of a curved grain boundary, which moves in a system with mobile particles, is more complicated than a planar boundary and can be easily analyzed only for steady-state motion of a grain boundary. This topic will be addressed in terms of its influence on the shape of a moving boundary in Sec. 3.4.3.

So far we have considered the migration of a boundary loaded with particles and the velocity dependent detachment of particles from the boundary. In reality, however, there will be a volume distribution of particles. For a stationary boundary ($v = 0$) an equilibrium distribution of particles on the boundary $\bar{n}_b(r)$ will be established, which is different from the volume distribution $\bar{n}_v(r)$ owing to the interaction energy $U_z = K_1 \pi r^2 \gamma$, between particle and boundary (in Zener approximation, K_1 is the geometry factor)

$$\bar{n}_b(r)dr = 2r\bar{n}_v(r)\exp\left(\frac{K_1\pi r^2\gamma}{kT}\right)dr \quad (3.77)$$

If a boundary would move from a particle free volume to a particle containing volume, the equilibrium distribution will be readily established. For a moving boundary, however, the equilibrium particle distribution can only be maintained for particles that are able to migrate with the boundary, i.e. for a given velocity only all particles with size $r < r_c(v)$. At an instant of time a moving

boundary will, therefore, be in contact with two types of particles, namely the thermally distributed particles for $r < r_c(v)$ and the volume distribution of particles with $r > r_c(v)$, to which the boundary is attached temporarily during its motion. Both kinds of particles, however, have quite a different effect on boundary migration. While the small particles, which migrate with the boundary, reduce the effective driving force, the large statistically touched particles constitute a “frictional” force, acting like pinning centers.

With increasing boundary velocity the number of particles attached to the boundary diminishes so that the net drag effect decreases, while the “frictional” forces increase owing to a growing number of contacted but unattached particles. Therefore, the dependence of boundary velocity on driving force does not reveal a discontinuity as in Fig. 3.14; rather, it will continuously change between the two branches [208].

It is stressed that for mobile obstacles, grain boundary behavior and finally microstructure evolution is not any longer determined by the distribution of obstacle spacings, but rather by the distribution of obstacle mobilities.

The discussion so far has been based on the assumption that the particle distribution in the system is temporally constant. However, it was shown that the particle distribution behind the moving grain boundary was different from the one in front of the boundary. Moreover, the particle distribution, observed behind the moving boundary, is shifted toward the large size particles as compared to the particle distribution ahead of the moving grain boundary [213, 214]. The authors explained this phenomenon by “the increased diffusion permeability of grain boundaries” [213]. Quantitative calculations show that for particle densities ($\sim 10^{13} \text{ cm}^{-3}$ given in [213, 214], grain growth rate (up to 10^{-4} cm/s), and rate of particles growth ($\sim 10^{-9} \text{ cm/s}$) the contribution of grain boundary diffusivity for a time, when a particle is in contact with the grain boundary, is negligibly small. The observed phenomena are more likely due to another effect of boundary-particle interaction. If the particles are large and thus practically immobile at a given driving force and temperature they act as pinning centers and cause the initially planar grain boundary to bow out between the particles. This bulging, however, increases the grain boundary area and, consequently, decreases the level of grain boundary adsorption, i.e. adsorption of the grain boundary becomes unsaturated. The only powerful source for solute atoms to replenish the concentration in the boundary are the second-phase particles, primarily the smallest of them, in accordance with the Gibbs-Thomson equation, which states that the chemical potential of atoms in a particle increases with decreasing radius of curvature (size of a particle). Consequently, the curved grain boundary tends to dissolve the attached second-phase particles, most rapidly the smallest of them. With decreasing particle size the mobility of the particle increases and eventually permits the particle to move together with the grain boundary, causing the latter to flatten. The locally flat grain boundary will now be oversaturated by adsorbed atoms, and in turn will redistribute the solute atoms to the particles, favoring the largest ones. A shift of the particle size distribution toward

a larger mean size is the consequence.

3.3.6 Groove Dragging

In the past, virtually all known techniques of studying grain boundary migration utilized the observation of the line of intersection of a grain boundary with a free surface. However, if a grain boundary is exposed to the surface a new situation arises. The result of this interaction between the grain boundary and the free surface is a new surface defect — a thermal groove. The displacement of this defect requires mass transport and consequently, energy dissipation, which makes itself felt as a drag force on the boundary. That a thermal groove hinders grain boundary migration can be easily understood from a very simple concept. Under the assumption of a stationary groove and a flat grain boundary, it is evident that the boundary has to increase its area when being displaced from the root of the groove. The corresponding drag force P_R is easily derived from Fig. 3.15

$$P_R = -\frac{2\gamma \cdot dy}{\delta \cdot dx} = -\frac{2\gamma}{\delta} \cdot \cot \frac{\Theta}{2} \cong -\frac{\gamma^2}{\delta \gamma_s} \quad (3.78)$$

using $2\gamma_s \cos \Theta/2 = \gamma$ and $\sin \Theta/2 \cong 1$, since Θ is close to π (the difference is a few degrees only). Evidently, groove dragging is particularly aggravating at small specimen thickness δ (γ_s — free surface tension).

In reality the situation is complicated by the fact that neither the groove remains stationary and symmetric nor the boundary remains flat; rather the boundary will bulge in the specimen interior (Fig. 3.16). In fact, in grain boundary migration experiments the mobility of the system grain boundary-thermal groove is actually measured. Mullins was the first who understood the role of the free surface for a grain boundary and the effect of a thermal groove on grain boundary motion [215]–[218]. Recently Mullins' approach was extended by Brokman et al. [219, 220] who considered the steady-state motion of a grain boundary in a thin film under the action of a thermal groove. Some simple groove models were considered in [221, 222]. It should be stressed that the approach by Brokman et al. maintained the principal Mullins' assumption: the angle Θ at the root of a groove (Fig. 3.15) remains constant during grain boundary motion and is determined by the equilibrium values of the surface tensions of grain boundary and free surface.

This can be looked at from a different perspective, however [210]. The equation of motion of a uniform isotropic boundary under the action of a driving force P and a curvature K may be written as

$$\dot{y} = m_b (P - \gamma K) \frac{ds}{dx}$$

$$\dot{y} = m_b \left\{ P + \gamma y'' \left[1 + (y')^2 \right]^{-3/2} \right\} \left[1 + (y')^2 \right]^{1/2} \quad (3.79)$$

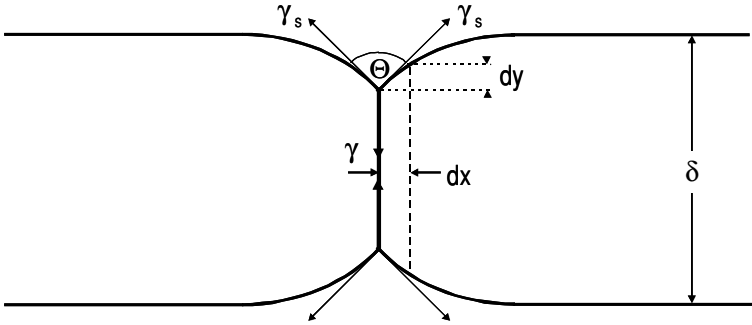


FIGURE 3.15

A groove exerts a drag on the boundary, since a small boundary displacement increases the grain boundary area. The drag force does not depend on the depth of the groove.

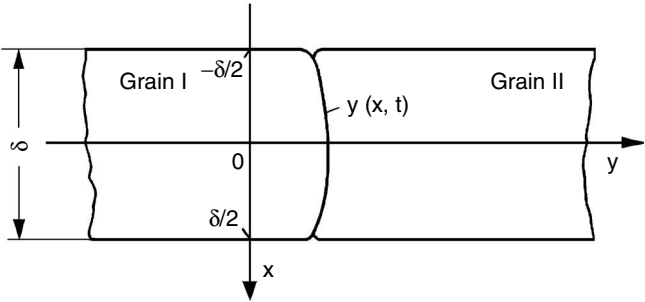


FIGURE 3.16

Through thickness grain boundary shape $y(x, t)$ under the action of a driving force for migration and surface grooves.

where s is the line element, $y(x, t)$, $-\delta/2 \leq x \leq \delta/2$ is the function describing the profile of the boundary (δ is the thickness of the specimen, Fig. 3.16). We also use the common notation $y' = dy/dx$, $y'' = d^2y/dx^2$. For a moderately curved boundary $(y')^2 \ll 1$ and Eq. (3.79) simplifies to

$$\dot{y} = m_b (P + \gamma y'') \quad (3.80)$$

Two boundary conditions are dictated by symmetry arguments

$$y(-\delta/2, t) = y(\delta/2, t) \quad \text{and} \quad y'(0, t) = 0 \quad (3.81)$$

and owing to the coincidence of the bottom of the groove and the terminal point of the boundary

$$V = \dot{y}(-\delta/2, t) + U y'(-\delta/2, t) \quad (3.82)$$

where V is the horizontal and U the vertical velocity component of the bottom of the groove (Fig. 3.17). To determine the velocities V and U we consider the formation, growth and migration of the thermal groove which appears along the intersection of the moving grain boundary with the crystal surface. In a general form, the kinetics of groove formation is given by

$$\dot{Y} = -\Omega_a (J_s + J_g + J_v) \left[1 + (Y')^2 \right]^{-1/2} + V Y' \quad (3.83)$$

$Y(x, t)$ is the shape of the groove (Fig. 3.18), Ω_a is the atomic volume, $J_s(x, t)$ is the surface diffusion flux, $J_g(x, t)$ is the flux perpendicular to the surface of atoms carried through the gas phase, $J_v(x, t)$ is the vacancy diffusion flux through the crystal. The last term in the right-hand part of Eq. (3.83) represents the convection flux due to the coordinate system moving with the groove velocity V , i.e.

$$\dot{Y} = \frac{\partial Y}{\partial t} + V Y' \quad (3.84)$$

The magnitude of each flux depends on the shape of the surface [215]–[218]. The equilibrium of the forces of grain boundary and free surface tension at the bottom of the groove γ and γ_s , respectively, requires (Fig. 3.18)

$$\begin{aligned} \gamma_s (\cos \Theta_+ - \cos \Theta_-) &= \gamma \sin \Theta \\ \gamma_s (\sin \Theta_+ + \sin \Theta_-) &= \gamma \cos \Theta \end{aligned} \quad (3.85)$$

It can be shown [210] that the increment of $\tan \Theta$ consists of two parts, the first due to the change of the slope of the boundary, and the second due to the increasing depth of the bottom of the groove (Fig. 3.17)

$$\frac{d(\tan \Theta)}{dt} = \dot{y}'(-\delta/2, t) + U y''(-\delta/2, t) \quad (3.86)$$

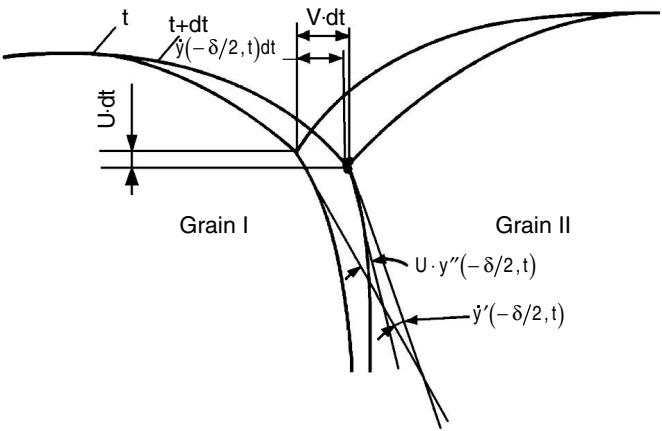


FIGURE 3.17
Variation in the surface profile during boundary migration with concomitant formation of a thermal groove.

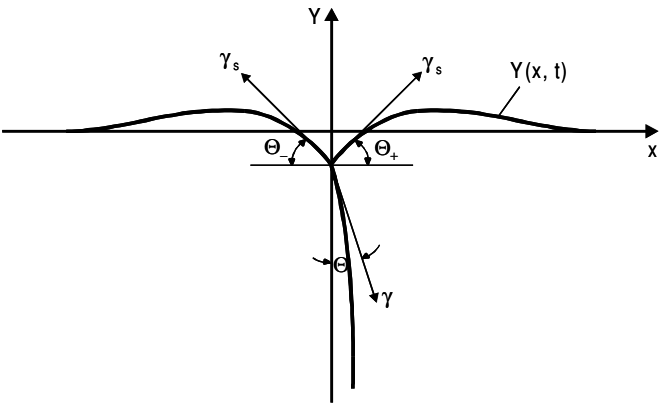


FIGURE 3.18
Equilibrium of forces due to surface and grain boundary tension.

For sufficiently “thick” specimens ($h/\delta \ll 1$), where h is the depth of the groove, we obtain by integration

$$\Theta \cong \tan \Theta = y'(-\delta/2, t) \quad (3.87)$$

With respective secondary assumptions regarding the mass transport and given initial conditions the problem can be solved. The authors of [210], however, used one considerable simplification, which they called the “approximation of an almost symmetrical groove.”

Let us now consider the motion of a boundary-surface junction. Its velocity can be described as

$$V = m_g \gamma \sin \Theta \quad (3.88)$$

where m_g is the mobility of the grain boundary-surface junction. The function $m_g(t)$ can be determined on the basis of the following arguments. At the beginning of motion the smooth, flat surface does not drag boundary motion. Formally, this means that $m_g(t) \rightarrow \infty$. As the groove grows, the mobility $m_g(t)$ decreases, and the near surface section of the boundary begins to move more slowly than the part of the grain boundary in the specimen interior. As a result the boundary becomes tilted with regard to the surface. Once it exceeds a certain critical angle it can detach from the groove without increasing its own area. This is accomplished when the angle between the tangent to the boundary at the surface and the tangent to the surface of the crystal at the bottom of the groove is 90° . Strictly speaking, this situation is impossible to reach if the angle between the surface tensions of a free surface and of the grain boundary is always in equilibrium. One possible mechanism of how the boundary can detach from the groove is given in [210]. After detachment a new groove begins to form and the process is repeated.

If the velocities $\dot{y}(x, t)$ of different points on the boundary differ very little, then the boundary can be considered to move as a whole with velocity $v = \dot{y}(x, t)$.

Integrating Eq.(3.80)

$$\int_{-\delta/2}^{\delta/2} \dot{y}(x, t) dx = m_b \{ P\delta + [y'(\delta/2, t) - y'(-\delta/2, t)] \gamma \} \quad (3.89)$$

Substituting $\dot{y}(x, t)$ by $V(t)$ and using Eqs. (3.79) and (3.87) we obtain

$$V(t) = \frac{Pm_b}{1 + \frac{2m_b}{\delta m_g(t)}} \quad (3.90)$$

Eq. (3.90) describes the velocity of a boundary as a whole which interacts with the free surface of a crystalline solid. It is evident from Eq. (3.90) that the joint motion of boundary and groove depends on the mobility of the boundary (m_b), the mobility of the groove (m_g) and the thickness of the crystal (δ).

The grain boundary is able to detach from the groove, if it flexes to an angle Θ that exceeds the critical angle $\Theta_c = \pi/2 - \Theta_-$ in Fig. 3.17, or

$$\frac{2P\delta}{\gamma\Theta_c} \geq 1 \quad (3.91)$$

The critical angle Θ_c can in first approximation (symmetrical groove) be estimated as

$$\Theta_c = \arcsin \gamma/2\gamma_s \quad (3.92)$$

If Eq. (3.91) is not satisfied the boundary will remain attached to the groove, in other words, it will move together with the groove. The mobility of a groove $m_g(t)$ is determined by the principal mechanism of groove development and can be calculated if the mechanism is known [210]. If the groove is shaped by surface diffusion

$$m_g(t) = c_1 t^{-3/4} \quad (3.93)$$

where $c_1 = (16\gamma_s^{5/4}/\gamma^2) (D_s \omega \Omega_a^2/kT)^{1/4}$, D_s is the coefficient of surface diffusion, ω is the surface density of atoms, Ω_a is the atomic volume [210]. Accordingly, for diffusion through the gas phase

$$m_g(t) = c_2 t^{-2/3} \quad (3.94)$$

$$c_2 = [Dp_0\Omega_a^2/(kT)^2]^{1/3} \gamma_s^{1/3}/2\gamma$$

D is the coefficient of gas diffusion, p_0 is the pressure of saturated vapor above the flat surface of a crystal. Finally, if the process of mass transport is limited by evaporation of atoms from the surface, the mobility of the groove can be determined as

$$m_g(t) = c_3 t^{-1/2} \quad (3.95)$$

$$c_3 = \left[\frac{p_0 \Omega_a^2}{\gamma_s (2\pi M)^{1/2} (kT)^{3/2}} \right]^{1/2}$$

(M is the atomic weight.)

The time dependence of grain boundary displacement $\ell(t)$ can be found by integration of Eq. (3.90). So, for the mechanism of surface diffusion

$$\ell(t) = \frac{4P(2c_1\delta)^{4/3}}{m_b^{1/3}} \left[\xi - \frac{1}{6} \ln \frac{(1+\xi)^3}{1+\xi^3} - \frac{1}{\sqrt{3}} \left(\arctan \frac{2\xi-1}{\sqrt{3}} + \pi/6 \right) \right] \quad (3.96)$$

with $\xi = (2m_b/(c_1\delta))^{1/3} t^{1/4}$.

In the beginning, when the groove drags grain boundary motion only weakly

$$\ell(t) \cong Pm_b t \quad (3.97)$$

in accordance with rate theory, but after a sufficiently long period of time

$$\ell(t) \sim t^\varepsilon \quad (3.98)$$

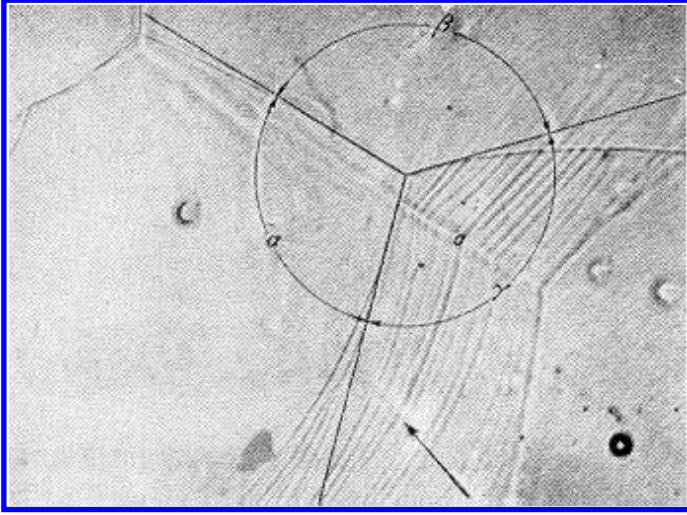
where ε is determined by the controlling mass transfer mechanism. The period τ between two consecutive detachments from the groove for different mechanisms $i = 1, 2, 3$ can be derived [210]

$$\tau_i = \left[\frac{2m_b}{c_i \delta} \left(\frac{P\delta}{\gamma \Theta_c} - 1 \right) \right]^{-\frac{1}{\varepsilon_i}} \quad (3.99)$$

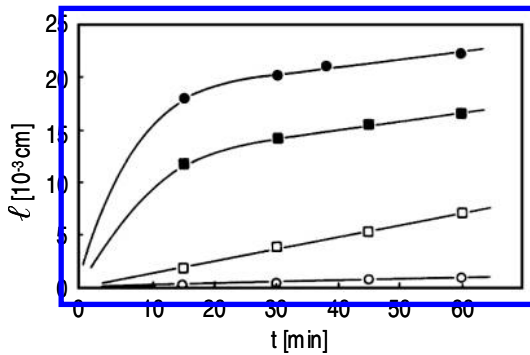
As the effective driving force P for grain boundary migration or the sample thickness δ decreases, the time between consecutive detachments increases, approaching infinity when the equal sign holds in relation (3.91). Physically this means that the grain boundary does not detach from the groove anymore. But the groove cannot stop grain boundary motion, although its migration rate decreases in the course of time, since $\ell(\infty) = \int_0^\infty v(t)dt$ diverges for all mechanisms of groove formation and displacement [210].

In summary, a characteristic feature of the interaction between a moving grain boundary and a free surface is the potential formation and growth of a thermal groove along the terminal line of the grain boundary at the free surface, joint motion and detachment of the boundary from a groove, formation of a new groove and so on. Experimentally, this has to manifest itself as periodic sudden changes in the velocity of the moving boundary.

This behavior corresponds to the common experience that grain boundary motion appears jerky on the surface [223]–[225]. This is demonstrated in Fig. 3.19, where surface grooves were formed during jerky motion of grain boundaries in steel [226]. The intermediate positions of a grain boundary, which had moved by stop-and-go during annealing in vacuum at very high temperatures, are distinctly revealed by the respective grooves (Fig. 3.19). The associated displacement increases proportionally with progressing annealing time at low temperatures, but highly non-linearly at high annealing temperatures [227] (Fig. 3.20). Fig. 3.21 shows the migration of a boundary in a zinc bicrystal as a function of time [228]. The effect of grooving is a retardation of grain boundary motion at the surface, such that the grain boundary in the bulk moves far ahead of the boundary at the surface (Fig. 3.22) until the boundary detaches itself from the groove [210, 225]. The evolution of the shape of a moving grain boundary between two detachments from the groove is apparent from Fig. 3.22. The theoretical curve of grain boundary displacement (Fig. 3.23) was found by numerical integration in the approximation of an almost symmetrical groove (Eq. (3.90)) [210]. There is good agreement between the experimental and theoretical curves. Within a complete cycle of detachment and regrooving, the experimental results are in reasonable agreement with the kinetics predicted from theory [210, 225] (Fig. 3.24). The curve can be subdivided into two linear sections, with a slope of 1:2 for the first and 1:3

**FIGURE 3.19**

Surface grooves due to jerky grain boundary migration in steel after annealing of 1h at 1100°C in a vacuum [226].

**FIGURE 3.20**

Grain boundary displacement vs. annealing time for oxide-forming specimens of Al annealed at different temperatures: 553°C (o); 567°C (□); 602°C (■); 616°C (●) [227].

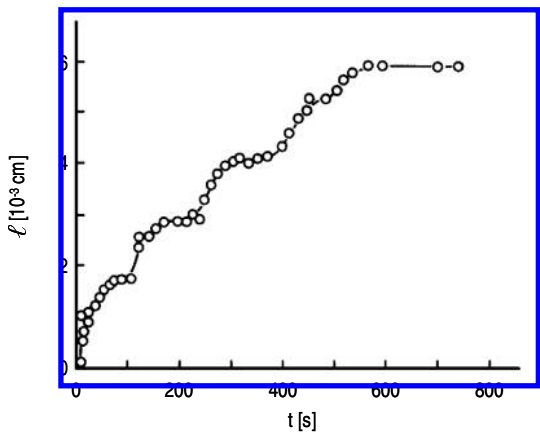


FIGURE 3.21
Measured grain boundary displacement in a Zn bicrystal under grooving conditions [228].

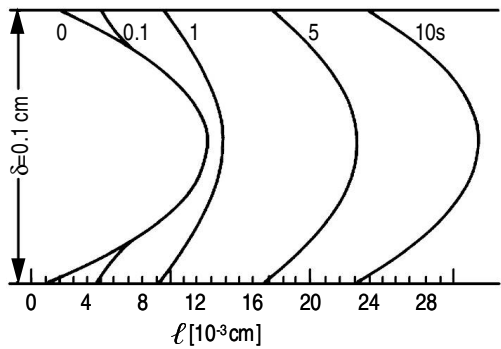


FIGURE 3.22
Development of through thickness grain boundary shape during consecutive steps of grain boundary motion with initial grooving at the surface.

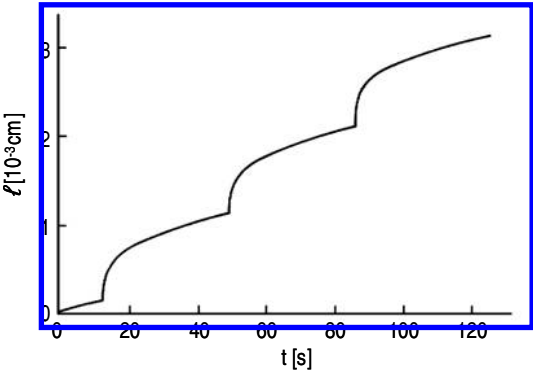


FIGURE 3.23
Theoretically predicted grain boundary displacement in Zn under the action of thermal grooving.

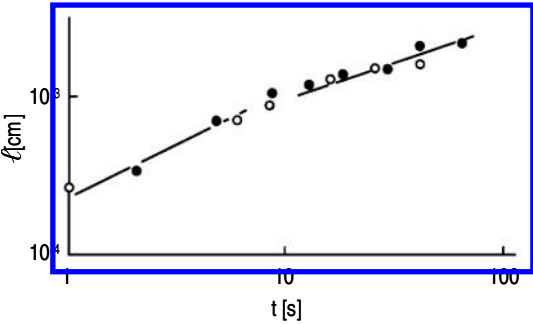


FIGURE 3.24
Time dependence of $\langle 10\bar{1}0 \rangle$ tilt boundary displacement in Zn with a single jump; •, ○ —points corresponding to different jumps.

for the second one. The two slopes correspond to groove control by transfer through the gas phase, which is natural for zinc. For small grooves the process is determined by the stages of evaporation and condensation, while for large grooves diffusion in the gas phase is rate controlling. For grain boundary motion in aluminum the slope of the corresponding lines for high temperatures equals 1:4, corresponding to groove development by surface diffusion [210].

3.4 Measurement of Grain Boundary Mobility

3.4.1 Polycrystal Methods

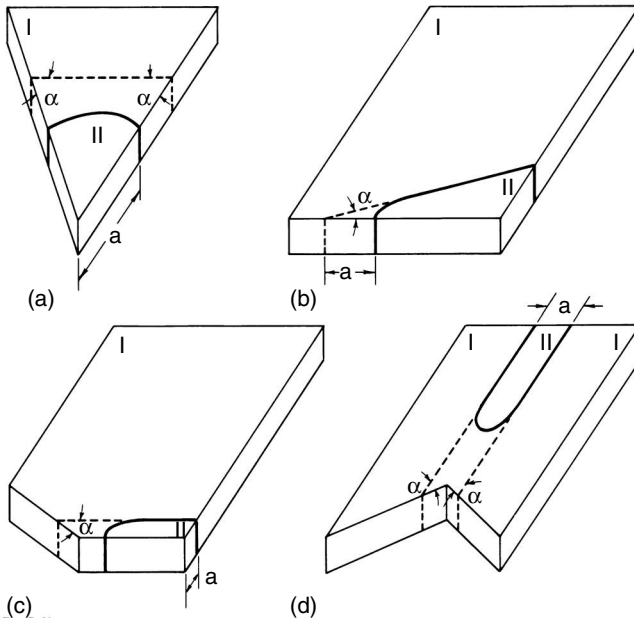
The capability of grain boundaries to move, and to move fast, has been known for a long time. This ability forms the basis for such important technological processes as recrystallization and grain growth. Thus, it seems natural to extract data on grain boundary motion, i.e. the grain boundary mobility, from the temporal evolution of grain size during recrystallization or grain growth in polycrystals. Indeed, this has been the case until recent times. A large amount of data was collected over decades. However, these data, while useful for every specific situation, fail to solve the physical problem underlying grain boundary migration. The development of statistical methods for treating experimental results does not alter the heart of the matter. Averaging over a large number of grains in this case is counterproductive, since it “spreads” the mobility over many differently migrating grain boundaries.

As a result, correlations between grain boundary property and structure cannot be obtained from such data. The relationship between grain boundary mobility and its crystallography, the effect of temperature, pressure, impurity content on the motion of specific grain boundaries, the mechanism of grain boundary migration and other fundamental aspects of grain boundary migration cannot be studied by recrystallization methods. Measurements of grain boundary mobility based on mean grain size data of polycrystals may give a rough estimate of this value only. Recrystallization and grain growth are multicomponent processes of microstructure evolution, involving strongly interacting elements of the polycrystal structure, namely grain boundaries and triple junctions. Therefore, in the following we shall confine our considerations to data obtained in bicrystal experiments.

3.4.2 Bicrystal Methods

3.4.2.1 Bicrystal Geometry

The driving forces considered in Sec. 3.2 constitute the basis of numerous experimental methods for the study of grain boundary migration. Most fre-

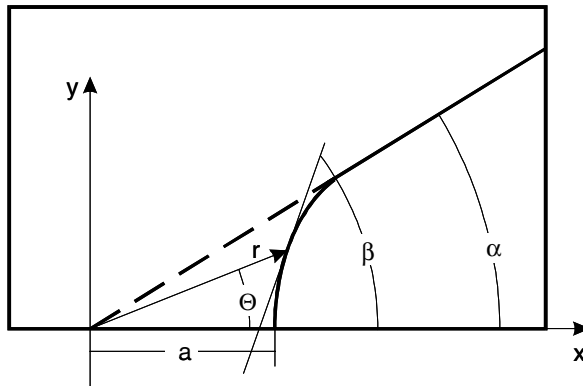
**FIGURE 3.25**

Various boundary geometries in bicrystalline specimens for the study of grain boundary migration: (a) wedge technique; (b) reversed-capillary technique; (c) constant driving force technique (quarter-loop technique); (d) constant driving force technique (half-loop technique) [229].

quently the capillary driving force is used in a variety of bicrystal geometries, which we shall consider in the following.

As repeatedly mentioned, only bicrystal techniques permit us to obtain reliable and reproducible physical data on grain boundary mobility. However, bicrystal techniques require substantial experimental efforts to manufacture bicrystals with given and precise orientations and misorientations as well as to prepare adequate specimens for investigation with the chosen technique. The different bicrystal arrangements designed to measure the grain boundary velocity and, eventually, the grain boundary mobility are given in Fig. 3.25 [229]. A basic advantage of all techniques, which utilize the capillary driving force, is that the surface tension of a grain boundary depends only slightly on temperature and, therefore, the driving force is practically constant over a wide temperature range.

The “wedge” bicrystal technique (Fig. 3.25a) was frequently used [230]–[233]. The main and, perhaps, the only advantage of this technique is a simple relation between driving force P and the macroscopic grain dimension a (ra-

**FIGURE 3.26**

Boundary geometry and definition of parameters for the reversed-capillary technique.

dus of curvature)

$$P = \gamma/a \quad (3.100)$$

where γ is the grain boundary surface tension. In this technique the driving force increases with progressing grain boundary displacement. So, the driving force is very small in the beginning, and sources of pinning forces can manifest themselves.

The reversed-capillary technique (Fig. 3.25b), first proposed and developed by Sun and Bauer [234, 235], was used many times to investigate grain boundary migration in crystals [234]–[241]. The major advantages of this technique are the relative ease of manufacture and preparation of specimens and the possibility to change the driving force by varying the angle α (Fig. 3.25b). Finally, the reversed-capillary technique allows one to obtain relatively large driving forces, although unfortunately only in the beginning of the experiment, which is usually sufficient to force the boundary to break free from potential pinning centers. The shape of a moving grain boundary for this method was analyzed by Mullins [242], Sun and Bauer [234, 235] and Shvindlerman et al. [236, 241].

With the driving force given by $f(\alpha)\gamma/a$, where $f(\alpha)$ is an amplification factor, a displacement da in a time interval dt has to satisfy the relation

$$da = m_b f(\alpha) \gamma dt / a \quad (3.101a)$$

or with $a = 0$ for $t = 0$

$$a^2 = 2m_b f(\alpha) \gamma t \quad (3.101b)$$

Such approximation is convenient for an angle α close to 90° ; otherwise other

approximations should be used [236]. The driving force for the reversed-capillary method is given by

$$P = \gamma/R = \frac{\gamma}{a}f(\alpha) \quad (3.102)$$

where R is the radius of boundary curvature.

An example is the circular arc shape [236] (Fig. 3.26). To solve the equation which describes the shape of a moving boundary in a two-dimensional sample, an assumption of shape invariance, i.e. a scaling behavior, must be introduced [234, 235]. If the (2D) shape of the boundary is given in polar coordinates (r, Θ)

$$f(\alpha) = \left. \frac{d\beta}{d\Theta} \right|_{\Theta=0^\circ} \quad (3.103)$$

where β is the inclination of the tangent at a given point of the grain boundary (Fig. 3.26). As shown in [242] this approach does not take into account the drag effect of mobile obstacles, e.g. impurity atoms, mobile particles or surface grooves [208, 210, 225]. (This problem will be addressed in Sec. 3.4.3.)

The important disadvantage of the reversed-capillary technique is the lack of steady-state motion of a grain boundary. This disadvantage is avoided by the half-loop technique, since the driving force remains constant (Fig. 3.25c,d). The grain boundary half-loop (Fig. 3.25d) or quarter-loop (Fig. 3.25c) moves as a whole, and its shape remains self-similar during migration [227, 244]. The average driving force on a half-loop (h.l.) [227, 243, 245] or on a quarter-loop (q. l.) [244, 246] is

$$P_{h.l.} = \frac{2\gamma}{a} \quad (3.104a)$$

or

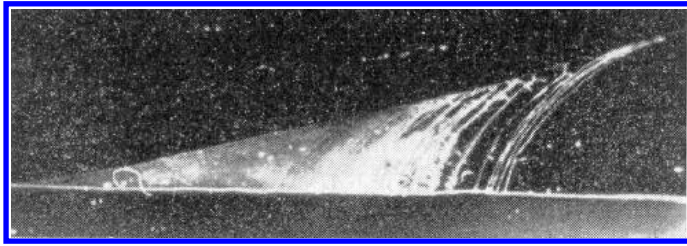
$$P_{q.l.} = \frac{\gamma}{a} \quad (3.104b)$$

respectively.

The contention is that the driving force for constant driving force techniques is substantially smaller than for the reversed-capillary techniques [229]. However, as shown in [247], it is possible to grow bicrystals with half-loop grain boundary geometry, where the size of the shrinking crystals does not exceed $\sim 0.1\text{mm}$. It is particularly emphasized that in all capillary techniques, except for half-loop geometry, the moving grain boundary is exposed to the free side surface of the bicrystal. In certain cases this may cause drag effects by the free surface, as will be discussed in Sec. 3.5.

3.4.2.2 Techniques to Monitor Grain Boundary Migration

As mentioned above, the observation of grain boundary migration is commonly performed by investigation of the motion of a macroscopic segment

**FIGURE 3.27**

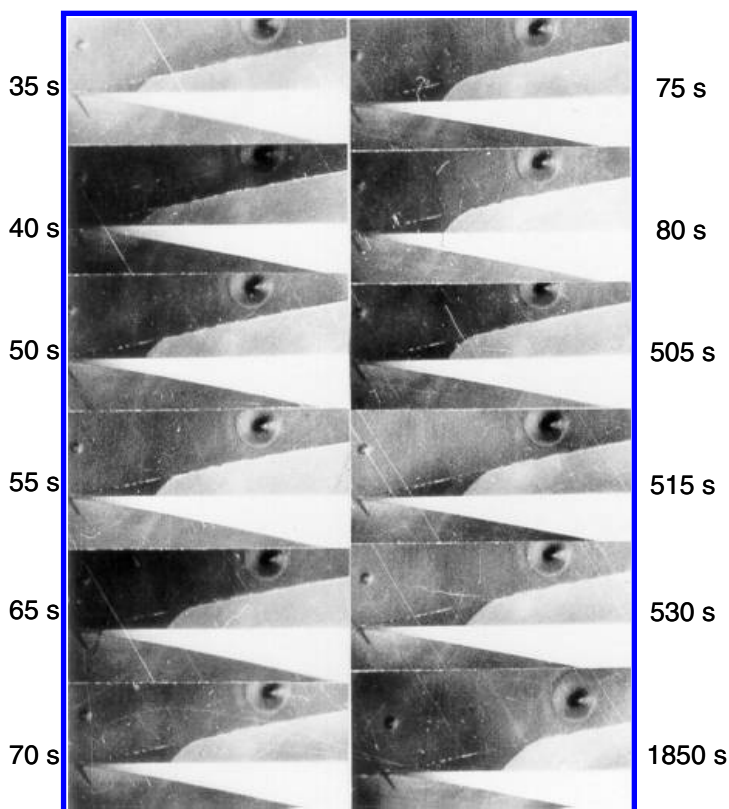
Traces of a moving boundary in a Zn bicrystal (reversed-capillary technique).

of the grain boundary. The velocity v of grain boundary motion is defined as the displacement Δx of this segment normal to itself in a time interval Δt : $v = \Delta x / \Delta t$. For this purpose the position of the segment has to be located. There are two essentially different ways to determine the position of a grain boundary in crystals and to measure the velocity of its motion: the continuous method and the discontinuous method.

The discontinuous method is most common. The location of the boundary is determined by its intersection with the crystal surface after discrete time intervals. The position of a boundary can be revealed by the groove, which forms on sample cooling or by chemical etching of the crystal surface. The boundary groove can easily be observed under an optical microscope. The principal advantage of this method is its simplicity; the major shortcoming is the necessity to average the measured boundary displacement over a large period of time between consecutive observations.

One variation of this method consists of periodic cooling of the sample by 20–30°C for a short time in the hot stage of a microscope [227, 245]. Such procedure causes the formation of a “vacancy” groove along the line of intersection of the grain boundary with the free surface of the crystal: an excess of thermal vacancies moves from the bulk of the crystals to the grain boundary and along the boundary to a free surface. Since the observation of grain boundary displacement occurs in this case “under a microscope” it is more “controlled,” which substantially reduces the principal shortcoming of this method [227, 236] (Fig. 3.27).

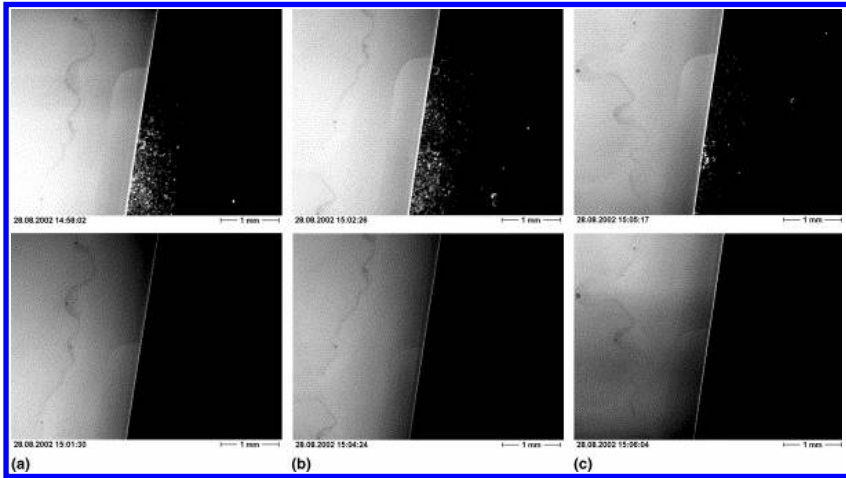
The continuous method requires determination of the boundary position at any moment in time and thus requires automation of the procedure to locate the boundary position. Correspondingly, the boundary has to be identified by the discontinuity of a physical property associated with the change in crystal orientation. There are various techniques to distinguish different crystal orientations such as reflection of polarized light [228, 248], photoemission [223], X-ray topography [249, 250], X-ray diffraction [251]–[253], or backscattered electron density [254]. The observation of grain boundary motion by orientation contrast is convenient and reliable, and does not only yield the location

**FIGURE 3.28**

Recorded grain boundary migration in a Zn bicrystal.

of a moving grain boundary, but also its shape at any moment. In Fig. 3.28 individual video frames of grain boundary migration in zinc bicrystals are given [228] as observed by polarized light in an optical microscope. Evaluation of this recording provides all parameters to determine the grain boundary mobility: time dependence of grain boundary displacement and radius of curvature of a moving grain boundary at any moment. The characteristic time resolution is about 10^{-2} s, the spatial resolution is a few μm , the thickness of the samples is insignificant [228]. Unfortunately, this technique is applicable only to optically anisotropic materials, i.e. of material with lower symmetry crystal structure, for instance, hexagonal crystals.

X-ray topography permits us to obtain an image of a grain boundary as the interface between the contiguous grains. Synchrotron white beam X-ray topography (SWBXRT) offers excellent time resolution and thus can be used for “in situ” studies of grain growth, recrystallization and grain boundary mo-

**FIGURE 3.29**

Shape of a moving $37.5^\circ\langle 111 \rangle$ grain boundary in Al at 480°C [268].

tion [249, 250]. SWBXRT allows a spatial resolution in the range of several μm , the time resolution is about 1 s, the field of view extends to $2\text{--}3\text{ cm}^2$, the sample thickness can range between $0.1\text{--}1\text{ mm}$ [250]. However, the study of grain boundary motion by SWBXRT is restricted to samples of high perfection: the dislocation density should not exceed 10^4 cm^{-2} . Moreover, the principal shortcoming of this technique is its limited availability and thus limited access.

Photoemission microscopy also can be utilized for continuous tracking of grain boundary migration [223]. However, this technique is restricted to metals with high melting points. A recently developed elegant method is the investigation of crystal shape evolution by backscattered electrons in an SEM, since the contrast by backscattered electrons is very sensitive to orientation. The method also allows for orientation evaluation by EBSD with the same set-up. The capabilities of the EBSD technique have been increased substantially in the past years. In particular, the migration and shape of the grain boundaries can be measured in situ in an SEM utilizing the orientation contrast revealed by an electron backscatter detector [266]. With a specially designed laser powered heating stage in situ investigations of grain boundary motion can be conducted at temperatures up to 1000°C [267]. The SEM is equipped with a digital image scanning system, which records series of orientation contrast images in predetermined time intervals. In Fig. 3.29 the shape of a moving grain boundary quarter-loop in Al at 480°C is presented [268].

A simple, precise and very versatile technique to identify the position of a grain boundary utilizes X-ray diffraction. X-ray diffraction is very sensitive to the structure and orientation of crystalline material and, therefore, it is an

excellent probe for differences in crystal structure or crystal orientation. The principle of the method is illustrated in Fig. 3.30 [251, 253]. The bicrystal is placed in a goniometer of the X-ray Interface Continuous Tracking Device (XICTD) in such a way that one grain (I) is in the Bragg position, while the other is not. The maximum intensity I_d of the reflected X-ray beam is measured as long as the X-ray spot is located solely on the surface of crystal I . If the spot is located on the grain boundary, the intensity of the reflected beam should be intermediate between I_d and I_0 . When the boundary moves the sample can be displaced accordingly so that the reflected X-ray intensity remains constant during grain boundary motion. Thus, the velocity of the moving grain boundary (generally speaking, the interface) is equal to the speed of sample movement at any moment in the course of the experiment. This procedure does not interfere with the process of grain boundary migration. The measurable velocity ranges from 1 to 1000 μms^{-1} with a temporal resolution of about five measurements per second. In Fig. 3.31 the displacement vs. time diagrams are shown for a grain boundary in Al, which moves under a constant driving force (Fig. 3.30) [255]. The hot stage of the XICTD allows the sample to be heated up to 1200°C in nitrogen or an inert gas atmosphere to suppress oxidation and grooving; the temperature is kept constant within $\pm 0.3^\circ\text{C}$. The accuracy of the velocity measurements of grain boundary motion is better than 2%.

It is stressed again that any reliable information on grain boundary mobility can be obtained only from a physically proper and reproducible experiment, carried out on specific single grain boundaries with given crystallography and defined chemistry. Respective experiments have to comply with several requirements: controlled or constant driving force of grain boundary migration, its reproducibility and potential to change it over a wide range free of interference with the process of grain boundary migration itself, feasibility of manufacturing bicrystals free of fabrication defects. Only under these conditions is it possible to observe “the free motion of a grain boundary,” which we define as the motion of a single grain boundary, when the influence of drag factors can either be neglected or can be accurately taken into account. Actually, the interaction of a moving grain boundary with point defects (impurity atoms, vacancies), dislocations or bulk defects (second-phase particles, voids) usually is taken into account, or such defects are eliminated by appropriate procedures.

Generally speaking there are two groups of basically different experimental techniques of grain boundary migration studies (Table 3.3). The first group includes the experimental techniques, where the driving force is determined by the difference of the free energy of adjacent grains but not affected by the geometry of the sample or by the shape and energy of the grain boundary. The second group comprises the experimental techniques in which the driving force is provided by the surface tension (free energy) of the grain boundary. The techniques of the latter group are advantageous due to the high stability of the driving force both with respect to time and under a change of tem-

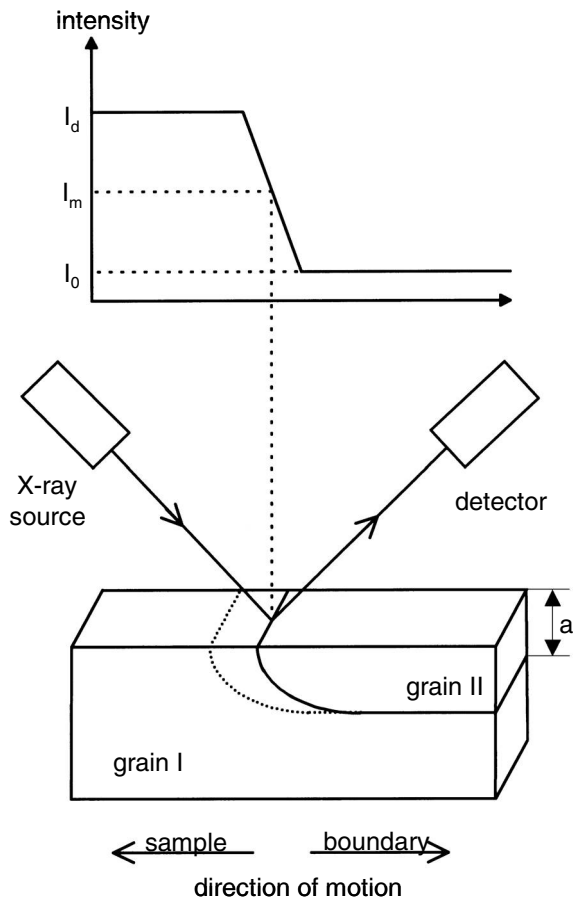


FIGURE 3.30
Principle of operation of the XICTD. The diffraction conditions generate an X-ray intensity gradient across the boundary. The specimen is moved to maintain a constant recorded intensity.

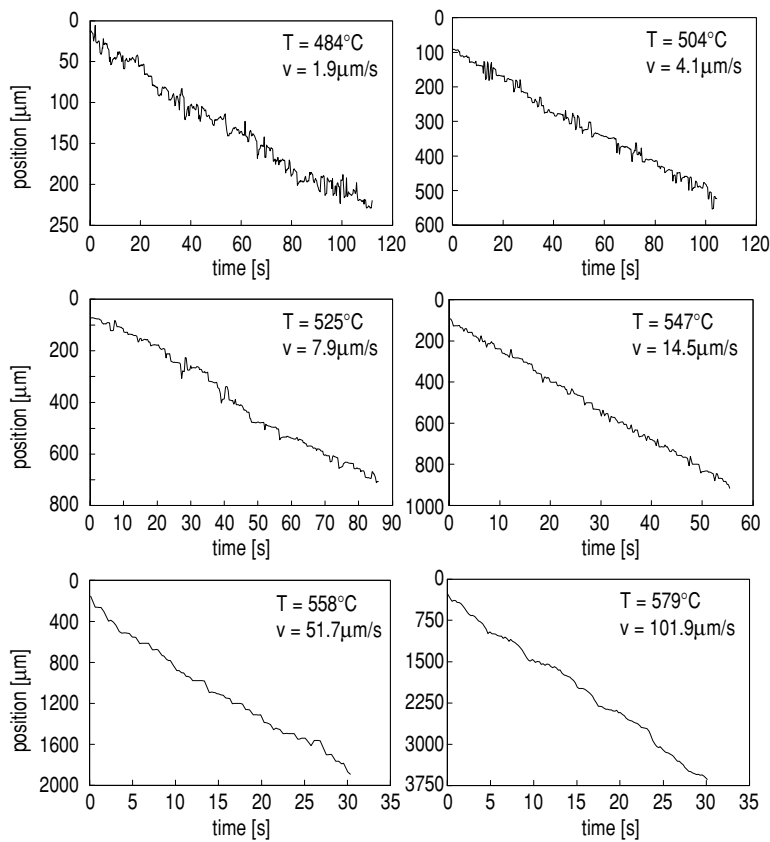


FIGURE 3.31
Typical XICTD recordings of grain boundary position vs. annealing time from low ($\approx 1\mu\text{m/s}$) to high ($\approx 100\mu\text{m/s}$) migration rates.

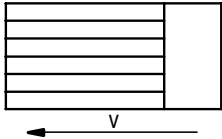
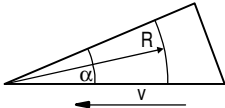
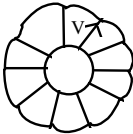
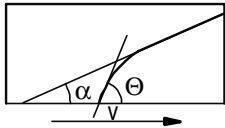
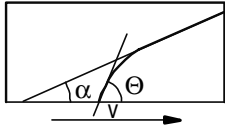
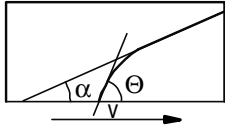
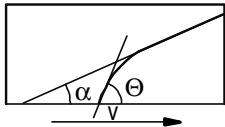
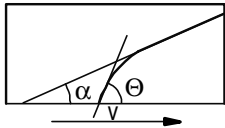
perature, its reproducibility and the feasibility to control the magnitude of the driving force. One shortcoming of the techniques in this group is that the influence of the free surface may interfere with the migration process (see groove dragging, [Sec. 3.3.6](#)).

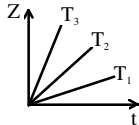
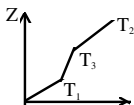
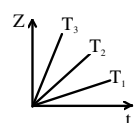
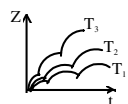
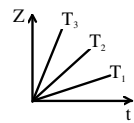
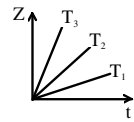
The techniques N11-13 and N9-10 ([Table 3.3](#)) are most advantageous. They stand out because of the constant driving force, no effect of the free surface on grain boundary motion and the feasibility to describe analytically the steady-state shape of the moving grain boundary. This permits us to find a relationship between the microscopic kinetic properties of the grain boundary and the macroscopic properties of a grain boundary half- or quarter-loop (the techniques N9 and N11, respectively), as will be considered below.

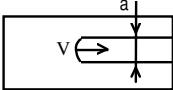
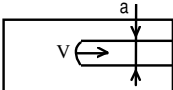
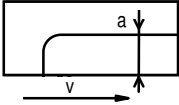
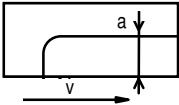
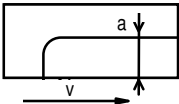
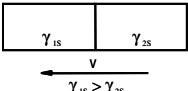
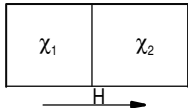
Regrettably, the techniques of grain boundary migration studies based on a reduction of the boundary area have the disadvantage that it is impossible to investigate the motion of a planar boundary. A curved grain boundary implies that its structure changes along the boundary, since it is composed of different grain boundary planes. The mobilities obtained can, therefore, be related to a specific misorientation and boundary character (tilt), but not to a specific grain boundary structure. A planar boundary can be forced to move in a bicrystal comprised of grains with some orientation-dependent properties like elastic constants or magnetic susceptibility. Unfortunately, only few materials show such strong anisotropy. An example is Bi, which exhibits a strong anisotropy of its magnetic susceptibility [189], or some other hexagonal metals.

This raises the fundamental question whether it is at all possible to study the mobility of grain boundaries in experiments with a curved boundary. The general solution of grain boundary motion under the effect of its own surface tension was given in [256]. Among other issues, it was comprehensively discussed what can be measured in experiments with a curved grain boundary. As shown in [256], experiments on steady-state motion of a curved grain boundary for half-loop or quarter-loop geometry, or in the case of the reversed-capillary technique, determine the average mobility only, i.e. averages over all boundary planes present. But, as stressed in [256], contrary to experiments on polycrystals, this averaging is a physical averaging, the same from experiment to experiment. Such averaged boundary mobility proves to be dependent on misorientation between grains, on purity of the material used and on other characteristics of the system, as will be presented in [Sec. 3.5](#).

TABLE 3.3
Bicrystal Techniques of Grain Boundary Migration

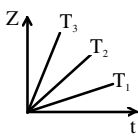
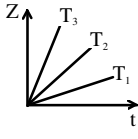
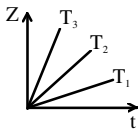
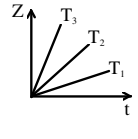
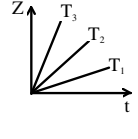
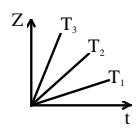
N	Source of driving force [Pa]	Experimental technique	δ [cm]	Metal	Grain boundary displacement recording
1	Energy of low-angle grain boundaries $P \cong 4 \cdot 10^2 = const.$		0.25	Pb	A
2	Energy of high-angle grain boundary $P = \gamma/R = 5 \cdot 10^2 - 10^3$		0.25–0.5	Al	B
3	Energy of deformed matrix $P \cong 10^6 - 10^7$		0.01	Au	B
4	Energy of high-angle grain boundary $P = \gamma/R \cong 10^2 - 10^3$		0.5	Al	B
5	Energy of high-angle grain boundary $P = \gamma/R \cong 10^2 - 10^3$		0.1	Cu	B
6	Energy of high-angle grain boundary $P = \gamma/R \cong 5 \cdot 10^2 - 10^3$		0.1–0.2	Zn	C
7	Energy of high-angle grain boundary $P = \gamma/R \cong 8 \cdot 10^2 - 2 \cdot 10^3$		0.2	Fe-Si	A
8	Energy of high-angle grain boundary $P = \gamma/R \cong 8 \cdot 10^2 - 2 \cdot 10^3$		0.2	Fe-Si	A

N	Time dependence of grain boundary displacement	Time interval $\Delta t(s)$ between consecutive measurements or speed of recording	Dependence $V(P)$	Criterion ρ	Ref.
1		$0.6 \cdot 10^2 - 1 \cdot 10^3$	—	$\rho = \frac{P\delta\gamma_s}{\gamma^2}$	[I]
2	—	$\sim 10^4$	$V \sim P$	$\rho = \frac{\gamma_s\delta}{R\gamma} \cong \frac{3\delta}{R}$ $\rho_{\text{exp}} = 0.5 - 4$	[II,III]
3		$6 \cdot 10^2 - 1 \cdot 10^4$	—	$\rho = \frac{P\gamma_s\delta}{\gamma^2}$ $\rho_{\text{exp}} = 5 \cdot 10^2 - 5 \cdot 10^3$	[IV]
4		$0.15 \cdot 10^2 - 2 \cdot 10^4$	$V \sim P$	$\rho = \frac{\gamma_s\delta}{R\gamma} = \rho_{\text{exp}} \cong 10$	[V]
5	—	—	$V \sim P$	—	[VI]
6		speed of recording: 1 frame per 3-15s	for the initial jumps $V \sim P$	$\rho_{\text{exp}} \cong 10$	[VII, VIII]
7		$\sim 5 \cdot 10^2 - 2 \cdot 10^3$	$V \sim P$	$\rho_{\text{exp}} \cong 5$	[IX]
8		$\sim 2 \cdot 10^4$	$V \sim P$	$\rho_{\text{exp}} \cong 10 - 15$	[X]

9	Energy of high-angle grain boundaries $P \cong 2\gamma/a =$ $10^3 - 3 \cdot 10^3 = \text{const.}$		0.15–0.2	Al	B
10	Energy of high-angle grain boundaries $P \cong 2\gamma/a =$ $5 \cdot 10^2 - 10^3 = \text{const.}$		0.1–0.2	Zn	C
11	Energy of high-angle grain boundaries $P \cong \gamma/a =$ $5 \cdot 10^2 - 5 \cdot 10^3 = \text{const.}$		0.2	Al	D
12	Energy of high-angle grain boundaries $P \cong \gamma/a =$ $5 \cdot 10^2 - 5 \cdot 10^3 = \text{const.}$		0.2	Al	D
13	Energy of high-angle grain boundaries $P \cong 2\gamma/a =$ $10^3 - 5 \cdot 10^3 = \text{const.}$		0.2	Fe-Si	D
14	Difference of surface tension of free surfaces of a foil $P = 2\Delta\gamma_s/\delta \cong$ $10^2 - 10^3 = \text{const.}$		0.15–0.3	Fe	A
15	Magnetic free energy in a bicrystal with anisotropic magnetic susceptibility $P = \omega_1 - \omega_2 =$ $\frac{\mu_0}{2} H^2 (\chi_1 - \chi_2)$		0.3	Bi	B

Annotations

1. δ is the thickness of a sample.
2. Δt is the interval between two consecutive recordings of the grain boundary position or displacement; the speed of recording of grain boundary motion.
3. ρ is a criterion describing the interaction of a moving grain boundary and the free surface of a crystal. ρ_{exp} is the magnitude of ρ in the series of experiments discussed.

9		30–300	$V \sim P$	$\rho = \frac{2\gamma_s\delta}{\gamma_a}$ $\rho_{\text{exp}} = 10\text{--}12$	[XI, XII]
10		speed of recording: 1 frame per 3–15s	$V \sim P$	$\rho = \frac{2\gamma_s\delta}{\gamma_a}$ $\rho_{\text{exp}} = 5\text{--}25$	[XIII]
11		–	–	$\rho = \frac{\gamma_s\delta}{\gamma_a}$ $\rho_{\text{exp}} = 10\text{--}15$	[XIV, XVII]
12		~4 measure- ments per second	$V \sim P$	$\rho_{\text{exp}} = 10\text{--}30$	[XVI, XVII]
13		~4 measure- ments per second	$V \sim P$	$\rho_{\text{exp}} = 10\text{--}100$	[X]
14	–	$10^3 - 10^4$	–	$\rho = \frac{6\Delta\gamma_s}{\gamma}$ $\rho_{\text{exp}} \approx 1$	[XVIII]
15		180 – 360	$V \sim P$	$\rho = \frac{P\delta\gamma_s}{\gamma^2} =$ $\frac{P\delta}{0.09\gamma_s}$ $\rho_{\text{exp}} \cong 2$	[XIX, XX]

4. The ratio γ_s/γ was taken as 3 [240, 263]. R is the radius of curvature of a moving grain boundary. For the reversed-capillary technique $R = \ell \sin \alpha [1 - \cos(\Theta - \alpha)]$ where ℓ is the displacement of a boundary along the specimen edge; values of α and Θ are given in the figures relevant to the reversed-capillary technique. For the experimental technique “15”; $\gamma = 0.3\gamma_s$; $\gamma_s = 0.521 \text{ J/m}^2$ at 239°C [254].

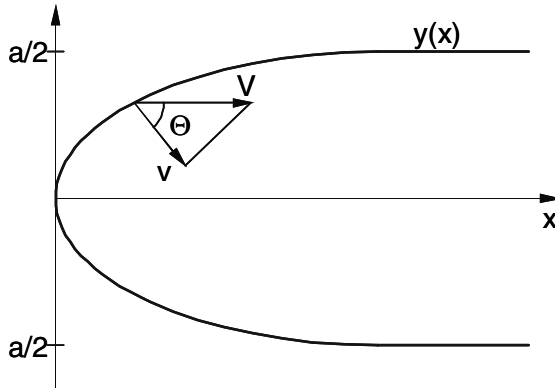
5. "A" means that the grain boundary position was determined by chemical etching; "B" by thermal grooving; "C" means that grain boundary motion was recorded by observation with polarized light in an optical microscope, the annealing of the sample was not interrupted; "D" means the grain boundary motion was determined via X-ray interface continuous tracking device (XICTD).
6. χ_1 and χ_2 are the susceptibilities of grains 1 and 2, respectively, along the magnetic field H ; μ_0 is the absolute permeability.

-
-
- | | |
|-------|--|
| I | Aust KT, Rutter JW, <i>Trans. AIME</i> , 215:119, 1959;
Aust KT, Rutter JW. <i>Trans. AIME</i> , 215:820, 1959;
Aust KT, Rutter JW. <i>Acta Metall.</i> , 12:181, 1965;
Rutter JW, Aust KT. <i>Trans. AIME</i> , 218:682, 1960. |
| II | Rath BB, Hu H. in Hu H, editor, <i>The Nature and Behaviour of Grain Boundaries</i> , Plenum Press, New York, 1972. |
| III | Rath BB, Hu H. <i>Trans. TMS – AIME</i> , 236:1193, 1966;
Rath BB, Hu H. <i>Trans. TMS – AIME</i> , 245:1243, 1969; |
| IV | Grünwald W, Haessner F. <i>Acta Metall.</i> , 18:217, 1970. |
| V | Deminczuk DM, Aust KT. <i>Acta Met.</i> , 21:1149, 1975. |
| VI | Viswanathan R, Bauer CL. <i>Acta Met.</i> , 21:1099, 1973. |
| VII | Antonov AV, Kopetskii ChV, Shvindlerman LS, Sursaeva VG.
<i>Sov. Phys. – Dokl.</i> , 18:736, 1974. |
| VIII | Sursaeva VG, Andreeva AV, Kopetskii ChV, Shvindlerman LS.
<i>Phys. Met. Metall.</i> , 41:98, 1976. |
| IX | Lejcek P, Paidar V, Adamek J, Kadeckova S. <i>Interface Sci.</i> , 1:187, 1993. |
| X | Furtkamp M, Gottstein G, Molodov DA, Semenov VN, Shvindlerman LS. <i>Acta Mater.</i> , 46:4103, 1998. |
| XI | Fridman EM, Kopetskii ChV, Shvindlerman LS, Aristov VJu.
<i>Zt. Metallk.</i> , 64:458, 1973. |
| XII | Fridman EM, Kopetskii ChV, Shvindlerman LS. <i>Zt. Metallk.</i> , 66:533, 1975. |
| XIII | Straumal BB, Sursaeva VG, Shvindlerman LS. <i>Phys. Met. Metalloved.</i> , 49:102, 1980. |
| XIV | Aristov VYu, Kopetskii ChV, Molodov DA, Shvindlerman LS.
<i>Sov. Phys. Solid State</i> , 22:1900, 1980. |
| XV | Molodov DA, Kopetskii ChV, Shvindlerman LS. <i>Sov. Phys. Solid State</i> , 23:1718, 1981. |
| XVI | Molodov DA, Czubayko U, Gottstein G, Shvindlerman LS.
<i>Scripta Metall. Mater.</i> , 32:529, 1995; Molodov DA, Czubayko U, Gottstein G, Shvindlerman LS. <i>Mat. Sci. Forum</i> , 207–209:133, 1998. |
| XVII | Gottstein G, Molodov DA, Czubayko U, Shvindlerman LS.
<i>J. Physique IV</i> , C3, 5:89, 1995. |
| XVIII | Walter JL, Dunn CG. <i>Trans. AIME</i> , 215:46, 1959. |
| XIX | Molodov DA, Gottstein G, Heringhaus F, Shvindlerman LS.
<i>Scripta Metall. Mater.</i> , 37:1207, 1997. |
| XX | Molodov DA, Gottstein G, Heringhaus F, Shvindlerman LS.
<i>Acta Mater.</i> , 46:5627, 1998; Molodov DA, Gottstein G, Heringhaus F, Shvindlerman LS. 1997 <i>NHFML Annual Report</i> , 165, 1998. |
-

3.4.3 Shape of a Moving Grain Boundary

Grain boundary motion during grain growth is controlled by the curvature of the grain boundary, which, in turn, is determined by the shape of the grain boundary. When considering the complex grain boundary geometry of polycrystals, this problem is simplified by the assumption that all grain boundaries possess equal mobilities and surface tensions irrespective of the misorientation of the grains and the crystallographic orientation of the boundary planes, and thus the shape of all grains is considered to be uniform and allows us to describe the grain boundary curvature by only one parameter — the mean grain size. However, when the shape of individual grains cannot be neglected, like in bicrystals — and truly also in polycrystals — it is necessary to determine the shape of a moving grain boundary. Besides, the shape of a moving grain boundary is a source of very useful data with regard to the orientation dependence of grain boundary surface tension and grain boundary mobility or the interaction between a moving grain boundary and different kinds of obstacles. In the following we will restrict our consideration predominantly to the steady-state motion of a single grain boundary.

The problem of the shape of a moving grain boundary was first considered by Mullins [242], and his equations provide a basis for all studies in this area. As mentioned, the general case of grain boundary steady-state motion under the influence of its own surface tension was considered in [256]. Although that study was dedicated to a *U*-shaped grain boundary (half-loop), all principal results can be successfully applied to any other type of steady-state grain boundary motion as to the quarter-loop geometry and to grain boundary systems with triple junctions (see below). In [256] a grain boundary was considered that moved steadily at a velocity V along the x -axis (Fig. 3.32). It was assumed that the system was homogeneous through the thickness of the bicrystal, i.e. independent of the z -axis, which in Fig. 3.32 is perpendicular to the plane of the diagram. Hence, there is a quasi-two-dimensional situation, as for all known experimental techniques of grain boundary migration studies where the driving force is generated by the surface tension of the curved boundary. The coordinate system was attached to the steadily moving boundary, i.e. all boundary elements were at rest with regard to this system. A slight displacement of a boundary element parallel to its tangential plane was assumed to cause no physical changes in the system and, hence, would not cause an energy change or dissipation. Therefore, each boundary element is solely under the influence of a force f normal to the boundary element plane. This force may be due to two reasons. First, it may stem from the difference of the chemical potentials of the atoms in the adjacent grains, caused by a tensorial external thermodynamic force (e.g. a magnetic field in a magneto-anisotropic material). Second, it may be due to the grain boundary energy dissipated when the grain boundary area is reduced. The first force component, f_0 , is the same for all boundary elements, whereas the second component, f_D , is related to the velocity v of boundary motion normal to the boundary element.

**FIGURE 3.32**

Grain Boundary shape $y(x)$ for the half-loop geometry. In steady state the grain boundary is displaced as a whole with velocity V due to the action of grain boundary curvature, which displaces each surface element of the boundary with normal velocity v .

When the motion of the boundary is considered under the effect of capillary forces only, $f_0 = 0$. The relationship $m = v/f_D$ shows that the boundary element mobility m is the physical property of the element.

In the following we will derive the shape of a grain boundary during steady-state motion under the action of a dissipative force $f_D = f$. For simplicity the coordinate system is attached to the boundary, i.e. moves together with the boundary. If the boundary runs straight through the thickness of a specimen, its shape is given by the 2D shape function $y = y(x)$ on the surface. In steady state the free energy assumes a minimum and, therefore, an infinitesimal virtual displacement δn perpendicular to the boundary will not change the free energy. Such displacement, however, will alter the area and thus the total energy of the boundary and dissipate the driving force in the swept area, i.e. in 2D

$$\delta G = \delta \int \gamma ds + \int f \delta n ds \quad (3.105)$$

where s is the line element of the shape curve $y(x)$, which can be expressed by $\mathbf{r}(t) = (x(t), y(t))$. With $\dot{x} = dx/dt$, $\dot{y} = dy/dt$

$$\begin{aligned} ds &= \sqrt{\dot{x}^2 + \dot{y}^2} dt; \\ \delta n ds &= \delta x dy - \delta y dx = (\dot{y} \delta x - \dot{x} \delta y) dt; \end{aligned} \quad (3.106)$$

Differentiation yields the Lagrange equations

$$\begin{aligned} -f\dot{y} &= \frac{d}{dt} \frac{\partial}{\partial \dot{x}} \left(\gamma \sqrt{\dot{x}^2 + \dot{y}^2} \right) \\ f\dot{x} &= \frac{d}{dt} \frac{\partial}{\partial \dot{y}} \left(\gamma \sqrt{\dot{x}^2 + \dot{y}^2} \right) \end{aligned} \quad (3.107)$$

Introducing the angle Θ between the normal to the boundary element and the direction of motion (Fig. 3.32) ($\sin\Theta = \dot{x}/\sqrt{\dot{x}^2 + \dot{y}^2}$, $\cos\varphi = \dot{y}/\sqrt{\dot{x}^2 + \dot{y}^2}$) we obtain the boundary shape

$$\begin{aligned} x(\Theta) &= \int_0^\Theta \frac{\left(\gamma + \frac{d^2\gamma}{d\theta^2} \right) \cos \Theta}{f} d\Theta \\ y(\Theta) &= \int_0^\Theta \frac{\left(\gamma + \frac{d^2\gamma}{d\theta^2} \right) \sin \Theta}{f} d\Theta \end{aligned} \quad (3.108)$$

Since the displacement rate V of the boundary and the migration rate v of a boundary element perpendicular to its plane (referred to as normal velocity in the following) are related by the angle Θ (Fig. 3.32)

$$v = V \cos \Theta \quad (3.109)$$

also

$$f = f_D = \frac{V \cos \Theta}{m_b} \quad (3.110)$$

Substituting Eq. (3.110) into Eq. (3.108), we obtain with the reduced mobility⁷

$$A_b = m_b \left(\gamma + \frac{d^2\gamma}{d\Theta^2} \right) \quad (3.111)$$

$$\begin{aligned} x &= \frac{1}{V} \int_0^\Theta A_b d\Theta \\ y &= \frac{1}{V} \int_0^\Theta A_b \tan \Theta d\Theta \end{aligned} \quad (3.112)$$

The shape of a boundary will be a smooth curve as long as the boundary surface tension varies continuously. If, however, it changes discontinuously with the angle Θ , as is inherent in crystalline interfaces, faceting of the moving

⁷In Sec. 3.5.2 we will introduce the simplified version $A_b = m_b\gamma$ for the reduced mobility, which assumes that the grain boundary energy does not vary notably with changing inclination. In the case of facetting, as discussed here, however, γ changes strongly with inclination.

boundary will occur. If at a given value of the angle $\Theta = \Theta_0$ the derivative changes by a step $\Delta\gamma'_{\Theta_0}$, then at that point

$$\frac{d^2\gamma}{d\Theta^2} = -\Delta\gamma'_{\Theta_0}\delta(\Theta - \Theta_0) \quad (3.113)$$

Substituted into Eq. (3.112), it yields the following finite change of x and y at a constant angle $\Theta = \Theta_0$

$$\begin{aligned} \Delta x &= \frac{m_b(\Theta_0) \Delta\gamma'(\Theta_0)}{V} \\ \Delta y &= \frac{m_b(\Theta_0) \Delta\gamma'(\Theta_0) \tan \Theta_0}{V} \end{aligned} \quad (3.114)$$

This means a facet occurs, the length of which

$$\Delta S_{\Theta_0}^s = \frac{m_b(\Theta_0) \Delta\gamma'(\Theta_0)}{V \cos \Theta_0} \quad (3.115)$$

depends on the given angle Θ_0 .

This facet length, however, is different from the length of a facet on a stationary (resting) boundary. Imagine a boundary that is pinned at its end and subjected to a volume driving force f_0 . In analogy to the shape of a free surface of a crystal, one obtains a facet if the grain boundary surface tension changes discontinuously by $\Delta\gamma'_{\Theta_0}$ at inclination Θ_0 . The length of the facet can be shown to be [257]

$$\Delta S_{\Theta_0}^e = \Delta\gamma'(\Theta_0) / f_0 \quad (3.116)$$

It is different, however, from the facet length on a boundary moving under the action of a driving force f_0 . For example, if Θ_0 and Θ_1 are two angles at which an energy step occurs, then the relation between the facet lengths reads with Eqs.(3.115) and (3.116)

$$\frac{\Delta S_{\Theta_0}^s}{\Delta S_{\Theta_1}^s} = \frac{\Delta S_{\Theta_0}^e}{\Delta S_{\Theta_1}^e} \cdot \frac{m_b(\Theta_0) \cos \Theta_1}{m_b(\Theta_1) \cos \Theta_0} \quad (3.117)$$

Note that the length of the facet at steady-state motion depends on its mobility and orientation relative to the direction of motion. The steady-state velocity of a U -shaped grain boundary (grain boundary half-loop technique (N9 in Table 3.3)) is

$$V = \frac{1}{a} \int_{-\pi/2}^{\pi/2} A_b d\Theta \quad (3.118a)$$

In experiments with grain boundary half-loops the steady-state velocity and, to a minor extent, the boundary shape depend on the half-loop width (driving force), the grain misorientation angle, the orientation of the half-loop as a

whole, i.e. on the direction of motion, on temperature, on material purity, and so on⁸.

In general, the reduced mobility of a boundary element depends on its orientation. To take that dependence into account, let us count the angle Θ in Eq. (3.118a) from a given fixed direction in the crystal, which may be defined by an angle β with regard to the x -axis of the coordinate system in Fig. 3.32.

$$V = \frac{1}{a} \int_{\beta-\pi/2}^{\beta+\pi/2} A_b d\Theta \quad (3.118b)$$

i.e. the velocity of the half-loop motion may depend on its orientation. If the reduced mobility of the boundary element does not depend upon the velocity of normal motion, i.e. in the case of a linear relationship between the velocity and the driving force⁹, the dependence of the steady-state velocity upon the half-loop orientation is determined by the difference between the mobilities of the straight (stationary) boundary sections.

$$\frac{dV}{d\beta} = \frac{A_b(\beta + \pi/2) - A_b(\beta - \pi/2)}{a} \quad (3.119)$$

If the crystal lattice has an inversion symmetry, then $A_b(\beta + \pi/2) = A_b(\beta - \pi/2)$, and the velocity would not depend on the half-loop orientation. In this case, experiments on half-loop migration determine the reduced mobility, averaged over all directions present in the half-loop. It is stressed that the averaged mobility thus determined basically differs from the so-called average grain boundary mobility, obtained by studying the kinetics of grain growth in a polycrystal, since in a polycrystal the average is taken over different boundaries, which differ not only in orientation, but also in misorientation. Averaging in a polycrystal is a statistical averaging; it is meaningful only for a statistical grain boundary distribution, i.e. for a random texture in the sample, a uniform distribution of the grain boundaries by misorientation parameters, etc. These assumptions are not commonly satisfied in experiments, which results in a relatively poor reproducibility of polycrystal properties. Contrary to the averaging in polycrystalline experiments, the averaging by Eq. (3.118) is a physical averaging, which remains unchanged from experiment to experiment. The orientation-averaged boundary mobility turns out to be dependent on the characteristics of the system, such as the misorientation between the grains, temperature, pressure, purity of the materials used, etc. Consequently, despite its average character, the evidence obtained by the techniques of single grain

⁸Of course, all principal consequences pertaining to the grain boundary half-loop hold for the steady-state migration of a grain boundary quarter-loop as well (technique N11, Table 3.3).

⁹It should be noted that the anisotropy of the reduced mobility is usually neglected. A nonlinear dependence of the velocity on the driving force can be due to an interaction of a moving boundary with impurity atoms, as will be discussed below.

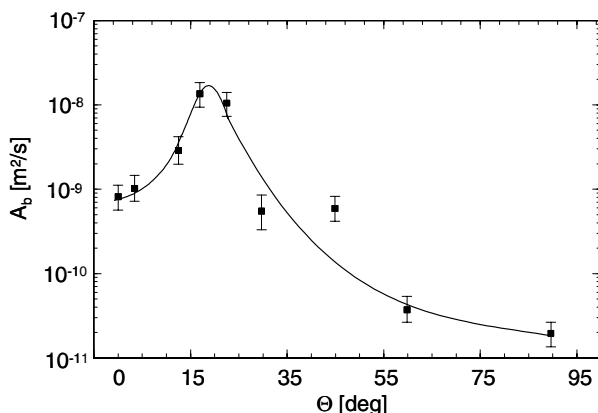


FIGURE 3.33

Dependence of the reduced mobility of a half-loop $86^\circ \langle 11\bar{2}0 \rangle$ tilt boundary in a Zn bicrystal vs. the half-loop inclination angle.

boundary migration studies discussed conveys important physical information on the kinetic properties of grain boundaries and reveals specific differences between dissimilar boundaries.

In crystal lattices that do not possess an inversion symmetry, the half- (or quarter-) loop velocity may depend on its orientation relative to specific crystallographic directions. This dependence was indeed discovered for the migration of $\langle 11\bar{2}0 \rangle$ tilt boundaries in zinc with a misorientation angle of 86° (Fig. 3.33). However, such a dependency may also be due to impurity drag, when the dependence between velocity and driving force becomes nonlinear due to breakaway of the boundary from adsorbed impurities. To answer the question as to whether the observed dependence was due to the absence of an inversion symmetry or to the nonlinearity due to breakaway effects, one has to consider the motion of a grain boundary half- (or quarter-) loop in a grain boundary system with impurities [243]. In the case of the results presented in Fig. 3.33, the half-loop velocity was high and the free boundary moved much faster than the impurity-loaded boundary. In such a case Eq. (3.119) holds and, therefore, the velocity was determined by the impurity free boundary segments, mutually related by a 180° rotation, whereas the role of non-linearity was insignificant [247].

In the following we consider the motion of a grain boundary half- (or quarter-) loop in detail, using the approximation of “Lücke-Detert” [193]. Far away from the vertex, the two branches of the boundary will be planar, and their planes are parallel to each other and perpendicular to the plane of the diagram. This renders the problem quasi-two-dimensional. The velocity of

normal motion of a boundary element is [242]

$$v = \frac{m_b \gamma}{R} \quad (3.120)$$

where R is the radius of curvature of the boundary, which changes along the boundary and, therefore, the velocity v varies along the boundary. Under steady-state conditions the shape of the half- (or quarter-) loop does not vary with time and

$$v = V \cos \Theta = V y' \left[1 + (y')^2 \right]^{-1/2} \quad (3.121)$$

where the function $y = y(x)$ describes the shape of the boundary in a coordinate system carried along by the boundary, $y' \equiv dy/dx$. We shall only consider the top part of the half-loop, i.e. $y \geq 0$ (for reasons of symmetry the shape of the bottom part is the mirror image of the top part).

The shape of the boundary during steady-state motion is given by Eqs. (3.120) and (3.121), and the well-known equation for the radius of curvature $R = -y'' / \left[1 + (y')^2 \right]^{3/2}$

$$y'' = -\frac{V}{\gamma m_b} y' \left[1 + (y')^2 \right] \quad (3.122)$$

under three boundary conditions (Fig. 3.32)

$$\begin{aligned} y(0) &= 0 \\ y(\infty) &= a/2 \\ y'(0) &= \infty \end{aligned} \quad (3.123)$$

The third boundary condition in Eq.(3.123) relates to a half-loop only. For a quarter-loop the boundary condition (Fig. 3.34) should be substituted by

$$y'(0) = \tan \tilde{\Theta} \quad (3.124)$$

where the angle $\tilde{\Theta}$ is defined by the surface tensions of the grain boundary and the free surfaces on the side of the sample [258]. Let us consider the shape of the boundary in the quarter-loop technique (Fig. 3.34). The free energy of the system in quasi-two-dimensional approximation can be represented as the sum of boundary and surface energies

$$G = \int_{b-a}^b \left[\gamma \delta \sqrt{1 + (y')^2} + 2\Delta\gamma_n \tilde{\Theta} \right] dx + \Delta\gamma_T y_0 \delta + c \equiv \int_{b-a}^b U dx + W \quad (3.125)$$

where $\Delta\gamma_n = \gamma_{n1} - \gamma_{n2}$, $\Delta\gamma_T = \gamma_{T1} - \gamma_{T2}$ are the differences between the specific free energies on the two sides of the boundary on the top and side surface of the sample, respectively (Fig. 3.34); c is some constant. Taking into

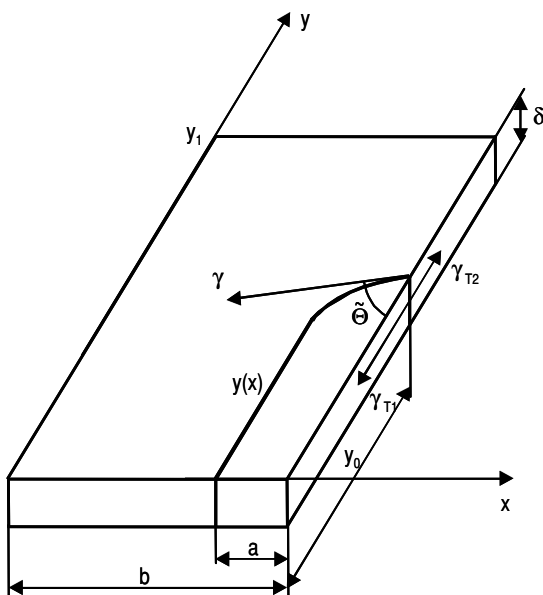
**FIGURE 3.34**

Illustration of the geometry and the surface tensions in the quarter-loop technique.

account that the right-hand end of the boundary moves freely along the line $x = b$, the equilibrium condition for this end can be found from

$$\left| \frac{dU}{dy'} - \frac{\partial W}{\partial y_0} \right|_{x=b} = 0 \quad (3.126)$$

From Eqs. (3.125) and (3.126) the equilibrium condition can be derived

$$\left| \frac{\gamma y' \delta}{\sqrt{1 + (y')^2}} - \Delta \gamma_T \delta \right|_{x=b} = 0 \quad (3.127)$$

or, expressing y' as a function of the contact angle $\tilde{\Theta}$,

$$\gamma \cos \tilde{\Theta} = \Delta \gamma_T \quad (3.128)$$

Eq. (3.128) can be utilized to determine the relative grain boundary surface tension γ and to estimate the free surface tension [259].

The actual form of the solution depends on how the surface tension and the mobility vary from point to point at the boundary [256]. In case of impurity drag some parts of the boundary may move freely, while the more slowly

moving section is loaded with impurities. If the boundary mobility depends only on temperature T and velocity v

$$m_b = m_L + (m_F - m_L) H(v - v^*) \quad (3.129)$$

where $H(\xi)$ is the Heavyside step function, defined by

$$H(\xi) = \begin{cases} 0, & \xi < 0 \\ 1, & \xi > 0 \end{cases} \quad (3.130)$$

and m_F and m_L are the mobilities of an impurity-free and an impurity-loaded boundary, respectively; v^* is the critical value of the boundary velocity, where the impurities can still move together with the boundary [193]. Because it is evident that the surface tension varies from point to point much more slowly than the mobility, it can be assumed [243] that $\gamma = \text{const.}$

The vertex of the half-loop moves fastest, and its velocity is equal to the velocity V of the half-loop as a whole. If $V < v^*$, the boundary remains attached to its impurities at any point, and its mobility is $m = m_L = \text{const.}$ Integration of Eq. (3.122) then yields [243]

$$y = y_0 + \frac{m_L \gamma}{V} \arccos \left[e^{-\frac{(x-x_0)V}{m_L \gamma}} \right] \quad (3.131)$$

where y_0 and x_0 are the constants of integration. With the boundary conditions (Eq. (3.123)), we obtain

$$V = \frac{\pi \gamma m_L}{a} = \frac{2\gamma}{a} \frac{\pi}{2} \cdot m_L \quad (3.132)$$

$$y = \frac{a}{\pi} \arccos \left(e^{-\pi x/a} \right) \quad (3.133)$$

The term $2\gamma/a$ can be referred to as the average driving force, and the quantity $\pi m_L/2$ then corresponds to the average half-loop mobility.

A half-loop, the velocity v of which exceeds v^* , consists of a boundary segment which became detached (free) from impurities as well as a loaded segment moving together with the impurities. The part of the boundary far from the half-loop vertex moves relatively slowly and, therefore, does not become detached from the impurities. The shape of the latter segment is given by an expression similar to Eq. (3.131)

$$y_L = y_{0L} + b_L \arccos \left(e^{-\frac{x-x_{0L}}{b_L}} \right) \quad (3.134)$$

where $b_L = m_L \gamma / V$.

If $V > v^*$, the boundary at the vertex becomes detached from the impurities, and its shape is then

$$y_F = y_{0F} + b_F \arccos \left(e^{-\frac{x-x_{0F}}{b_F}} \right) \quad (3.135)$$

where $b_F = m_F \gamma / V$.

At the point x^* on the boundary, which moves exactly with the velocity v^*

$$\begin{aligned} y_L(x^*) &= y_F(x^*) \\ y'_L(x^*) &= y'_F(x^*) \end{aligned} \quad (3.136)$$

The boundary cannot be discontinuous or contain kinks, since at a kink the curvature of the boundary and, consequently, the driving force would become infinite.

The conditions (3.123) now change to

$$\begin{aligned} y_F(0) &= 0 \\ y_L(\infty) &= \frac{a}{2} \\ y'_F(0) &= \infty \end{aligned} \quad (3.137)$$

and the integration constants y_{0L} , y_{0F} , x_{0L} , and x_{0F} are completely defined

$$y(x) = \left\{ \begin{array}{l} b_F \arccos \left(e^{-\frac{x}{b_F}} \right), \quad 0 \leq x \leq x^* \\ \frac{a}{2} - b_L \arcsin \left(e^{-\frac{x-x^*(1-b_L/b_F)}{b_L}} \right), \quad x^* < x < \infty \end{array} \right\} \quad (3.138)$$

where

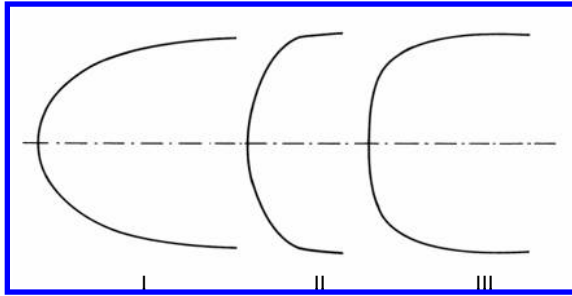
$$x^* = -\frac{m_F \gamma}{V} \ln \frac{v^*}{V} \quad (3.139)$$

and the half-loop velocity is given by

$$v^* = V \sin \left(\frac{\pi}{2} \frac{V_F - V}{V_F - V_L} \right) \quad (3.140)$$

where $V_F = \pi \gamma m_F / a$ and $V_L = \pi \gamma m_L / a$.

The change of shape of a half-loop on detachment from its impurities is shown schematically in Fig. 3.35. The detachment from the impurities flattens the grain boundary. This effect does not only apply to impurity atoms but also to mobile particles. It follows from Eq. (3.140) that the detachment of a grain boundary half-loop, more generally of a curved boundary, from its impurities is more complicated than for a planar boundary. The dependence (3.140) is plotted in Fig. 3.36. The various curves correspond to different values of the ratio $\alpha = V_F / V_L$. The diagram reflects the behavior of a grain boundary half-loop at different values of v^* / V_F but for a constant V_L / V_F . If v^* / V_F is large, the boundary moves together with its impurities, and its velocity is V_L (line $a - b$ in Fig. 3.36). If v^* / V_F decreases and reaches the value V_L / V_F (point b), some impurities become detached from the half-loop vertex, and the boundary segment abruptly assumes the velocity corresponding to point c (Fig. 3.36). Furthermore, as v^* / V_F decreases, more and more impurity atoms become detached from the boundary, i.e. increasingly larger segments of the

**FIGURE 3.35**

Changes in the shape of a half-loop boundary in the course of its detachment from impurities: (I) before detachment; (II, III) different stages of detachment.

boundary move freely, and the half-loop velocity approaches V_F . In turn, if the value v^*/V_F is increased again, the half-loop velocity follows the same curve to point d in Fig. 3.36, and then discontinuously changes to V_L (impurity attachment).

The following transformation is very useful for the interpretation of the calculations. It is clear from Eq.(3.121) that

$$y' = \frac{v/V}{\sqrt{1 - v^2/V^2}} \quad (3.141)$$

Substituting (3.136) into (3.117) and integrating with respect to $\xi = v/V$

$$V = \frac{2\gamma}{a} \int_0^1 \frac{m_b(\xi V) d\xi}{\sqrt{1 - \xi^2}} \equiv \frac{2\gamma}{a} M(V) \quad (3.142)$$

where $2\gamma/a$ is the average driving force acting on the half-loop; V is the velocity of the half-loop as a whole; $M(V)$ is the average mobility of the half-loop. If $V < v^*$ and $m(V) = m_L = \text{const.}$, we find $M = \pi m_L/2$ in full agreement with the above analysis. Eq. (3.142) allows us to determine the steady-state half-loop velocity as a function of the driving force, if we know the dependence $m(v)$, which determines the microscopic mobility of a segment of the boundary with regard to its normal displacement. However, experimental investigations usually give the macroscopic velocity of a half-loop, and we come up against the inverse problem: knowing the dependence of V on the driving force on the half-loop of width a , we have to find the dependence $m(v)$. With this in mind, we will represent Eq. (3.142) in the form

$$\frac{a(V)V}{2\gamma} = \int_0^V \frac{m_b(v) dv}{\sqrt{V^2 - v^2}} \equiv \int_0^{V^2} \frac{\frac{m_b(v)}{v} d(v^2)}{2\sqrt{V^2 - v^2}} \quad (3.143)$$

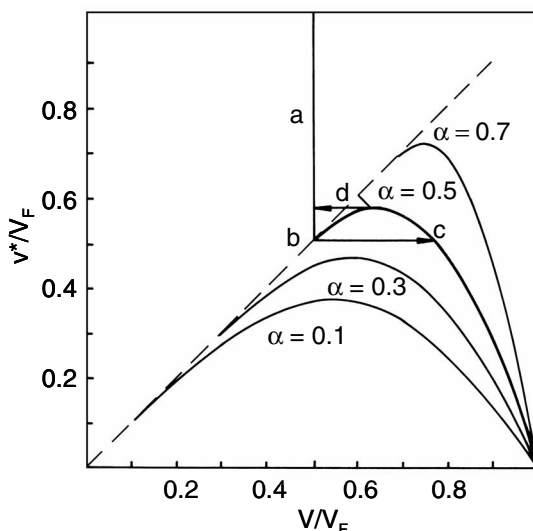
**FIGURE 3.36**

Diagram used to determine the velocity of steady-state motion of a half-loop (see text).

where $a(V)$ is the inverse function of $V(a)$. This integral equation can be solved with regard to $m_b(v)$

$$m_b(v) = \frac{1}{\pi\gamma v} \int_0^v \frac{\frac{da(V)}{dv} V + 2a(V)}{\sqrt{v^2 - V^2}} V^2 dV \quad (3.144)$$

This establishes the full relationship between the microscopic kinetic properties of a grain boundary and the macroscopic properties of a half-loop.

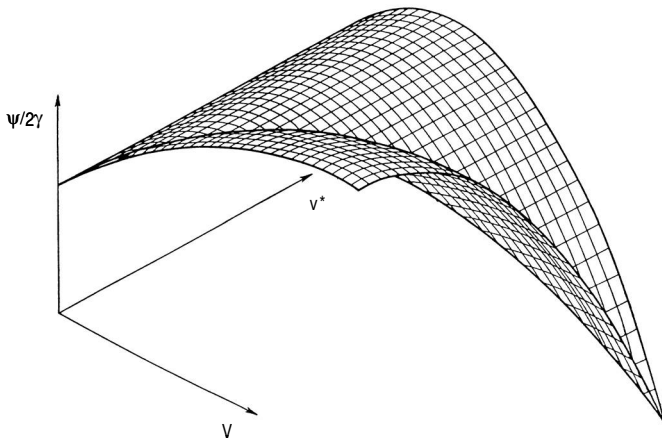
The macroscopic approach provides a way for a pictorial interpretation of the solution of the problem in the Lücke-Detert approximation. The average mobility of a half-loop given by Eq. (3.142) can be easily deduced

$$M(V) = \left\{ m_L \arcsin \frac{v^*}{V} + m_F \arccos \frac{v^*}{V}, V > v^* \right\} \quad (3.145)$$

and the substitution of Eq. (3.145) into Eq. (3.142) yields Eq. (3.140). It is obvious that the relation (3.142) corresponds to the extremum of the function

$$\psi(V) = \left[2\gamma V - a \int_0^V \frac{V dV}{M(V)} \right] \quad (3.146)$$

since (3.146) is obtained by integrating (3.142) in the form $2\gamma - aV/M(V) = 0$. It is easily seen that only the maxima of this function correspond to stable

**FIGURE 3.37**

Generalized dissipative function (see text).

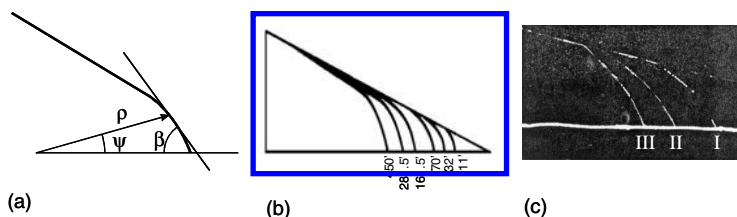
steady-state motion. The velocities conforming to the minima of $\Psi(V)$ decrease with increasing driving force, which is physically incorrect, and the solutions are totally unstable. The function $\Psi(V)$ for different values of v^* in the Lücke-Detert approximation is plotted in Fig. 3.37. Finally, it is noted that for a linear dependency of the velocity on the driving force ($M = \text{const.}$) the function Ψ is equivalent to the rate of dissipation (loss) of the free energy of the system, which is related to the Onsager principle in the thermodynamics of irreversible processes [260].

The grain boundary half- (and quarter-) loop are the only known experimental techniques at present, where the grain boundary moves steadily. For the reversed-capillary technique (N4, Table 3.3) additional assumptions are needed to solve the equation for the shape of a moving boundary [229, 242]

$$\frac{\rho(\Psi, t) d\rho(\Psi, t)}{dt} = \frac{m_b(\varphi) \gamma \partial \beta(\Psi)}{\partial \Psi} \quad (3.147)$$

where $\rho(\Psi, t)$ is the radius-vector of a point on the grain boundary in polar coordinates; $\beta(\Psi)$ is the angle between the tangent vector $d\rho$ to the grain boundary at this point and the vector $\rho(\Psi = 0, t)$; $m_b(\varphi)$, $\gamma(\varphi)$ are the mobility and surface tension of the grain boundary, respectively; φ is the angle of misorientation of the grain boundary (Fig. 3.38). If $m_b(\varphi)$ and $\gamma(\varphi)$ are independent of time, the space and time variables can be separated. In this case the shape of the grain boundary does not change during motion, in other words, the scaling condition is satisfied.

A general calculation of the grain boundary shape for the reversed-capillary technique is difficult and will not be presented here. In this respect a thermodynamic concept [261] proved to be very beneficial. Assuming as the physical

**FIGURE 3.38**

Grain boundary displacement for reversed-capillary technique. (a) Boundary geometry. (b) Calculated successive positions of a moving grain boundary in a bicrystal. Numbers indicate annealing time in minutes ($A_b = 10^{-3} \text{ m}^2/\text{s}$; $B = 10^{-2} \text{ m/s}$; $\gamma\delta = 5 \cdot 10^{-5} \text{ J/m}$; $\Delta\gamma_n = 10^{-5} \text{ J/m}^2$; $\Delta\gamma_e\delta = 10^{-5} \text{ J/m}$; $\tan \alpha = 0.275$). (c) Traces of grain boundary motion in a Zn bicrystal (x400).

condition that an intermediate equilibrium of the boundary is always attained, the free energy of the system at each instant is at a — relative — minimum, despite the fact that irreversible processes occur in the system. One of the merits of such an approach is that it is possible to determine the transition process parameters. In this approach the problem can be reduced to determining a conditional extremum (minimum) of the free energy of the system. The corresponding equations of motion are the coupling equations for this free energy functional. It is finally noted that such concept is close to the Onsager principle and to the principle of maximum rate of change of the thermodynamic potential of the system [260]. In this approach [261] the shape of a grain boundary moving under the action of its own curvature or other driving forces can be determined (Fig. 3.25b,c). The reader is referred to [261] for details.

There are important reasons why we consider the problem of the shape of a moving grain boundary so comprehensively. First, the description given above is based on a visual concept, where all changes associated with the joint motion of grain boundary and impurity cloud, the detachment from the impurity cloud, and the motion of the free grain boundary are clearly defined in the shape of the moving boundary. Second, up to now the grain structure of a polycrystal is characterized by only one parameter — the mean grain size — in spite of the fact that practically all grain boundaries are curved. Further, we think that the given considerations are important and necessary because of the discrepancy that all theories of grain boundary motion assume planar grain boundaries, while real grain boundaries are curved, i.e. the theories are applied without any corrections to grain boundary motion in polycrystals. The analysis of the shape of the moving boundaries will become increasingly interesting for computer simulations of grain growth and recrystallization.

Despite its importance, there has been only little research dedicated to the shape of moving grain boundaries. A satisfactory agreement between exper-

iment and theory was found when the shape of a grain boundary, moving under the conditions of the reversed-capillary technique, was compared to the theoretical shape approximated by a circular arc [236]. A recent investigation [244] was conducted to compare the experimentally observed shape in the quarter-loop technique with the corresponding calculations in the framework of the Lücke-Detert approximation to analyze the principal question whether boundary motion in the quarter-loop technique complies with scaling conditions, and, in particular, to estimate the influence of the impurity atoms on the shape of a moving grain boundary.

The quarter-loop technique was chosen since, on the one hand, considerable detailed experimental research has been conducted about the effect of grain boundary mobility using this method, and on the other hand, it can be easily treated theoretically [243]. Contrary to the “half-loop” situation, in this case the grain boundary steady-state motion is a motion together with a triple junction which is formed by three surfaces (the grain boundary and two free surfaces) and, naturally, by the three corresponding surface tensions γ , γ_{T1} and γ_{T2} (Fig. 3.34). Equilibrium in that triple junction can be conserved if there is no mass transfer (diffusion etc.) to change the shape of the triple junction in this point. The problem can be considered under the assumption of uniform grain boundary properties and quasi-two-dimensionality [244] by using Eqs. (3.120)–(3.124). Eq. (3.148) describes the shape of a freely moving quarter-loop, i.e. which does not interact with impurity atoms and other obstacles.

$$y(x) = \xi \arccos \left(e^{-x/\xi + c_1} \right) + c_2$$

$$\xi = \frac{a}{2\Theta}; \quad c_1 = \ln(\sin \Theta); \quad c_2 = \xi \left(\frac{\pi}{2} - \Theta \right) \quad (3.148)$$

The solution for a quarter-loop influenced by impurity drag can be derived by the procedure extensively considered above (Eqs. (3.134)–(3.140)) except that boundary condition (3.137) must be replaced by (3.124).

$$y(x) = \begin{cases} -(b_F - b_L) \arccos \left(\frac{\sin \Theta}{e^{\frac{x^*}{b_F}}} \right) + \frac{a}{2} - b_L \frac{\pi}{2} + b_F \arccos \left(e^{\frac{b_F \ln(\sin \Theta) - x}{b_F}} \right) & 0 \leq x \leq x^* \\ \frac{a}{2} - b_L \frac{\pi}{2} + b_L \arccos \left(e^{\frac{b_L \ln(\sin \Theta) - x^* \left(\frac{b_L}{b_F} - 1 \right) - x}{b_L}} \right) & x \geq x^* \end{cases} \quad (3.149)$$

where b_L is:

$$b_L = \frac{b_F \left[\arccos \left(\frac{\sin \Theta}{e^{\frac{x^*}{b_F}}} \right) + \Theta - \frac{\pi}{2} \right] - \frac{a}{2}}{\arccos \left(\frac{\sin \Theta}{e^{\frac{x^*}{b_F}}} \right) - \frac{\pi}{2}} \quad (3.150)$$

The parameters in the function (3.149) are the width of the shrinking grain $a/2$, the angle Θ of the grain boundary with the free surfaces in the triple junction.

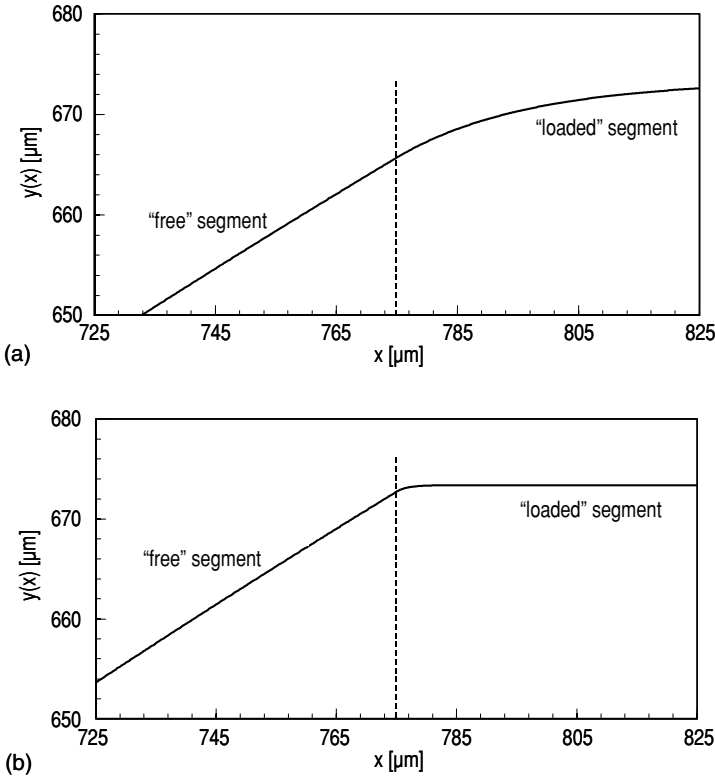


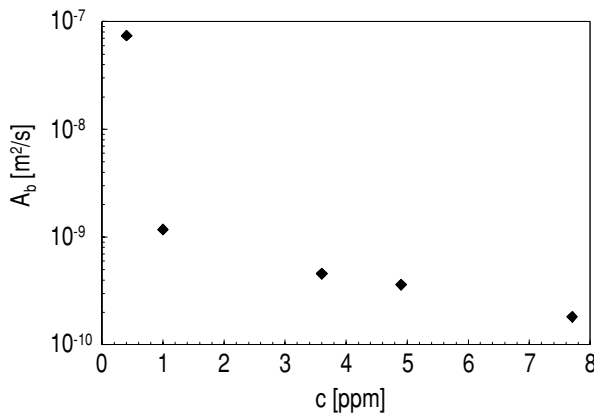
FIGURE 3.39

Intersection of “free” and “loaded” segment of the calculated grain boundary shape (a) $m_L/m_F = 0.0292$, (b) $m_L/m_F = 0.00245$ (x^* - dashed line).

tion, the critical point x^* , and b_F . The first two parameters can be measured directly in the experiment. The latter two have to be chosen in an appropriate way to fit the experimentally derived grain boundary shape. As can be seen from Eqs.(3.134) and (3.135), $b_L/b_F = m_L/m_F$. The point x^* is the point of intersection of the “free” and “loaded” segments of the grain boundary.

The value m_L/m_F is a measure for how drastic the change between the “free” and the “loaded” part in the point of intersection will be. Even if there is no kink or discontinuity in the calculated grain boundary shape at point x^* the change from the “free” to the “loaded” part will be more and more abrupt for smaller and smaller values of m_L/m_F (Fig. 3.39).

Corresponding experiments were carried out on aluminum bicrystals with a $40.5^\circ\langle 111 \rangle$ tilt boundary. The samples differed by the amount of dissolved impurities. Bicrystals with a total impurity content of 0.4 ppm, 1.0 ppm,

**FIGURE 3.40**

Dependence of the reduced grain boundary mobility on impurity content in high purity Al.

3.6 ppm, 4.9 ppm and 7.7 ppm were studied. The grain boundary mobility was extracted from in situ experiments of grain boundary motion (see Sec. 3.4.2). After the measurement of grain boundary mobility the samples were rapidly cooled to room temperature, and the grain boundary shape was recorded with an image analysis system. The accuracy of locating the grain boundary was about $15\mu m$. The used mobility data [244] are given in Fig. 3.40.

A major change in the mobility was observed in the regime between 0.4 ppm and 1.0 ppm, where the mobility drops drastically with increasing impurity content. This may be due to the attachment of impurities to the grain boundary [244]. In the specimen with 0.4 ppm solute atoms the grain boundary had a mobility of $7.4 \cdot 10^{-8} m^2/s$ which can be assumed to be the mobility m_F of the “free” moving grain boundary. In this context “free” means that there are no additionally adsorbed atoms at the grain boundary, i.e. the concentration of the solute atoms in the grain boundary does not differ from the concentration of the solute atoms in the bulk. At larger impurity content the mobility is no longer determined by the intrinsic grain boundary mobility, but rather by the mobility m_L of the impurities. The investigation proves that the influence of the impurity atoms on grain boundary properties and behavior is rather strong even in very pure materials. The experimentally measured shape of a moving grain boundary (Al with 1.0 ppm impurities) and the shape, calculated according to Eq. (3.148), which does not take into consideration impurity drag, are compared in Fig. 3.41. The large discrepancy is obviously and apparently due to the neglect of boundary-impurity interactions. However, with m_L and m_F determined as explained above, the measured boundary shape

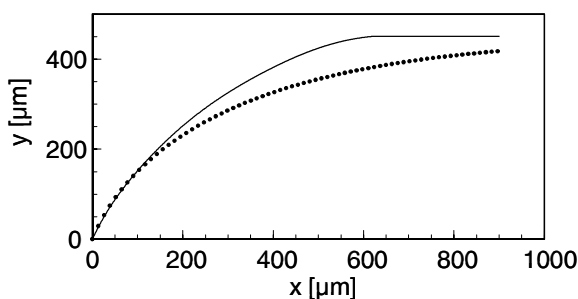


FIGURE 3.41

Comparison between experimental data (solid line) and calculated shape (dotted line) disregarding segregation.

can be successfully fitted by Eq. (3.149) using only x^* as a free fit parameter (Fig. 3.42).

The same holds for the reversed-capillary technique. Any attempt to fit the shape by assuming a freely moving boundary fails, but good agreement between experiment and theory can be observed when impurity drag and thus different mobilities are taken into account (Fig. 3.43) [241].

As mentioned above, the shape of a moving grain boundary is a new source of information on grain boundary migration. One example is given in Fig. 3.44, where the value of the critical distance x^* , normalized by the driving force (in terms of the quarter-loop width a) is plotted vs. the impurity content. In accordance with the Lücke-Detert theory [193] the critical velocity v^* (and rigidly bound to it the position of the critical point x^* on the quarter-loop) is determined by the balance between the maximum force of interaction of the impurity atoms with the boundary and the force, which is imposed by the energy dissipation caused by boundary motion across the matrix. The difference in the impurity drag for grain boundaries in samples with different amount of impurities is caused by the adsorption of impurities at the grain boundary. According to theory the velocity should decrease proportionally to the inverse of the concentration of adsorbed atoms. Therefore, x^* should increase with decreasing impurity content, as observed qualitatively (Fig. 3.44) [244]. However, a linear relation between the inverse of the impurity concentration and v^* , i.e. x^* , is not observed over the whole concentration range, which indicates a more complicated interaction of adsorbed atoms with the grain boundary. In such a case x^*/a should increase more strongly with decreasing impurity content than linearly. This tendency is indeed observed (Fig. 3.44).

Evidently, even in very — although not perfectly — pure metals there is no agreement between the experimentally observed and calculated shape of a moving grain boundary, if the impurity influence is not taken into account. This has to be kept in mind to avoid serious misinterpretation when evaluating

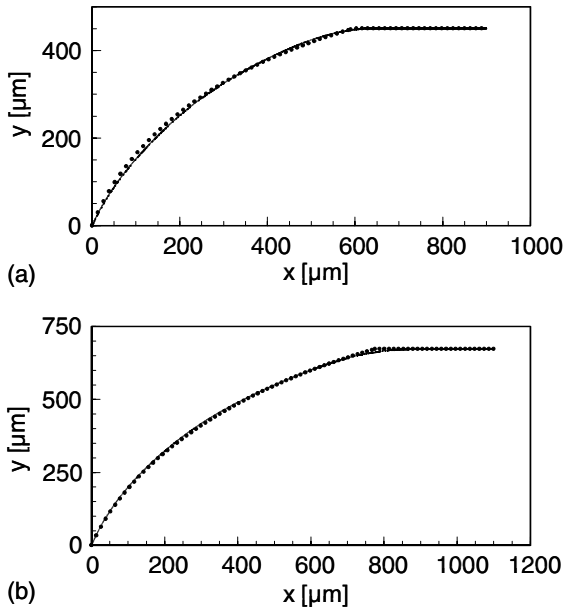


FIGURE 3.42

Experimentally observed (solid line) and calculated (Eq. (3.149), dotted line) grain boundary shape for Al with an impurity content of (a) 1.0 ppm (b) 3.6 ppm (quarter-loop technique).

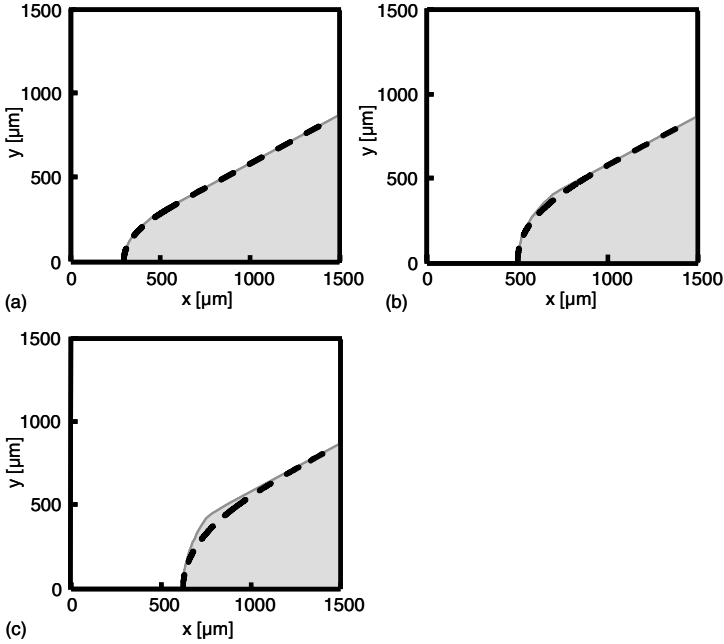


FIGURE 3.43

Experimentally observed and calculated shape accounting for drag effect: (shaded area), neglecting the drag effect (dashed line) (Fe-3%Si, reversed-capillary technique): (a) theoretically predicted grain boundary shape; (b) accounting for drag effect; (c) without regard to drag effect.

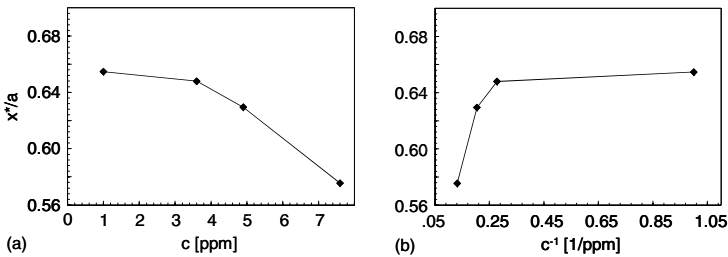


FIGURE 3.44

Dependence of critical point x^*/a on (a) impurity content; (b) reciprocal impurity content.

experimental mobility data.

3.5 Experimental Results

3.5.1 Relation between Driving Force and Migration Rate

As elaborated in Sec. 3.1 the driving force for grain boundary migration is always small compared to the thermal energy. Therefore, grain boundary migration is a drift motion following the trend to reduce the energy content of the crystalline aggregate. A drift velocity, however, is always proportional to the driving force, as derived in Sec. 3.1 (Eq. (3.6))

$$v = m_b P$$

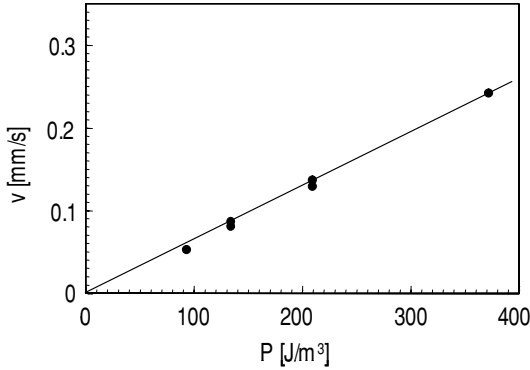
and the proportionality factor m is the grain boundary mobility

$$m_b = v/P \quad (3.151)$$

In accurate experiments relation (3.6) is unambiguously confirmed, most precisely for the motion of a planar grain boundary under the action of a magnetic driving force (Fig. 3.45). In this case the grain boundary crystallography is exactly defined and remains unchanged during boundary motion. Moreover, the driving force can be precisely calculated and varied in a defined manner. Also for the motion of curved grain boundaries Eq.(3.6) is obeyed (Fig. 3.46), although for very small driving forces a deviation to lower migration rates is observed. This deviation is likely to be due to drag effects (solute drag, groove dragging) which necessarily have to show up when the driving force tends to zero since no material is absolutely pure. A proportionality between mean migration rate and elastically stored energy was even reported for growing grains in polycrystals (Fig. 3.47). Despite this conceptually necessary and experimentally confirmed relation (3.6) there have been reports in pertinent literature which contended that Eq.(3.6) does not hold, rather

$$v \sim P^n \quad (3.152)$$

with $n \gg 1$ and as high as $n = 12$ would more adequately comply with experimental results. The crucial experiment to prove this complication was due to Rath and Hu [230]–[233] (Fig. 3.48), who conducted experiments on aluminum bicrystals using wedge-shaped specimens (Sec. 3.4.2.1, Fig. 3.25a). These results have worried the scientific community for many years since such results cannot be understood from fundamental principles (Sec. 3.1) and also preclude a determination of grain boundary mobility without further theoretical treatment of relation (3.152). It can be shown, however, that the observed

**FIGURE 3.45**

Measured grain boundary migration rate vs. driving force of a flat boundary in a bicrystal of Bi exposed to a magnetic field.

relation (3.152) is due to improperly conducted experiments and, therefore, a misinterpretation of experimental data.

The experiments of Rath and Hu [230]–[233] were carried out on aluminum in a hydrogen (reducing) atmosphere which strongly promotes grooving since aluminum does not form a protective oxide layer on its surface under these conditions. Also, they used a discontinuous method to measure the grain boundary displacement with large intervals of annealing time. So, the experimental results corresponded to an average displacement including a large number of detachment-attachment processes of the moving boundary from its groove. In this case [210, 225] the average boundary migration

$$v = \lim_{t \rightarrow \infty} \frac{\int_0^t v(q) dq}{t} = \frac{\int_0^\tau v(q) dq}{\tau} \quad (3.153)$$

where τ is the time between two consecutive detachments according to Eq.(3.99). Since the principal mechanism of groove development in aluminum is surface diffusion, the average grain boundary velocity is obtained by differentiation of Eq. (3.96) (Sec. 3.3.6) and (3.153)

$$v = 4PA_b \left\{ \left[\frac{1}{\chi^3} - \frac{1}{6\chi^4} \ln \frac{(1+\chi)^3}{1+\chi^3} \right] - \frac{1}{\chi^4 \sqrt{3}} \left(\arctan \frac{2\chi-1}{\sqrt{3}} + \frac{\pi}{6} \right) \right\} \quad (3.154a)$$

where

$$\chi = \left(\frac{P\delta}{2\gamma\Theta_c} - 1 \right)^{-1/3} \quad (3.154b)$$

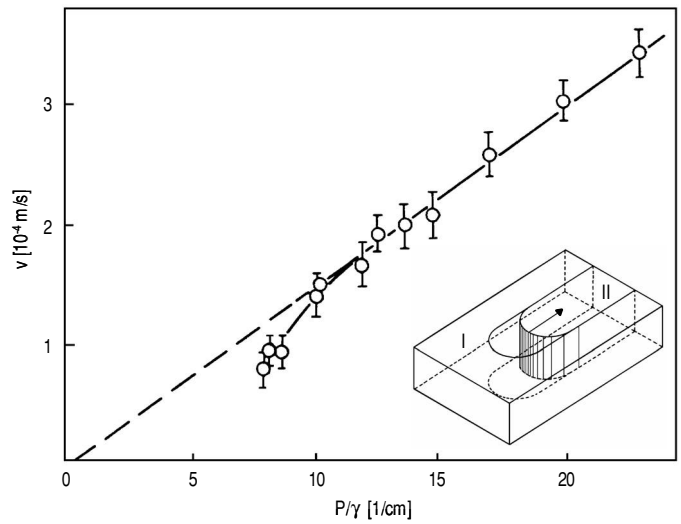


FIGURE 3.46
Measured grain boundary migration rate vs. reduced driving force of *U*-shaped boundaries in Al bicrystals (half-loop technique).

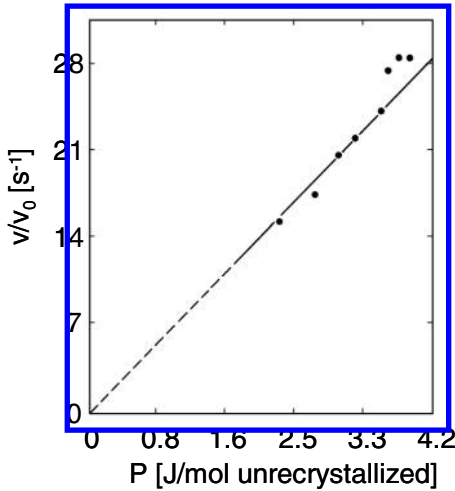
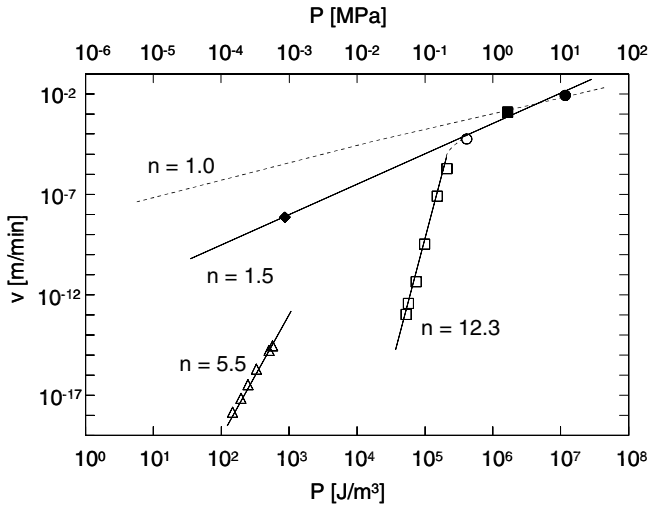


FIGURE 3.47
Average growth rate (normalized by a constant v_0) as a function of the driving force for a polycrystalline aluminum alloy containing 17 ppm Cu during primary recrystallization at 125°C [262].

**FIGURE 3.48**

Boundary migration rate vs. driving force as reported by Rath and Hu [231] for wedge-shaped Al bicrystals.

Correspondingly, the kinetics in the experiments mentioned are entirely controlled by thermal grooving and groove dragging rather than by an intrinsic relation between migration rate and driving force [225] (Fig. 3.49).

The concept derived in Sec. 3.3.6 provides a basis for formulating the requirements to be satisfied by an experiment aimed at a physically correct study of grain boundary motion. It is important to note that a necessary condition [210] for grooving to be negligible is the magnitude of the criterion ρ

$$\rho = \frac{P\delta}{\gamma\Theta_c} \cong \frac{P\delta\gamma_s}{\gamma^2} \gg 1 \quad (3.155)$$

An analysis of this criterion applied to the series of experiments by Rath and Hu [230]–[233] reveals the following scenario: driving force $P = \gamma/R$ with $R = 1.02 - 0.2$ cm, sample thickness 0.25 cm thick. Taking $\gamma/\gamma_s \cong 0.3$ [263], one obtains for the beginning of motion $\rho \cong 0.5$ and at the end $\rho \cong 4$, i.e. only toward the end can one expect a free motion of the boundary, while groove dragging controls most of the experiments. In conclusion, the results obtained do not pertain to free boundary motion.

Rath and Hu [230]–[233] surmised that the nonlinearity $v \sim P^n$ was due to impurity drag such that the boundary was in the transition regime between loaded and free state (Sec. 3.3.2, Fig. 3.6). This is not feasible, however, since the boundary will assume either the loaded or the free state, if the transition is discontinuous, as observed experimentally (Fig. 3.7). Only for very small

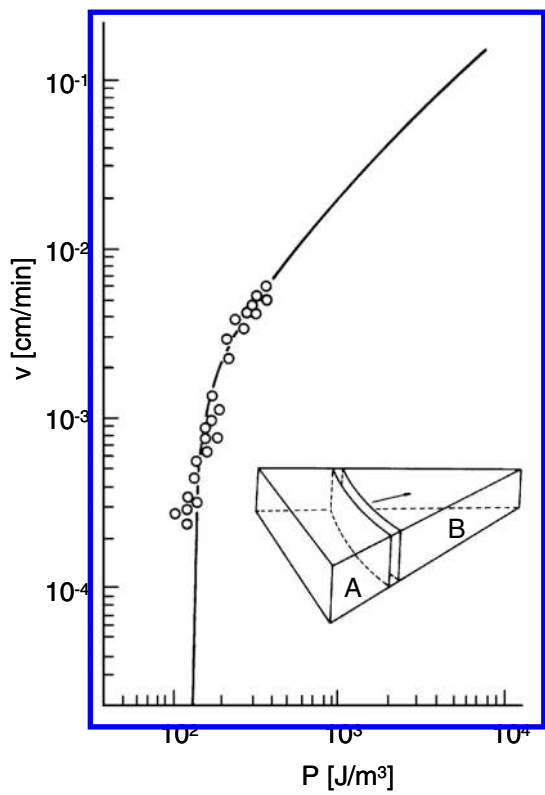


FIGURE 3.49
Calculated $v(P)$ dependency (curve) in the presence of groove dragging. Symbols are values reported by Rath and Hu (see Fig. 3.48).

impurity contents and driving forces is there a continuous transition from the loaded state to the free motion state which, however, is limited to a small driving force interval, much smaller than the driving force noted in the experiments of Rath and Hu.

With the proportionality between migration rate and driving force being unambiguously established, Eq.(3.151) can be applied to extract the grain boundary mobility from grain boundary motion experiments and to determine the influence of temperature, hydrostatic pressure, grain boundary crystallography, chemical composition etc. on grain boundary mobility.

3.5.2 Kinetic Parameters of Grain Boundary Mobility

As evident from Sec. 3.1 grain boundary migration is a thermally activated process. Thus, its kinetics follow an Arrhenius-type temperature dependence

$$v = v_0 \exp \left(-\frac{H_m}{kT} \right) \quad (3.156)$$

Since the driving force is independent of temperature, the temperature dependence of v is the temperature dependence of the grain boundary mobility

$$m_b = \frac{v}{P} = m_0 \exp \left(-\frac{H_m}{kT} \right) \quad (3.157)$$

where H_m is the activation enthalpy of grain boundary migration and m_0 the corresponding preexponential mobility factor. It is noted that

$$H_m = E_m + pV^* \quad (3.158)$$

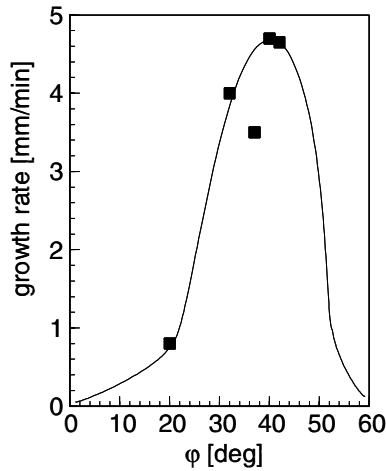
(E_m — activation energy) depends on the pressure p , which can be used to determine the activation volume V^* (Sec. 3.5.4). However, for all practical purposes grain boundary migration proceeds under a constant (ambient) pressure.

Since most results referred to in the following were obtained for the migration of curved grain boundaries, we introduce for simplicity the reduced mobility (see footnote in [Sec. 3.4.3](#))

$$A_b = m_b \cdot \gamma = A_0 \exp \left(-\frac{H_m}{kT} \right) \quad (3.159)$$

For the half-loop geometry it can be obtained from the boundary velocity by $A_b = va/2$, for the quarter-loop geometry $A_b = va$ (Sec. 3.4.2.1).

Any influence on grain boundary mobility will be reflected in a change of H_m , V^* , and/or m_0 (resp. A_0). Therefore, in the following we will discuss the dependence of these kinetic parameters on the structure and chemistry of grain boundaries.

**FIGURE 3.50**

Change of boundary migration rate with orientation difference about a common $\langle 111 \rangle$ axis in Al [264].

3.5.3 Misorientation Dependence of Grain Boundary Mobility

The long-known observation that pronounced crystallographic textures develop during annealing of deformed metals was the first indication that grain boundary mobility may depend on misorientation. Correspondingly, the first findings on the orientation dependence of grain boundary velocity were obtained in recrystallization experiments (Fig. 3.50) [264, 265, 269]. Such dependencies were confirmed subsequently with experiments on bicrystals, which do not only permit us to investigate all orientation relationships, but also to determine the influence of various factors on grain boundary mobility, e.g. temperature, pressure, nature and content of impurities etc. However, in the majority of investigations grain boundary migration was considered for a very few specific boundaries and provides only an incomplete characteristic of the migration capability of grain boundaries [230]–[235], [270]–[272]. The misorientation dependence was studied extensively for lead, aluminum and zinc.

The misorientation dependence of the velocity of single boundaries in zone refined lead was studied under a constant driving force (striation/subgrain/structure, experimental technique N1, Table 3.3) and in a range of temperatures [182] (Fig. 3.51). Well-pronounced extrema (maxima of grain boundary velocity, minima of activation energy and preexponential factor, respectively) could be associated with low Σ coincidence boundaries.

In aluminum the misorientation dependency of grain boundary mobility

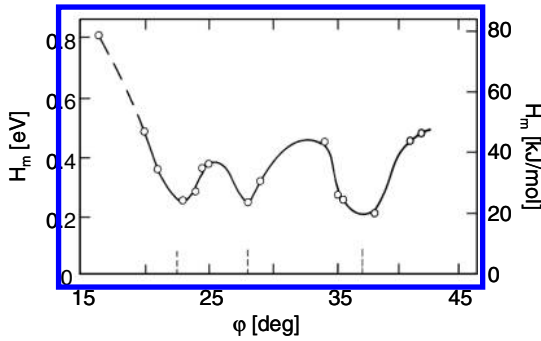


FIGURE 3.51

Measured activation enthalpies H_m vs. misorientation angle φ for $\langle 100 \rangle$ tilt boundaries in zone refined lead [182].

and its kinetic parameters (enthalpy of activation and pre-exponential factor) was investigated for $\langle 100 \rangle$, $\langle 111 \rangle$ and $\langle 110 \rangle$ tilt grain boundaries with a total amount of impurities of $(2 - 5) \cdot 10^{-4}$ at% by the grain boundary half-loop technique (N9, Table 3.3) (Fig. 3.52) [273]–[275].

The misorientation dependency of the activation enthalpy of migration for $\langle 10\bar{1}0 \rangle$ and $\langle 11\bar{2}0 \rangle$ tilt boundaries in zinc with a total impurity content of $5 \cdot 10^{-4}$ at% and $5 \cdot 10^{-3}$ at%, respectively, are shown in Fig. 3.53 [70, 239, 276]. The data were obtained by the reversed-capillary technique (technique N6, Table 3.3). Qualitatively, the behavior of the migration activation enthalpy in Zn is akin to fcc metals. Evidently, the dependency $H_m(\varphi)$ reflects structural peculiarities of the grain boundaries. However, the situation is complicated by the fact that exact CSLs for hexagonal close-packed structures exist only for rotations around $\langle 0001 \rangle$ and for hypothetical structures with a rational ratio c/a . This problem can be alleviated by including also superlattices close to coincidence. A comparison of the misorientation dependencies of mobility (Fig. 3.53) with the computed misorientation dependency of Σ revealed for hcp metals that there is a correlation between the extrema of the curves $A_b(\varphi)$, $H_m(\varphi)$, $A_0(\varphi)$ (φ — angle of rotation) and the misorientation of low Σ grain boundaries. We will refer to low Σ coincidence boundaries also as special grain boundaries in the following.

In essence, all misorientation dependencies of grain boundary mobility and its parameters considered are non-monotonous, and the corresponding extrema correspond to low Σ misorientations of the CSL lattice. The magnitude of the oscillations is large: for the grain boundary mobility about 2 orders of magnitude, for the activation enthalpy ~ 60 – 120 kJ/mol. Therefore, one has to address the question of what is the origin of this misorientation dependence. In other words, is there a fundamental correlation between the structural properties of a grain boundary, e.g. the value of Σ , and grain boundary mobility?

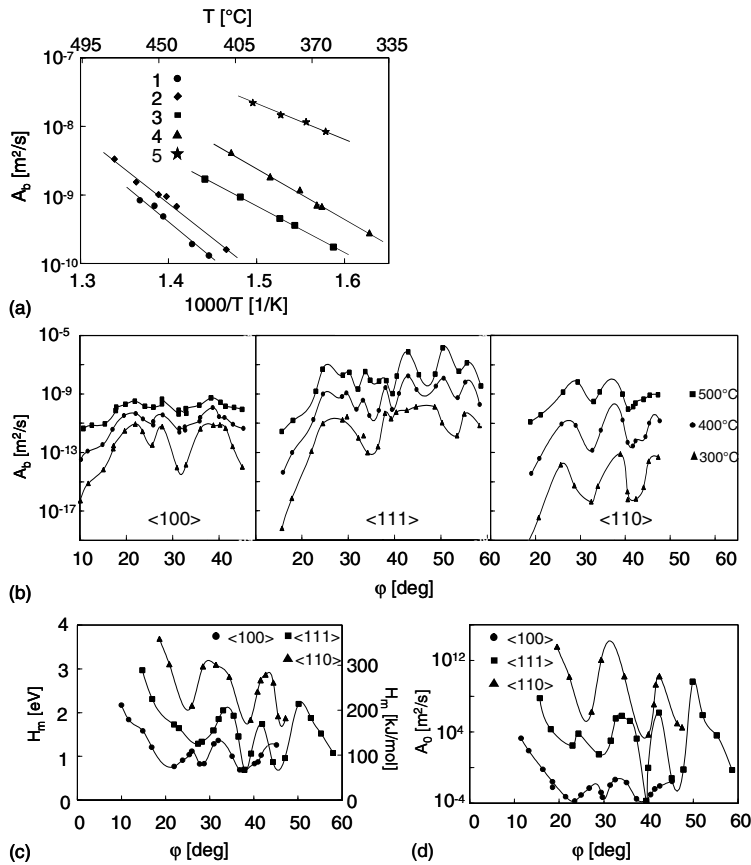


FIGURE 3.52

Temperature and misorientation dependencies of reduced grain boundary mobility for $\langle 100 \rangle$, $\langle 111 \rangle$ and $\langle 110 \rangle$ tilt grain boundaries in aluminum. (a) Temperature dependence, $\langle 111 \rangle$ tilt grain boundaries with various angles φ of misorientation 1 – $\varphi = 33^\circ$; 2 – 35.5° ; 3 – 28° ; 4 – 36.5° ; 5 – 45° . (b) Misorientation dependence at 500°, 400° and 300°C, respectively. (c) Enthalpy of activation vs. misorientation angle φ for motion of $\langle 100 \rangle$, $\langle 111 \rangle$ and $\langle 110 \rangle$ tilt boundaries in Al. (d) Pre-exponential factor of reduced grain boundary mobility for tilt boundaries in Al.

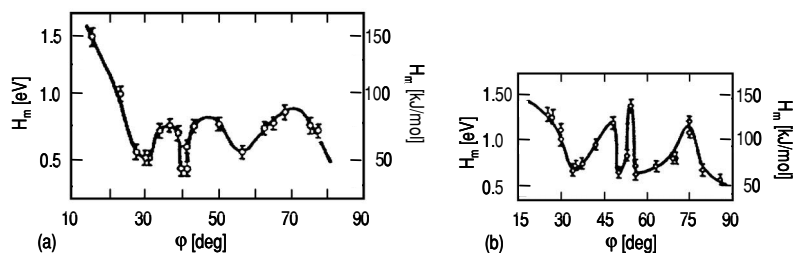


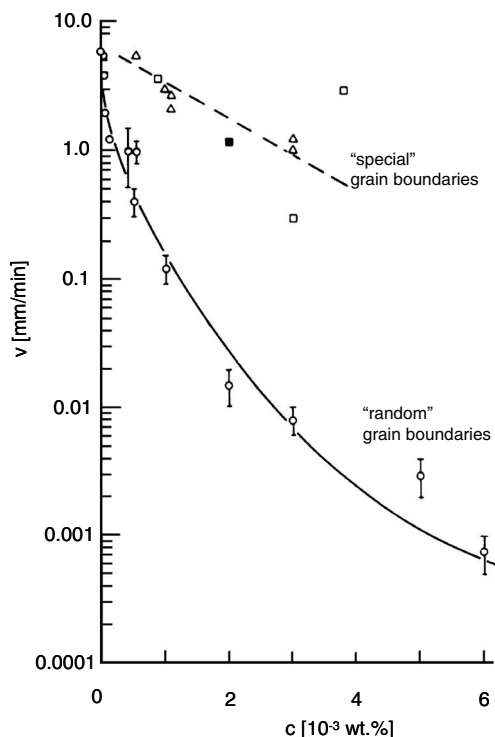
FIGURE 3.53

Misorientation dependence of activation enthalpy of grain boundary motion for $\langle 10\bar{1}0 \rangle$ (a) and $\langle 11\bar{2}0 \rangle$ (b) tilt boundaries in Zn.

One is tempted to attribute the observed orientation dependence to the misorientation dependence of grain boundary structure (Chapter 2), specifically to changes in the apparently structure-dependent transfer of atoms across the boundary. However, while the observed misorientation dependence certainly reflects the variance of grain boundary structure with changing misorientation, it is not an effect of migration mechanism but rather an effect of misorientation dependence of grain boundary segregation. If grain boundaries segregate less, they are less hindered by impurity drag and thus more mobile. Special boundaries are considered to be more perfectly structured and, therefore, less liable to segregation. This would explain the observation that special boundaries are more mobile than non-special boundaries.

The classical work in this field is Aust and Rutter, who studied the influence of tin additions on the velocity of grain boundary migration and its activation energy in lead [180]–[182]. They observed that the migration rates of boundaries with misorientation close to a coincidence relationship — i.e. special grain boundaries — and others — the random boundaries — were substantially different: lead doped with tin the special boundaries moved faster than the random ones, and the migration rate of random boundaries depended much more strongly on tin content than the migration rate of special boundaries (Fig. 3.54). The situation for the energy of activation was similar: for special grain boundaries the activation energy of migration was practically unaffected by the tin content, whereas for random grain boundaries the activation energy rose dramatically with increasing tin concentration (Fig. 3.55).

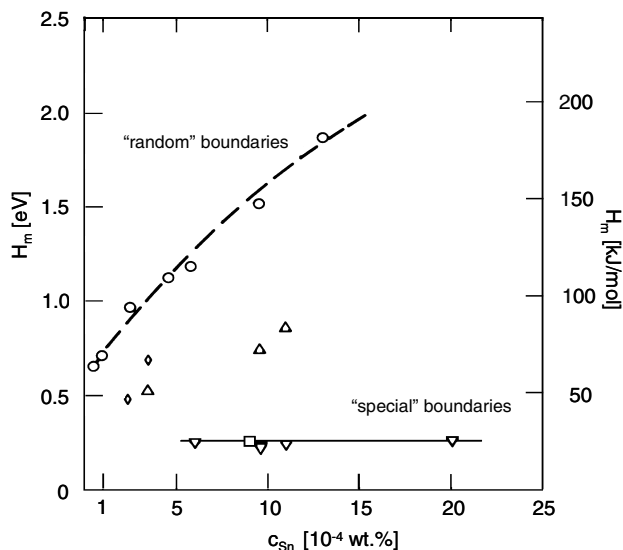
The structure dependence of segregation is most convincingly demonstrated by mobility measurements on Al and Zn of different purity [239, 255, 273, 276, 278, 279]. Fig. 3.56 shows the dependence of the activation enthalpy for the mobility of $\langle 100 \rangle$ tilt boundaries vs. misorientation in Al with different contents of impurities [274]. For low-angle boundaries the activation enthalpy is seen to decrease with increasing misorientation. For high-angle boundaries ($\phi \geq 20^\circ$) the activation energy depends strongly on impurity level. For both

**FIGURE 3.54**

Migration rate vs. Sn concentration in Pb bicrystals according to Aust and Rutter [180, 277]. Special and random boundaries behave differently.

ultrapure (99.99995%) and low purity (99.98%) materials the activation energy does not depend on the misorientation angle, but the absolute value of the activation energy is higher for the impure material by a factor of three. For a less-than-ultrapure material (99.9992%), referred to as high purity material, the activation energy oscillates and attains minima for special misorientations, which correspond to low Σ CSL rotations. For these special misorientations the activation energy is practically identical for high purity and ultrapure material. Thus, experimental results of single grain boundaries confirm the finding that in high purity materials special boundaries have a smaller migration activation enthalpy [180]–[182] and as a consequence, in some cases (to be considered below) a higher mobility than random boundaries.

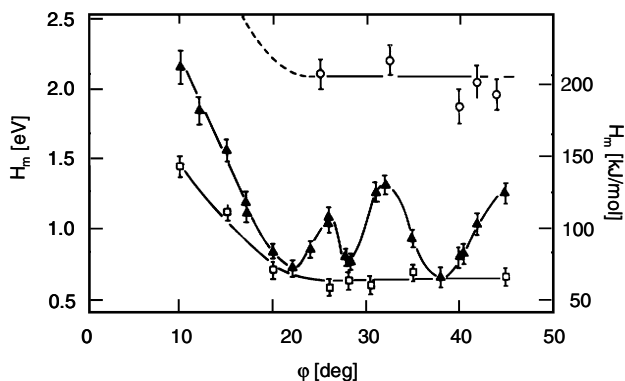
From the bicrystal experiments on differently pure materials, it can be concluded that the orientation dependence of grain boundary mobility is due to segregation effects [279]. In fact, high-angle tilt grain boundaries in ultrapure metals do not show any misorientation dependence of boundary mobility at

**FIGURE 3.55**

Activation enthalpy of migration for experiments shown in [Fig. 3.53](#).

all. Correspondingly, the orientation dependence of grain boundary mobility for high purity material merely reflects the orientation dependence of segregation such that special grain boundaries are less liable to segregation than random grain boundaries and, therefore, less affected by impurity drag. It should be remembered that the segregation capability is an intrinsic grain boundary property which is strongly connected with the boundary structure. In this regard the orientation dependence of grain boundary mobility and its parameters reflect the structural properties of a grain boundary. But the influence of impurity drag, which in turn is determined by boundary segregation, is much greater than the intrinsic orientation dependence of boundary mobility. Therefore, we can state with reasonable confidence that the misorientation dependence of boundary mobility on concentration is mainly determined by boundary segregation.

This effect and, therefore, the distinction between the mobility of special and random boundaries is, however, limited to a relatively small range of impurity content. At a purity level of 99.98%, all tilt grain boundaries in Al were found saturated with impurities, irrespective whether special or random boundaries. The ability of special boundaries to resist segregation appears to be very sensitive to the atomic arrangement even for low Σ boundaries. For the same impurity level special $\langle 10\bar{1}0 \rangle$ tilt boundaries in zinc demonstrate selective segregation while $\langle 11\bar{2}0 \rangle$ tilt boundaries remain unaffected by segregation ([Figs. 3.57a,b](#)).

**FIGURE 3.56**

The dependence of the activation enthalpy of migration for $\langle 100 \rangle$ tilt grain boundaries in Al of different purity: \square — 99.99995at%; \blacktriangle — 99.9992at%; \circ — 99.98at%.

Thus, we can conclude that the orientation dependence of grain boundary mobility is a consequence of segregation and can only be observed in a relatively small window of impurity content. The extent of this regime also depends on misorientation. Outside of this concentration range the mobility of high-angle grain boundaries apparently does not depend on misorientation. This conclusion has serious consequences for our understanding of the boundary mobility and the mechanism of impurity influence on it. The results on the purest material seem to indicate that grain boundary mobility does not depend on misorientation. However, owing to the lack of extremely pure materials and with our current level of information on the behavior of ultrapure metals, it cannot be ruled out that the apparent invariance of mobility with misorientation represents only an intermediate case and with increasing purity of the material the mobility again becomes dependent on orientation. It is conceivable that in the absence of impurities, random grain boundaries move more easily than special boundaries, since the lower energy and well-ordered structure of special boundaries would provide an enhanced resistance to a temporary modification of the structure, as necessary for grain boundary motion. Correspondingly, four regimes of purity level may be distinguished, which reflect a different orientation dependence of grain boundary mobility (Fig. 3.58) [279]. Three branches (1–3) in Fig. 3.58 have been experimentally confirmed, while the fourth still remains at the level of speculation.

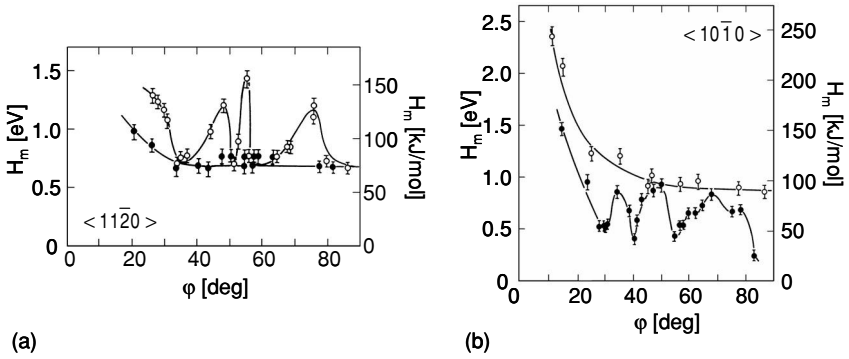


FIGURE 3.57

The dependence of the activation enthalpy of migration on angle of rotation for (a) $\langle 11\bar{2}0 \rangle$ and (b) $\langle 10\bar{1}0 \rangle$ tilt grain boundaries in Zn of different impurity: \circ — 99.995 at%; \bullet — 99.9995 at%.

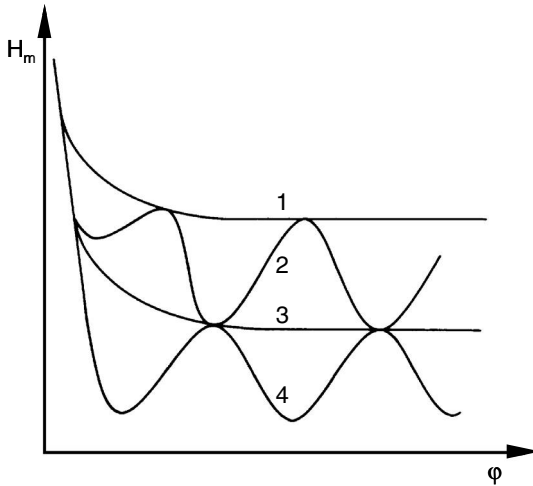


FIGURE 3.58

Schematic dependence of activation enthalpy of grain boundary mobility for differently pure materials. 1 — low purity; 2 — high purity; 3 — ultra high purity; 4 — completely pure material.

3.5.4 Correlation of Grain Boundary Migration and Diffusion

While we pointed out in Sec. 3.1 that grain boundary migration is not to be confused with diffusion across the boundary, it is interesting to compare the misorientation dependence of grain boundary diffusion with the misorientation dependence of grain boundary mobility. For this purpose the data for grain boundary diffusion of zinc in $\langle 100 \rangle$ and $\langle 111 \rangle$ tilt boundaries in aluminum can be utilized [280]–[282]. Fig. 3.59 shows the misorientation dependence of the migration activation enthalpy for $\langle 111 \rangle$ tilt boundaries in Al and the activation enthalpy for zinc diffusion along $\langle 111 \rangle$ tilt grain boundaries in aluminum. The migration activation enthalpy of both migration (H_m) and boundary diffusion (H_{DG}) depend upon the misorientation in a non-monotonous manner; maxima on the diffusion activation enthalpy curve strictly correspond to minima on the migration activation enthalpy curve, and vice versa. In both cases extrema are observed at angles which correspond to special (CSL) boundaries. Apparently, the misorientation dependence of boundary diffusion is complementary to the misorientation dependence of boundary migration. Of course, it has to be kept in mind that the measured diffusion data [280] reflect the diffusion along grain boundaries, while migration is at most akin to diffusion across the boundary. Also, boundary migration is more related to self-diffusion, whereas impurity (zinc) diffusion was measured experimentally [280, 282]. Unfortunately, there are no methods to measure the diffusion across grain boundaries. In a high-accuracy study [283] the grain boundary diffusion of ^{195}Au and grain boundary self-diffusion of ^{64}Cu along symmetrical $\langle 001 \rangle$ tilt boundaries with misorientation close to $\Sigma 5$ (36.9°) were measured under identical experimental conditions as a function of temperature and tilt angle (Fig. 3.60). The parameter $\pi = S\delta D_b$ (segregation factor $S = 1$ for grain boundary self-diffusion, $2 \leq S \leq 6$ for Au in Cu; grain boundary width $\delta = 0.5\text{nm}$; D_b grain boundary diffusion coefficient) manifests the same characteristic orientation dependence for both grain boundary self-diffusion and grain boundary impurity diffusion of Au in Cu. A qualitatively similar orientation dependence was observed in both cases. Furthermore, this orientation dependence was independent of the purity of the Cu material used (Fig. 3.60a). High purity Cu bicrystals of two different original Cu materials (Cu1 and Cu2) were grown. The total impurity amount in both types of Cu was small and comparable, although different. Clearly segregation effects cannot account for the observed variations of the parameter π .

The activation enthalpy and pre-exponential factor of grain boundary migration do not correspond to the relevant parameters for diffusion, however. As evident from Figs. 3.52, 3.59, and 3.60, the activation enthalpy of grain boundary migration for the majority of grain boundaries investigated is much larger than that of grain boundary diffusion, frequently even larger than that of bulk diffusion. The calculated values of the pre-exponential factor of grain boundary mobility, based on the grain boundary diffusion data, are presented

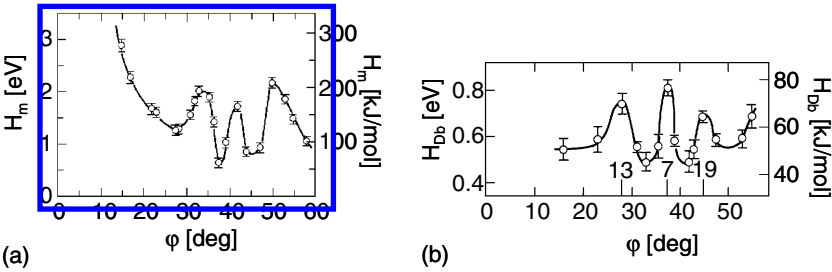


FIGURE 3.59
(a) Migration activation enthalpy of $\langle 111 \rangle$ tilt grain boundaries in Al. (b) Activation enthalpy of Zn diffusion along $\langle 111 \rangle$ tilt grain boundaries in Al.

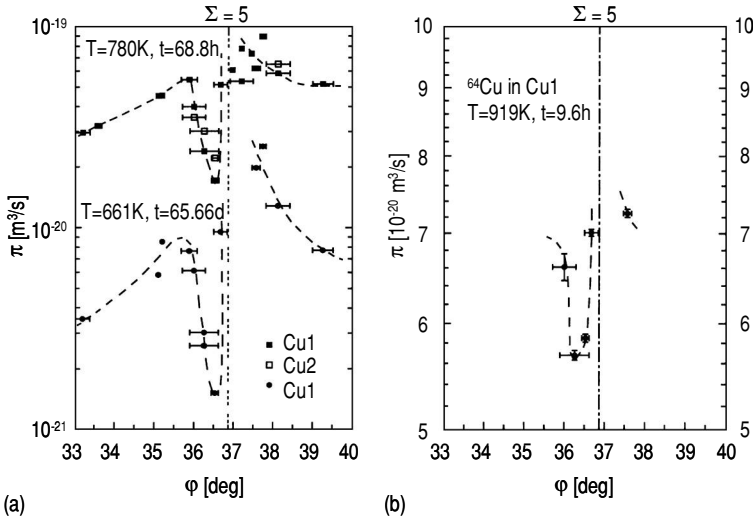


FIGURE 3.60
Misorientation dependence of the quantity $\pi(\phi)$ of grain boundary diffusion along $\langle 100 \rangle$ tilt boundaries in Cu for different temperatures.

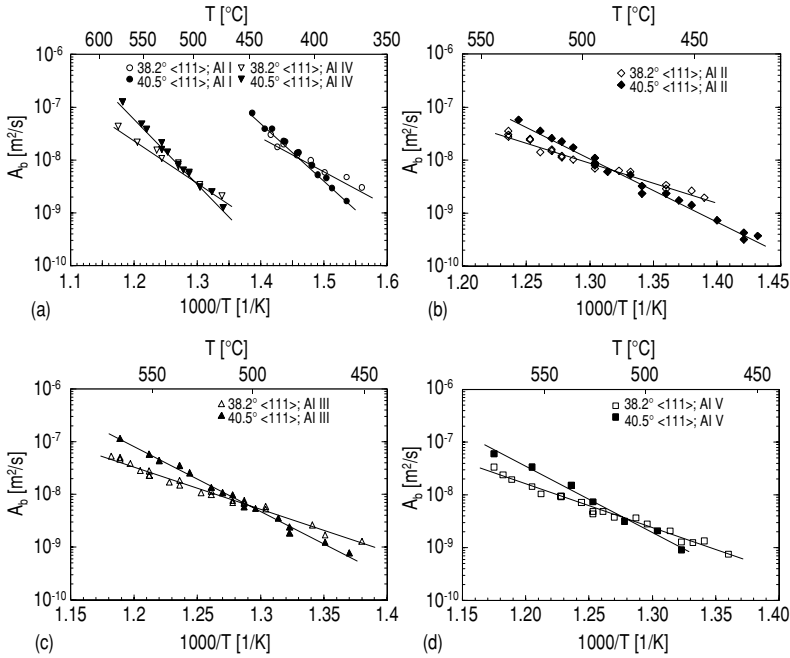
in Fig. 3.52. For $\langle 100 \rangle$ tilt grain boundaries only a few of the calculated values correlate with experiments. As a rule, the experimental pre-exponential factor is 2–15(!) orders of magnitude larger than the factor calculated from the theory of hopping motion of individual atoms across the grain boundary. A difference between the mechanisms and activation parameters of grain boundary migration and grain boundary diffusion was also found in atomistic simulations (see Chapter 5).

3.5.5 Segregation Effects Other Than Misorientation

We have shown in Sec. 3.5.3 that the misorientation dependence of grain boundary mobility is mostly due to segregation effects, and it is not clear to date whether even in ultrapure material the intrinsic mobility of grain boundaries was measured. In this sense even high purity material has to be considered as a very dilute solution affected by segregation. In addition to the influence on misorientation dependence of grain boundary mobility, there are two important issues for a more quantitative treatment of segregation effects on grain boundary migration.

1. The total impurity content is always composed of different elements, but it is common experience that different elements have varying degrees of effect on grain boundary motion. Fe, Ti and Sc impurities are known to very effectively hinder boundary migration in Al. P in Cu or Nb in steels are comparably effective. Conversely, some other elements may have only minor influence on boundary mobility, like Ag in Al. In essence, the question has to be addressed which elemental concentration is to be considered most relevant for the overall migration behavior of the boundary.
2. Even if the impurity content in the volume is small, the concentration in the boundary may be high, if the interaction energy with the boundary is large. Then the impurity drag theory may fail, since it also assumes a dilute solution of impurities in the boundary, i.e. it neglects impurity interactions in the boundary.

In this context, the motion of pure $\langle 111 \rangle$ tilt boundaries with misorientation angles in the vicinity of the special misorientation $\Sigma 7$ (38.2°) was studied under the action of a constant driving force (technique N12, Table 3.3) [197, 255]. Here we will confine our consideration to the motion of $\langle 111 \rangle$ tilt boundaries with misorientation $\varphi = 38.2^\circ$ (special misorientation $\Sigma 7$) and 40.5° . These boundaries are of special interest because of their dominant role in recrystallization of Al [284]. The velocity of grain boundary motion was measured

**FIGURE 3.61**

Temperature dependence of the reduced mobility A_b for 38.2° and 40.5° $\langle 111 \rangle$ tilt grain boundaries in different types of pure aluminum.

by continuous tracking of the moving grain boundary (XICTD). The experiments were carried out on bicrystals produced from high purity aluminum of different production. The total impurity content in each material was defined as the sum of the concentration of all elements found as determined by glow discharge mass spectrometry (Table 3.4 [197, 255]). With regard to the question which elemental concentration to consider as most relevant for the overall migration behavior of the boundary, it was proposed to consider the total impurity concentration as the relevant concentration for grain boundary migration. There are several reasons to justify this assumption. All materials used in the investigation were high purity aluminum, which were produced by multiple pass zone refining. During zone melting only those impurities which strongly interact with lattice defects remain in the solid phase, the structure of which is more disordered than the crystalline solid and, therefore, more akin to a liquid.

The temperature dependencies of the reduced mobility (Sec. 3.5.2) of 38.2° and 40.5° $\langle 111 \rangle$ tilt grain boundaries in aluminum of different purity and the concentration dependence of the activation enthalpy for these boundaries are

represented in Figs. 3.61 and 3.8a, respectively. As evident from Fig. 3.8a, even at the lowest impurity content, i.e. in the material of highest purity, the activation enthalpy rises with increasing impurity concentration contrary to predictions of impurity drag theory (Sec. 3.3.2).

There are several reasons for the discrepancy between the theories of impurity drag and the experimental data. All theories are based on the assumption of a small concentration both in the bulk and in the grain boundary. However, the boundary impurity concentration may be high despite a small bulk impurity concentration. Furthermore, for high impurity concentrations in the boundary it is necessary to take into account the mutual interaction of adsorbed atoms in the boundary. Also, as shown experimentally [285, 286] and theoretically [35], grain boundaries are inhomogeneous, i.e. not every site in the grain boundary is equally favorable for impurity segregation. Thus the interaction between the adsorbed atoms also should be taken into account.

The interaction of impurities with grain boundaries can be taken into ac-

TABLE 3.4

Impurity Content of Investigated Aluminum Samples

Material	RRR	Measured impurity content (ppm)
Al I	21400	0.4
Al II	15000	1.0
Al III	5100	3.6
Al IV	6500	4.9
Al V	11500	7.7
(RRR — residual resistivity ratio = $R(293K)/R(4.2K)$).		

count in terms of adsorption [197, 255]. The advantage of such an approach is that it allows us to express the influence of adsorption on both the activation enthalpy and the pre-exponential mobility factor. As shown above (Sec. 3.3.3), impurity drag theory can be extended to take into account an interaction of adsorbed impurities in the grain boundary and thus, provide a reasonable agreement with experimental results for the concentration dependence of the activation enthalpy and also for the pre-exponential mobility factor (Figs. 3.9 and 3.10). It should be noted that the chosen values of the parameters in the equation of grain boundary mobility are physically reasonable. For example, the enthalpy of adsorption in the grain boundary ranges from 0.82 eV to 0.86 eV, the product of the coordination number and the heat of mixing extends from 0.17 eV to 0.24 eV etc.. We emphasize once again that the best agreement between theory and experiment can be achieved if the difference in the partial activation areas ω_i of the adsorbed atoms in the grain bound-

ary is taken into account. Best agreement is obtained for a ratio $\beta = 0.05$ of the partial areas of impurity atoms and matrix atoms (see Sec. 3.3.3). The boundary activity of the impurities can be described by the derivative of the boundary surface tension γ with respect to the chemical potential μ_i of the impurity atoms

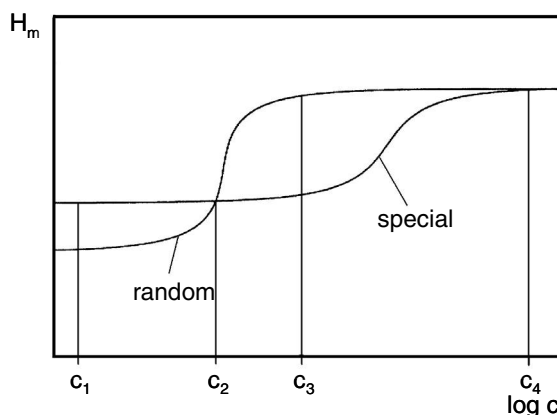
$$\frac{d\gamma}{d\mu_i} \cong -\frac{1}{\omega_i} \quad (3.160)$$

This relation indicates that the impurity which most actively interacts with the boundary should possess the smallest partial area. Despite the obvious importance of the partial area in grain boundary thermodynamics, ignoring it is the rule rather than the exception in current grain boundary physics.

The approach discussed in Sec. 3.3.3 principally allows us to explain the orientation dependence of migration activation parameters in different regimes of impurity concentration (Fig. 3.58, Table 3.4). Fig. 3.62 shows the migration activation enthalpy as a function of impurity concentration for special and random grain boundaries using the Fowler-Guggenheim isotherm under the natural conditions for the heat of mixing $\varepsilon = \varepsilon_{\text{special}} < \varepsilon_{\text{random}}$ (the difference between $\varepsilon_{\text{special}}$ and $\varepsilon_{\text{random}}$ is small), $H_i^{sp} < H_i^{\text{rand}}$. It is seen that the result of the calculation complies with the scheme in Fig. 3.58. Actually, for a very low impurity concentration (c_1) the migration activation enthalpy for a random grain boundary is lower than for a special one. The rate of increase of the migration activation enthalpy with impurity content for a random grain boundary is higher than for a special one, and at a defined concentration c_2 the enthalpy for both boundaries becomes equal. There is a large gap between the values of enthalpy of activation at a concentration c_3 which belongs to regime 2 in Fig. 3.58. With further increase in the impurity concentration the migration activation enthalpies also become equal (c_4 , case 1 in Fig. 3.58).

3.5.6 Impurity Drag and Breakaway

According to the previous sections (Sec. 3.5.3–3.5.5) both pure metals and dilute alloys have to be treated as solid solutions with regard to grain boundary migration because of the impact of segregation. In this section we shall consider the results obtained on single-phase materials more quantitatively in the framework of the impurity drag theories as put forward by Lücke and Detert, Cahn, Lücke and Stüwe, Westengen and Ryum [193]–[195], [287] (Sec. 3.3.2). A comparison of theory and experiment can be carried out in two principally different directions. The first way is the analysis of the experimental data in terms of impurity drag, i.e. the analysis of the changes in grain boundary velocity, mobility, migration, energy (enthalpy) of activation as a function of the nature and content of impurity atoms. The theories of impurity drag include the nature of the impurities as the energy of interaction U_0 between the impurity atoms and grain boundary and the volume diffusion coefficient of the

**FIGURE 3.62**

Computed dependence of activation enthalpy of grain boundary motion on impurity concentration for special and random grain boundaries.

impurities. The second way consists of searching for effects predicted by the theories, in particular the effect of detachment of the moving grain boundary from adsorbed atoms. The requirements which are imposed by the theory on experiments are tough: exactly known driving force of grain boundary migration; well-defined grain boundary crystallography and geometry; physically correct and reproducible experiments; and, finally, what is of critical importance, a pure metal doped with a defined content of specific impurities. There are no investigations capable of complying with all requirements mentioned, and we shall only consider those closest to the ideal, i.e. an extremely small number of investigations dedicated to the interaction of a moving single grain boundary with impurities. We even will violate our principles and discuss some experiments on polycrystals.

The concentration dependence of the grain boundary migration rate in lead doped with Sn, Ag, Au is represented in Fig. 3.63 [277]. This dependence is in qualitative agreement with the Lücke-Detert relationship (strictly speaking, according to the Lücke-Detert theory the velocity should vary inversely proportionally to the impurity content of the sample, but for a narrow range of impurity content and a low concentration the predicted dependency can be approximated by the observed exponential variation) and was observed for all impurities studied by Aust and Rutter [277]. Evidently, the influence of silver and gold is much stronger than the influence of tin. A reasonable agreement between theory and experiment was also observed by Frois and Dimitrov [288, 289] who studied grain growth in aluminum doped with Cu and Mg (Fig. 3.64). Two branches of the concentration dependence were observed: at low concentrations the velocity of grain growth did not depend on

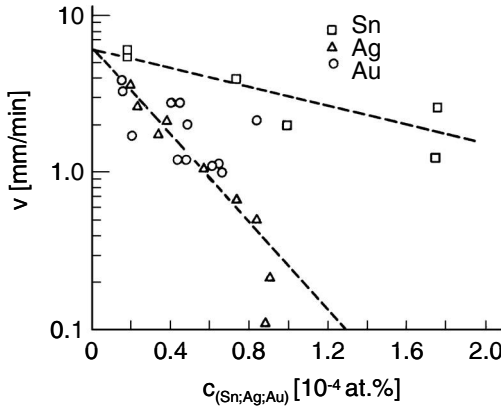


FIGURE 3.63

Grain boundary migration rate vs. impurity concentration in lead crystal for special (low Σ) (top curve) and non-special (bottom curve) boundaries [277].

the impurity content, whereas at larger concentrations the velocity decreased linearly with increasing concentration.

The concentration dependence of the activation enthalpy of grain boundary migration comprised two different regimes: at low content of Mg the enthalpy of activation did not depend on concentration and equaled the value observed for grain growth in pure Al (0.65eV). With rising concentration there was an abrupt change of the activation enthalpy to 1.5eV, i.e. close to the activation enthalpy of bulk self-diffusion [288, 289].

“Pure” Al doped with silver (Fig. 3.65) exhibited a slightly different concentration dependency. The enthalpy of activation rose with increasing Ag concentration, starting from a certain critical content of silver. A similar behavior was observed by Aust and Rutter for the concentration dependence of the migration activation enthalpy of single grain boundaries in lead doped with silver and gold (Fig. 3.66) [277]. Note the dramatic change in the migration activation enthalpy in Fig. 3.66.

The mobility of random grain boundaries and $\langle 100 \rangle$ non-special tilt grain boundaries in aluminum bicrystals of different purity was studied in a concentration range of solute atoms between $5 \cdot 10^{-5}$ and $2 \cdot 10^{-2}$ at% principal impurities in at%: Si ($5 \cdot 10^{-6} - 1 \cdot 10^{-3}$); P ($5 \cdot 10^{-6} - 5 \cdot 10^{-3}$), Zn ($1 \cdot 10^{-6} - 1 \cdot 10^{-3}$), Ti ($1 \cdot 10^{-6} - 5 \cdot 10^{-3}$); Fe ($5 \cdot 10^{-5} - 5 \cdot 10^{-4}$); Cu ($1 \cdot 10^{-6} - 1 \cdot 10^{-2}$) [227, 273]. The concentration dependence of the activation enthalpy for the motion of a single random grain boundary is shown in Fig. 3.67a [227, 273]. The curve can be subdivided into three segments. The first segment is characterized by an activation enthalpy independent of impurity content. The second segment stands out by a considerable increase

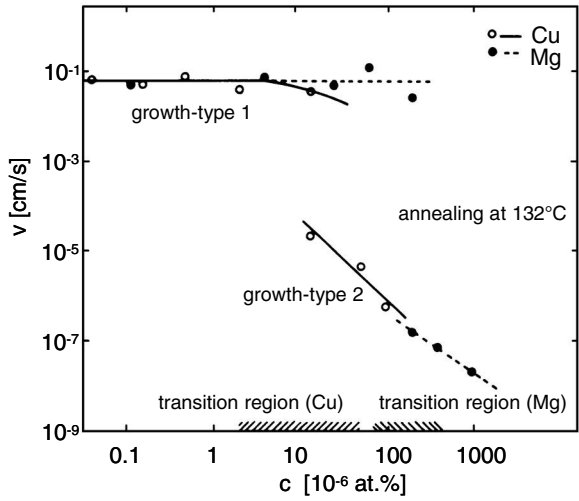


FIGURE 3.64
Concentration dependence of grain growth rate in Al doped with Cu and Mg [288, 289].

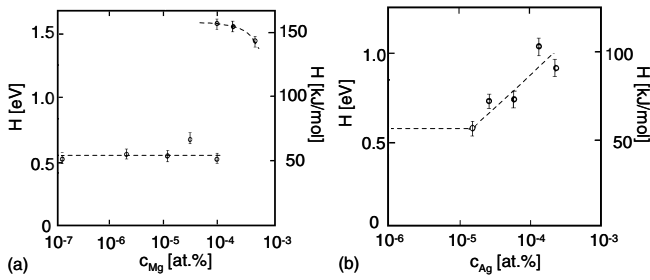


FIGURE 3.65
Enthalpy of activation of grain growth in Al doped with Mg and Ag [288, 289].

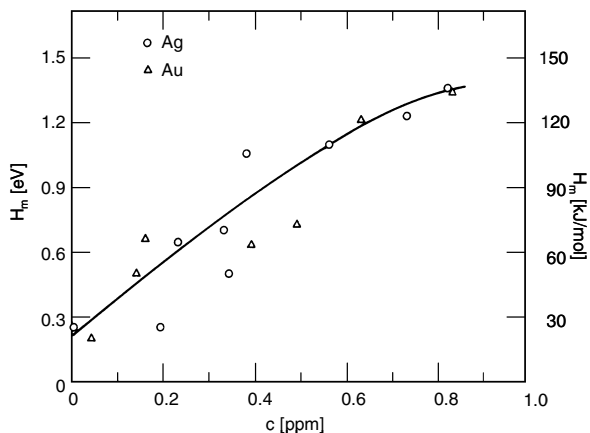
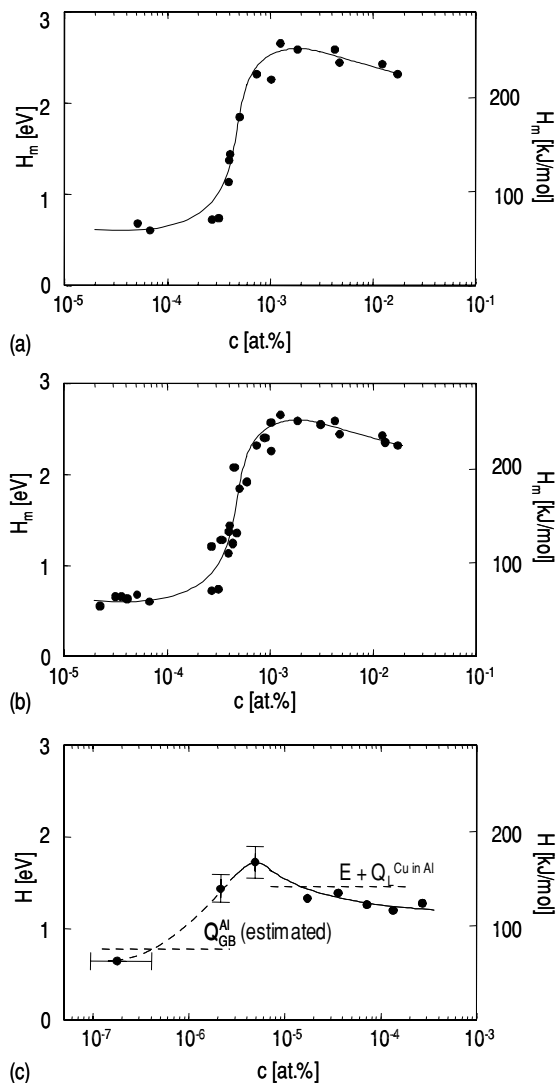


FIGURE 3.66

Concentration dependence of migration activation enthalpy in lead doped with Ag and Au [277].

in the activation enthalpy with rising solute content. Such variation in the activation enthalpy can be described [227] on the basis of a concept of adsorption of interacting atoms on a non-homogeneous boundary. In the third segment of the $H_m(c)$ curve the activation enthalpy of grain boundary migration does not only fail to increase with growing concentration, but even a slight decrease in the activation enthalpy is observed. A maximum value of the $H_m(c)$ function can be interpreted by the assumption that not all impurity atoms contribute to the increase of the migration activation enthalpy, since only a fraction $\bar{\Gamma} < \Gamma_0$ of impurity atoms moves jointly with the boundary. Therefore, when the boundary adsorption Γ tends to saturate, the activation enthalpy attains a maximum. A respective calculation predicts a reasonable concentration for the maximum ($\sim 10^{-4} - 10^{-3}$ at% [273]). The results obtained from bicrystal experiments for random grain boundaries (Fig. 3.67a) and $\langle 100 \rangle$ tilt boundaries in Al (Fig. 3.67b) agree with data of the activation enthalpy of grain growth in aluminum doped with copper as measured by Gordon and Vandermeer [290, 291] (Fig. 3.67c).

Thus far the impurity influence on migration of random grain boundaries (or grain boundaries far from a coincidence misorientation) has been considered. That is the reason why the results of single grain boundary migration were considered in context with grain growth, i.e. “polycrystal” experiments. Apparently, in some investigations a reasonable agreement between experiment and predictions of the impurity drag theory was observed. However, the majority of experimental studies reveals fundamental and essential dis-

**FIGURE 3.67**

Migration activation enthalpy for random (a) and non-special (b) $\langle 100 \rangle$ tilt boundaries in Al of different total impurity content. (c) Enthalpy of activation for grain growth in zone refined Al doped with Cu [290, 291].

crepancies between theory and experiment, in particular a much too strong dependence of the activation enthalpy on the impurity content. We shall investigate whether such behavior is only a consequence of the nature of random grain boundaries or whether it also pertains to special boundaries.

Theory predicts that a grain boundary breaks away from an impurity cloud at large velocities and high temperatures. A study of this breakaway phenomenon allows us to extract additional information on the interaction of a moving grain boundary with impurities. In the original Lücke-Detert theory detachment occurs when the impurity atoms are not able to move with the velocity prescribed by the boundary. The more refined theories of Lücke-Stüwe and Cahn took into account that the concentration not only decreases with increasing temperature, but also with increasing boundary migration rate (see [Sec. 3.3.2](#)) which considerably speeds up detachment and results in a discontinuous breakaway of the boundary from the adsorbed impurities.

The abrupt change in the velocity of a grain boundary during its detachment from an impurity cloud can be considered as a kinetic phase transition [292]. An experimental support of this viewpoint is the observed hysteresis of the transition temperature. On heating, the detachment occurs at a higher temperature than the re-attachment of the impurities to the boundary on cooling [293, 294].

Also important is the dependence of the detachment parameters on the ratio of grain boundary to bulk diffusion coefficient: D_b/D . An increase of D_b/D shifts the detachment point toward higher driving forces. This has an obvious physical explanation: the impurity atoms near the boundary become more mobile as D_b/D increases, and continue to move with the boundary at a greater velocity, corresponding to a larger driving force. There is, however, an interesting theoretical inconsistency. Having compared theoretical predictions with experimental results, we see that for Al already at $D_b/D \cong 10^2$ the detachment temperature exceeds the melting point. The calculated detachment temperatures agree with those observed, if the diffusion coefficient $D_b \sim 10D$. Evidently, D_b cannot be identified with the coefficient of impurity diffusion along the boundary, since at the respective temperatures the boundary diffusion coefficient is usually $10^5 - 10^6$ times the bulk value [295].

The effect of grain boundary detachment from impurities was experimentally observed and studied on single $\langle 111 \rangle$ tilt grain boundaries in gold [296] and aluminum [293, 294, 297]; $\langle 10\bar{1}0 \rangle$ and $\langle 11\bar{2}0 \rangle$ tilt boundaries in zinc [292, 293, 298, 299]; and $\langle 110 \rangle$ tilt boundaries in Fe-3%Si [300]. [Figs. 3.68-3.72](#) give the temperature and driving force dependencies of grain boundary velocity (mobility) in gold, aluminum, zinc and Fe-3%Si. A characteristic feature of the dependencies considered is a dramatic change in the grain boundary velocity (more correctly, mobility) in a narrow temperature range. Above and below the breakaway regime the grain boundary mobility shows a usual Arrhenius type temperature dependence.

A considerable body of experimental data has been accumulated to date. The effect was observed on special and close to special grain boundaries, but

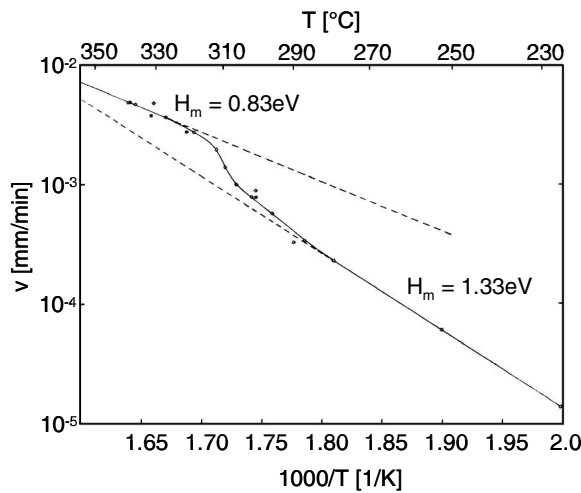


FIGURE 3.68
Temperature dependence of the migration rate of $\langle 111 \rangle$ tilt boundaries ($\varphi = 30^\circ$) in rolled gold [296].

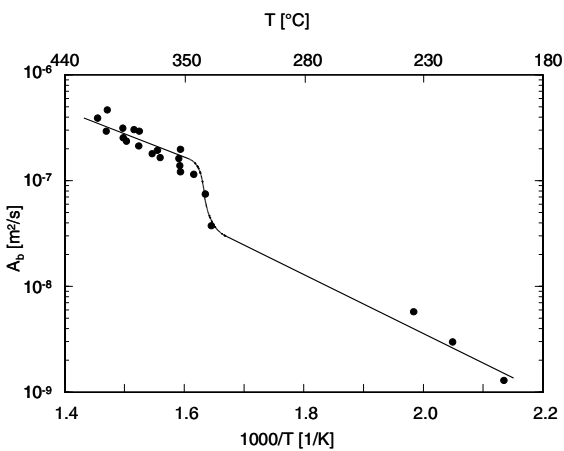


FIGURE 3.69
Temperature dependence of the reduced mobility of $30^\circ \langle 10\bar{1}0 \rangle$ tilt grain boundaries in Zn.

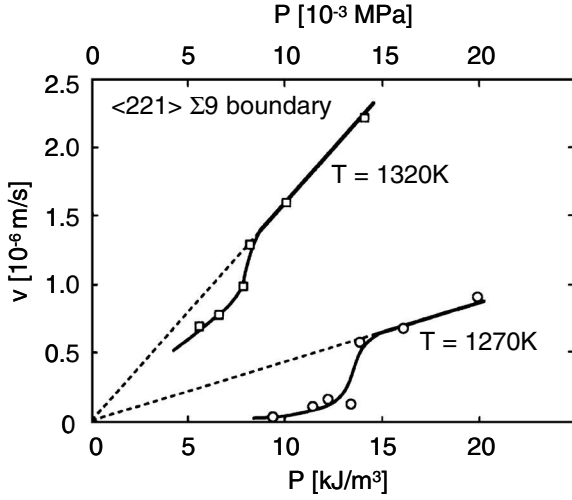


FIGURE 3.70

Variation of boundary velocity v with driving force P for $\langle 221 \rangle$ tilt grain boundaries in Fe-Si at 1270K and 1320K [300].

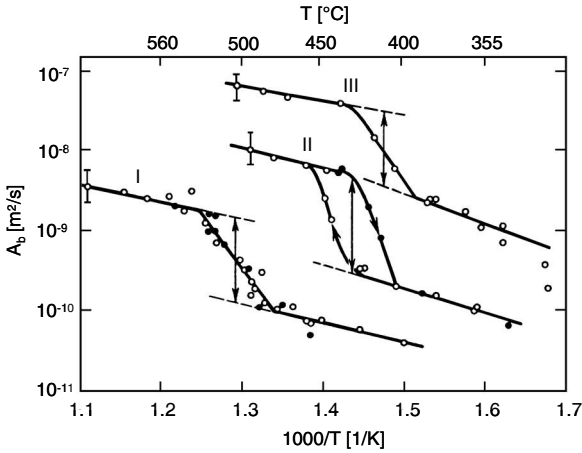
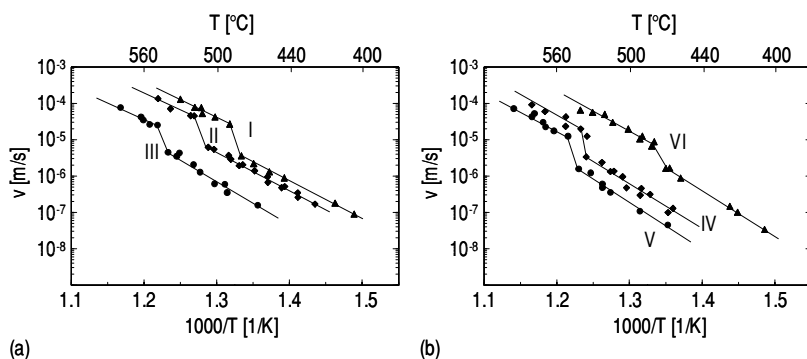


FIGURE 3.71

Temperature dependence of the reduced mobility of $38^\circ \langle 111 \rangle$ tilt grain boundaries in Al. (For the meaning of I, II, III see Table 3.5.)

**FIGURE 3.72**

Temperature dependence of the velocity of a $36.5^\circ\langle 111 \rangle$ tilt grain boundary in iron-doped aluminum. (For meaning of I, II, III, IV, V, VI see [Table 3.6](#).)

no effect was found on random (non-special) grain boundaries and in materials with high impurity content. Apparently, it has been experimentally impossible to create a sufficiently large driving force to detach a grain boundary of high adsorption capability from its impurity cloud. An analysis of the data obtained in the framework of the Lücke, Stüwe or Cahn approach showed that the phenomena observed for $\langle 111 \rangle$ tilt boundaries in aluminum and $\langle 10\bar{1}0 \rangle$, $\langle 11\bar{2}0 \rangle$ tilt boundaries in zinc were related to the drag effect of adsorbed iron atoms in aluminum and to adsorbed aluminum atoms in zinc [292, 301]. The conceptual framework to determine the major parameters of interaction between grain boundary and impurities from experimental data of the breakaway effect is given below.

Fig. 3.72 shows the temperature dependence of the mobility of $\langle 111 \rangle$ tilt grain boundaries, $\varphi = 36.5 \pm 0.5^\circ$ in high-purity aluminum samples (I–VI) specially doped with iron. The iron concentration, though rather low, was significantly larger than the concentration of any other dissolved element [297] (Table 3.6). A constant driving force was provided by the surface tension of a curved grain boundary (grain boundary quarter-loop technique). The measurements were carried out by continuous boundary tracking (XICTD). The effect was observed in the temperature range 460–550°C; the specific temperature depended on the driving force and impurity (iron) content (Fig. 3.72, Table 3.6). The experimental data correlated well with predictions of the impurity drag theory. The energy of interaction between grain boundary and impurity iron was found to be 0.134 ± 0.02 eV [297].

Of special interest are the nature and number of adsorption sites at a grain boundary. The adsorption capacity of a special grain boundary is in the range of $\sim 10^{14} \text{ cm}^{-2}$. This is distinctly lower than that measured by Auger spec-

TABLE 3.5

Grain Boundary Detachment I

Number of the sample	Active impurity Fe		
	I	II	III
Concentration of the active impurities [at%]	$2 \cdot 10^{-5}$	$1 \cdot 10^{-5}$	$5 \cdot 10^{-6}$
Temperature of detachment [T_0 , K]	775	700	680
Driving force P_i [J/m ³]	$6 \cdot 10^2$	$6 \cdot 10^2$	$6 \cdot 10^2$
D_m [m ² /s] at T_0 (experimental)	$4.1 \cdot 10^{-10}$	$1.7 \cdot 10^{-9}$	$8.3 \cdot 10^{-9}$
D_{im} [m ² /s] at T_0 (experimental)	$4 \cdot 10^{-17}$	$1.4 \cdot 10^{-16}$	$3.3 \cdot 10^{-16}$
D_{m0} [m ² /s] (experimental)	$6.1 \cdot 10^{-7}$	$9.2 \cdot 10^{-6}$	$6.7 \cdot 10^{-6}$
D_{0im} [m ² /s] (experimental)	$1.2 \cdot 10^{-13}$	$2.5 \cdot 10^{-12}$	$1.4 \cdot 10^{-11}$
H_m^D [eV]	0.50	0.53	0.40
H_{im}^D [eV] (experimental)	0.52	0.60	0.64
H_{im}^D , diffusion	0.60	0.60	0.60
Fe in Al D_{0im} [m ² /s]*)	$4.1 \cdot 10^{-13}$	$4.1 \cdot 10^{-13}$	$4.1 \cdot 10^{-13}$
U_0 [eV]	0.17	0.24	0.24
Z [cm ⁻²]	$2.3 \cdot 10^{14}$	$7 \cdot 10^{13}$	$2.4 \cdot 10^{14}$

*) Mirano K, Agarwala RP, Cohen M, *Acta Metall.*, 10:857, 1962.

troscopy on random grain boundaries in polycrystals, which proves a much higher adsorption capability of non-special grain boundaries.

The temperature dependency of the mobility of $\langle 111 \rangle$ tilt grain boundaries ($\varphi = 46.8^\circ$, $\Sigma 19$) in iron-doped aluminum samples (Figs. 3.73a,b) exhibits two consecutive steps, followed by a dramatic decrease of the migration activation enthalpy. An analysis of the data obtained shows that the observed mobility jumps are related to the breakaway of the migrating grain boundary from adsorbed iron atoms, and the sequence of the breakaway is attributed to the existence of two types of adsorption centers in the special grain boundaries mentioned, which differ in interaction energy ($U_{01} = 0.12 \pm 0.01$ eV, $U_{02} = 0.3 \pm 0.02$ eV). The density of the adsorption centers are $z_1 = (1.5 \pm 0.2) \cdot 10^{14}$ cm⁻² and $z = (4.4 \pm 0.3) \cdot 10^{12}$ cm⁻², respectively. It appears [294] that z_1 correlates with an average (with respect to the inclination angle deviating from the symmetric position) surface density of coincidence sites ($\sim 1.8 \cdot 10^{14}$ cm⁻²). Hence, the active centers of type I may be interpreted as most distorted regions between the coincidence sites. It was suggested that the interaction centers of type II may be associated with grain boundary dislocations.

It counts in favor of the hypothesis that the observed abrupt change in the migration velocity is due to grain boundary detachment from its impurities so that the value of the calculated interaction energy U_0 and the number of adsorption sites z (within the limits of experimental uncertainty) remain constant for a given grain boundary type but different impurity content (Table

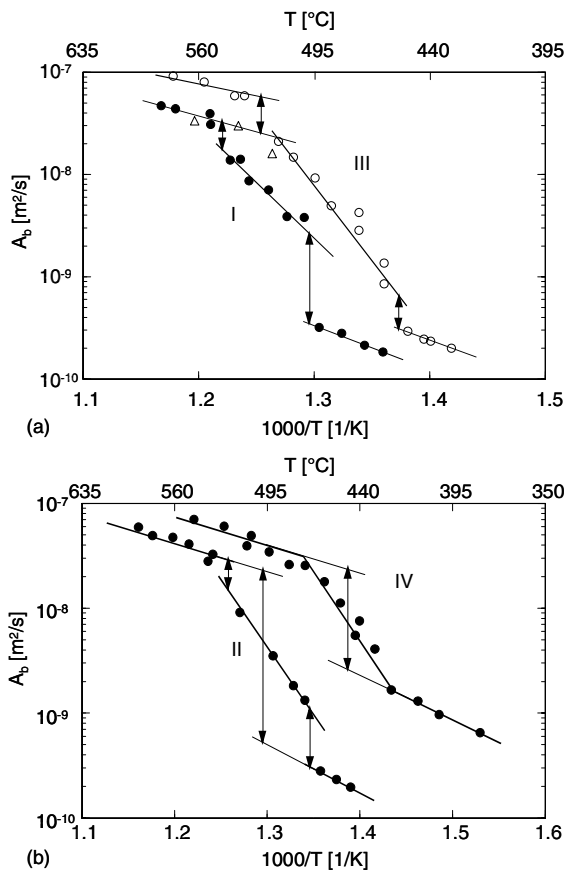


FIGURE 3.73
Temperature dependence of the reduced mobility of a 46.5°⟨111⟩ tilt boundary in iron-doped aluminum. (For meaning of I, II, III, IV see [Table 3.6](#).)

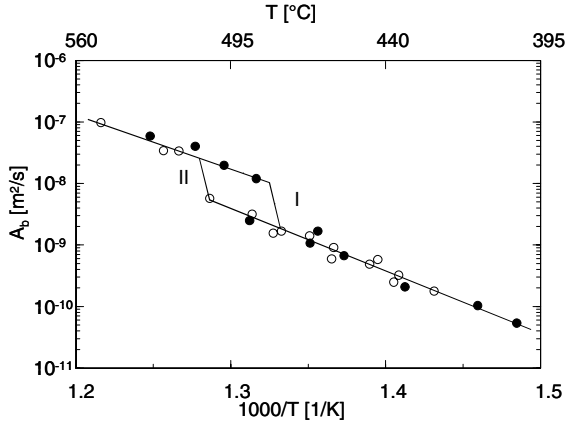


FIGURE 3.74

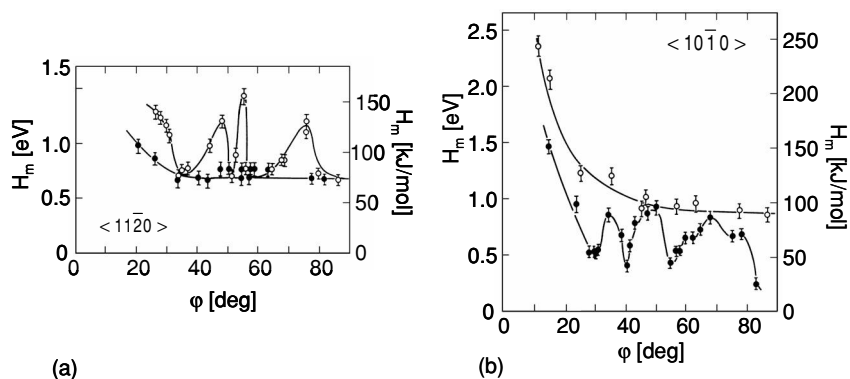
Temperature dependence of the reduced mobility of a $36.5^\circ\langle 111 \rangle$ tilt grain boundary for samples I and II (Table 3.6).

3.6): the detachment temperature correctly shifts with increasing impurity concentration and driving force. The temperature dependence of the velocity of a $36.5^\circ\langle 111 \rangle$ grain boundary for two samples (I and II) with equal iron content but different driving force ($P_I/P_{II} = 1.6$, the absolute value of the driving force in this experiment being rather small, $P/kT \sim 10^{-6}$) is presented in Fig. 3.74. The velocities and breakaway temperature intervals differ for the two samples, but the mobilities in the low- and high-temperature regimes are the same. This confirms that the driving force determines the temperature interval of the effect. The good quantitative agreement also supports the proposed idea of the nature of the effect [294]. It should be noted that the change in the driving force by a factor of 1.5 was sufficient to shift the detachment temperature by 25K.

The difference in the number of adsorption sites (adsorption centers), especially obvious for grain boundaries in zinc (Table 3.6), gives rise to a number of effects. So, at the same bulk impurity concentration the orientation dependencies for $\langle 10\bar{1}0 \rangle$ and $\langle 11\bar{2}0 \rangle$ tilt grain boundaries in zinc are quite different (Fig. 3.75). The difference in the adsorption capacity leads to a faster adsorption saturation on $\langle 10\bar{1}0 \rangle$ grain boundaries than on $\langle 11\bar{2}0 \rangle$ boundaries [239, 276].

3.5.7 Athermal Motion of Grain Boundaries

Low adsorption capacity may result in athermal grain boundary migration and was experimentally observed for both special and close to special $\langle 11\bar{2}0 \rangle$

**FIGURE 3.75**

Dependence of activation enthalpy of migration on misorientation angle for (a) $\langle 11\bar{2}0 \rangle$ and (b) $\langle 10\bar{1}0 \rangle$ tilt grain boundaries in Zn of different purity: ○ – 99.995 at%; ● – 99.9995 at%.

tilt grain boundaries in zinc (Figs. 3.76, 3.77) [298, 299]. The temperature dependence of the reduced mobility $A_b(T)$ is characteristic for breakaway of a migrating boundary from its adsorbed impurities. An essential new feature is that after the detachment from the impurity atmosphere the grain boundary velocity becomes temperature independent¹⁰.

Experiments on $86^\circ \langle 11\bar{2}0 \rangle$ tilt grain boundaries under constant driving force (grain boundary half-loop, technique N 10, Table 3.3) showed a strong dependence of the mobility on grain boundary orientation (inclination) in the athermal regime (Figs. 3.33, 3.76–3.79) [247]. The mobility maximum approximately coincided with the grain boundary plane $\{10\bar{1}2\}$ of the shrinking grain.

It is interesting to analyze what mechanism may control the athermal motion of a grain boundary. It is conceivable that linear defects (grain boundary dislocations or steps) move along the grain boundary in an athermal fashion. Once a step (or dislocation) moves it will sweep along the grain boundary at the speed of sound ($c \approx 3 \cdot 10^5$ cm/s). For a step height $h \cong 10^{-8}$ cm, the grain boundary mobility can be estimated as $A \cong hc \approx 10^{-3}$ cm²/s, a magnitude which is close to the maximum mobility observed in experiment (Fig. 3.33). The macroscopic observations presented above are closely connected with the motion of faceted grain boundaries.

¹⁰The term athermal does not mean that the activation energy of grain boundary is exactly equal to zero. It reflects only the experimentally established fact that the motion does not depend on temperature, which also can occur for $E \ll kT$, i.e. every trial to overcome the activation barrier will be successful.

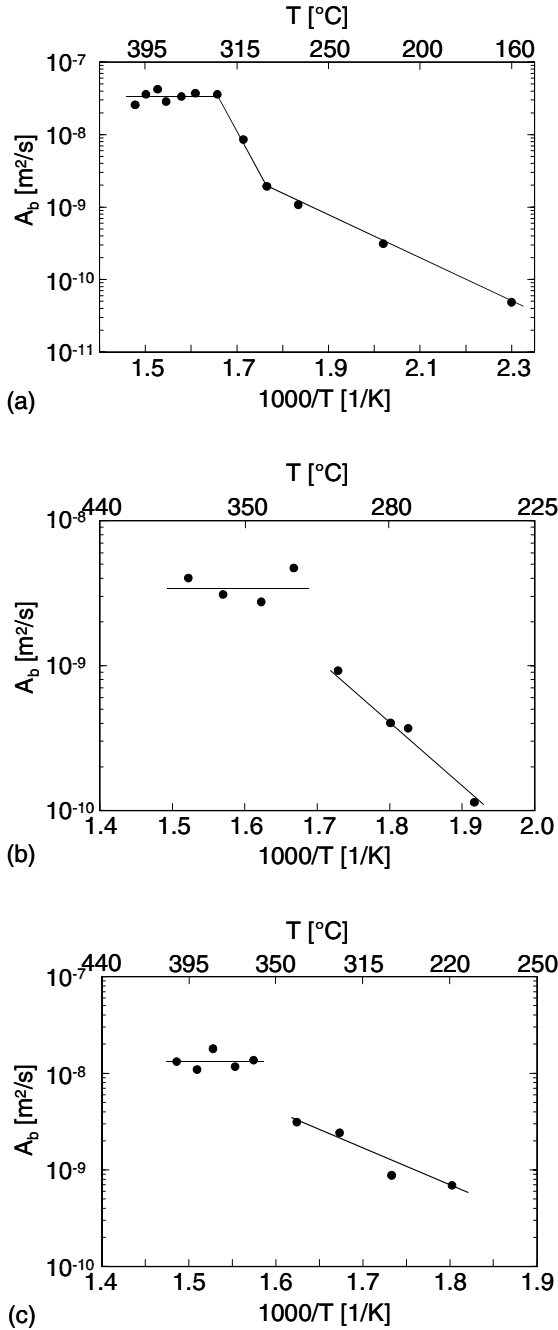


FIGURE 3.76

Temperature dependence of the reduced mobility of $\langle 11\bar{2}0 \rangle$ tilt grain boundaries in Zn: (a) $\varphi = 34^\circ$ ($\Sigma 23$); (b) $\varphi = 56^\circ$ ($\Sigma 36$); (c) $\varphi = 85^\circ$ ($\Sigma 11$).

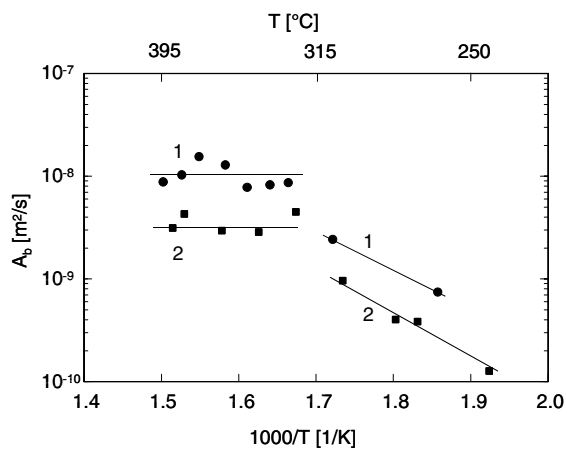


FIGURE 3.77
Temperature dependence of the reduced mobility of $56^\circ\langle 11\bar{2}0 \rangle$ tilt grain boundaries in Zn with $1 \cdot 10^{-5}\text{at\%Al}$ (1) and $3 \cdot 10^{-5}\text{at\%Al}$ (2).

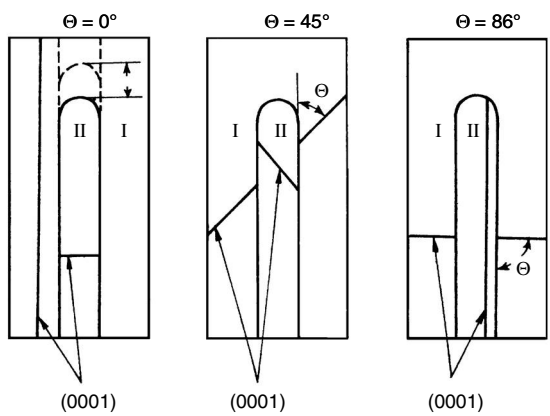


FIGURE 3.78
Bicrystals (half-loop geometry) with different inclination angle Θ of a tilt grain boundary $86^\circ\langle 11\bar{2}0 \rangle$.

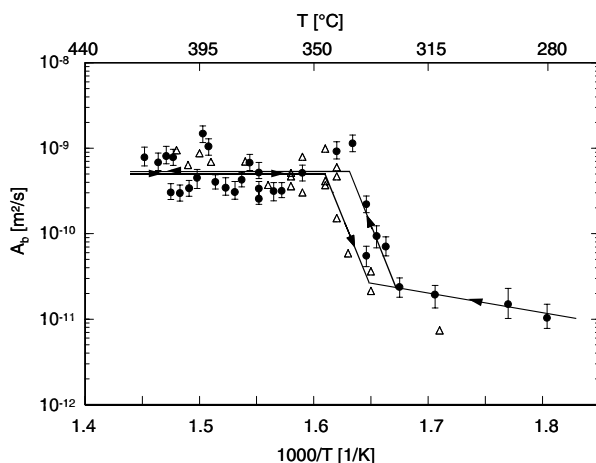


FIGURE 3.79

Temperature dependence of the grain boundary reduced mobility: tilt boundary $\langle 11\bar{2}0 \rangle$ in Zn: $\varphi = 86^\circ$; $\theta = 4^\circ$. The solid circles pertain to heating experiments.

3.5.7.1 Effect of Faceting on Grain Boundary Motion

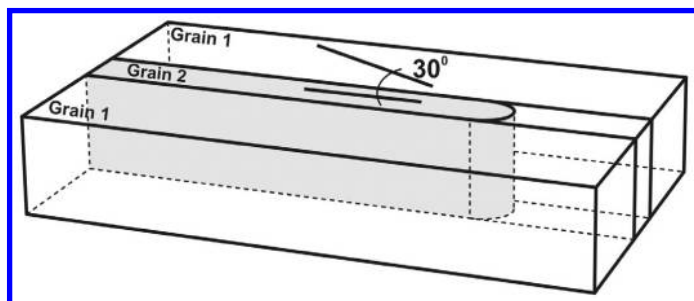
The surface of minerals is often composed of planar faces which are referred to as facets. They are due to the crystalline nature of the materials and reflect an anisotropy of the surface energy. However, facets are not only observed on crystal surfaces but can also occur on internal interfaces, like grain boundaries, and appear as straight grain boundary segments in an optical micrograph. Prominent examples are coherent twin boundaries in low stacking fault energy materials [310]. The relation between grain boundary (GB) faceting and grain boundary behavior, in particular, grain growth and grain boundary migration, was the subject of investigation in the past [141], [312]–[314]. However, only recently have quantitative methods been put forward to tackle this problem [315]–[317]. The migration of incoherent twin grain boundaries with facets was studied by Straumal et al. [316]. It was demonstrated that the rather complicated kinetics of grain boundary motion, in particular the strong non-Arrhenius temperature dependence, could be explained by considering the motion of two competing facets. Rabkin considered the influence of grain boundary faceting on grain growth and the motion of a 2D grain boundary half-loop [317]. Using several simplifying assumptions he showed that faceting might modify the Von Neumann-Mullins relationship for 2D grain growth; it was also found that the length of a facet on a half-loop depended on its mobility, i.e. the length of a facet increased with rising facet mobility.

TABLE 3.6
Grain Boundary Detachment II

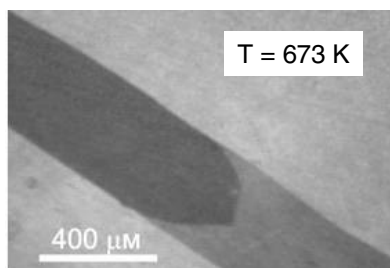
Metal	Tilt boundary	Drag- ging atoms	Concen- tration of dragging impurity c_1 10^{-5} at %	Energy of inter- action U_0 [eV]	Number of adsorption sites at grain boundary Z_1 [cm ⁻²]	Adsorption Γ [at/cm ²]
Al	$\langle 111 \rangle$ $\varphi = 38^\circ$	Fe	2	0.17	$2.3 \cdot 10^{14}$	$8 \cdot 10^8$
			1	0.24	$7 \cdot 10^{13}$	-
			1	0.23	$2.4 \cdot 10^{14}$	-
Zn	$\langle 11\bar{2}0 \rangle$ $\varphi = 81^\circ$ $\langle 11\bar{2}0 \rangle$ $\varphi = 56^\circ$	Al	1	0.36	$9.0 \cdot 10^{13}$	$4.8 \cdot 10^9$
			1	0.34	$8.0 \cdot 10^{13}$	$4.8 \cdot 10^9$
Zn	$\langle 11\bar{2}0 \rangle$ $\varphi = 45^\circ$ $\langle 11\bar{2}0 \rangle$ $\varphi = 88^\circ$ $\langle 10\bar{1}0 \rangle$ $\varphi = 57^\circ$ $\langle 10\bar{1}0 \rangle$ $\varphi = 30^\circ$	Al	3	0.35	$4.8 \cdot 10^{13}$	$1.5 \cdot 10^{10}$
			3	0.33	$5.9 \cdot 10^{13}$	$1.5 \cdot 10^{10}$
			3	0.35	$8.8 \cdot 10^{13}$	$1.5 \cdot 10^{10}$
			3	0.19	$1.4 \cdot 10^{15}$	$1.5 \cdot 10^{10}$
			3	0.18	$1.4 \cdot 10^{15}$	$1.3 \cdot 10^{10}$
Al	$\langle 111 \rangle$ $\varphi = 36.5^\circ$	Fe	7*	0.15	$1.0 \cdot 10^{14}$	$7.1 \cdot 10^8$
			sample I			
			7*	0.12	$1.4 \cdot 10^{14}$	$6.0 \cdot 10^8$
			sample II			
			8	0.12	$1.4 \cdot 10^{14}$	$6.2 \cdot 10^8$
Al	$\langle 111 \rangle$ $\varphi = 36.5^\circ$	Fe	sample III			
			1.15	0.12	$1.4 \cdot 10^{14}$	$8.9 \cdot 10^8$
			sample III			
			1.6	0.12	$1.1 \cdot 10^{14}$	$11.3 \cdot 10^8$
			sample V			
Al	$\langle 111 \rangle$ $\varphi = 46.5^\circ$	Fe	1.65	0.12	$1.3 \cdot 10^{14}$	$15.9 \cdot 10^8$
			sample VI			
			8**	0.12	$1.4 \cdot 10^{14}$	$6.1 \cdot 10^8$
			sample I	0.30	$4.9 \cdot 10^{12}$	$2.1 \cdot 10^8$
			6**	0.12	$1.7 \cdot 10^{14}$	$7.4 \cdot 10^8$
Al	$\langle 111 \rangle$ $\varphi = 46.5^\circ$ ***	Fe	sample II	0.32	$4.2 \cdot 10^{12}$	$2.6 \cdot 10^8$
			5**	0.14	$1.3 \cdot 10^{14}$	$5.6 \cdot 10^8$
			sample III	0.32	$3.8 \cdot 10^{12}$	$1.9 \cdot 10^8$

* $P_I/P_{II} = 1.6$ (Fig. 3.74).
** The experimental data were analyzed in the framework of the model with two kinds of adsorption sites.
*** Sample IV corresponds to the initial aluminum.

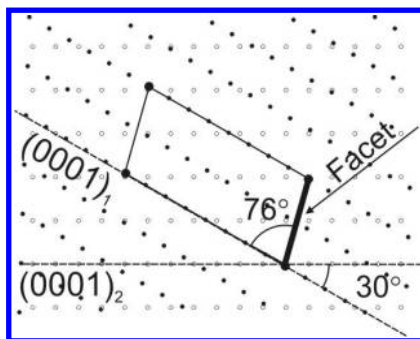
The impact of faceting on the motion of a high-angle grain boundary in Zn was investigated in [320, 321]. The study was conducted [320, 321] for

**FIGURE 3.80**

Scheme of a Zn bicrystal containing $[10\bar{1}0]$ tilt GBs with misorientation angles of 30° . The lines on the top faces of the crystals denote the orientation of basal plane (0001) in each grain $[320]$.



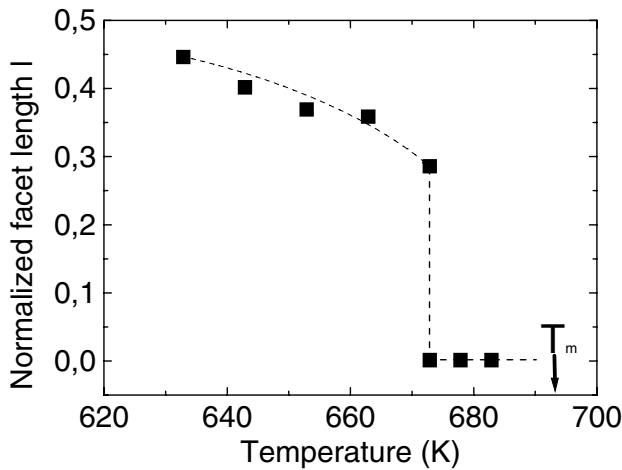
(a)



(b)

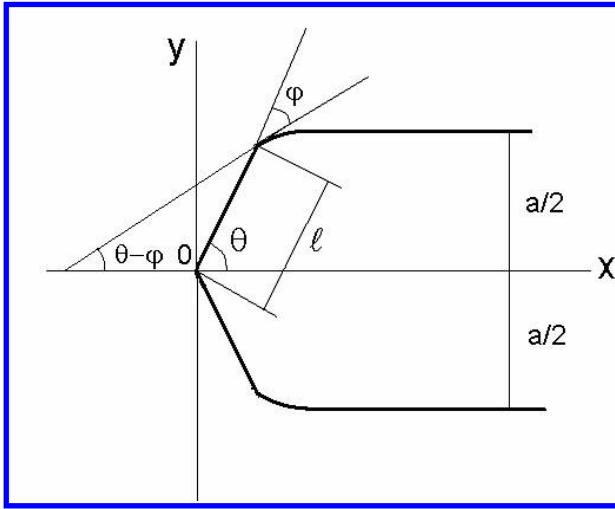
FIGURE 3.81

(a) Video frame of a moving grain boundary half-loop with facets $[320]$. (b) Section of CCSL perpendicular to the $[10\bar{1}0]$ tilt axis for GBs with misorientation angle θ of 30° . Filled and empty circles mark the sites of the two misoriented Zn lattices. Large circles mark CCSL sites. The reciprocal density of coincidence sites is $\Sigma = 17$. The unit cell of the respective CCSL, the position of the basal plane (0001) for grain 2 and the CCSL plane parallel to the facet on the moving GB are also shown $[320]$.

**FIGURE 3.82**

Observed temperature dependence of the facet length ℓ [320].

steady-state motion of the individual grain boundary — $[10\bar{1}0]$ and $[11\bar{2}0]$ tilt grain boundary half-loop (Figs. 3.80, 3.81) — and in situ recording of grain boundary motion. Above a certain temperature (673K for $[10\bar{1}0]$ boundaries) the migrating GB half-loop was continuously curved. Below this temperature a facet appeared and coexisted with the curved GB. The length of the facet increased with decreasing temperature (Fig. 3.82 [320]). The formation of a grain boundary facet is usually due to a low grain boundary energy for the specific facet inclination. From geometrical arguments, a low GB energy can be associated with a high density of coincidence points of a coincidence site lattice (CSL) [166, 316, 322]. The c/a ratio of the lattice spacing a in the basal plane (0001) and c perpendicular to (0001) is irrational in Zn. Therefore, exact coincidence site lattices exist in Zn only for GBs with $[0001]$ rotation axis. In all other cases, including $[10\bar{1}0]$ tilt GBs, a so-called constrained coincidence site lattice (CCSL) exists [323]. A section of the CCSLs perpendicular to the $[10\bar{1}0]$ tilt axis is shown in Fig. 3.81 for a GB with misorientation angle of 30° . Filled and open circles, respectively, mark the lattice points of the two mis-oriented Zn lattices. Large gray circles mark the CCSL sites. Evidently, the points of both lattices do not coincide exactly, and the difference may reach a few percent of the lattice spacing. This situation is similar to near-coincidence GBs of materials with cubic lattice, when the misorientation angle is close but not equal to the misorientation of exact coincidence θ_Σ , although still inside the range for special GBs [320, 324]. The reciprocal density of coincidence

**FIGURE 3.83**

Geometry of a grain boundary half-loop with a facet [320].

sites for the studied $30^\circ[10\bar{1}0]$ GB is $\Sigma = 17$, for the $85^\circ[11\bar{2}0]$ grain boundary $\Sigma = 11$.

Let us consider the steady-state motion of a grain boundary half-loop with a facet. A schematic sketch of the considered faceted boundary is given in Fig. 3.83 [320]. It resembles closely the experimentally observed shape (Figs. 3.80, 3.81).

The equation of motion and the boundary conditions which define the steady-state shape and the velocity V of a moving half-loop are given in [320]. In case of a partially faceted boundary the respective equations of motion and the boundary conditions ($a - c$) for the curved boundary read (Fig. 3.83)

$$y'' = -\frac{V}{\gamma m_b} y' (1 + y'^2)$$

$$(a) \quad y'(\ell \cos \theta) = \tan(\theta - \varphi)$$

$$(b) \quad y(\infty) = a/2$$

$$(c) \quad y(\ell \cos \theta) = \ell \sin \theta$$

(3.161)

Since the facet is flat with inclination θ (Fig. 3.83) the shape of the curved part of the moving half-loop with a facet is given by the equation

$$y = \frac{a}{2} - \frac{m_b \gamma}{V} \frac{\pi}{V} + \frac{m_b \gamma}{V} \arccos \left[\sin(\theta - \varphi) \exp \left(\frac{V}{m_b \gamma} (\ell \cos \theta - x) \right) \right] \quad (3.162)$$

The velocity of the moving half-loop can be extracted from the boundary condition (c) which renders

$$V = \frac{m_b \gamma (\theta - \varphi)}{\frac{a}{2} - \ell \sin \theta} \quad (3.163)$$

Since for steady-state motion the faceted and curved segments of the half-loop have to move with the same velocity, the migration rate of the grain boundary half-loop with a facet is also controlled by the facet motion. Formally the facet velocity can be expressed as

$$V = m_f \gamma_f \kappa \quad (3.164)$$

where m_f , γ_f are the mobility and surface tension of the facet, $\gamma_f = \gamma \cos \varphi$ (see Fig. 3.83). The equivalent curvature of the facet κ can be found from the so-called weighted mean curvature approach [73, 318]. The weighted mean curvature is defined by the reduction of the total interfacial free energy in the course of an infinitesimal facet displacement divided by the volume swept by the displaced facet. Then the velocity of the facet can be expressed as (Fig. 3.83))

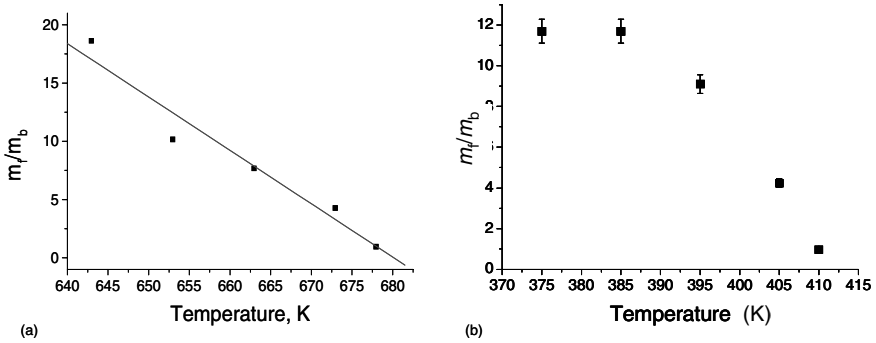
$$V = \frac{m_f \gamma \sin \varphi \sin \theta}{\ell} \quad (3.165)$$

From Eqs. (3.162) and (3.165) we obtain the length of a moving facet

$$\ell = \frac{\frac{a}{2}}{\sin \theta + \frac{m_b (\theta - \varphi)}{m_f \sin \varphi \sin \theta}} \quad (3.166)$$

Eq. (3.166) allows us to derive the mobility of the facet and its temperature dependence from experimentally measured values of the facet length. For example, the normalized facet mobility (m_f/m_b) for the facet in a $[10\bar{1}0]$ grain boundary system as extracted from experimental data is presented in Fig. 3.84 [320].

Apparently, a reduction of the facet length with rising temperature is mainly caused by a decrease in the ratio m_f/m_b . On the other hand, the absolute value of the facet mobility can be extracted if the grain boundary mobility is known from an independent experiment (Fig. 3.85) [320, 321]. As can be seen the facet has a high mobility with a very low activation enthalpy (~ 0.1 eV). An increase in the facet length with increasing facet mobility seems counterintuitive, since it is a frequent observation that faceted boundaries move with low mobility [310, 324]. The high mobility of the facet is associated with a low activation energy and attributed to a high step mobility on the facet [247, 320]. Such interpretation tacitly assumes that the production rate of steps on the facet is sufficiently high and will not affect the facet velocity. For instance, steps may be injected into the facet from the shrinking part of the boundary. This may not be true, though, for smooth low energy facets like coherent twin grain boundaries. In such case the migration rate may be

**FIGURE 3.84**

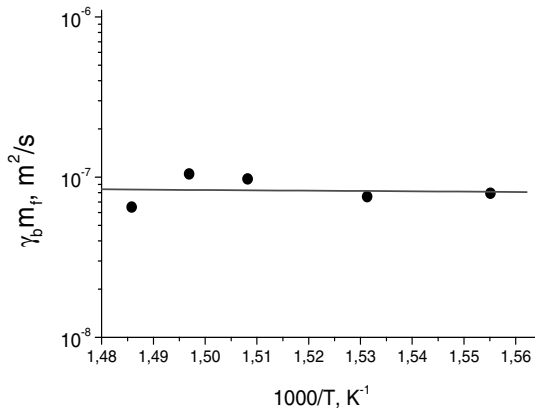
(a) Temperature dependence of the ratio of the normalized facet mobility m_d/m_b for a $[10\bar{1}0]$ tilt grain boundary [320]. (b) Temperature dependence of the ratio of the facet mobility and boundary mobility m_f/m_b for a $[11\bar{2}0]$ tilt grain boundary [321].

determined by the production rate of steps on the facet rather than by step migration and consequently, a steady-state motion with a facet of finite length may not be possible according to Eq. (3.166). Yoon [325] proposed that besides the faceting transition there may also be a roughening transition where smooth facets become rough owing to entropy-driven defect generation (steps, vacancies).

It is noted that the dynamic facet length given by Eq. (3.166) is equivalent to a maximum rate of free energy decrease [321]. As shown in Sec. 3.4.3 the velocity V of a half-loop as a whole corresponds to an extremum of the function $\Psi(V)$ (3.146). Only maxima of this function correspond to stable steady-state motion. For a linear dependence of the velocity on the driving force ($M(V) = \text{const.}$) the extremum of the function $\Psi(V)$ is equivalent to the maximum rate of reduction of free energy of the system (dissipation rate), in other words, the system tries to reduce the free energy as fast as possible, i.e. with the maximum possible rate.

For the steady-state motion of a grain boundary half-loop with a facet the average mobility can be defined in two ways, either by the facet motion or by the motion of the curved boundary. In the first case — the half-loop motion is controlled by the facet motion — the average mobility can be expressed as [321]

$$M_f(V) = \frac{V}{2\gamma/a} = \frac{m_f a \sin \varphi \sin \theta}{2\ell} \quad (3.167)$$

**FIGURE 3.85**

Temperature dependence of the facet mobility for a $[10\bar{1}0]$ tilt grain boundary [321].

When the half-loop migration rate is determined by the motion of the curved grain boundary the average mobility is

$$M_b(V) = \frac{m_b(\theta - \varphi)a}{2\left(\frac{a}{2} - \ell \sin \theta\right)} \quad (3.168)$$

A maximum rate of free energy reduction of the system is obtained for a constant average mobility

$$M_f(V) = M_b(V) \quad (3.169)$$

Obviously condition (3.169) is satisfied by relation (3.166). In essence, the facet changes its length in the course of motion in order to permit the system to reduce its free energy with the highest rate, which in turn is related to the Onsager principle of irreversible thermodynamics.

3.5.8 Effect of Pressure on Grain Boundary Migration: Activation Volume

As derived in Sec. 3.5.2, the grain boundary mobility is given by Eqs. (3.157) and (3.158)

$$m_b = \frac{v}{P} = m_0 \exp\left(-\frac{H_m}{kT}\right)$$

$$H_m = E_m + pV^*$$

If an experiment is carried out at constant pressure the pre-exponential factor m_0 and the enthalpy of activation H_m can be derived from the temperature dependency of grain boundary mobility. However, the enthalpy of activation and the pre-exponential factor are not independent of each other (compensation effect, Sec. 3.7). Therefore, from mobility measurements at different temperatures only information on a single activation quantity can be obtained.

The measured activation enthalpies for grain boundary motion are difficult to interpret. The problem of impurity influence on boundary mobility and, in particular, on migration activation enthalpy was discussed above. It was shown that despite a decrease in the activation enthalpy of boundary migration with rising impurity content, the activation enthalpy of migration for most grain boundaries is significantly greater than the activation enthalpy of grain boundary diffusion and, in many instances, can even exceed the activation enthalpy of bulk diffusion (Figs. 3.51, 3.55, 3.56). Even if the interaction between the adsorbed atoms is taken into account, at least in a very pure material, there is a drastic difference between the rate theory of single atom hopping and experimental results.

A more direct measure of the migration mechanism is the activation volume. The activation volume reflects the difference between the volume of the system in the activated and in the ground state. The activation volume V^* can be obtained from measurements of the pressure dependence of Gibbs free energy of activation

$$G = H - TS = E + pV^* - TS \quad (3.170)$$

$$\left. \frac{\partial \ln v}{\partial p} \right|_T = -\frac{V^*}{RT} \quad (3.171)$$

$$\left. \frac{\partial \ln v}{\partial 1/T} \right|_p = -\frac{H}{R} \quad (3.172)$$

For instance, the activation volume for bulk self-diffusion ought to be in the order of one atomic volume. In this case the activated state consists of the vacancy production and the local lattice expansion caused by the diffusing atom in the saddlepoint configuration. The relaxed volume of a vacancy roughly corresponds to a little less than an atomic volume, and the lattice expansion during the diffusive jump will be small compared to an atomic volume. The activation volume for grain boundary diffusion is only a little less than that for bulk diffusion (Table 3.7). This can be easily understood, because the density of grain boundaries is not very different from the bulk density of the crystal (even during melting the density of a metal drops only a few percent) (see Chapter 1). With regard to grain boundary motion the value of the activation volume is expected to provide information on essentials of the grain boundary migration mechanism.

Despite the relative ease of interpretation of the activation volume compared to the activation enthalpy, there have been only very few studies on

the pressure dependence of grain boundary migration [302]–[304]. The main reason for this deficiency is the serious experimental problems that have to be overcome in order to successfully conduct experiments on grain boundary migration at high hydrostatic pressure. Beginning with the pressurizing medium, either a gas or a liquid should be stable up to high temperatures and must be inert to the material of the sample to avoid contamination of the specimen. Moreover, the high pressure device must be designed to provide a stable and homogeneous temperature field. The displacement of a grain boundary during annealing at high pressure is given by

$$\ell = vt = v_0 t \exp\left(-\frac{E_m}{RT}\right) \exp\left(-\frac{pV^*}{RT}\right) \quad (3.173)$$

where v is the grain boundary velocity, t is the annealing time, v_0 is the pre-exponential velocity factor. For a fluctuation of temperature δT and pressure δp and an inaccuracy of time measurement δt , the relative error of the grain boundary displacement reads [304]

$$\frac{\Delta \ell}{\ell} = \left[\frac{E_m}{RT^2} \delta T \right] + \left[\frac{V^*}{RT} \delta p \right] + \frac{\delta t}{t} \quad (3.174)$$

Obviously, the uncertainty of grain boundary displacement will be essentially determined by the stability of pressure and temperature in addition to the magnitude of the activation energy and activation volume. For $E_m \cong 1.3$ eV, $T \cong 10^3$ K, $V^* \cong 10$ cm³/mol, at a pressure of the order of 100 MPa, a minor fluctuation of temperature by $\delta T \cong 1$ K is equivalent to a change of pressure by 15 MPa. Therefore, a high stability of pressure and temperature is required for an accurate measurement.

TABLE 3.7

Parameters of Bulk Diffusion

Metal	Specimen	H_D^{bulk} [eV]	D_0 [m ² /s]	$V_{\text{bulk}}^*/\Omega_a$
Ag self-diffusion [I]	polycrystals	2.0	$8.9 \cdot 10^{-3}$	
Ag self-diffusion [II]	$\langle 001 \rangle$ tilt grain boundary $\varphi = 28^\circ$	1.97	$7.2 \cdot 10^{-5}$	
Ag self-diffusion [III]	polycrystals	1.87	$2.78 \cdot 10^{-5}$	
Ag self-diffusion	single crystal “pure” silver			0.66 [IV] 0.88 [V]
Al-Zn	polycrystals $\varphi = 32^\circ$ $\varphi = 37^\circ$ $\langle 111 \rangle$ tilt grain boundary	1.28 [VI] 1.35 [X]	$2.45 \cdot 10^{-5}$ [VI] $1.4 \cdot 10^{-4}$ [X]	1.1 [VII]
Al self-diffusion				1.23 – 1.35 [XII]
Al-Cu	single crystal			1.16
Al-Ag	“pure” Al single			1.19
Al-Au	crystal of Al			1.18 [V]
Au self-diffusion	polycrystals	1.8 [XIII]	$9.1 \cdot 10^{-6}$	0.67 – 0.81 [XII]
Cd self-diffusion	polycrystals 99.9995 at%	$Q^{\parallel} = 0.79$ $Q^{\perp} = 0.82$ [XI]	$= 1.3 \cdot$ $(D_{\parallel} + 2D^{\perp})$ $D_0^{\perp} = 5 \cdot 10^{-6}$ $D_0'' = 1 \cdot 10^{-5}$ [XV]	$\perp C$ $\parallel C$ 0.53 – 0.59 [XVII]
Pd self-diffusion	Polycrystals 99.95%	1.1 [XVIII]	$1.17 \cdot 10^{-4}$ [XVIII]	single crystal 0.71 – 0.84 [XIX] 0.57 – 0.715 [XX]
Pd self-diffusion	$\langle 001 \rangle$ tilt and twist grain boundary 99.999 at%	1.07 [XXIV]	$6.26 \cdot 10^{-5}$ [XXIV]	
Sn self-diffusion	polycrystals 99.99%	0.99 [XXI]	$7.8 \cdot 10^{-5}$	single crystal $\perp C$ 0.304 – 0.362 $\parallel C$ 0.321 – 0.329

TABLE 3.8
Parameters of Grain Boundary Diffusion

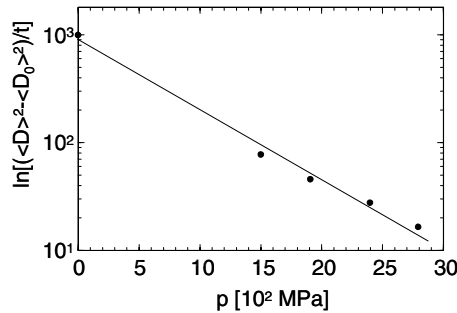
Metal	H_D^b [eV]	$(\delta D_b)_0$ [m ³ /s]	V^*/Ω_a
Ag self-diffusion [I]	0.92	$5.76 \cdot 10^{-15}$	
Ag self-diffusion [II]	1.05	$2 \cdot 10^{-16}$	
Ag self-diffusion [III]	0.67	$1.16 \cdot 10^{-16}$	1.09
Ag self-diffusion Al-Zn	0.54 [VIII] 0.52 $\varphi = 32^\circ$ 0.87 $\varphi = 37^\circ$ $\langle 111 \rangle$ tilt grain boundary [XI]	$3.1 \cdot 10^{-15}$ [VIII]	0.8 – 1.08 [IX]
Au self-diffusion	0.88 [XIV]	$3.1 \cdot 10^{-16}$ [XIV]	
Cd self-diffusion	0.48 [XVI]	$3.35 \cdot 10^{-14}$	
Pd self-diffusion	0.68 [XVIII]	$8.17 \cdot 10^{-14}$	
Pd self-diffusion	Twist grain boundary [XXV] 0.35 tilt grain boundary $\varphi = 30^\circ$ 0.2		
Sn self-diffusion	0.43 [XXIII]	$3.22 \cdot 10^{-15}$	
I — Hoffmann RE, Turnbull D. <i>J. Appl. Phys.</i> , 22:634, 1951.			
II — Turnbull D, Hoffmann RE. <i>Acta Metall.</i> , 2:419, 1954.			
III — Kaigorodov VN, Klotsman SM, Timofeev AN, Trakhtenberg IS. <i>Phys. Met. Metall.</i> , 25:910, 1968.			
IV — Rein G, Mehrer H. <i>Phil. Mag.</i> , A45:767, 1982.			
V — Beyeler M, <i>These Université Paris</i> , 1968.			
VI — Beke DL, Godeny I. <i>Phil. Mag.</i> , A47:281, 1983.			
VII — Erdelyi G, Lojkowski W, Beke DK, Gödeny I, Kedves JL. in <i>Diffusion in Metals and Alloys</i> , Kedves FJ, Beke DL, editors. Aldermannsdorf, p. 398, 1983.			
VIII — Gödeny I, Beke DK, Kedves FJ. <i>Trans. Japan. Inst. Metals (suppl.)</i> , 27:525, 1986.			
IX — Erdelyi G, Lojkowski W, Beke DK, Gödeny I, Kedves JL. <i>Phil. Mag.</i> , A56 : 673, 1987.			
X — Ovsienko DY, Zasimcuk IK. <i>Phys. Met. Metall.</i> , 10:743, 1960.			

-
- XI — Aleshin AN, Aristov VJ, Bokstein BS, Shvindlerman LS. *Phys. Stat. Sol. (a)*, 45:359, 1978.
 - XII — Beyeler M, Adda Y. *J. Phys. (Paris)*, 345, 1978.
 - XIII — Makin SM, Rowe AH, Claire AD. *Proc. Phys. Soc. Lond.*, 70:545, 1957.
 - XIV — Gupta D. *J. Appl. Phys.*, 44:4455, 1973.
 - XV — Wadja ES, Shirn GA, Huntington HB. *Acta Metall.*, 3:39, 1955.
 - XVI — Günther F, Haessner A, Oppermann L. *Isotopenpraxis*, 5:461, 1969.
 - XVII — Buescher BJ, Gilder HM, Shea N. *Phys. Rev.*, B7:2261, 1973.
 - XVIII — Okkerse B. *Acta Metall.*, 2:551, 1954.
 - XIX — Nachtrieb NH, Resing HA, Rice SA. *J. Chem. Phys.*, 31:135, 1959.
 - XX — Hudson JB, Hoffman RE. *Trans. Met. Soc. AIME*, 221:71, 1961.
 - XXI — Lange W, Haessner A, Berthold I. *Phys. Stat. Sol.*, 1:50, 1961.
 - XXII — Curtin HR, Decker DL, Vanfleet HB. *Phys. Rev.*, A139:1551, 1965.
 - XXIII — Smithells CJ. *Metals Reference Book*, 5th ed, Butterworths, London, 1976.
 - XXIV — Star, JP, Upthegrove WR. *Trans. ASM*, 59:479, 1966.
 - XXV — Hudson JB. in *Aeronautical Research Laboratory Technical Report*, Wright Air Development Center, Dayton, OH, cited from Ref. XXIV, Report 60-321, 1966.
-

Moreover, Eq. (3.174) shows that high values of pressure are necessary to obtain an impact on grain boundary motion by pressure comparable to the measured temperature influence. To compensate for the effect on grain boundary mobility by a temperature change of the order of ~ 250 K the pressure should be changed by the order of ~ 1 GPa. This demonstrates the serious experimental problems which have to be overcome to properly measure the pressure dependence of grain boundary mobility.

Grain boundary migration is the result of a net flux of lattice sites across the grain boundary. This means that the transfer of an atom across the boundary causes a new lattice site to be produced on the grain boundary face of the growing crystal, while a lattice site at the grain boundary face of the shrinking crystal is removed. If the process of grain boundary migration occurs by both the hopping of single atoms across the boundary for the diffusion migration and activation volume, both close to an atomic volume is to be expected.

Owing to the substantial experimental difficulties, there are only few sources in the literature that address this item. Hahn and Gleiter [305] studied grain growth in pure Cd (99.9999%) under high pressure (up to 28 kbar (2.86 GPa)) and at annealing temperatures 180-260°C. The activation volume was not calculated by Hahn and Gleiter, but their data permit us to derive it [304]. In Fig. 3.86 the rate of grain growth in Cd is given as a function of pressure calculated in [124] from the data of [304]. It yields an activation volume for grain growth, which can be associated with grain boundary migration:

**FIGURE 3.86**

Pressure dependence of the mobility ($\sim D^2/t$) during grain growth [304, 305].

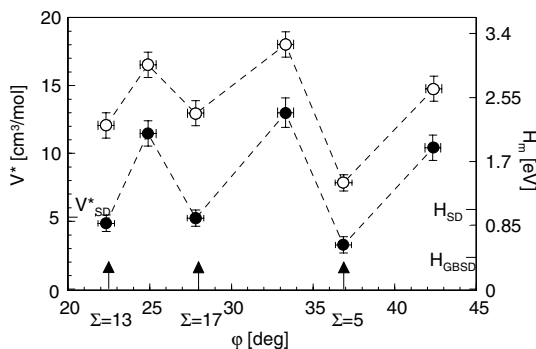
$V^* = 6.39 \text{ cm}^3/\text{mol}$, or $V^* = 0.49 \cdot \Omega_a$ (Ω_a — atomic volume). Since the ratio V_{SD}^*/Ω_a for bulk self-diffusion in Cd ranges from 0.53 to 0.59, there is reasonable agreement between V^*/Ω_a and V_{SD}^*/Ω_a .

Lojowski [306] studied grain growth in Al (99.99%) under a pressure up to 25 kbar (2.5 GPa) at 400°C. The activation volume ranged from 0.65–0.8 Ω_a and depended on the thermomechanical history, i.e. on crystallographic texture of the polycrystals. The values of the activation volume for self-diffusion in Al given in the literature are contradictory and range from 0.52–1.35 Ω_a (Table 3.7). The latter reference seems to provide more accurate data. In any event, $V^* \leq V_{SD}^*$.

As stressed many times, experiments on polycrystals provide only an average picture of the phenomenon. Also, as the majority of grain boundaries in polycrystals have the character of random boundaries, the activation volume of grain growth most likely reflects the activation volume of migration of random grain boundaries.

Special and non-special $\langle 001 \rangle$ tilt grain boundaries were studied in tin [302, 303, 307]. Grain boundary migration was measured at atmospheric pressure and at high hydrostatic pressure up to 16 kbar. The orientation dependencies of activation enthalpy and activation volume of migration are given in Fig. 3.87. The activation enthalpy for the migration of special grain boundaries is 1.5–2 times larger than the energy of activation for bulk self-diffusion and almost by an order of magnitude larger than for grain boundary self-diffusion, whereas the activation volume for special grain boundaries amounts to 0.6–0.96 V_{SD}^* . However, for non-special grain boundaries the activation volumes exceed V_{SD}^* by a factor of 2–2.5. This is a first indication that the activation volume of grain boundary migration can substantially exceed the diffusion activation volume.

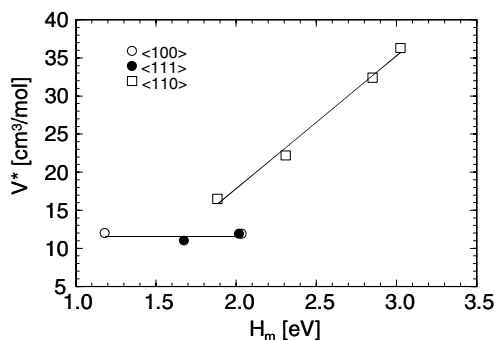
The results of a comprehensive study of the temperature and pressure de-

**FIGURE 3.87**

Activation enthalpy (o) and activation volume (•) of $\langle 001 \rangle$ tilt grain boundary migration in tin.

dependencies of $\langle 100 \rangle$, $\langle 110 \rangle$, and $\langle 111 \rangle$ tilt grain boundaries in bicrystals of pure Al are given in Figs. 3.88 and 3.89 [304]. The activation volumes for $\langle 100 \rangle$ and $\langle 111 \rangle$ tilt boundaries are identical and independent of the angle of rotation, quite in contrast to the behavior of the activation enthalpy. The absolute value of about $12 \text{ cm}^3/\text{mol}$ corresponds to slightly more than one atomic volume in aluminum and is, therefore, close to the activation volume for bulk self-diffusion. As mentioned above, the activation volume is the difference between the volume of the activated and the ground state. For self-diffusion this is essentially the volume of a vacancy, which has to be provided for the elementary diffusive step. The finding of an activation volume for grain boundary migration close to that of bulk self-diffusion suggests that a diffusion process controls the boundary migration rate. On the other hand, the intrinsic grain boundary mobility, e.g. in the absence of impurities, is not likely to yield activation volumes very different from a single atomic volume, since a diffusive jump across the boundary by detaching an atom from the shrinking grain and attaching it to the growing one requires the generation of a lattice site at the internal surface of the growing crystal. If large structural vacancies do not exist in the boundary, then the creation of a lattice site in the boundary requires a volume change close to an atomic volume. In fact, computations of grain boundary structure at 0 K do not predict large excess volumes in grain boundaries, at least not in special boundaries. The results for $\langle 100 \rangle$ and $\langle 111 \rangle$ tilt boundaries are, therefore, quite in line with our current understanding of grain boundary motion by the hopping of single atoms across the boundary.

By contrast the activation volume for $\langle 110 \rangle$ tilt boundaries increases with increasing departure from the exact low Σ coincidence misorientation, as is also the case for the activation energy (Fig. 3.88). For a $30^\circ \langle 110 \rangle$ bound-

**FIGURE 3.88**

Activation volume vs. activation enthalpy of tilt grain boundary migration in Al (tilt axis indicated).

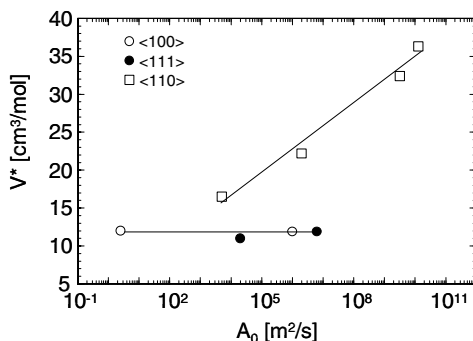
ary, which deviates by $\sim 8^\circ$ from the $\Sigma 9$ boundary, the activation volume amounts to $36 \text{ cm}^3/\text{mol}$ equivalent to more than three atomic volumes. Such large activation volume cannot be justified in terms of individual atomic jump mechanisms of grain boundary migration. Rather, such values are evidence that more than a single atom is involved in the fundamental process of grain boundary migration.

Migration mechanisms, based on groups of atoms, can consist either of the concomitant migration of groups or a cooperative motion (chain transfer) by coordinated serial motion of atoms. Group mechanisms of grain boundary migration have been proposed by several authors in the past, but without any proof of evidence. In his island model of grain boundary structure, Mott proposed that little patches of perfect crystal structure will detach from one crystal and attach at the other side of the boundary [162]. Such a model of grain boundary migration, however, is not compatible with our current knowledge of grain boundary structure. Grain boundaries are very narrow with little excess volume and do not give room for floating crystal patches across the boundary. In a computer simulation carried out by Shan and Bristowe [308], as well as Schönfelder, Wolf et al. [309], it was found that concurrent shuffling of groups of atoms may take place during migration.

3.5.9 Effect of Grain Boundary Orientation

3.5.9.1 Anisotropy of Grain Boundary Motion

Thus far, we have considered the dependency of grain boundary mobility on misorientation between the adjacent grains only. A grain boundary, how-

**FIGURE 3.89**

Activation volume vs. preexponential reduced mobility factor of tilt grain boundary migration in Al (tilt axis indicated).

ever, is also defined by its spatial orientation (inclination), which is commonly changing along the boundary between adjacent grains. It is usually tacitly assumed that the (spatial) orientation of a boundary does not seriously affect grain boundary mobility. This is not always true, however, as evident from recrystallized microstructures of fcc materials with low stacking fault energy, which exhibit a high density of slim annealing twins (Fig. 3.90). Despite a common orientation relationship the mobility of the long straight coherent twin boundaries is obviously much lower than that of the other, incoherent twin boundaries. Not only twin boundaries exhibit an anisotropy of mobility for a given misorientation relationship. This is most easily demonstrated from bicrystal experiments where a boundary is allowed to freely expand in a volume.

Such a case can be achieved by utilizing growth selection in a steep temperature gradient of a slightly deformed single crystal with the shape of a shovel [310] (Fig. 3.91). Growth selection is set off at the top of the handle and is terminated when the remaining single grain boundary has reached the bottom of the handle. Subsequently, the entire shovel is subjected to an annealing treatment, during which the boundary freely expands into the blade of the shovel, driven by the stored energy of cold work in the slightly rolled single crystal shovel.

Although during growth selection certain orientations are strongly preferred over others in growth competition, other orientation relationships also are occasionally observed to survive. From a large number of experiments it is evident that grain boundaries with $\langle 100 \rangle$ and $\langle 110 \rangle$ rotation axis grow fairly isotropically, i.e. the final shape of the growing grain is a semicircle (Fig. 3.92). For a $\langle 111 \rangle$ rotation axis a very anisotropic grain boundary mobility is apparent, and the growing grain assumes the shape of a rectangle (Fig. 3.93).

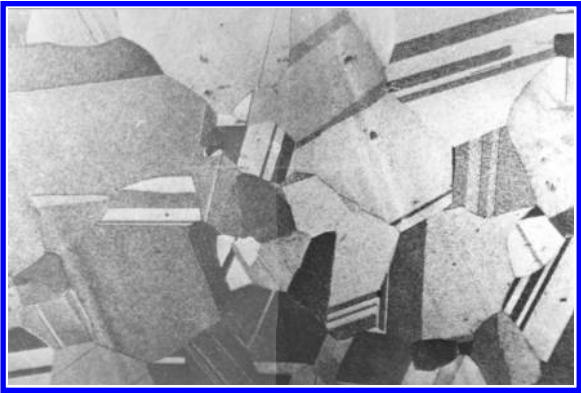


FIGURE 3.90
Microstructure of recrystallized brass. Note anisotropic grain shape of annealing twins.

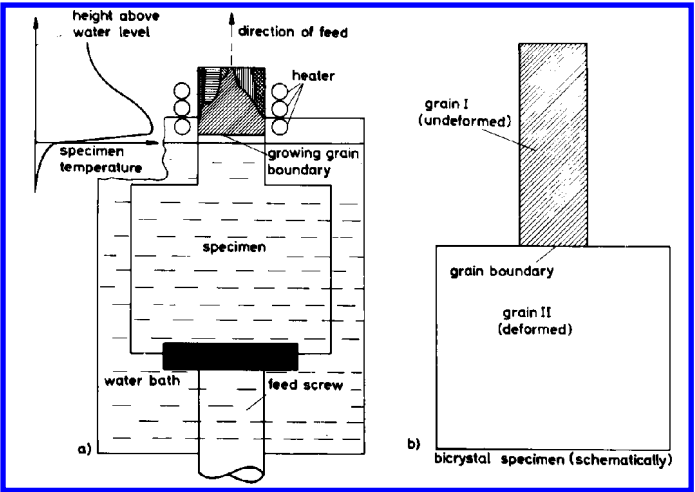
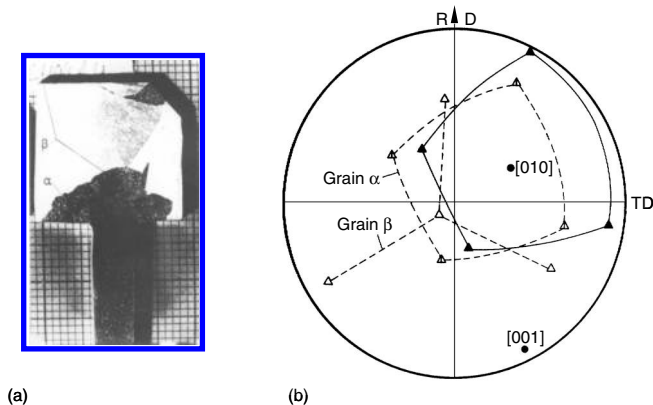


FIGURE 3.91
(a) Principle of the production of a bicrystal from a deformed single crystal in a gradient furnace; (b) idealized form of the used bicrystal.

**FIGURE 3.92**

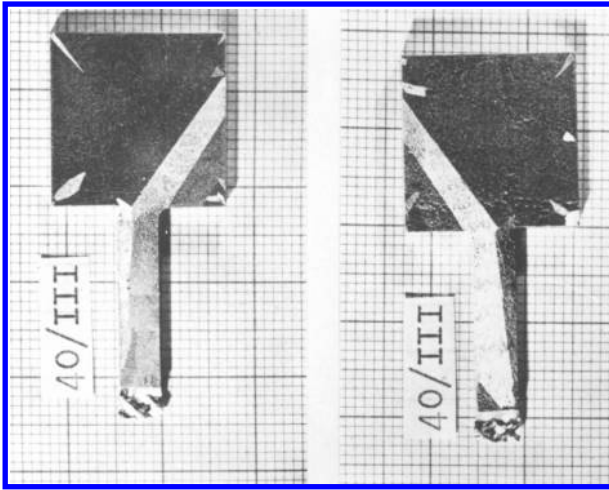
Isotropic grain growth of grain boundaries with $\langle 100 \rangle$ rotation axis. (a) Grain β was nucleated spontaneously from the surface (b).

The long straight facet of the grown grain, i.e. the slowly moving boundary, is determined by the crystallography of the growing grain rather than by the shovel geometry. If the shovel is machined out differently from the rolled single crystal, the spatial orientation of the slowly growing facet follows exactly the change of the crystallographic directions in the deformed single crystal (Fig. 3.94). The long facet is always perpendicular to the $\langle 111 \rangle$ rotation axis, i.e. this slowly moving facet is a twist boundary. The degree of anisotropy Λ , defined by

$$\Lambda = \frac{\text{elongation}}{\text{broadening}} \quad (3.175)$$

of the grain, is not a function of angle of rotation, but rather is strongly dependent on the deviation of the actual rotation axis from an ideal $\langle 111 \rangle$ axis (Fig. 3.95). The more perfect the twist character of the boundary, the larger Λ , up to a factor of 100 for the ideal $\langle 111 \rangle$ twist boundary, which is most perfectly achieved for the coherent twin boundary. A deviation by 2 degrees reduces the anisotropy already by a factor of 10. An ideal $\langle 111 \rangle$ twist boundary consists of two perfectly flat $\{111\}$ planes of the adjacent crystals, and it is easy to imagine that it is difficult to remove or attach atoms to these planes, i.e. to make the grain boundary move.

It was frequently observed that the growing grain assumed the shape of a triangle rather than a rectangle (Fig. 3.96). One of the straight faces was identified as a twist boundary, while the other triangular boundary was faceted comprising piecewise twist boundary facets. For a single crystal orientation symmetrical with regard to the growth direction in the handle of the shovel, two symmetrically equivalent orientations frequently survived the

**FIGURE 3.93**

Rectangular-shaped grain obtained by free planar growth in Al. Deformed grain in Goss orientation (110)[001]. Orientation relationship between grains approximately $46^\circ(111)$.

growth competition, one of which became rectangular while the other one assumed a triangular shape (Fig. 3.97). Although the reason for this behavior is not yet clear, it may be related to the dependence of grain boundary mobility on direction of motion, as will be shown in Sec. 3.5.9.2.

This anisotropy of grain boundary mobility manifests itself by an ellipticity of grain morphology during free growth of a grain in a homogeneous environment. The first-order twin boundaries ($60^\circ(111)$) are the most prominent, but not the only example. For a general mathematical description of grain shape evolution, the displacement of a grain boundary element parallel to its normal has to be considered (Fig. 3.16). Including forces by grain boundary surface tension γ and a volume driving force P for its motion, we arrive at the shape evolution equation $y(x, t)$ (see also Sec. 3.3.6)

$$\frac{\partial y}{\partial t} = V - Pm_b + m_b\gamma\kappa \quad (3.176)$$

where V is the speed of a (dragging) groove, and κ is curvature. If the boundary slope is small ($(\partial y/(\partial x) \ll 1)$) then a linear equation is obtained

$$\frac{\partial y}{\partial t} = V + m_b \left(\gamma \frac{\partial^2 y}{\partial x^2} - P \right) \quad (3.177)$$

The solution of this partial differential equation depends on the magnitude of the driving forces and the orientation dependent mobility of the boundary.

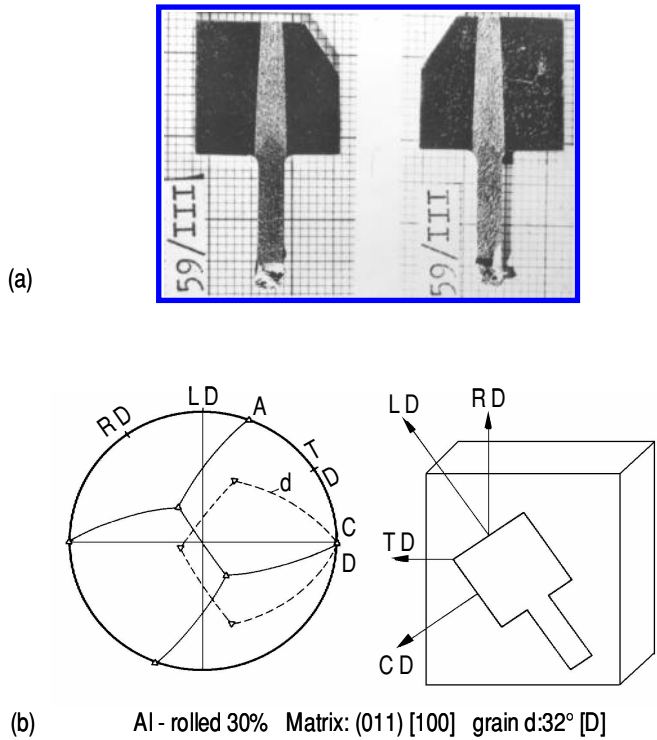


FIGURE 3.94

The same rolling sample as Fig. 3.93, (a) shovel cut in such a way that the {111} plane is parallel to longitudinal direction (b).

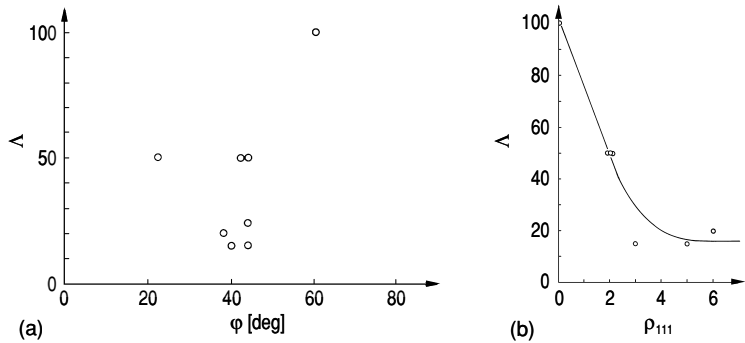
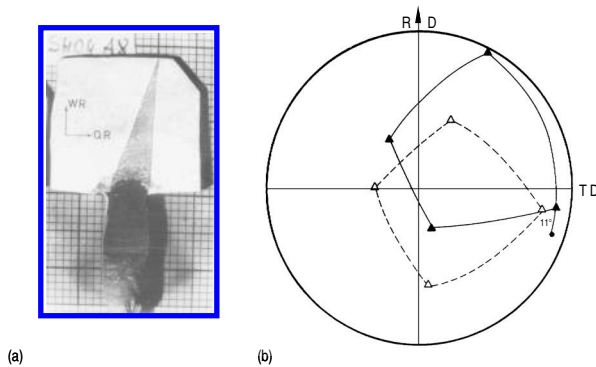


FIGURE 3.95

Shape anisotropy A of grain grown with <111> rotation axis to consumed grain in Al. (a) Dependence on rotation angle; (b) dependence on deviation of the actual rotation axis from the ideal <111> axis.

**FIGURE 3.96**

Triangular-shaped grain (a); the orientation of the triangular-shaped grain (b).

For an isotropically moving boundary the solution will be a sphere in three dimensions or a circle in two dimensions. For the general case, i.e. more complicated conditions with regard to mobility and surface tension, solutions are yet to be derived.

3.5.9.2 Impact of Boundary Orientation on the Steady-State Motion of Curved Grain Boundaries

The growth selection experiments have shown the high anisotropy of $\langle 111 \rangle$ grain boundaries in the course of grain growth [310].

The steady-state motion of a grain boundary under the action of its own surface tension was analyzed in Sec. 3.4.3. Since the differently inclined boundary elements may have different reduced mobilities, in general the velocity of a curved boundary moving in steady state depends on its orientation [256]. The only exception are tilt grain boundaries in a crystal lattice with inversion symmetry ($\langle 100 \rangle$ tilt boundaries). Such effect was observed, for instance, for half-loop migration of $\langle 11\bar{2}0 \rangle$ tilt boundaries in Zn [247].

In [311] an attempt was undertaken to consider this phenomenon for the steady-state motion of $\langle 111 \rangle$ tilt and mixed tilt-twist grain boundaries in Al bicrystals. The steady-state motion of a quarter-loop boundary in two configurations was studied (Fig. 3.98). The boundary configuration sketched in Fig. 3.98a can be represented by a series of differently inclined “pure tilt” elements whereas the boundary with the configuration of Fig. 3.98b is composed of a series of mixed tilt-twist elements with changing twist component along the boundary.

The motion of curved grain boundaries with rotation axis $\langle 111 \rangle$ and misorientation angles between 34° and 42° in both configurations shown in

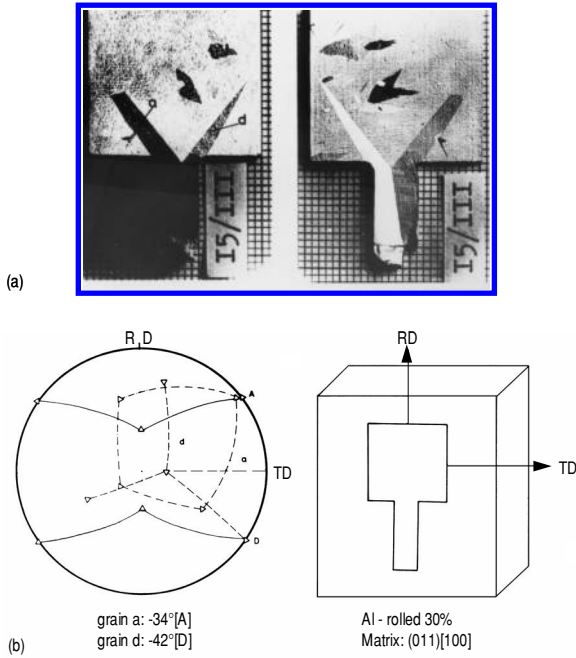


FIGURE 3.97

Examples of two growing grains in Al with equivalent orientation relationships to the consumed grain but different shapes (a); the orientation of the shovel cut (b).

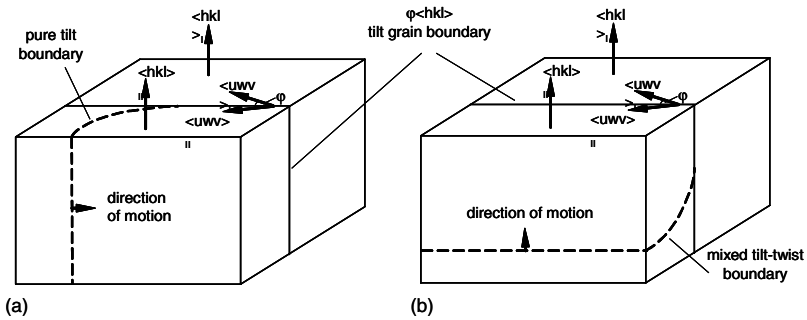
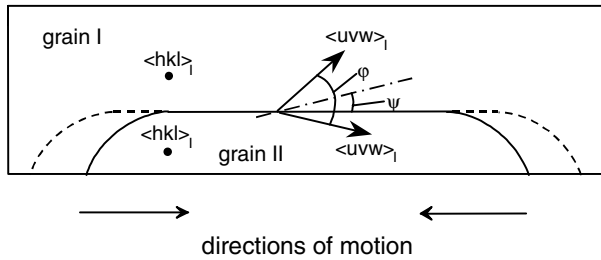


FIGURE 3.98

Sketch of a bicrystal with initially straight symmetrical $\phi(hkl)$ tilt grain boundary, which moves under a capillary driving force as (a) a pure tilt and (b) a mixed tilt-twist boundary [311].

**FIGURE 3.99**

Motion of a curved tilt boundary with different sets of boundary planes. The straight section of the boundary is asymmetrical with an inclination from a symmetrical position [311].

Fig. 3.98 was investigated. The initial straight grain boundary in the investigated bicrystals was mostly a symmetrical tilt boundary. The curved boundary in the Fig. 3.98a configuration keeps its tilt character, and only the inclination of the boundary plane changes in the curved part. By contrast, the character of the curved boundary in the configuration of Fig. 3.98b changes along the boundary and becomes mixed with increasing twist and decreasing tilt components. The motion of such a mixed tilt-twist grain boundary was investigated. Since the moving curved part of the boundary consists of different boundary planes, it is impossible to study directly the effect of grain boundary inclination on its mobility by utilizing the grain boundary curvature as a driving force. That is why in experiments [311] the orientation of the whole moving curved boundary was changed by an inclination of the initial part of the boundary from its symmetrical position ($\Psi > 0$, Fig. 3.99). Therefore, the motion of different sets of boundary planes for the same $\varphi\langle hkl \rangle$ tilt boundary can be measured and compared. The motion of $34^\circ \langle 111 \rangle$ and $36^\circ \langle 111 \rangle$ boundaries with asymmetrical straight tilt boundary having an inclination angle Ψ up to 7° (Fig. 3.99) was studied as well. The higher the Ψ , the greater the difference in the orientations of the corresponding curved sections. If the boundary mobility depends on boundary inclination, this would affect the velocity of steady-state motion of a curved boundary.

The results of measurements of the motion of $\langle 111 \rangle$ tilt boundaries in opposite directions are shown in Figs. 3.100 and 3.101. As seen, practically no difference has been found either in the case of an asymmetrical initially straight boundary (Fig. 3.100), or in the case of an asymmetrical boundary with inclination angles $\Psi = 5.5^\circ$ or $\Psi = 7.1^\circ$ (Fig. 3.101).

Another feature which reflects both the kinetic and thermodynamic property of the grain boundary during steady-state motion is the shape of a moving grain boundary (see Sec. 3.4.3). Pure twist boundaries are planar boundaries. By definition, it is impossible to measure their motion by utilizing grain

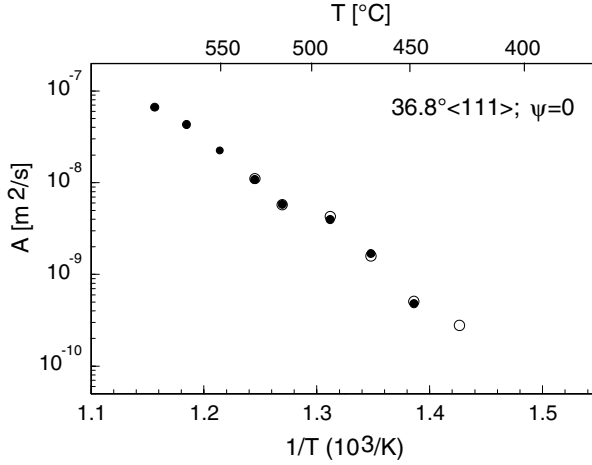


FIGURE 3.100

Reduced boundary mobility vs. temperature for the motion of a 36.8°<111> tilt boundary with a symmetrical ($\Psi = 0$) straight boundary section [311].

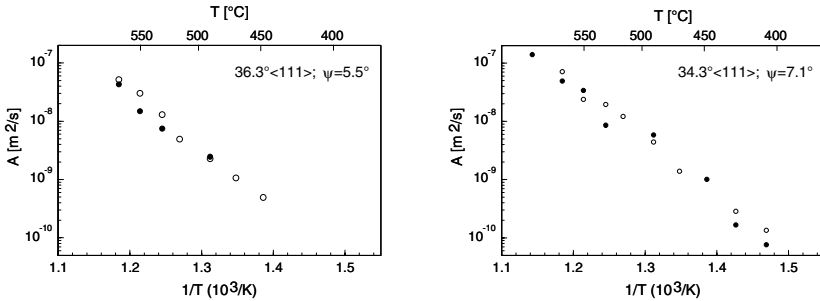
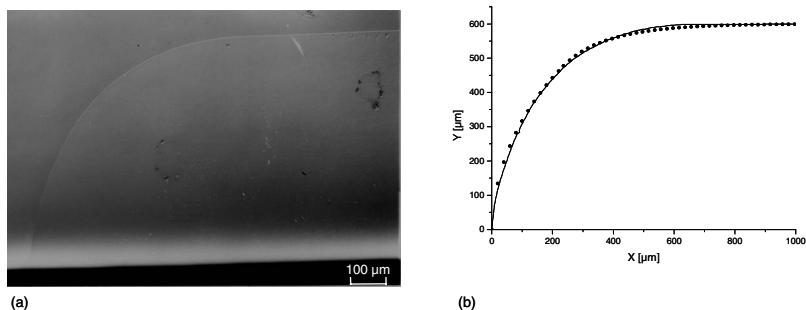


FIGURE 3.101

Temperature dependence of the mobility of two curved tilt grain boundaries with asymmetrical straight boundary sections. Open and filled symbols indicate the boundary motion in opposite directions [311].

**FIGURE 3.102**

(a) Measured and (b) calculated shape of a moving $40.6^\circ \langle 111 \rangle$ mixed tilt-twist boundary in pure Al (99.999%) at $T = 602^\circ\text{C}$ (solid line is measured shape, dotted line is calculated shape) [311].

boundary curvature as a driving force. However, it is possible to study the motion of mixed boundaries which comprise both tilt and twist components (Fig. 3.98b). In such a configuration the boundary character changes from pure tilt to almost pure twist along its curved part, although the boundary retains the same misorientation angle φ and axis $\langle hkl \rangle$ of rotation. In [311] the shape of a “mixed” grain boundary which comprises both tilt and twist components has been studied (Fig. 3.98b). In such a configuration the boundary character changes from pure tilt to almost pure twist along its curved part, although the boundary retains the same misorientation angle φ and axis $\langle hkl \rangle$ of rotation (Fig. 3.102). The theoretical basis of such examination is given by Eqs. (3.122), (3.148)–(3.150).

The consistency of measured and calculated grain boundary shape (Fig. 3.102) allows us to conclude that different elements of the investigated boundary have the same reduced mobility, irrespective of grain boundary character, i.e. their composition of tilt and twist components. That means an increase in the twist component along a curved mixed boundary in such geometrical configuration does not affect its steady-state motion. The motion of $\langle 111 \rangle$ mixed boundaries was measured in [311] in the angular misorientations interval between 37° and 42° in the vicinity of the special $\Sigma 7$ orientation. It was shown that both activation parameters of grain boundary migration — the enthalpy of activation and the pre-exponential factor — changed non-monotonically with a minimum at the $\Sigma 7$ misorientation and very similar to the respective dependencies for a $\langle 111 \rangle$ tilt grain boundary.

3.5.9.3 Motion of Flat Boundaries

In the previous sections we discussed the dependency of grain boundary mobility on crystallography and impurity content on results obtained in experiments where the motion of curved grain boundaries was studied. The only exceptions were the experiments of Aust and Rutter, where planar grain boundaries moved under driving forces provided by the striated microstructure (sub-boundaries) [180]–[182]; however, the boundaries were not perfectly planar, and the striations may have caused other difficulties (Chapter 4).

A curved grain boundary implies that its structure changes the boundary, since it is composed of different grain boundary planes. The mobilities obtained cannot, therefore, be related to a specific grain boundary structure. However, a planar boundary can be forced to move, if a bicrystal with grains that have some orientation-dependent property, like elastic constants or magnetic susceptibility, are utilized. Under the impact of a respective directed external field the property anisotropy will generate a free energy difference between adjacent grains that creates a driving force for grain boundary displacement. This driving force does not depend on boundary properties and moves a boundary from the grain with lower free energy toward the one with higher free energy. In particular, such conditions can be obtained by the action of a magnetic field on a bicrystal of a material with anisotropic magnetic susceptibility.

The origin of the driving force for grain boundary migration in a magnetically anisotropic material was considered by Mullins [185]. The expression for the driving force, as applied to bismuth, reads

$$P = \mu_0 \frac{\Delta\chi}{2} H^2 (\cos^2\theta_1 - \cos^2\theta_2) \quad (3.178)$$

where H is the magnetic field strength, $\Delta\chi$ the difference of the susceptibilities parallel and perpendicular to the trigonal axis, θ_1 and θ_2 are the angles between the magnetic field and the trigonal axes in both grains of the Bi bicrystal.

Several efforts were made in the past to utilize a magnetic field for the study of grain boundary kinetics in Bi. The orienting effect of a magnetic field on the solidification and grain growth of Bi was investigated by Goetz [326] and Mullins [185], respectively. Fraser et al. [327] showed that a grain, which was generated by recrystallization following a local deformation of a Bi single crystal, grew and consumed the initial single crystal under the action of a magnetic driving force. However, no specific boundary motion was investigated. Since the available magnetic driving force was rather small, the magnetic field in the experiments of Mullins and Fraser et al. was superimposed on growing grains, i.e. a magnetic force was applied to boundaries that were already moving under the force exerted by their surface tension and curvature.

In a recent investigation grain boundary motion was measured by applying a magnetic field to a specially prepared bicrystal, i.e. to a system that

was completely in equilibrium without an applied magnetic field [189]. The experiments were carried out on bicrystals of high purity (99.999%) bismuth. The $90^\circ\langle 112 \rangle$ boundary was examined. The misorientation angle between the trigonal axes in both crystals of the bicrystal was chosen to be 90° in order to gain the maximum possible magnetic driving force (Eq. (3.178)). The investigated boundary was a mixed $90^\circ\langle 112 \rangle$ boundary with a deviation of the boundary plane from the ideal tilt position of $15^\circ \pm 2^\circ$ (twist component) due to the systematical deviation from the pure tilt position by $13 - 17^\circ$ during crystal growth [189, 328]. Prior to their exposure to a magnetic field (the field strength used was $1.63 \cdot 10^7 \text{ A/m}$) the samples were annealed for 10 hours at 230°C in vacuum. To ensure sufficient boundary mobility the magnetic field was imposed on the samples at a temperature of 255°C ($0.97T_m$).

The experiments unambiguously confirmed that grain boundaries in Bi bicrystals actually moved under the action of a magnetic driving force (Fig. 3.103). The observed linear dependence of boundary displacement on annealing time proves the free character of its motion (Fig. 3.104). It was found that after the application of the magnetic field the initially inclined grain boundary plane changed its position and inclination as illustrated in Fig. 3.105 to become a planar grain boundary perpendicular to the free surfaces, which minimized the boundary area. This planar boundary was an asymmetrical (near tilt) grain boundary, inclined 45° to the symmetrical boundary plane. The rotation of the boundary plane during the initial stage of its movement may be explained by the action of an additional driving force for boundary motion, provided by the boundary surface tension. Evidently, this additional driving force was not sufficient to move the grain boundary during annealing without a magnetic field, but it forced the boundary into a position with minimum surface area once it started moving under the action of the magnetic field.

To prove that boundary motion was caused exclusively by the magnetic driving force, the experiment was carried out in two different ways. First, a specimen was mounted in a holder such that the c -axis ($\langle 111 \rangle$) of crystal 1 was directed parallel to the field (Fig. 3.105a). The $\langle 111 \rangle$ axis in crystal 2 in this case was perpendicular to the field, and the grain boundary moved in the direction of the latter crystal due to its higher magnetic free energy. Second, a specimen was mounted in a position where the axis $\langle 111 \rangle$ in crystal 2 was close to the field direction, and the corresponding axis in crystal 1 was perpendicular to the field. The direction of boundary motion in this case was opposite, from crystal 2 toward crystal 1 (Fig. 3.105b). This result provides unambiguous evidence that the grain boundaries in the bicrystals were forced to move by the magnetic driving force only. In addition, some bicrystals were annealed in a magnetic field in both positions, and boundary motion in the opposite direction was observed in the same specimen depending on its position with regard to the magnetic field.

The grain boundary mobility m is given by the ratio of velocity v and driving force P , $m = v/P$. The measurement of boundary motion under a

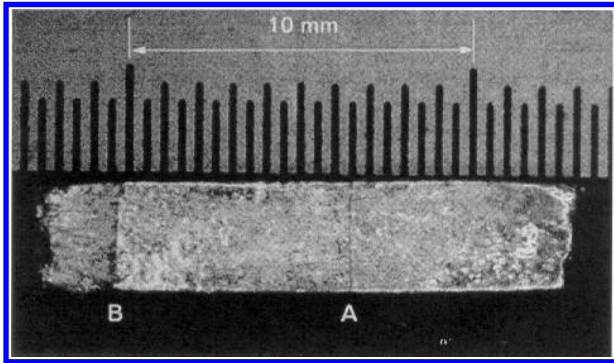


FIGURE 3.103

Displacement of a flat grain boundary in a Bi bicrystal during annealing in a magnetic field. A and B are the initial and final positions of the boundary.

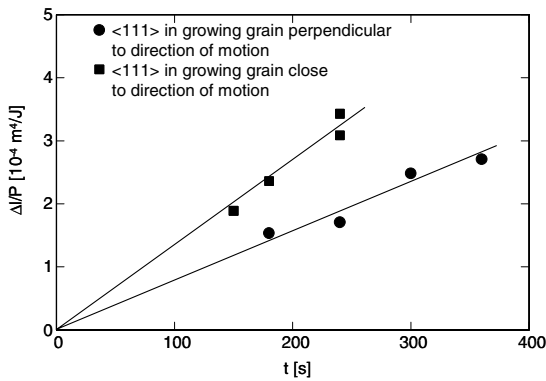
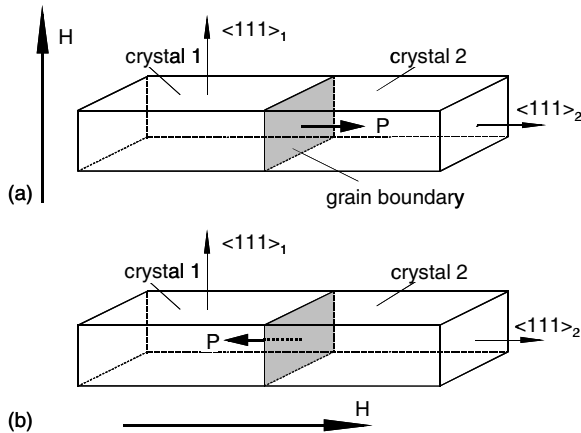


FIGURE 3.104

Normalized displacement of a grain boundary vs. annealing time for the same grain boundary moving in opposite directions.

**FIGURE 3.105**

Geometry of investigated bicrystals and sense of driving force P with regard to direction of the magnetic field H . (a) The axis $\langle 111 \rangle$ in the crystal 1 is directed parallel to the field. (b) The axis $\langle 111 \rangle$ in the crystal 2 is directed parallel to the field, while the axis $\langle 111 \rangle$ in the crystal 1 is perpendicular to the field.

constant magnetic driving force provides a unique opportunity to determine the absolute value of grain boundary mobility. In experiments with curved grain boundaries only the reduced mobility $A_b = m_b \gamma$, where γ is the not exactly known boundary surface tension, can be obtained. For the driving force provided by a striation microstructure, both the surface tension of the low-angle grain boundaries, which form the substructure, and their density are unknown. Also, the average surface tension of the subgrain boundaries and their density may vary along the way of the moving high-angle grain boundary in the sample. The mobility of the boundaries investigated in Bi bicrystals was found to be rather high: on average $m_b \approx 1.1 \cdot 10^{-7} \text{ m}^4/\text{J}\cdot\text{s}$ at 250°C ($= 0.97 T_m$), which results in a very high velocity $v \approx 40 \mu \text{ m/s}$ at a comparably small driving force $P \approx 350 \text{ J/m}^3$. For comparison, the driving force acting on a curved boundary with a radius of curvature of $\approx 0.5 \text{ mm}$, which is typical for experiments on curvature driven boundaries in bicrystals of high purity aluminum, is $\approx 10^3 \text{ J/m}^3$ (assuming $\gamma \approx 0.5 \text{ J/m}^2$), and the boundary mobility at 480°C is $m_{\text{Al}}^{480^\circ\text{C}} \approx 5 \cdot 10^{-7} \text{ m}^4/\text{J}\cdot\text{s}$ [190]. The boundary mobility in high purity aluminum has not been measured at a homologous temperature $T/T_m = 0.97$, as used in the current experiment with Bi but an extrapolation of experimental data to this temperature (which is $T = 630^\circ\text{C}$ for Al) would yield a boundary mobility $m_{\text{Al}}^{630^\circ\text{C}} \approx 5 \cdot 10^{-5} \text{ m}^4/\text{J}\cdot\text{s}$.

In contrast to the symmetric tilt boundary, for the asymmetric tilt boundary the measured boundary mobilities were found to be distinctly different for mo-

tion in opposite directions (Fig. 3.106). For the chosen crystallography of the bicrystals the boundary was less mobile when the c ($\langle 111 \rangle$)-axis in the growing grain was perpendicular to the direction of motion ($m_{\perp} = 8.0 \cdot 10^{-8} \text{ m}^4/\text{J}\cdot\text{s}$) and moved faster when the trigonal c -axis in the growing grain was close to the direction of motion ($m_{\parallel} = 1.3 \cdot 10^{-7} \text{ m}^4/\text{J}\cdot\text{s}$). There are several potential reasons for this anisotropy. First, there is an essential difference in the distance between the crystallographic planes on each side of the boundary. An estimation shows that this factor may change the velocity of grain boundary motion; however, this factor is unlikely to change the velocity by more than 20%, which is distinctly less than the observed effect. Second, because grain boundary motion in Bi bicrystals may be influenced by impurity drag, the difference in the diffusivity of impurities in two opposite direction in the anisotropic structure of Bi should be taken into consideration. In this respect it is interesting that the symmetric tilt boundary exhibited a much higher mobility than the asymmetric tilt boundary and did not show a dependence of boundary mobility on the sense of motion (Fig. 3.106).

It is finally noted that a flat grain boundary can also be moved by the application of other external fields, e.g. an electrical field in anisotropic dielectric materials or an elastic stress in elastically anisotropic materials. The latter has been studied extensively by experiments [341]–[357] and computer simulations [358]. In this context it was proposed that the motion of grain boundaries is always associated with a shear deformation. This is the subject of current research

3.5.9.4 Generation of electrical currents and magnetic fields by grain boundary motion

The motion of a grain boundary in a magnetic field can be considered as a motion of a conductor in a magnetic field, which causes an electromotive force in accordance with the Faraday effect. Such approach was put forward and has been considered comprehensively in [340]. It is evident that the structure of a grain boundary including the electronic structure is different from the structure of the interior of the adjacent crystals. Thus, in principle, the migration of a grain boundary can also be considered as the motion of an electrical conductor with electromagnetic properties different from the bulk. The motion of a conductor in a magnetic field causes an electromotive force (Faraday, 1831), i.e. dissipates energy.

In a microscopic model a grain boundary is assumed to migrate by the exchange of lattice sites across the boundary. In the mesoscopic model the grain boundary is associated with a volume of different magnetic susceptibility. The atomic exchange will take a small, but nevertheless finite time τ . In the course of the time τ the magnetic induction changes in the volume where the atomic rearrangement takes place. This leads to the generation of an electric field in accordance with Faraday's law. The induced electrical current generates its own magnetic field H_G (Biot-Savart-Laplace law). The

directions of the induced current and the magnetic field H_G are determined by the Lenz rule in such a way that the generated magnetic flux counteracts the imposed magnetic field, which corresponds to an electromotive force. As a result the magnetic driving force decreases. This can be expressed as a reduction of grain boundary mobility m .

The migration process can be described as a displacement of a grain boundary area $S \approx r^2$ by a distance r with the velocity $v \approx \frac{r}{\tau}$. The change of the magnetic flux $\Delta\Phi$ which occurs in a time τ through the area r^2 normal to the direction of the magnetic field with the strength H can be estimated as $\Delta\Phi \approx \Delta\chi H r^2$, where $\Delta\chi$ is the difference of the magnetic susceptibilities of adjacent grains along the magnetic field direction.

This induces an electromotive force

$$E_{\text{ind}} \approx \frac{\Delta\Phi}{c\tau} = \frac{\Delta\chi H r^2}{c\tau} \quad (3.179)$$

(c — speed of light) and, in turn, the magnetic field

$$H_G = \frac{r^2\sigma}{c^2\tau}\Delta\chi H \equiv \frac{\tau_0}{\tau}\Delta\chi H \quad (3.180)$$

where σ is some effective conductivity of a nano-region in close proximity to the grain boundary for the time of its rearrangement. It is conceivable that this conductivity is different from the bulk conductivity. The characteristic time $\tau_0 = \frac{\sigma r^2}{c^2}$ has a physical meaning. It is the time for attenuation of electromagnetic perturbations in the volume $V \approx r^3$. The effect can be considered in terms of a reduction in the driving force of grain boundary motion, or as a reduction in grain boundary mobility m . This conclusion as well as the derivation is quite general and may be applied to any moving interface. In particular, it can be applied to the asymmetry of grain boundary mobility for grain boundary motion in opposite directions in a magnetic field as experimentally observed in Bi. So, for the motion of an asymmetrical grain boundary in opposite directions the parameter $\beta = \frac{\Delta m}{m}$ should be essentially different where m is the mobility at zero field. The only exception is a symmetrical grain boundary where β must be exactly the same. The induced perturbation will eventually be converted to Joule heat Q which contributes additionally to the grain boundary slowdown. However, the calculations show that this contribution is negligible.

As an alternative approach let us consider the motion of a grain boundary with constant velocity v . The induced magnetic field H_G and the dragging force F can be expressed as

$$H_G = \frac{I}{c}\ell = \frac{\sigma v \ell}{c^2}\Delta\chi H \quad (3.181)$$

$$F = H_G H \ell^2$$

correspondingly. ℓ is the thickness or width of the sample.

In this case the reduction in grain boundary mobility is equal to

$$\frac{\Delta m}{m} \approx \frac{\sigma v \ell}{c^2} \quad (3.182)$$

The approach put forward in [340] permits us to analyze the different configurations of a grain boundary in the magnetic field. For example, for the configuration considered in Fig. 3.105a the relations for H_G can be expressed as

$$H_G = \frac{I}{c\ell} = \frac{2\sigma v d_m \Delta \chi H}{c^2} \quad (3.183)$$

The magnetic field H_G (Eq.(3.183)) acts as a dragging force F which causes a change in grain boundary mobility

$$\frac{\Delta m}{m} \approx \frac{2\sigma v d_m \Delta \chi}{c^2} \quad (3.184)$$

The magnetic thickness d_m may be much larger than the “crystallographic” grain boundary thickness, since it does not have to be smaller than the “formation length” of the magnetic susceptibility.

Generally, the relative change in grain boundary mobility is reasonably described by the order of magnitude given by Eq. (3.184). The comparatively large magnetic field generated in the volume $V \sim \ell^3$ (contrary to r^3 for the microscopic approach, where r is in the range of the lattice constant) in the course of grain boundary motion increases essentially the dragging force due to the conversion of magnetic energy into Joule heat and in turn the change of grain boundary mobility

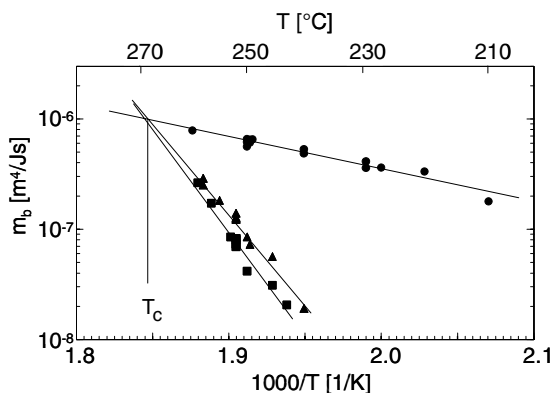
$$F_{\text{Joule}} = \left(\frac{\sigma v \ell}{c^2} \right)^3 \frac{\ell^2}{d_m^2} (\Delta \chi H)^2 \quad (3.185)$$

$$\frac{\Delta m_{\text{Joule}}}{m} = \left(\frac{\sigma v \ell}{c^2} \right)^3 \left(\frac{\ell}{d_m} \right)^2 \frac{\Delta \chi}{\kappa} \quad (3.186)$$

where κ is the “configuration” coefficient of the magnetic driving force $\kappa = \frac{P}{\Delta \chi H^2}$. One can see that the Joule dragging force F_{Joule} is proportional to v^4 contrary to the Lenz dragging force F , which is associated exclusively with the magnetic field induced by grain boundary motion $F \sim v^2$.

The numerical estimates do not render very high values of the magnetically induced dragging force — in the range of 10^{-3} : $\frac{\Delta m}{m} \approx 10^{-3}$ for the effect of Joule dragging [340]. However, it is stressed that the very strong dependency of the mobility reduction on the grain boundary velocity (Eq. (3.186)) can tangibly affect the final result.

The approach put forward in [340] is one way to explain the strange results of grain boundary mobility measured during the boundary motion in opposite directions, as described in Sec. 3.5.9.3. The electromagnetic dragging force in

**FIGURE 3.106**

Temperature dependence of symmetrical and asymmetrical tilt boundaries in Bi.

a strong magnetic field cannot quantitatively explain the observed results, though. We would like to emphasize that the discussed effects are applicable to the motion of any defect in solids, especially for the high speed movement of dislocations in a magnetic field. In any event, if this asymmetry of grain boundary mobility also holds for other metals, it would have a serious impact on our understanding of grain boundary motion, since the mobility of a grain boundary is commonly conceived not to depend on its direction of motion.

3.6 Effect of Wetting Phase Transitions on Grain Boundary Migration

Grain boundaries are liable to undergo phase transitions under certain conditions. The character of grain boundary structure may change from a strongly ordered CSL type (special) to a disordered (non-special or random) type with rising temperature as discussed in Chapter 2. This structural transition must, of course, be reflected in a discontinuous mobility change at the transition temperature as was indeed observed experimentally (Fig. 3.107) [329]. In the presence of alloying elements the boundary may be loaded with impurities or break free from its segregated solutes, which again corresponds to a grain boundary phase transition and thus markedly affects grain boundary mobility as discussed at length in Secs. 3.3, 3.5.3 and 3.5.5.

If the alloying elements can give rise to a chemical phase transformation

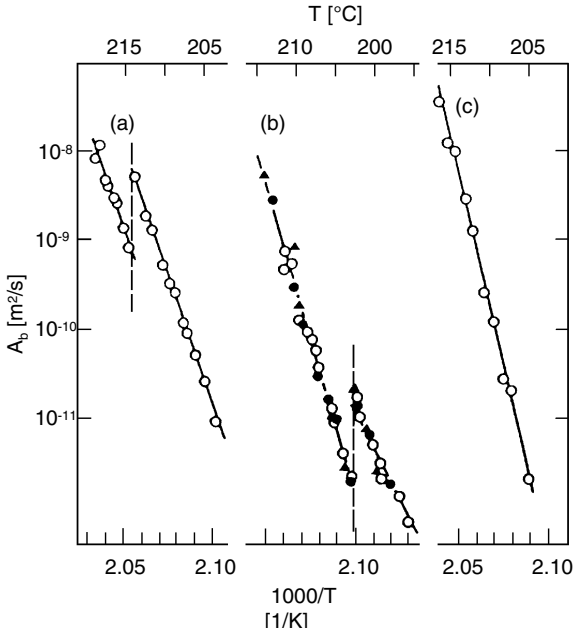


FIGURE 3.107

Temperature dependence of the reduced mobility of $\langle 001 \rangle$ tilt boundaries in tin in the vicinity of a structural phase transition. Misorientation angles: (a) 28.2° ; (b) 29.0° ; (c) 29.5° . Fig. 3.107b presents data for samples with different migration driving force. The temperature T_c of the structural transition is seen to be independent of the migration driving force.

(dissociation) in the boundary, complex phenomena may arise due to the different properties of the bulk and boundary phase, e.g. in terms of composition and melting. In this section we will consider grain boundary wetting phase transitions in the systems Al-Ga and Al-Pb and their effect on grain boundary mobility.

All known experiments on bicrystals have demonstrated a reduction in the rate of grain boundary migration by impurities. Theoretically, this is accounted for by the impurity drag theories, which predict a decrease in the boundary mobility by adsorbed impurities. However, there are some remarkable exceptions to the common rule that can cause unexpected and surprising results. Examples of such unusual impurity effects on grain boundary motion were observed recently in aluminum doped with a minor amount of Ga (10 ppm, Fig. 3.108) [330] or lead [331]. In contrast to other alloying elements Ga (as well as Pb at high temperatures) raises the mobility and thus accelerates grain boundary migration in Al. This effect was studied on $\langle 111 \rangle$ tilt grain boundaries with the angles of misorientation 38.2° ($\Sigma 7$) and 40.5° . The dramatic rise in grain boundary mobility with the addition of 10 ppm Ga was interpreted in [330] as a consequence of a change in the boundary structure and the mechanism of boundary migration owing to a pre-wetting phase transition and formation of a liquid (or quasi-liquid) Ga-rich layer on the grain boundary.

In [332] this phenomenon was studied on the same $\langle 111 \rangle$ tilt grain boundaries (angles of misorientation are 38.2° and 40.5°), over a wide range of Ga concentration. Fig. 3.108 demonstrates the temperature dependence of boundary mobility for the boundaries investigated. The migration activation enthalpy was found to be constant for a given grain misorientation over the entire temperature range investigated for all Al alloys despite different Ga content. The concentration dependence of boundary mobility is presented in Fig. 3.109. After the initial drastic rise, compared to pure Al, the boundary mobility in Ga-doped aluminum decreases with increasing concentration of Ga.

The behavior of a moving grain boundary in Al-Pb alloys differs substantially from both the motion in pure Al and in Al-Ga alloys (Fig. 3.110). At a certain temperature T_w , which depends on the misorientation angle, the migration parameters (enthalpy of activation and pre-exponential factor) change abruptly for both grain boundaries studied. Qualitatively, the same was observed for $\langle 111 \rangle$ tilt boundaries with misorientation 38.2° (special boundary $\Sigma 7$ and 40.5° non-special boundary) [330]. The characteristic temperature T_w is higher for the special boundary $\Sigma 7$ than for the 40.5° boundary. At relatively low temperatures $T < T_w$ boundary motion is unstable (Fig. 3.110), and the activation enthalpy of it in this temperature range is mostly smaller than that for grain boundary migration in pure aluminum (Fig. 3.110). The observed features of grain boundary motion in the Al-Pb alloy along with the abrupt change in the boundary mobility and its parameters can be associated with a grain boundary wetting phase transition [331]. The unstable boundary

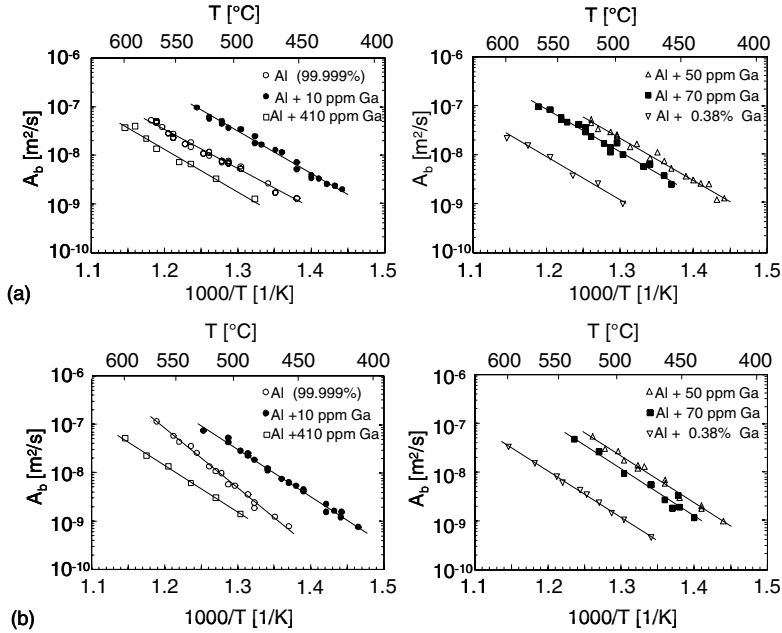


FIGURE 3.108

Temperature dependence of reduced boundary mobility for $\langle 111 \rangle$ tilt boundaries in Al with different contents of Ga (a) 38.2° ; (b) 40.5° .

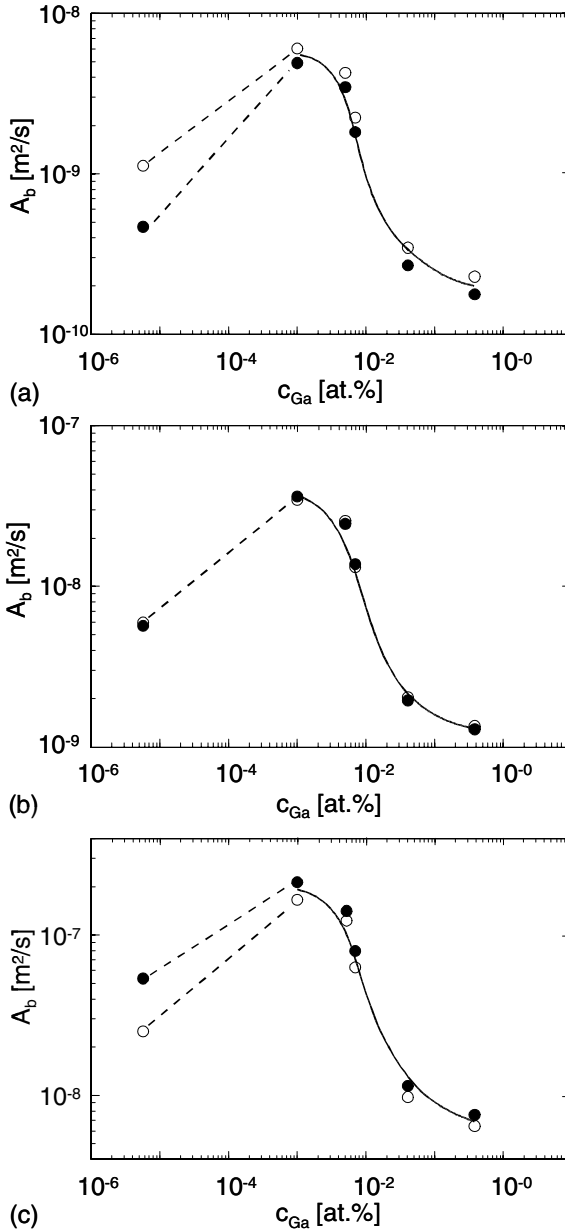


FIGURE 3.109

Dependence of reduced boundary mobility on Ga concentration for 38.2° (○) and 40.5° (●) $\{111\}$ tilt boundaries in Al at different temperatures: (a) — 450°C; (b) — 500°C; (c) — 550°C.

motion at somewhat lower temperatures is most probably related to the interaction of the grain boundary with mobile liquid lead droplets. Above the wetting transition temperature, the boundary is completely wetted by liquid lead, and this drastically changes the mechanism of grain boundary motion. Therefore, the observed temperature dependence of grain boundary migration in Al doped with minor amounts (20 ppm) of Pb [331] suggests that the lead solubility in Al is indeed negligible, so that even at concentrations as low as 20 ppm lead exists in aluminum as a second phase.

The size of lead particles can be estimated [331] using the experimentally determined grain boundary mobilities at $T < T_w$ (Fig. 3.110). For fine particles their dominant mechanism of motion is the mechanism of surface diffusion [207] (Table 3.2). The experimentally determined velocity of grain boundary motion at $T < T_w$ can be considered as the critical velocity for the joint motion of grain boundary and particles. From this the radius of the particles was estimated as $5 \cdot 10^{-8} \leq r \leq 10^{-7} \text{ m}$.

If grain boundary migration at $T < T_w$ is controlled by the mobility of liquid lead droplets, then the activation enthalpy of grain boundary motion should be close to the activation enthalpy of droplet motion [208]. This conclusion is supported by the experimental data. As is well known, the activation enthalpy for surface diffusion is significantly lower than that for the bulk diffusion. The activation enthalpy for bulk self-diffusion in Al is $H_D \sim 1.5 \text{ eV}$, whereas the activation enthalpy for boundary migration at $T < T_w$ was found to be 0.8–1.0 eV for both grain boundaries studied.

Wetting phenomena at grain boundaries require two phases (liquid and solid) being in equilibrium with each other. The contact angle Θ depends on the grain boundary surface tension γ and the surface tension of solid-liquid interface γ_{SL} : $\gamma = 2\gamma_{SL}\cos\Theta$ (Fig. 3.111).

For $\gamma \geq 2\gamma_{SL}$ the boundary is completely wetted by the liquid phase, and $\Theta = 0$. In the latter case the boundary cannot coexist with the liquid and is replaced by a layer of the liquid phase. The temperature dependencies of the surface tensions γ and γ_{SL} are schematically shown in Fig. 3.112. The wetting transition at the grain boundary occurs at the temperature T_w , where $\gamma(T)$ intersects $2\gamma_{SL}(T)$. If two grain boundaries have different surface tensions, we may expect that their wetting transitions occur at different temperatures: namely the lower the γ , the higher the T_w . This agrees with experimental results [331]: the energy of the $\Sigma 7$ special boundary is lower than the energy of the 40.5° non-special boundary, and the wetting transition temperature for the special grain boundary ($T_{w,s.} = 560^\circ\text{C}$) is noticeably higher than that for the non-special one ($T_{w,ns.} = 535^\circ\text{C}$) (Fig. 3.110).

Usually the wetting transition at a grain boundary is observed under circumstances where a bicrystal is in contact (equilibrium) with a large amount of liquid. Such type of wetting may be called an “external” wetting in contrast to the “internal” wetting, when the wetting liquid is distributed as fine particles (droplets) in the bulk of the grains. For an internal wetting transition, when the grain boundary becomes covered by a liquid layer of thickness λ at

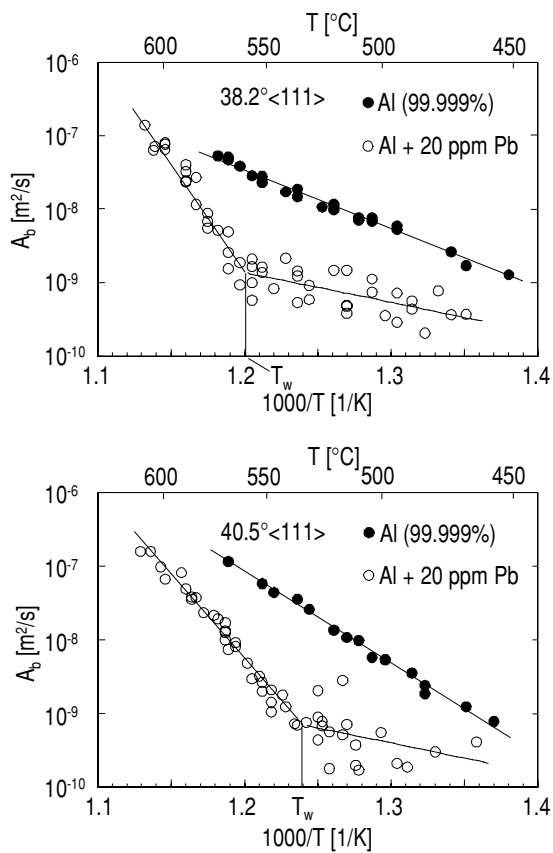


FIGURE 3.110
Temperature dependence of reduced grain boundary mobility in pure Al and Al-20 ppmPb.

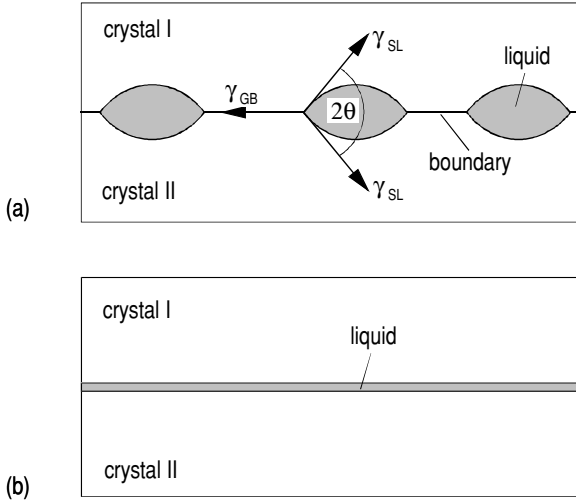


FIGURE 3.111

Illustration of the prewetting transition in a grain boundary. (a) Incomplete wetting ($2\Theta > 0$); (b) complete wetting ($2\Theta = 0$).

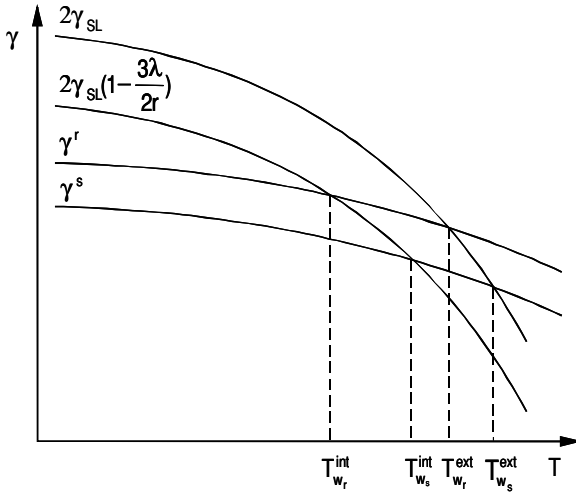


FIGURE 3.112

Schematic temperature dependence of surface tension at the solid/liquid interface ($2\gamma_{SL}(T)$), special boundary (γ^s) and random grain boundaries (γ^r).

the expense of droplets in the bulk, the change in free energy of the system can be written as

$$\Delta G = -\gamma + 2\gamma_{SL} - \frac{3\lambda}{r}\gamma_{SL} \quad (3.187)$$

The third term on the right-hand side of Eq.(3.187) describes the gain in free energy due to the reduction of the total interphase (solid-liquid) area when the liquid inclusions of radius r are transformed into a liquid boundary layer. According to Eq. (3.187) and Fig. 3.112 the temperature of an internal wetting transition should be lower than that of an external wetting transition, which also corresponds to experimental observations [333].

In addition to the grain boundary wetting phase transition, where the boundary is covered by a thin layer of a second phase, which is also a bulk equilibrium phase under the given conditions, there is a prewetting (or pre-melting) grain boundary transition when the grain boundary becomes covered by a layer of definite thickness of a phase which is not an equilibrium bulk phase under such conditions. The grain boundary phase transformation in Al-Ga alloys is attributed to this kind of interfacial phase transitions. The obtained results, i.e. decrease of boundary mobility and invariance of migration activation enthalpy with increasing Ga concentration, are in agreement with the hypothesis [330] that a change of boundary migration mechanism upon Ga addition is associated with the formation of an interlayer of Ga-rich wetting phase on the grain boundary. The rate controlling process of grain boundary migration in this case cannot be the mass transport across the wetting phase interlayer, because the activation enthalpy should then be on the order of 0.1 eV (activation enthalpy for diffusion in liquids), i.e. much smaller than observed in experiment. Rather, grain boundary motion is apparently controlled by the detachment of atoms from the shrinking grain, which occurs on the crystal/interlayer interface. The magnitude of activation enthalpy is determined by the boundary migration mechanism, and must depend on structure and properties of the crystal/interlayer interface, but obviously should be independent of the bulk impurity concentration. This was actually confirmed by the experimental results (Fig. 3.108a).

A rise in the bulk Ga concentration leads to an increase in the boundary thickness after the prewetting phase transition on the grain boundary, as can be easily demonstrated in a quasi-chemical ideal solution approach of the involved phases [334, 335].

3.7 Compensation Effect in Grain Boundary Motion

3.7.1 The Fundamental Rate Equation

It is textbook knowledge that the temperature dependence of the absolute rate ρ of thermally activated processes is governed by the Arrhenius relation

$$\rho = \rho_0 \exp\left(-\frac{H}{kT}\right) \quad (3.188)$$

where ρ_0 denotes the preexponential factor, H the enthalpy of activation and k is the Boltzmann constant. For evaluation of experimental data the activation enthalpy is commonly determined from the slope $-H/k$ of an Arrhenius plot $\ln \rho$ vs. $1/T$. Little attention is usually paid to the preexponential factor ρ_0 , although it has been long known that ρ_0 changes, if the system is biased such as to vary H . However, as we will show below, there is overwhelming experimental evidence that the preexponential factor is strongly related to the activation enthalpy: ρ_0 increases or decreases if H increases or decreases according to the relation

$$H = \alpha \ln \rho_0 + \beta \quad (3.189)$$

Here α and β are constants, the meaning of which will be dealt with below. Eq. (3.189) is referred to as compensation effect (CE), since it strongly moderates the effect of a variation of H on the value of the absolute reaction rate ρ , such that above a so-called compensation temperature, $T_c = \alpha/k$, the process with the highest activation enthalpy has the highest reaction rate, while for $T < T_c$ the process with the lowest value of H proceeds fastest.

Although the CE has been also reported for bulk processes, e.g. bulk diffusion of solute atoms in a crystalline matrix [336, 337] or diffusion in whiskers of different size [338], it is most pronounced in surface and interfacial reaction phenomena, since in such cases the changes of H and ρ_0 can be quite substantial. This was found for diffusion along grain boundaries and interfaces [339, 359, 367], grain boundary migration [274, 303] and spreading of extrinsic grain boundary dislocations [368].

The CE probably was first reported by Constable [369] for dehydrogenation of ethanol on a copper catalyst. More recently it has been found in other thermally activated chemical, physical and biological processes and systems [370]–[372]. The compensation effect in surface reactions and catalysis has been associated with the interaction of adatoms in adsorbed surface layers [373]–[377]. The variation of enthalpy and preexponential factor was attributed to the number of ways in which the heat bath can furnish the energy needed to overcome the barrier [378]. This, however, is closely connected with the interactions in the adsorbed layers.

In this section we will review much of the existing data on the compensation effect in thermally activated interface processes, although the fundamental

concepts hold for surfaces and bulk processes as well. Since it is difficult to track details of data published by other authors, we shall restrict ourselves to the considerable body of data obtained in our own interface research activities.

We will show that the compensation effect can be rationalized from thermodynamic fundamentals and how it applies to select solid state kinetics, in particular grain boundary migration.

3.7.2 Examples

The CE manifests itself by a linear relation between the preexponential factor ρ_0 and the activation enthalpy H , as expressed by Eq. (3.189). This equation implies the existence of a temperature $T_c = \alpha/k$, the compensation temperature (CT), where all reaction rates ρ of the considered group of thermally activated processes are the same, i.e. the lines for the corresponding Arrhenius plots intersect at temperature T_c . Inserting Eq. (3.189) into Eq. (3.188) at $T = T_c$ yields

$$\rho(T_c) = \exp\left(-\frac{\beta}{kT_c}\right) \quad (3.190)$$

In effect, the “Arrhenius coordinates” T_c and β govern the kinetics of the thermally activated process, since they uniquely link H and $\ln\rho_0$ according to Eq. (3.189). In the following we present some pertinent examples for different grain boundary processes.

The compensation lines $H(\ln A_0)$ for the reduced mobility $A = A_0 \exp(-H/kT)$ of $\langle 111 \rangle$ [274] and $\langle 100 \rangle$ [379] tilt boundaries in Al, $\langle 11\bar{2}0 \rangle$ tilt boundaries in Zn [380] and $\langle 001 \rangle$ tilt boundaries in Sn [302] are given in Figs. 3.113–3.116. The corresponding compensation temperatures are for Al $\langle 111 \rangle$: 450°C, Al $\langle 100 \rangle$: 770°C, Zn $\langle 11\bar{2}0 \rangle$: 420°C, and Sn $\langle 001 \rangle$: 236°C. Fig. 3.117 shows results for Zn diffusion along tilt and twist boundaries in Al [381]. In this case T_c is in the range 450–500°C. The CE is not confined to single phase systems as is obvious from Figs. 3.118–3.120 [359, 382]. For interface diffusion in $\langle 001 \rangle$ twist boundaries between Sn and Ge monocrystals in two temperature ranges, namely 40°C and 184°C, the compensation temperature equals 27°C in the former and 220°C in the latter temperature regime. It is noted in this context that the gray-white phase transition in tin takes place at a temperature of 20°C.

3.7.3 Thermodynamics of the Activated State

3.7.3.1 Nature of the Activated State

The preexponential factor in the Arrhenius relation (Eq. (3.188)) consists of some geometrical constants ρ_1 , a frequency factor ν and an entropy term $\exp(S/k)$, which depend on the kinetic quantity under consideration, like dif-

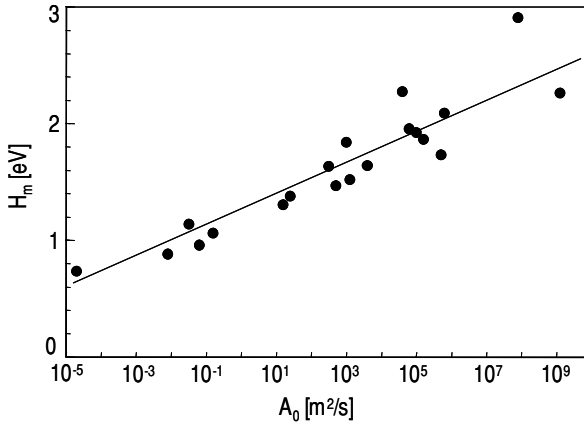


FIGURE 3.113

Dependence of migration activation enthalpy H_m on the (reduced) pre-exponential mobility factor A_0 for $\langle 111 \rangle$ tilt grain boundaries in Al.

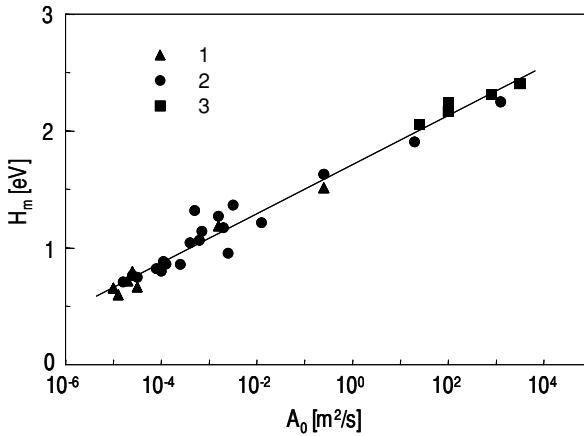


FIGURE 3.114

Dependence of migration activation enthalpy H_m on the (reduced) pre-exponential mobility A_0 factor for $\langle 100 \rangle$ tilt grain boundaries in Al; 1 — Al 99.99995at.%; 2 — Al 99.9992at.%; 3 — Al 99.98at.%.

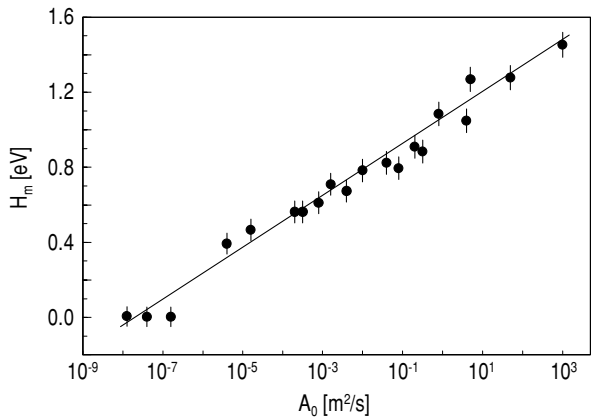


FIGURE 3.115
Dependence of migration activation enthalpy H_m on the (reduced) preexponential mobility factor A_0 for $\langle 11\bar{2}0 \rangle$ tilt grain boundaries in Zn.

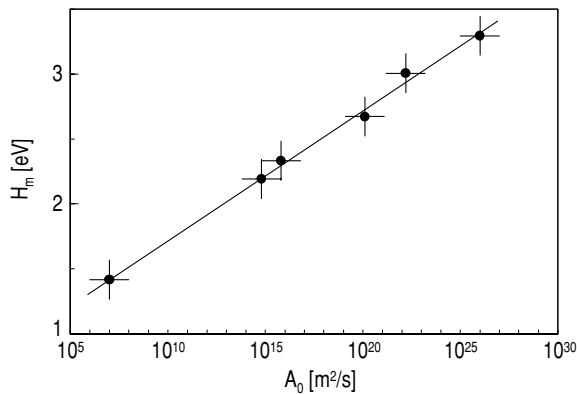


FIGURE 3.116
Dependence of migration activation enthalpy H_m on the (reduced) preexponential mobility factor A_0 for $\langle 001 \rangle$ tilt grain boundaries in Sn.

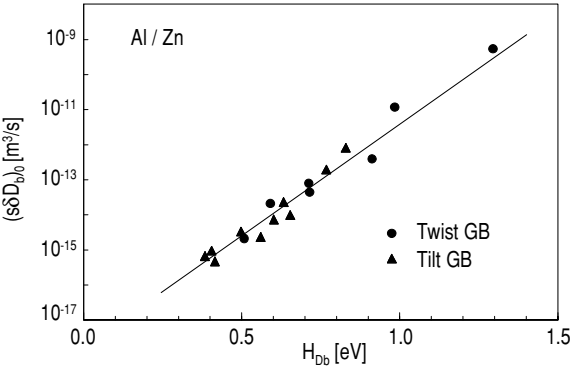


FIGURE 3.117
Dependence of the preexponential factor $(s\delta D_b)$ on activation enthalpy H_{Db} for grain boundary diffusion of Zn along tilt and twist grain boundaries in Al.

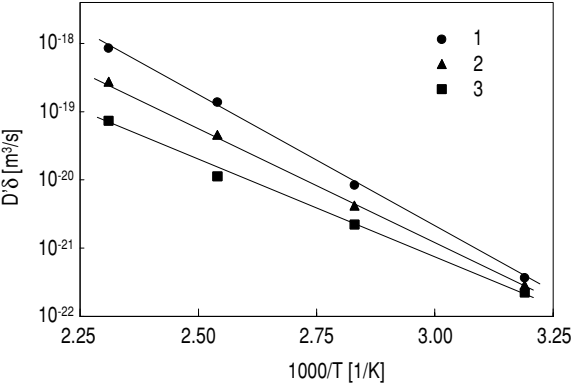


FIGURE 3.118
Temperature dependence of the diffusional permeability of In in $\langle 001 \rangle$ twist interphase boundaries in Sn-Ge. Misorientation angles: 1–2°; 2–6°; 0–3°.

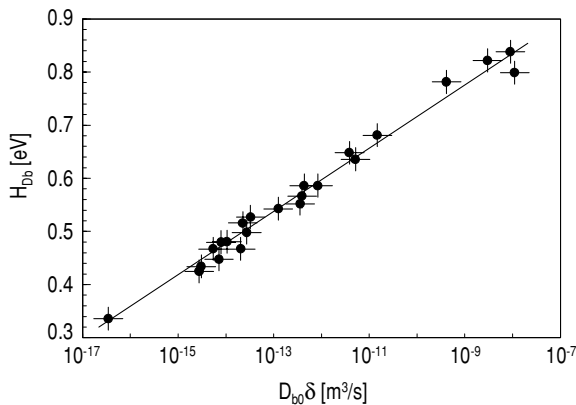


FIGURE 3.119
Dependence of the activation enthalpy H_{Db} for In diffusion along $\langle 001 \rangle$ twist interphase boundaries in Sn-Ge on the preexponential factor $D_{b0}\delta$ in the temperature range 313–433K.

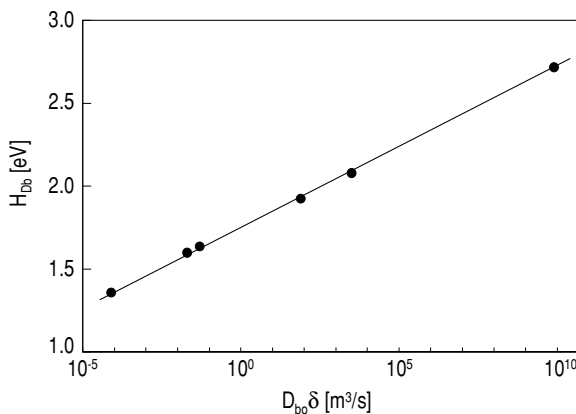


FIGURE 3.120
Same as Fig. 3.119, but in the temperature range 457–490K.

fusivity, mobility, chemical reaction rate etc. For a given material and kinetic process, $\rho_1\nu$ is constant and for convenience the dimensionless quantity $\rho/(\rho_1\nu) \cong \tilde{\rho}$ can be considered instead, i.e.

$$\tilde{\rho} = \exp\left(-\frac{G}{kT}\right) = \exp\left(\frac{S}{k}\right) \exp\left(-\frac{H}{kT}\right) = \tilde{\rho}_0 \exp\left(-\frac{H}{kT}\right) \quad (3.191)$$

A linear relationship between H and $\log \tilde{\rho}_0$ is equivalent to the fact that the entropy of activation is linearly related or even proportional to the activation enthalpy. This observed coupling of entropy and enthalpy of activation suggests that the activated state is not a random energy fluctuation in space and time, but a defined and thus reproducible although unstable state, which is described by its respective thermodynamic functions. Its attainment from the stable ground state corresponds to a first-order phase transformation. In an interface we can associate the activated state with a local change of the interface structure, or more precisely, of a structure that the interface could attain if a more stable state would not exist for the given thermodynamic conditions. In this sense we consider the saddle point configuration of the activated state as the minimum free energy configuration of all potential metastable states for the given thermodynamic system (Fig. 3.121) and the attainment of the activated state as a displacive phase transformation of first order. In this concept the compensation temperature is the equilibrium temperature for such a virtual phase transformation.

The compensation relation (Eq. (3.189)) can be easily derived under these conditions. As an example we consider the grain boundary mobility m , which is known to depend on grain boundary structure and chemistry. Application of the Arrhenius relation (Eq. (3.191)) to the grain boundary mobility m_b yields

$$\ln m_b = \ln m_0 - \frac{H}{kT} = \frac{S}{k} - \frac{H}{kT} \quad (3.192)$$

where $S = k \ln m_0$ and H represent the activation entropy and enthalpy of grain boundary mobility, respectively.

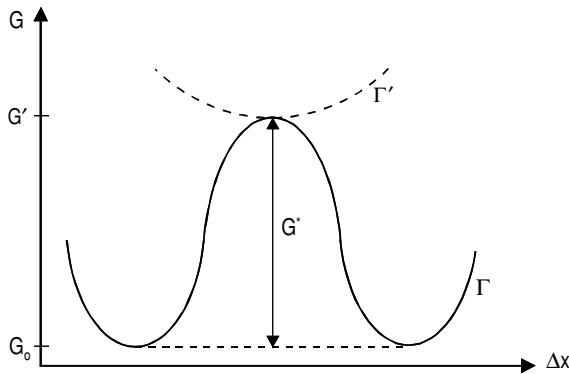
Let the parameter λ denote some intensive structural or chemical specification, like angle of misorientation, composition, surface tension etc. If λ changes slightly from the reference state λ_0 , then S and H change accordingly

$$\ln m_0(\lambda) = \frac{S(\lambda)}{k} = \frac{1}{k} \left[S(\lambda_0) + \left. \frac{dS}{d\lambda} \right|_{\lambda=\lambda_0} \cdot (\lambda - \lambda_0) + \dots \right] \quad (3.193)$$

$$H(\lambda) = H(\lambda_0) + \left. \frac{dH}{d\lambda} \right|_{\lambda=\lambda_0} \cdot (\lambda - \lambda_0) + \dots \quad (3.194)$$

As S and H change only slightly, since $G = H - T \cdot S$ is at minimum, a linear approximation is sufficient, and solving Eq. (3.193) for $\lambda - \lambda_0$ yields

$$\ln m_0(\lambda) = \frac{S(\lambda_0) - H(\lambda_0)/T_c}{k} + \frac{H(\lambda)}{kT_c} \quad (3.195a)$$

**FIGURE 3.121**

Simplified correspondence of thermally activated state Γ and thermodynamically metastable state Γ' .

where

$$T_c = \frac{\left. \frac{dH}{d\lambda} \right|_{\lambda=\lambda_0}}{\left. \frac{dS}{d\lambda} \right|_{\lambda=\lambda_0}} = \left. \frac{dH}{dS} \right|_{\lambda=\lambda_0} \quad (3.195b)$$

is the compensation temperature, i.e. the equilibrium temperature between ground state and activated state, or equilibrium phase and “barrier” phase. This result implies that the barrier phase, i.e. the activated state, is a metastable phase closely related to the equilibrium state. It corresponds to a configuration of atoms with the smallest increase of potential energy with respect to the ground state. It seems obvious that equilibrium states occurring in the vicinity of the compensation temperature most easily satisfy this requirement. These conclusions are supported by the observation that the compensation temperature is often close to the equilibrium temperature of a nearby phase transition [382]. Of course, when considering interface phenomena, potential metastable phases need not be confined to bulk phases.

3.7.3.2 Equilibrium Thermodynamics Approach

The simplified treatment given above already delivers the CE, i.e. Eq. (3.189) and defines the compensation temperature. In the following we shall give a more complete treatment of the thermodynamics of the activated state, based on the previously rationalized assumption that the transition from the equilibrium state to the activated state is a first-order phase transition.

Let $G_0 = H_0 - TS_0$ denote the Gibbs free energy (referred to as free energy in the following) of the equilibrium phase and $G' = G_0 + G^* \equiv (H_0 + H^*) - T(S_0 + S^*)$ the respective function of the barrier phase. We want to investigate the behavior of the barrier phase close to the point of

phase transformation. Enthalpy and entropy of the barrier phase are assumed to depend on temperature, pressure and a constitutional parameter λ , as referred to in the previous section, which varies with modification of the interfacial system but does not noticeably affect the transformation temperature.

At a temperature T and pressure p near the transition point (T_c, p_c)

$$\begin{aligned} \Delta G' &= (G' - G_0) = G^* \cong (\Delta G')_{T_c, p_c} + \\ &+ \frac{\partial}{\partial T} (\Delta G')_{T_c, p_c} \Delta T + \frac{\partial}{\partial p} (\Delta G')_{T_c, p_c} \Delta p + \dots \end{aligned} \quad (3.196a)$$

where

$$\Delta T = T - T_c, \quad \Delta p = p - p_c \quad (3.196b)$$

Introducing the thermodynamic functions

$$\Delta G' = G^* = E^* - TS^* + pV^* \cong -S^*(T_c, p_c, \lambda) \Delta T + V^*(T_c, p_c, \lambda) \Delta p \quad (3.197)$$

we obtain

$$\begin{aligned} E^* &= S^*(T_c, p_c, \lambda) T_c + T [S^*(T, p, \lambda) - S^*(T_c, p_c, \lambda)] - \\ &- V^*(T_c, p_c, \lambda) p_c + p [V^*(T_c, p_c, \lambda) - V^*(T, p, \lambda)] \end{aligned} \quad (3.198)$$

Approximating the terms in the square brackets by a series expansion to first-order

$$S^*(T, p_c, \lambda) - S^*(T_c, p, \lambda) \cong \frac{(C_p^*)_{T_c, p_c, \lambda}}{T_c} \Delta T + \Delta \left(\frac{C_p^*}{T} \xi \right)_{T_c, p_c, \lambda} \Delta p + \dots$$

because of $c_p/T = (dS/(dT))_{p, N}$, where N is the number of particles, and introducing

$$\xi = \left(\frac{\partial T}{\partial p} \right)_{V, N}, \quad \eta = \left(\frac{\partial V}{\partial T} \right)_{p, N}, \quad \zeta = \left(\frac{\partial V}{\partial p} \right)_{T, N} \quad (3.199)$$

we arrive at

$$\begin{aligned} E^* &\cong S^*(T_c, p_c, \lambda) T_c + T \left(\frac{C_p^*}{T_c} \right)_{T_c, p_c, \lambda} \Delta T + \\ &+ T \left(\frac{C_p^*}{T} \xi \right)_{T_c, p_c, \lambda} \Delta p - V^*(T_c, p_c, \lambda) p_c + \\ &+ p(\eta)_{T_c, p_c, \lambda} \Delta T + p(\zeta)_{T_c, p_c, \lambda} \Delta p \end{aligned} \quad (3.200)$$

Then, if the intensive parameters of an experiment are not too different from their value at compensation, i.e. $\Delta T/T_c, \Delta p/p_c \ll 1$, Eq. (3.200) simplifies to

$$E^* \cong S^*(T_c, p_c, \lambda) T_c - V^*(T_c, p_c, \lambda) p_c \quad (3.201)$$

Eq. (3.201) manifests a linear relation between the enthalpy and entropy (or volume) of activation, i.e. there is a special, metastable, “barrier” phase, which is attained by a first-order phase transformation at a critical temperature, pressure, etc. and which we refer to as compensation temperature, pressure, etc.

Thus, in analogy to the (temperature) compensation effect for constant pressure at variable temperature, there is also a (pressure) compensation effect for constant temperature at variable pressure. For a temperature $T \neq T_c$ close to the transition temperature the free energy change owing to a change of pressure from p_c to p reads

$$\Delta G' \equiv G^* = E^*(\lambda) - TS^*(T, p_c, \lambda) + pV^*(T, p_c, \lambda) = V^*(T, p_c, \lambda) \Delta p \quad (3.202)$$

Combining Eqs. (3.201) and (3.202)

$$TS^*(T, p_c, \lambda) - T_c S^*(T_c, p_c, \lambda) \cong p_c [V^*(T, p_c, \lambda) - V^*(T_c, p_c, \lambda)] \quad (3.203)$$

or in first-order approximation, introducing the coefficient of thermal expansion $\alpha^* = 1/V^* (dV^*/dT)_{p,N}$

$$S^*(T, p_c, \lambda) \cong p_c V^* \alpha^* - c_p^* \quad (3.204)$$

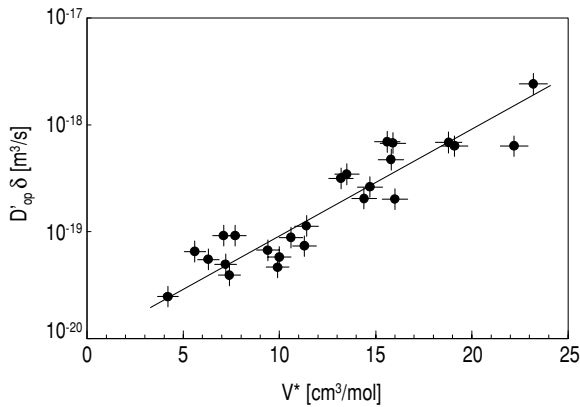
i.e. the entropy S^* is linearly related to the activation volume V^* . In fact, such relation was experimentally verified (Fig. 3.122) [359]. In essence, the considerations prove that the compensation effect can be derived from equilibrium thermodynamics of the activated state which, in turn, can be associated with a potential metastable state.¹¹

3.7.3.3 Irreversible Thermodynamics Approach

The activated state is not a stable equilibrium state and, therefore, the return of the system to the equilibrium state ought to comply with the laws of irreversible thermodynamics. One of the fundamental principles of nonequilibrium thermodynamics is the principle of maximum rate of change of the thermodynamic potential of the system [260, 261, 383]. This means, as stated by Ziegler [260], that a system with given thermodynamic forces strives for equilibrium on the shortest way, i.e. at constant temperature and pressure with the maximum rate of Gibbs free energy reduction. It is noted that this pertains to relative rather than absolute minima of the thermodynamic potential function, i.e. to the most stable intermediate state of the system.

In application of these principles to interface processes let us consider, as

¹¹It is noted that Eq. (3.196a) also holds if T is rather different from T_c . Since the higher-order terms $d^n S/dT^n$ are practically zero, the series expansion of $S(T)$ can always be truncated after the first-order term.

**FIGURE 3.122**

Dependence of the product under zero pressure on activation volume at 161°C.

an example, the case of grain boundary motion under a constant driving force P . The rate of reduction of the free energy of the system dG/dt ,

$$\frac{dG}{dt} = -vP \quad (3.205)$$

where $v = m_b P$ is the velocity of grain boundary motion, m_b the grain boundary mobility. Accordingly,

$$\frac{dG}{dt} = -vP = -m_b P^2 \quad (3.206)$$

and

$$m_b = m_0 e^{-\frac{H^*}{kT}}; \quad m_0 = e^{\frac{S^*}{k}} \quad (3.207)$$

where $G^* = E^* - TS^* + pV^* = H^* - TS^*$ is the Gibbs free energy of activation.

Let us consider the extremum of the function in Eq. (3.206) with respect to an arbitrary state parameter λ :

$$\frac{d}{d\lambda} \left(\frac{dG}{dt} \right) = \frac{d}{d\lambda} (-m_b P^2) = 0 \quad (3.208)$$

and since P is independent of λ

$$\frac{d}{d\lambda} (m_b) = 0 \quad (3.209)$$

With $\lambda = \lambda_0$ at the maximum of dG/dt and using Eqs.(3.206) and (3.207)

$$\frac{d}{d\lambda} (H^* - TS^*)_{\lambda=\lambda_0} = 0 \quad (3.210)$$

Again we obtain the compensation temperature

$$T_c = \left(\frac{dH^*}{dS^*} \right)_{\lambda=\lambda_0} \quad (3.211)$$

As a result, the CE is in agreement with the principles of nonequilibrium thermodynamics and yields the previously derived CT.

It is noted that there are several atomistic approaches of the activation process. Either the energy dissipation into the adjoining finite volume is considered [384]–[386], or, alternatively, the transition state is examined as a heterophase fluctuation [387].

3.7.4 Applications

3.7.4.1 The Island Model of Grain Boundary Migration

To reveal the meaning and significance of the CE and the CT we will study a simple model system, namely grain boundary migration according to the “island” model as proposed by Mott long ago [162]. The model assumes that groups of n atoms “melt” on the side of the vanishing grain and become attached to the side of the growing grain. The activated, metastable state is identified with a frozen liquid state. This permits one to determine the entropy and enthalpy of activation, namely

$$S^* = \frac{nL}{T_m}, \quad H^* = nL \quad (3.212)$$

where L is the heat of melting per atom, and T_m is the melting temperature. The velocity v of the grain boundary according to this model reads

$$v = b\nu n \frac{\Delta G}{kT} \exp\left(\frac{S^*}{k}\right) \exp\left(-\frac{H^*}{kT}\right) \quad (3.213)$$

where b is the atomic spacing and ν the Debye frequency.

It is obvious from Eq. (3.213) that the model complies with the compensation effect: the enthalpy of activation is proportional to the activation entropy.

$$H^* = T_m S^* \quad (3.214)$$

and, therefore,

$$T_c = \frac{dH^*}{dS^*} = T_m \quad (3.215)$$

An identical result can be obtained in terms of irreversible thermodynamics according to Eq. (3.211).

3.7.4.2 Brown-Ashby Relations

Brown and Ashby [388] analyzed diffusion data for a wide range of solids (metals and ceramics) and, as a result, found three correlations for a given structure and bond type

$$D(T_m) = \kappa_1 \quad (3.216)$$

$$\frac{H^*}{kT_m^0} = \kappa_2 \quad (3.217)$$

and

$$V^* = \frac{H^*}{T_m^0} \left(\frac{dT_m^0}{dp} \right) \quad (3.218)$$

where κ_1 and κ_2 are constants, which in first order are independent of the pressure p ; T_m^0 is the melting point at atmospheric pressure and k is the Boltzmann constant.

We will show that Eqs. (3.216)–(3.218) are in full agreement with the concepts of the CE as developed above [389]. If “for a given structure and bond type” [388] the compensation effect is obeyed, the compensation temperature necessarily coincides with the melting point, as for pure elements not undergoing a phase transition in solid state, T_m is the only temperature for a first-order phase transition in the temperature range discussed. Then, in accordance with Eq. (3.191) we obtain for bulk diffusion

$$H^* = kT_m \ln D_0 + \beta \quad (3.219)$$

and at $T = T_m$

$$D(T_m) = e^{-\frac{\beta}{\kappa T_m}} \quad (3.220)$$

Apparently Eq. (3.220) exactly corresponds to the empirical relation given by Eq. (3.219). We shall not discuss Eq. (3.217), which is a special case of the more general relation (3.218). Most interesting is the third relation, Eq. (3.218). Let us consider this relation in terms of the “activation-barrier-phase.” The change in the transition point (compensation temperature T_c) with pressure p is given by the Clausius-Clapeyron equation

$$\frac{\Delta V}{\Delta S} = \frac{dT_c}{dp} \quad (3.221)$$

With

$$\Delta V = V' - V_0 = V^* \quad \text{and} \quad \Delta S = S' - S_0 = S^* \quad (3.222)$$

we obtain

$$\frac{V^*(\lambda)}{S^*(\lambda)} = \frac{dT_c}{dp} \quad (3.223)$$

Since

$$T_c^0 S^*(\lambda) = E^*(\lambda) \quad (3.224)$$

Eq. (3.223) can be rewritten as

$$\frac{V^* \cdot T_c^0}{E^*} = \frac{dT_c}{dp} \quad (3.225)$$

If the compensation temperature coincides with the melting point we arrive at the Brown-Ashby relation

$$V^* = \frac{E^*}{T_m^0} \frac{dT_m}{dp} \quad (3.226)$$

Therefore, the Brown-Ashby relation can be considered a direct consequence of the CE [389].

3.7.4.3 Impact of the CE on Thermally Activated Processes

Fig. 3.50 gives the measured rate of boundary migration vs. the misorientation angle about a common $\langle 111 \rangle$ tilt axis [264]. The maximum velocity is attained for a misorientation angle of $\sim 41^\circ$. Over many years this result worried scientists (including the authors themselves [390]). The point is that close to the $41^\circ \langle 111 \rangle$ tilt grain boundary there is the special grain boundary $\Sigma 7$: $38.2^\circ \langle 111 \rangle$ with apparently high mobility and low activation energy of migration [190, 275, 280, 299]. Therefore, the $41^\circ \langle 111 \rangle$ boundary was tacitly assumed to represent a scatter of the $\Sigma 7$ boundary. Nevertheless, numerous growth selection experiments provided strong experimental evidence that the maximum mobility was attained at misorientation angles above 40° , i.e. close to 41° and not 38.2° .

The misorientation dependence of activation enthalpy for migration of $\langle 111 \rangle$ tilt grain boundaries in the vicinity of the special grain boundary $\Sigma 7$ (38.2°) as obtained from bicrystal experiments [190] is given in Fig. 3.123. Obviously, the activation enthalpy is at maximum for a misorientation angle close to 41° . However, the misorientation dependence of the preexponential factor behaves the same way, i.e. attains a maximum for 41° misorientation (Fig. 3.124). In fact, the CE with a CT of $\sim 450^\circ\text{C}$ (Fig. 3.125) causes the grain boundaries with the lowest activation energy to be most mobile at $T < CT$, whereas for $T > CT$ the opposite is the case (Fig. 3.126). As a result, due to the CE, which boundary moves fastest depends on the temperature range (relative to CT), and this reconciles the contradiction between recrystallization and growth selection experiments mentioned above.

As a general rule the compensation temperature divides the temperature range into two regimes with different relations between the magnitude of reaction rate and energy of activation. When the experiments are conducted below T_c , then the processes with low energies of activation prevail. The reverse is also true; if the measurements are taken above T_c , then the processes with high energies of activation dominate the kinetics (Fig. 3.127).

The example given above also elucidates another consequence of the CE, namely the drastically mitigated influence of the activation enthalpy. For

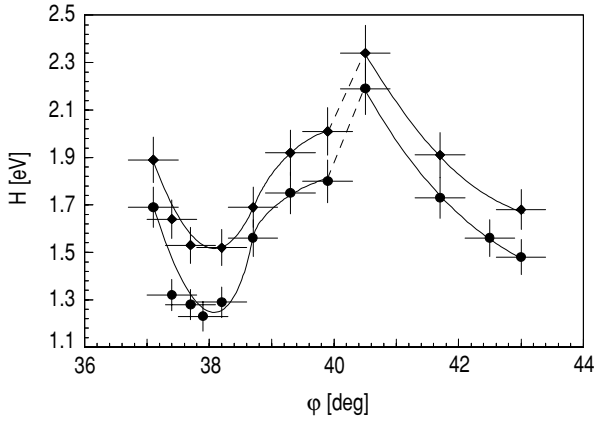


FIGURE 3.123

Activation enthalpy H_m for migration of $\langle 111 \rangle$ tilt grain boundaries as a function of misorientation angle φ for two different aluminum charges: Al I - 0.4 ppm of impurity; Al II - 1.0 ppm of impurity.

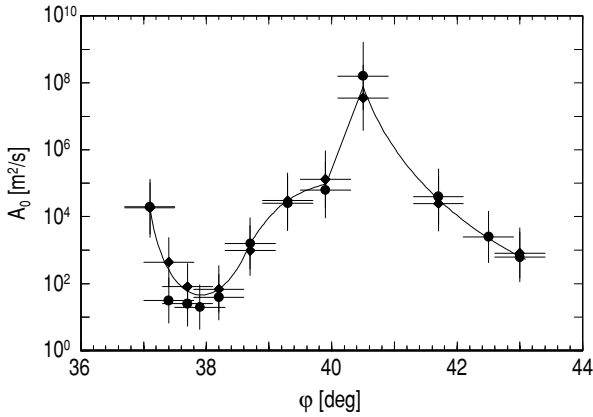


FIGURE 3.124

Reduced mobility preexponential factor A_0 of $\langle 111 \rangle$ tilt grain boundaries as a function of misorientation angle φ for two different aluminum charges: (● - Al I; ♦ - Al II).

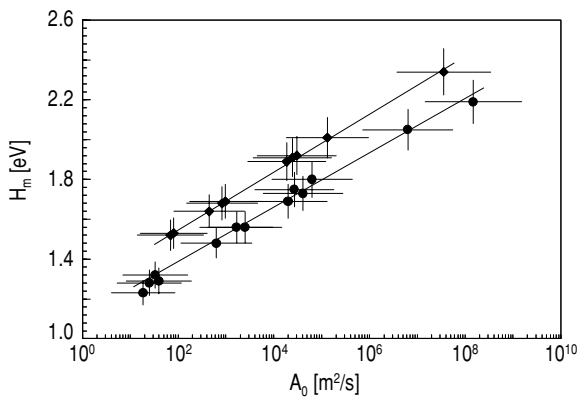


FIGURE 3.125
Dependence of migration activation enthalpy H_m on the preexponential reduced mobility factor A_0 for the investigated $\langle 111 \rangle$ tilt grain boundaries in high-purity aluminum of two different charges: (● - Al I; ◆ - Al II).

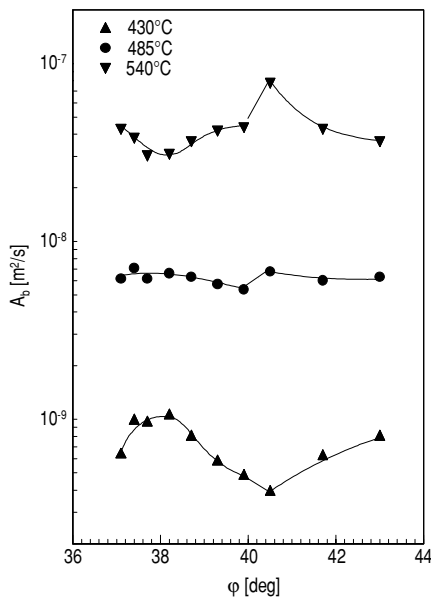


FIGURE 3.126
Misorientation dependence of grain boundary reduced mobility A for $\langle 111 \rangle$ tilt boundaries in Al II at different temperatures.

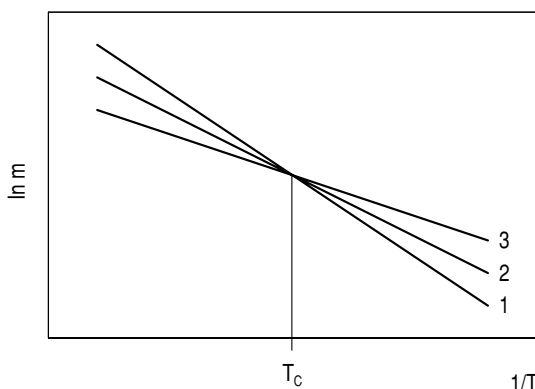


FIGURE 3.127

Schematic sketch demonstrating the impact of the CE on grain boundary mobility m above and below the CT. ($H_1^* > H_2^* > H_3^*$; $m_{01} > m_{02} > m_{03}$; $T > T_c$: $m_1 > m_2 > m_3$; $T < T_c$: $m_1 < m_2 < m_3$.)

instance, in the case of two different $\langle 111 \rangle$ tilt grain boundaries ($\Sigma 7$ and $40.5^\circ \langle 111 \rangle$) in Al the activation enthalpies for grain boundary migration are ~ 1.24 eV and 2.1 eV, respectively. If we take into account the difference of the activation enthalpy only, then at 480°C the mobilities of the two boundaries would differ by six orders of magnitude, while, in reality, due to the CE, they differ by not more than a factor of 3!

However, very often conclusions are drawn only on the basis of the magnitude of the activation energy. For instance, on this basis it is contended a small amount of impurities (0.001% Mn) in Al reduces the rate of boundary migration by many orders of magnitude (up to 10^{11} times) [390, 391]. Because of the CE this is very unlikely to happen and has never been observed. In essence, the compensation effect controls the kinetics of the processes (at least, interfacial reactions), restricting and compensating the influence of the involved activation parameters, in particular of the activation enthalpy.

3.7.4.4 The CE in Thermally Activated Bulk Processes

The CE is not restricted to interface phenomena. Brief mention has already been made of CE observations on bulk activation processes [336]–[338]. But nowhere is the role of the CE as important as in grain boundary activation processes. As an example let us consider bulk diffusion. In this case the preexponential factor is predicted by Zener's theory [392], which assumes that the Gibbs free energy G^* of an atom in the transition state — i.e. in the saddle

point configuration — is defined by the work of elastic deformation

$$G^* = \frac{1}{2}\mu\varepsilon_0^2 \quad (3.227)$$

where ε_0 is some effective elastic strain, μ the relevant elastic modulus [392]. Since G_m^* is a free energy, the corresponding entropy

$$S^* = - \left(\frac{\partial G^*}{\partial T} \right)_p \quad (3.228)$$

and, taking into account the very weak temperature dependence of the elastic modulus μ

$$S^* \cong -G_0^* \frac{d(\mu/\mu_0)}{dT} = -H_0^* \frac{d(\mu/\mu_0)}{dT} \quad (3.229)$$

where $G_0^* = H_0^*$ is the Gibbs' free activation energy and enthalpy and μ_0 the shear modulus at 0K, respectively.

Introducing $\chi = d(\mu/\mu_0)/d(T/T_m)$, where T_m is the melting temperature of the solvent: $S^* \cong (\chi H^*)/(T_m)$. According to Zener's theory the preexponential factor for bulk diffusion can change by less than 2–3 orders of magnitude. This is negligible compared to the 7–10 orders of magnitude (!) for grain boundary diffusion or migration. It is emphasized again that this large variance in the preexponential factor is a consequence of the collective nature of grain boundary processes. This is why the CE plays such an important role in interfaces and especially grain boundary kinetics.

3.8 Mechanisms of Grain Boundary Migration

In Sec. 3.1 we mentioned that there is actually no theory of grain boundary migration and hitherto, we have no detailed information on the atomic mechanism of grain boundary migration, except from preliminary results of molecular dynamics computer simulations [309] or high-resolution TEM studies of boundary migration [393]. Because of the importance of this issue to the major topic of this text, we at least want to review and critically assess proposals made in the past.

Early models [162, 178] of grain boundary structure assumed that the grain boundary comprised a certain volume of thickness $\delta \gg b$, i.e. much broader than the spacing of atoms in the adjacent lattices, in other words a wide boundary (Fig. 3.128). Corresponding phenomenological theories of grain boundary motion have to consider that for steady-state motion the three fluxes

$$j_{1b} = j_c = j_{b2} \quad (3.230)$$

where j_{1b} is the flux of atoms detaching from the consumed crystal, j_{b2} is the flux of atoms attaching to the growing crystal and $j_c = v/\Omega_a$ is the convection flux in the boundary, i.e. a flux of atoms that an observer attached to the boundary would see. The attachment and detachment processes will be thermally activated and may occur in a specific respective process (Fig. 3.128b)

$$\begin{aligned} j_{b1} &= c_{11} \frac{b}{\Omega_a} \nu \exp\left(-\frac{G_m}{kT}\right) - c_{12} \frac{b}{\Omega_a} \nu \exp\left(-\frac{G_m + P\Omega_a/2}{kT}\right) \quad (3.231) \\ j_{b2} &= c_{21} \frac{b}{\Omega_a} \nu \exp\left(-\frac{G_m - P\Omega_a/2}{kT}\right) - c_{22} \frac{b}{\Omega_a} \nu \exp\left(-\frac{G_m}{kT}\right) \\ j_c &= \frac{v}{\Omega_a} \end{aligned}$$

where c_{ij} are geometrical constants, G_m the activation free energy of the diffusive atomic motion. Assuming similar structural conditions on both shores of the boundary: $c_{11} = c_{22}$, $c_{12} = c_{21}$ yields $c_{11} = c_{12}$ and with $\Omega_a \approx b^3$

$$\begin{aligned} v &= c_{11} b \nu \left[\exp\left(-\frac{G_m - P\Omega_a/2}{kT}\right) - \exp\left(-\frac{G_m + P\Omega_a/2}{kT}\right) \right] \quad (3.232) \\ &\cong c_{11} \frac{b^4 \nu}{kT} e^{-\frac{G_m}{kT}} \cdot P \end{aligned}$$

which is the fundamental equation already derived in Sec. 3.1.

The detachment and attachment process may be composed of several steps, each of which may be associated with a specific flux equation, which will complicate the system of Eq. (3.231) but yield a similar solution to contain the activation energies for the elementary steps considered. Also, vacancies may be involved in the diffusion process at the boundary edges so that the boundary vacancy concentration can be introduced in Eq. (3.232). Such an approach allows us to introduce crystallography in the modeling of grain boundary migration. This was first proposed by Gleiter [177], who treated grain boundary migration like an evaporation/condensation process on the internal crystal surfaces (Fig. 3.129) and, therefore, tacitly assumed the existence of a wide grain boundary. This concept can, in principle, account for the observed anisotropy of grain boundary migration. Unfortunately, this theory lacks predictive power since most involved crystallographic parameters are unknown. A more serious objection to the theory, however, is the assumption of a wide grain boundary, which is in obvious contradiction to the narrow structure of real grain boundaries observed (Chapter 2).

Mott [162] assumed in his theory of boundary migration (Island model) that the boundary contains small patches of perfect crystal structure which become detached and attached to the crystal surfaces by partial melting and solidification processes. The migration process can be modeled in analogy to Eq. (3.232), except that the free activation energy is the energy of melting of a cluster of n atoms and correspondingly the attachment of the island will move the boundary by a distance nb . While this model is also based on unrealistic

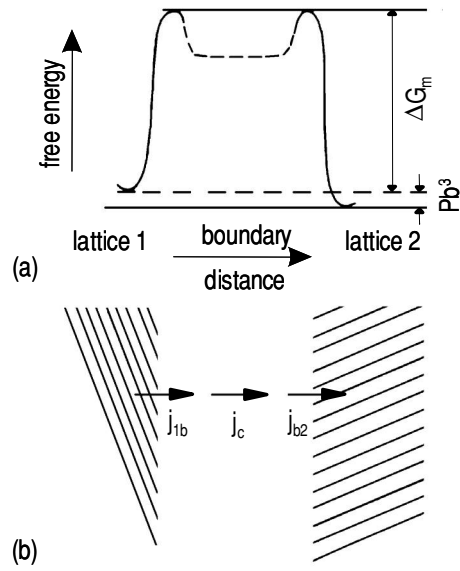


FIGURE 3.128 Wide grain boundary (schematically); (a) free energy barrier; (b) fluxes across the boundary.

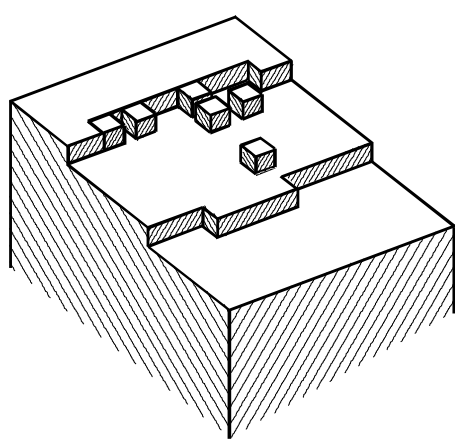


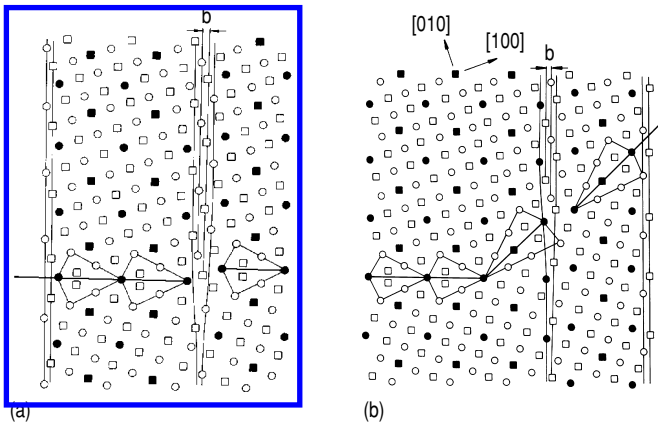
FIGURE 3.129 Model of grain boundary motion according to Gleiter [177]. Atoms are removed from ledges on the surface of the shrinking grain and become attached to ledges on the growing grain surface.

assumptions of the boundary structure and does not incorporate boundary crystallography, it is the first attempt to describe boundary migration as a group motion of atoms. In Sec. 3.5 we reported the frequent observation of high activation energies and large activation volumes of boundary migration which are very difficult to reconcile with a single atom hopping motion as a mechanism of boundary migration. Rather, the measured large activation parameters hint at collective or cooperative motion of atomic groups. Nevertheless, in spite of their interesting approaches to account for specific experimental observations, models based on a wide grain boundary structure are unacceptable since there is unambiguous evidence that boundaries are narrow and not wide (Chapter 2).

The rate theory of boundary migration for narrow boundaries is commonly reduced to a single diffusive step as derived in Sec. 3.1 to yield Eq. (3.232) for the migration rate. Such an approach cannot account for the observed orientation dependence of activation energy and activation volume, since no grain boundary structure is taken into account.

Substantial progress in the understanding of grain boundary phenomena was achieved from the geometrical models of grain boundary structure, predominantly the CSL model (Chapter 2). With regard to grain boundary motion the CSL theory provided two important details. First, as already pointed out by Kronberg and Wilson [394], low Σ CSL boundaries are expected to segregate less and, therefore, are less affected by impurity drag. Second, non-structural — or extrinsic — secondary grain boundary dislocations (SGBD) cause steps¹² on the boundary at the dislocation cores (Fig. 3.130). The displacement of an SGBD along the boundary — an SGBD can only exist in the boundary — is associated with the displacement of the step, which is equivalent to the displacement of the boundary (perpendicular to its plane). The model is particularly attractive for grain boundary migration during recrystallization, because it conveniently unifies the process of dislocation decomposition in the grain boundary and the process of grain boundary migration [395]–[397]. Since the glide motion of dislocations is fundamentally associated with a shear deformation, the process of SGBD motion results in a combined migration and sliding process of the grain boundary. However, during recrystallization and grain growth no macroscopic shape changes are observed. Thus we have to assume that the sum of shears is zero or, correspondingly, that the total Burgers vector strength is zero. The attractive feature of this concept is that it easily predicts orientations of rapid growth. This is the case if the threshold of thermal activation is low, for instance, for SGBDs moving in the grain boundary by simple glide. Even if the Burgers vector is parallel to the grain boundary plane, SGBD glide motion will displace the grain boundary, owing to the step in the boundary associated with the core of the SGBD (Fig. 3.130). An example is the motion of a $\Sigma 3$ coher-

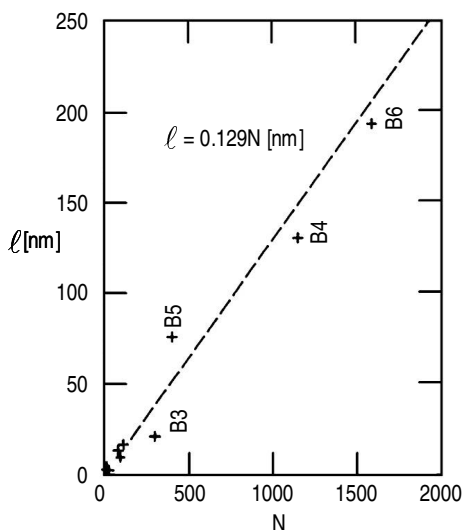
¹²Recently also referred to as disconnections [376].

**FIGURE 3.130**

Secondary grain boundary dislocation in a $\Sigma 5$ tilt boundary [395]. Note step of boundary at dislocation core. (a) Burgers vector parallel to boundary. Dislocation is glissile along the boundary. (b) Burgers vector inclined to boundary. Climb is necessary for dislocation motion in the boundary.

ent twin plane by glide of Shockley partial dislocations in fcc crystals. In fact, Shockley partials are the SGBDs of the twin orientation.

Recent experiments, however, cast doubt on this dislocation concept of grain boundary migration. Babcock and Balluffi [224] conducted in situ experiments on grain boundary migration and sliding in thin-film Au bicrystals in a hot stage of a TEM. The structure of the boundary (an orientation close to $\Sigma 5$) could be exactly defined in terms of SGBD. They confirmed the dislocation model of combined grain boundary sliding and migration by correlating successfully the amount of sliding and migration with the number of moving SGBD and their Burgers vectors (Fig. 3.131). However, this well-defined and correlated motion constituted only a negligible part of the entire grain boundary migration. Occasionally the authors observed jerky motion with very high migration rate, but without any noticeable change in the dislocation structure of the grain boundary. The authors concluded from such results that the normal process of grain boundary migration is not related to the motion of SGBD. Rather, they propose a shuffling mechanism of atoms for the migration process (Fig. 3.132). Such a shuffling model would be supported by recent computer simulations of the motion of a $\Sigma 5$ boundary under the pressure of its curvature. The study revealed cooperative motion of groups of atoms during certain steps of grain boundary migration. The authors concede, however, that this coordinated motion may be facilitated by the high degree of order in the grain boundary and may be less likely in random grain boundaries which, however, also have been observed to move very fast.

**FIGURE 3.131**

Observed boundary displacement ℓ due to slip of N secondary grain boundary dislocations in a thin-film gold bicrystal [224].

The concept of grain boundary migration by coordinated movement of atoms is not new and the current results do not substantiate a model of cooperative motion beyond the state of conjecture. But the findings make it obvious that a closer look at the movement of atoms during the process of grain boundary migration will be necessary to gain a deeper understanding of this seemingly so trivial, but in detail so complicated, process.

More recent molecular dynamics computer simulations on flat $\langle 100 \rangle$ twist boundaries [309] have confirmed such cooperative processes, although the actual trajectory of atoms during boundary migration is very complex owing to a high level of thermal activation in and close to the boundary causing concomitant rapid diffusive motion and high defect (vacancy) concentration. A more detailed analysis of such results is provided in Chapter 5.

Finally, we should mention that there also have been attempts to observe grain boundary migration in situ in an HREM. In fact, such a motion was observed in thin-film bicrystals of Au. However, in analogy to the highly perturbed boundary structure reported from molecular dynamics computer simulations, the high resolution image of the atoms (columns) in the boundary is blurred and prevents elementary steps of motion to be discriminated (Fig. 3.133). However, the comparison of the atomic arrangement of the crystal surfaces in the boundary definitely reveals that ledges on the boundary are dismantled on one (shrinking) side and extended on the other (growing)

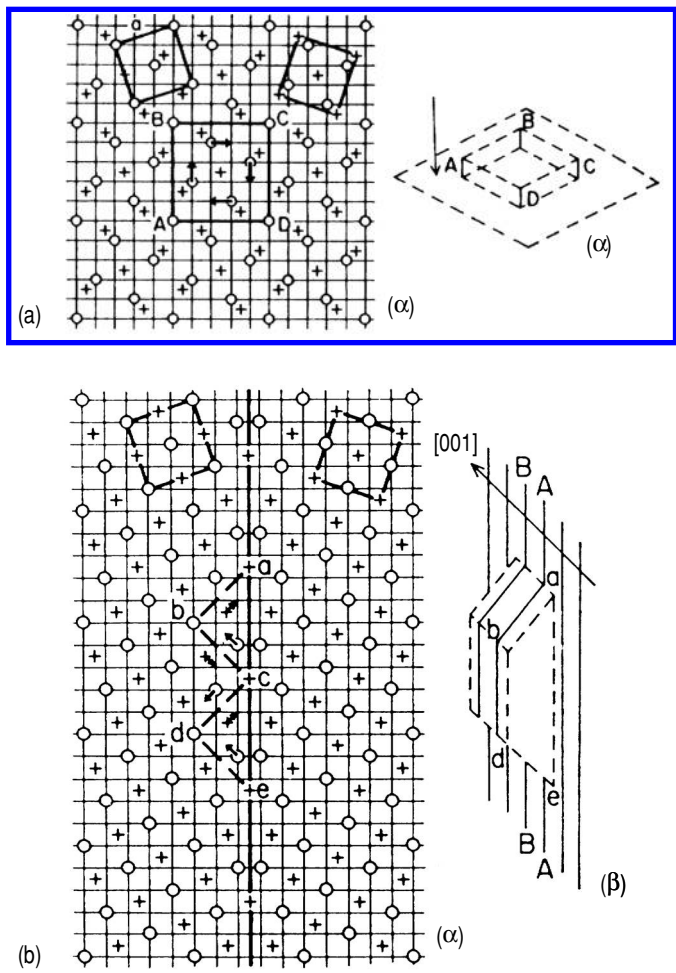


FIGURE 3.132

Shuffling model of grain boundary motion as proposed by Babcock and Balluffi for $\Sigma 5[001]$ twist boundary (a) ((α) The first planes of crystal 1 (0's) and 2 (+'s)) and the same for $\Sigma 5[001]$ tilt grain boundary (b) ((α) the first planes of the crystals 1 and 2; (β) the view of the boundary edge) $[224]$.

side of the boundary (Fig. 3.134).

Eventually, the compensation effect opens up possibilities to look at the mechanisms of grain boundary motion from quite a different perspective. The compensation lines $H(\log A)$ for $\langle 111 \rangle$ tilt grain boundaries in aluminum with different total impurity content or different misorientation, respectively, are given in Figs. 3.135a,b. Obviously, these lines have different slopes and converge toward a range ($H \cong 0.5$ eV, $A_0 \cong 10^{-4}$ cm²s) which is shaded in Fig. 3.135. Interestingly, these magnitudes of activation enthalpy and pre-exponential factor correspond to the values predicted theoretically for grain boundary migration under the assumption that the boundary moves by diffusional jumps of individual atoms across the boundary [164]. We interpret this result and the fact that the actually observed values of H_m and A_0 are much higher, as strong indications that grain boundaries move by the transfer of groups of atoms across the boundary rather than by diffusional jumps of single atoms. This approach is supported by the measurement of the activation volume of boundary migration as reported in Sec. 3.5.8 [304]. In fact, Fig. 3.135 substantiates that a group mechanism is the intrinsic mechanism of grain boundary migration, which would also be engaged for completely pure material. The respective investigation [197] provides evidence that the pre-exponential factor is only little affected by changing solute concentration, i.e. for any impurity content the activation parameters A_0 and H are far higher than any reasonable estimate for a single atom jump mechanism of boundary motion.

Prompted by the results of Rath and Hu [230]–[233] who found a nonlinear relationship between grain boundary migration rate and driving force (erroneously, as explained in Sec. 3.5.1), there have been various attempts to account for this finding theoretically. The impurity drag and vacancy drag theory already predict a nonlinear dynamics of grain boundary motion in very dilute alloys, but only in a very narrow range of conditions which were unlikely to be maintained experimentally. The only way to account for stable nonlinear dynamics is a velocity-dependent mobility in Eq. (3.6), since grain boundary motion is always a drift motion and thus, its velocity proportional to the driving force, as shown in Sec. 3.1.

The grain boundary mobility can depend on velocity only if the migration mechanism is affected by the migration rate. One possible mechanism is the spiral growth mechanism as proposed by [399] in analogy to crystal growth. The centers of the spirals are grain boundary screw dislocations which are assumed to be decomposition products of crystal dislocations, absorbed in the grain boundary during grain boundary motion. Accordingly, the spiral density is proportional to the dislocation density, i.e. proportional to the driving force

$$v = m(P) \cdot P \sim P^2 \quad (3.233)$$

Indeed, spiraling grain boundary screw dislocations were observed experimentally (Fig. 3.136).

While this spiral mechanism at least would account for a nonlinear grain

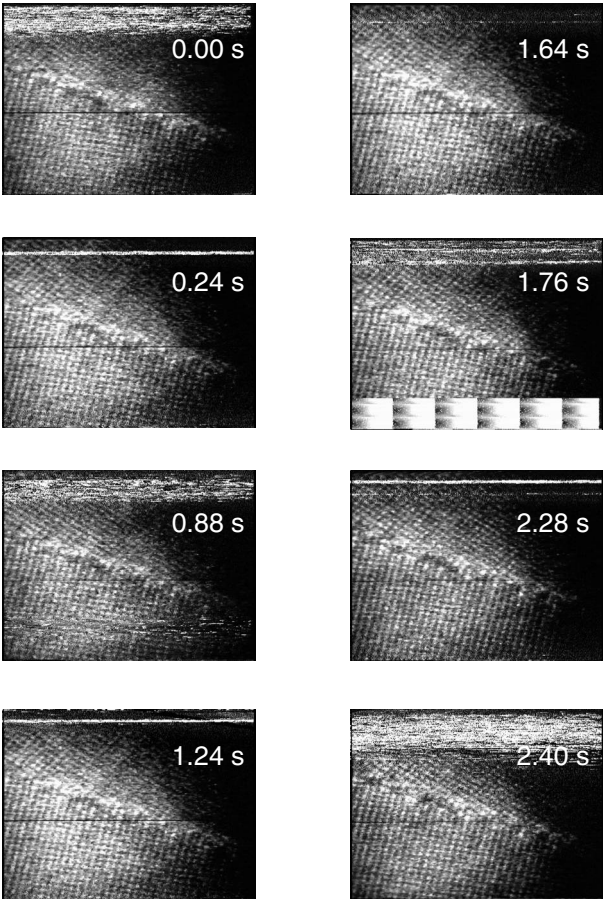


FIGURE 3.133
Selected video frames of HREM images of a moving boundary in a thin-film gold bicrystal.

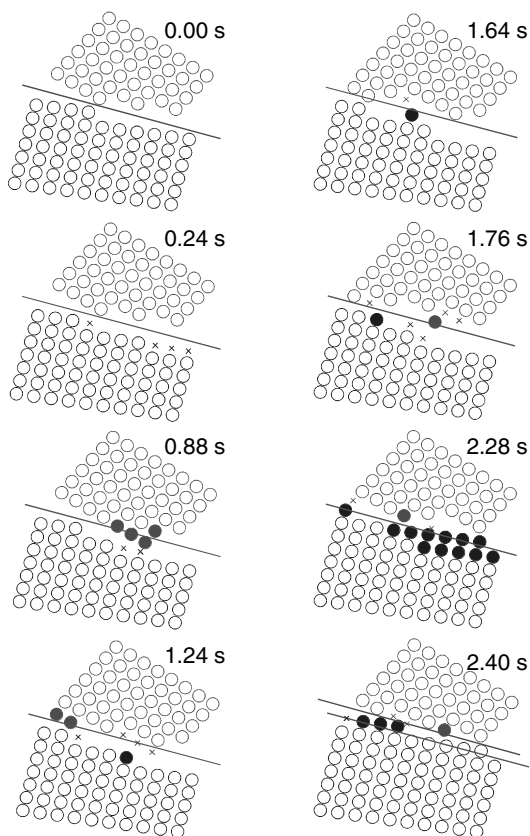


FIGURE 3.134

Resolved atomic positions on video frames shown in [Fig. 3.133](#). The boundary moves first down and then back up. Filled circles denote newly attached atoms, x indicates removed lattice sites. The two lines shown at 2.40 s represent the initial and final positions of the boundary.

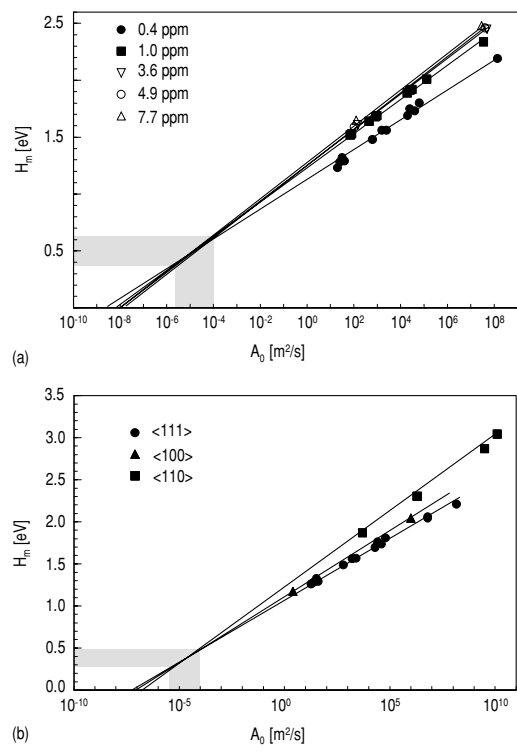


FIGURE 3.135
Compensation lines $H(\log A_0)$ for various tilt grain boundaries in Al: (a) same misorientation but different impurity content; (b) same impurity content but different orientation.

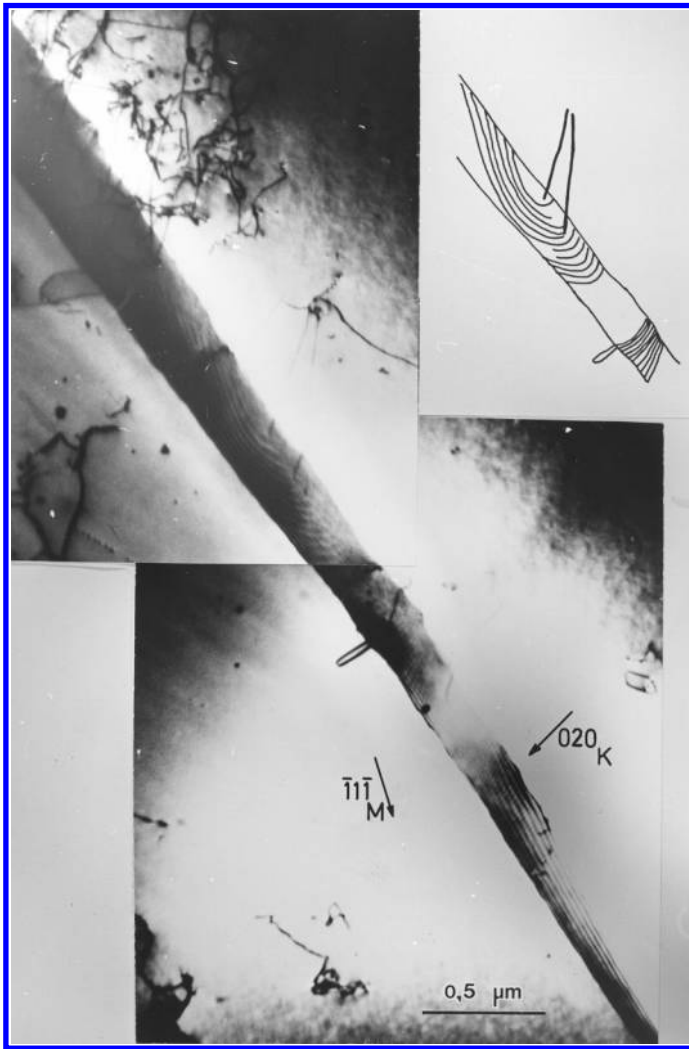
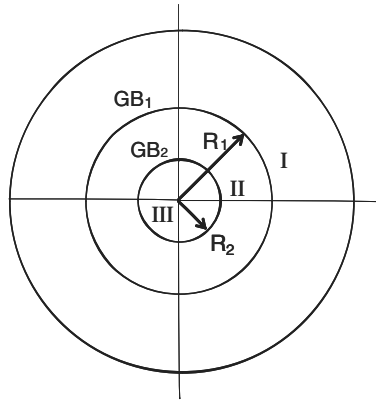


FIGURE 3.136

Generation of a spiral SGBD source by interaction of a crystal dislocation with a moving grain boundary in dynamically recrystallizing Cu at 930°C [398].

boundary dynamics, all accurate measurements so far have ruled out the need for such dependency. It is finally noted that the spiral mechanism is easily combined with vacancy drag owing to the annihilation of the crystal dislocations in the boundary, since the dislocation decomposition will provide both free excess volume (vacancies) as well as secondary grain boundary screw dislocations, i.e. the center of a growth spiral.

**FIGURE 3.137**

Cylindrical tricrystal of Al under hydrostatic pressure at 500°C.

3.9 Problems

PROBLEM 3.1

Evaluate the driving force of grain growth in a sample with boundary excess volume V^{ex} under hydrostatic pressure P .

PROBLEM 3.2

A hydrostatic pressure 10^{10} Pa ($\sim 10^5$ atm) is applied to an Al cylindrical specimen at 500°C (see Fig. 3.137).

The grain boundary excess free volume of the grain boundary GB₁ is equal to $1.4 \cdot 10^{-10} \text{ m}^3/\text{m}^2$, of the grain boundary GB₂ $V^{\text{ex}} = 0.6 \cdot 10^{-10} \text{ m}^3/\text{m}^2$, respectively. The mobility of grain boundaries GB₁ and GB₂ under atmospheric pressure are: $m_{01} = m_{02} = 2 \cdot 10^{-6} \text{ m}^4/\text{J.s}$. The activation volume of grain boundary migration is equal to $V_{ac} = 10^{-5} \text{ m}^3/\text{mol}$ for both grain boundaries (Eq. 3.159).

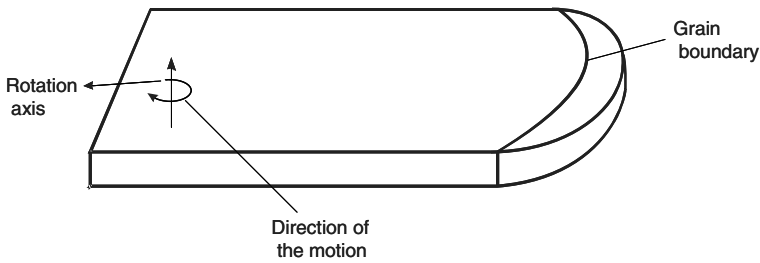
Calculate the time when the grain II will disappear, in other words, the time when grain boundary GB₁ will catch the boundary GB₂.

PROBLEM 3.3

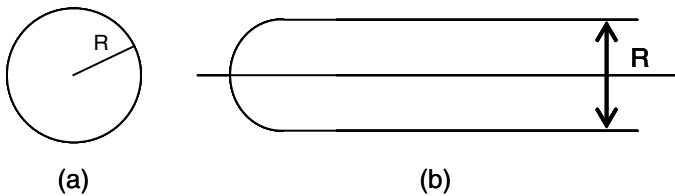
Solve Problem 3.2 for the case that the grains are spheres. The values of all other parameters remain unchanged.

PROBLEM 3.4

Determine the driving force for grain boundary migration in a polycrystal

**FIGURE 3.138**

A turbine blade with a grain boundary during angular motion.

**FIGURE 3.139**

Circular grain (a) and grain boundary half-loop (b).

(e.g. turbine blade) during angular motion (Fig. 3.138).

PROBLEM 3.5

Compare the rate of reduction of the surface free energy for two 2D configurations: a circle with radius R and a half-loop of the size $a = R$ (see Fig. 3.9).

PROBLEM 3.6

Use the so-called weighted mean curvature approach to determine the driving force for grain boundary motion of the following configurations:

- (1) a circular cylinder of radius R ;
- (2) a sphere of radius R ;
- (3) a grain boundary quarter-loop;
- (4) a grain boundary system with triple junctions;
- (5) a 2D regular n -sided polygon under junction kinetics. How does the driving force change with the topological class n of the grain?

Hint: Grains in a 2D system at junction kinetics are bordered by straight lines and tend to form regular polygons.

PROBLEM 3.7

(a) Derive the Lücke-Detert relation for grain boundary motion in a system with impurities in the case of negative adsorption.

(b) Examine when the system satisfies the principle of maximal rate of free energy reduction.

PROBLEM 3.8

Consider the effect of grain boundary detachment of a $38^\circ\langle 111 \rangle$ tilt grain boundary from impurities in Al bicrystals. The driving force for grain boundary motion is $6 \cdot 10^2 \text{ J/m}^3$; the concentration of impurities (at. %): Si = $1 \cdot 10^{-5}$; Zn = $1 \cdot 10^{-5}$; P < $3 \cdot 10^{-4}$; Cu = $7 \cdot 10^{-5}$; Ti < $3 \cdot 10^{-6}$; K = $1 \cdot 10^{-4}$; Cl = $1 \cdot 10^{-4}$. The temperature dependence of grain boundary mobility is given in Fig. 3.70.

Use the Lücke-Detert, Cahn, Lücke-Stüwe approaches to find:

- (1) the impurity which dominates solute drag;
- (2) the diffusion characteristics of this impurity;
- (3) the kinetic properties of the grain boundary;
- (4) the adsorption characteristics of the grain boundary and the impurities.

PROBLEM 3.9

Consider grain growth in a system with mobile particles. The radius of the particles is r , the volume fraction of the particles is c . The number of the particles is constant and the particles are distributed uniformly in the bulk of the sample.

- (1) Derive an expression for the grain growth kinetics when the grain boundary sweeps up the particles during its motion.
- (2) Calculate the time dependency of the mean grain radius.

PROBLEM 3.10

Estimate the efficiency of retardation of grain growth in an Al polycrystal at 673 K by mobile particles. The radius of the particles $r = 50 \text{ nm}$, grain boundary mobility at 673 K $m_b = 2 \cdot 10^{-12} \text{ m}^4/\text{J}\cdot\text{s}$, $\gamma = 0.5 \text{ J/m}^2$. The volume fraction of the particles is $c = 10^{-4}$.

PROBLEM 3.11

Consider a polycrystal with mobile second-phase particles. Show that there is a certain radius of the particles which makes the particle drag most efficient. Hint: Consider a single size particle distribution.

PROBLEM 3.12

Consider three grain boundaries with the following activation parameters of grain boundary migration [404]:

Grain Boundary I (GBI): $H = 1.4 \text{ eV}$, $A_0 = 10^2 \text{ m}^2/\text{s}$

Grain Boundary II (GBII): $H = 2.2 \text{ eV}$, $A_0 = 10^8 \text{ m}^2/\text{s}$

Grain Boundary III (GBIII): $H = 1.67 \text{ eV}$, $A_0 = 10^4 \text{ m}^2/\text{s}$ (1) Prove that the compensation plots of all three grain boundaries intersect in one point.

(2) Determine the compensation temperature of this system.

(3) Calculate the ratio of the grain boundary mobilities at 380°C and 520°C .

PROBLEM 3.13

Consider the migration of a grain boundary in a magnetic field as the motion of an electric conductor. This causes an electromotive force, i.e. generates a drag force on the grain boundary. The change of grain boundary mobility m can be described as

$$\frac{\Delta m}{m} = \frac{\sigma v \ell}{c^2} \quad (3.234)$$

where σ is the conductivity, ℓ is the thickness (or the width) of the sample, c is the speed of light, v is the velocity of grain boundary motion.

Find the time dependency of the mean grain size of a polycrystal during grain growth in a magnetic field.

Thermodynamics and Kinetics of Connected Grain Boundaries

“... You’re the only one who seems to understand about tails. They don’t think — that’s what’s the matter with some of these others. They’re no imagination. A tail isn’t a tail to them, it’s just a Little Bit Extra at the back.”

— *A.A. Milne*

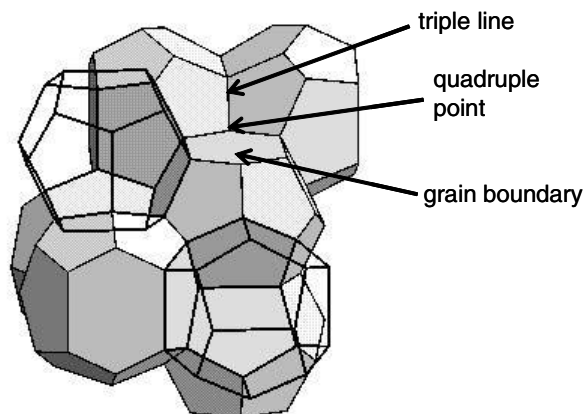
“Expediency, therefore, concurs with Nature in stamping the seal of its approval upon Regularity of conformation; nor has the Law been backward in seconding their efforts. ‘Irregularity of Figure’ means with us the same as, or more than, a combination of moral and criminality with you, and is treated accordingly.”

— *Edwin A. Abbott*

4.1 Microstructural Elements of Polycrystals

The major elements of a polycrystalline structure are grain boundaries. The energy of these grain boundaries is the source of the driving force of grain growth; their motion and interaction either mutually or with crystal dislocations constitute the mechanisms of recrystallization. The main properties of the boundaries, which are essential for the migration process, are the surface tension γ and mobility m_b . As repeatedly mentioned, these properties are likely to differ for different grain boundaries. Furthermore, grain boundary surface tension and mobility can depend on the boundary orientation (inclination). The motion of a grain boundary segment is determined by the grain boundary shape in its closer vicinity.

In the course of motion grain boundaries interact with other grain boundaries. These interactions occur along the lines of intersection of grain boundaries, which are called triple junctions (Fig. 4.1). Besides grain boundaries and triple junctions there is only one more topological element of a 3D arrangement

**FIGURE 4.1**

Grain structure with grain boundary triple lines and quadruple points.

of connected boundaries, a grain boundary quadruple point at the location where four grains meet. At the same time this point is the location where four grain boundary triple lines intersect (Fig. 4.1). There is a large variety of potential triple lines and quadruple junctions in polycrystalline materials since their geometry is determined by the constituting grain boundaries, each of which has five degrees of freedom. Hence, a triple line is defined by 12 independent geometrical parameters; a quadruple point requires 21 quantities for a unique geometrical characterization. Six grain boundaries, four grains and four triple junctions meet in one quadruple point (junction). All other intersections are energetically unprofitable and as a consequence unstable.

These junctions possess specific physical properties (line tension γ^ℓ [1, 400, 402], triple junction and quadruple point mobility m_{tj} and m_{qp} [403]) and move under the action of the surface tension of grain boundaries which join at the junction and, in the case of triple lines, by their own line tension [401].

In the context of triple junctions we will consider only the intersection of three boundaries. It is obvious that a line of intersection of two boundaries does not make sense physically. More than three boundaries might, in principle, intersect along one line; however, such configuration is energetically unprofitable and splits into several triple junctions. More than three grain boundaries do not intersect along a line, but can meet in one point, the so-called quadruple point or quadruple junction of grain boundaries.

4.2 Thermodynamics of Triple Junctions

The thermodynamics of triple junctions might be treated in analogy to Gibbs' thermodynamics of interfaces. We may here remark that a nearer approximation in the theory of equilibrium and stability might be attained by taking special account, in our general equations, of the lines in which surfaces of discontinuity meet. These lines might be treated in a manner entirely analogous to that in which we have treated surfaces of discontinuity. We might recognize linear densities of energy, of entropy, and of the several substances which occur about the line, also a certain linear tension. With respect to these quantities and the temperature and potentials, relations would hold analogous to those which have been demonstrated for surfaces of discontinuity ([1]). The properties of the triple junction line can be determined formally according to Gibbs as a difference between a real system, in which the triple junction line is a distinct configuration, connected to three boundaries (interfaces) and an ideal system, where the structure and the properties of the three boundaries are assumed to be unaffected by their line of intersection. However, generally a change in the length of a triple junction line and in the area of the grain boundaries are rigidly connected. Therefore, changes of triple junction and boundary extensions should be considered in conjunction. Namely, if M is a certain extensive parameter of the system (energy, volume, etc.), then the triple junction and the boundary part can be determined as a difference between the total value of M and its bulk part

$$M^\ell + M^S = M - (M^\alpha + M^\beta) \quad (4.1)$$

where $M^\alpha + M^\beta = M^V$ is the bulk part of the system, α and β are two parts of the system, in particular, the grains; M^ℓ and M^S are the triple junction and boundary parts of the system, respectively.

In accordance with the concepts considered (Chapter 1), we assume that not only the excess surface volume is equal to zero ($V^s = 0$), but also the excess triple junction volume V^ℓ is equal to zero: $V^\alpha + V^\beta = V$, where V is the total volume of the system. Geometrically it means that its 3-D shape, e.g. (column or prism) of a triple junction, is replaced by a line. In analogy to Eq. (1.27) we obtain

$$M = m^\alpha V^\alpha + m^\beta V^\beta + m^s \tilde{A} + m^\ell \ell \quad (4.2)$$

where m^α and m^β are the bulk densities, m^s is the surface excess density, m^ℓ is the triple junction line excess density of the property M , \tilde{A} is the area of the boundaries (interfaces) in the system, ℓ is the length of the triple junction line. Let us introduce one of the most important surface and linear excesses — the adsorption. For the i -th component in accordance with Eq. (1.28) we obtain

$$N_i = n_i^\alpha V^\alpha + n_i^\beta V^\beta + \Gamma_i \tilde{A} + \Gamma_i^\ell \ell \quad (4.3)$$

(N_i is the number of atoms of the i -th component, n_i is the respective atomic densities, Γ_i is the boundary adsorption, Γ_i^ℓ is the triple junction (triple line) adsorption.)

The fundamental thermodynamic characteristic of a triple junction is the tension line γ^ℓ . The work required for a reversible increase of the triple junction length ℓ by $\delta\ell$ is

$$\delta W^\ell = \gamma^\ell \delta\ell \quad (4.4)$$

As mentioned above, it is more reasonable to consider the joint change of the length of the triple junction line and the area of the boundaries

$$\delta W^{\ell s} = \left(\gamma + \gamma^\ell \frac{\partial \ell}{\partial \tilde{A}} \right) d\tilde{A} \quad (4.5)$$

For a constant temperature T , volume V , and the invariant chemical potentials μ_i of the components ($i=1,2,\dots,k$)

$$\delta W^{\ell s} = d\Omega_{T,V,\mu_i} \quad (4.6)$$

where Ω is the Gibbs grand potential.

For a system with a boundary and a triple junction

$$d\Omega = -pdV - SdT - \sum_1^k N_i d\mu_i + \left(\gamma + \gamma^\ell \frac{\partial \ell}{\partial \tilde{A}} \right) d\tilde{A} \quad (4.7)$$

or (see Eqs. (1.5) and (1.6))

$$\Omega = -pV + \gamma\tilde{A} + \gamma^\ell \ell \quad (4.8)$$

For the surface-junction parameters Eq. (1.17) reads

$$d\Omega^{\ell s} = -pdV^{\ell s} - S^{\ell s}dT - \sum_1^k N_i^{\ell s}d\mu_i + \left(\gamma + \gamma^\ell \frac{\partial \ell}{\partial \tilde{A}} \right) d\tilde{A} \quad (4.9)$$

Then, from Eqs. (1.41) and (4.9)

$$\tilde{A} \left(d\gamma + d\gamma^\ell \frac{\partial \ell}{\partial \tilde{A}} \right) = -S^{\ell s}dT - \sum_1^k N_i^{\ell s}d\mu_i + V^{\ell s}dp \quad (4.10)$$

Introducing the specific values $s^{\ell s} = \frac{S^{\ell s}}{A}$, $\Gamma_i^{\ell s} = \frac{N_i^{\ell s}}{A}$, $v^{\ell s} = \frac{V^{\ell s}}{A}$

$$\left(d\gamma + d\gamma^\ell \frac{\partial \ell}{\partial \tilde{A}} \right) = -s^{\ell s}dT - \sum_1^k \Gamma_i^{\ell s}d\mu_i + v^{\ell s}dp \quad (4.11)$$

Eq. (4.11) is the triple junction variant of the well-known Gibbs equation

which in this instance connects the change of boundary and triple junction surface tension with a variation in temperature, pressure and chemical potentials. For example, for a binary system at constant temperature and pressure, using the Gibbs-Duhem relation (1.55) we arrive at

$$\left(d\gamma + d\gamma^\ell \frac{\partial \ell}{\partial A}\right) = -\Gamma_1^{\ell s} d\mu_1 - \Gamma_2^{\ell s} d\mu_2 = -\left(\Gamma_2^{\ell s} - \frac{c}{1-c} \Gamma_1^{\ell s}\right) d\mu_2 \quad (4.12)$$

where c is the concentration. In the framework of this approach, we cannot achieve more. There is no dividing surface, either between the grain boundary and the bulk (see Chapter 1), or between the boundaries and the triple junction, and it is not possible to make one adsorption $\Gamma_1^{\ell s}$ equal to zero by changing the position of the dividing surface.

Let us consider a binary system with the concentrations c_1 and c_2 under the assumption that the triple junction is in thermodynamic equilibrium with its constituent boundaries and with the bulk. Then

$$\begin{aligned} \mu_1^\ell(\gamma^\ell, T, c_1^\ell) &= \mu_1^s(\gamma, T, c_1^b) = \mu_1^v(p, T, c_1) \\ \mu_2^\ell(\gamma^\ell, T, c_2^\ell) &= \mu_2^s(\gamma, T, c_2^b) = \mu_2^v(p, T, c_2) \end{aligned} \quad (4.13)$$

where μ_1^ℓ , μ_2^ℓ , μ_1^s , μ_2^s , μ_1^v , μ_2^v are the chemical potentials of the first and second component in the triple junction, at the grain boundaries, and in the bulk, respectively, c_1^ℓ , c_2^ℓ , c_1^s , c_2^s denote the respective triple junction and grain boundary concentrations. The line tension stretches (or compresses, depending on whether the line γ^ℓ is positive or negative) the triple junction, and the equilibrium conditions can be written as

$$\begin{aligned} \mu_1^v(p, T, c_1) &= \mu_1^\ell(T, c_1^\ell) - \gamma^\ell \bar{\ell}_1; \\ \mu_2^v(p, T, c_2) &= \mu_2^\ell(T, c_2^\ell) - \gamma^\ell \bar{\ell}_2 \end{aligned} \quad (4.14)$$

$\bar{\ell}_i$ is the length of an atom of the i -th component in the triple junction line.

If it can be assumed that $\bar{\ell}_1 = \bar{\ell}_2 = \bar{\ell}$, then

$$\mu_1^v(p, T, c_1) - \mu_1^\ell(T, c_1^\ell) = \mu_2^v(p, T, c_2) - \mu_2^\ell(T, c_2^\ell) \quad (4.15)$$

Taking both the bulk and triple junction as ideal solutions

$$\begin{aligned} \mu_1^v &= \mu_{10}^v + kT \ln c_1 \\ \mu_1^\ell &= \mu_{10}^\ell + kT \ln c_1^\ell \end{aligned} \quad (4.16)$$

The difference $\mu_{10}^v - \mu_{10}^\ell = -\gamma_1^\ell \bar{\ell}_1$, inasmuch as the value $\gamma_1^\ell \bar{\ell}_1$ is the excess energy of an atom of the first component in the triple junction in comparison with the same atom in the bulk; γ_1^ℓ and γ_2^ℓ are the line tensions of the triple junction in pure first and second component, respectively. Combining Eqs. (4.15) and (4.16)

$$c_1^\ell = \frac{c_1 B^\ell}{1 - c_1 + c_1 B^\ell} \quad (4.17)$$

where $B^\ell = \exp \left[\frac{\gamma_2^\ell - \gamma_1^\ell}{kT} \bar{\ell} \right]$. More complicated isotherms of triple junction adsorption can be derived in analogy to the interface adsorption [197].

It is of interest to find a relation between interface (in particular, grain boundary) concentration and adsorption on a triple junction. Let us consider the equilibrium between the grain boundary and triple junction constitution, taking into account that the boundary is stretched by the surface tension γ and the triple junction is stretched (or compressed) by the line tension γ^ℓ . Then from Eqs. (4.14) and (4.15)

$$\begin{aligned}\mu_1^s(T, c_1^s) - \gamma \bar{A}_1 &= \mu_1^\ell(T, c_1^\ell) - \gamma^\ell \bar{\ell}_1 \\ \mu_2^s(T, c_2^s) - \gamma \bar{A}_2 &= \mu_2^\ell(T, c_2^\ell) - \gamma^\ell \bar{\ell}_2\end{aligned}\quad (4.18)$$

where A_i is the area of an atom of the i -th component in the grain boundary.

Considering both the grain boundary and triple junction chemistry as ideal solutions

$$\begin{aligned}\mu_1^s &= \mu_{10}^s + kT \ln c_1^s \\ \mu_1^\ell &= \mu_{10}^\ell + kT \ln c_1^\ell\end{aligned}\quad (4.19)$$

By subtraction we obtain $\mu_{10}^s - \mu_{10}^\ell = -(\gamma_1^\ell \bar{\ell}_1 - \gamma_1 \bar{A}_1)$ and $\mu_{20}^s - \mu_{20}^\ell = -(\gamma_2^\ell \bar{\ell}_2 - \gamma_2 \bar{A}_2)$. These values represent the difference of the excess energy of an atom of the first and second component, respectively, in the triple junction and in the interface; γ_1 and γ_2 are the grain boundary surface tensions in the respective pure components. For the simplest situation, when $\bar{\ell}_1 = \bar{\ell}_2 = \bar{\ell}$, $\bar{A}_1 = \bar{A}_2 = \bar{A}$ combining (4.18) and (4.19), we arrive at

$$c_1^\ell = \frac{c_1^s B^{\ell s}}{1 - c_1^s + c_1^s B^{\ell s}}\quad (4.20)$$

where

$$B^{\ell s} = \exp \left[\frac{(\gamma_2^\ell - \gamma_1^\ell) \bar{\ell} - (\gamma_2 - \gamma_1) \bar{A}}{kT} \right]$$

One can see from Eqs. (4.17) and (4.20) that the concentration in the triple junction is rigidly bound not only to the concentration in the bulk of the sample, but to the concentration in the interface, in particular, in the grain boundary. It is felt that the detachment of adsorbed atoms from the grain boundary should initiate the same phenomenon in the triple junction. In this case the triple junction will no longer be in equilibrium with the bulk, but, nevertheless, and what is of importance, is that it might still be in equilibrium with the boundaries.

As already mentioned by Gibbs [1], although the line tension of a triple junction might be negative, still the line of the triple junction (termed “filament” by Gibbs) should be stable, and the phase of the triple junction would differ from the phase in the interfaces. “We may here add that the linear

tension there mentioned may have a negative value. This would be the case with respect to a line in which three surfaces of discontinuity are regarded as meeting, but where nevertheless there really exists in stable equilibrium a filament of different phase from the three surrounding masses" [400]. The triple junction with a negative linear tension should manifest unusual thermodynamic properties. In particular, the adsorption of impurities on a triple junction, as a rule, should be negative and, therefore, definitely lower than at grain boundaries. Further, the behavior of a triple junction with negative line tension can be manifested in the attempt to increase its length. The description given above complies with this requirement. Computer simulations of the energy of a grain boundary triple junction indicate the feasibility of such an effect [405].

4.2.1 Grain Boundary Triple Line Tension — Experimental Approach

The influence of grain boundary junctions on grain growth, stability and evolution of the grain microstructure was recognized recently [360, 361, 411]. This effect is especially pronounced in fine-grained and nanocrystalline materials. The influence of the line tension of grain boundary triple junctions on grain growth and stability of nanocrystalline materials is not confined to its contribution to the driving force of grain growth but determines the adsorption on the triple junctions and in turn their mobility, as well.

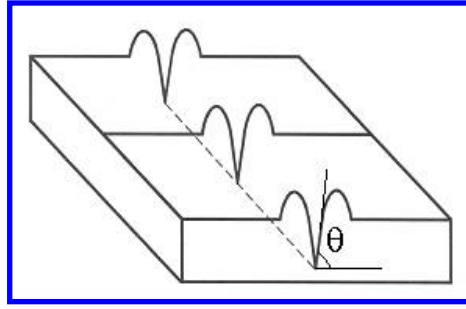
The problem of triple line energy was discussed by Gibbs who came to the conclusion that the excess free energy of a triple line between fluid phases might be positive or negative [1, 362]. McLean [23] contended that triple junctions should have a positive energy owing to the influence of three connected grain boundaries. The attempts to extract the triple line energy from simple geometrical model were undertaken in [406]–[408]. More recent computational studies by Srinivasan et al. [364] and Van Swygenhoven [363, 365] came to contradictory conclusions. The authors of [364] concluded that a negative triple line energy is possible although the value of the triple line tension obtained in the simulation studies [365] was always positive. Unfortunately, there is a poor body of experimental data to resolve this issue by properly conducted experiments. This is mainly due to both the experimental difficulties and the lack of a rigorous theoretical basis of such measurements [366].

The theoretical foundations of the measurement of triple line tension along with the experimental technique were put forward and developed in [366, 421].

It is well known that the equilibrium at the straight root of a thermal groove satisfies the condition

$$\gamma = \gamma_{S1}\sin\Theta_1 + \gamma_{S2}\sin\Theta_2 \quad (4.21)$$

where Θ_1 , Θ_2 and γ_{S1} , γ_{S2} are the respective angles and surface energies to both sides of the groove. In the case that the grain boundary is curved in the

**FIGURE 4.2**

Grain boundary formed at a flat grain boundary with a curved groove root [366].

root of the groove (Fig. 4.2), one has to take into account an additional term, the so-called line tension γ^ℓ of the groove root triple line, i.e.

$$\gamma - \gamma^\ell \frac{\frac{\partial^2 u}{\partial r^2}}{\left[1 + \left(\frac{\partial u}{\partial r}\right)^2\right]^{3/2}} = \gamma_{S1} \sin \xi_1 + \gamma_{S2} \sin \xi_2 \quad (4.22)$$

The term $u(r)$ mathematically describes the profile of the groove root. The multiplier of γ^ℓ is the Laplace curvature. The dihedral angles denoted by ξ_1 and ξ_2 have the same meaning like Θ_1 and Θ_2 in Eq. (4.21) but are different in magnitude owing to the curvature. The topography of a triple junction [366] after thermal annealing is formed by three grain boundaries which meet in a way schematically shown in Fig. 4.3. The three groove roots are curved towards the triple junction but remain straight far away from this point.

If one associates a line tension with the triple line, an equilibrium of the four competing line tensions (the three groove line tensions γ_{i-j}^ℓ and the triple line tension γ_{tj}^ℓ) at the triple junction will be established. The line tension of these groove roots at the triple junction is

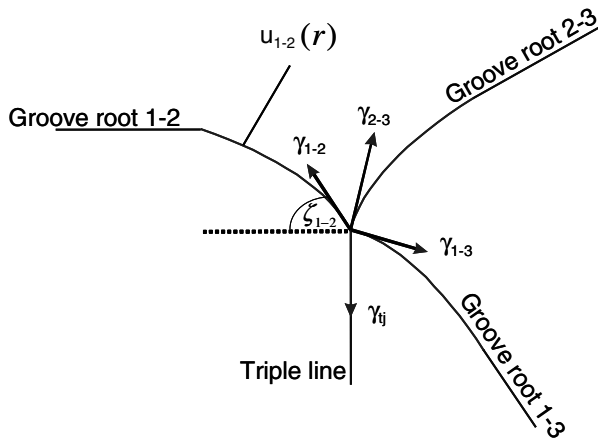
$$\gamma_{i-j}^\ell = \frac{\gamma_{i-j} - \gamma_{Si} \sin \xi_i - \gamma_{Sj} \sin \xi_j}{\frac{\partial^2 u_{ij}}{\partial r^2} \Big|_{r=0}} \left[1 + \left(\frac{\partial u_{ij}}{\partial r} \Big|_{r=0} \right)^2 \right]^{3/2} \quad (4.23)$$

From the equilibrium of the four line tensions it follows for the triple line tension

$$\gamma_{tj}^\ell = \gamma_{1-2}^\ell \sin \zeta_{1-2} + \gamma_{1-3}^\ell \sin \zeta_{1-3} + \gamma_{2-3}^\ell \sin \zeta_{2-3} \quad (4.24)$$

Eq. (4.24) constitutes the theoretical basis of the presented approach and can be used to calculate the triple line energy from the geometry of the boundaries merging at the triple junction [366].

The first measurements were performed on polycrystalline copper with

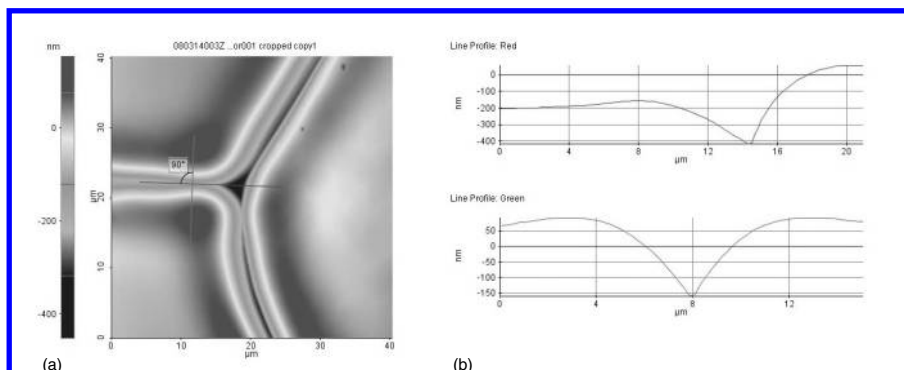
**FIGURE 4.3**

Schematic 3D view of the line tension equilibrium in the triple junction [366].

rather large grains [366]. The topography in the close vicinity of the triple junctions was measured by means of atomic force microscopy. An example for groove formation at grain boundaries intersecting the crystal surface is given in Fig. 4.4. In the center of the figure there is a triple junction of the three adjoining grain boundaries (Fig. 4.4(a)) [366]. From AFM measurements (Fig. 4.4) all necessary parameters can be derived to extract the triple line tension, such as the grain boundary groove angles Θ_i , the groove root angles in the center of the triple junction ξ_i , and the profile of the groove roots. The measured value of the line tension of grain boundary groove root γ_{i-j}^ℓ and grain boundary triple junction γ_{tj}^ℓ are positive and equal to $(17.0 \pm 7.0) \cdot 10^{-9}$ J/m and $6.5 \pm 2.5) \cdot 10^{-9}$ J/m, respectively. The analysis given in [366] shows that the negative value of γ_{tj}^ℓ can be expected only for the line tension of grain boundary groove root γ_{i-j}^ℓ smaller than $-4 \cdot 10^{-7}$ J/m. A comprehensive description of the approach and the experimental technique of the measurements was put forward in [366].

4.3 Motion of a Grain Boundary System with Triple Junctions

It is usually tacitly assumed in all studies of grain boundary migration and grain growth that the line tension of a triple junction is of minor importance

**FIGURE 4.4**

Top view (a) of an AFM topography measurement in the vicinity of a triple junction; (b) surface profiles along lines indicated in (a) [366].

and that a triple junction does not drag grain boundary motion. Thus, their role in the migration process is reduced to maintaining the thermodynamic equilibrium in terms of fixed dihedral angles during grain boundary motion.

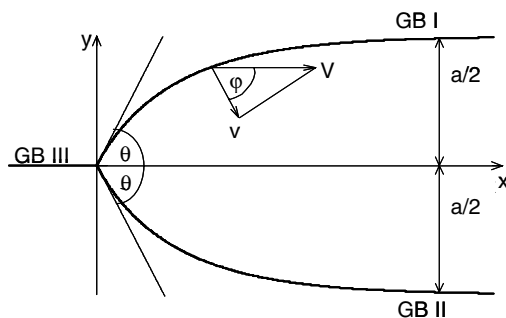
However, as shown in [403], the movement of triple junctions caused by boundary migration can involve additional energy dissipation, in other words, a triple junction can have a finite mobility. The concept of a specific triple junction mobility was first introduced in [403].

Steady-state motion of a system of boundaries with a triple junction is only possible in a narrow range of geometrical configurations. One of them is shown in Fig. 4.5 [403]. The triple junction in Fig. 4.5 is rectilinear and perpendicular to the plane of the diagram. Far from the triple junction all three boundaries are planar, their planes parallel to each other and perpendicular to the plane of the diagram. This makes the problem quasi-two-dimensional.

Of course, this is very different from situations that arise in a polycrystal, and real triple junctions are unlikely to experience steady-state motion. But a detailed analysis of this problem allows us to isolate the main physical aspects of triple junction motion.

The next assumption relates to the driving forces of grain boundary and triple junction motion in this system. It is commonly assumed that the system only migrates under the action of the surface tensions γ of the adjoining grain boundaries. The problem can be considered in the framework of a uniform boundary model, i.e. all grain boundaries possess equal surface tensions and mobilities irrespective of the misorientation of the adjacent grains and the crystallographic orientation of the boundaries, and the mobilities of grain boundary and triple junction are independent of their velocity.

The given assumptions require symmetry with respect to the x -axis. The normal displacement of each element of a boundary, the velocity of grain

**FIGURE 4.5**

Geometry of the grain boundary system with triple junction in the course of steady-state motion.

boundary motion, the differential equation of the shape $y(x)$ of a moving grain boundary, and the boundary conditions are identical to the problem of the shape of a moving boundary (Chapter 3, Eqs. (3.117)–(3.119)) and are repeated here for convenience:

$$y'' = -\frac{V}{m_b \gamma} y' [1 + y'^2] \quad (4.25)$$

$$y(0) = 0 \quad (4.26)$$

$$y(\infty) = a/2$$

$$y'(0) = \tan \Theta$$

The meaning of the length a and angle Θ is clear from Fig. 4.5.

Since a driving force $\gamma(2 \cos \Theta - 1)$ is applied to the triple junction, the velocity of its motion can be expressed as

$$V = m_{tj} \gamma (2 \cos \Theta - 1) \quad (4.27)$$

where m_{tj} is the mobility of the junction.

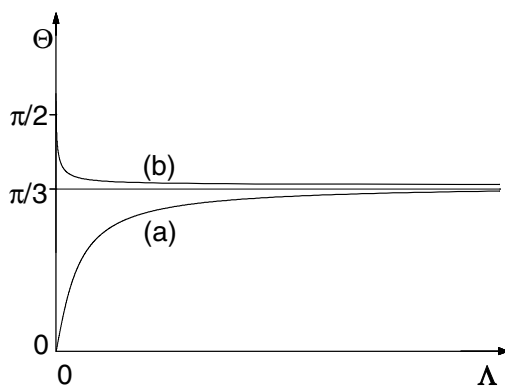
Eqs. (4.25)–(4.27) define the problem completely. The shape of a steady-state moving grain boundary was already described by Eq. (3.143):

$$y(x) = \xi \arccos \left(e^{-\frac{x}{\xi} + C_1} \right) + C_2 \quad (4.28)$$

$$\xi = \frac{a}{2\Theta}$$

$$C_1 = \ln(\sin \Theta)$$

$$C_2 = \xi (\pi/2 - \Theta)$$

**FIGURE 4.6**

Geometry of the grain boundary system with triple junction in the course of steady-state motion.

As can be seen, a steady-state motion of the grain boundary system with a triple junction is possible indeed. The velocity of steady-state motion V of the system is equal to

$$V = \frac{2\Theta m_b \gamma}{a} \quad (4.29)$$

From (4.27) and (4.29) we arrive at the equation which determines the steady-state value of the angle Θ :

$$\frac{2\Theta}{2 \cos \Theta - 1} = \frac{m_{tj} a}{m_b} = \Lambda \quad (4.30)$$

This equation associates the angle Θ with the value of the dimensionless parameter $\Lambda = m_{tj} a / m_b$, which characterizes the inhibiting influence of the triple junction on grain boundary migration.

It should be stressed that the dimensions of m_{tj} , triple junction mobility, and m_b , the grain boundary mobility, are different, so that their ratio m_b / m_{tj} has the dimension of a length.

For small Λ , $m_{tj} a / m_b \ll 1$, the contact angle Θ approaches zero. For large Λ the junction does not influence boundary migration, and the angle Θ tends to its equilibrium value $\pi/3$. The dependency of Θ vs. Λ is shown in Fig. 4.6. When $\Lambda \gg 1$ the value V is independent of the mobility of the junction and governed only by the boundary properties and the driving force, which is proportional to $1/a$

$$V = \frac{2\pi m_b \gamma}{3a} \quad (4.31)$$

When $\Lambda \ll 1$ the velocity is controlled by the mobility of the junction

$$V = \gamma m_{tj} \quad (4.32)$$

These relations comprise the theoretical background for experimental studies of triple junction mobility and how it affects grain boundary migration.

4.4 Triple Junctions Motion in the Presence of Impurities

Until now we have considered the migration of a grain boundary system which does not interact with impurities. In the following we analyze the main effects introduced by impurities on the motion of a grain boundary system with a triple junction. First of all we would like to emphasize that, contrary to the motion of a single grain boundary, there are two aspects of the problem where impurity influence can manifest itself, namely grain boundary motion and triple junction motion. Let us consider more comprehensively the latter aspect of the problem.

The theories of impurity influence on grain boundary motion also can be applied, with certain corrections, to triple junction motion. Actually, if a triple junction moves under the action of a driving force P with a certain number of impurity atoms Γ^ℓ (per unit line length) the velocity of such a triple junction is given by

$$V_{tj} = m_{tj} P_{eff} \quad (4.33)$$

where the P_{eff} is the effective driving force. (Please note that the dimension of triple junction mobility and its driving force, respectively, are different from the respective quantities for grain boundary migration.) P_{eff} can be written as

$$P_{eff} = P - \Gamma^\ell f \quad (4.34)$$

where f is the attraction force between the triple junction and an impurity atom, Γ^ℓ is the adsorption on the triple junction.

On the other hand the velocity of an impurity atom and, therefore, also of the triple junction in the case that both move together reads with the Nernst-Einstein relation

$$m_{im} = \frac{D}{kT} \quad (4.35)$$

where m_{im} is the mobility of an impurity atom

$$v = m_{im} f \quad (4.36)$$

From Eq. (4.33)-(4.36) we find

$$v = \frac{Pm_{tj}}{1 + \Gamma^\ell \frac{m_{tj}}{m_{im}}} \quad (4.37)$$

or, for $\Gamma^\ell \frac{m_{tj}}{m_{im}} \gg 1$

$$v \cong \frac{Pm_{im}}{\Gamma^\ell} = \frac{PD}{\Gamma^\ell kT} = \frac{PD_0 e^{-\frac{H_D}{kT}}}{\Gamma^\ell kT} \quad (4.38)$$

where D_0 is the pre-exponential factor and H_D the activation enthalpy of impurity diffusion, respectively.

Correspondingly, the triple junction mobility, with regard to the impurity effect, can be defined as

$$m_{tj} = \frac{D}{\Gamma^\ell kT} = \frac{D_0 e^{-\frac{H_D}{kT}}}{\Gamma^\ell kT} \quad (4.39)$$

Eqs. (4.37) and (4.39) describe the triple junction motion in the presence of impurities in the Lücke-Detert approximation [193] (see Chapter 3). In analogy to grain boundary motion in this approximation, an impurity atom can move together with a triple junction at a velocity not exceeding

$$v^* = \frac{D_0 e^{-\frac{H_D}{kT}}}{\Gamma^\ell kT} \cdot \frac{U_0}{r_0} \quad (4.40)$$

where r_0 is the smallest dimension of the defect (grain boundary or triple junction width), and the ratio U_0/r_0 is an estimate of the maximum force of interaction between the impurity atom and the triple junction. (It should be remembered that the dimension of U_0 for a triple junction line is [energy/length].) If the velocity exceeds v^* , the triple junction detaches from the impurities.

However, apart from the influence of the impurity atoms on triple junction motion, there is also an influence of these atoms on the motion of the adjoining grain boundaries. As mentioned, the motion of a grain boundary system with a triple junction is akin to the motion of a grain boundary quarter-loop. Therefore, the general solution for Eq. (4.25) is in accordance with [243, 244]

$$y = y_0 + \frac{m\gamma}{V} \arccos \left[e^{-\frac{(x-x_0)V}{m\gamma}} \right] \quad (4.41a)$$

where y_0 and x_0 are integration constants.

The grain boundary velocity V is at a maximum at the triple junction and reduces to zero at the straight, immobile sections. The critical velocity v^* can be described as the velocity of such point on the grain boundary system with a triple junction (Fig. 4.5) which separates two boundary segments, namely a segment detached from the impurity atoms (to the left in Fig. 4.5) and a

segment loaded with impurities (to the right in Fig. 4.5), in other words, for $0 \leq x \leq x^*$ the velocity $V > v^*$ and for $x > x^*$ the velocity $V < v^*$ (see Chapter 3, Sec. 3.4.3).

The final solution for the shape of a moving grain boundary half-loop with a triple junction is quite similar to the moving grain boundary quarter-loop [244] (Eq. (4.41b))

$$y(x) = \begin{cases} - (b_F - b_L) \arccos \left(\frac{\sin \Theta}{e^{\frac{x^*}{b_F}}} \right) \\ + \frac{a}{2} - b_L \frac{\pi}{2} + b_F \arccos \left(e^{\frac{b_F \ln(\sin \Theta) - x}{b_F}} \right) & 0 \leq x \leq x^* \\ \frac{a}{2} - b_L \frac{\pi}{2} + b_L \arccos \left(e^{\frac{b_L \ln(\sin \Theta) - x^* (\frac{b_L}{b_F} - 1) - x}{b_L}} \right) & x \geq x^* \end{cases} \quad (4.41b)$$

From the relation for b_L and b_F

$$b_L = \frac{b_F \left[\arccos \left(\frac{\sin \Theta}{e^{\frac{x^*}{b_F}}} \right) + \Theta - \frac{\pi}{2} \right] - \frac{a}{2}}{\arccos \left[\frac{\sin \Theta}{e^{\frac{x^*}{b_F}}} \right] - \frac{\pi}{2}}$$

where b_F and b_L relate to the “free” and “loaded” part of the boundary

$$\begin{aligned} b_F &= \frac{m_F \gamma}{V} \\ b_L &= \frac{m_L \gamma}{V} \end{aligned} \quad (4.42)$$

we obtain the mobilities of “free” and “loaded” boundary m_F and m_L , respectively.

The angle Θ in Eq. (4.41b) is defined by Eq. (4.30), in which the criterion Λ is a function of triple junction and grain boundary mobility in the presence of impurities.

There is a variety of possible situations. Besides the grain boundary impurity attachment-detachment processes the phenomena of triple junction impurity attachment-detachment have to be considered, and in addition the combinations “free” grain boundary — “free” triple junction, “free” grain boundary — “loaded” triple junction etc. Unfortunately, little is known about triple junction mobility, and there are no data at all about the interaction between triple junctions and impurity atoms.

4.5 Experimental Investigations of Triple Junction Motion

As mentioned above, triple junctions along with grain boundaries comprise the main structural elements of polycrystals. In spite of its importance for microstructural evolution the influence of triple junctions on boundary migration has not been treated at all experimentally and has been hardly investigated theoretically, mainly by computer simulations [409]. In comparison the motion of grain boundaries has been studied actively, especially in the past 20–30 years [410]. In all studies concerning grain boundary migration and grain growth it was tacitly assumed that triple junctions do not have an influence on the motion of the boundaries; rather, their role in this process was reduced to establishing the thermodynamic equilibrium angles at the junction during boundary motion.

The lack of experimental results for triple junction motion is mainly due to the experimental difficulties of obtaining reliable data. Not only the velocity of the junction motion must be measured, but also the shape of the intersecting grain boundaries during the motion, as will be discussed below. For conducting experiments a technique had to be developed which allowed continuous monitoring of the position and the geometrical arrangement of such boundary system during the experiment. Moreover, the steady-state motion of a grain boundary system with a triple junction is only possible in a very narrow range of geometrical configurations with specific restrictions imposed on the properties of the grain boundaries in the system. In particular, it was suggested that all grain boundaries in the system are identical. The equations considered for the motion of the grain boundary system with a triple junction (4.28)–(4.31) retain their validity for the following boundary system, a so-called symmetrical boundary system, which is shown in Fig. 4.5: two identical curved boundaries (GB I and II) and a different straight boundary (GB III). Such a system is much more convenient for experimental realization than a system comprising only ideal uniform boundaries. In the following this defined boundary system will be considered [183]. The respective surface tensions and the mobilities of the boundaries are

$$\begin{aligned}\gamma_1 &= \gamma_2 \equiv \gamma \neq \gamma_3 \\ m_{b1} &= m_{b2} \equiv m_b \neq m_{b3}\end{aligned}\tag{4.43}$$

If the angles at the triple junction are in equilibrium, the driving force is equal to zero and for a finite triple junction mobility the velocity v_{tj} should vanish as well. Consequently, for a finite m_{tj} , a motion of the triple junction detunes the equilibrium angles and, as a result, drags the motion of the boundaries. For the situation given in Fig. 4.5

$$v_{tj} = m_{tj} (2\gamma \cos\Theta - \gamma_3)\tag{4.44}$$

In the case of steady-state motion of the entire boundary system the velocity of the triple junction equals the velocity of the grain boundaries. Therefore, the steady-state value of the angle Θ is determined by Eqs. (4.29) and (4.44)

$$\frac{2\Theta}{2 \cos\Theta - \frac{\gamma_3}{\gamma}} = \frac{m_{tj}a}{m_b} = \Lambda \quad (4.45)$$

The dimensionless criterion Λ reflects the drag influence of the triple junction on the migration of the system. One can distinguish two limiting cases:

a) $\Lambda \rightarrow 0$: In this case the angle Θ tends to zero, i.e. the motion of the entire boundary system is governed by the mobility of the triple junction and the corresponding driving force. For the limit $\Theta = 0^\circ$ the velocity of the system is given with Eq. (4.44) by:

$$v = m_{tj} (2\gamma - \gamma_3) \quad (4.46)$$

b) $\Lambda \rightarrow \infty$: In this case the angle Θ tends to assume its value at thermodynamic equilibrium:

$$\Theta = \arccos \left(\frac{\gamma_3}{2\gamma} \right) = \Theta_{eq} \quad (4.47)$$

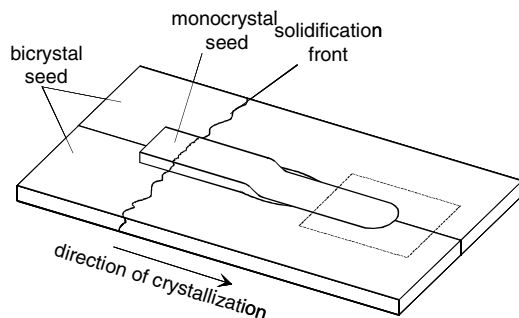
The motion of the system is independent of the triple junction mobility and is governed only by the grain boundary mobility and the corresponding driving force. The velocity of the boundary system in this case with Eq. (4.29) and (4.47) is given by

$$v = \frac{2\Theta_{eq}m_b\gamma}{a} \quad (4.48)$$

The two states of motion of the entire grain boundary system can be distinguished experimentally for a known ratio γ_3/γ by measuring the contact angle Θ .

Experimentally, this idea was first realized in [183, 411]. The experiments were carried out on zinc tricrystals with a grain boundary geometry as shown in Fig. 4.5. The tricrystals were produced of high purity Zn (99.999 at%) by a technique of directional crystallization in a high purity Argon atmosphere (Fig. 4.7). The characteristics of the tricrystals studied are given in Table 4.1. The orientations of the three adjacent grains of each sample were determined by the Laue-technique, Electron Back Scatter Diffraction (EBSD) and by an investigation of the fracture surface of a cracked sample. For the latter method small cracks were induced by a sharp knife in the sample cooled by liquid nitrogen. The cracks propagated along the basal plane of each grain. Hence, the misorientation could be determined by the orientation of the surface of the cracks.

For measuring the migration rate and the geometry of the grain boundary system during the motion temperatures a modified optical microscope operating with polarized light and a hot stage was used. An additional polarization filter applied in the reflected beam allowed us to distinguish the different

**FIGURE 4.7**

Method of tricrystal fabrication; the rectangular area represents the tricrystal used for migration experiments.

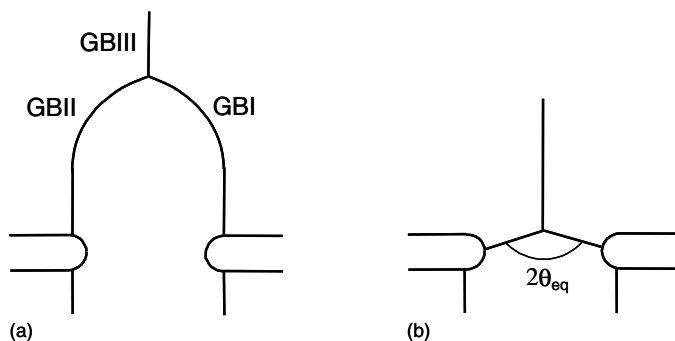
orientations of the grains by the different intensity of the reflected light. A color video camera was attached to the microscope and connected to a video cassette recorder to record the motion of the triple junction system during the experiment. For each temperature the velocity of the triple junction system, the angle Θ , and the width a of the vanishing grain were measured. For this, single video frames were grabbed by a computer and in accordance with Eq. (4.28) a computed shape of the grain boundary system was superimposed. By fitting the computed shape to the shape observed, the angle Θ and the width a of the shrinking grain were determined.

TABLE 4.1

Misorientations of the Used Tricrystals

Sample	GB I	GB II	GB III
S1	$82^\circ \langle 01\bar{1}0 \rangle$	$81^\circ \langle 01\bar{1}0 \rangle$	$4^\circ \langle 12\bar{3}0 \rangle$
S2	$61^\circ \langle 01\bar{1}0 \rangle$	$62^\circ \langle 01\bar{1}0 \rangle$	$3^\circ \langle 0001 \rangle$
S3	$25^\circ \langle 10\bar{1}0 \rangle$	$23^\circ \langle 10\bar{1}0 \rangle$	$48^\circ \langle 10\bar{1}0 \rangle$
S4	$14^\circ \langle 10\bar{1}0 \rangle$	$16^\circ \langle 10\bar{1}0 \rangle$	$30^\circ \langle 10\bar{1}0 \rangle$

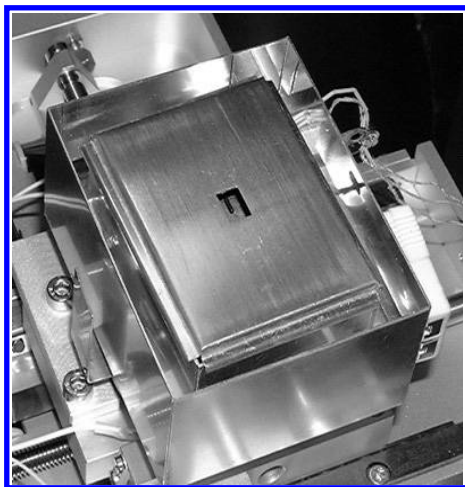
Note: The numbering of the boundaries corresponds to Fig. 4.5.

**FIGURE 4.8**

Sketch of an experiment to determine Θ_{eq} . (a) grain boundary system with triple junction and notches to avoid a complete disappearance of the grain enclosed by GBI and GBII; (b) the same system after annealing at 655°C.

Unfortunately, this technique cannot be applied to tricrystals of Al. Early in the development of this research the migration rate of a grain boundary system with triple junction in Al was measured by the XICTD technique. (The XICTD technique is discussed in greater detail in Chapter 3.) The main disadvantage of an X-ray-diffraction-based technique is the difficulty to visualize the shape of a moving boundary. That is why in [436] the following procedure was used. For each temperature the velocity V , the angle Θ and the width of the shrinking grain α were determined. For this the sample was rapidly cooled down after measurements of the migration rate at each temperature. The position of the grain boundary system and the angle Θ were recorded from the grain boundary grooves. Before subsequent heating to measure the migration rate the specimen was polished to remove the grooves. Measurements of Θ during annealing close to the melting point were carried out by the following experiment. A sample with grain boundaries was annealed at a temperature close to the melting point ($T = 655^\circ\text{C}$) for 5 minutes. To avoid the complete vanishing of the shrinking grain enclosed by GBI and GBII (4.8a) the sample was notched. After annealing the sample was rapidly cooled down, and the position of the grain boundaries and the angle $2\Theta \approx 2\Theta_{eq}$ (Fig. 4.8b) were measured by optical microscopy. To determine Λ for the samples SII and SIII (Table 4.1) the grain boundary energy data calculated by Hasson and Goux were used [184].

However, electron backscatter diffraction (EBSD) is nowadays widely used for the investigation of grain microstructure evolution. Since the contrast by backscattered electrons (BSE) is sensitive to crystallographic orientation, the

**FIGURE 4.9**

Heating stage for in situ measurements of grain boundary motion in an SEM [430, 431].

shape of a moving grain boundary can, in principle, be visualized in an SEM (see Chapter 3). The major difficulty is obtaining good orientation contrast at elevated temperatures. A hot stage was specifically designed and fabricated at the Institute of Physical Metallurgy and Metal Physics of RWTH Aachen University, for the study of grain boundary migration in the SEM [430, 431]. To reduce the heat radiation and to protect the BSE detector the hot stage was surrounded by double reflecting walls (Fig. 4.9). An Everhart-Thornley backscattered electron detector was used to obtain the orientation contrast. The hot stage allowed to heat the specimens up to 640°C; the temperature could be held constant within $\pm 2^\circ$. A video frame grabber system recorded a sequence of BSE images with a scanning rate between 1 to 30 seconds per frame. The recorded video frames contained the whole information to determine triple junction and grain boundary mobility and the magnitude of the criterion Λ , the time dependency of the triple junction and boundary displacement and the shape of the moving grain boundaries (Fig. 4.10).

The motion of four different triple junctions (Table 4.1) with a grain boundary configuration as in Fig. 4.8 was investigated in the temperature range between 330°C and 405°C [183]. The triple junctions of samples S1 and S2 consisted of two nearly identical high-angle tilt grain boundaries (curved boundaries, GB I and II) and a low-angle tilt boundary (straight boundary, GB III). Due to the different properties of low-angle grain boundaries and high-angle boundaries, the triple junction systems of samples S1 and S2 were symmetrical junctions as described above. Under the assumption that the properties of a high-angle boundary vary only little with misorientations, the

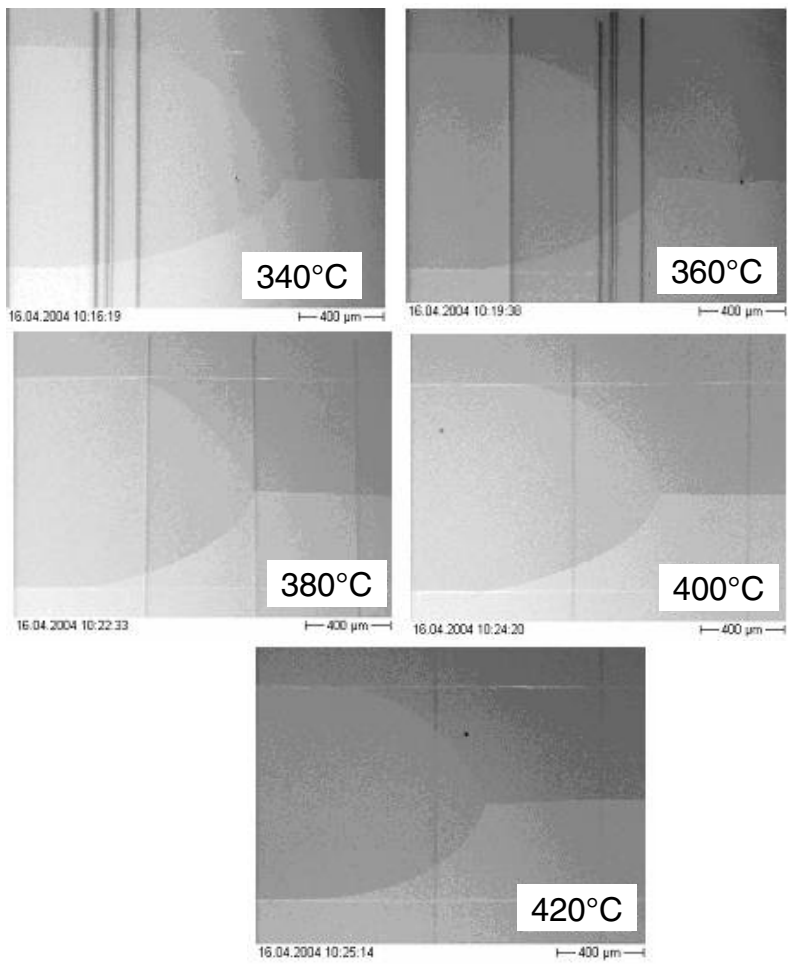


FIGURE 4.10
Set of recorded SEM images of steady-state motion at different temperatures of grain boundary systems with triple junction in Al [433].

behavior of the triple junction system of samples S3 and S4 can be considered as an ideal triple junction as referred to in [403]. For both types of triple junctions the shape of the moving grain boundary system was similar to the shape predicted by theory. Fig. 4.11 shows a series of video frames of a moving symmetrical triple junction in a Zn tricrystal. The straight grain boundary (GB III) is invisible due to the small orientation difference (3°) of the adjacent grains. The solid line in the lower right picture was computed in accordance with Eq. (4.28) and fit the shape of the curved grain boundaries quite well. The small deviation between the theoretical and observed shape of the boundaries at the transition from the straight part of GB I and II to the curved part may have been caused by faceting, i.e. a dependency of γ on the inclination of the boundary, which was neglected in the derivation of Eq. (4.28). For the ideal triple junction the same behavior was observed (Fig. 4.12). Because of the different ratio γ_3/γ the angle Θ for the ideal junction was smaller than for a symmetrical one. As can be seen from this consideration, there is no reason to take an impurity influence into account.

For all samples the velocities v (Fig. 4.13) and the angles Θ (Fig. 4.14) were found to be constant for a given temperature over the entire temperature range investigated. Evidently, the assumption of a steady-state motion of the entire grain boundary system was justified.

As obvious from Figs. 4.11 and 4.12, Θ increased with increasing temperature. In particular for the symmetrical triple junction the change of Θ was dramatic (Fig. 4.15). In accordance with the temperature dependence of Θ , the criterion Λ , determined by Eqs. (4.30) and (4.45), was found to be constant for a given temperature, but increased with increasing temperature (Figs. 4.16, 4.17). At low temperatures Λ was on the order of unity and increased with rising temperature up to 3 orders of magnitude. For the calculation of Λ for symmetrical triple junctions (samples S1, S2) the ratio γ_3/γ was determined under the assumption that for temperatures near the melting point the value of Θ reaches the thermodynamic equilibrium value.

The drag effect of a grain boundary triple junction was readily illustrated in [434]. The authors undertook the attempt to compare “directly” the mobility of a “free” grain boundary and a grain boundary system with triple junction (Fig. 4.18). Actually, the boundary configuration in Fig. 4.1 without triple junction constitutes a grain boundary half-loop (Fig. 4.19).

Essentially, the procedure was as follows: the motion of a grain boundary half-loop in Zn of 99.995% purity was studied. Independently, the motion of practically the same half-loop attached to a flat low-angle boundary (Fig. 4.18) was investigated. “Practically the same” means that the incorporation of a low-angle grain boundary changed the misorientation of curved grain boundaries only negligibly. Hence, one can conduct a direct comparison between the motion of a grain boundary half-loop and the motion of practically the same half-loop with a triple junction. In other words, we can determine the mobility of a moving grain boundary system with and without triple junction. It was mentioned above that the approach used for an analysis of a uniform

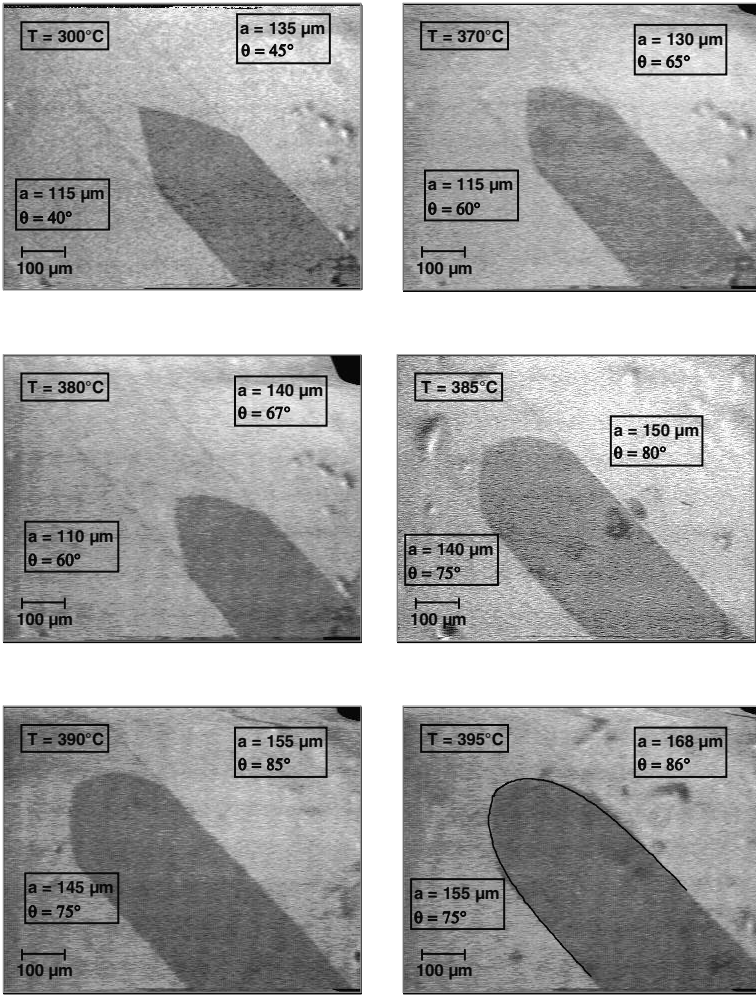
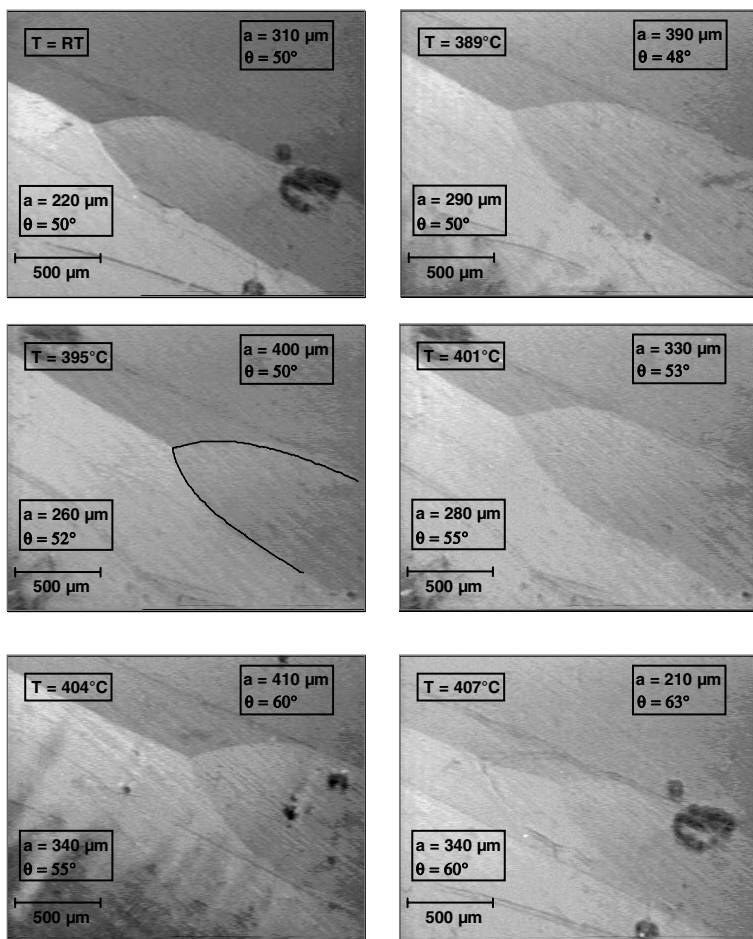


FIGURE 4.11

Video frames for different temperatures of a moving symmetrical triple junction (sample S2). GB III (see Fig. 4.5) is invisible, located at the tip of the two visible boundaries. At $T = 300^\circ\text{C}$ the grain boundary system did not move at all. The solid line generated according to Eq. (4.28) in the lower right frame fits the boundary shape.

**FIGURE 4.12**

Video frames for different temperatures of an ideal triple junction of sample S3. The room temperature (RT) frame shows the initial position. The solid line was computed according to Eq. (4.28). It fits the shape of the boundaries.

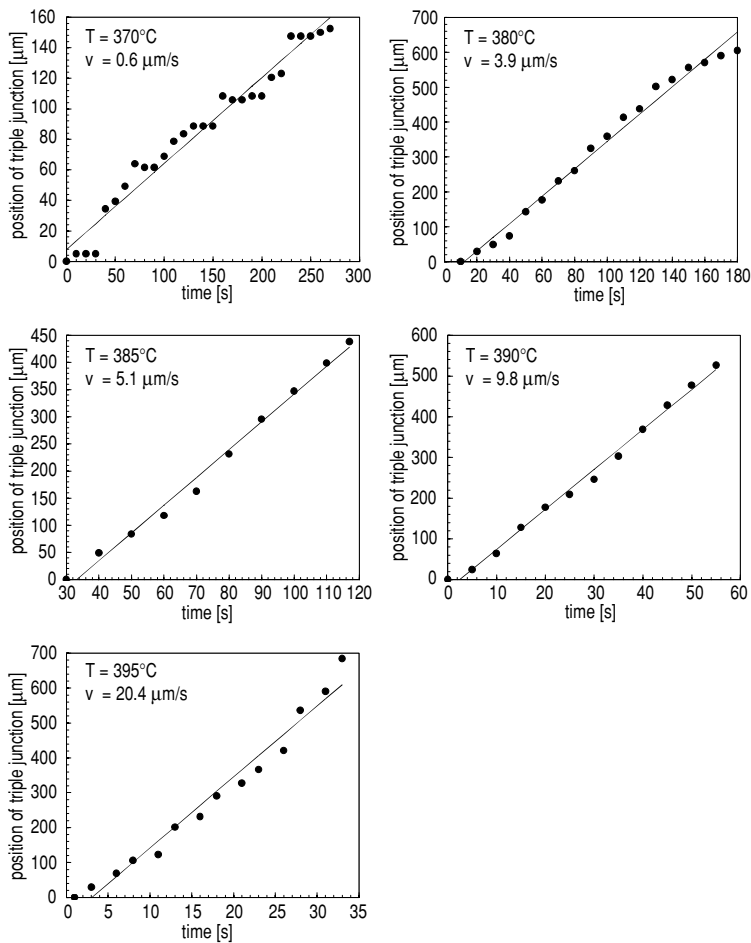


FIGURE 4.13
Triple junction position vs. time for different temperatures for sample S2.

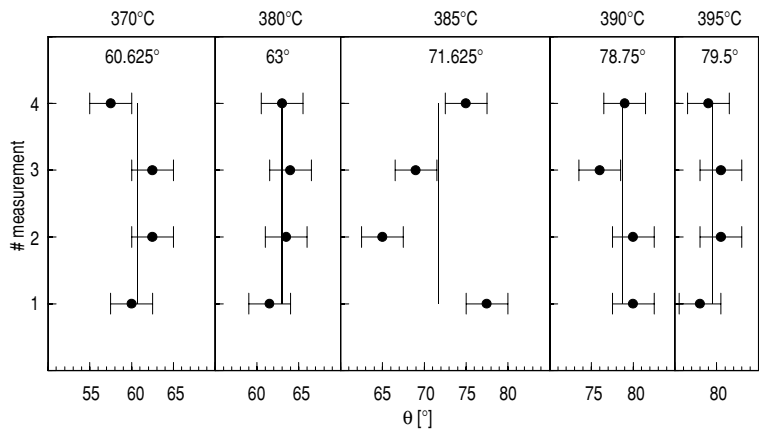


FIGURE 4.14
Reproducibility of measurements of the angle Θ at different temperatures for sample S2.

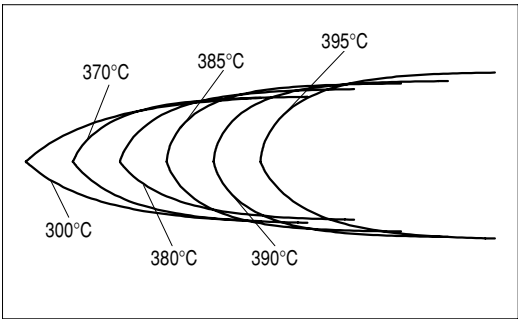


FIGURE 4.15
Evolution of the shape of the grain boundary system of sample S2 with increasing temperature.

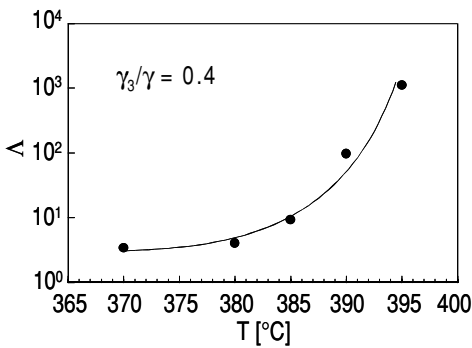


FIGURE 4.16
Temperature dependence of the criterion Λ for a symmetrical triple junction (sample S2).

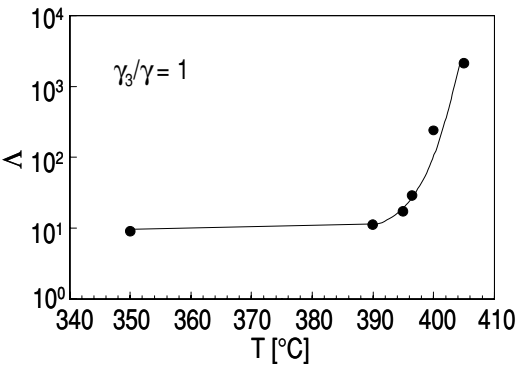


FIGURE 4.17
Temperature dependence of the criterion Λ for an ideal triple junction (sample S3).

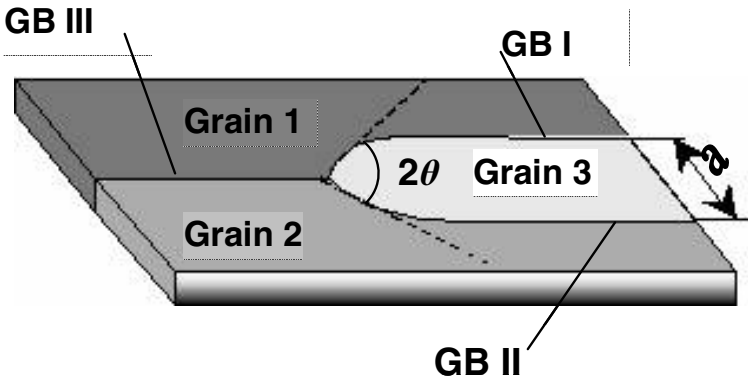


FIGURE 4.18

Geometry of grain boundary system with triple junction.

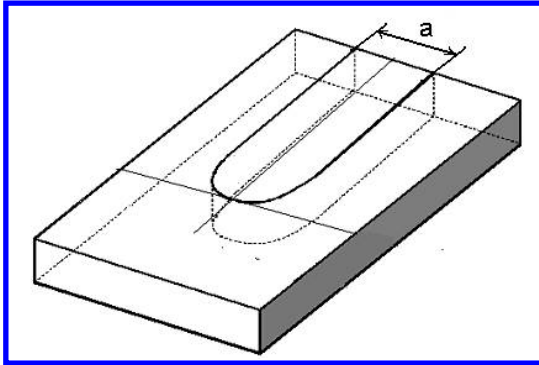


FIGURE 4.19

Geometry of a grain boundary half loop, i.e. the grain boundary system in Fig. 4.18 without triple junction.

grain boundary system (Fig. 4.18) can be applied completely to a symmetrical system, where grain boundaries I and II are the same, but different from the rectilinear grain boundary III. This difference manifests itself in the relation for the dimensionless criterion Λ and in the value of the equilibrium angle Θ_{eq} Eqs. (4.44) and (4.45). The essential issue is the problem how to determine Θ_{eq} . In [434] this problem was treated by two methods. In the first method one grain boundary system was stopped by notches near the triple junction; it gave a possibility to measure Θ_{eq} . An alternative way consists of using literature data of grain boundary surface tension in Al. In our case we used the Read-Shockley equation to estimate the ratio between the surface tension of low-angle and high-angle grain boundaries.

Two grain boundary systems were studied: a $\langle 11\bar{2}0 \rangle$ tilt boundary system with 84° misorientation of the curved boundaries (half-loop); the misorientation across the straight boundary was about 3° . The second grain boundary system was a system of $\langle 10\bar{1}0 \rangle$ tilt boundaries. The misorientation for the half-loop was 62° , the misorientation of straight boundary was also about 3° . The velocities and mobilities of the grain boundary systems for the two types of motion were compared; i.e. in free motion — half-loop — and in constrained motion — half-loop with triple junction. In the following the product of the displacement of the grain boundary vertex and the width of the grain a , i.e. $al(t)$ will be referred to as reduced displacement.

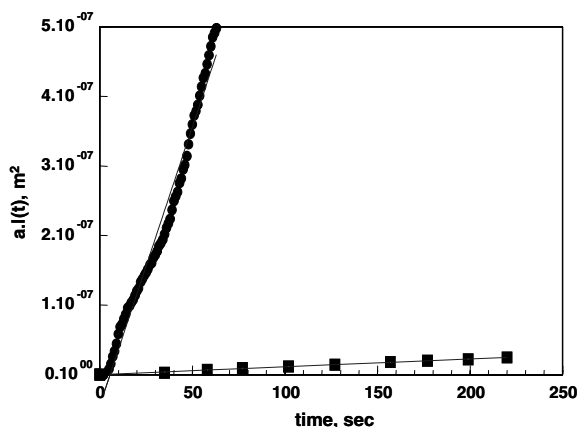
In Fig. 4.20 the dependency of the reduced displacement $al(t)$ on time for a grain boundary half-loop and a half-loop with a triple junction are presented. Although half-loops (and half-loops with triple junction) of different width were studied experimentally, the comparison of the product $al(t)$ compensates the discrepancy between the major parameter of driving force — the width a . Strictly speaking, in the driving force for the half-loop and half-loop with triple junction would be $\frac{2\gamma}{a}$ and $\frac{2\gamma}{a} - \frac{\gamma_{III}}{a}$ respectively, and should be taken into consideration as well; however, since GBIII is a low-angle boundary, we reason that such small correction may be disregarded. One can see, the performed experiment brings out clearly that the triple junction strongly drags grain boundary motion.

Let us consider the mobility of grain boundary and triple junction. Since the exact value of γ , the grain boundary surface tension, is usually unknown it is convenient to use the reduced mobility, A_b and A_{tj} , which can be expressed, respectively, as

$$A_b = \frac{Va}{\pi} = m_b\gamma \quad - \text{ for a half-loop} \quad (4.49)$$

$$A_b = \frac{Va}{2\Theta} = m_b\gamma \quad - \text{ for a grain boundary system with triple junction} \quad (4.50)$$

$$A_{tj} = \frac{Va}{2 \cos \Theta - \frac{\gamma_{III}}{\gamma}} \quad - \text{ for a grain boundary system with triple junction} \quad (4.51)$$

**FIGURE 4.20**

Time dependence of reduced displacement $a.l(t)$ for $\langle 10\bar{1}0 \rangle$ tilt grain boundary half-loop (solid circles) and triple junction configuration (solid squares) for misorientation angle 62° at $T = 390^\circ\text{C}$ [434].

(Contrary to m_b and m_{tj} , the quantities A_b and A_{tj} have the same dimension).

The temperature dependency of A_b and A_{tj} for system I and II is presented in Figs. 4.21 and 4.22. It can be seen that the dependency can be subdivided into two regions. The first one can be characterized by the relation $A_{tj} < A_b$. In this region the motion of the system is controlled by the triple junction mobility. The second region is defined by the relationship $A_b < A_{tj}$. In this region the motion of a grain boundary system is determined by the grain boundary mobility.

In Fig. 4.21 some experimental points that reflect the motion of a grain boundary system with triple junction were recalculated according to the equation for boundary kinetics (Eq. 4.50). We are dealing with the points lying above the intersection point with the line $A_b (\frac{1}{T})$ — mobility of the half-loop. One can see that the recalculated points — open circles — are in good agreement with the half-loop mobility (solid circles). It should be borne in mind that the transition temperature between these two kinetics regimes might be higher than the melting point. In such case the motion of the grain boundary system will be governed by the triple junction mobility in the whole temperature range.

The results obtained in the experiments on Zn tricrystals [434] were qualitatively confirmed by investigations on Al tricrystals [436], [437].

Since the mobility of grain boundaries in Al has been well investigated in bicrystal experiments, such measurements permit a direct comparison of grain

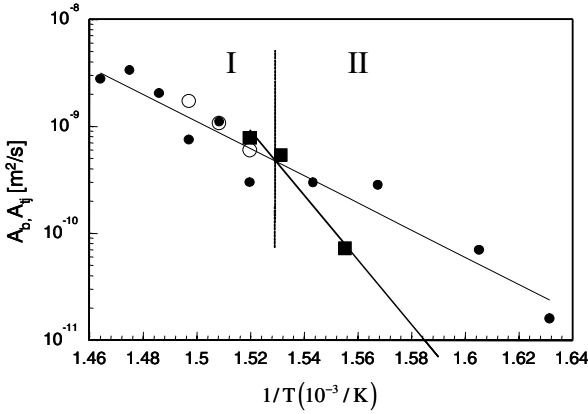


FIGURE 4.21
Temperature dependence of reduced grain boundary mobility A_b (solid circles) and reduced triple junction mobility A_{tj} (solid squares) for $\langle 10\bar{1}0 \rangle$ tilt boundaries in Zn; the regions I and II are the regions of grain boundary and triple junction kinetics, respectively [434].

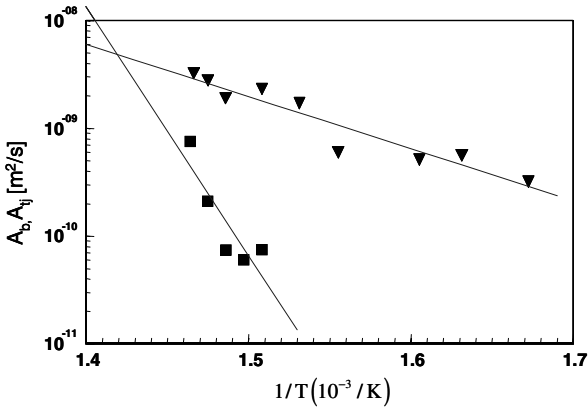


FIGURE 4.22
Temperature dependence of reduced grain boundary mobility A_b (solid triangles) and reduced triple junction mobility A_{tj} (solid squares) for $\langle 11\bar{2}0 \rangle$ tilt boundaries in Zn [434].

boundary and triple junction properties. The experiments were carried out on tricrystals of high purity (99,999%) aluminium with a grain boundary geometry as shown in Fig. 4.18. The crystallographic characteristics of the studied tricrystals are given in Table 4.2. The orientations of the three contiguous grains of each sample were determined by the Laue technique and electron back scatter diffraction (EBSD).

The motion of three grain boundaries systems with triple junctions (Ta-

TABLE 4.2

Misorientation of the Investigated
Tricrystals

Sample	GB I	GB II	GB III
S I	$21^\circ \langle 111 \rangle$	$18^\circ \langle 111 \rangle$	$3^\circ \langle 111 \rangle$
S II	$27^\circ \langle 110 \rangle$	$22^\circ \langle 110 \rangle$	$5^\circ \langle 110 \rangle$
S III	$44^\circ \langle 110 \rangle$	$29^\circ \langle 110 \rangle$	$15^\circ \langle 110 \rangle$

ble 4.2) was investigated in the temperature range between 400 and 590°C [436]. The investigated triple junctions consisted of two high-angle tilt grain boundaries (GBI and GBII) and a low-angle tilt boundary (GB III). Due to different properties of low-angle and high-angle grain boundaries and under the assumption that the properties of high-angle grain boundaries vary only little with changing misorientation, the investigated grain boundary systems can be regarded as symmetrical junctions.

For all samples investigated the velocities V were found to remain constant during an experiment at a given temperature over the entire investigated temperature range. This supports the idea of a steady-state character of motion. The angle Θ was seen to increase with increasing temperature (Table 4.3). Due to the temperature dependence of Θ , the criterion Λ , determined by Eqs (4.30) and (4.45), was found to increase with increasing temperature as well. For a calculation of Λ for the motion of grain boundaries in sample SI the ratio γ_{III}/γ was determined under the assumption that for temperatures near the melting point the value of Θ reaches the thermodynamic equilibrium value¹ ($\Theta_{eq} = \arccos\left(\frac{\gamma_{III}}{2\gamma}\right)$). The values of the ratio γ_{III}/γ for all investigated systems are given in Table 4.3.

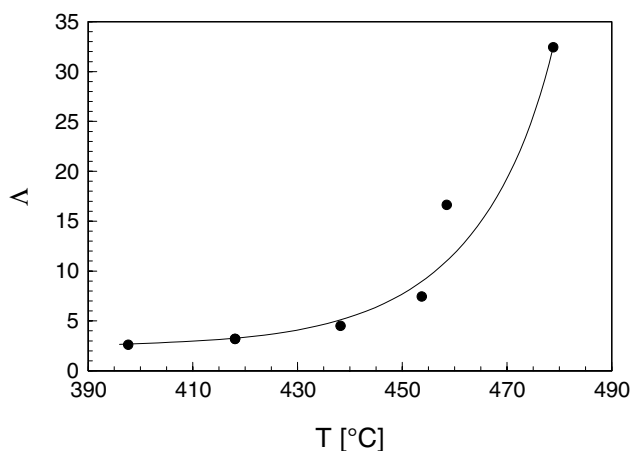
The measured quantities in the current experiments were the migration rate V of the grain boundary system with triple junction and the triple junction angle Θ . Using the measured values of Θ , the dimensionless parameter Λ was calculated for each annealing temperature, and the temperature depen-

¹It is obvious that $\Theta \rightarrow \Theta_{eq}$ when the kinetics of the system become grain boundary controlled. In other words $\Theta_{measured} \cong \Theta_{eq}$ can be expected near the melting point.

TABLE 4.3
Parameters of the Motion of Investigated Grain Boundary Systems with Triple Junctions in Al Tricrystals [436]

Sample	$T^{\circ}\text{C}$	Θ	Λ	V m/s	A_b m^2/s	A_{tj} m^2/s	H_b eV	H_{tj} eV
SI	398	58.5	2.6	$0.58 \cdot 10^{-6}$		$8.7 \cdot 10^{-10}$		
	418	62	3.19	$1.1 \cdot 10^{-6}$		$2.0 \cdot 10^{-9}$		3.2
	418	62	3.19	$1.17 \cdot 10^{-6}$		$2.5 \cdot 10^{-9}$		
	$\frac{\gamma_3}{\gamma} =$	438	67	4.5	$5.52 \cdot 10^{-6}$	$2.8 \cdot 10^{-9}$	$1.3 \cdot 10^{-8}$	
	0.261	454	72.5	7.4	$1.47 \cdot 10^{-5}$	$7.0 \cdot 10^{-9}$	$5.2 \cdot 10^{-8}$	1.4
		459	78	16.6	$6.4 \cdot 10^{-6}$	$3.4 \cdot 10^{-9}$	$5.7 \cdot 10^{-8}$	
SII	479	80	32.4	$1.45 \cdot 10^{-5}$	$7.6 \cdot 10^{-9}$	$2.5 \cdot 10^{-8}$		
	479	55	2.2	$5.8 \cdot 10^{-7}$		$6.6 \cdot 10^{-10}$		
	489	61.5	3.2	$1.13 \cdot 10^{-6}$		$1.7 \cdot 10^{-9}$		2.7
	510	61.5	3.2	$4.79 \cdot 10^{-6}$		$6.0 \cdot 10^{-9}$		
	530	62	3.3	$1.85 \cdot 10^{-5}$	$7.4 \cdot 10^{-9}$			
	$\frac{\gamma_3}{\gamma} =$	551	63.5	3.7	$3.3 \cdot 10^{-5}$	$1.4 \cdot 10^{-8}$		
SIII	0.286	571	70	6.1	$4.32 \cdot 10^{-5}$	$1.9 \cdot 10^{-8}$		1.4
		591	72	7.4				
	530	61.5	9.8	$5.11 \cdot 10^{-7}$	$2.7 \cdot 10^{-9}$			
	551	62	10.9	$1.0 \cdot 10^{-5}$	$5.3 \cdot 10^{-9}$			
$\frac{\gamma_3}{\gamma} =$	0.735	571	64	16.4	$1.86 \cdot 10^{-5}$	$9.8 \cdot 10^{-9}$		
		591	67	50.7	$2.06 \cdot 10^{-6}$	$9.4 \cdot 10^{-9}$		

dency of Λ was determined. Fig. 4.23 shows this dependency for the samples of type SI. According from the approach outlined above, at low temperatures, where Λ is of the order of unity, the motion of the grain boundary system is controlled by the mobility of the triple junction. A rise of Λ with increasing temperature reflects the transition from triple junction to grain boundary controlled motion of the grain boundary system. The technique used for measuring the angle Θ raises the important question whether the angle measured after the sample was cooled down corresponded to the real triple junction angle at annealing temperature. There are two main factors, which may affect the angle Θ : a thermodynamical influence, which reflects the temperature dependence of the grain boundary surface tension, and a kinetic influence, defined by the relation between grain boundary and triple junction mobilities and the width of the vanishing grain a . The thermodynamical effect is negligible, since the boundary surface tension depends only slightly on temperature, although how slightly is not exactly known. In any event, if the grain boundary surface tensions and their temperature coefficients are comparable, then the angle Θ should be essentially temperature independent. The kinetic factor can really affect the magnitude of the angle Θ . Taking into account that triple junction kinetics predominate at relatively low temperatures [436, 437], the observed value of Θ may be reduced compared to the real angle at annealing temperature. However, due to the strong temperature dependence of grain

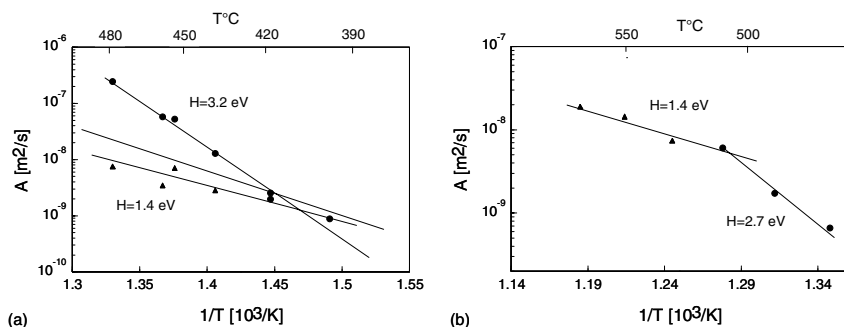
**FIGURE 4.23**

Temperature dependence of the criterion Δ for triple junctions in Al [436].

boundary mobility and the high cooling rate of the sample this change in the real value of Θ is likely to be sufficiently small.

The reduced mobilities for grain boundaries and triple junctions are given in Fig. 4.24 where the triangles represent the (reduced) grain boundary mobility, whereas the circles denote the respective triple junction mobility. The system is obviously controlled by the slowest moving constituent, i.e. the triple junction at low temperatures and the grain boundary at high temperatures. According to their respective linear behavior in the Arrhenius plot the activation enthalpy can be determined as indicated in the figure. Obviously, there is a distinct transition from triple junction kinetics at low temperatures to grain boundary kinetics at elevated temperatures, and the activation enthalpy for triple junction motion H_{tj} is considerably higher than for grain boundary migration (H_b). The behavior of the grain-boundary-controlled branch in Fig. 4.24 compares well with measurements of the reduced grain boundary mobility obtained from the data (see Chapter 3) of independent bicrystal experiments. The corresponding evaluation for system SI is given in Fig. 4.24(a) and yields comparable behavior.

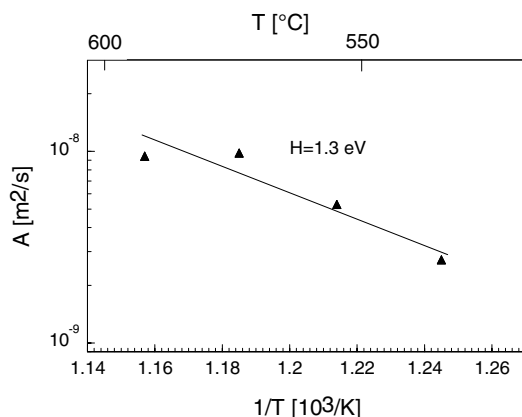
We would like to stress two points. First, there is a transition temperature between two kinetic regimes, namely between grain boundary and junction regime. This transition temperature between these two kinetics regimes might be either higher than the melting point, or a rather low temperature, in particular lower than the temperature range of measurements. In this latter case the motion of a grain boundary system will be governed by the grain boundary mobility in the whole temperature range. One example is given in Fig. 4.25. The measurements of grain boundary motion in the sample SIII

**FIGURE 4.24**

Temperature dependence of triple junction (●) and grain boundary mobility (▲) in samples SI (a) and SII (b). Dotted line represents the mobility of a $21^\circ\langle 111 \rangle$ tilt boundary in Al as reconstructed from literature data (see Chapter 3) ($H = 1.6\text{eV}$; $A_0 = 10^3\text{m}^2/\text{s}$) [436].

were performed at a relatively high temperature. The persistently higher values of A and the constant but comparatively low activation enthalpy in the entire investigated temperature range (Fig. 4.25) indicate that the system always moves in the boundary-controlled regime. Obviously, this has to be attributed to the structure and property of the rectilinear grain boundary in sample SIII which is practically a high-angle boundary contrary to the respective boundaries in the samples SI and SII, which are low-angle boundaries. It is noteworthy that the motion of system SII, also consisting of $\langle 110 \rangle$ tilt boundaries, in this temperature range is controlled by boundary motion as well.

Further, we would like to draw the attention of the reader to the essential difference in the activation enthalpy of grain boundary and triple junction motion. The activation enthalpy of triple junction motion is much larger than the respective quantity for grain boundaries. However, these data are not enough to determine the kinetic regime which controls the motion of the grain boundary system with a junction. The explanation for this phenomenon can be provided on the basis of the compensation effect. The compensation effect manifests itself in a linear dependence between the logarithm of the pre-exponential factor and the enthalpy of activation in the mobility relation. A comprehensive description of this effect is given in Chapter 3. It was shown that the compensation effect can be derived in the framework of a first-order phase transition between the equilibrium state and the metastable “activation barrier” state. The temperature and pressure of compensation correspond to the temperature and the pressure of equilibrium between the “barrier” and ground state. Experimental data indicate also that the compensation temperature is often close to the equilibrium temperature of a first-order phase

**FIGURE 4.25**

Temperature dependence of the reduced mobility of grain boundaries in sample SIII [436].

transformation in the bulk. As has been shown, the compensation effect rather than the energy of activation or the pre-exponential factor individually controls the kinetics of thermally activated interfacial processes. The results of [437] where the motion of a rather large number of grain boundary systems with triple junction in specially grown Al tricrystals was studied are very useful to analyze this phenomenon. The crystallography and the kinetic parameters of grain boundaries and triple junctions investigated in [437] are presented in Table 4.4. (Table 4.4 includes also some data listed in Table 4.2.)

Fig. 4.26 demonstrates the compensation effect for the mobility of grain boundary systems with triple junction and individual tilt grain boundaries in Al.

It is of interest to compare the transition temperature from triple junction kinetics to grain boundary kinetics with the compensation temperature (Table 4.5). Apparently, the kinetic transition temperature compares to the compensation temperature for all grain boundary systems with triple junctions, i.e. is in accordance with the concept put forward in Sec. 3.7: the compensation temperature is the equilibrium temperature between ground state and activated state. As shown in Sec. 3.7, this concept is supported by numerous observations that the compensation temperature is close to the temperature of a nearby phase transition. From the experimental data discussed above it transpires that for the motion of a grain boundary system with triple junction the compensation temperature coincides with the temperature of the kinetic phase transition from the grain boundary regime to the junction regime.

In other words, the compensation temperature is the border between two kinetic regimes: grain boundary kinetics and triple junction kinetics. Below

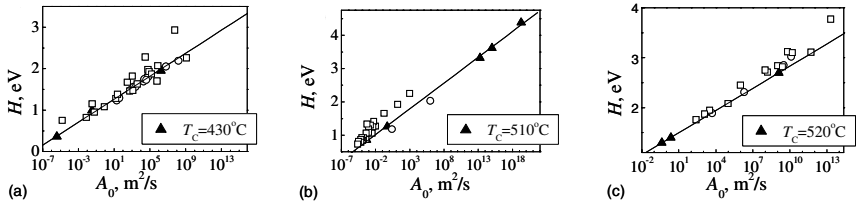
TABLE 4.4
Crystallography and Kinetic Parameters of Grain Boundary and Triple Junction Mobility in Al [437]

No.	GB I	GB II	GB III	$\Delta T, ^\circ\text{C}$ temp. inter- val invest- igated	H_b eV	A_{0b} m^2/s	H_{tj} eV	A_{tj} m^2/s
1	21° $\langle 111 \rangle$	18° $\langle 111 \rangle$	3° $\langle 111 \rangle$	398–479	1.0	0.03	1.8	$4.5 \cdot 10^4$
2	20° $\langle 111 \rangle$	25° $\langle 111 \rangle$	5° $\langle 111 \rangle$	380–420			2.0	$1.8 \cdot 10^6$
3	20° $\langle 111 \rangle$	10° $\langle 111 \rangle$	30° $\langle 111 \rangle$	470–510	0.4	$1.8 \cdot 10^6$		
4	22° $\langle 100 \rangle$	28° $\langle 100 \rangle$	6° $\langle 100 \rangle$	460–495			3.3	$1.8 \cdot 10^{13}$
5	12° $\langle 100 \rangle$	25° $\langle 100 \rangle$	37° $\langle 100 \rangle$	590–620	1.3	0.5		
6	37° $\langle 100 \rangle$	25° $\langle 100 \rangle$	12° $\langle 100 \rangle$	500–550			3.6	$6.8 \cdot 10^{14}$
7	12° $\langle 100 \rangle$	37° $\langle 100 \rangle$	25° $\langle 100 \rangle$	520–570	0.9	$4.7 \cdot 10^{-4}$	4.4	$1.8 \cdot 10^{19}$
8	27° $\langle 110 \rangle$	22° $\langle 110 \rangle$	5° $\langle 110 \rangle$	469–591	1.4	2.3	2.7	$1.3 \cdot 10^9$
9	44° $\langle 110 \rangle$	29° $\langle 110 \rangle$	15° $\langle 110 \rangle$	530–591	1.3	0.4		

TABLE 4.5
Transition Temperature (T_{trans}) and Compensation Temperature (T_{comp}) for Al Bi- and Tricrystals [437]

Grain boundaries in Al bicrystals			Triple junctions in Al tricrystals	
$T_{\text{comp.}}/T_{\text{melt.}}$			$T_{\text{comp.}}/T_{\text{melt.}}$	$T_{\text{trans.}}/T_{\text{melt.}}$
$\langle 100 \rangle$	1.08 [437]	0.82 [436]	0.84	0.85
$\langle 111 \rangle$	0.77 [434]	0.75 [436]	0.75	0.76
$\langle 110 \rangle$	0.92 [434]	0.93 [436]	0.85	0.85

T_C triple junctions drag the motion of the system, whereas at temperatures above T_C the motion is governed by the grain boundary mobility.

**FIGURE 4.26**

Activation enthalpy H vs. pre-exponential factor A_0 for: a) $\langle 111 \rangle$: triple junctions in Al tricrystals [437] — \blacktriangle ; grain boundaries in Al bicrystals — \circ [274], \square [435]; b) $\langle 100 \rangle$: triple junctions in Al tricrystals [437] — \blacktriangle ; grain boundaries in Al bicrystals — \circ [379], \square [435]; c) $\langle 110 \rangle$: triple junctions in Al tricrystals — \blacktriangle ; grain boundaries in Al bicrystals — \circ [435], \square [274].

4.5.1 Motion of a Grain Boundary System with Triple Junction in a Material with Impurities

At the beginning of this chapter we considered in general terms the influence of impurity atoms on the motion of a grain boundary system with triple junction. It was shown that the concurrent interaction between foreign atoms and the two types of moving structural elements makes the process more complicated and more intricate than for grain boundary motion. The first experiments in this area were reported in [433]. The experiments were conducted on tricrystals manufactured from high pure Al (99.9999 wt.%) with different contents of Mg.

The total impurity concentration [433] includes a large number of chemical elements of different concentration. Since each element may interact differently with grain boundary and junction it is important to select the element which is most effective for migration. This problem is hard to address experimentally as it is impossible to produce a “pure” binary alloy with a rather low concentration of the alloying element.

That is why in [433] alloys were produced where the concentration of one species (Mg, “alloying element”) exceeded the total amount of other impurities in the specimen. It was assumed that just this element in the given concentration is responsible for the impurity influence on grain boundary migration (Table 4.6).

All tricrystals studied had the same crystallographic parameters and differed only in Mg concentration. (The concentration of Mg in specimen Al II is distinctly smaller than the total impurity concentration; however, the author of [433] used it as a starting point for the alloys studied.) The shape and orientation of the grown tricrystals is shown in Fig. 4.27. The two curved grain boundaries GB1 and GB2 were identical in terms of misorientation angle

TABLE 4.6
Concentration of Mg in the Al Alloys
Studied [433]

Al Alloys	Al II	Al III	Al IV	Al V
Main solute element	Mg	Mg	Mg	Mg
Concentration wt. ppm	0.2	50	100	1000

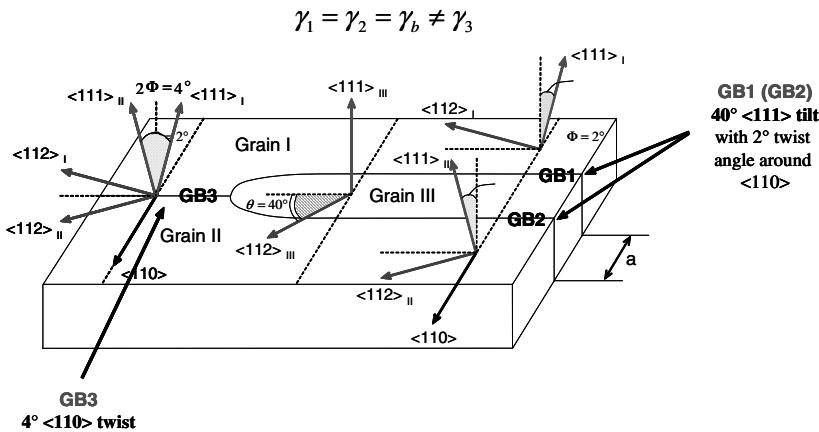


FIGURE 4.27
Geometry and crystallography of grown tricrystals [433].

and rotation axis. The $40^\circ\langle 111 \rangle$ tilt grain boundary (GB1, GB2) was superimposed by a rotation around the axis perpendicular to the grain boundary plane by an angle $\psi = \pm 4^\circ$. Thus, such a boundary can be described as a $40^\circ\langle 111 \rangle$ tilt boundary with a $\pm 4^\circ$ twist component. GB3 is a low-angle twist grain boundary with rotation axis $\langle 110 \rangle$ and misorientation angle $2\psi = 4^\circ$. The width of the shrinking grain a (Grain III) was about $900\text{--}1000\ \mu\text{m}$ in all specimens studied. The shape of the grain boundaries and the displacement of the triple junction were recorded in situ using SEM. A sequence of video frames of the recorded motion is presented in Fig. 4.28 [433].

For all specimens the velocity, the dihedral angle at the triple junction and the criterion Λ were found to remain constant at constant temperature. This confirms the assumption of a steady-state motion of the grain boundary system. In Fig. 4.29 the temperature dependence of the reduced grain boundary and triple junction mobility, A_b and A_{tj} , respectively, and the dihedral angle 2Θ at the triple junction for a specimen with 1000 wt ppm Mg are presented. The kinetic parameters of the grain boundaries and triple junctions studied

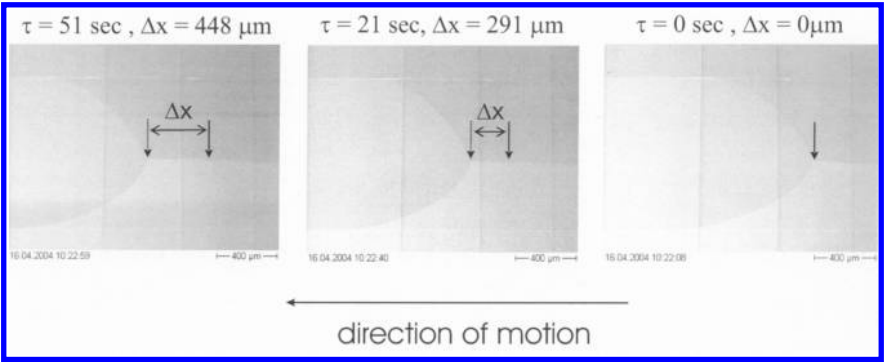


FIGURE 4.28 Set of video frames of recorded SEM images for the motion of grain boundary system with a triple junction in Al with 50 wt ppm of Mg [433].

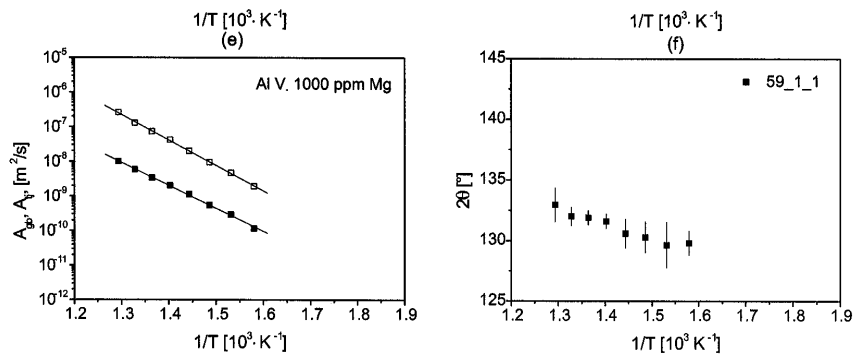


FIGURE 4.29 Temperature dependence of the reduced mobility A_{gb} (solid symbols), A_{tj} (open symbols), and the dihedral angle 2Θ in an Al specimen with 1000 wt % Mg [433].

are given in Table 4.7.

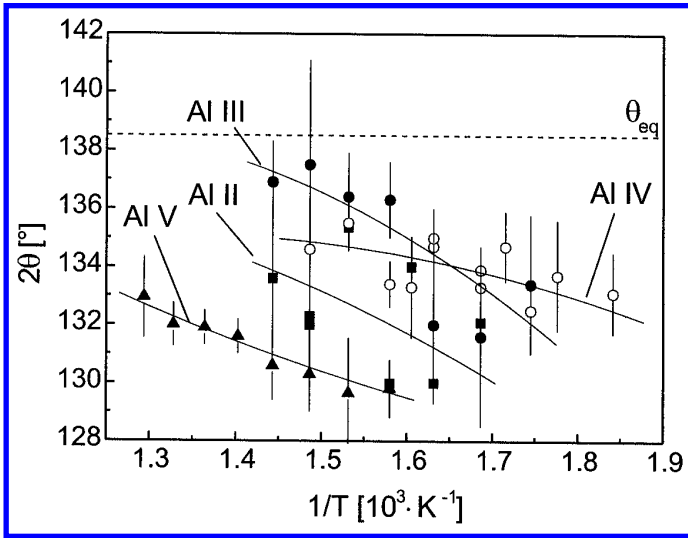
TABLE 4.7
The Activation Enthalpy and Pre-Exponential Factor for Grain Boundary and Triple Junction Migration

	H_{gb}, eV	$A_{gb0}, \text{m}^2/\text{s}$		H_{tj}, eV	H_{tj0}, eV	
Al II	1.45 ± 0.16	$7.173 \cdot 10^2$	$+1.152 \cdot 10^4$ $-6.752 \cdot 10^2$	1.60 ± 0.24	$1.098 \cdot 10^8$	$+1.096 \cdot 10^8$ $-9.182 \cdot 10^7$
Al III	1.49 ± 0.01	$8.938 \cdot 10^2$	$+2.269 \cdot 10^2$ $-1.809 \cdot 10^2$	2.01 ± 0.14	$7.005 \cdot 10^8$	$+8.089 \cdot 10^9$ $-6.446 \cdot 10^8$
Al IV	1.47 ± 0.08	$3.867 \cdot 10^2$	$+3.348 \cdot 10^3$ $-3.005 \cdot 10^2$	1.57 ± 0.11	$8.597 \cdot 10^4$	$+5.969 \cdot 10^5$ $-7.514 \cdot 10^4$
Al V	1.32 ± 0.02	$3.589 \cdot 10^0$	$+1.488 \cdot 10^0$ $-1.052 \cdot 10^0$	1.46 ± 0.02	$7.324 \cdot 10^2$	$+2.211 \cdot 10^2$ $-1.702 \cdot 10^2$

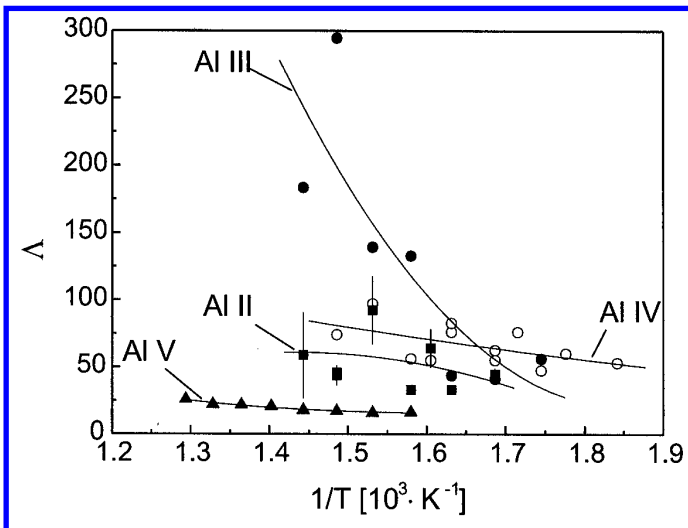
As shown in [433] the dihedral angle 2Θ and the criterion Λ remain constant at a given temperature, however, they increase with rising temperature (Figs. 4.29–4.31).

The criterion Λ decreases dramatically toward lower temperatures, revealing that triple junction drag increases at low temperatures. However, the absolute value of the criterion Λ even at the lowest temperature studied was still rather large ($\Lambda \approx 12$). Probably, the motion of the grain boundary system was still controlled by grain boundary kinetics. It is of interest how the criterion Λ changes with Mg concentration at constant temperature (Fig. 4.32). Obviously, a rising impurity content markedly decreases the criterion Λ . Since Λ is proportional to the ratio of grain boundary and triple junction mobility such a behavior substantiates that foreign atoms affect triple junction mobility much more strongly than grain boundary mobility. Hence, there is a significant difference in interaction of solute atoms with grain boundaries and triple junctions. This is evident also from the concentration dependency of triple junction and grain boundary mobility (Fig. 4.33).

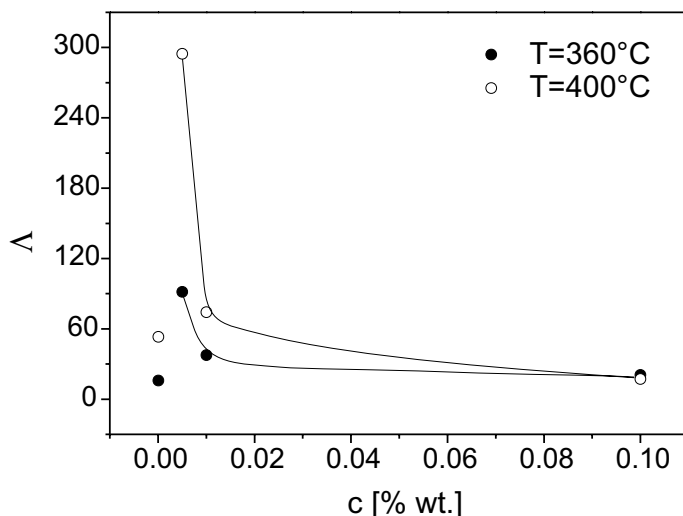
In essence, the two different regimes of coupled triple junction and grain boundary motion can be observed by a change in the angle Θ with temperature. At low temperatures, where Λ is of the order of unity (Figs. 4.16 and 4.17), the motion of the boundaries is dragged by the hardly mobile triple junction. Accordingly, the angle Θ is smaller than predicted by the equilibrium of grain boundary surface tensions (Figs. 4.11 and 4.12), and the motion of the entire boundary system is controlled by the mobility of the triple junction. With increasing temperature the triple junction becomes more mobile compared to the grain boundary as indicated by an increasing value of Λ (Figs. 4.16 and 4.17). Therefore, triple junction drag decreases and at high

**FIGURE 4.30**

Dihedral angle 2θ vs. temperature in different Al alloys: ■ — Al II; ○ — Al III; ● — Al IV; ▲ — Al V [433] (see Table 4.6 for composition of alloys).

**FIGURE 4.31**

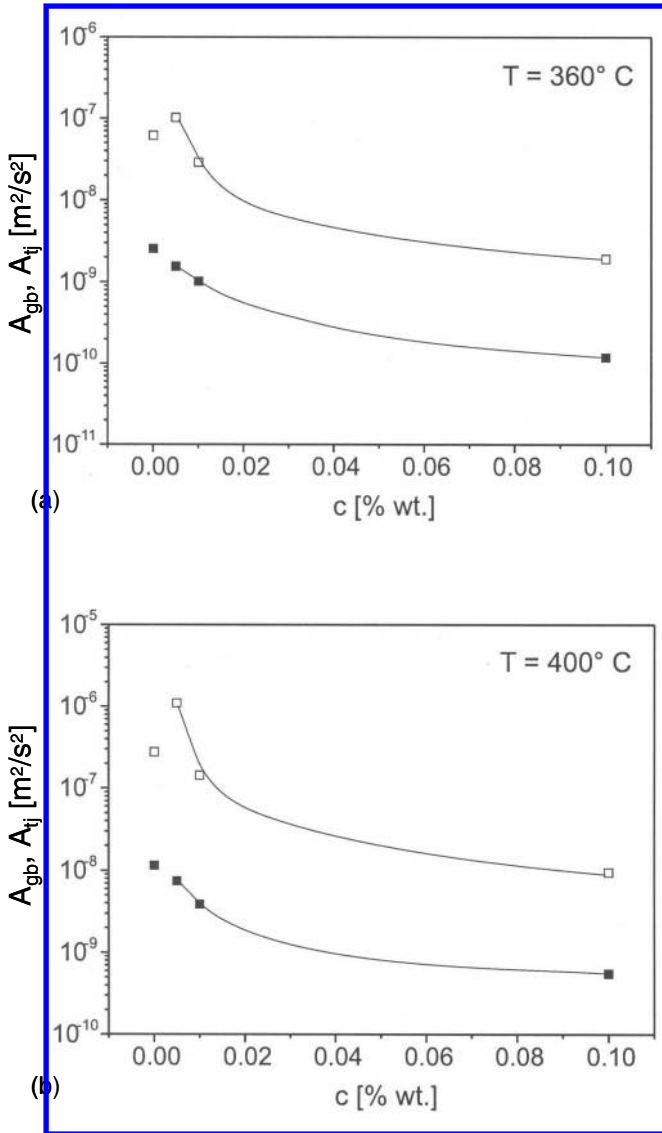
Parameter Λ vs. temperature for different Al alloys: ■ — Al II; ○ — Al III; ● — Al IV; ▲ — Al V [433] (see Table 4.6 for composition of alloys).

**FIGURE 4.32**

Criterion Λ vs. concentration of Mg atoms at constant temperature [433].

temperatures, close to the melting point, the motion of the entire boundary system is governed by the grain boundary mobility only. As a consequence of this transition of the state of motion the angle Θ tends to attain its thermodynamic equilibrium value with increasing temperature (Fig. 4.15). One might argue that the grain boundary surface tension will also change with temperature and may effect a change in Θ . However, the observed temperature dependence of Θ cannot be explained in terms of a different temperature coefficient of the grain boundary surface tension. First, the temperature coefficient of the surface tension is much higher for high-angle grain boundaries than for low-angle boundaries. Thus, the change of Θ for samples S1 and S2 should be opposite to the experimental observations, i.e. the angle Θ would have to decrease with increasing temperature. Secondly, the order of change of Θ is too large to be explained by thermodynamic reasons in terms of different temperature coefficients of the surface tension, in particular for samples S3 and S4, which comprise nearly identical boundaries [183]. Consequently, the temperature dependence of Θ for all samples must result from a change of the kinetics of motion, reflected by the temperature dependence of Λ (Figs. 4.16, 4.17).

The reported investigations unambiguously prove the existence of a specific mobility of triple junctions. The dimensionless criterion Λ specifies the ratio of triple junction mobility to grain boundary mobility (Eq. (4.45)). For low temperatures Λ is on the order of unity and thus the mobility of triple junctions is comparable to the grain boundary mobility (normalized by the width

**FIGURE 4.33**

Reduced mobility A_{gb} (solid symbols) and A_{tj} (open symbols) as a function of Mg concentration c at a constant temperature of (a) 360° and (b) 400°C [433].

a of the shrinking grain). The mobility of the grain boundary and of the triple junction was determined on the basis of the given approach (Eqs. (4.29) and (4.44)). For convenience we use the reduced form (4.50, 4.51). For all triple junctions investigated the activation enthalpy of triple junction migration H_{tj} was found to be higher than for grain boundary migration H_b . It is particularly stressed that in contrast to A_b the reduced triple junction mobility A_{tj} does not only depend on the intrinsic mobility but on the grain size a as well (Eq. (4.51)). With increasing grain size the triple junction becomes more mobile (in terms of its reduced mobility) in comparison to the grain boundary mobility. As a consequence, the transition temperature between the two kinetic regimes, where A_b is comparable to A_{tj} , changes with grain size. Fig. 4.34 [183] shows schematically the temperature dependencies of the reduced mobility of a triple junction and the corresponding grain boundary mobility for different grain sizes. For a large grain size (a_3), as characteristic for grain growth experiments, the mobility of grain boundaries is comparable to the mobility of triple junctions² at relatively low temperatures (Fig. 4.34). The kinetics in the temperature regime, which is characteristic for conventional recrystallization treatments, is controlled by the more slowly moving grain boundary. For a very small grain size (a_1), as characteristic for ultrafine-grained material, e.g. nano-crystalline material, the situation is opposite. The transition temperature is comparatively high, and the kinetics in the same temperature regime is controlled by the triple junction mobility. Moreover, the absolute value of the triple junction mobility and thus its migration rate at a given temperature is distinctly lower for fine-grained than for coarse-grained microstructures, and there is circumstantial evidence that the surprising thermal stability of ultrafine-grained materials is due to insufficient triple junction mobility [412, 413].

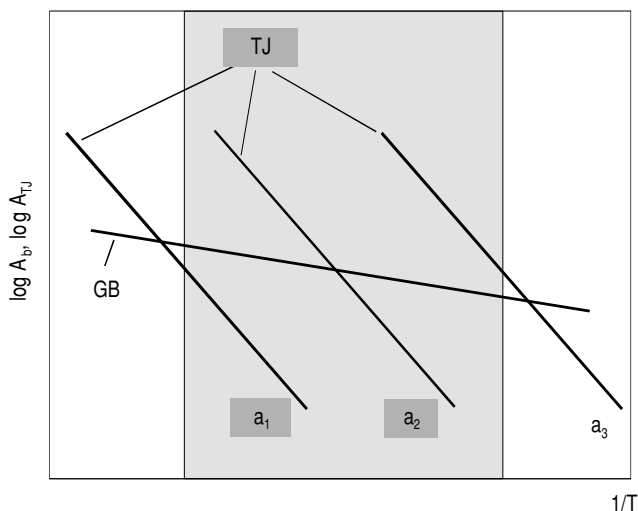
We feel that the results reported above are of particular importance for the field of grain growth. If during grain growth the motion of the grain boundary system is controlled by the mobility of the grain boundaries, the velocity v is proportional to the grain boundary curvature ($\sim 1/a$) (Eq. (4.29)). By contrast, in the case of triple junction controlled motion the velocity v is constant (Eq. (4.27)). The kinetics of the evolution of the mean grain size in the former case will be determined by the dependency

$$v = \frac{da}{dt} \sim \frac{1}{a} \Rightarrow \langle a \rangle \sim \sqrt{t} \quad (4.52)$$

i.e. the mean grain size increases in proportion to the square root of the annealing time. By contrast, in the latter case

$$v = \frac{da}{dt} = \text{const.} \Rightarrow \langle a \rangle \sim t \quad (4.53)$$

²In other words, $m_b \cong m_{tj} \cdot a_3$.

**FIGURE 4.34**

Sketch of the temperature dependence of the reduced grain boundary mobility A_b and reduced triple junction mobility A_{tj} for different grain size a_i ; $a_i < a_2 < a_3$; the shaded area indicates the temperature regime characteristic for recrystallization experiments.

i.e., the mean grain size increases in proportion to the time of annealing.

4.6 Triple Junction Drag and Grain Growth in 2D Polycrystals

4.6.1 Introduction

The grain microstructure in a polycrystal is a mosaic. A 2D mosaic is a surface, in particular, a plane, which is closely packed by 2D shapes. Similarly, if a space is closely filled by 3D bodies, we can call this construction a 3D mosaic. Grain growth in 2D and 3D polycrystals is a living mosaic. During grain growth the grains are growing, shrinking, or disappearing. The grain boundaries are moving as if they are trying to escape the sample, without much success, though.

The observation and study of 2D grain growth in polycrystals — in real polycrystals or in computer simulations — afford, beside pure scientific pleasure, a great aesthetic enjoyment. That is why we admire the mosaics of Seville

or the wonderful engravings of Escher.

The driving force for grain growth is the excess free energy of grain boundaries — their surface tension. Under this driving force grain boundaries migrate through the crystal. This motion leads to the shrinking of some grains and growth of others but on average to an increase in the mean grain size. Other examples of domain growth phenomena are antiphase domains and soap froth. The described change in the grain microstructure conspicuously affects some of the physical, mechanical, and chemical properties of the materials. A polycrystal is an inhomogeneous system, and the characteristic scale of this inhomogeneity is the grain size \bar{R} . This quantity is of concern in a number of theoretical and empirical relationships and model considerations: the Hall-Petch relation for plastic deformation, diffusion creep (Nabarro-Herring and Coble relations), diffusivity, and so on. The dependence of \bar{R} on time and the influence of different factors on the grain size such as temperature, impurity content, etc. are the most important issues of grain growth kinetics. In many cases not only the characteristic grain size \bar{R} is important, but more specific features of the system as well, e.g. grain size distribution, orientation distribution, topological aspects of grain microstructure, the effect of the second-phase particles, voids, etc. It is well known that the major thermodynamic and kinetic properties of grain boundaries depend markedly on the misorientation of adjacent grains and on the spatial orientation of the boundaries (inclination) (see Chapters 1 and 3). In this chapter these aspects of the problem will not be taken into account. Consideration and discussion will be given in the framework of the so-called uniform grain boundary model (to be explained below). The second distinctive property of this chapter is that, contrary to other reviews and books (for instance [416]–[418]), special consideration is given to the influence of grain boundary triple junctions and quadruple points on grain growth.

The first part of this section is dedicated to the grain growth in 2D subjects — foils, thin films, adsorbed phases, 2D phases, etc.

The second part addresses grain growth in 3D systems, the influence of triple junctions and quadruple points on the kinetics of grain growth in such a system and the generalized relation between the topological class of a grain and the volume rate of change.

Finally, the kinetics of grain growth affected by vacancy generation is considered. The reduction in grain boundary area in the course of grain growth is accompanied by a reduction in the grain boundary excess free volume which, in turn, can be viewed as a flux of vacancies into the bulk of the sample, as a cause of elastic stresses and plastic deformation, and may even lead to voids and crack formation.

4.6.2 Topology of Grain Structures

The different topological elements in a polycrystal are related by the Euler theorem

$$-G + F - E + V = 1 \quad (4.54)$$

where G , F , E and V are the numbers of grains, boundaries, triple junctions and vertices. For each grain another version of Euler's theorem holds

$$f_i - e_i + v_i = 2 \quad (4.55)$$

where f_i , e_i , v_i are the numbers of grain boundaries, triple junctions and quadruple points (vertices) which are forming the i th-grain.

Important restrictions apply because of the conditions imposed on grain boundary junctions; all lines of the junctions are triple lines and the points are quadruple points. For a given grain this leads to the relation

$$2e_i = 3v_i \quad (4.56)$$

From Eqs. (4.55) and (4.56) it follows that there is only one independent parameter, for example, f_i . At the same time grains with the same f_i may be topologically different [416].

The topological structure of a polycrystal can be described by the mean values \bar{f} , \bar{e} , \bar{v}

$$\bar{f} = \frac{1}{G} \sum_{i=1}^G f_i = \frac{2F}{G} \quad (4.57)$$

$$\bar{e} = \frac{1}{G} \sum_{i=1}^G e_i = \frac{3E}{G} \quad (4.58)$$

$$\bar{v} = \frac{1}{G} \sum_{i=1}^G v_i = \frac{3V}{G} \quad (4.59)$$

Another important characteristic of the grain structure is the mean number of vertices per boundary. Note that the average here is taken over the whole ensemble of boundaries, not grains [416, 417]:

$$\bar{\eta} = \frac{6}{G\bar{f}} \sum_{i=1}^F Gv_i \quad (4.60)$$

This quantity relates to \bar{f} by the well-known Coxeter relation:

$$\bar{f} = \frac{12}{6 - \bar{\eta}} \quad (4.61)$$

There are more restrictions on polycrystal topology. For example, the relations discussed above allow $\bar{f} = 4$ which is to say that all grains are tetrahedra.

However, it is impossible to fill space by tetrahedra and at the same time to comply with the requirements of connectivity: all junctions are triple lines and quadruple points. The second example is related to 2D grain growth under the action of triple junctions. In this case, as will be shown, the grains should be transformed to polygons with rectilinear grains boundaries. Unfortunately, the requirements of the connectivity are difficult to formalize.

The topological structure of 3D polycrystals is rather complex [401, 404, 419]. The structure of a 2D polycrystal is much simpler. The topology of a 2D grain is described by one scalar integer parameter n , for instance, by the number of triple junctions n which belong to the grain or, what is the same, by the number of adjacent grains. The parameter n is commonly referred to as the topological class of a 2D grain. The Euler relation for a 2D arrangement leads to

$$G - E - V = 1 \quad (4.62)$$

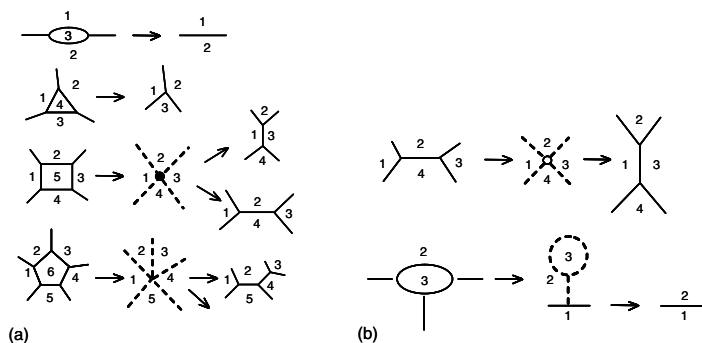
where G , E and V are the number of grains, boundaries (lines) and triple junctions (points), respectively. Since three grain boundaries meet at a junction, and every grain boundary connects two junctions, we arrive at

$$3V = 2E = \bar{n}G \quad (4.63)$$

where \bar{n} is the mean number of junctions per grain. For a representative polycrystal ($G \gg 1$) $\langle n \rangle = 6$ as evident from Eq. (4.62) and the fact that one grain boundary belongs to two grains. The second consequence is that the minimal value of n is two because there is no grain with a simple triple junction, which would require that a boundary border two regions of the same grain.

4.6.3 Elementary Topological Rearrangements

The topological structure of a polycrystal changes in the course of grain growth. These changes are very important: grain growth proceeds by a decrease in the total number of grains and thus, is connected with the loss of grains and the corresponding topological rearrangements. Not only does the area of each grain vary with time, but so does the value of its topological parameter n . The elementary topological rearrangements of a 2D structure are shown in Fig. 4.35. In accordance with Eq. (4.61) the loss of a grain is accompanied by the disappearance of two junctions and three grain boundaries (Fig. 4.35) [409, 416]. Such grain switching is called compulsory. Besides the compulsory switching other spontaneous rearrangements are possible. Their occurrence essentially affects the structure of a polycrystal and grain growth kinetics. The shrinking of grains with $n = 2$ and $n = 3$ is completely determined (Fig. 4.35). For $n = 4$ there are two topologically alternative possibilities and for $n = 5$ there are five possible ways (Fig. 4.35). A spontaneous switching occurs when the length of a boundary shrinks to zero and an unstable fourfold junction is formed (Fig. 4.35). This junction splits into two new

**FIGURE 4.35**

Topological rearrangements in a 2D system due to grain vanishing (a) and due to grain boundary switching (b). For $n = 5$ there are five possible configurations [416].

junctions connected by a new boundary. Eventually, two grains decrease their topological class by one and two grains increase their topological class by one; so the total number of grains, boundaries and junctions remains unchanged after the switching.

For a 3D system the topological rearrangements are much more complicated. Parallel to the vanishing of grains there is a large spectrum of rearrangements in which the number of grain boundaries and junctions change in accordance with the Euler theorem.

4.6.4 Grain Growth Kinetics

In this paragraph we will consider the role of different structural elements of a polycrystal during grain growth.

The major structural elements of a polycrystal are the grain boundaries. They are the main source of driving force for grain growth; their motion and interaction define the mechanism of grain growth. The major grain boundary parameters essential to this process are grain boundary surface tension γ and grain boundary mobility m_b . These parameters can differ for different grain boundaries and depend on boundary inclination. The motion of a grain boundary element is determined by the grain boundary shape in the close proximity of the element.

Neglecting anisotropy the equation of grain boundary motion can be written (Eq. (3.115)) as

$$v = -m_b \gamma \kappa = -A_b \kappa \quad (4.64)$$

where v is the velocity of the normal displacement of the boundary element, κ is the local curvature. Eq. (4.62) represents a nonlinear partial differential equation of first order in time and second order in space.

During their motion grain boundaries interact at triple junctions and quadruple points. Let us restrict our consideration here to grain boundaries and triple junctions (the influence of quadruple points will be considered later). Then the velocity of triple junction motion can be represented as

$$\vec{V}_{tj} = m_{tj} \left(\sum_{i=1}^3 \gamma_i \vec{\tau}_i - \frac{\gamma^\ell \vec{r}}{r^2} \right) \quad (4.65)$$

where m_{tj} and $\gamma^\ell \cdot \vec{r}$ are triple junction mobility and line tension, respectively, the vector \vec{V}_{tj} is directed normal to the junction and the unit vectors $\vec{\tau}_i$ are directed along the adjacent boundaries. The vector \vec{r} is the radius of the triple line curvature. Relation (4.65) defines the boundary conditions for the equations of grain boundary motion (Eq. (4.64)). The vector relation determines two conditions at any point of a triple junction. However, three grain boundaries are intersecting at the triple junction; in other words, we need three boundary conditions. The third condition is of geometrical origin: it is the requirement for three surfaces (grain boundaries) to intersect along one line, the triple junction.

If the role of triple junctions is neglected, the boundary conditions may be simplified to the condition of equilibrium of the dihedral angles between the three intersecting boundaries

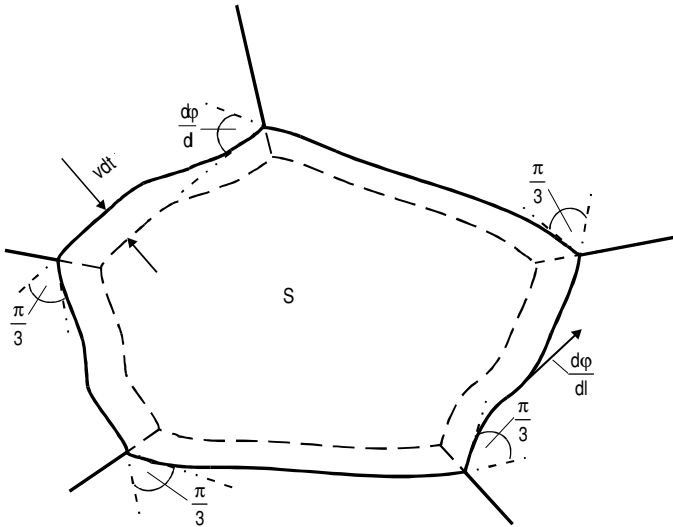
$$\sum_{i=1}^3 \gamma_i \vec{\tau}_i = 0 \quad (4.66)$$

In many cases grain growth is considered under the assumption that the triple junction line tension is rather small while grain mobility is rather large, so for sufficiently large grains the effect of triple junctions can be neglected. We will discuss this issue in greater detail later. However, we would like to stress here that even for a polycrystal with rather large mean grain size it is impossible to avoid a contribution of triple junctions to grain growth kinetics: the vanishing grains necessarily experience a stage with extremely small grain size.

A configuration where more than three boundaries intersect along one line is energetically unfavorable and thus unstable. It will split into several triple junctions (see problem 2.3.4). We would like to remind the reader that this holds in the framework of the uniform grain boundary model.

However, there is a stable configuration where more than three grain boundaries meet. These are so-called quadruple junctions (points). In such a point six grain boundaries, four grains and four triple lines meet. All other configurations of intersections are energetically unprofitable and, as a consequence, unstable.

If the line tension of the triple junctions is neglected, the quadruple points

**FIGURE 4.36**

Definition of parameters for the effect of triple junctions for a calculation of the rate of grain area change.

do not introduce new boundary conditions — the equilibrium angles at the triple junctions unambiguously determine the grain boundary configuration in the vicinity of the quadruple junctions [421]. In the case that the structure and energy of the triple junction line depend on the line direction the line tension has to be taken into account for the equilibrium angles between grain boundaries. It is stressed that the considerations made above relate to stationary grain boundaries.

4.6.5 Uniform Grain Boundary Model and the Von Neumann-Mullins Relation

For grain growth in a 2D system, Mullins [242] derived a fundamental relation, which was originally formulated by Von Neumann for 2D soap froth [476]. The respective model makes very fundamental assumptions, namely: (1) All grain boundaries possess equal mobilities and surface tensions, irrespective of their misorientation and the crystallographic orientations of the boundaries, the so-called uniform grain boundary model; (2) the mobility of a grain boundary is independent of its velocity; (3) the triple junctions do not affect grain boundary motion; therefore, the contact angles at triple junctions are always in equilibrium and, due to the first assumption, are equal to 120° .

Let us consider a 2D grain with area S [242, 476]. In the time interval

dt all points on the grain boundaries of the grain will be displaced normal to the grain boundaries by the amount Vdt , where V is the grain boundary migration rate. Accordingly, the rate of change of the grain area S can be expressed by

$$\frac{dS}{dt} = - \oint V d\ell \quad (4.67)$$

where $d\ell$ is an element of the grain perimeter. For grain growth

$$V = \gamma m_b \kappa \equiv A_b \kappa \quad (4.68)$$

where m_b is the grain boundary mobility, γ is the grain boundary surface tension, K is the local curvature of the grain boundary

$$K = \frac{d\varphi}{d\ell} \quad (4.69)$$

where φ is the tangential angle at any given point of the grain boundary.

From Eqs. (4.67)–(4.69), it follows that

$$\frac{dS}{dt} = -A_b \oint d\varphi \quad (4.70)$$

If the grain were bordered by a smooth line, the integral in Eq. (4.70) would be equal to 2π . However, because of the discontinuous angular change at every triple junction, the angular interval $\Delta\varphi = \pi/3$ is subtracted from the total value 2π for each triple junction. Consequently

$$\frac{dS}{dt} = -A_b \left(2\pi - \frac{n\pi}{3} \right) = \frac{A_b\pi}{3} (n - 6) \quad (4.71)$$

where n is the number of triple junctions for each respective grain, i.e. the topological class of the grain. Thus the rate of area change is independent of the shape of the boundaries and determined by the topological class n only. Grains with $n > 6$ will grow and those with $n < 6$ will disappear [242, 476]. Eq. (4.71) is referred to as the Von Neumann-Mullins relation.

What should especially be stressed is the generality of the approach considered and the versatility of the consequences; in part, the result expressed in Eq. (4.71) does not depend on the shape of moving boundaries. The rate of grain area changes along with the sign of the right-hand side of Eq. (4.71), which is determined only by the number of the adjacent (neighboring) grains, or, what is the same, by the topological class of the grain — the number of triple junctions of the grain. That is why every attempt to revise either the derivation of the Von Neumann-Mullins relation or its consequences attracts considerable attention from materials scientists. However, Gusak and Tu declared that they found an invalidity of the Von Neumann-Mullins (VN-M) theorem [242, 476]. “To prove the invalidity of any theorem,” as the authors wrote quite rightly, “it is enough to have just one example showing that it

is wrong.” For this purpose the authors considered the shrinkage of a regular convex triangle, using the VN-M theorem and a “direct derivation,” to compute the area change of a regular convex triangle [477].

The VN-M relation yields $\frac{dS}{dt} = \pi m_b \gamma$, whereas the “direct derivation” of the grain area change in the case of a shrinking regular convex triangle results in: $\frac{dS}{dt} = 2(\pi - \sqrt{3}) m_b \gamma$. Gusak and Tu attempted to explain the discrepancy by considering in greater detail the motion of different parts of a moving grain boundary, which cannot, of course, replace the general and powerful VN-M derivation. As can be seen, a correct derivation for a regular three-sided grain only deviates on the order 3% from the VN-M result, and the difference is thus clearly a second-order effect.

Hunderi and Ryum [478] tried to solve the problem of the configuration considered by Gusak and Tu by numerical methods on the basis of the major equations of the VN-M approach. Since their calculations were carried out in the framework of the VN-M approach, the result is quite evident and predictable from the very beginning: the VN-M relation is correct.

Nevertheless, one issue remains open: what is the reason for such a discrepancy?

A more sophisticated treatment of the phenomenon is given in [479]. The reason for the discrepancy between the VN-M approach and the approach of Gusak and Tu are the different boundary conditions. Whereas the VN-M approach associates the motion of a grain boundary element with the local curvature when an element is displaced normal to itself, the approach put forward by Gusak and Tu requires that the boundaries have a constant curvature such that the contact angles at the triple junctions are in equilibrium. For each displacement of a boundary, for instance a triangular grain, the curvature has to be readjusted to account for equilibrium at the junctions. In fact, the curvature will increase with progressing grain growth owing to the fact that the grain shrinks. Therefore an additional adjustment of the grain boundary geometry has to occur in order to maintain the proper curvature. In the VN-M approach, such an adjustment is not enforced, since the boundary shape can be arbitrary. Equilibrium at the junctions is established locally, and the curvature driven grain boundary motion maintains or reduces the curvature in contrast to the Gusak-Tu approach. In the Gusak-Tu approach two steps of motion are involved, curvature driven growth and subsequent readjustment of the curvature to re-establish constant curvature and junction equilibrium. The VN-M approach considers only curvature driven growth and disregards curvature adjustment at junctions as an effect of second order. There is actually no physical principle that would require constant curvature, and the Gusak-Tu approximation is a very special case determined entirely by geometry, which however is not realized in nature.

Finally, it can be stated that the evolution of a “regular convex triangle” during grain growth does not follow the scenario of Gusak and Tu [477], namely the shrinkage as a self-similar regular triangle. If a regular convex triangle is left to its own devices, it becomes an isosceles triangle and collapses

as a triangle of irregular shape. Its state as a regular triangle is only one possibility among infinitely many others. The correctness of the VN-M relation cannot be judged from the behavior of a grain of a particular shape.

Thus, the phenomenon can be expressed like this. The configuration described and discussed by Gusak and Tu can appear in the course of grain growth, however this is a configuration without future, by increasing this configuration will be transformed to another, not so symmetrical configuration (isosceles triangle) and, finally, collapse as a triangle of irregular shape. Eq. (4.71) follows from the general Gauss-Bonnet theorem about the integral of the Gaussian (total) curvature κ_G . For two dimensions it coincides with the Laplacian (mean) curvature κ_L . Just this curvature determines the capillary pressure and, as a consequence, the capillary driven grain boundary motion. In three dimensions, however, these two curvatures are different; even their dimensionality is different:

$$\kappa_G = \frac{1}{R_1} \cdot \frac{1}{R_2} \quad (4.72)$$

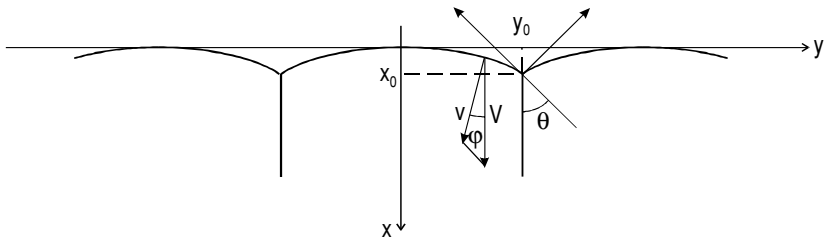
$$\kappa_L = \frac{1}{R_1} + \frac{1}{R_2} \quad (4.73)$$

where R_1 and R_2 are the principal radii of curvature. That is why a direct transfer of Eq. (4.71) to 3D systems is impossible. There have been attempts to extend the results of the VN-M approach to a 3D situation. The successes and failures of this attempt will be analyzed in further considerations.

4.6.6 Effect of Triple Junction Drag on the Von Neumann-Mullins Relation

Evidently, the existence of triple junctions dramatically affects the kinetics of grain growth. However, we will show below that the interaction of moving grain boundaries with triple junctions also impacts our conception of microstructure evolution.

Let us consider the system shown in Fig. 4.5 [183, 403, 474]. This system was analyzed comprehensively above. As can be seen from Fig. 4.5 this system comprises three grains (three grain boundaries) with a common triple junction. If a triple junction is mobile and does not drag grain boundary motion, then parameter Λ (Eq. (4.30)) tends to infinity and the angle $\Theta \rightarrow \pi/3$, i.e. the equilibrium angle at a triple junction in the uniform grain boundary model. By contrast, however, when the mobility of the triple junction is relatively low (strictly speaking, when $m_{tj}a \ll m_b$ then $\Theta \rightarrow 0$). It is particularly emphasized that the angle Θ is completely defined by the dimensionless parameter Λ , which, in turn, is a function of not only the ratio of triple junction and grain boundary mobilities, but of the grain size as well. In the following, we shall use the term “triple junction of low mobility” when we mean “small value of Λ ”.

**FIGURE 4.37**

Configuration of grain boundaries at triple junctions during steady-state motion for $n > 6$.

One of the cornerstones of the VN-M relation is the assumption that the triple junctions do not drag grain boundary motion. However, the fact that the kinetics of triple junctions may be different from the kinetics of the adjoining grain boundaries affects the kinetics of microstructure evolution during grain growth, as formulated in terms of the VN-M relation.

The rate of area change for a grain with $n < 6$ can be expressed as

$$\frac{dS}{dt} = -m_b \gamma \oint d\varphi = -A_b [2\pi - n(\pi - 2\Theta)] = A_b (\pi - 2\Theta) \left(n - \frac{2\pi}{\pi - 2\Theta} \right) \quad (4.74)$$

Since the limited mobility of the triple junction reduces the steady-state value of the angle Θ as compared to the equilibrium angle, the shrinking rate of grains with $n < 6$ decreases, as obvious in the case when the mobility of the triple junction becomes very low. In other words, for grains with $n < 6$ the influence of the triple junction mobility slows down the process of grain structure evolution, decreasing the vanishing rate of grains with small topological class ($n < 6$).

For grains with topological class greater than 6 let us consider the steady-state motion of a grain boundary system shown in Fig. 4.37 with the same set of assumptions applied to the previous boundary system, namely, uniform grain boundary properties and quasi-two-dimensionality [473]. The steady-state motion of this system is determined by Eq. (4.25) only with different boundary and initial conditions

$$\begin{aligned} y'(0) &= \infty \\ y'(x_0) &= \tan \Theta \\ y(0) &= 0 \end{aligned} \quad (4.75)$$

The velocity of triple junction motion can be expressed as

$$V_{tj} = m_{tj} \gamma (1 - 2 \cos \Theta) \quad (4.76)$$

As in the previous case, Eqs. (4.25) and (4.75) fully define the problem considered.

$$y(x) = -\frac{x_0}{\ln \sin \Theta} \arccos \left(e^{\frac{\pi}{x_0} \cdot \ln \sin \Theta} \right) \quad (4.77)$$

The velocity of steady-state motion of the system is

$$V = -\frac{m_b \gamma}{x_0} \ln \sin \Theta \quad (4.78)$$

The length x_0 replaces the role of the grain size a in the previous case (Fig. 4.37) or

$$y_0 = y(x_0) = -\frac{x_0}{\ln \sin \Theta} \arccos \left(e^{\ln \sin \Theta} \right) = -\frac{x_0}{\ln \sin \Theta} \left(\frac{\pi}{2} - \Theta \right) \quad (4.79)$$

From Eqs. (4.76) and (4.78) we obtain Λ , which describes the influence of the triple junction mobility on grain boundary migration

$$-\frac{\ln \sin \Theta}{1 - 2 \cos \Theta} = \frac{m_{tj} x_0}{m_b} = \Lambda \quad (4.80)$$

Obviously, for $\Lambda \gg 1$, when the boundary mobility determines the kinetics of the system, the angle Θ tends to its equilibrium value ($\pi/3$).

Again, the angle Θ changes when a low mobility of the triple junction starts to drag the motion of the boundary system. However, as evident from Eq. (4.80) and Fig. 4.6, in this case the steady-state value of the angle Θ increases as compared to the equilibrium state. (Otherwise the triple junction would move in the negative direction of the x -axis, increasing the free energy of the system.)

For $\Lambda \ll 1$ the angle Θ (Eq. (4.80)) tends to approach $\pi/2$. The dependency $\Theta = \Theta(\Lambda)$ for both $n < 6$ and $n > 6$ are shown in Fig. 4.6.

Such an increase of the angle Θ also decreases the magnitude of $(n - 2\pi/\Theta)$ in Eq. (4.74), in other words, it decreases the “effective” magnitude of the topological class of the growing grain with $n > 6$. Consequently, microstructural evolution will slow down due to triple junction drag for any n -sided grain. The only exception holds for $n = 6$, since a hexagonal grain structure becomes unstable when the contact angle $2\Theta \neq 2\pi/3$. Since the actual magnitude of Θ is determined by the triple junction and grain boundary mobility as well as the grain size and is independent of the number of sides of a grain, there is no unique dividing line between vanishing and growing grains with respect to their topological class anymore, like $n = 6$ in the VN-M approach.

The generality of the approach considered and the diversity of the consequences should be stressed. In particular, the result expressed in Eq. (4.71) does not depend on the shape of the moving boundaries: the rate of grain area change along with the sign of the right-hand side of Eq. (4.71) is determined only by the number of the adjacent (neighboring) grains, or, what is same, by the topological class of the grain — the number of triple junctions of the grain.

4.6.6.1 Triple Junction Motion and Grain Microstructure Evolution

The classical concepts of grain growth in polycrystals are based on a dominant role of grain boundaries. Since metals are not transparent, we are used to imaging crystalline microstructures by means of 2D sections, for instance in optical micrographs.

The 2D model of grain growth provides the basis for our understanding of the thermodynamics and kinetics of grain microstructure evolution. However, 2D grain microstructures are not pure mathematical abstractions. In modern materials science objects with 2D grain structure are physically meaningful and have achieved great importance. Metal sheet, thin films, coatings and thin layers are prominent examples of objects with 2D grain microstructure.

For a variety of problems it is possible to obtain an exact physical solution for 2D microstructures. The most famous example is the VN-M relation which was considered above. This relation is based on three fundamental assumptions.

The first assumption agrees with the described uniform boundary model and is likely to be realized in many cases. Of course, grain boundary mobility is significantly affected by grain boundary character (see, for instance Chapter 3), and an anisotropy of grain boundary properties manifests itself also in grain microstructure evolution [422]. Nevertheless, in polycrystals with random texture and in commercial alloys non-special boundaries are likely to prevail [273, 424]. For a more refined analysis, anisotropic boundary properties also have to be taken into account; however, they will not change the fundamental conclusions of the approach presented in the following [425].

The second assumption complies with the principles of absolute reaction rates. The third assumption — the infinite mobility of grain boundary triple junctions — is a mere hypothesis and needs to be checked experimentally. For this it is necessary to measure the triple junction mobility.

As shown in the previous paragraphs the theoretical approaches and experimental technique developed make it possible to measure quantitatively the mobility of triple junctions [183, 427, 436]. It was shown that the behavior of a grain boundary system with triple junction is determined by the dimensionless criterion $\Lambda = \frac{m_{tj}a}{m_b}$. For steady-state motion of the grain boundary system with triple junction the criterion Λ can be expressed as a function of the angle Θ at the tip of triple junctions (relation 4.30). The line between Λ and Θ makes it possible to measure the value of Λ and, in turn, the triple junction mobility for different metals and grain boundary systems. Experimental investigations on grain boundary systems with triple junctions in Zn and Al have shown that the triple junction mobility is finite and may be low. Molecular dynamics simulation studies of triple junction migration, performed for the same geometrical configuration as used in real experiments [183, 421, 436], confirmed that the triple junction mobility, contrary to the VN-M assumption, can be limited [439, 440] (see Chapter 5). On the whole, the simulations sup-

port the experimental observations of non-equilibrium triple junction angles and ascertain a substantial triple junction drag.

4.6.6.2 The Generalized Von Neumann-Mullins Relation

Since the assumptions made to derive the VN-M relation can obviously be violated it is of interest to consider this relation for the case of non-equilibrium contact angles at the triple junction. Such an attempt was undertaken in [427, 441, 442]. To conserve the central idea of the VN-M relation let us consider first a situation when the influence of the triple junction is rather large, but, nevertheless, the motion of the system can be viewed as grain boundary motion, since the driving force is still due to grain boundary curvature, i.e. the triple junction is reduced to a change in the angle Θ (Eq. 4.74)).

Since $\Lambda = \Lambda(\Theta)$ the relation between the rate of grain area change and the criterion Λ can be found. In [442] such a relation was derived expanding the function $2\cos\Theta - 1$ into a power series in the vicinity of $\Theta = \pi/3$ for $n < 6$ and $n > 6$, respectively. For $n < 6$

$$\Theta \cong \frac{\sqrt{3}\pi\Lambda}{6 + 3\sqrt{3}\Lambda} \quad (4.81)$$

and, respectively,

$$\dot{S} = \frac{m_b\gamma\pi}{3} \left(n \frac{6 + \sqrt{3}\Lambda}{2 + \sqrt{3}\Lambda} - 6 \right) \quad (4.82)$$

For $\Lambda \rightarrow \infty$ — free boundary kinetics regime — Eq. (4.82) is identical to the classical VN-M relation.

The topological class n^* of grains for which $\dot{S} = 0$ is equal to

$$n^* = \frac{2 + \sqrt{3}\Lambda}{1 + \frac{\sqrt{3}}{6}\Lambda} \quad (4.83)$$

Evidently n^* increases with Λ and for $\Lambda \rightarrow \infty$ $n^* \rightarrow 6$. For $n > 6$

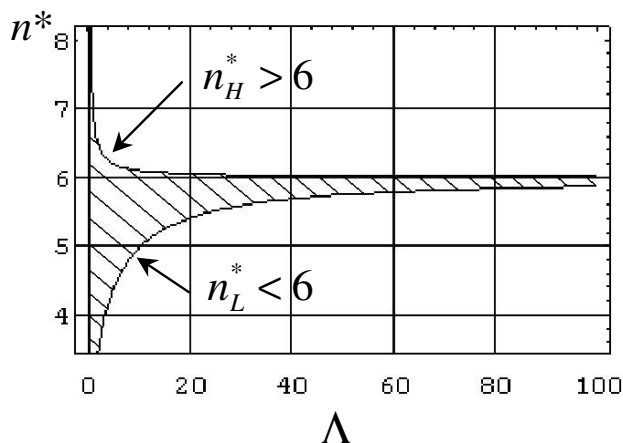
$$\Theta \cong \pi/3 + \frac{1}{\Lambda B} \quad (4.84)$$

where $B = -\frac{\sqrt{3}}{\ln \sin(\pi/3)}$ and, correspondingly

$$\dot{S} \cong \frac{m_b\gamma\pi}{3} \left[n \left(1 - \frac{6}{\pi\Lambda B} \right) - 6 \right] \quad (4.85)$$

Apparently, for $n < 6$ and for $n > 6$, the equation for the rate of grain area change becomes identical for $\Lambda \rightarrow \infty$; the value of n^* for $n > 6$ reads

$$n^* = \frac{6}{1 - \frac{6}{\pi\Lambda B}} \quad (4.86)$$

**FIGURE 4.38**

Dependence of n_H^* and n_L^* on Λ .

The drag effect of grain boundary triple junctions results in a change in the topological limit between the classes of shrinking and growing grains such that the limit decreases for shrinking grains but increases for growing grains. This behavior $n^*(\Lambda)$ becomes obvious from Fig. 4.38, where the cases $n < 6$ and $n > 6$ are distinguished as $n_L^*(\Lambda)$ and $n_H^*(\Lambda)$, respectively.

4.6.6.3 Grain Stability

Since there is a gap between $n_L^*(\Lambda)$ and $n_H^*(\Lambda)$ it is an interesting question how grains behave with $n_L^*(\Lambda) < n < n_H^*(\Lambda)$. From the above discussion it appears that such grains are not capable of growing or of shrinking (Fig. 4.38), i.e. grains of the topological classes in the hatched area of Fig. 4.38 will be stable. This can be understood from the following consideration.

According to Eq. (4.74) \dot{S} becomes zero for

$$\Theta = \frac{\pi}{2} \left(1 - \frac{2}{n} \right) \quad (4.87)$$

For any integer n , $\Theta(n)$ is exactly the (half) junction angle for an n -sided polygon, i.e. $\Theta = 60^\circ \left(\frac{\pi}{3} \right)$ for $n = 6$, $\Theta = 54^\circ$ for $n = 5$, $\Theta = 45^\circ \left(\frac{\pi}{4} \right)$ for $n = 4$, $\Theta = 67.5^\circ \left(= \frac{3\pi}{8} \right)$ for $n = 8$, etc.

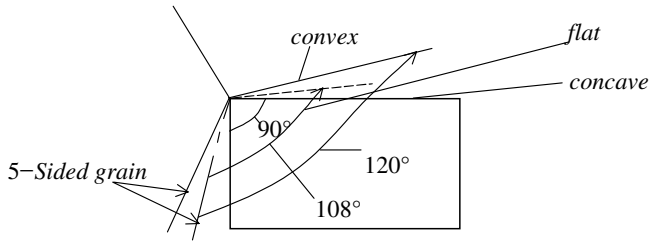
This means for a given (integer) n^* the angle Θ corresponds to the (half) internal angle of an n^* -sided polygon, i.e. the boundaries are flat, and without curvature the polygon is stable. The important point to consider is that the angle Θ is a dynamical angle, i.e. it develops during motion of the boundaries that are connected at the triple junction. Prior to motion boundaries

at a triple junction will adjust Θ to attain the equilibrium angle ($\Theta = 60^\circ$). Therefore, 6-sided grains have flat boundaries, $n < 6$ -sided grains have convex boundaries, $n > 6$ -sided grains have concave boundaries. If the system is allowed to move the curved boundaries will move and adjust Θ to the dynamic value, which is less than 60° for $n < 6$ and larger than 60° for $n > 6$.

The 6-sided grain will not change since it has flat boundaries to begin with, so there is no driving force for grain boundary motion and, therefore, no change of $\Theta = m\pi/3$. Let us consider a 5-sided grain under the condition $n^* = 4$, i.e. a 4-sided grain will attain flat boundaries and, therefore, is stable (Fig. 4.39). Prior to motion the 5-sided grain has convex boundaries with $\pi/3 = \Theta$ at the junctions. Triple junction drag will change the angle to $\Theta = \pi/4$. Corresponding to $n^* = 4$, the angle $\Theta = \pi/4 = 45^\circ$ is smaller than the junction angle for a 5-sided grain with flat boundaries. During the change of the angle from initially $\Theta = 60^\circ$ to $\Theta = 45^\circ$ for the given Λ the angle will pass through $\Theta = 45^\circ$, where the boundaries become flat and the driving force ceases. The configuration is locked. The junction angle may return to $\Theta = 60^\circ$ to establish static equilibrium at the junction, but this will make the boundary convex and drive the junction angle back to 54° . In essence, if the 5-sided grain were to attain the angle $\Theta = 45^\circ$ from initially 60° , it would have to change the curvature from convex to concave. For this to happen it must pass through a flat configuration, where the driving force ceases and the system becomes locked.

The same holds for a grain with $n^* > 6$. Let us consider $n^* = 8$ and a 7-sided grain. Initially, Θ is in static equilibrium with $\Theta = 60^\circ$. The boundaries are concave. Because of $n^* = 8$ the dihedral angle of the 7-sided grain will change to a terminal 67.5° . At $\Theta = \frac{5\pi}{14} = 64.3^\circ$ the 7-sided grain will arrive at a configuration with flat boundaries. Again, the boundaries at static equilibrium are concave. A 7-sided grain for $\Theta = 67.5^\circ$ with a Λ corresponding to $n^* = 8$ would have convex boundaries. It never can get there, since the change in curvature requires a transient flat boundary, where the system will become locked, when only curvature drives the boundary system.

In summary, grains with n -sides and $n_L^* < n < n_H^*$ become locked and can neither grow nor shrink. This phenomenon might be essential for understanding the high stability of grain microstructures in ultrafine-grained and nanocrystalline materials, specifically in 2D thin layers and films. For $\Lambda \rightarrow \infty$, i.e. for $\Theta = \pi/3 = \text{const.}$, the border between growing and shrinking grains is the singular value $n^* = 6$. It dissociates to an interval (between n_L^* and n_H^*) for rather small Λ . Such an effect is expected to further stabilize the grain microstructure. Since Λ depends on grain size, this stabilization is more pronounced in fine-grained and nanocrystalline systems.

**FIGURE 4.39**

Geometry of a 5-sided grain during transition from static to dynamic equilibrium for $n^* = 4$.

4.6.6.4 Triple Junction Controlled Growth

For a large grain size, or more correctly, for a rather large criterion Λ , the system moves under boundary kinetics while triple junctions only slightly disturb grain boundary motion. However, as the criterion Λ decreases, grain boundary migration and grain growth, respectively, become controlled by the motion of triple junctions. The triple junction kinetics are characterized by some distinctive properties which we will discuss in more detail. To begin with, we will show that under triple junction control in the course of grain growth in 2D systems the grains will eventually be bordered by straight (flat) boundaries, i.e. they will assume a polygonal shape.

Let us consider the curvature κ of a grain boundary system with triple junctions (for configurations which relate to $n < 6$ and $n > 6$). As derived in [441] for a system with $n < 6$ we obtain for the curvature κ

$$\kappa = \frac{1}{\xi} e^{-x/\xi + \ln \sin \Theta} = \frac{2\Theta}{a} e^{-(2\Theta/a)x} \sin \Theta = \frac{\Lambda}{a} \sin \Theta (2\cos \Theta - 1) e^{-(2\Theta/a)x} \quad (4.88a)$$

where $\xi_i = \frac{a}{2\Theta}$. For a system with $n > 6$ it was shown that

$$\kappa = \frac{\ln \sin \Theta}{x_0} e^{(x/x_0) \ln \sin \Theta} = \frac{\Lambda}{x_0} (1 - 2\cos \Theta) e^{(x/x_0) \ln \sin \Theta} \quad (4.88b)$$

Since for triple junction kinetics $\Lambda \rightarrow 0$, the grain boundary curvature $\bar{\kappa}$ also approaches zero, i.e. the grain structure of 2D polycrystals comprises straight grain boundaries. In other words, under triple junction kinetics the grains in a 2D polycrystal represent a system of contiguous polygons.

More specifically, as shown in [441], in the framework of triple junction kinetics a polygon of arbitrary shape will be transformed into an equilateral polygon, and any deviation from an equilateral polygon will generate a force to restore the equilibrium shape. The only exception is a triangle, i.e. a grain of topological class $n = 3$ is always unstable and must disappear. Eventually,

all other shrinking polygons must by necessity go through this stage, when grain growth is controlled by the motion of triple junctions.

This phenomenon has important consequences for the development of grain growth. To demonstrate this we take a look at the evolution of a shrinking grain in the course of grain growth. The topological class of such a grain must be lower than 6, taking into account naturally all corrections to the VN-M relation, given above. We emphasize that the transition between boundary and triple junction kinetics does not only depend on grain boundary and triple junction mobility, but on the size of a grain as well. When the size of a grain diminishes progressively there comes a time when boundary kinetics become replaced by junction kinetics. This will happen to grains of the topological class $n = 4$ or $n = 5$ which are bound to shrink even after such a transition to triple junction kinetics. Grains of topological class $n = 3$ will collapse without transforming into a regular polygon. Since the kinetics of triple junctions are significantly slower than boundary kinetics, the four- and five-side polygons will shrink, and eventually contract to a point although at a markedly smaller rate. How this phenomenon reveals itself during grain growth will be considered below.

The final stage of grain growth under triple junction kinetics is a regular n -sided polygon. Let us finally consider the behavior of a regular n -sided polygon. As shown in [441, 442], the rate of grain area change \dot{S} can be expressed as

$$\dot{S} = -m_{tj}\gamma n \tilde{R} \sin\left(\frac{2\pi}{n}\right) \left[2\sin\left(\frac{\pi}{n}\right) - 1\right] = -2m_{tj}\gamma n \tilde{r} \sin\left(\frac{\pi}{n}\right) \left[2\sin\left(\frac{\pi}{n}\right) - 1\right] \quad (4.89)$$

where \tilde{r} and \tilde{R} are an interior and exterior radius, respectively.

In essence, a limited triple junction mobility always slows down the evolution of grain microstructure of polycrystals, irrespective of whether the topological class of the considered grain is smaller or larger than 6. Formally, for grains with $n < 6$, the sluggish motion of the triple junctions “reduces” the effective topological class of growing grains, whereas for grains with $n > 6$ the triple junction behavior makes the topological class of vanishing grains appear larger.

The mere fact that there is a growing grain with triple junctions of low mobility requires the existence of other grains with $n < 6$ to surround it. There is no point in discussing to which grain their common junction belongs. The only exception holds for $n = 6$, since under triple junction control a hexagonal grain structure with contact angle $2\Theta = 2\pi/3$ becomes unstable. Since the actual magnitude of Λ is determined by the triple junction and grain boundary mobility as well as by the grain size and is independent of the number of sides of a grain, there is no unique dividing line between vanishing and growing grains with respect to their topological class anymore, like $n = 6$ in the VN-M approach. As has been detailed above for sufficiently small Λ the border between shrinking and growing grains degenerates to an interval bounded by

the lines $n_H^*(\Lambda)$ and $n_L^*(\Lambda)$ (Fig. 4.39) which contracts to a point for $\Lambda \rightarrow \infty$.

In the following we consider the consequences of the two approaches for the evolution of grain microstructures. The distinguishing feature of the VN-M model is the infinite mobility of grain boundary triple junctions. This requires that grains in a “Von Neumann-Mullins” polycrystals are bordered by curved boundaries. This should manifest itself in linear dependences of the mean grain area on time and of the rate of grain area change on the topological class. For a given reduced boundary mobility $A_b = m_b \cdot \gamma$ a grain with topological number n is characterized by a unique value of its rate of area change $\frac{dS}{dt} \equiv \dot{S}$. The slope of the relation³ $\dot{S}(n)$ is only determined by the reduced grain boundary mobility: $\frac{d\dot{S}}{dn} = \frac{m_b \gamma \pi}{3}$.

In the opposite case, for pure triple junction kinetics the grains in a 2D polycrystal are bordered by straight lines, i.e. the grain microstructure is represented by a system of space-filling polygons. The temporal evolution of such a system is defined by Eq. (4.89).

A practically relevant and theoretically interesting case is an intermediate situation, when the triple junction influence is tangibly large, but nevertheless, the evolution of the system can be still considered as governed by grain boundary motion. In this case the time dependence of the average grain area $\langle S \rangle$ is practically linear; however, the rate of grain area change \dot{S} is defined not only by the topological class n but by the criterion Λ as well (Eqs. (4.82) and (4.83)), respectively. So, there is no unique relation anymore between \dot{S} and topological class n of the grain; the dependence $\dot{S}(n)$ is blurred by the impact of criterion Λ .

The discussed consequence afforded by the developed approach is probably the most significant one, but the new approach also allows us to make some more quantitative predictions.

- i) Grains are not capable of growing nor of shrinking in the intermediate situation that manifests itself in the dependency $\dot{S} = 0$ and $n^* = n^*(\Lambda)$.
- ii) Under triple junction kinetics grains should be bordered by flat boundaries, i.e. straight lines in 2D.
- iii) Under triple junction kinetics a system of polygons tends to transform to a system of equilateral polygons. The only exception is the triangle which will collapse without transforming into a regular polygon.
- iv) For triple junction kinetics the rate of grain area change can be described by Eq. (4.89).

³We would like to remind the reader that both the VN-M model and the model discussed in [441, 442] are based on the uniform grain boundary and triple junction approach.

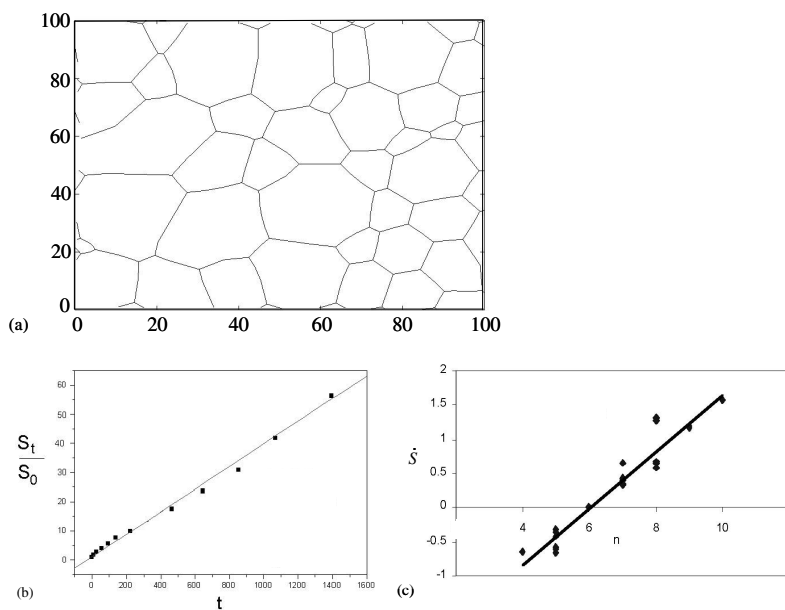
4.6.6.5 Computer Simulations

In both theoretical approaches only a single grain and its behavior are considered in an unspecified, i.e. average environment. The effect of discrete grain arrangements was studied by computer simulations of 2D grain growth [442]. Curvature and boundary-tension-driven grain growth is best represented by a (virtual) vertex model [443, 444]. In such a model the driving force is the net grain boundary surface tension at a vertex. A vertex can be a triple junction or any point on a polygonized grain boundary. For a given time interval the equation of motion is solved concomitantly for all vertices. Each vertex is assigned a mobility so that different mobilities for triple junctions and boundaries can easily be implemented.

In Fig. 4.40 the simulated evolution of the microstructure of a 2D polycrystal is presented at various stages of grain growth. The evolution was fully controlled by grain boundary kinetics. The time dependence of the mean grain area was computed. As apparent from Fig. 4.40a the grains are bordered by curved boundaries. The dependence of the mean grain area on time, and particularly the dependence of the rate of grain area change \dot{S} vs. the topological class n of a grain are shown in Fig. 4.40b,c. They reflect all features that are peculiar to a “Von Neumann-Mullins” polycrystal: $\langle S \rangle$ increases linearly with annealing time; the rate of grain area change \dot{S} is linear in n , and the line $\dot{S}(n)$ intersects the axis n at $n = 6$, i.e. $\dot{S} = 0$ at $n = 6$. The slope of the line $\dot{S}(n) = \frac{\pi m_b \gamma}{3}$ is as predicted by the Von Neumann-Mullins relation. A decrease in the criterion Λ increases the effect of triple junctions on grain growth.

Two essentially different situations were considered [442]. The first case related to the kinetics when the triple junction influence is tangibly large, but nevertheless, the evolution of the system can be described as a result of curvature-driven grain boundary motion. In contrast to unconstrained grain boundary motion, however, the boundaries are much more straight (Fig. 4.41a). When Λ is still relatively large, $0.4 \leq \Lambda \leq 5.0$, the mean grain area $\langle S \rangle$ changes linearly with time t , which reflects the nature of the controlling grain boundary kinetics of the system at this stage (Fig. 4.41b). The quantitative variation of the rate of grain area change \dot{S} on topological class n , which is a straight line for pure grain boundary kinetics (Fig. 4.40c), is transformed to an area under the constraint of a finite triple junction mobility (Fig. 4.41c). For all topological classes a large scatter of $\dot{S}(n)$ is observed. While for unconstrained grain boundary kinetics (infinite junction mobility) \dot{S} is a function of n only, for a system with finite junction mobility \dot{S} becomes a function of both n and Λ , $\dot{S} = \dot{S}(n, \Lambda)$ (Fig. 4.41c). The straight line in Fig. 4.41c, which describes the Von Neumann-Mullins relationship, has the slope $\frac{\pi m_b \gamma}{3}$ and $\dot{S}(n = 6) = 0$.

As the parameter Λ decreases the influence of triple junction drag becomes obvious not only in the $\dot{S} - n$ diagram, but also in changes of the dependency $S(t)$ (Fig. 4.42). Hence, grain growth cannot be considered any longer

**FIGURE 4.40**

Simulation results for a 2D polycrystal for grain boundary kinetics ($\Lambda \rightarrow \infty$). (a) Microstructure at $S(t)/S_0 = 1.72$; (b) normalized area $S(t)/S_0$ vs. time t ; (c) \dot{S} as function of n .

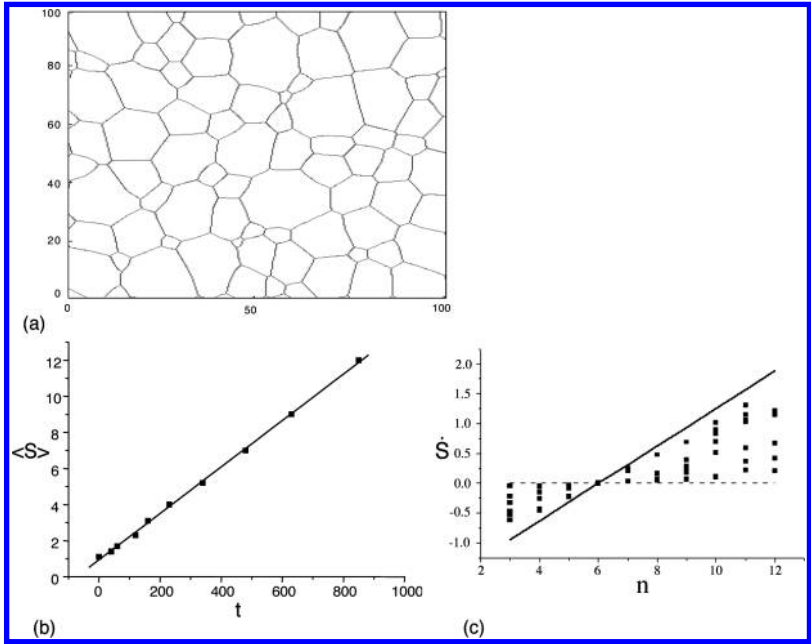


FIGURE 4.41

Simulation results for $0.1 < \Lambda < 1.0$. (a) Microstructure at $S_t/S_0 = 10.0$; (b) average area $\langle S \rangle$ vs. time t ; (c) \dot{S} as function of n for $0.1 < \Lambda < 10$. Solid squares are the results of computer experiments; the line represents the Von Neumann-Mullins relation.

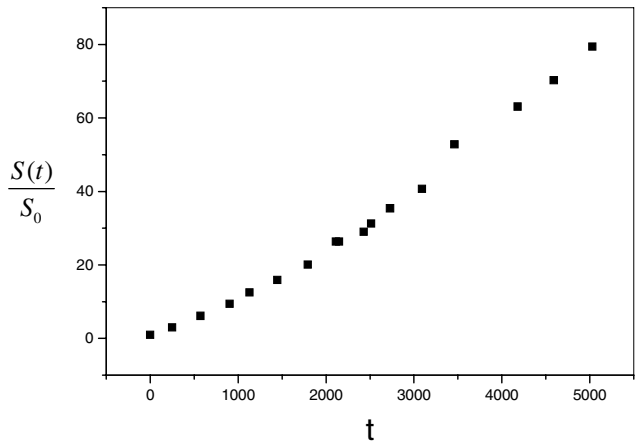


FIGURE 4.42

Grain size vs. time for $0.01 < \Lambda < 1.0$.

to be controlled by purely boundary kinetics, affected by triple junction drag, rather the dependency $\dot{S}_n(\Lambda)$ clearly demonstrates that a finite triple junction mobility fundamentally changes the character of the function. For a given n , $\dot{S}(n)$ is not represented by a point anymore, but by a line (Fig. 4.43). There are two issues which should be stressed. Firstly, a good agreement between the computer experiments and theory is observed. Further, according to the presented theoretical approach, Eqs. (4.82) and (4.84) perfectly describe in close proximity to equilibrium, i.e., for rather large Λ , the influence of a finite triple junction mobility on the rate of grain area change, \dot{S}_n , given that all Von Neumann-Mullins conditions, except the infinite triple junction mobility, are fulfilled. The expressions

$$\lambda_{n<6} \equiv \frac{\dot{S}_{n<6}^{TJ}}{\dot{S}_{n<6}^{VNM}} \cong \frac{n^{\frac{6+\Lambda\sqrt{3}}{2+\Lambda\sqrt{3}}}}{n-6} \quad (4.90a)$$

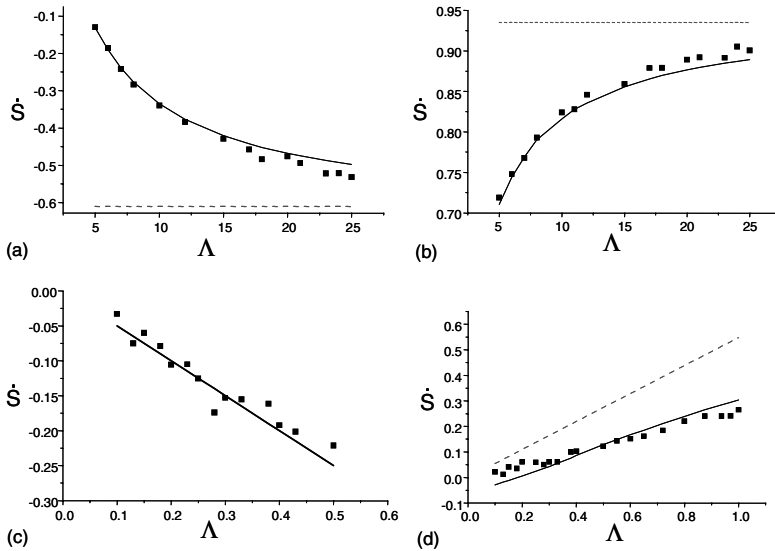
$$\lambda_{n>6} \equiv \frac{\dot{S}_{n>6}^{TJ}}{\dot{S}_{n>6}^{VNM}} \cong \frac{n \left(1 - \frac{6}{\pi\Lambda B}\right) - 6}{n-6} \quad (4.90b)$$

represent the ratio of the rate of grain area change for finite triple junction mobility and for the pure Von Neumann-Mullins case. For the same value of Λ , grains with $n < 6$ deviate more strongly from pure grain boundary kinetics than do grains with $n > 6$. Therefore, grains with $n = 4$ are under triple junction control (Fig. 4.43), whereas the growth of grains with $n = 9$ is still governed by boundary kinetics (Fig. 4.43). In other words, triple junction drag does not only slow down the rate of grain growth, but also changes the grain microstructure of 2D polycrystals. This is also evident in experimental observations of grain growth in thin foils [445]. At the stage of the process where triple junction influence becomes obvious, i.e. when the time dependency of the mean grain size is linear, the grain size distribution becomes wider.

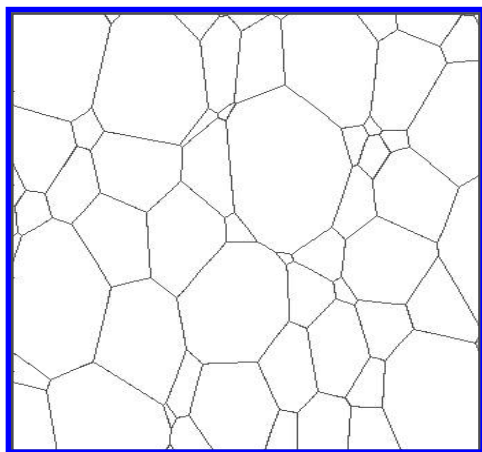
For grain growth strictly controlled by triple junction motion, theory predicts that the grain boundaries become flat and that the grains approach the shape of equilateral polygons. A polygon of arbitrary shape will be transformed into an equilateral polygon, and any deviation from an equilateral polygon will generate a force to restore the equilibrium shape. The only exception is a triangle, i.e. a grain of topological class $n = 3$ is always unstable and bound to disappear. The computer simulations fully confirm the theoretical predictions. Fig. 4.44 represents the grain microstructure developed under triple junction kinetics. The grains are bordered by straight lines. The

ratio $\eta = \frac{\sum_{i=1}^n \frac{L_{\text{curv}}^i}{L_{\text{str}}}}{n}$ gives a quantitative measure of grain boundary curvature, where L_{curv} is the length of a curved boundary and L_{str} is the distance between the two corresponding triple junctions (Fig. 4.45). When Λ tends to zero, $\eta \rightarrow 1$ (Fig. 4.46).

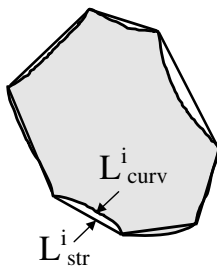
To assess the theoretical prediction that under triple junction kinetics all 2D grains of arbitrary shape become converted to equilateral polygons —

**FIGURE 4.43**

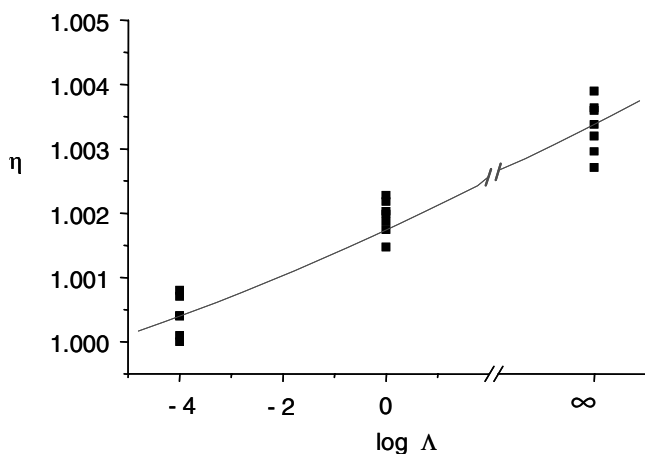
The rate of grain area change \dot{S} as a function of Λ (a) for grains with $n = 4$. Filled squares are the results of computer simulations. The solid line represents the theoretical prediction of intermediate kinetics (Eqs. (4.30) and (4.71)) ($5 < \Lambda < 25$); the dotted line corresponds to the Von Neumann-Mullins relation. (b) For grains with $n = 9$. The solid line represents the theoretical prediction for intermediate kinetics (Eqs. (4.62) and (4.71)). The dotted line corresponds to the Von Neumann-Mullins relation. (c) For grains with $n = 4$, and $0.1 < \Lambda < 1.0$. The solid line represents the theoretical prediction for triple junction kinetics (Eq. (4.89)). (d) For grains with $n = 9$. The solid line is the theoretical prediction for intermediate kinetics (Eqs. (4.62) and (4.71)); the broken line represents triple junction kinetics.

**FIGURE 4.44**

Simulation results for a 2D polycrystal at $\Lambda \sim 10^{-4}$. Microstructure at $S_t/S_0 = 10.0$.

**FIGURE 4.45**

Measure of boundary straightness. The diagram explains how the value η was measured.

**FIGURE 4.46**

Computer simulation (filled squares up to $S_t/S_0 = 10$) and theoretical prediction (solid line) of $\eta(\log \Lambda)$.

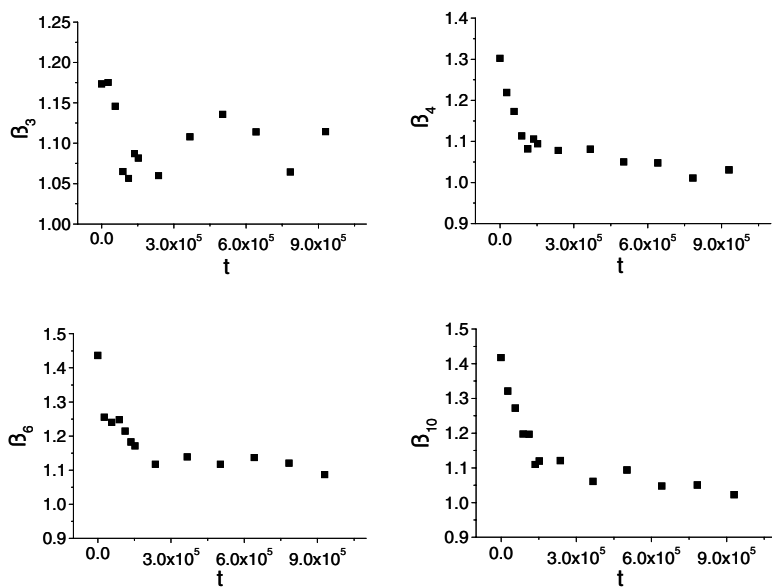
except for triangles — we define the parameter

$$\beta_n = \frac{\frac{L_1}{L_2} + \frac{L_2}{L_3} + \dots + \frac{L_{n-1}}{L_n} + \frac{L_n}{L_1}}{n} \quad (4.91)$$

where L_i is the length of the i -th side of an n -sided grain. When the shape of a grain approaches an equilateral polygon, $\beta_n \rightarrow 1$. The only exception is a triangle, which is unstable and has to disappear, i.e. β_3 should not converge toward $\beta_3 = 1$. The behavior of β_n with time was determined from the computed microstructure, including β_3 (Fig. 4.47). Apparently for all studied n -sided polygons $\beta_n \rightarrow 1$, except for β_3 which changes randomly. Fig. 4.48 confirms that such behavior of β_n holds for triple junction kinetics only. The value β_n was measured up to $S_t/S_0 = 10$. As apparent from Figs. 4.47 and 4.48 a grain size ten times larger than the initial grain size was reached in a much shorter time for boundary kinetics.

The function $\dot{S}(n)$ for triple junction kinetics is presented in Fig. 4.49. The curve is calculated according to Eq. (4.89) whereas the symbols represent simulation results. Except for the intrinsically unstable triangular grains ($n = 3$), the theoretical predictions are in good agreement with the computer experiment. We note that \dot{S} rises with n and approaches a limit (Eq. (4.89)) contrary to the predictions of the Von Neumann-Mullins relation.

The evolution of a 2D grain system with triple junctions was comprehensively studied by computer simulations in [445, 446]. The results of [446] are in good agreement with the approach discussed above.

**FIGURE 4.47**

Time dependence of β_n for various n under triple junction kinetics ($\Lambda \approx 10^{-4}$ up to $S_t/S_0 = 10$).

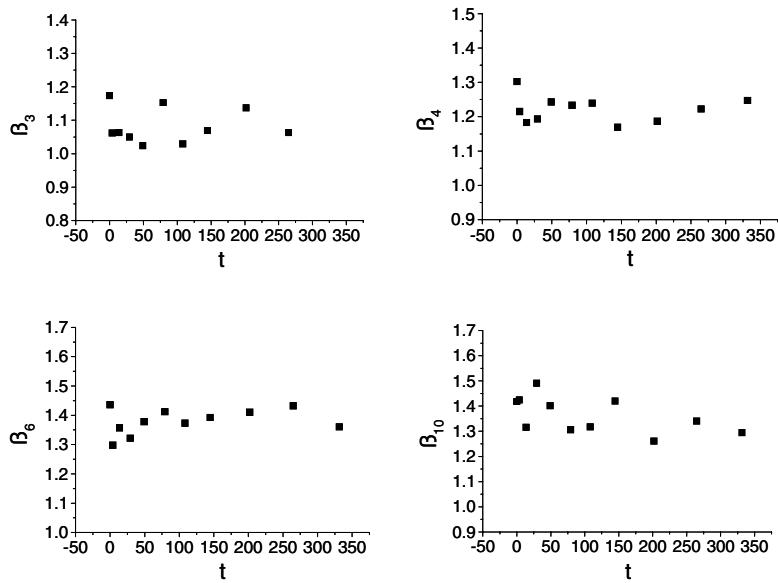


FIGURE 4.48
Time dependence of the “rectilinearity” β_n under grain boundary kinetics ($\Lambda \gg 1$) for $S_t/S_0 = 10.0$.

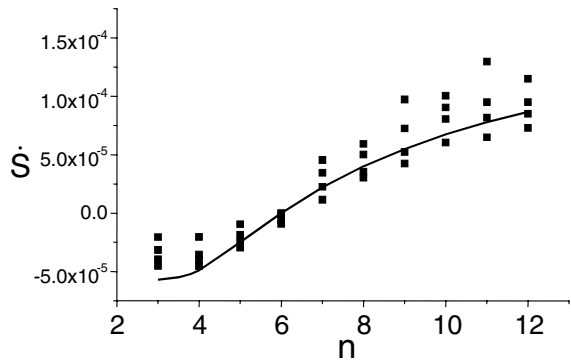


FIGURE 4.49
 \dot{S} vs. topological class n . Simulation results (filled squares) for $\Lambda \sim 10^{-4}$. The solid line represents the dependency predicted by Eq. (4.89).

4.6.6.6 Grain Growth in a System with Boundary Junctions of Finite Mobility: Experiments on Metallic Materials

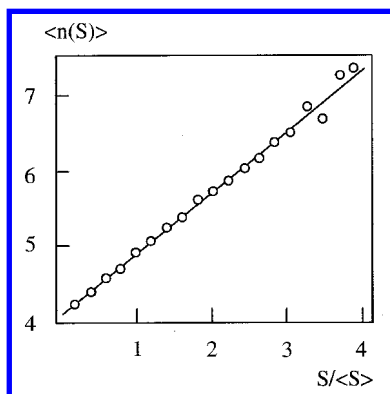
Doubtlessly, the experimental observation of the effects described above and the general influence of grain boundary junctions on grain growth and evolution in polycrystals especially in nanocrystalline materials is of great interest. Unfortunately, there are only very few experimental investigations where this attempt was undertaken. First we consider experimental studies of grain growth in 2D Al foils [448].

As mentioned for junction-controlled grain growth all grains assume the shape of a regular polygon, irrespective of their number of sides, except for triangles. As shown in [441] a grain with the shape of a regular polygon remains stable, i.e. does not undergo a shape change except for a triangular shape.

Correspondingly, a 2D arrangement of grains with regular polygonal shape would “freeze,” except if it contains triangular grains. The hexagonal structure belongs to this set of stable geometries only if it is equilateral. On the other hand, any other space-filling arrangement of regular polygons is a potentially stable structure, if it can be attained⁴. The only exception is a triangle, and any arrangement of regular polygons which contains at least a single triangle would also be observed to behave in an unstable manner.

We reason that this phenomenon has important consequences for the development of grain growth. Let us take a look at the evolution of a shrinking grain in the course of grain growth. The topological class of such a grain should be smaller than $n = 6$, naturally taking into account all corrections to the Von Neumann-Mullins relation. As shown above the transition between boundary and triple junction kinetics does not only depend on grain boundary and triple junction mobility, but on the size of a grain as well. When the size of a grain progressively diminishes there comes a time where boundary kinetics is replaced by junction kinetics. This will happen to grains of the topological class $n = 4$ or $n = 5$ which are bound to shrink even after such a transition to triple junction kinetics. Grains of topological class $n = 3$ will collapse without transforming into a regular polygon. Since the kinetics of triple junctions are significantly slower than the boundary kinetics, the four- and five-side polygons will shrink, and eventually contract to a point although at a markedly smaller rate. Experimentally this phenomenon will manifest itself in the mean value of the topological class of vanishing grains. In Fig. 4.50 experimental data of grain growth in aluminum foil with 2D (columnar) structure are presented, in terms of the grain size dependence of the mean topological class $\langle n \rangle$ [448]. Extrapolation of this experimental dependence to zero area yields the mean value of the topological class of vanishing grains. As can be seen $\langle n \rangle(0) \cong 4.2$, i.e. $n = 4$ is the smallest topological class to shrink in

⁴We do not know whether space-filling topological arrangements of regular polygons exist besides regular hexagons that satisfy the force equilibrium at junctions.

**FIGURE 4.50**

Dependence of the mean topological class $\langle n(s) \rangle$ on “grain size” $S/\langle S \rangle$ (normalized by the average grain size) for pure Al [448].

a stable manner. In [429]–[432], the motion and geometry of connected (by triple junctions) grain boundaries in 2D Al foils were investigated in situ in an SEM with a specially designed heating stage. The experiments were carried out on polycrystalline Al sheets of thickness $120\ \mu\text{m}$. The materials was recrystallized to a mean grain size of $150\ \mu\text{m}$. This allowed us to realize an approximately 2D microstructure.

EBSD measurements were carried out before and after in situ grain growth experiments to determine the misorientation of the grains and to confirm the quasi-two-dimensionality of the grain structure. These EBSD checks were necessary to ascertain that no grains from beneath surfaced and interfered with the measurement.

The experiments were performed in a temperature range from 250 to 300°C . The SEM was upgraded by a digital image scanning system, which collected the images and saved them in AVI format. In post-processing the images were analyzed by a special routine that measured the displacement of the triple junctions and the vertex angles at the triple junctions.

The authors tried to fulfil the main physical criteria, which were used as a basis for the analysis of steady-state motion of the grain boundary system with triple junction: uniform grain boundary model, the geometrical configuration (Fig. 4.51), and the steady-state motion of the junction. Two specific configurations were studied: for $n < 6$ and for $n > 6$ (Fig. 4.51, Tables 4.8, 4.9).

Figs. 4.52 and 4.53 reveal steady-state motion of the investigated triple junction in the course of grain growth triple junction displacement is linear vs. time; vertex angles remain constant over the time of experiment.

The diagram obtained of the vertex angle Θ vs. the dimensionless criterion

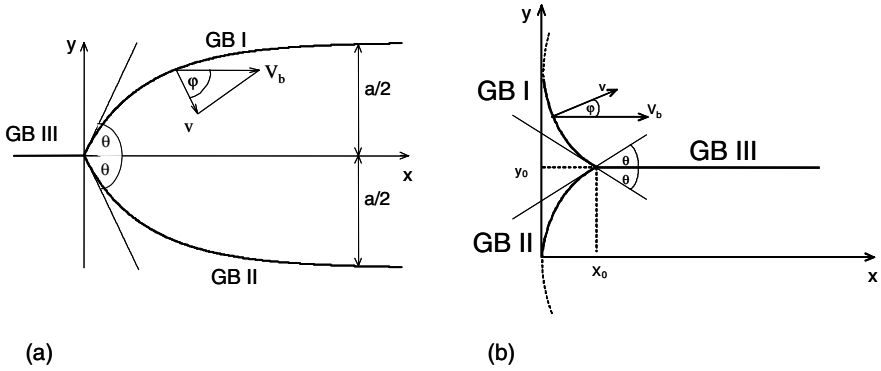


FIGURE 4.51

The two basic configurations of a grain boundary system with triple junction during steady state motion studied in [429].

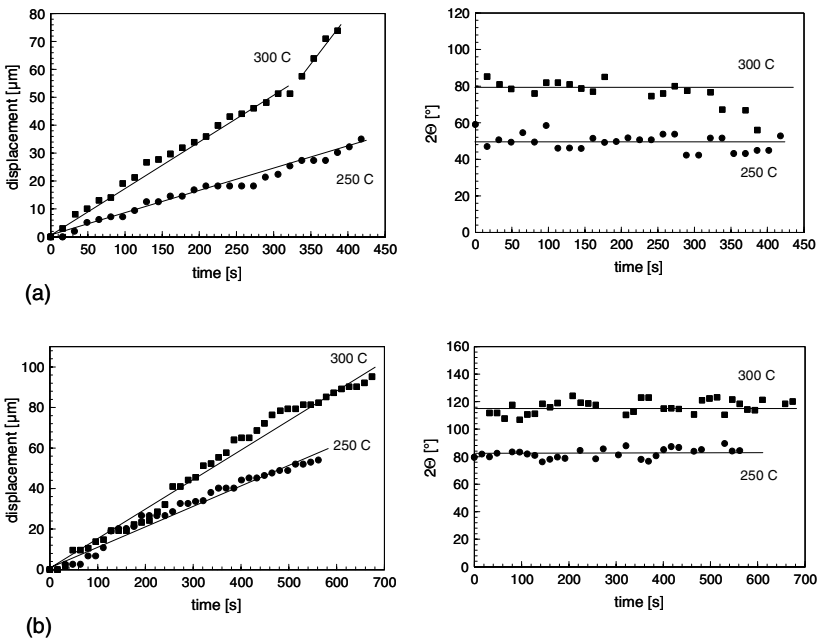


FIGURE 4.52

(a) Displacement and vertex angle 2Θ vs. time for triple junction TP-S2 with a configuration of Fig. 4.51a at 250°C and 300°C. (b) Displacement and vertex angle 2Θ vs. time for triple junction TP-S3 with a configuration of Fig. 4.51a at 250°C and 300°C.

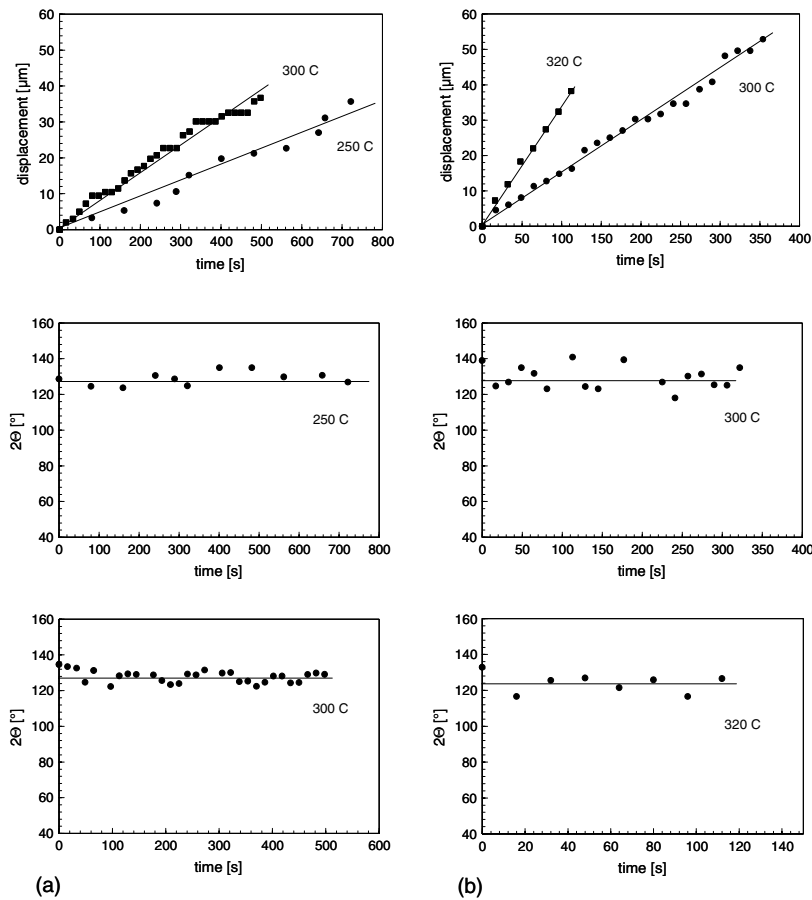


FIGURE 4.53
(a) Displacement and (b) vertex angle 2Θ vs. time for triple junction (a) TP-G1 and (b) TP-G3 with a configuration of Fig. 4.51b at two different temperatures.

TABLE 4.8
Misorientation of Three Contiguous
Grains at Investigated Junctions

Junction	GB I	GB II	GB III
TP-S2	19°[021]	43°[433]	39°[212]
TP-S3	35°[310]	53°[434]	46°[112]
TP-G1	28°[223]	31°[100]	30°[123]
TP-G3	26°[014]	23°[100]	12°[032]

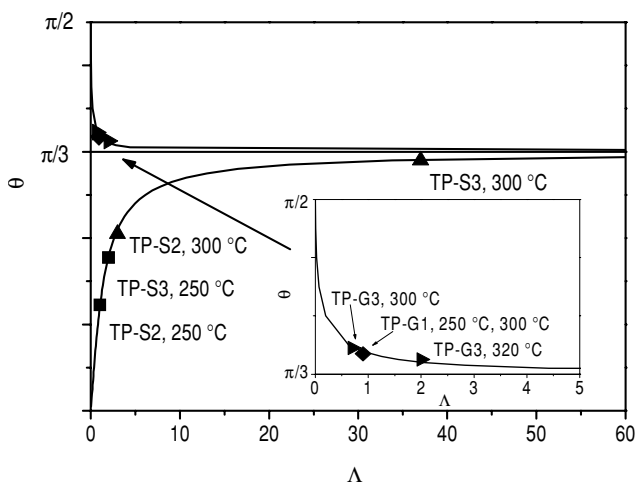
TABLE 4.9
Parameters of Motion of the Investigated
Boundary System with Triple Junction

Junction	T(°C)	$v(\mu\text{m/s})$	2Θ	Λ
TP-S2	250	0.08	49	1
	300	0.17 (0.35)	79	2
TP-S3	250	0.10	82	3
	300	0.15	116	37
TP-G1	250	0.05	127	0.9
	300	0.08	127	0.9
TP-G3	300	0.15	129	0.7
	320	0.35	124	2

Λ confirms the results of computer simulations (Fig. 4.54), where the Λ dependency of n^* — the topological class for which $\dot{S} = 0$ — was constructed. However, the direct and conclusive way to estimate quantitatively the drag effect of triple junctions on grain growth is to measure the rate of area change of individual grains.

To attribute the rate of grain area change to triple junction drag and specifically to a definite value of Λ, some rather strict criteria should be fulfilled in experiment. In particular, the grain growth should be driven in a boundary regime (Eqs. (4.82, 4.85)), and the motion of the triple junction has to be in steady state.

It was shown that at constant temperature $S \sim t$. This confirms the boundary kinetics of the observed grain growth [429]. The main result, obtained in [429], is the experimentally measured diagram $\dot{S} = f(n)$ (Figs. 4.54 and 4.55). The diagram revealed that the rate \dot{S} was not constant for a given n , as it needs to be in accordance with the Von Neumann-Mullins concept, but follows the relations (4.82, 4.85), which take into account the triple junctions drag. Apparently, the grains which exhibited higher rates \dot{S} were not (or were less) affected by triple junctions. The Von Neumann-Mullins limit is represented in the diagram of Fig. 4.55 by the straight line connecting the maximal values of \dot{S} and the point $\dot{S} = 0$ for $n = 6$. The slope of this line is determined by the reduced grain boundary mobility $A_b = m_b\gamma$. The measured value of

**FIGURE 4.54**

Vertex angle Θ vs. criterion Λ . The symbols denote the measured values for the analyzed junctions; the lines are calculated according to Eqs. (4.81 and 4.82).

A_b ($\sim 10^{-10} \text{m}^2/\text{s}$) is in a good agreement with mobility data of random grain boundaries in Al [450].

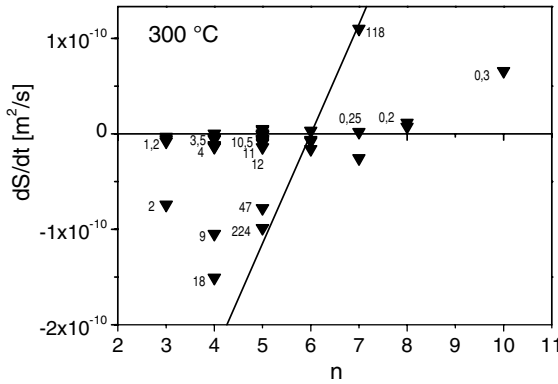
On the other hand, if A_b is known, the values of Λ can be calculated for each experimental point from equations (4.82) and (4.85). The more a measured value of \dot{S} deviates from the Von Neumann-Mullins limit the stronger the drag effect exerted by triple junctions and, respectively, the smaller the value of Λ .

The experimental results are in a good agreement with predictions of vertex simulations of grain growth, in particular with Fig. 4.41 [442]. We would like to stress again that due to the finite mobility of the triple junctions there is no more a unique linear dependence between grain growth rate and the topological class of the grain; in other words, the growth rate \dot{S} does not only depend on the topological class of the grain but on the criterion Λ as well.

4.6.6.7 How to Evaluate the Mobility of Grain Boundary Junctions? Phenomenological Approach

The main consequence of the consideration given above can be formulated as follows: in order to predict and describe the kinetics and geometry of grain microstructure evolution the mobility of grain boundary junctions needs to be known.

Undoubtedly, the most correct way to determine the mobility of boundary

**FIGURE 4.55**

Rate of grain area change dS/dt vs. topological class n of a grain for 300°C. The values of Λ are given next to the data point.

junctions is the study of a grain boundary system with a single junction in a steady-state motion or a certain grain of defined topological class in the course of grain growth [183, 436]. However, in general this is a cumbersome procedure which requires a sophisticated technique of grain microstructure analysis and the results of independent measurements of grain boundary mobility.

In [447] a rather simple approach was used for evaluation of the mobility of grain boundary junctions, namely from the temporal evolution of the grain size. Let us consider the motion of a grain boundary driven by grain boundary curvature κ with triple and quadruple junctions which have their own mobility. The motion of such a boundary can be considered as the motion of a boundary with mobile defects [441, 447]. The velocity of such a boundary is given by

$$V = P_{\text{eff}} m_b \quad (4.92)$$

where P_{eff} is the effective driving force for grain growth

$$P_{\text{eff}} = \gamma\kappa - \frac{f_1}{a_1} - \frac{f_2}{a_2} \quad (4.93)$$

and a_1 and a_2 are the spacings of the respective junctions. Since a_1 and a_2 are of the same order of magnitude we assume for simplicity $a_1 = a_2 = a$ in the following. f_1 and f_2 are the drag forces of triple and quadruple junctions, respectively. In accordance with the Nernst-Einstein relation

$$\begin{aligned} f_1 &= \frac{V}{m_{tj}} \\ f_2 &= \frac{V}{m_{qp}} \end{aligned} \quad (4.94)$$

we arrive at

$$V \left[1 + \frac{m_b}{am_{tj}} + \frac{m_b}{a^2 m_{qp}} \right] = m_b \gamma \kappa \quad (4.95)$$

Eqs. (4.92)–(4.95) yield

$$V = \frac{m_b \gamma \kappa}{1 + \frac{1}{\Lambda} + \frac{1}{\Lambda_{qp}}} \quad (4.96a)$$

where $\Lambda_{qp} = \frac{m_{qp} a^2}{m_b}$.

$$\frac{1}{m_b \gamma} (< R^2 > - < R_0^2 >) + \frac{1}{m_{tj} \gamma} (< R > - < R_0 >) + \frac{1}{m_{qp} \gamma} \ln \frac{< R >}{< R_0 >} = t \quad (4.96b)$$

where $< R >$ is the mean grain size.

Eqs. (4.99a) or (4.99b) define the different types of grain growth kinetics in polycrystals. The first one is the well-known grain boundary kinetics: $\frac{1}{\Lambda}, \frac{1}{\Lambda_{qp}} \ll 1$, the velocity V is proportional to the grain boundary curvature, and the mean grain size increases in proportion to the square root of the annealing time: $V = \frac{d<R>}{dt} \sim \frac{1}{<R>} \rightarrow <R> \sim \sqrt{t}$. If grain boundary motion is controlled by the mobility of triple junctions ($\frac{1}{\Lambda} \gg 1$ and $\frac{1}{\Lambda} \gg \frac{1}{\Lambda_{qp}}$), the velocity V is constant: $V = \frac{d<R>}{dt} = \text{const.} \rightarrow <R> \sim t$. Finally, if the mobility of the quadruple junctions (points) determines the motion of the grain boundary system ($\frac{1}{\Lambda_{qp}} \gg 1$ and $\frac{1}{\Lambda} \gg \frac{1}{\Lambda_{qp}}$) the velocity V is proportional to the radius of curvature: $V = \frac{d<R>}{dt} \sim <R> \rightarrow <R> \sim e^t$. Under grain boundary kinetics we observe the classical grain growth kinetics, which is to hold for rather large grains. The schematic diagram of the mean grain size vs. time dependence of different kinetic regimes is given in Fig. 4.56.

There is only a very restricted number of studies where the grain growth in nanocrystalline and ultrafine-grained materials was observed, and much less where it was quantitatively evaluated. Experimental data relevant to such kinetics were actually obtained for grain growth in thin ($\sim 1000\text{\AA}$) silver films [415]. Fig. 4.57 shows the dependence of the mean grain size on annealing time at the early stage of grain growth. For all temperatures investigated the mean grain size changed linearly with annealing time. At a later stage of annealing, when the mean grain size reached a sufficiently large value, corresponding to Fig. 4.55, the kinetics were ruled by the grain boundary mobility, and the linear time dependence was replaced by a parabolic relationship.

In Fig. 4.58 the results of grain growth in nanocrystalline iron are presented [451, 452]. In [451, 452] grain growth for a rather small grain size is characterized by a linear dependence of the mean grain size on annealing time. It should be stressed that at large annealing time the linear dependence $<R> \sim t$ transforms to the classical grain boundary kinetics $<R> \sim \sqrt{t}$.

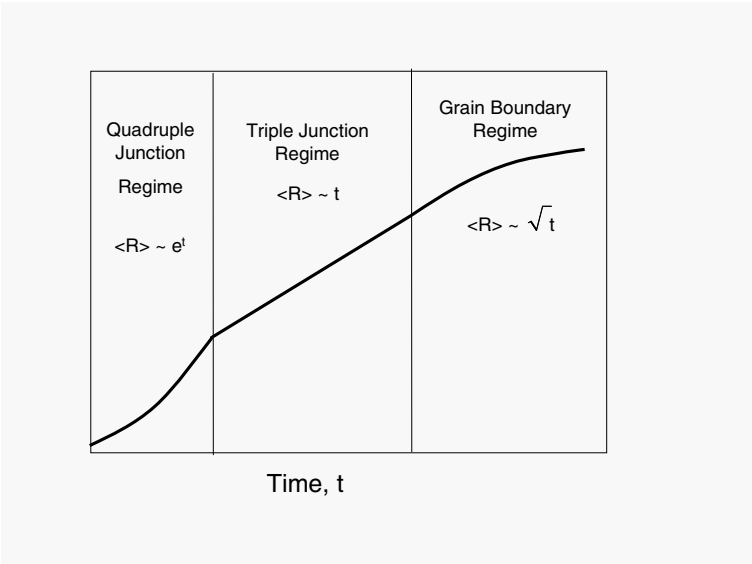


FIGURE 4.56
Grain growth kinetics at different regimes.

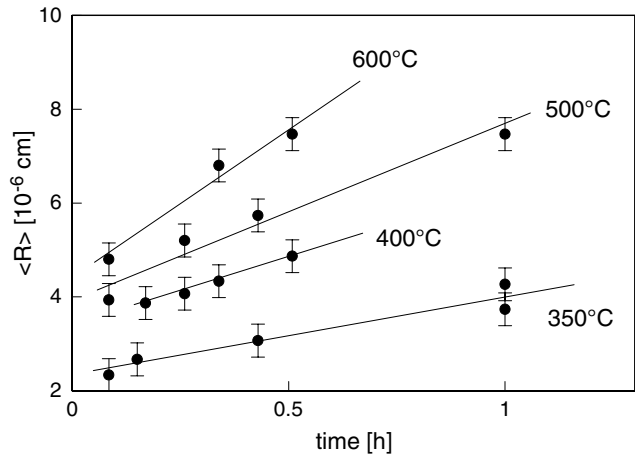


FIGURE 4.57
Temporal evolution of the mean grain size $\langle R \rangle$ in thin silver films [415].

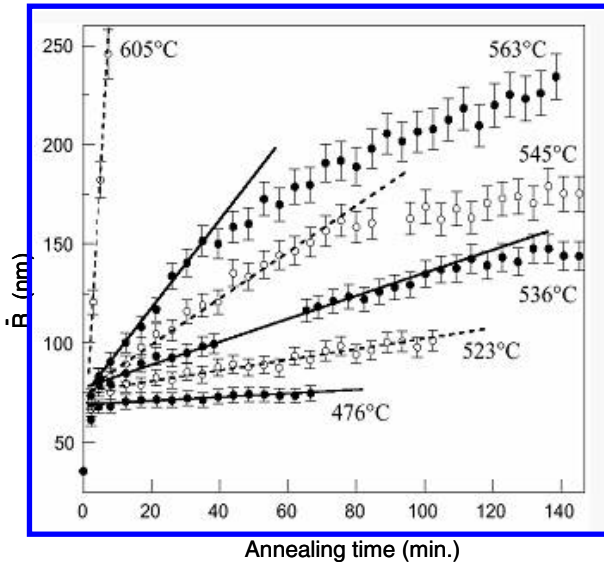


FIGURE 4.58

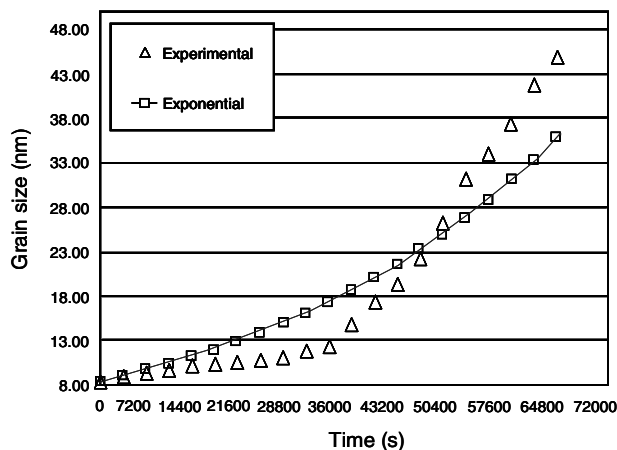
Mean grain size (radius) in nanocrystalline iron vs. annealing time [452].

There are indications that in the course of grain growth in nanocrystalline materials quadruple junction kinetics were also observed [453, 454]. The quadruple junction mobility $m_{qp}\gamma$ extracted from the experimental results of [453] is given in [447]: $m_{qp}\gamma \cong 2 \cdot 10^{-4} \text{s}^{-1}$.

In Fig. 4.59 the experimental data of grain growth in nanocrystalline Pd are presented [454]. We would like to draw the reader's attention to the distinctive property of the experimental curve: at the early stage of annealing the shape of the curve is concave. The approach discussed gives us the possibility to extract the values of the triple junction and quadruple junction mobility from the time dependency of the mean grain size: $m_{tj}\gamma = 3 \cdot 10^{-11} \text{s}^{-1}$; $m_{qp}\gamma = 3 \cdot 10^{-5} \text{s}^{-1}$.

The agreement between equation (4.96a) for $\frac{1}{m_{qp}\gamma} \gg \frac{1}{m_b\gamma}, \frac{1}{m_{tj}\gamma}$ and experiment (Fig. 4.59) is reasonable [454]. This agreement can be improved if the initial region of the curve, where grain growth does not take place in reality, is neglected.

The inverse problem has been investigated by Novikov. He studied by computer simulation the grain growth in 2D and 3D systems for different grain sizes as well as triple junction and quadruple point mobilities [445, 446]. For a rather small grain size and (or) low triple junction and quadruple junction mobility the curves $\langle R \rangle \sim t$ have just the same peculiarities: linearity for rather small $\Lambda_{tj} = \frac{m_{tj}a}{m_b}$ and an exponential dependence $\langle R \rangle \sim \exp(t)$ for small $\Lambda_{qp} = \frac{m_{qp}a^2}{m_b}$.

**FIGURE 4.59**

“Grain growth” in nanocrystalline Pd [454]; \triangle — experiment, \square — Eq. (4.99b).

4.7 Grain Growth in 3D Systems

4.7.1 Analytical Approaches

As mentioned in Sec. 4.6.5 a direct transfer of the Von Neumann-Mullins relation to 3D systems is impossible. However, the beauty and mathematical clarity of the Von Neumann-Mullins relation encouraged a number of attempts to search for a 3D analogy of this relation. All approaches share the assumption that a 3D polycrystal can be represented as an assembly of polyhedra. However, as shown in [545], a polycrystal cannot be completely constructed from convex polyhedra, rather than piecewise convex or concave. First of all let us consider grain growth in a case when the grain system is nearly two dimensional. Levine et al. represented the Von Neumann-Mullins relation as [544]

$$\frac{dS}{dt} = m_b \gamma \left[\frac{\pi}{3} (n - 6) + S_i \bar{\kappa}_G \right] \quad (4.97)$$

where $\bar{\kappa}_G$ is the Gaussian curvature measured over the area of a grain. For $\bar{\kappa}_G > 0$ the area of the grains at the surface will increase exponentially, whereas for the grains inplane the area will change linearly with time. Finally, the entire surface will constitute a single grain. On the other hand the negative Gauss curvature ($\bar{\kappa}_G < 0$) stabilizes the grain microstructure (see Eq. (4.97)) for a definite grain area.

Mullins [546] proceeded from the assumption that grain growth in 3D sat-

ifies the hypothesis of statistical self-similarity and that the grain boundary normal velocity at any point of the grain boundary is proportional to the local mean curvature. The volume rate of change \dot{V} for a given grain can be described as

$$\dot{V} = \sum_i \int_i v_n dS \quad (4.98)$$

and integration over all grain faces results finally in the kinetic equation

$$\dot{V} \cdot V^{-1/3} = \left(\frac{3}{4\pi} \right)^{1/3} m_b \gamma G_1(N) \cdot G_2(N) \quad (4.99)$$

where N is the number of faces of the polyhedron considered

$$\begin{aligned} G_1(N) &= \pi/3 - 2 \arctan \left[\frac{1.86(N-1)^{1/2}}{N-2} \right] \\ G_2(N) &= 5.35n^{2/3} \left[\frac{N-2}{2(N-1)^{1/2}} - \frac{3}{8} G_1(N) \right] \end{aligned} \quad (4.100)$$

The dependency (4.99) manifests some interesting features, in particular, grains with $N \leq 13$ shrink whereas grains with $N \geq 14$ grow. The consideration reflects the major properties of analogous approaches: the final kinetic relation is based on a large number of approximations, the most essential of which is the substitution of a real 3D grain by idealized polyhedra, bordered by flat faces, and so on.

Hilgenfeldt's approach [545] is based on the famous theorem of Hermann Minkowski from 1903. Minkowski had shown that the mean curvature over the surface of a convex body is linked to the caliper radius, which is the distance between the coordinate origin (the center of mass of the body) and the plane touching the body in the direction (Θ, ϕ)

$$\int_{4\pi} c(\Theta, \phi) dw = \int_s H dA \quad (4.101)$$

where the integrals are over all solid angles and the total area of the convex body.

Hilgenfeldt applied Eq. (4.101) to two different polycrystals: to polyhedra K with curved edges and its skeleton polyhedron K_0 , i.e. a polyhedron with the same vertex positions, however, with flat surfaces to obtain

$$\left(\frac{dV}{dt} \right) V^{-1/3} = m_b \gamma G(N) \quad (4.102a)$$

where

$$G(N) = \frac{3[(n-2)\tan\pi/\eta_N]^{2/3} \tan^{1/3}(\chi_N)}{2^{1/3}} \cdot (\pi/3 - \chi_N)$$

with $\eta_N = G - \frac{12}{N}$ and

$$\chi_N = 2 \arctan \left\{ 4 \sin^2 (\pi/\chi_N)^{1/2} \right\} \quad (4.102b)$$

Glicksman and Rios [547]–[551] developed the so-called “average N -hedra” (ANH) model. The authors [547]–[551] describe ANH as a symmetric, i.e. isometric N -hedron, consisting of N identical faces, meeting at $3(N-2)$ pairs of identical symmetrical vertices, each separated from adjacent vertices by constant distance. In other words, an ANH is a polycrystal of equidistant (from volume centroid) vertices. Every pair of adjacent faces intersects at the topologically required average internal dihedral angle of 120° . Each ANH in this infinite set manifests unique geometric properties, all of which are determined by the index $N \geq 4$ [547]–[551]. In this model all grains in a polycrystal have the same vertex-to-vertex distance.

The expression for the grain volume rate of change renders

$$\left(\frac{dV}{dt} \right) V^{-1/3} = m_b \gamma c_1 \left(\sqrt{N} - \sqrt{N_c} \right) \quad (4.103)$$

where $c_1 \cong 1.51$ and $N_c \cong 13.397$ is the critical number of faces or critical topological class of ANH; this polyhedron would neither grow nor shrink.

It is emphasized that all approaches introduced so far are based on the assumption that a 3D polycrystal can be represented by a system of convex bodies (polyhedra).

In 2007 MacPherson and Srolovitz [552] derived a strict relation between the rate of grain volume change and the topological and geometrical characteristics of a polycrystal. It was shown that the integral curvature H (the sum of the principal curvatures) for a domain D with mean width $L(D)$ bounded by a surface ∂D consisting of smooth surfaces that meet along curves (edges) with dihedral exterior angle $\alpha = \pi/3$ measured in the plane perpendicular to the edges with length $e_i(D)$ can be expressed as [552]

$$\int_{\partial D} H \, dA = 2\pi \left(L(D) - \frac{1}{G} \sum_{i=1}^N e_i(D) \right) \quad (4.104)$$

The significance of average mean curvature for quantitative metallography was already shown by Cahn [553]. In particular it was described how the average value of the mean curvature of surfaces in a specimen can be precisely determined by simple measurements performed on random sections or on projections of these surfaces. The inverse problem reads

$$\bar{\kappa}_p = (1/L) \int \kappa_p \, d\ell \quad (4.105)$$

where κ_p is the curvature, $\kappa_p = \frac{y''}{(1+y'^2)^{3/2}}$, $d\ell = \sqrt{1+y'^2} dx$, and $L = \int d\ell$ is the total length of the curve. The integral in Eq. (4.105) can be called the

total curvature κ^T . The average curvature $\bar{\kappa}_p$ can also be expressed as

$$\bar{\kappa}_p = \left(\frac{1}{L} \right) (\Delta\Theta) \quad (4.106)$$

where $\Delta\Theta$ gives the change in the direction of the tangent to the end of the curve considered ($\Theta = \arctan(y')$). For a closed curve $\Delta\Theta = \pm 2\pi$ and $\bar{\kappa}_p = \pm 2\pi/L$. In accordance with [553] $\bar{\kappa}_p$ is positive for the concave curve and negative for the convex curve.

Then for a given grain

$$\frac{dV}{dt} = -m_b\gamma \int_{\partial D} H dA = -2\pi m_b\gamma \left(L(D) - \frac{1}{6}e(D) \right) \quad (4.107)$$

or if the volume of the grain is known at any time

$$\left(\frac{dV}{dt} \right) V^{-1/3} = -2\pi m_{gb}\gamma \left(L(D) - \frac{1}{6}e(D) \right) \cdot V^{-1/3} \quad (4.108)$$

As the Von Neumann-Mullins relation, the new relation (Eq. (4.108)) depends only on the geometrical characteristics of the grain.

However, contrary to the Von Neumann-Mullins relation Eq. (4.104) is not purely topological. The rate of grain volume change depends on the mean width of the grain and the total length of the triple junctions. However, it does not depend distinctly on the shape of the grain. If the right-hand side of Eq. (4.104) is proportional to the grain size then the kinetics of grain growth are governed by a parabolic law.

It is stressed that all approaches so far considered assumed (tacitly [545]–[551], or explicitly [552]) that grain boundaries move slowly enough to maintain the equilibrium dihedral angles at triple junctions. In other words, the mobility of all junctions is assumed to be infinite.

For an isolated convex polyhedral grain with curved faces bounded by sharp edges the total curvature κ^T is equal to $\kappa^T = \frac{1}{2}\Delta\Theta L + \bar{\kappa}_s S = 2\pi\bar{D}$ where $\bar{\kappa}_s$ is the average mean curvature of just the grain surfaces (faces), $\Delta\Theta$ is the complement of the average dihedral edge angle, S is the total area and L is the edge length. Then

$$\bar{\kappa}_s = \frac{2\pi}{S} \left[\bar{D} - \frac{\Delta\Theta}{4\pi} L \right] \quad (4.109)$$

For the particular case of polyhedra with flat faces $\bar{\kappa}_s$ is zero and the caliper diameter \bar{D} is equal to $\bar{D} = \frac{\Delta\Theta}{4\pi} L$. Cahn's equation can be considered a particular solution of the general Eq. (4.104). In what follows the approach based on relation (4.104) will be called the Cahn-MacPherson-Srolovitz relation.

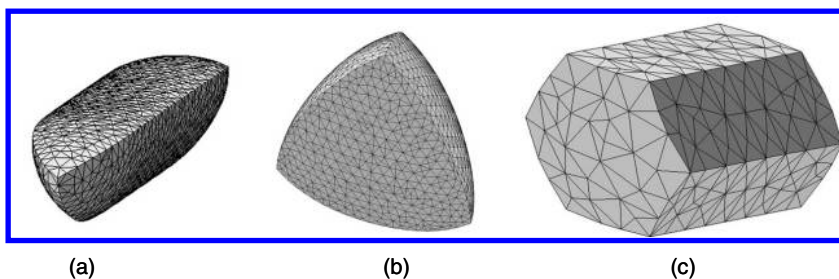


FIGURE 4.60 (SEE COLOR INSERT FOLLOWING PAGE 424)

Configurations used for the simulation of the diverse analytical expressions corresponding to (a) a 3-sided grain, (b) a tetrahedral grain and (c) a hexagonal prismatic grain. The grains surrounding these grains and forming the granular aggregates are not shown. The case of the hexagonal prism is special since it is surrounded by other hexagonal prisms and thus presents steady-state motion of its grain boundaries [554].

4.7.2 Computer Simulations of 3D Grain Growth

4.7.2.1 Solitary Grains

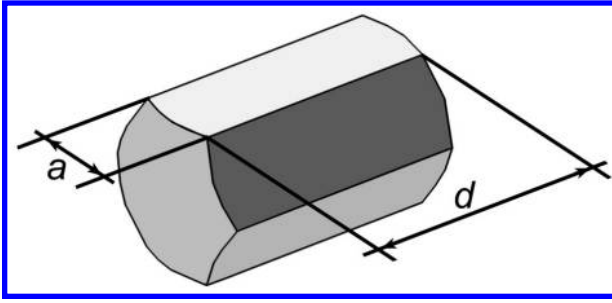
In [554] a three-dimensional vertex model was utilized to study grain growth in 3D systems and to analyze how the aforementioned approaches represent reality.

Contrary to the 2D situation the details of grain growth in 3D systems can be quantitatively studied only by computer simulations since the techniques for continuous characterization of 3D grain structures are still at their infancy.

The problem was considered in two stages. Firstly, the grain growth of a single grain was examined and the results were compared quantitatively with analytical approaches developed by MacPherson and Srolovitz [552]. In the second stage the kinetics of grain growth in 3D polycrystals obtained by computer simulations were compared to analytical predictions [541, 542, 554].

Three simple singular grain shapes were considered in [554] (Fig. 4.60). Although these configurations are unlikely to be found in a normal polycrystal (the tetrahedron is an exception) their simplicity makes them a good subject to test the different approaches discussed above.

We would like to stress again that the Cahn-MacPherson-Srolovitz approach is the only one that considers the metrics of the grains, which change dynamically in the course of grain growth. As a result this approach predicts a non-constant time dependency of the normalized volume rate of change ($\dot{V}V^{-1/3}$). All other models depend only on the topological class and thus predict a constant value of ($\dot{V}V^{-1/3}$). Comparison of the Cahn-MacPherson-Srolovitz approach with experimental results is somehow complicated because the parameters of this approach have to be determined from the current ge-

**FIGURE 4.61**

A hexagonal prismatic grain and the two dimensions a and d are shown [542].

ometry of the grains. A vertex model allows us to define all the parameters for this calculation during the evolution of the volume of a grain. In the following we will explain more comprehensively how the Cahn-MacPherson-Srolovitz relation (4.104), (4.108) can be computed from the simulated microstructure [554].

For this we consider the example of a hexagonal prismatic grain [542] (Fig. 4.61)

$$L(D) = \frac{1}{2\pi} \sum_i^{n_{ef}} \beta_i e_i \quad (4.110)$$

$$e(D) = \sum_i^{n_{tj}} e_i^{tj} \quad (4.111)$$

The term $e(D)$ is the length of the triple junctions of a given grain and is equal to the sum of the length of all triple lines N_{tj} of such a grain.

The term $L(D)$ reflects the local variation of the surface with respect to a fixed reference. To better understand this we need to imagine that the surface is also divided into very small surface elements. The normal to each element of the surface dS characterizes its spatial orientation, which may be different from all other pieces of surface surrounding the element dS ; the angle β is known as the turning angle and represents precisely the variation of one surface element with respect to another. The term e_i in Eq. (4.110) comprises the length of the junction between the dS elements. The sum over all junctions n_{ef} corresponds to the mean width of the whole domain. The orientation difference β across a triple junction corresponds to the external dihedral angle which in the equilibrium is established by the surface tensions of the adjoining grain boundaries. Another interesting feature of this term is that it introduces implicitly the curvature of the surface in Eq. (4.104).

As an example in Fig. 4.61 two new variables, a and d , define the dimensions of the grain: d is the length of the longitudinal triple line grain and a is the length of a side of the hexagonal cross section; the curvature of the triple line

is included in this parameter. Now we can calculate first the term $e(D)$ for this grain as follows:

$$e(D) = \sum_i^{n_{tj}} e_i^{tj} = 6d + 12a \quad (4.112)$$

the term $L(D)$ can also be easily calculated:

$$L(D) = \frac{1}{2\pi} \sum_i^{n_{ef}} \beta_i e_i = \frac{1}{2\pi} \left(2L_k + \frac{1}{3}\pi \cdot 6d + \frac{1}{3}\pi \cdot 12a \right) = \frac{L_k}{\pi} + d + 2a \quad (4.113)$$

where L_k is the unknown mean width of the two curved grain boundaries of the grain. Because all other grain boundaries are flat, $\beta = 0$ and their surfaces do not contribute to the mean width.

From Eqs. (4.105), (4.112) and (4.113), we arrive at

$$\frac{dV}{dt} = -2\pi m_b \gamma \left(\frac{L_k}{\pi} + d + 2a - d - 2a \right) = -2m_b \gamma L_k \quad (4.114)$$

The volume change rate for the configuration considered is determined by the term L_k which represents only the curved grain boundaries. It can be seen that Eq. (4.114) delivers a constant rate dV/dt and complies with reality since the configuration in Fig. 4.61 demonstrates a steady-state evolution of its volume.

In order to compare the different approaches the volume rate of change was normalized by the cubic root of the volume of the grains at any time, and for the case of the Cahn-MacPherson-Srolovitz approach Eq. (4.108) was used.

Fig. 4.62 shows the temporal evolution of the volume and the normalized volume rate of change for a 3-sided grain (Fig. 4.60). The volume is seen to decrease non-linearly with time (Fig. 4.62) indicating that, as predicted by Eqs. (4.104) and (4.108), there is not a constant volume rate of change (\dot{V}) for a particular topological class. Since the parameters in Eq. (4.104) change with time, \dot{V} cannot have a constant value unless special conditions are met as in the case of the hexagonal prism [542]. The normalized volume rate of change (Fig. 4.62b) also does not seem to be constant with time. A comparison of $\dot{V}V^{-1/3}$ for the different approaches evidences best agreement of the simulations with the Cahn-MacPherson-Srolovitz approach Mullins' model (Eq. (4.99)) also yields reasonable agreement. This indicates that the expression $\dot{V}V^{-1/3}$ of this particular grain is not far from the mean of the topological class $n = 3$. The models of Hilgenfeldt et al. [545] and Glicksman-Rios [551] cannot deliver a value for the topological class $n = 3$ since Eqs. (4.102) and (4.103) become undetermined for this number of grain faces.

The evolution of the tetrahedral grain shows similar features, a non-linear dependency of the volume on time (Fig. 4.64) and, consequently, a non-constant \dot{V} ; however, $\dot{V}V^{-1/3}$ is closer to a constant value (Fig. 4.64b). As in the previous case, the agreement with Eq. (4.108) is good. The observed

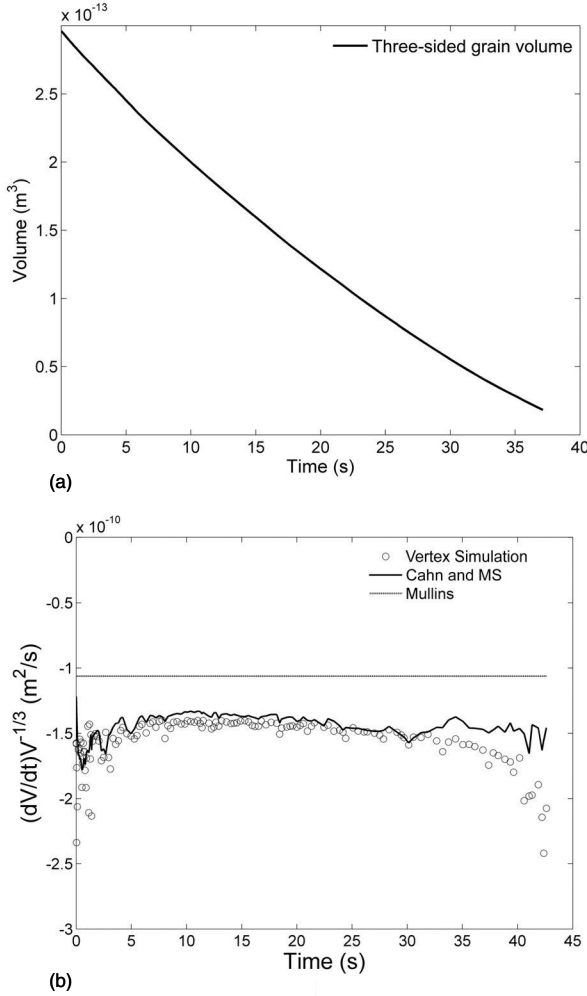
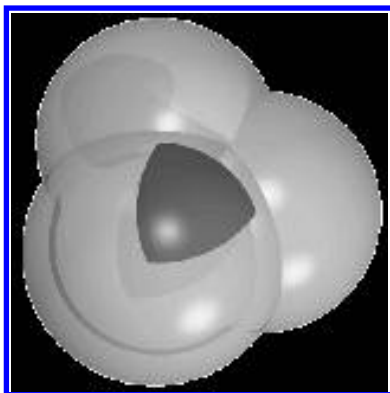


FIGURE 4.62

Volume evolution with time (a) and comparison of the volume rate of change of a 3-sided grain with the different model as calculated from the simulation data. (b) The Hilgenfeldt and Glicksman-Rios models do not appear because the volume rate of change of a grain with a topological class $n = 3$ cannot be calculated with their approaches (Eqs. (4.102) and (4.103) become undetermined [554]).

**FIGURE 4.63**

Reuleaux tetrahedron.

deviations in the beginning of the simulation are caused by the fact that the starting configurations have flat grain boundaries and thus need a certain relaxation time to attain the necessary curvature and equilibrium at the triple lines. The tetrahedral grain is of special interest for the Glicksman-Rios model [551]; the point is that the tetrahedral grain has a particular geometry, since it resembles a Reuleaux tetrahedron that is formed by the intersection of four spheres of equal radius with centers located at the surfaces of the neighboring spheres (three-dimensional equivalent of the Reuleaux triangle (Fig. 4.63)).

This geometry is optimal to study the Glicksman-Rios approach [551] because during its evolution it meets the condition of a constant vertex-to-vertex distance λ_4 that is assumed in this model, and thus Eq. (4.103) represents an exact solution for the growth rate of this grain. The simulation results show, in fact, excellent agreement with this model. The Hilgenfeld and Mullins models [545] also show reasonable agreement.

As shown in [542] the evolution of a hexagonal prism takes place in the steady-state regime and $\dot{V} = \text{const}$. Fig. 4.65 shows the calculated parameters $L(D)$ and $e(D)$ taken directly from the geometry of the evolving grain [542]. For a grain which evolves in a steady-state regime ($\dot{V} = \text{const}$) the curves $L(D, t)$ and $e(D, t)$ need to be parallel (Eq. (4.104)). One can see that this condition is evidently fulfilled (Fig. 4.65).

The results for the hexagonal prism (Fig. 4.66) show that the Cahn-MacPherson-Srolovitz approach [552] is the only one that reproduces almost exactly the evolution of the mean volume rate of change of the prism whereas other approaches deviate from the simulation results since they can only render a constant value, yet, on average with reasonable agreement. It is also confirmed that neither a constant \dot{V} nor a constant $\dot{V}V^{-1/3}$ can be expected for a given topological class because of the dependency of the growth rate on the metrics of the grain. For the 3-sided and tetragonal grain a constant

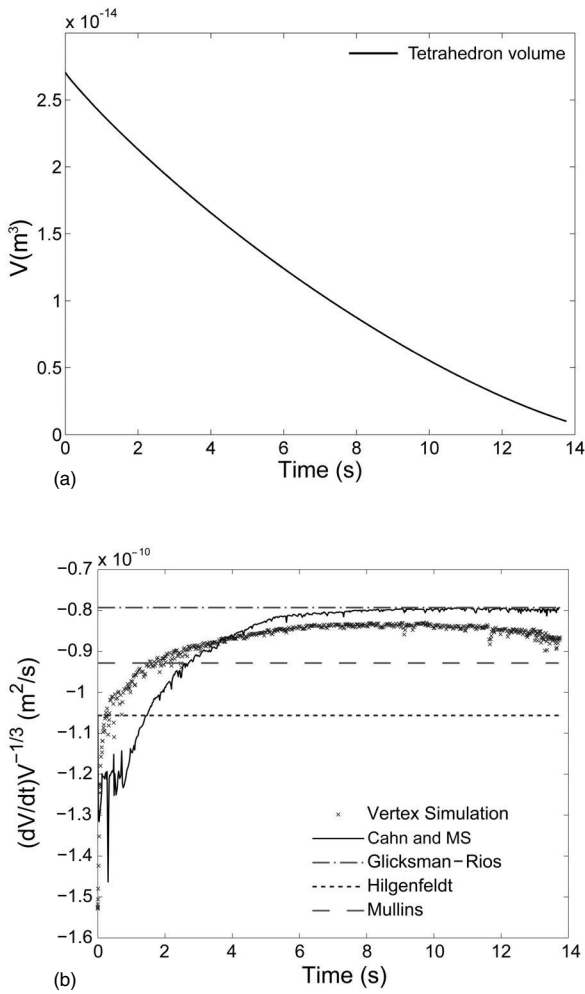
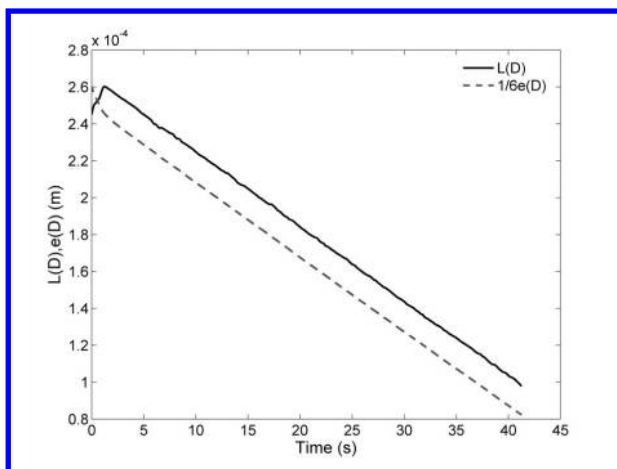


FIGURE 4.64 Volume evolution with time (a) and comparison of the volume rate of change of a tetrahedral grain using the different models as calculated from the simulation data (b) [554].

**FIGURE 4.65**

The temporal evolution of the parameters $L(D)$ and $e(D)$ for a hexagonal prism [554].

\dot{V} cannot be achieved. It is stressed that even in these cases a constant $\dot{V}V^{-1/3}$ is highly debatable since any perturbation in the geometry of the grains from the assumed ones will lead to deviations from the expected values. The hexagonal prism shrinks at constant \dot{V} and, therefore, cannot deliver a constant $\dot{V}V^{-1/3}$.

The analysis of the data of Fig. 4.66b reveals another interesting feature. The deviation between the Cahn-MacPherson-Srolovitz relation and the normalized volume rate of change remains constant for the entire simulation (with the exception of the incipient relaxation time). This occurs because the area of the grain boundaries that provides the driving force for the reduction of the volume of the grain does not change and, accordingly, the surface is represented by about the same quantity of triangular facets. Thus, the numerical error remains constant. The reduction of the grain boundary area and, hence, of the free energy, occurs at the expense of the lateral flat grain boundaries of the grain.

The results presented demonstrated that the Cahn-MacPherson-Srolovitz relation 4.104 delivers the best description for the curvature-driven grain volume change under specific controlled conditions. Despite the simplicity of the configurations studied, the results indicate that a grain of a given topological class can only shrink or grow with a constant $\dot{V}V^{-1/3}$ or \dot{V} under special conditions. The volume rate of change of normal closed domains for constant topological class will scatter over a certain range depending on the change in the metrics of the grain $L(D)$ and $e(D)$ in Eq. (4.104) until a topological transformation occurs that changes the topological class of the grain.

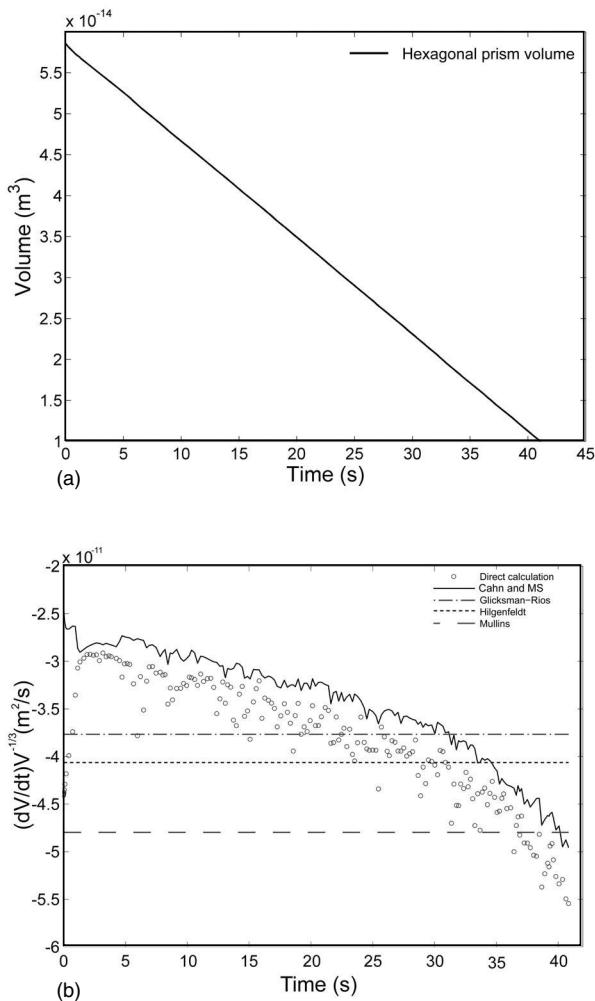


FIGURE 4.66 Volume evolution with time (a) and comparison of the volume rate of change of a hexagonal prismatic grain predicted by different models and simulation data (b) [554].

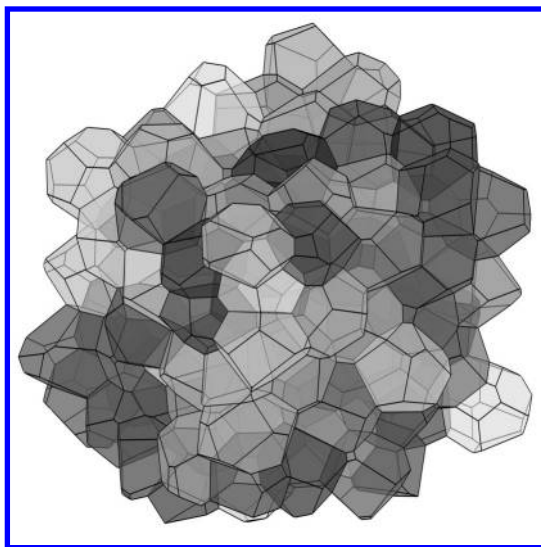


FIGURE 4.67 (SEE COLOR INSERT FOLLOWING PAGE 424)

Polycrystal used in the simulation composed of 125 grains with periodic boundary conditions [554].

4.7.2.2 3D Polycrystals

In the previous section we considered how the results of computer simulations of the temporal evolution of the volume of solitary grains compare to the different analytical approaches [541, 542, 554]. However, the behavior of a single grain is not the major goal of the approaches discussed. The main objective is to find a key to describe the grain growth in 3D polycrystal, to compute the rate of change of the volume of the grains in complex grain assemblies. This problem was considered in [554], where the grain growth in a polycrystal composed of 125 grains (Fig. 4.67) was studied quantitatively. The volume rate of change of all grains showed very good agreement with the Cahn-MacPherson-Srolovitz relation. In Fig. 4.68, an example of three grains with different growth rates is shown. During growth the grains suffer topological changes by gaining and losing grain boundaries [554]. One can see that the volume rate of change \dot{V} is apparently affected less by the change in the topological class than by the change in the metrics of the grains as substantiated also by the good agreement of the Cahn-MacPherson-Srolovitz relation with simulation results. In ([554]) it was shown that the evolution of individual grains and grain growth in polycrystal are well described by the Cahn-MacPherson-Srolovitz relation. An agreement between this relation

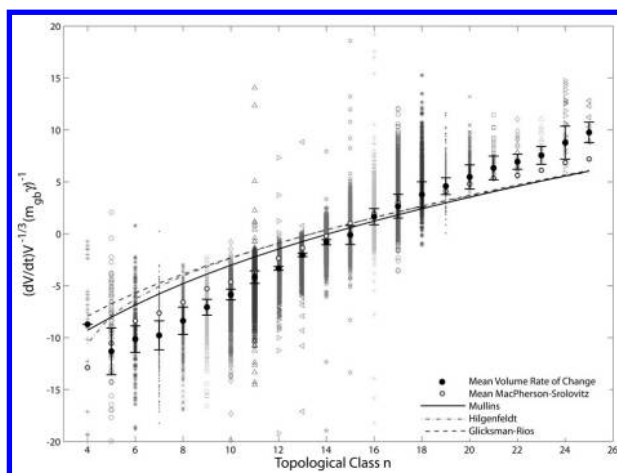


FIGURE 4.68 (SEE COLOR INSERT FOLLOWING PAGE 424)

Volume rate of change as a function of the topological class; the lines represent the analytical approaches of Mullins, Rios, and Glicksman, and Hilgenfeldt et al. The normalized volume rate of change was calculated directly from the change of grain volume with time [554].

and computer simulations signifies that there is no constant growth rate for a given topological class. Hence, grains with the same number of triple junctions may exhibit different growth rates depending on the difference between the mean width and the length of the triple junctions. Since this is the case, none of the approaches that formulate the growth rate as a function of the topological class (4.99, 4.102, 4.103) can be entirely valid for single crystals, since they can yield a correct result only under very specific conditions, i.e. if, at a certain time, there are grains fulfilling the relations. In order to test the predictive power of these approaches, the volume rate of change as a function of the topological class is plotted for these relations in Fig. 4.68 and compared to simulation results ([554]). It is evident that each topological class can have various growth rates in accordance with the Cahn-MacPherson-Srolovitz relations (4.104, 4.108). The mean normalized volume rate of change $\langle \dot{V} V^{-1/3} \rangle$ for each topological class is represented as a solid black circle, whereas open circles represent the mean according to the Cahn-MacPherson-Srolovitz relation that was calculated from the mean $L(D)$, $e(D)$, and volume for each topological class, i.e. $\langle \dot{V} V^{-1/3} \rangle = 2\pi m_{gb} \gamma (\langle L(D) \rangle_n - 1/6 \langle a(D) \rangle_n) \cdot \langle V \rangle_n^{-1/3}$. If only the mean values for each topological class are compared, all approaches show very good agreement with the simulation results. This has also been pointed out by Wakai [555], Weygand [556] and in phase-field simulations by Kim [557]. The mean value determined by the Cahn-MacPherson-Srolovitz

relation renders also a good agreement; however, it must be stressed that this relation is not meant to be used as a general descriptor of the average $\langle \dot{V}V^{-1/3} \rangle$.

The main property which distinguishes the observed analytical geometrical approaches is that all of them, except the Cahn-MacPherson-Srolovitz relation, do not include the metrics of the grain.

The theories of Mullins, Glicksman and Rios and Hilgenfeldt et al. are constructed by analogy with the Von Neumann-Mullins approach, they are purely topological. That is why the major weakness of the approaches mentioned are not quantitative discrepancies in computer simulations. All of these approaches give asymptotically a reasonable rate of the grain volume evolution, but in the absence of metrics. This is the reason why it has been impossible in the frame work of these approaches to consider problems connected to grain growth in systems with finite mobility of grain boundary junctions. The influence of the metrics comes particularly into play when it is impossible to assume that grain boundary junctions have an infinite mobility. Such an attempt was undertaken in [542].

When deriving Eq. (4.104) Cahn, MacPherson and Srolovitz assumed that the dihedral angles at triple lines attain their equilibrium value of 120° . Consequently, the angle between triple lines at quadruple junctions must reach the tetrahedral angle of $\sim 109.47^\circ$ [542]. Since a finite mobility of the junctions influences the value of these angles, one might expect that the Cahn-MacPherson-Srolovitz relation will not be able to predict adequately the volume rate of change of a grain in the case of a finite mobility of grain boundary junctions. This principal problem was studied in [542, 554] for different triple junction and quadruple junction mobility. In all cases a tangible deviation from the values predicted by Eq. (4.104) was observed. However, for a finite quadruple junction mobility the effect is much smaller than for a finite triple junction mobility.

In Fig. 4.69 the results of computer simulation and different analytical approaches are presented. Under the action of a finite mobility of triple lines ($\Lambda_{tj} = 0.2$), the different analytical approaches predict values of the volume change rate which depart greatly from the simulation results both in a quantitative and qualitative sense. For a better agreement the diverse approaches need to consider the change of curvature that comes with a boundary junction of finite mobility. One major effect of a finite quadruple junction mobility is a change in the curvature of the adjoining triple lines, which implicitly alters also their length. The total length of the triple lines $d(D)$ for the configuration shown in Fig. 4.61 is given by the sum of all triple line lengths a and d . The length of the triple lines for a hexagonal cross section can be easily calculated as (Figs. 4.37 and 4.61) [427, 441]

$$a = 2\ell = \frac{2x_0}{\ln \sin \Theta} \ln \left(\frac{1 + \cos \Theta}{\sin \Theta} \right) \quad (4.115)$$

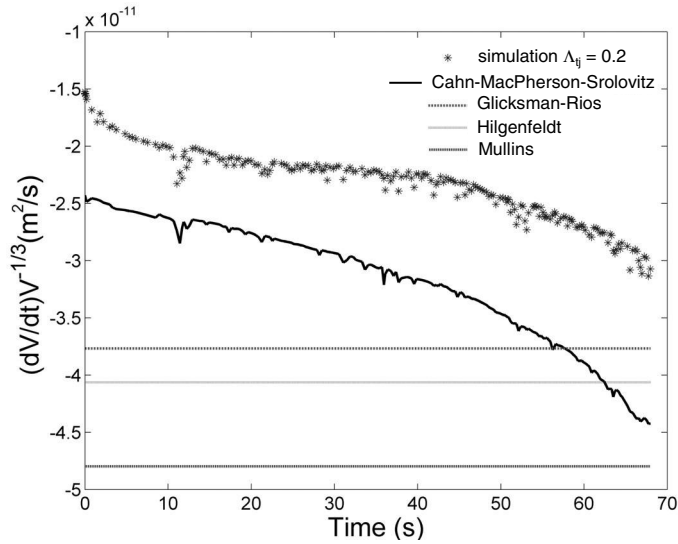


FIGURE 4.69
A comparison of the different approaches with simulation results for the case of a finite triple junction mobility reveals a strong discrepancy [542, 554].

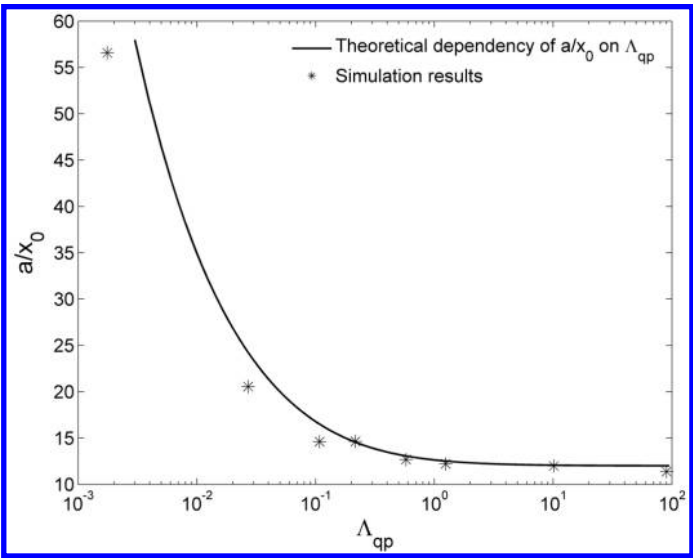
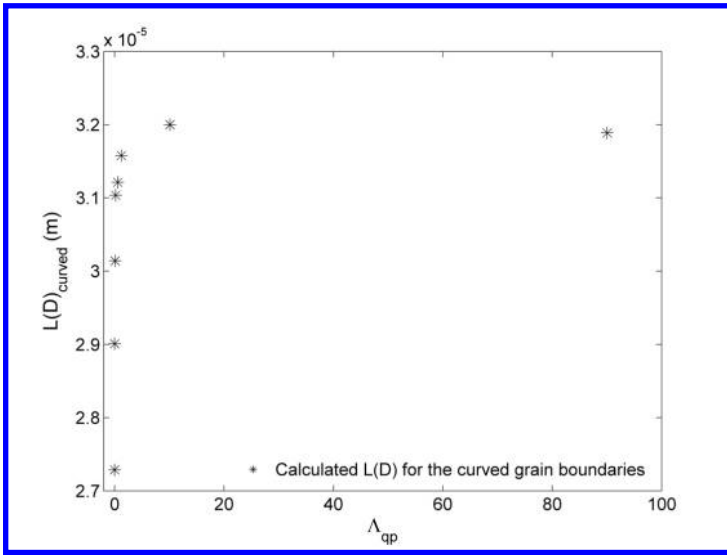


FIGURE 4.70
Dependency of the triple line length on the parameter Λ_{qp} [542].

**FIGURE 4.71**

A comparison of the different approaches and with the simulation results for the case of a finite triple mobility reveals a strong discrepancy [542].

where Θ can be expressed as a function of the criterion Λ_{qp}

$$\Theta \cong \frac{2\Lambda_{qp}}{3\Lambda_{qp} + \sqrt{\Lambda_{qp}(9\Lambda_{qp} + 2)}} + \frac{\pi}{2} \quad (4.116)$$

On the other hand the length d can be represented as

$$d = d_0 - 2v_b t \quad (4.117)$$

where d_0 is the length of the longitudinal triple line at $t = 0$, v_b is the velocity of the front and rear faces of the grain.

The simulation gives us the possibility of extracting the dependency of the parameters a and $L(D)$ on Λ_{qp} (Figs. 4.70 and 4.71). One can see that $L(D)$ increases rapidly for rather small Λ_{qp} to a value of $L(D)$, which corresponds to the curvature of the grain boundary for $\Lambda_{qp} \rightarrow \infty$. The dependence of the parameters $L(D)$ and $e(D)$ on a finite quadruple junction mobility questions, strictly speaking, the applicability of the Cahn-MacPherson-Srolovitz relation to grain growth in real 3D systems. However, it can be expected that, similar to the generalized Von Neumann-Mullins relation [427, 441, 442] there is a generalized Cahn-MacPherson-Srolovitz relation

$$\frac{dV}{dt} = f(L[\Lambda_{qp}, \Lambda_{tj}]) e[\Lambda_{qp}, \Lambda_{tj}] \quad (4.118)$$

4.8 Kinetics of Grain Growth Inhibited by Vacancy Generation

Even for a crystal of a pure element it is thermodynamically profitable to contain “intrinsic impurities” — the vacancies. It is a rather elaborate problem to account for the effect of vacancies on the processes in solids. Even if we restrict ourselves to processes where the vacancies are generated as a product of a kinetics process the list is long enough. Vacancy production by moving jogs on dislocations during plastic deformation, by a progressing solid/liquid interface in solidification, or, generally, in every first-order phase transition, which includes the crystalline phase, shrinking voids in sintering, or, finally, during grain growth due to the different density of grain boundary and the ideal crystal [20], [455]–[457] (grain boundary excess free volume — see Chapter 1). As for the latter example of vacancy production, which is the subject of this paragraph, the point is that the excess of grain boundary free volume liberated by the reduction of total grain boundary area can be considered a flux of vacancies into the bulk of a sample, a cause of elastic stresses or a source of plastic deformation. However, in principle, the approach which considers the elimination of volume excess by vacancies is most versatile. In fact, the way to reduce the excess through elastic stresses is a deadlock. The relaxation of elastic stresses is a long-term and slow process. That is why in a short time the reduction of grain boundary area will result in a strong increase of free energy. Moreover, as mentioned above, the relaxation of elastic stresses occurs by a directed flux of vacancies. The inhibiting effect of vacancies on the very process in which they are generated will be considered from a thermodynamics viewpoint [11, 12], [458]–[460].

The excess free volume a system has to get rid of in such processes can be released as vacancies which have to be accommodated by the crystal bulk. A vacancy can be understood as an “impurity atom” which is dissolved in a crystal, and the distinctive property of which (compared to ordinary impurities) is that a vacancy is born from vacuum and disappears in vacuum, i.e. there is no conservation rule. Other than that the properties of vacancies are similar to the usual impurities: creating a solution even in absolutely pure crystals, vacancies decrease the free energy; if the vacancy concentration exceeds the solubility limit — the equilibrium concentration of vacancies c^{eq} — vacancies try to leave the crystal or to precipitate as second-phase particles, i.e. voids. The kinetics aspect of vacancy influence on grain growth was considered in [198, 199]. In [11, 12], [458]–[460] it was shown that in the course of grain growth a self-drag of grain boundaries can be observed, caused by the libration of excess free volume in terms of vacancy emission.

In the most general terms, the Gibbs free energy G of a system with vacancies can be written as

$$G = G_{\text{non-vac}} + G_{\text{vac}} \quad (4.119)$$

where $G_{\text{non-vac}}$ is the non-vacancy part of the Gibbs free energy and G_{vac} is the contribution due to vacancies.

Obviously small deviations of the vacancy concentration c from its equilibrium value c^{eq} will increase the last term in Eq. (4.119), irrespective of the sign of the difference $c - c^{\text{eq}}$. As shown in [459]

$$\left(\frac{d^2 G_{\text{vac}}}{dc^2} \right)^{\text{eq}} = \frac{NkT}{c^{\text{eq}}} \left[1 + \exp \left(\frac{-H_v^f}{kT} \right) \right] \cong \frac{NkT}{c^{\text{eq}}} \quad (4.120)$$

Here n and N are the number of vacancies and the number of atomic sites per unit volume, respectively, and H_v^f is the vacancy formation enthalpy. Then, taking into account that at equilibrium $\frac{dG_{\text{vac}}}{dc} = 0$, we arrive at

$$G = G_{\text{non-vac}} + G_{\text{vac}}(c^{\text{eq}}) + \frac{1}{2} \frac{NkT}{c^{\text{eq}}} (c - c^{\text{eq}})^2 \quad (4.121)$$

Higher order terms in $c - c^{\text{eq}}$ have been neglected. It is noted that this compact formula for the vacancy part of the free energy embraces both the vacancy formation enthalpy term and the entropy contribution,

The formulation given in [459] makes it possible to look at the kinetic processes involving vacancies from a viewpoint of their thermodynamic feasibility. Obviously, a kinetic process will be promoted thermodynamically if the derivative of G with respect to time t , \dot{G} , is negative, i.e.

$$\dot{G} = \dot{G}_{\text{non-vac}} + \frac{NkT}{c^{\text{eq}}} (c - c^{\text{eq}}) \dot{c} < 0 \quad (4.122)$$

The time derivative of the vacancy concentration \dot{c} can be written as

$$\dot{c} = \dot{c}^+ - \dot{c}^- \quad (4.123)$$

representing a competition between the vacancy production (\dot{c}^+) and the vacancy removal (\dot{c}^-) rates. While the latter quantity can be expressed in a generic form

$$\dot{c}^- = \frac{D_v}{d^2} (c - c_{\text{sink}}) \quad (4.124)$$

where D_v is the vacancy diffusivity, d is the sink spacing and c_{sink} the vacancy concentration at a sink, the vacancy production rate depends on the particular mechanism of vacancy generation and is related to the rate of variation of the first, “non-vacancy,” term of the free energy \dot{G} . In what follows, kinetic processes which are significantly affected by this coupling with their “by-product,” i.e. the vacancies produced, will be investigated.

As a “by-product” of this process, vacancies are released into the crystal bulk. Indeed, the density of a grain boundary is generally lower than that of the bulk (see Chapter 1).

The excess free volume released during the reduction of the grain boundary area has to be accommodated by the bulk. This assumption is supported by

recent computer simulations of grain boundary motion [457]. The supply of vacancies by moving grain boundaries may produce a vacancy supersaturation in the bulk, raising the Gibbs free energy and producing a thermodynamic force on the boundary. As can be expected intuitively, particularly by analogy with the Le Chatelier principle, this thermodynamic force will oppose grain boundary migration. Under certain conditions considered in [11, 458, 459], this effect may be strong enough to temporarily suppress grain growth altogether. In the approach proposed uninhibited grain growth was considered to occur only during a limited time t^* (Eq. (4.125)). After that time, on reaching the condition when the time derivative of the free energy of the system becomes positive, “locking” of grain growth occurs

$$t \geq t^* = \frac{1}{24} \cdot \frac{\gamma c^{\text{eq}} R^2}{NkT(V^{\text{ex}})^2 V} \quad (4.125)$$

Under the assumption that $t^* \ll \tau = d^2/D_v$ the expression for the effective velocity of grain growth V_{eff} can be written as

$$V_{\text{eff}} = \frac{t^*}{\tau} V = \frac{1}{24} \cdot \frac{\gamma D_{SD}}{NkTZ(V^{\text{ex}})} \left(\frac{R}{d} \right)^2 \quad (4.126)$$

Here d and D_v are the average spacings between vacancy sinks and the vacancy diffusivity, correspondingly. V is the “unperturbed” rate of grain growth driven by the boundary energy; γ , δ , β and m are grain boundary characteristics: free energy per unit area, thickness, the relative excess free volume, and mobility, respectively; \bar{R} is the average grain size (radius), D_{SD} is the bulk self-diffusion coefficient, N is the number of atoms per unit volume and Z is the coordination number; kT has its usual meaning. Clearly it is more correct to express the product $\beta\delta$ as a grain boundary excess free volume V^{ex} [m^3/m^2]. The ratio $\frac{d^2}{D_v}$ determines the characteristic vacancy annihilation time. Smoothing the discontinuous solution by replacing V_{eff} with the time derivative of the average grain size $d\bar{R}/dt$ and solving Eq. (4.125) yields the time law for the grain growth model of [11, 459]

$$\frac{1}{\bar{R}_0} - \frac{1}{\bar{R}} = \frac{1}{24} \cdot \frac{\gamma D_{SD} t}{NkTZ(V^{\text{ex}})^2 d^2} \quad (4.127)$$

where \bar{R}_0 is the initial grain size.

The model outlined above accounts for the inhibiting effect of vacancies on grain growth, but, of course, it is not more than an approximation of the real continuous process of grain growth. Guided by the principle that “*natura non facit saltus*,” the authors of [12, 460] suggested a description of grain growth as a continuous process.

An equation expressing the balance of energy associated with an increment of grain size dR within a time increment dt can be written as

$$-\frac{d}{d\bar{R}} \left(\frac{3\gamma}{2\bar{R}} \right) d\bar{R} = \frac{3}{2} \cdot \frac{1}{\bar{R}} \cdot \frac{(d\bar{R}/dt)^2}{m_b} dt + \frac{NkT}{c^{\text{eq}}} (c - c^{\text{eq}}) \frac{6V^{\text{ex}}}{\bar{R}^2} d\bar{R} \quad (4.128)$$

Eq. (4.128) expressed the energy balance: the energy release associated with the reduction of the GB area (the left-hand side of Eq. (4.128)) is distributed between the dissipation due to the drag forces (first term on the right-hand side of (4.128) and the vacancy sub-system — second term on the right-hand side of Eq. (4.128)).

$$\dot{c} = \frac{6V^{\text{ex}}}{\bar{R}^2} \cdot \frac{d\bar{R}}{dt} - \frac{D_v}{d^2} (c - c^{\text{eq}}) \quad (4.129)$$

Eqs. (4.128) and (4.129) render a full description of the evolution of the grain system in terms of the average grain radius and the vacancy concentration. In a dimensionless form they can be rewritten as

$$\xi \frac{d\xi}{dt} + A\Psi C - A = 0 \quad (4.130)$$

$$\frac{dC}{dt} = \frac{p}{\xi^2} \frac{d\xi}{dt} - C \quad (4.131)$$

Here $\xi = \bar{R}/d$, $C = c - c^{\text{eq}}$, $A = m_b\gamma/D_v$, $\Psi = \frac{4NkT(V^{\text{ex}})}{c^{\text{eq}}\gamma}$, $p = 6V^{\text{ex}}/d$; the time t is now non-dimensional and is measured in units of d^2/D_v .

Numerical solutions of the above set of equations for a broad range of parameters have shown that for sufficiently small initial grain size $\xi_0 = R_0/d$ the grain growth uninhibited by vacancies is preceded by an incubation time during which the growth rate is substantially reduced, the time dependence of the grain size exhibiting a plateau-like behavior (Fig. 4.72). For large values of ξ_0 no incubation time is observed. The incubation time is defined as the time at which the grain growth rate is a maximum. This time corresponds to the termination of the plateau-like behavior and a transition to uninhibited, parabolic grain growth (Fig. 4.72). During the incubation time the vacancy concentration stays approximately constant (Fig. 4.72). Numerical results also show that the non-dimensional incubation time is inversely proportional to ξ_0 and can be represented by the following formula

$$\tau_{\text{incubation}} = \frac{P\Psi}{\xi_0} \quad (4.132)$$

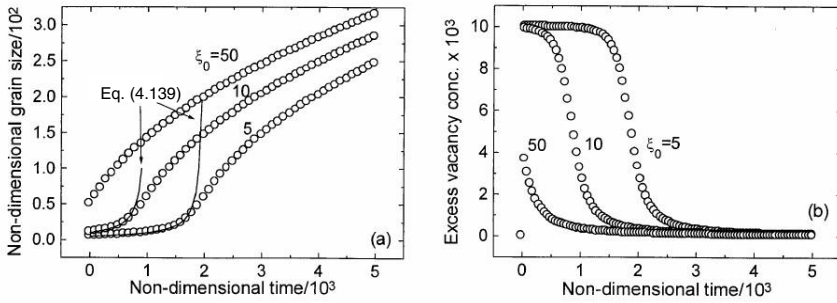
or in dimensional form

$$t_{\text{incubation}} = 24 \frac{NkT(V^{\text{ex}}d)^2}{\gamma\bar{R}_0D_{\text{SD}}} \quad (4.133)$$

where D_{SD} is the bulk self-diffusion coefficient.

For times larger than the incubation time a common parabolic grain growth law follows, while within the incubation time an approximate analytical solution of the set of Eqs. (4.132) and (4.133) reads

$$C = 1/\Psi \quad (4.134)$$

**FIGURE 4.72**

Dependence of non-dimensional grain size (a) and of excess vacancy concentration (b) on the non-dimensional time calculated from Eqs. (4.130), (4.131) for the following values of parameters: $A = 10$, $\Psi = 100$, and $p = 100$ [12].

$$\frac{1}{\xi_0} - \frac{1}{\xi} = \frac{1}{P\xi} \quad (4.135)$$

or rewritten in dimensional form

$$\frac{1}{R_0} - \frac{1}{R} = \frac{1}{24} \cdot \frac{\gamma D_{SD} t}{NkT(V^{\text{ex}})^2 d^2} \quad (4.136)$$

This demonstrates that the approximation [11, 458] based on the intermittent locking-unlocking scheme with smoothing, provides a quantitatively adequate representation of continuous grain growth in the regime where the inhibiting effect of grain growth-induced vacancies is operative. Indeed, Fig. 4.72 demonstrates an excellent match between the $\xi(t)$ dependencies over the incubation period given by Eqs. (4.135) and (4.136).

The condition for the occurrence of the vacancy-induced stabilization against grain growth can be extracted from a comparison of the inhibited grain growth with the common, parabolic grain growth kinetics. In fact, parabolic growth occurs if the vacancy effect can be neglected, i.e. if the vacancy concentration is sufficiently close to its equilibrium value. From Eq. (4.130) it then follows

$$\xi^2 - \xi_0^2 = 2At \quad (4.137)$$

Obviously, the solution of the set of Eqs. (4.130) and (4.131) coincides with the parabolic law given by Eq. (4.137) for a time tending to zero and also for times much larger than the incubation time, when C tends to zero, cf. Fig. 4.72. A real inhibition of grain growth means that the rate of growth in the plateau region, described by Eq. (4.135) is much smaller than that corresponding to “free” uninhibited growth described by Eq. (4.137). This condition reads

$$\xi \ll (Ap\Psi)^{1/3} \quad (4.138)$$

or in the dimensional form

$$\bar{R}_0 \ll \bar{R}_c^* = \left[24NkTZ(V^{\text{ex}})^2 d^2 \frac{m_b}{D_{\text{SD}}} \right]^{1/3} \quad (4.139)$$

One can see that this condition is not very material sensitive, particularly due to the fact that the ratio of the grain boundary mobility and the coefficient of bulk self-diffusion is not strongly material dependent, and also due to the power of $1/3$. One possible source of structural dependence is the sink spacing d , for example if it is related to the inverse of the square root of the dislocation density that may bring about some variability of the quantity on the right-hand side of inequality (Eq. (4.139)).

One particular case needs to be considered separately, though. It is the case when the initial grain size is so small that no other vacancy sinks but the grain boundaries themselves are available, so that d is to be identified with the grain size \bar{R} . Eq. (4.136) then changes to

$$\frac{dC}{dt} = \frac{1}{\xi^2} \left(6 \frac{d\xi}{dt} - C \right) \quad (4.140)$$

Eq. (4.135) remains unchanged. However, the meaning of the non-dimensional grain size and the non-dimensional time are different now: $\xi = \bar{R}(V^{\text{ex}})$, and time is measured in units of $(V^{\text{ex}})^2/D_v$.

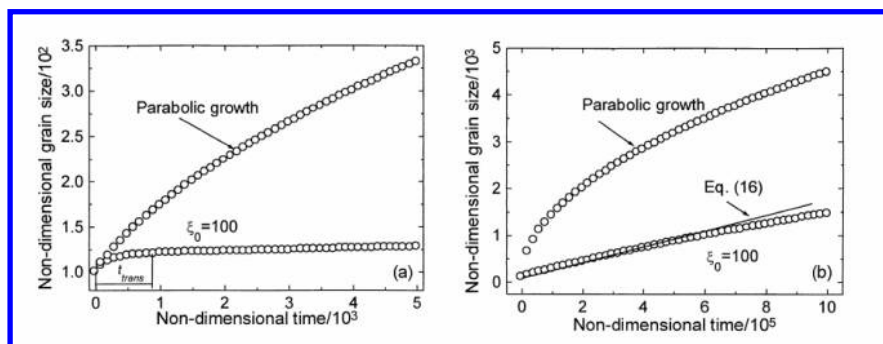
Solving the set of Eqs. (4.135) and (4.140) numerically, one can see that the temporal behavior of the grain size in this case is different from the behavior in the case of constant sink spacing d . After a short initial period of time t_{trans} the case of vacancy-inhibited growth slows down considerably (Fig. 4.73). After that grain growth effectively stays inhibited for very long times. The growth rate is thus always lower than the respective rate of usual parabolic growth (Fig. 4.73). Again, using the fact that after the transient period t_{trans} the vacancy concentration is sustained at an approximately constant level and that the grain size does not change significantly, we arrive at an approximate solution of the set of Eqs. (4.135) and (4.140) which reads

$$\bar{R} - \bar{R}_0 = \frac{1}{24} \cdot \frac{\gamma D_{\text{SD}} t}{NkTZ(V^{\text{ex}})^2} \quad (4.141)$$

From Fig. 4.73 one can see that Eq. (4.140) indeed provides a good analytical approximation for sufficiently short times, which nevertheless should be longer than t_{trans} .

The stability condition of nanocrystalline material against grain growth can be expressed by the inequality

$$\bar{R}_0 \ll \bar{R}_c = 24NkTZ(V^{\text{ex}})^2 \frac{m_b}{D_{\text{SD}}} \quad (4.142)$$

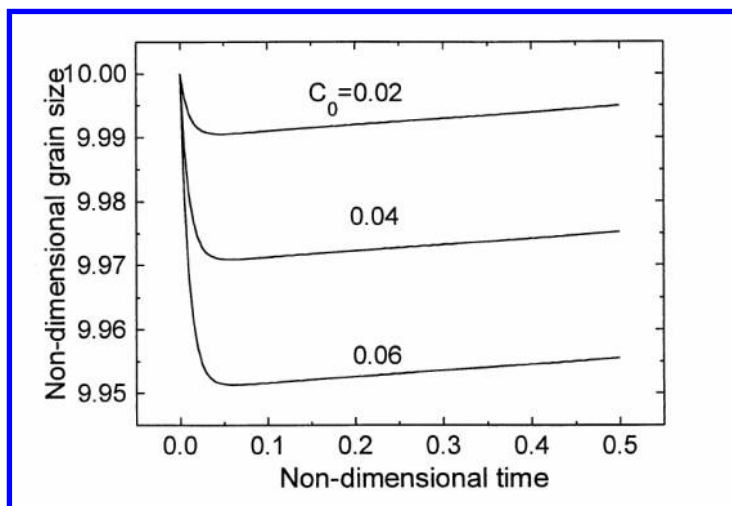
**FIGURE 4.73**

Dependence of non-dimensional grain size on the non-dimensional time calculated from Eqs. (4.130) and (4.140) for the following values of parameters: $A = 10$, $\Psi = 100$ for two different time scales [12].

These results have an interesting interpretation: a nanocrystalline material cannot be stable if condition (4.142) or (4.139) (whichever is relevant) is violated. In that sense, the critical radius \bar{R}_c or \bar{R}_c^* can be regarded as a limiting stable grain size above which grain growth uninhibited by vacancies is possible. Obviously, as seen from (4.139) and (4.142) the critical grain size is temperature dependent. As the activation energies for grain boundary mobility are generally different, the sense of the temperature variation of the critical grain size will depend on the interplay of the temperature dependencies of the mobility and self-diffusion coefficient. It is emphasized that the grain boundary mobility may depend very strongly on the type of the boundary, the texture in the material and its purity (see Chapter 3), which makes an estimation of the critical radius to a fairly difficult task. In [12] such an estimation was attempted for Al, the only material for which m_b is known with some confidence. At 300°C one obtains both \bar{R}_c and $\bar{R}_c^* = (\bar{R}_c d^2)^{1/3}$ of the order of 100 nm. These estimates can, from our viewpoint, explain the relative stability of nanocrystalline materials against grain growth.

The results of the described approach were compared with grain growth experiments in nanocrystalline Fe [452]. As intimated by the authors of [452] the theory developed is able to account for the growth rate discrepancy between nanocrystalline and microcrystalline Fe without recourse to impurity effects.

We would like to remind the reader that the results of [452] were considered in the previous paragraph as an experiment, which supports the grain boundary junction drag approach, predicting under definite conditions a linear dependence between average grain size \bar{R} and annealing time. The vacancy drag concept suggests also another explanation. A quantitative experiment only can say which approach gives more adequate description of reality. The set of Eqs. (4.135) and (4.136), or (4.132) and (4.133) yields solutions that predict a

**FIGURE 4.74**

Dependence of non-dimensional grain size on the non-dimensional time calculated from Eqs. (4.130) and (4.131) for various levels of initial vacancy supersaturation.

decrease of the average grain size for the case of an initial vacancy supersaturation. In other words, it can be speculated that grain refinement can be induced by a high vacancy concentration, which can be created in different ways, e.g. by quenching from a high temperature, irradiation with energetic particles or plastic deformation. An example of the computed variation of the average grain size with time for three different initial excess vacancy concentrations is shown in Fig. 4.74. Although the magnitude of grain size decrease is small the very possibility of vacancy-induced grain refinement appears interesting. The physical reason for this grain refinement is similar to the well-known effect of grain refinement during discontinuous precipitation [462], diffusion-induced grain boundary migration [463] and discontinuous ordering reactions [464]. In all cases the loss of energy associated with an increase of grain boundary area is compensated for by the energy gain in the bulk due to decomposition of a supersaturated solution, formation of a solid solution, or bulk ordering of the quenched disordered alloy behind moving grain boundaries.

In [460] the discussed approach was applied to grain growth in thin films, one of the most important subjects of modern information technology. Grain growth in thin films has some distinctive properties, which are mainly connected with the stresses developing in thin films and with a strong influence of the free surface on grain boundary motion [465, 466]. The consideration of the first feature dates back to Chaudhari [13, 14] [467]–[469]. First, the cohesion between a film and a substrate should lead to internal stresses in

the film. Second, under certain conditions an equilibrium grain size can exist beyond which no grain growth occurs. The latter results from consideration of the interplay between the elastic strain energy and the total grain boundary energy during grain growth. The model proposed by Chaudhari appears to be commonly accepted, see, e.g., a review [14]. In that approach it was tacitly assumed that the excess free volume of grain boundaries released during grain growth disappears instantly, giving rise to a tensile stress. This strong assumption limits the applicability of the model, as the free volume release would normally occur via generation of lattice defects, notably the injection of vacancies into the bulk of the material [457].

Let us consider briefly the situation analyzed in [13, 14]. A polycrystalline thin film is deposited on a substrate, and we assume the film is initially in a stress-free state. In the course of grain growth the reduction of the excess grain boundary free volume would lead to a decrease in the free volume, and, as a result (at constant film thickness), to a decrease in the area of the film. Then the stress in a given direction of the isotropic film can be estimated as

$$\sigma = \frac{E}{2(1-\nu)} V^{\text{ex}} \left(\frac{1}{R_0} - \frac{1}{R} \right) \quad (4.143)$$

Here $E/(1-\nu)$ is the biaxial elastic modulus expressed in term of Young's modulus E and Poisson's ratio ν .

However, Eq. (4.143) going back to [13] does not take into account the elongation of the specimen due to the generation of vacancies. One possibility is to convert it into individual vacancies. As long as the vacancies thus generated stay in the film, no net volume change occurs. (This implies that the excess free volume is considered to be equal to the total volume of vacancies generated, i.e. possible relaxation effects are neglected.) However, when vacancy removal by diffusion (e.g. to the film surface) occurs, film shrinkage due to loss of grain boundary area will outweigh its extension due to vacancies. If an individual vacancy leads to the specimen elongation αb , where b is the atomic spacing in the direction of interest and α is the numerical coefficient of the order of unity, the resulting stress reads [460]:

$$\sigma = \frac{E}{(1-\nu)} \left\{ \frac{1}{2} V^{\text{ex}} \left(\frac{1}{R_0} - \frac{1}{R} \right) - \alpha (c - c^{\text{eq}}) \right\} \quad (4.144)$$

The coefficient α can be extracted from a simple consideration. In the case when no vacancy removal occurs the stress should vanish:

$$\frac{1}{2} V^{\text{ex}} \left(\frac{1}{R_0} - \frac{1}{R} \right) = \alpha (c - c^{\text{eq}}) \quad (4.145)$$

On the other hand one has under such "adiabatic" condition

$$c - c^{\text{eq}} = V^{\text{ex}} \left(\frac{1}{R_0} - \frac{1}{R} \right) \quad (4.146)$$

From (4.145) and (4.146) we get $\alpha = 0.5$.

As mentioned above, Chaudhari's approximation presumes that the excess volume disappears instantaneously, while in our approach part of it is contained in the vacancies. In this case the resulting stress can be expressed by

$$\sigma = \frac{E}{2(1-\nu)} \left\{ V^{\text{ex}} \left(\frac{1}{R_0} - \frac{1}{R} \right) - (c - c^{\text{eq}}) \right\} \quad (4.147)$$

The Gibbs free energy of the film (per unit volume) can be written as a sum of three contributions:

The elastic energy:

$$G_{\text{el}} = \frac{\sigma^2}{2E} (1-\nu) \quad (4.148)$$

the grain boundary free energy (per unit volume):

$$G_{\text{gb}} = \frac{\gamma}{R} \quad (4.149)$$

where γ is the boundary surface tension; the relation (4.149) is derived under the assumption that the grains are cylindrical with height equal to the film thickness; and, finally the "vacancy" free energy:

$$G_{\text{vac}} = \frac{NkT}{2c^{\text{eq}}} (c - c^{\text{eq}})^2 \quad (4.150)$$

Consider the derivative of the full Gibbs free energy $G = G_{\text{el}} + G_{\text{GB}} + G_{\text{vac}}$ with respect to the average grain size R

$$\begin{aligned} \frac{dG}{dR} = & \left[\frac{NkT}{c^{\text{eq}}} (c - c^{\text{eq}}) - \frac{\sigma}{2} \right] \cdot \frac{dc}{dR} + \\ & + \left\{ \frac{1}{4} \frac{E}{(1-\nu)} V^{\text{ex}} \left[V^{\text{ex}} \left(\frac{1}{R_0} - \frac{1}{R} \right) - (c - c^{\text{eq}}) \right] - \gamma \right\} \frac{1}{R^2} \end{aligned} \quad (4.151)$$

The behavior of the system can be diagnosed by an analysis of the sign of this derivative. The thermodynamic viability of the grain growth process requires that the derivative be negative.

The evolution of the vacancy concentration with time t is given by

$$\frac{dc}{dt} = \frac{V^{\text{ex}}V}{R^2} - \frac{D_v}{d^2} (c - c^{\text{eq}}) \quad (4.152)$$

The first term on the right-hand side represents the rate of vacancy generation accompanying grain growth (V being the grain growth rate, which is proportional to the velocity of grain boundary migration). The second term describes the vacancy removal by diffusion to the film surface, with D_v being the vacancy diffusivity and d the film thickness.

Two essentially different situations of grain growth in thin films were considered in [460]. When vacancy removal can be neglected (which can be referred

to as the “adiabatic” case), $\sigma = 0$, and the last term in (4.152) can be dropped leading to

$$\frac{dc}{dR} = \frac{V^{\text{ex}}}{R^2} \quad (4.153)$$

Equation (4.151) then assumes the form

$$\frac{dG}{dR} = \frac{1}{R^2} \left\{ -\gamma + (V^{\text{ex}})^2 \frac{NkT}{c^{\text{eq}}} \left(\frac{1}{R_0} - \frac{1}{R} \right) \right\} \quad (4.154)$$

It is seen that in the early stages of grain growth, when R is close to R_0 , the derivative $\frac{dG}{dR}$ is negative, meaning that the process is favorable thermodynamically. However, at a certain critical value of R given by

$$R_c = \frac{R_0}{1 - \frac{\gamma c^{\text{eq}} R_0}{(V^{\text{ex}})^2 NkT}} \quad (4.155)$$

the derivative $\frac{dG}{dR}$ vanishes. This critical value of R can be seen as an “equilibrium” grain size beyond which no growth will occur. Obviously, such a critical grain size is only possible if the denominator of Eq. (4.155) is positive, i.e. if

$$R_0 < \frac{(V^{\text{ex}})^2 NkT}{\gamma c^{\text{eq}}} \quad (4.156)$$

A simple estimate using representative values of the parameters

$$V^{\text{ex}} = 2 \cdot 10^{-11} \text{m}^3/\text{m}^2, \quad \gamma = 1 \text{J}/\text{m}^2, \quad T = 500 \text{K}, \quad c^{\text{eq}} = 10^{-8}$$

shows that this condition is fulfilled for $R_0 < 1.5 \cdot 10^{-5} \text{m}$. The estimation is given for $V^{\text{ex}} = 2 \cdot 10^{-11} \text{m}^3/\text{m}^2$ [460]. However, the direct measurements of grain boundary excess free volume (Chapter 1) show that V^{ex} might be in the range of $5 \cdot 10^{-11} \text{m}^3/\text{m}^2$, which gives us the value of R_0 equal to $R_0 \approx 10^{-4} \text{m}$. Of course, this value is strongly temperature dependent, primarily through the thermal equilibrium vacancy concentration. If inequality (4.156) is not fulfilled, grain growth will be unrestricted.

The second situation, which can be called the “Chaudhari” approximation [467], also follows from Eqs. (4.152) and (4.153). Indeed, assuming the existence of such a critical radius and thus setting V to zero and further assuming that the vacancy concentration is equal to its thermal equilibrium value (a tacit assumption in Chaudhari’s paper [467]) we find that

$$R \cong \frac{R_0}{1 - \frac{4\gamma R_0(1-\nu)}{E(V^{\text{ex}})^2}} \quad (4.157)$$

This formula produces Chaudhari’s result [13] which was revisited by Thompson and Carel [14].

The modified energy balance equation reads

$$\frac{\gamma}{R^2} \frac{d\bar{R}}{dt} = (1 - \nu) \cdot \frac{\sigma}{E} \frac{d\sigma}{dt} + \frac{NkT}{c^{\text{eq}}} (c - c^{\text{eq}}) \frac{\beta\delta}{R^2} \frac{dR}{dt} + \frac{V^2}{m_b R} \quad (4.158)$$

The set of Eqs. (4.158) and (4.153) with σ given by Eq. (4.144) describes this problem completely.

A convenient non-dimensional form of this set of equations reads

$$\frac{dc}{dt} = \frac{d\chi}{\chi^2 dt} - c \quad (4.159)$$

$$\begin{aligned} & \left[A + (1 - B)C - \left(\frac{1}{\chi_0} - \frac{1}{\chi} \right) \right] \frac{d\chi}{\chi^2 dt} = \\ & = - \left(\frac{1}{\chi_0} - \frac{1}{\chi} - C \right) \frac{dC}{dt} + Q \frac{1}{\chi} \left(\frac{d\chi}{dt} \right)^2 \end{aligned} \quad (4.160)$$

where $C = c^{\text{eq}} - c$, $\chi = \frac{R}{V^{\text{ex}}}$, $\chi_0 = \frac{R_0}{V^{\text{ex}}}$, $A = \frac{4\gamma}{V^{\text{ex}}E}(1 - \nu)$,

$$B = \frac{4NkT}{Ec^{\text{eq}}}(1 - \nu) \quad \text{and} \quad Q = \frac{4(1 - \nu)V^{\text{ex}}D_v}{d^2Em_b} \quad (4.161)$$

D_v is the vacancy diffusivity, d is the sink spacing.

The set of equations (4.159) and (4.161) describing the evolution of the grain size and the vacancy concentration provide a full description of the system [460]. Some results of a detailed numerical study are given below.

The maximum growth rate is observed at the very beginning of the process. An almost uninhibited, nearly parabolic growth regime is observed at large times (Fig. 4.75).

The length of the plateau-like incubation stage depends on the value of model parameters and the initial grain size χ_0 . An interesting feature should be noted — during the incubation time the vacancy concentration remains constant (Fig. 4.76). The end of the incubation period is signified by a precipitous drop in C and a peak in the time dependence of the grain growth rate $\frac{d\chi}{dt}$ (Fig. 4.77) [460]. The dependence of the incubation time τ on $1/\chi_0$ is shown in Fig. 4.78; this dependence can be represented by a simple formula

$$\tau = \frac{B}{A} \cdot \frac{1}{\chi_0} \quad (4.162)$$

It should be stressed that τ is not sensitive to the dissipation parameter Q .

The formula (4.162) can be rewritten as a dimensional relation

$$\tau_{\text{inc.}} = \frac{(V^{\text{ex}})^2 NkT}{\gamma R_0} \cdot \frac{d^2}{D_v c^{\text{eq}}} \quad (4.163)$$

expressing the incubation time $\tau_{\text{inc.}}$ in terms of the physical parameters of the system, temperature and sink spacing [460].

The thermodynamic-kinetic approach developed in [11], [460] makes it possible to give a full description of the evolution of the average grain size for many systems. Similar consideration can be applied to grain growth in reinforcement particles in a composite to grain growth in a multiphase system, or the kinetics of void dissolution [459].

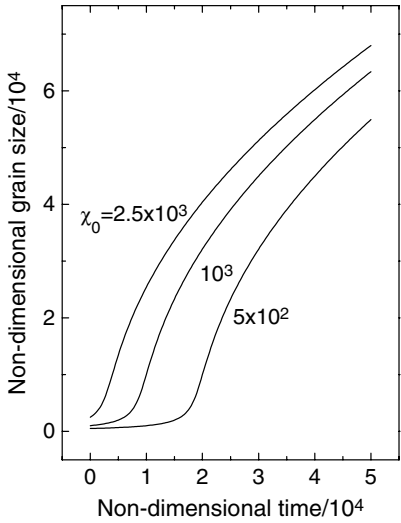


FIGURE 4.75
Variation in the grain size time for various values of the initial grain size. (All quantities are given in dimensionless units [460].)

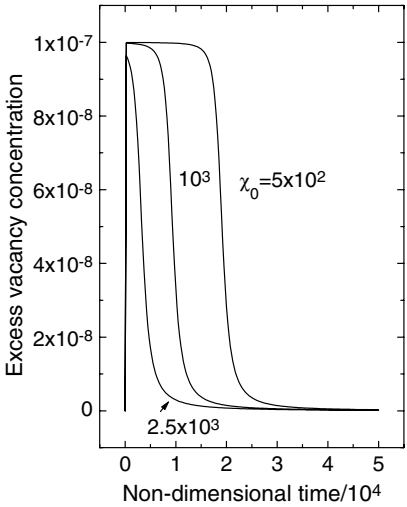


FIGURE 4.76
Evolution of the excess vacancy concentration with the non-dimensional time for three different values of the initial grain size [460].

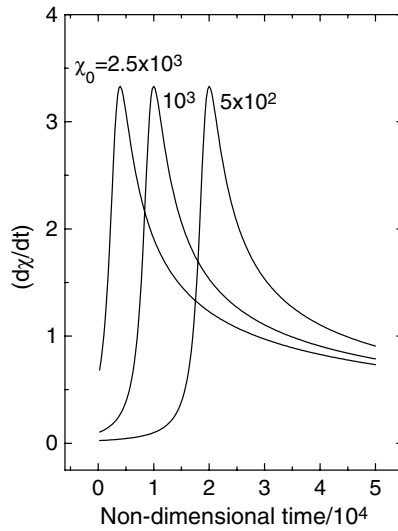


FIGURE 4.77

The grain growth rate as a function of time for three different values of the initial grain size. (All quantities are given in dimensionless units [460].)

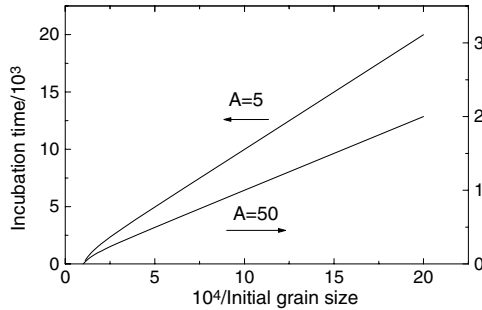


FIGURE 4.78

The initial grain size dependence of the incubation time. (Note the different scales for the two different values of the parameter A used [460].)

4.8.1 Diffusion-Controlled Creep in Nanocrystalline Materials under Grain Growth

The developed approach to the processes in materials where vacancy generation is considered as an integral part of grain growth was applied to creep in nanocrystalline materials governed by diffusion [558]–[560], [563]. Let us consider a frequent situation in polycrystals when creep deformation occurs in parallel with grain growth.

The amount of vacancy supersaturation and the corresponding grain size variation, as mentioned before, can be described by a set of coupled differential equations (Eqs. 4.130, 4.131, and 4.158). One expresses the balance of energy associated with an increment dR of the mean grain size R , and the other describes the change of vacancy concentration in the bulk.

As shown in [561] for nanocrystalline materials it is natural to assume that no vacancy sink of dislocations type are available in the bulk of a grain, in other words, the sink spacing d can be identified with average grain size R . The vacancies generated at grain boundaries will be firstly adsorbed by the boundaries and then directed to the free surface of a sample by boundary diffusion. Nevertheless, the main concept of the approach developed in [11], [458]–[460] is valid in this case as well. Although the concept discussed above related to non-equilibrium processes, like grain growth in polycrystals and in thin films on a substrate, void dissolution, and sintering, it considered the phenomena in terms of equilibrium thermodynamics, i.e. the change of vacancy concentration of the system was felt as a change of the vacancy part of the free energy. So, in our case the increase in the local vacancy concentration in a boundary results, in accordance with equilibrium between the grain boundary and the adjacent bulk, in an increase in the vacancy concentration in the grain.

We would like to remind the reader that qualitatively the physics of the phenomenon can be described as follows. Grain growth is suppressed over a characteristic incubation time $t_{incubation}$, followed by “normal” grain growth characterized by a parabolic time law. During this time, the average vacancy concentration in the bulk is maintained at a nearly constant level above the equilibrium one. After the incubation time the vacancy concentration drops down to thermal equilibrium.

The vacancy concentration during the incubation time can be estimated by setting the rate of the concentration variation \dot{c} to zero and substituting for dR/dt an expression following from [460]

$$dR/dt = \frac{1}{24} \cdot \frac{\gamma D_v c^{eq}}{NkT(V^{ex})^2} \quad (4.164)$$

The resulting vacancy concentration reads

$$c = \left[1 + \frac{\gamma}{4NkT(V^{ex})} \right] c^{eq} \quad (4.165)$$

Estimates show that the second term stemming from the vacancy generation effect is at least an order of magnitude larger than the first one so that

$$c = \frac{\gamma}{4NkT(V^{\text{ex}})}c^{\text{eq}} \equiv \lambda c^{\text{eq}} \quad (4.166)$$

holds. At first glance, it may appear strange that the magnitude of the effect is inversely proportional to the “vacancy efficiency” of grain boundaries represented by the grain boundary excess free volume V^{ex} . However, the level of vacancy supersaturation is the result of an interplay between the number of vacancies injected in the bulk due to the shrinkage of the total volume of the boundaries and the rate of this shrinkage. While the first quantity is proportional to V^{ex} , the latter is inversely proportional to the square of V^{ex} , as seen from Eq. (4.164). It should be noted that the time

$$t_{\text{incubation}} = 24 \frac{NkT(V^{\text{ex}})^2 R_0}{\gamma D_v c^{\text{eq}}} \quad (4.167)$$

during which the increased vacancy concentration is maintained is proportional to $(V^{\text{ex}})^2$. Here R_0 is the initial grain size.

We would like to discuss here one long-standing misconception in the scientific literature. If we take into account that the vacancy concentration is increased during grain growth the expressions for Nabarro-Herring or Coble [558]-[560] creep need to be modified. However, according to a standard textbook treatment of diffusional creep, no effect of this enhancement of the vacancy concentration would follow. It is customary to attribute diffusional creep to the non-uniform vacancy concentration in an inhomogeneously stressed solid. In this case the diffusive flux is determined by the gradient of the vacancy concentration and an overall increase in the vacancy concentration, as with grain growth-induced vacancies, would not affect the creep rate. This concept is physically wrong, though, because the vacancies in an inhomogeneously stressed solid are in thermodynamic equilibrium and, therefore, their chemical potential is zero everywhere, even though their concentration is non uniform. As Herring [559] pointed out correctly, it is the inhomogeneous chemical potential distribution of the atoms that gives rise to a diffusion flux in diffusion creep. In the presence of a stress σ the chemical potential of an atom is changed by an amount $\sigma\Omega$. A uniaxial stress causes a chemical potential gradient of the order $\sigma\Omega/R$ on a grain scale, which gives rise to a diffusion flux, and hence, diffusion creep. The overall vacancy concentration does affect the creep rate since the atomic mobility is proportional to the total local vacancy concentration. The atom flux across a grain is then given by

$$j = \frac{D}{kT} N \cdot \frac{\Omega\sigma}{R} \quad (4.168)$$

where D denotes the bulk diffusivity of atoms. For the vacancy mechanism of bulk diffusion it can be written as

$$D = D_v c \quad (4.169)$$

The plastic strain rate associated with the grain shape variation is then given by

$$\dot{\epsilon}_{NH} = A \frac{j\Omega}{R} = A \frac{\Omega\sigma}{kT} \frac{1}{R^2} D_v c \quad (4.170)$$

Here A is a numerical coefficient; use was made of the relation $N\Omega = 1$ that holds for a pure material. In a similar way an expression for the plastic strain rate can be obtained for the case when creep is controlled by diffusional mass transfer via grain boundaries (Coble creep [560]) assuming a vacancy mechanism of grain boundary diffusion

$$\dot{\epsilon}_{\text{Coble}} = A\pi \frac{\Omega\sigma}{kT} \frac{\delta}{R^2} D_v^{GB} c^{GB} \quad (4.171)$$

Here D^{GB} is the vacancy diffusivity and c^{GB} the vacancy concentration in grain boundaries. (An interesting modification of the diffusion-controlled creep, in which the $1/R^2$ dependence is combined with the grain boundary diffusion, was discussed in [562].)

The value V^{ex} , the excess of grain boundary free volume, is the vacancy capacity of the grain boundary. However, when considering Coble creep [560], the authors of [561] were forced to separate β and δ : the difference in the density between grain boundary and the bulk β and the grain boundary width δ . The diffusion flux during grain boundary diffusion is determined by the grain boundary width δ . Nevertheless, we would like to stress that a physical meaning has only the parameter V^{ex} . V^{ex} , as shown in [20, 564] (see also Chapter 1) can be measured experimentally. For instance, for a $40^\circ\langle 111 \rangle$ tilt grain boundary in Al $V^{\text{ex}} \cong 5 \cdot 10^{-11} \text{m}^3/\text{m}^2$.

In the case when no grain growth-induced vacancies are present, c in Eq. (4.170) (and also in Eq. (4.171) where it enters implicitly, provided that grain boundary diffusion is controlled by the vacancy mechanism) is equal to c^{eq} . However, in the case when a vacancy supersaturation due to grain growth prevails, $c = \lambda c^{\text{eq}}$, i.e. the actual vacancy concentration in the grain interior needs to be substituted. The modified creep rates by the Nabarro-Herring and the Coble mechanism are then given by

$$\dot{\epsilon}_{NH}^* = \lambda \dot{\epsilon}_{NH} = \frac{\gamma}{4NkTV^{\text{ex}}} \cdot \dot{\epsilon}_{NH} \quad (4.172)$$

Similar considerations can be applied to Coble creep. If thermodynamic equilibrium between the grain interior and the grain boundaries is assumed to be reached quasi-instantaneously (i.e. within a time much smaller than the incubation time $t_{\text{incubation}}$), the actual vacancy concentration in the grain boundaries c^{GB} will be enhanced, as compared to the thermal equilibrium value by the same factor of λ . This leads to an enhanced rate of Coble creep

$$\dot{\epsilon}_{\text{coble}}^* = \lambda \dot{\epsilon}_{\text{coble}} = \frac{\gamma}{4NkTV^{\text{ex}}} \cdot \dot{\epsilon}_{\text{coble}} \quad (4.173)$$

While an enhancement of the creep rate by a factor of λ is quite significant, the strain increment acquired during the incubation time, when the vacancy

concentration stays at a higher level, is even more impressive. It is given by

$$\Delta\varepsilon_{NH} = \int_0^{\text{incubation}} \dot{\varepsilon}_{NH}^* dt = 6A \frac{V^{\text{ex}}}{\delta} \frac{\Omega\sigma}{kT} \frac{\delta}{R_0} \quad (4.174)$$

and

$$\Delta\varepsilon_{\text{coble}} = \int_0^{\text{incubation}} \dot{\varepsilon}_{\text{coble}}^* dt = \frac{4\pi}{3} A \frac{V^{\text{ex}}}{\delta} \frac{\Omega\sigma}{kT} \left(\frac{D^{GB}}{D_v c^{\text{eq}}} \right) \left(\frac{\delta}{R_0} \right)^2 \frac{\Omega\sigma}{kT} \frac{\delta}{R_0} \quad (4.175)$$

for the Nabarro-Herring and the Coble type of creep, respectively. As shown in [561], for creep accompanied by grain growth the “extra” strain $\Delta\varepsilon$ for $t > t_{\text{incubation}}$ can be significant. Thus, for the Nabarro-Herring mechanism $\Delta\varepsilon_{NH} \cong 2\%$. For the Coble mechanism the effect is much stronger.

We would like to emphasize once more that the commonly accepted approach to diffusional creep based on a vacancy concentration gradient is insensitive to the effect discussed, as grain growth-induced vacancy generation does not give rise to additional concentration gradients. The principal idea of Herring that the diffusion creep mechanism is based on a gradient of the chemical potential of atoms has to be utilized instead.

4.9 Problems

PROBLEM 4.1

Find the pinning force that particles exert on a boundary.

(a) The radius of the particles is $r = 10^{-8}\text{m}$; the number of the particles per unit volume is $N = 10^{21}\text{m}^{-3}$; the surface tension of the grain boundary is equal to $\gamma = 0.5\text{J/m}^2$.

(b) $r = 5 \cdot 10^{-9}\text{m}$, $N = 10^{22}\text{m}^{-3}$; $\gamma = 0.5\text{J/m}^2$.

PROBLEM 4.2

Find the pinning force that particles exert on triple junctions.

(a) The radius of the particles $r = 10^{-8}\text{m}$, the number of particles per unit volume $N = 10^{21}\text{m}^{-3}$, the surface tension of the grain boundary is $\gamma = 0.5\text{J/m}^2$; the triple line tension $\gamma^\ell = 10^{-9}\text{m}$, the mean grain size $\langle D \rangle = 10^{-6}\text{m}$.

(b) $r = 10^{-9}\text{m}$; $N = 10^{22}\text{m}^{-3}$; $\gamma = 0.5\text{J/m}^2$; $\gamma^\ell = 10^{-8}\text{J/m}$; $\langle D \rangle = 10^{-7}\text{m}$. Compare the result with the result of (a).

PROBLEM 4.3

Find the pinning force that particles exert on grain boundary quadruple junctions.

(a) The radius of the particles is $r = 10^{-8}$, the number of the particles per unit volume is $N = 10^{21}\text{m}^{-3}$, the surface tension of the grain boundary is 0.5J/m^2 ; the mean grain diameter is $\langle D \rangle = 10^{-6}\text{m}$.

(b) The radius of the particles is $r = 10^{-7}\text{m}$, the number of the particles per unit volume is $N = 10^{21}\text{m}^{-3}$, $\gamma = 0.5\text{J/m}^2$, the mean grain diameter $\langle D \rangle = 10^{-6}\text{m}$.

PROBLEM 4.4

Show that the rate of change of the total area S in a polycrystal in the course of grain growth is proportional to S^3 .

PROBLEM 4.5

Find the dependency of the grain area change rate $\frac{dS}{dt}$ as a function of the topological class n for a system with triple junction for different parameters Λ :

$$\Lambda = 10.39(n < 6); \Lambda = 10^3(n < 6)$$

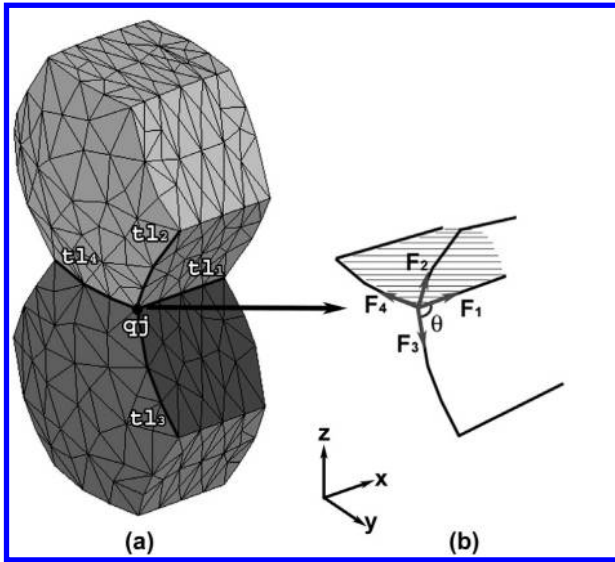
$$\Lambda = 1.11(n > 6); \Lambda = 10.39(n > 6)$$

$$\Lambda = 200(n > 6); \Lambda = 10^3(n > 6)$$

$$\gamma m_b = 10^{-9}\text{m}^2/\text{s}$$

PROBLEM 4.6

Consider the steady-state motion of a grain boundary half-loop with facets

**FIGURE 4.79**

- (a) Geometry of four triple lines (tl) meeting at the quadruple junction (qj).
 (b) Forces acting on the quadruple junction.

and triple junction. Find relations between the facet length, the facet mobility, and the mobilities of grain boundary and junction.

PROBLEM 4.7

Use dimensional analysis to obtain

- (a) a relation between the mean grain size and the annealing time for grain growth.
 (b) the dimensionless parameters which determine the motion of connected grain boundaries, i.e. grain boundaries and grain boundary junctions.
 (c) a relation for the velocity of a flat grain boundary which moves in a system with impurities.

PROBLEM 4.8

In Chapter 4 the steady-state motion of the boundary system with triple and quadruple junctions is considered. It was shown that the behavior of such a system is controlled by the dimensionless parameter Λ_{gp}

$$\Lambda_{gp} = -\frac{\ln \sin \Theta}{1 + 3 \cos \Theta} = \frac{m_{qp}x_0}{m_{tj}} \quad (4.176)$$

where Θ is the tetrahedral dihedral angle Θ (Fig. 4.79).

In equilibrium $\Theta = \Theta_{\infty} = \arccos(-1/3) \approx 109.47^\circ$, m_{gp} is the mobility

of the quadruple junction, x_0 the length which characterizes the grain size, m_{tj} the mobility of the triple junction.

Use the results [$m_b\gamma = 2 \cdot 10^{-14}\text{m}^2/\text{s}$, $m_{tj}\gamma = 4 \cdot 10^{-12}\text{m}/\text{s}$, $m_{gp}\gamma = 9 \cdot 10^{-5}\text{s}^{-1}$] to find the criterion Λ and the angle Θ for 2D configurations $n < 6$ and $n > 6$ in Al. Use $\langle R \rangle = 5 \cdot 10^{-8}\text{m}$ to find the tetrahedral angle at the tip of the quadruple point.

Computer Simulation of Grain Boundary Motion

“The steady state
Is out of date
Unless my eyes deceive me ...”
— *George Gamow*

“If this be true, (and they affirm it with great Confidence)
it is much to be wished that their Observations were made public”
— *Jonathan Swift*

5.1 Introduction

With the advent of high performance computers new tools have become available to study grain boundary motion and related phenomena like recrystallization and grain growth. Already in the 1970s the structure and energy of low Σ grain boundaries had been computed and important information on the relaxed structure of coincidence boundaries was obtained (see Chapter 2) but the dynamics of grain boundaries could not be addressed with the computer power available at that time. Molecular-dynamics (MD) simulations are widely used to study the atomic-level behavior of GBs at finite temperatures. The method itself is nowadays well established in the field of atomistic simulations. As early as the late 1950s [492] and early 1960s the first MD simulations were performed and the basis of this method was established [491]. During the following decades, refinements of the MD method by introducing finite temperature thermostats [493, 494, 497, 498], progress in deriving sophisticated interatomic potentials [495, 496, 499] and extending the MD method by introducing the simulation box vectors as variables [500, 501] steadily increased the potential of the method.

Wolf et al. [480] were the first to address the motion of flat grain boundaries by molecular dynamics (MD) simulations. Srolovitz and coworkers also used MD to study the curvature driven motion of a grain boundary half-loop, a geometry akin to experimental approaches [481]–[488].

In this chapter we will describe the fundamentals of the simulation method and the essential results obtained so far. Overviews on MD simulations of grain boundary energy and mobility were recently published [489, 490].

5.1.1 Classical Molecular Dynamics

The classical MD method utilizes concepts of classical mechanics. The aim of this method is to compute the time evolution of a system of N particles, usually atoms or molecules. Since in classical mechanics a particle system can be successfully characterized by a Lagrangian or Hamiltonian function, an equivalent approach can be utilized for an atomistic system. The simplest case of an interatomic interaction only depends on the distance r_{ij} between two atoms, i and j , and not on their orientation or the local environment. In such case the Lagrangian, L , reads

$$L(\{\mathbf{r}_i\}, \{\dot{\mathbf{r}}_i\}) = \mathbf{K}(\{\dot{\mathbf{r}}_i\}) - \mathbf{V}(\{\mathbf{r}_i\}) = \sum_{i=1}^N \frac{\mathbf{m}_i}{2} \dot{\mathbf{r}}_i^T \cdot \dot{\mathbf{r}}_i - \frac{1}{2} \sum_{i=1}^N \sum_{j=1}^N \mathbf{V}(\mathbf{r}_{ij}) \quad (5.1)$$

where $K(\{\dot{\mathbf{r}}_i\})$ represents the overall kinetic energy and $V(\{\mathbf{r}_i\})$ the overall potential energy of the system¹. The equations of motion of each atom, i , are then derived by the Newtonian equation of motion

$$m_i \cdot \frac{d^2 \mathbf{r}_i}{dt^2} = - \sum_{j=1}^N \frac{dV(r_{ij})}{d\mathbf{r}_i} = - \sum_{j \neq i}^N \frac{1}{r_{ij}} \cdot \frac{dV(r_{ij})}{dr_{ij}} \cdot \mathbf{r}_{ij}, \quad (5.2)$$

where $\mathbf{r}_{ij} = \mathbf{r}_i - \mathbf{r}_j$ and $r_{ij} = |\mathbf{r}_{ij}|$. In this case the Hamiltonian, $H(\{\mathbf{r}_i\}, \{\mathbf{p}_i = m_i \cdot \dot{\mathbf{r}}_i\})$, reads

$$H(\{\mathbf{r}_i\}, \{\mathbf{p}_i\}) = E = \sum_{i=1}^N \frac{1}{2m_i} \mathbf{p}_i^T \cdot \mathbf{p}_i + \frac{1}{2} \sum_{i=1}^N \sum_{j=1}^N \mathbf{V}(\mathbf{r}_{ij}) \quad (5.3)$$

E represents the total energy of the system and is conserved during motion. Time integration of Eq. (5.2) gives the trajectories of each particle, i , under the constraints that $E = \text{const.}$, $V = \text{const.}$, and $N = \text{const.}$, i.e. the particle system represents a microcanonical ensemble [491].

For most MD simulations it is desired to set the macroscopic temperature T , constant. Then the constraints are $T = \text{const.}$, $V = \text{const.}$, and $N = \text{const.}$, and the system represents a canonical ensemble. For this, Eq. (5.2) as well as the Lagrangian need to be altered (see Sec. 5.1.5).

¹ A^T denotes the transpose of A , where A is a tensor of rank one or two.

5.1.2 Parrinello-Rahman Method

A simulation based on the Parrinello-Rahman scheme [501] allows the simulation box to vary in shape and size. This feature is important for GBs due to the two-dimensional (2D) nature of the defect. For instance GBs have an excess volume [503, 504] which can only be modelled correctly if the box dimensions are allowed to adjust to internal and/or external stresses. In this particular case the dimension parallel to the GB normal is allowed to expand or contract according to the internal stress. The in-plane dimensions within the GB plane remain fixed since it is assumed that the in-plane dimensions are determined by the bulk properties far away from the GB region. In the

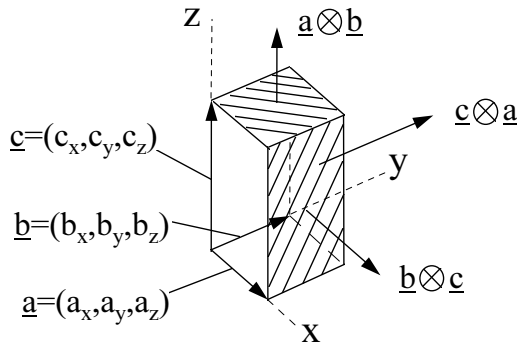


FIGURE 5.1

Simulation box notation according to the Parrinello-Rahman scheme: The vectors \mathbf{a} , \mathbf{b} and \mathbf{c} span the edges of the simulation box and its orientation is described by the vectors $\mathbf{b} \times \mathbf{c}$, $\mathbf{c} \times \mathbf{a}$ and $\mathbf{a} \times \mathbf{b}$. It should be noted here that these vectors do not necessarily need to be parallel to the (x, y, z) coordinate system.

following the matrix convention introduced by Parrinello-Rahman is used, i.e. the simulation box is described by a matrix $\underline{\underline{h}}$ the columns of which represent the simulation box vectors \mathbf{a} , \mathbf{b} and \mathbf{c} , $\underline{\underline{h}} = (\mathbf{a}, \mathbf{b}, \mathbf{c})$.

A schematic of a simulation box is shown in Fig. 5.1. The Parrinello-Rahman scheme adds nine new degrees of freedom to the already $3N$ degrees of freedom of an atomistic system composed of N atoms. To derive a new set of equations of motion for each atom and the simulation box matrix $\underline{\underline{h}}$, the scaling of the real space coordinates of each atom by the simulation box matrix, $\underline{\underline{h}}$, needs to be introduced into the Lagrangian which is expressed by $\mathbf{r}_i = \underline{\underline{h}} \cdot \mathbf{s}_i$ or $\mathbf{s}_i = \underline{\underline{h}}^{-1} \cdot \mathbf{r}_i$, where \mathbf{r}_i and \mathbf{s}_i are the coordinates in real and reduced space,

respectively. The new Lagrangian is then given by

$$\begin{aligned}
 L(\{\mathbf{s}_i\}, \{\dot{\mathbf{s}}_i\}, \{\underline{\mathbf{h}}\}, \{\dot{\underline{\mathbf{h}}}\}) \\
 = K(\{\dot{\mathbf{s}}_i\}, \{\underline{\mathbf{h}}\}) - V(\{\mathbf{s}_i\}, \{\underline{\mathbf{h}}\}) + \mathbf{K}_{\text{box}}(\{\dot{\underline{\mathbf{h}}}\}) - \mathbf{V}_{\text{elastic}}(\{\underline{\mathbf{h}}\}) \\
 = \sum_{i=1}^N \frac{m_i}{2} \dot{\mathbf{s}}_i^T \cdot \underline{\mathbf{G}} \cdot \dot{\mathbf{s}}_i - \frac{1}{2} \sum_{i=1}^N \sum_{j=1}^N V(r_{ij}) + \frac{1}{2} W \cdot TR(\dot{\underline{\mathbf{h}}}^T \cdot \dot{\underline{\mathbf{h}}}) - V_{\text{elastic}}(\{\underline{\mathbf{h}}\})
 \end{aligned} \quad (5.4)$$

where W is constant and has the dimension of mass and TR stands for the trace of a (3×3) matrix or second-rank tensor. Furthermore, $\underline{\mathbf{G}} = \underline{\mathbf{h}}^T \cdot \underline{\mathbf{h}}$, and in the derivation of Eq. (5.4) it was assumed that $\dot{\mathbf{r}}_i$ can be approximated by $\dot{\mathbf{r}}_i = \dot{\underline{\mathbf{h}}} \cdot \mathbf{s}_i + \underline{\mathbf{h}} \cdot \dot{\mathbf{s}}_i \approx \underline{\mathbf{h}} \cdot \dot{\mathbf{s}}_i$.

For a general stress state the elastic energy $V_{\text{elastic}}(\{\underline{\mathbf{h}}\})$ reads

$$V_{\text{elastic}}(\{\underline{\mathbf{h}}\}) = p \cdot (\Omega - \Omega_0) + \Omega_0 \cdot TR((\underline{\mathbf{g}} - p \cdot \underline{\mathbf{1}}) \underline{\mathbf{\varepsilon}}) \quad (5.5)$$

where Ω is the volume of the simulation box.

The equations of motion for each atom in reduced space do not depend on the specific form of $V_{\text{elastic}}(\{\underline{\mathbf{h}}\})$ or the kinetic energy of the box $K_{\text{box}}(\{\dot{\underline{\mathbf{h}}}\})$, because the reduced coordinates \mathbf{s}_i do not appear in these terms as obvious from Eqs. (5.4) and (5.5). Utilizing the Lagrangian equation of motion for the coordinate $s_{i,x}$, $s_{i,y}$ and $s_{i,z}$ yields

$$m_i \cdot \frac{d^2 \mathbf{s}_i}{dt^2} = m_i \cdot \ddot{\mathbf{s}}_i = - \sum_{j \neq i}^N \frac{1}{r_{ij}} \cdot \frac{dV(r_{ij})}{dr_{ij}} \cdot \mathbf{s}_{ij} - \mathbf{m}_i \cdot \underline{\mathbf{G}}^{-1} \cdot \dot{\underline{\mathbf{G}}} \cdot \dot{\mathbf{s}}_i \quad (5.6)$$

To derive the equations of motion for the simulation box represented by the matrix $\underline{\mathbf{h}}$; the strain tensor $\underline{\mathbf{\varepsilon}}$ in Eq. (5.5) needs to be expressed in terms of the components of the simulation box vectors. In a linear approximation, the strain tensor, $\underline{\mathbf{\varepsilon}}$, is given by

$$\underline{\mathbf{\varepsilon}} = \frac{1}{2} \cdot \left(\left(\underline{\mathbf{h}} \underline{\mathbf{h}}_0^{-1} - \underline{\mathbf{1}} \right) + \left(\underline{\mathbf{h}} \underline{\mathbf{h}}_0^{-1} - \underline{\mathbf{1}} \right)^T \right) \quad (5.7)$$

and the rotation tensor, $\underline{\mathbf{\omega}}$ by

$$\underline{\mathbf{\omega}} = \frac{1}{2} \cdot \left(\left(\underline{\mathbf{h}} \underline{\mathbf{h}}_0^{-1} - \underline{\mathbf{1}} \right) - \left(\underline{\mathbf{h}} \underline{\mathbf{h}}_0^{-1} - \underline{\mathbf{1}} \right)^T \right). \quad (5.8)$$

For the derivations of Eqs. (5.7) and (5.8) it is assumed that the atomistic system deforms homogeneously, i.e. the displacement, \mathbf{u}_j , of an atom, j , is fully determined by the deformation of the simulation box $\underline{\mathbf{h}}$ when changing from state $\underline{\mathbf{h}}_0$ to $\underline{\mathbf{h}}$. The displacement, \mathbf{u}^j , of an atom, j , is given by

$$\begin{aligned}
 \mathbf{u}^j &= \mathbf{r}^j - \mathbf{r}_0^j = \underline{\mathbf{h}} \cdot \mathbf{s}_0^j - \underline{\mathbf{h}}_0 \cdot \mathbf{s}_0^j = \left(\underline{\mathbf{h}} \cdot \underline{\mathbf{h}}_0^{-1} - \underline{\mathbf{1}} \right) \cdot \mathbf{r}_0^j \\
 &= \left(\underline{\mathbf{h}} \cdot \underline{\mathbf{h}}_0^{-1} - \underline{\mathbf{1}} \right) \cdot \begin{pmatrix} x_{0,1}^j \\ x_{0,2}^j \\ x_{0,3}^j \end{pmatrix} = \begin{pmatrix} u_1^j \\ u_2^j \\ u_3^j \end{pmatrix}
 \end{aligned} \quad (5.9)$$

Utilizing the displacement vector \mathbf{u}^j , the strain tensor components, $\varepsilon_{\mu,\nu}$, and the rotation tensor components, $\omega_{\mu,\nu}$, can be derived from

$$\varepsilon_{\mu,\nu} = \frac{1}{2} \left(\frac{\partial u_{\mu}^j}{\partial x_{0,\nu}^j} + \frac{\partial u_{\nu}^j}{\partial x_{0,\mu}^j} \right) \quad (5.10)$$

$$\omega_{\mu,\nu} = \frac{1}{2} \left(\frac{\partial u_{\mu}^j}{\partial x_{0,\nu}^j} - \frac{\partial u_{\nu}^j}{\partial x_{0,\mu}^j} \right) \quad (5.11)$$

The equations of motion of the simulation box can be derived under the assumption that the strain tensor, $\underline{\underline{\varepsilon}}$, is given by the non-linear expression

$$\underline{\underline{\varepsilon}} = \frac{1}{2} \cdot \left(\underline{\underline{h}}_0^{T-1} \cdot \underline{\underline{G}} \cdot \underline{\underline{h}}_0^{-1} - \underline{\underline{1}} \right) \quad (5.12)$$

and reads

$$\begin{aligned} W \ddot{\underline{\underline{h}}} &= (\underline{\underline{P}} - p \cdot \underline{\underline{1}}) \cdot \underline{\underline{h}}^{T-1} \Omega - \underline{\underline{h}} \cdot \underline{\underline{\Sigma}} \\ &= \underline{\underline{h}} \cdot \underline{\underline{h}}^{-1} \cdot (\underline{\underline{P}} - p \cdot \underline{\underline{1}}) \cdot \underline{\underline{h}}^{T-1} \Omega - \underline{\underline{h}} \cdot \underline{\underline{\Sigma}} = \underline{\underline{h}} \cdot \underbrace{\underline{\underline{DP}}}_{\text{symmetric}} \end{aligned} \quad (5.13)$$

During an MD simulation with an adjustable simulation box, Eq. (5.13) will be numerically integrated and the evolution of $\underline{\underline{h}}$ and $\underline{\underline{\varepsilon}}$ with time can be calculated. The incorporation of the simulation box vectors as dynamical quantities of the system is far from being trivial. Following Ray and Rahman finally leads to new equations of motion² for each atom, i .

$$m_i \cdot \ddot{\mathbf{s}}_i = - \sum_{j \neq i}^N \frac{1}{r_{ij}} \cdot \frac{dV(r_{ij})}{dr_{ij}} \cdot \mathbf{s}_{ij} - \mathbf{m}_i \cdot \underline{\underline{h}}^{-1} \cdot \ddot{\underline{\underline{h}}} \cdot \mathbf{s}_i - 2 \cdot \mathbf{m}_i \cdot \underline{\underline{h}}^{-1} \cdot \dot{\underline{\underline{h}}} \cdot \dot{\mathbf{s}}_i \quad (5.14)$$

5.1.3 Time Integration Schemes

The main goal of MD simulations is to determine the temporal evolution of a many particle system in phase space and to determine the structural and thermodynamic properties of the system. This can be achieved by time integration schemes based on finite difference approaches for the equations of motion of the particle system (Eq. (5.2) or (5.6)). Several schemes to integrate the equations of motion exist, which usually are derived from a Taylor series expansion for position, velocity, acceleration and higher order time derivatives of each atom at times $t + \delta t$ and $t - \delta t$. Here δt is the time step used to integrate

²Eqs. (5.6) and (5.14), are slightly different owing to the fact that in the second calculation scheme, the term $\dot{\underline{\underline{h}}} \cdot \mathbf{s}_i$ was not dropped from the equation $\dot{\mathbf{r}}_i = \dot{\underline{\underline{h}}} \cdot \mathbf{s}_i + \underline{\underline{h}} \cdot \dot{\mathbf{s}}_i$ in contrast to the original calculation scheme of Parrinello and Rahman [505].

the equations of motion. The Verlet time integration scheme [491] defines for an atom i

$$\mathbf{r}_i(\mathbf{t} + \delta\mathbf{t}) = \mathbf{r}_i(\mathbf{t}) + \frac{d\mathbf{r}_i(\mathbf{t})}{d\mathbf{t}} \cdot \delta\mathbf{t} + \frac{d^2\mathbf{r}_i(\mathbf{t})}{d\mathbf{t}^2} \frac{\delta\mathbf{t}^2}{2} + \dots \quad (5.15)$$

$$\mathbf{r}_i(\mathbf{t} - \delta\mathbf{t}) = \mathbf{r}_i(\mathbf{t}) - \frac{d\mathbf{r}_i(\mathbf{t})}{d\mathbf{t}} \cdot \delta\mathbf{t} + \frac{d^2\mathbf{r}_i(\mathbf{t})}{d\mathbf{t}^2} \frac{\delta\mathbf{t}^2}{2} \pm \dots \quad (5.16)$$

A second equation for the position of atom i , $\mathbf{r}_i(\mathbf{t} + \delta\mathbf{t})$, is found when adding Eqs. (5.15) and (5.16) and taking into account terms up to third order. Such equation does not explicitly depend on the velocity of atom i , $\frac{d\mathbf{r}_i(\mathbf{t})}{dt}$, at time t and reads

$$\Rightarrow \mathbf{r}_i(\mathbf{t} + \delta\mathbf{t}) = 2 \cdot \mathbf{r}_i(\mathbf{t}) - \mathbf{r}_i(\mathbf{t} - \delta\mathbf{t}) + \frac{d^2\mathbf{r}_i(\mathbf{t})}{d\mathbf{t}^2} \cdot \delta\mathbf{t}^2 \quad (5.17)$$

Eq. (5.17) renders the temporal evolution of the real space positions of each atom. The velocity of atom, i , at time t , $\frac{d\mathbf{r}_i(\mathbf{t})}{dt}$, is found when subtracting Eq. (5.15) from (5.16)³

$$\frac{d\mathbf{r}_i(\mathbf{t})}{dt} = \frac{\mathbf{r}_i(\mathbf{t} + \delta\mathbf{t}) - \mathbf{r}_i(\mathbf{t} - \delta\mathbf{t})}{2 \cdot \delta t} \quad (5.18)$$

For an adequate choice of the time step δt one uses the energy scale, length scale, or the atomic mass. For instance, the x component of force, F_x , has the SI unit $[F_x] = N = \frac{J}{m}$. The units of J and m are not the natural units when dealing with atomic-level systems. These are rather the units eV and a_0 . Hence the unit of the x component of force is $[F_x] = \left[\frac{eV}{a_0} \right]$. The contribution of a force, $F_x(t)$, exerted on atom i at position x at time $t + \delta t$ within a Taylor series expansion, allows one to formulate an equation of all entering units which eventually defines the unit of the simulation time step, δt :

$$\begin{aligned} [x] &= a_0^{Cu} = \frac{[F_x]}{[m_{Cu}]} \cdot [dt]^2 = \frac{eV}{a_0^{Cu} \cdot u} \cdot [dt]^2 \\ \Leftrightarrow [dt] &= t_{unit} = a_0^{Cu} \cdot \sqrt{\frac{u}{eV}} = 3.68 \cdot 10^{-14} \text{s} \end{aligned} \quad (5.19)$$

where u is the atomic mass unit which is equal to $1.66055 \cdot 10^{-27} \text{ kg}$, and a_0^{Cu} is the zero Kelvin lattice parameter of Cu. It is noted that δt depends on the studied material since it is proportional to its zero Kelvin lattice parameter.

³A different class of integration schemes only uses the information of the atom position, velocity and higher time derivatives at time t to predict the $t + \delta t$ situation. The predicted atom position, velocity and higher time derivatives at $t + \delta t$ are then refined by a corrector procedure. This class of integration schemes is called predictor-corrector scheme. A standard scheme is the Gear-predictor-corrector algorithm [491] which can be used in different forms with respect to the order of time derivatives used.

A typical time step is $\delta t = 0.05 \cdot t_{unit} = 1.84 fs$ for Cu potentials. A proper choice of the used time step can be verified by checking conservation laws within the utilized MD method like energy conservation and/or conservation of the linear momentum of the overall system. From a physical point of view the time step should be at least only a fraction of the minimal period related to the highest vibrational frequencies of the system. The Debye frequency, ν_D , can be considered as a good first reference to assess this aspect. Since ν_D is the order of $10^{13}/s$, $\delta T \ll \frac{1}{\nu_D}$.

5.1.4 Boundary Concepts

Different boundary concepts are utilized in atomistic systems depending on the physical properties to be studied. Commonly periodic boundary concepts are applied to simulation boxes to suppress finite size effects of the atomistic systems due to the limited number of atoms that can be considered in atomistic simulations. 3D periodic boundary conditions are common in atomistic simulations of crystalline materials. They are most adequate for ideal crystal simulations and for bicrystal simulation boxes where a strong interaction of the adjacent GBs, which exist in such systems due to the periodicity, can be ruled out.

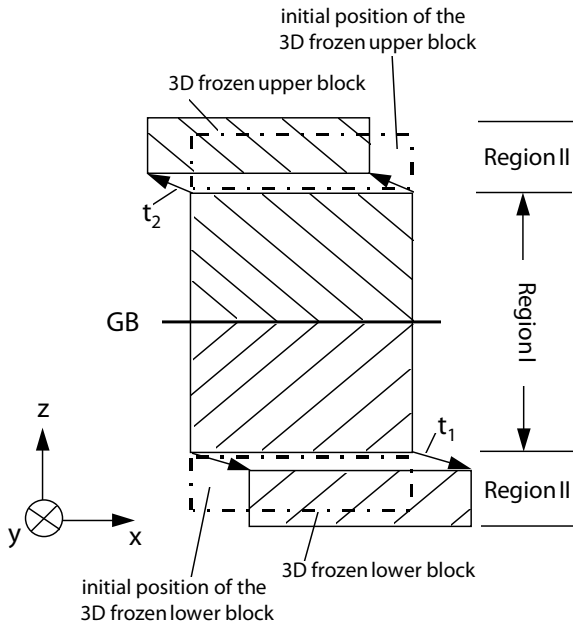
For pure twist GBs 3D periodic boundary conditions can be used when the GBs spacing is sufficiently large and no massive GB sliding occurs. For low-angle twist GBs GB sliding becomes increasingly important so that a 3D periodic border concept may not be the best choice. All tilt GBs have a strong tendency for GB sliding.

If sliding at a GB becomes an issue, 3D periodic boundary conditions may give rise to artificial, unphysical interactions of the two GBs. In such case a free surface normal to the GB would offer an alternative if the used interatomic potential is able to represent the free surfaces realistically and an interaction of the free surfaces and the GB can be neglected. Another concept is the frozen block approach [507] (Fig. 5.2) or its variants [524].

5.1.5 Finite Temperature MD Simulations

To perform finite temperature MD simulations one has to first define whether the temperature T is a thermodynamic variable or not. In the case of microcanonical simulations, T is not a thermodynamical variable, but an MD system will equilibrate to a certain temperature, which depends on the initial choice of kinetic energy introduced to the system [491].

In a canonical ensemble the temperature is a thermodynamic variable besides the number of atoms N , and the volume of the simulation box V . They are kept thermodynamically fixed during the complete course of a simulation run. Two major MD methods exist, namely an isokinetic method [491] which does not really represent a canonical ensemble, and finite temperature ther-

**FIGURE 5.2**

Region I/II 3D frozen block border concept according to Lutsko and Wolf. Here the blocks of region II are rigid frozen atomistic blocks which are shifted about the translations vectors, t_1 and t_2 respectively, according to the net force exerted by region I on either of the region II blocks.

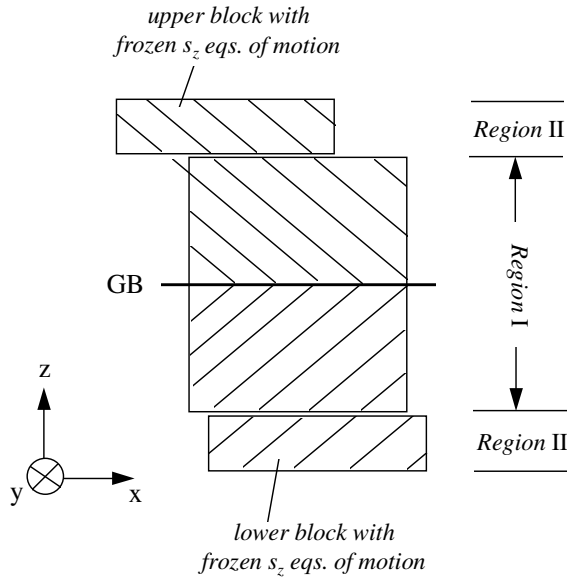


FIGURE 5.3
Restricted free surface border concept. Here the free surfaces are stabilized in the normal direction of the surfaces since during performed MD simulations the s_z component of region II atoms is held fixed. According to this procedure even for simple pair potentials stable surfaces can be obtained even in the presence of a DF.

mostats [491, 493].

In the case of isokinetic simulations, the desired temperature T can be established by rescaling the atoms' velocities after each time step according to the ratio of the desired kinetic energy in the overall system to the actual kinetic energy in the overall system [491], which, however, does not represent the canonical ensemble [491]. Hoover [498] and Nose [494, 497] introduced a different approach which utilizes frictional forces, a kinetic term for the variable associated with the heat bath and a logarithmic potential function to introduce the heat bath.

5.2 Driving Force Concepts

5.2.1 Introduction

GB migration is caused by a driving force. The introduction and quantification of driving forces for GB migration play a key role for the atomistic modeling of the migration of planar GBs. The study of planar GBs offers the advantage that the grain boundary structure is unambiguously defined whereas in curved grain boundaries the grain boundary character changes with location. However, planar GBs do not experience a curvature driving force.

To exert a driving force (DF) on a planar GB an energy gradient across the boundary has to be introduced into the system. In the following three different forms of DFs will be introduced to drive planar GBs. Bicrystal simulation boxes will be used exclusively in the simulations. The first approach utilizes the anisotropy of elastic constants which will cause an elastic energy differential across the boundary upon elastic loading [508]. A second approach makes use of a Peach-Koehler force owing to the coupling of an external stress state with the GB structure itself. A third DF scheme introduces an excess energy term to the orientation dependence of the atoms.

5.2.2 Elastic Driving Force

To introduce an elastic driving force one has to apply an appropriate strain or stress to a bicrystal simulation box that will cause an elastic energy difference in the two grains. Such an approach will only work in materials which behave elastically anisotropically since then the orientation will determine the elastic energy of a grain. Furthermore, only certain strain or stress states will give rise to an elastic driving force on a GB. For individual planar GBs such states need to be identified. This can be achieved by linear-elastic energy calculations for distinct GB geometries. Due to the gradient of stored elastic energy across a GB, the GB will migrate toward the grain with the higher elastic energy. The elastic driving force itself is then simply given by the difference in the

stored elastic energy density of the two grains. From the orientation of each grain with respect to the coordinate system (x, y, z) of the simulation box the rotation matrix can readily be derived that relates each grain orientation to the principal coordinate system of the crystal structure studied. These rotation matrices can then be used to transform the applied strain or stress tensor into the principal coordinate system of grain A and grain B in order to calculate the elastic energy density of each grain. The reference state of a cubic material in its principal coordinate system is defined by the situation where the $\langle 100 \rangle$ directions of the crystal are aligned with the coordinate system that defines the atom coordinates within the grain and where the primitive cell of the system is given by a cube as illustrated in Fig. 5.4(a). The misorientation relationship between the MD simulation box coordinate system (x, y, z) and those of either grain, A and B , are illustrated in Fig. 5.4(b) for the case of a $[001]$ planar twist GB.

We will confine our consideration to cubic materials. In the following the elastic driving force for a cubic crystal structure will be derived. The elastic energy density for a cubic crystal in its principal cubic coordinate system reads

$$\begin{aligned} E_{elast} &= \frac{1}{2} C_{ijkl} \varepsilon_{ij} \varepsilon_{kl} = \frac{1}{2} C_{1111} (\varepsilon_{11}^2 + \varepsilon_{22}^2 + \varepsilon_{33}^2) + 2C_{4444} (\varepsilon_{12}^2 + \varepsilon_{13}^2 + \varepsilon_{23}^2) + \\ &\quad C_{1122} (\varepsilon_{11} \cdot \varepsilon_{22} + \varepsilon_{11} \cdot \varepsilon_{33} + \varepsilon_{22} \cdot \varepsilon_{33}) \\ &= \frac{1}{2} S_{ijkl} \sigma_{ij} \sigma_{kl} = \frac{1}{2} S_{1111} (\sigma_{11}^2 + \sigma_{22}^2 + \sigma_{33}^2) + 2S_{4444} (\sigma_{12}^2 + \sigma_{13}^2 + \sigma_{23}^2) + \\ &\quad S_{1122} (\sigma_{11} \cdot \sigma_{22} + \sigma_{11} \cdot \sigma_{33} + \sigma_{22} \cdot \sigma_{33}), \end{aligned} \quad (5.20)$$

where the Einstein summation convention is implied. Transformation of the strain or stress tensor into the principal coordinate system of grains A and B , and a calculation of the difference between the elastic energy densities in both grains, A and B , finally yields the elastic driving force p_{elast} .

$$\begin{aligned} p_{elast} &= E_{elast}^B - E_{elast}^A \\ &= \frac{1}{2} C_{ijkl} (\varepsilon_{ij}^B \varepsilon_{kl}^B - \varepsilon_{ij}^A \varepsilon_{kl}^A) = \frac{1}{2} S_{ijkl} (\sigma_{ij}^B \sigma_{kl}^B - \sigma_{ij}^A \sigma_{kl}^A) \end{aligned} \quad (5.21)$$

For $[001]$ twist or tilt GBs this reads

$$\begin{aligned} p_{elast} &= E_{elast}^B \left([001], +\frac{\theta}{2} \right) - E_{elast}^A \left([001], -\frac{\theta}{2} \right) \\ &= \frac{1}{2} C_{ijkl} (\varepsilon_{ij}^B \varepsilon_{kl}^B - \varepsilon_{ij}^A \varepsilon_{kl}^A) \\ &= \sin(2\theta) \overbrace{(2C_{4444} - C_{1111} + C_{1122})}^{=C_A} \varepsilon_{12} (\varepsilon_{22} - \varepsilon_{11}) \\ &= \frac{1}{2} S_{ijkl} (\sigma_{ij}^B \sigma_{kl}^B - \sigma_{ij}^A \sigma_{kl}^A) \\ &= \sin(2\theta) \underbrace{(2S_{4444} - S_{1111} + S_{1122})}_{=S_A} \sigma_{12} (\sigma_{22} - \sigma_{11}) \end{aligned} \quad (5.22)$$

if the [001] axis is aligned with the z -direction of the simulation box coordinate system. The angle θ represents the rotation angle about the [001] axis. This result implies a choice of the strain tensor as follows:

$$\underline{\underline{\varepsilon}} = \begin{pmatrix} \varepsilon_{11} & \varepsilon_{12} & 0 \\ \varepsilon_{12} & \varepsilon_{22} & 0 \\ 0 & 0 & 0 \end{pmatrix}, \quad \mathbf{p} = (2\mathbf{C}_{4444} - \mathbf{C}_{1111} + \mathbf{C}_{1122}) \cdot \varepsilon_{12} \cdot (\varepsilon_{22} - \varepsilon_{11}) \cdot \sin(2\theta) \quad (5.23)$$

where C_{ijkl} are the elastic constants. To apply a coupled xy shear state seems reasonable since no further components of the strain tensor do appear in the elastic driving force equation (5.23). Hence, any additional strain tensor component would not result in a change of magnitude of the elastic driving force. To further simplify the situation and to avoid a volume change of the simulation box, the following strain tensor can be chosen for [001] twist GB migration simulations:

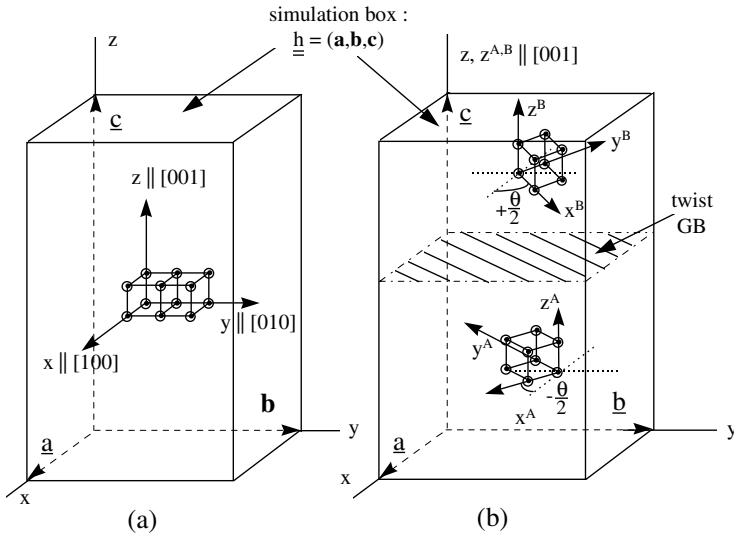
$$\underline{\underline{\varepsilon}} = \begin{pmatrix} \frac{\varepsilon}{2} & \varepsilon & 0 \\ \varepsilon & -\frac{\varepsilon}{2} & 0 \\ 0 & 0 & 0 \end{pmatrix}, \quad \text{leading to } \mathbf{p} = -(2\mathbf{C}_{4444} - \mathbf{C}_{1111} + \mathbf{C}_{1122}) \cdot \varepsilon^2 \cdot \sin(2\theta) \quad (5.24)$$

It is important to realize that the simulations can be performed either strain or stress controlled. In some cases it is crucial to chose appropriate boundary conditions for observing continuous GB migration. From a practical point of view, the strain-controlled MD simulations are robust to set up, since the MD simulation box remains fixed and does not need to be adapted to an imposed external stress state. From a physical point of view, the stress controlled simulations are more favorable since the simulation box can adjust its size and shape to the applied external stress tensor. This is a very important feature for finite temperature GB simulations if one pays attention to the fact that GBs can change their structure and character with temperature.

5.2.3 Peach-Koehler Driving Force

The well-established Peach-Koehler force exerted on single lattice dislocations due to internal or external stress states can also be used to study the effect of external stresses on GBs. This implies that the structure of such GBs still contains discrete GB dislocations. It is well known that low-angle GBs are composed of discrete GB dislocations. Their spacing D is large but decreases with rising misorientation angle Θ according to $\sin(\Theta/2) = b/2D$ where b is the Burgers vector. Frequently, high-angle GBs are assumed to have a disordered structure, but in principle, any grain boundary can be represented by a superposition of primary and secondary grain boundary dislocations.

It has been shown experimentally [511] that low-angle GBs can be driven by Peach-Koehler forces. The force \mathbf{F}_{Disl} , exerted on a single dislocation of

**FIGURE 5.4**

Geometry of MD simulation box: (a) shows a schematic of a MD simulation box of a perfect crystal while (b) presents a bicrystalline MD simulation box containing two grains labelled A and B for the case of an arbitrary $[001]$ twist GB. The direction of grain rotation and the primitive cells for a simple cubic material are illustrated in the figure as well. Note that both grains are symmetrically misoriented with respect to the MD simulation box coordinate system (x, y, z) . The box vectors \underline{a} , \underline{b} and \underline{c} that span out the simulation box and which are essential to apply any form of periodic border conditions are given in the figures as well. More details on the general aspects of the generation scheme and the geometry of the box are given in the text.

length L , Burgers vector $\mathbf{b}_{\text{Disl.}}$ and line vector $\mathbf{s}_{\text{Disl.}}$ by a stress state $\underline{\underline{\sigma}}$ at the dislocation is given by

$$\frac{\mathbf{F}_{\text{Disl.}}}{L} = (\underline{\underline{\sigma}} \cdot \mathbf{b}_{\text{Disl.}}) \times \mathbf{s}_{\text{Disl.}} \quad (5.25)$$

Recently it was shown experimentally that even high-angle tilt GBs can be driven by an external stress [512]. The simulations show that appropriately chosen pure shear stress states will result in Peach-Koehler forces on pure edge GB dislocations at least in the case of low-angle tilt GBs.

5.2.4 Orientation-Correlated Driving Force

To avoid artifacts due to the coupling of the stress state with the grain boundary structure an artificial driving force for GB migration can be used [396, 524]. The driving force itself is only artificial in the sense that it does not specify its source but can be considered like a magnetic or electrical driving force in materials with anisotropic magnetic susceptibility or dielectric constant. An atom of a specific crystal will experience an anisotropic excess energy due to an externally applied field. Therefore, one can construct an excess energy term for each atom as a function of the structure factor $|S(\mathbf{k}_\alpha)|^2$ associated with the orientations present in the system and which are calculated in the vicinity of each atom. The vicinity of an atom is considered a sphere of a certain radius centered around the atom. The radius will be the same as the one used to evaluate the interatomic forces on an atom, or its potential energy. Thus, for each atom j an excess energy term, e_j^{corr} , can be obtained by a simple analytical expression. The sum over all atoms can then simply be added to the potential energy of the overall system. By doing so this orientation-correlated driving force (OCDF) term will enter the Lagrangian or Hamiltonian and, hence, new equations of motion for each atom will be obtained. The OCDF will be identified by p_{corr} .

In the following the respective equations of motion will be derived. The structure factor of an orientation α represented by a respective reciprocal lattice vector \mathbf{k}_α is given by

$$\begin{aligned} |S(\mathbf{k}_\alpha)|^2 &= \frac{1}{N^2} \sum_{m=1}^N \sum_{l=1}^N \exp(i \cdot \mathbf{k}_\alpha \cdot (\mathbf{r}_m - \mathbf{r}_l)) \\ &= \frac{1}{N^2} \left(\left(\sum_{m=1}^N \cos(\mathbf{k}_\alpha \cdot \mathbf{r}_m) \right)^2 + \left(\sum_{m=1}^N \sin(\mathbf{k}_\alpha \cdot \mathbf{r}_m) \right)^2 \right) \quad (5.26) \end{aligned}$$

The overall excess energy contribution to the system $E_{\text{corr.DF}}$, as well as the excess energy e_j^{corr} for each atom j in a bicrystal consisting of an orientation,

1 and 2 is, therefore, given by

$$E_{corr.DF} = \sum_{j=1}^N e_j^{corr} = \sum_{j=1}^N \sum_{\alpha=1}^2 a_{\alpha} \cdot |S(\mathbf{k}_{\alpha})|_j^2 = \sum_{j=1}^N a_1 \cdot |S(\mathbf{k}_1)|_j^2 + a_2 \cdot |S(\mathbf{k}_2)|_j^2 \quad (5.27)$$

where a_1 and a_2 are coefficients which determine the strength of the excess energy due to an externally applied field, and are chosen such that the magnitude of the driving force is represented, for instance, $8.0 \cdot 10^{-3}$ eV/atom, and $2.0 \cdot 10^{-3}$ eV/atom, respectively. In order to evaluate Eq. (5.27), the value N in Eq. (5.26) will be replaced by N_j which is the number of neighbors within the cut off sphere around atom j .

The concept of an OCDF can be introduced into the utilized Parrinello-Rahman method as follows, e.g. using pair potentials. The adapted Lagrangian now reads

$$L(\{\mathbf{s}_i\}, \{\dot{\mathbf{s}}_i\}, \{\underline{\mathbf{h}}\}, \{\dot{\underline{\mathbf{h}}}\}) = K(\{\dot{\mathbf{s}}_i\}, \{\underline{\mathbf{h}}\}) - V(\{\mathbf{s}_i\}, \{\underline{\mathbf{h}}\}) - \mathbf{E}_{corr.DF}(\{\mathbf{s}_i\}, \{\underline{\mathbf{h}}\}) + K_{box}(\{\dot{\underline{\mathbf{h}}}\}) - V_{elastic}(\{\underline{\mathbf{h}}\}) \quad (5.28)$$

Utilizing the Lagrangian equation of motion for the coordinates $s_{i,x}$, $s_{i,y}$ and $s_{i,z}$ one obtains new equations of motion with the incorporated OCDF

$$m_i \cdot \ddot{\mathbf{s}}_i = - \sum_{j \neq i}^N \frac{1}{r_{ij}} \cdot \frac{dV(r_{ij})}{dr_{ij}} \cdot \mathbf{s}_{ij} - \underline{\underline{\mathbf{G}}}^{-1} \cdot \frac{d\mathbf{E}_{corr.DF}(\{\mathbf{s}_i\}, \{\underline{\mathbf{h}}\})}{d\mathbf{s}_i} - \mathbf{m}_i \cdot \underline{\underline{\mathbf{G}}}^{-1} \cdot \underline{\underline{\dot{\mathbf{G}}}} \cdot \dot{\mathbf{s}}_i \quad (5.29)$$

There are some advantages of the OCDF over the elastic DF. Both DFs share a temperature dependence. The temperature dependence of the OCDF for fixed coefficients a_1 and a_2 , is equivalent to the one for an elastic DF for a fixed strain, namely it decreases with increasing temperature. This behavior is associated with increasing thermal vibrations with rising temperature, which cause the structure factor to decrease. Accordingly, the temperature dependence of the OCDF is realistic. The main advantage of the OCDF over the elastic DF, however, is that now elasticity and/or processes that lead to plasticity can be separated from the DF.

Of course, the calculation of the additional force contributions are more demanding and complex compared to a standard pair potential procedure and, therefore, computation time goes up.

Even though the computational routines are more complicated and require more computation time, this approach has many advantages over the elastic DF approach. In order to obtain noticeable grain boundary migration in the short time frame of nanoseconds a large DF has to be applied to the simulation box, i.e. large strains when introducing an elastic DF. This may cause artifacts in grain boundary behavior and is limited by the theoretical shear stress. In case of an OCDF the driving force can easily be set to any desirable value by choosing appropriate coefficients a_1 and a_2 , and this is a convenient way to overcome unphysical elastic strain magnitudes.

5.3 Migration of [001] Twist Grain Boundaries

5.3.1 Procedure

Almost all results on GB migration and GB self-diffusion of planar [001] twist GBs that will be presented were obtained by utilizing the 3D LJ potential and applying a 3D periodic boundary concept. For the GB migration simulations due to an OCDF different boundary concepts and various atomistic potentials were applied. This is especially true for the simulations of the $\Sigma 5$ [001] twist GB, where simulations with the Cu EAM potential of Doyama and Kogure also were performed.

After the simulation cell has been set up, the grain boundary structure has to be relaxed prior to its motion. The GB properties and atomic-level structures of fully relaxed GB systems are obtained by performing lattice-statics (LS) simulations according to the steepest gradient method. These zero Kelvin relaxation simulations are necessary for most GBs due to their strictly geometric CSL generation scheme. The must to perform such simulations results from the fact that most GBs differ substantially in their equilibrium structure from the geometrical CSL GB construct. An important feature of equilibrated GBs is the volume expansion ΔV^{GB} which was found to be proportional to the GB energy and, therefore, a key parameter of any GB [503]. The volume expansion manifests the tendency of a GB to expand or shrink parallel to the GB normal. This is the case since for all performed simulations the in-plane dimensions of the CSL GBs are held fixed. If MD simulations were performed on unrelaxed high energy GBs with fixed finite time steps, the time integration scheme would fail to yield the true atomistic trajectories of each atom and cause a crash of the MD simulation by a destruction of the crystalline GB system. Thus, an initial relaxation procedure is essential for the simulation of GB migration. Furthermore, other important information on GBs like the GB energy and the volume expansion can be obtained from these computations.

In the case of [001] twist GBs a sequence of LS simulations is sufficient to yield fully relaxed GB properties, whereas for tilt GBs a combined LS/MD strategy has to be used to finally yield relaxed GBs.

5.3.2 Atomistic Structure of the Relaxed [001] Twist GBs

Since the atomistics of twist GBs are difficult to visualize the arrangement within (002) planes facing each other at the GB is used to gain insight into the atomic-level situation and will be referred to as in-plane data plots. It is accomplished by showing the closest *A*-type (002) planes of either of the two grains in one plot. This illustrates to what extent atomic-level relaxation had occurred in the vicinity of the GBs, e.g. by the coherency of the CSL points of the relaxed GB structures. The exact atomistic arrangement of the $\Sigma 29$

TABLE 5.1
Studied [001] Twist GBs

GB plane	θ	Σ	$E^{GB} [\frac{J}{m^2}]$	No. of CSL cells	$\Delta V^{GB} [a_o]$
(001)	43.60°	29	0.716	1;4	0.12204
(001)	36.87°	5	0.715	9	0.12080
(001)	28.07°	17	0.700	4	0.11623
(001)	22.62°	13	0.677	4	0.11144
(001)	16.26°	25	0.625	2	0.10350
(001)	12.68°	41	0.582	1	0.09801
(001)	8.80°	85	0.490	1	0.08517
(001)	6.03°	181	0.404	1	0.07324

Note: The table gives the misorientation angle, θ , the GB energy, E^{GB} , the number of CSL cells within each (002) plane, and the volume expansion of the GBs, ΔV^{GB} .

and $\Sigma 5$ twist GBs is given by Figs. 5.5 and 5.6. For [001] twist GBs in fcc crystals one finds the following relation for the volume of the primitive CSL cell, V_{CSL} , namely

$$\Sigma \cdot \Omega = V_{CSL} = d_{(001)} \cdot A_{CSL} = \frac{1}{2} a_o \cdot A_{CSL} = \Sigma \cdot \frac{a_o^3}{4} \Leftrightarrow A_{CSL} = \Sigma \cdot \frac{a_o^2}{2}$$

In general this means that the in-plane CSL area, A_{CSL} , is given by $A_{CSL} = \mathbf{a}_{CSL} \cdot \mathbf{b}_{CSL}$ where \mathbf{a}_{CSL} and \mathbf{b}_{CSL} are the in-plane CSL vectors. Assuming a square for the in-plane CSL cell, the in-plane area A_{CSL} is related in a simple manner to the magnitudes of the in-plane CSL vectors, a_{CSL} and b_{CSL} ,

$$A_{CSL} = \sqrt{\frac{\Sigma}{2}} \cdot a_o \cdot \sqrt{\frac{\Sigma}{2}} \cdot a_o \quad \Leftrightarrow \quad a_{CSL} = b_{CSL} = \sqrt{\frac{\Sigma}{2}} \cdot a_o$$

The relaxed low-angle twist grain boundaries reveal the structural screw dislocation in terms of non-ideal fcc atoms. The $\Sigma 25$ twist GB is on the border between low-angle and high-angle twist GB but also reveals discrete structural dislocations.

All studied GBs were simulated in three-dimensional atomistic systems. Hence, the GBs were truly two-dimensional defects. For the LJ potential, simulations with 3D periodic boundary conditions (BC) as well as with 2D periodic border conditions within the GB plane and stabilized free (002) surfaces were performed. Apart from the LJ potential, simulations with the EAM potential by Doyama and Adams and the Finnis-Sinclair potential according to Sutton and Chen were conducted as well. An overview of the performed GB migration simulations is given in Table 5.2.

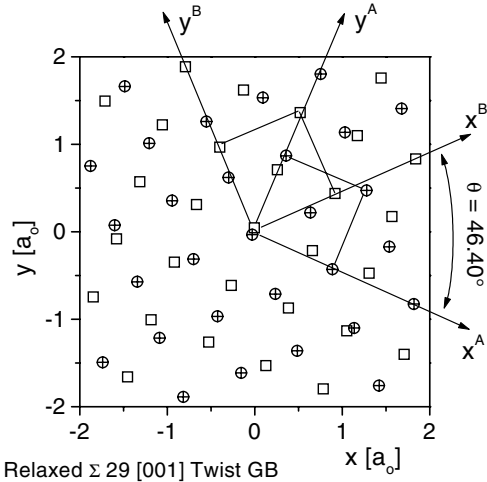


FIGURE 5.5

Atomistics of the $\Sigma 29$ [001] 43.60° twist GB. Here the closest A-type (002) planes facing each other at GB₂ are plotted. Atoms within plane A of grain A are given by filled circles while the atoms within plane A' of grain B are given by squares.

TABLE 5.2

Overview of conducted GB migration simulations on the studied [001] twist GBs

Σ	θ	Elastic DF	Orientation-Correlated DF
29	43.60°	LJ 3D periodic BC	—
5	36.87°	LJ 3D periodic BC	Doyama 2D periodic BC and free (002) surfaces LJ 2D periodic BC and stab. free (002) surfaces
17	28.07°	LJ 3D periodic BC [530]	LJ 3D periodic BC LJ 2D periodic BC and stab. free (002) surfaces
13	22.62°	LJ 3D periodic BC [530]	LJ 3D periodic LJ 2D periodic BC and stab. free (002) surfaces
25	16.26°	LJ 3D periodic BC [530]	—
41	12.68°	LJ 3D periodic BC	—
85	8.80°	LJ 3D periodic BC	LJ 3D periodic BC
181	6.03°	—	LJ 3D periodic BC

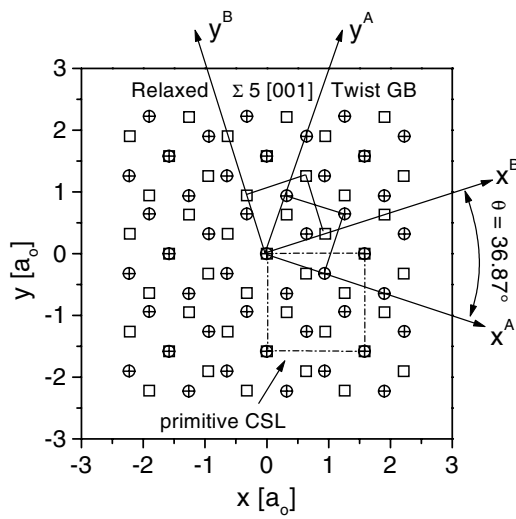
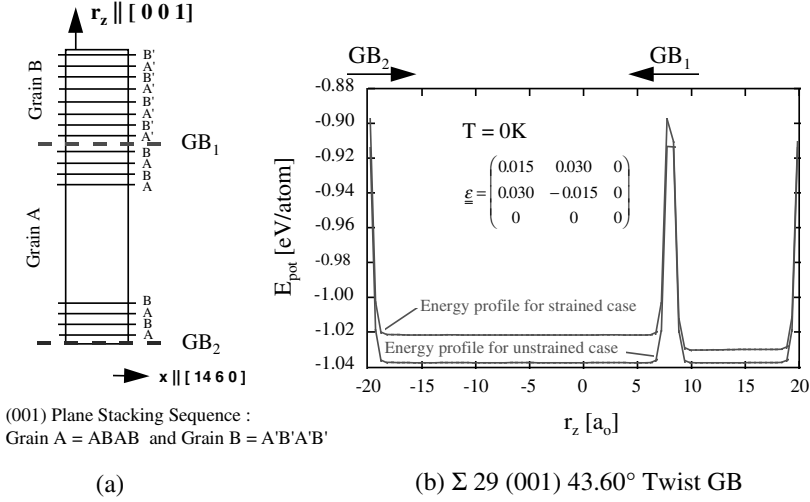


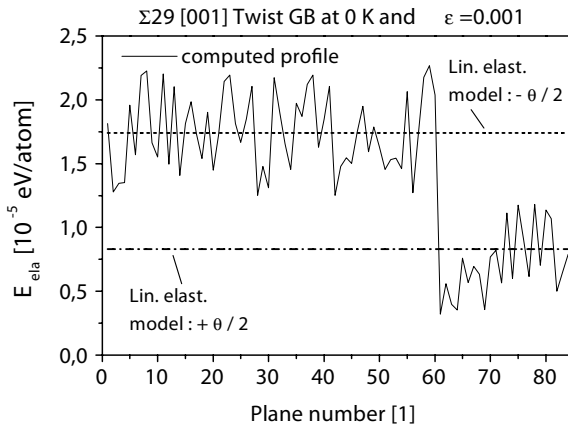
FIGURE 5.6
Atomistics of the $\Sigma 5$ [001] 36.87° twist GB. Here the closest A-type (002) planes facing each other at GB_2 are plotted. Atoms within plane A of grain A are given by filled circles while the atoms within plane A' of grain B are given by squares.

**FIGURE 5.7**

$\Sigma 29$ [001] 43.60° twist GB, $\gamma = 0.708 \frac{J}{m^2}$: (a) shows a schematic of the GB system showing the stacking sequence of (002) planes in the GB system. GB₁ and GB₂ identify the GB positions. (b) presents the verification of an elastic driving force for $\varepsilon = 0.03$ at 0 K for a 3D LJ system. Here the bulk regions of either grain for the unstrained case can be identified by having a potential energy equal to the cohesive energy of the ideal crystal of $E_{coh} = -1.037824$ eV/atom. Applying the strain homogeneously to the MD box leads to a shift of the unstrained energy profile by the amount of stored elastic energy within each grain. Thus this allows one to obtain the magnitude of stored elastic energy by subtracting the energy profiles of the strained and unstrained system. Here the two GBs, GB₁ and GB₂, are associated with the energy peaks in the profiles of (b).

5.3.3 GB Migration Due to an Elastic Driving Force

According to Fig. 5.7(b) the elastic energy stored within each grain can be determined by subtracting the energy profiles of the strained and unstrained system. The obtained energy profile thus represents the elastic energy variation along the [001] direction within the GB system which can be compared with the analytical linear elastic model as discussed in Sec. 5.2.2. Fig. 5.8 shows such a plane-by-plane elastic energy profile for the $\Sigma 29$ twist GB at a strain of $\varepsilon = 0.001$ and 0 K. In addition to the computed simulation data the analytical linear elastic model data are given as well by the broken lines which demonstrate that for a strain in the range of the classical elastic range the computed and model data agree very well. Since the simulation covers only

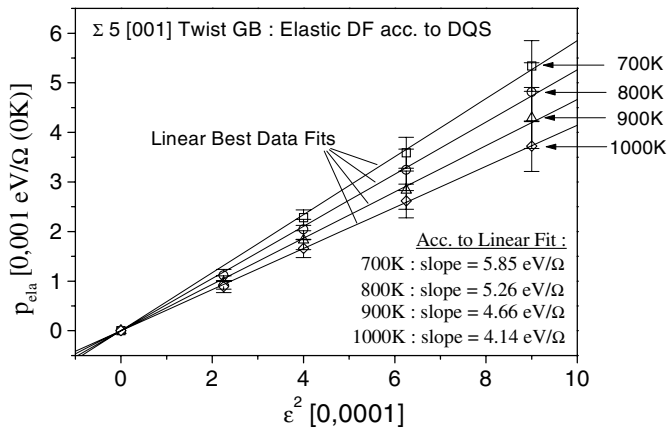
**FIGURE 5.8**

Plane-by-plane elastic energy profile of the $\Sigma 29$ twist GB at 0 K for $\varepsilon = 0.001$. The zick-zack energy profile in the bulk of the two grains is due to the fact that in this example a not fully relaxed $\Sigma 29$ GB system was used.

a time interval of maximum ns , the GB velocity must be at least in the range of m/s in order to be detected within these simulations. Hence, the applied strain ranged from 0.01 up to 0.035, where effectively a linear elastic behavior was observed, since no other defects were present in the system.

5.3.4 Data Analysis with Respect to GB Migration

To determine and track the position of the GBs throughout the MD simulations the so-called common-neighbor structural analysis (CNA) [516, 517] method was applied. A few simple criteria were imposed on the atomistic data to distinguish true GB atoms from the rest. First, according to the CNA method true ideal fcc atoms were determined in the system where each true ideal fcc atom could be recognized by its sharing of (421) triplets with the twelve nearest neighbors. Any atom that was not identified a true ideal fcc atom was then considered a potential GB atom. These non-ideal fcc atoms sometimes were bulk vacancies, and further data analysis was needed to rule them out as true GB atoms. Therefore, the system was sliced into slabs of e.g. discrete (002) planes, and a histogram of all non-fcc atoms was obtained. From these histograms, the centers of mass of the GBs were calculated and their temporal evolution was tracked. This data analysis was not carried out during the MD simulation runs but rather on stored atomistic configurations. The storing intervals used were one box after every 1000 time steps. This data analysis yielded the GB position vs. time, the slope of which corresponded to the GB velocity.

**FIGURE 5.9**

$\Sigma 5$ [001] twist GB. Elastic DF according to the DQS scheme for temperatures ranging from 700 K up to 1000 K and different strains.

5.3.5 Mobility of [001] Twist GBs

MD simulations were conducted for a $\Sigma 5$ GB in a temperature range from 700 K up to 1100 K. Utilizing the DQS scheme it was possible to calculate the elastic DF in situ during the MD GB migration simulations. The DF is proportional to the square of the strain, ε^2 , at a fixed temperature (Fig. 5.9). The slope equals $c_A \cdot \sin(2 \cdot \theta)$. It only differs by about 10 percent from the theoretical value calculated from linear elastic theory due to non-linear effects. Fig. 5.10 shows the temporal evolution of the GB position vs. time at 800 K for different elastic DFs. Due to the 3D periodic bicrystalline box geometry and the direction of the imposed DF, the upper grain usually shrank finally leaving behind a single grain with the orientation of the lower grain. The presented data manifest a linear dependency, the slope of which corresponds to the GB velocity.

The GB mobility for a certain temperature was then determined as the slope of a best linear data fit of GB velocity vs. elastic DF plots (Fig. 5.11). It is important to realize that many GB migration simulations for a fixed temperature at different DF levels are needed to yield reliable data of GB mobility at a given temperature.

An Arrhenius plot of the temperature dependence of the GB mobility for all studied [001] twist GBs in this study is given in Fig. 5.12. The slope of a best fit of each of the GB data yielded the activation parameters, namely the activation enthalpy, Q_{GBM} , and the GB mobility pre-exponential factor, m_o , as listed in Table 5.3. The results demonstrate that [001] twist GBs in an fcc material move continuously in the presence of an elastic DF. Strains of 0.01 to

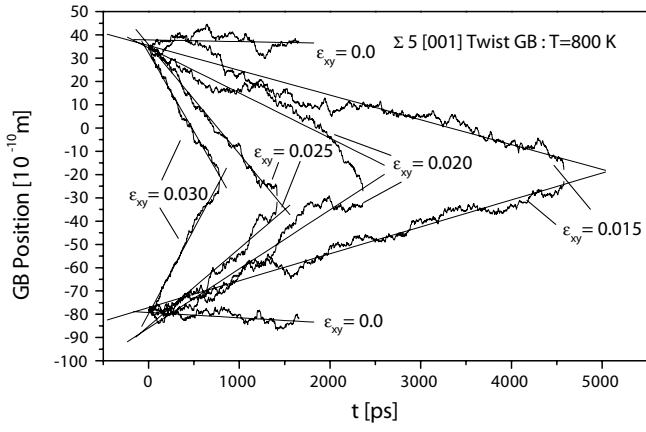


FIGURE 5.10
 $\Sigma 5$ [001] twist GB. GB position vs. time at 800 K for different elastic DFs.

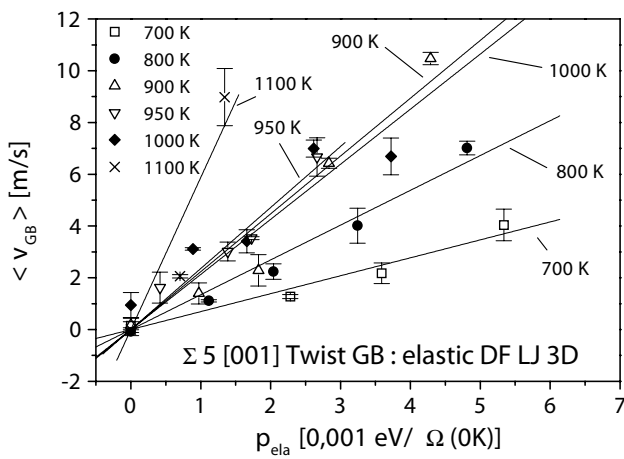


FIGURE 5.11
 $\Sigma 5$ [001] twist GB. GB velocity vs. elastic DF from 700 K up to 1100 K.

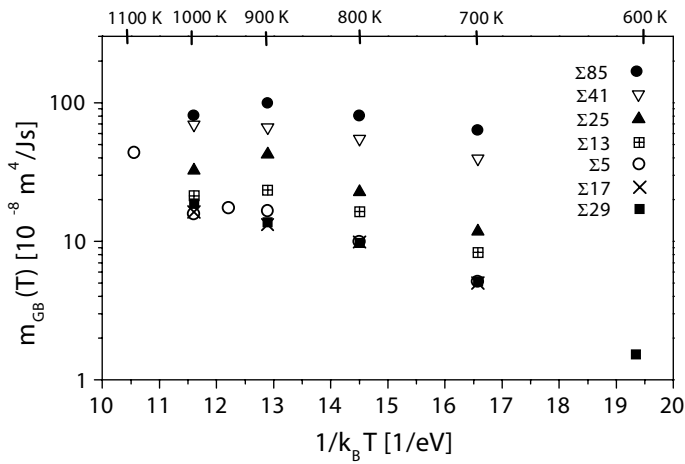


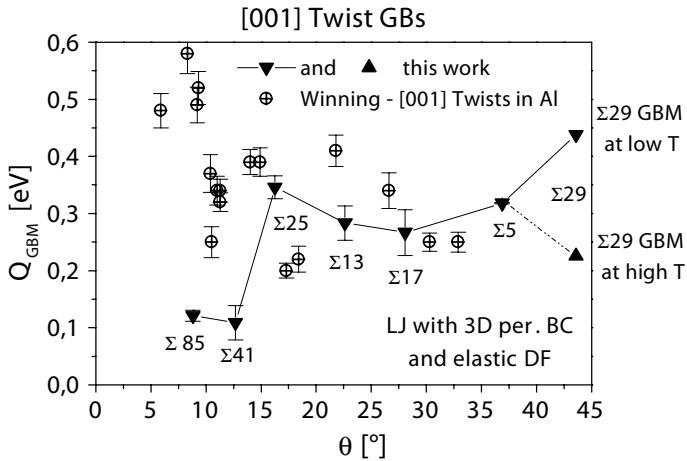
FIGURE 5.12
Arrhenius plot of GB mobility for the [001] twist GBs studied. The determined activation parameters are listed in Table 5.3.

TABLE 5.3
GB Migration Activation Parameters of the [001] Twist GBs Studied

GB plane	θ	Σ	Q_{GBM} [eV]	m_o [$10^{-6} \frac{m^4}{Js}$]
(001)	43.60°	29	0.438 ¹	73.06 ³
	43.60°	29	0.226 ² ± 0.008	2.57 ⁴
(001)	36.87°	5	0.319 ± 0.001	10.21
(001)	28.07°	17	0.267 ± 0.040	4.32
(001)	22.62°	13	0.284 ± 0.030	9.39
(001)	16.26°	25	0.346 ± 0.020	35.94
(001)	12.68°	41	0.109 ± 0.030	2.19
(001)	8.80°	85	0.121 ± 0.010	4.69

Note: The results were obtained for the LJ potential with 3D periodic BC and an elastic DF.

¹ according to low temperature regime
² according to high temperature regime
³ according to low temperature regime
⁴ according to high temperature regime



The distinction between high-angle and low-angle GBs was captured in the simulations, as evident from the GB migration activation parameters. The GB migration activation enthalpy for the two true low-angle twist GBs, $\Sigma 41$ and $\Sigma 85$, was about 0.12 eV. As confirmed in the simulations, the low-angle twist GBs consist of discrete screw dislocation networks that remain stable throughout the studied temperature range. Hence, the migration mechanism of the low-angle twist GBs must be linked to a movement of the screw dislocation network itself. By contrast, the high-angle twist GBs can move in the low temperature regime by collective shuffle mechanisms [522, 537] which are usually in-plane rearrangements. At elevated temperatures, an out-of-plane component of the atomic displacement appears which might be the cause for a change of the GB migration mechanism as reflected by the drop of the GB mobility above 900 K.

Using the OCDF as the DF concept for the studied twist GBs yields identical results for the GB mobility [524], the activation parameters of GBM [524] as well as for the found GBM mechanism [524].

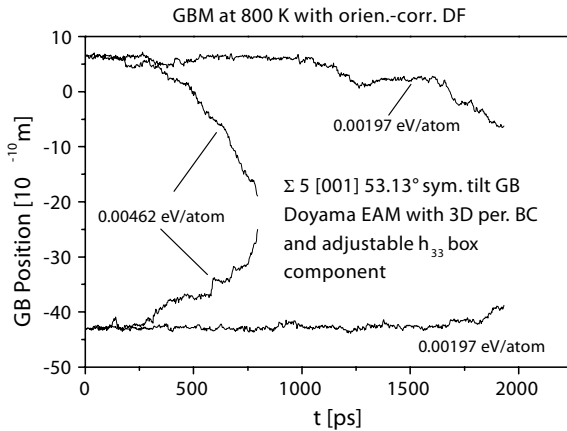
5.4 Motion of Tilt Boundaries

While the application of an elastic strain on the simulation box worked successfully to drive a twist boundary, it failed for tilt boundaries [524]. This is due to the fact that the application of any stress or strain state necessary to yield an elastic DF to a tilt boundary whose structure is composed of edge dislocations invariably caused GB sliding in addition to GB migration [524]. This eventually will stall GB migration and, therefore, renders MD simulations of GB migration unsuccessful [524]. These deficiencies can be overcome by the use of an OCDF.

All simulations of the migration of $\Sigma 5$, $53.13^\circ[001]$ tilt boundaries were obtained by MD simulations utilizing the Doyama EAM potential and by applying 3D periodic boundary conditions.

The studied GB system consisted of 100 (210) planes, where initially 60 (210) planes belonged to the lower grain and 40 (210) planes to the upper grain. Eight (002) planes were stacked in x -direction and the overall number of atoms was 4800. The relaxed GB energy was 0.899 J/m². The interatomic distance of (210) planes was 0.2236068 a_0 .

Finite temperature simulations were performed where only the h_{33} box variable was allowed to adjust to the present stress state according to the Rahman-Parrinello scheme. Under this constraint for the simulation box it was found that indeed the $\Sigma 5$ (210) tilt GB can move continuously in the presence of an OCDF. Two examples of GB position vs. time profiles are

**FIGURE 5.14**

GB position profiles at 800 K of the $\Sigma 5$ (210) symmetrical tilt GB with adjustable h_{33} box variable and OCDF.

shown in Figs. 5.14 and 5.15. At 800 K and low DF the GBs hardly move at all, but at high DFs they move quite rapidly. From a linear regression of the displacement vs. time dependencies the GB velocities of GB₁ and GB₂ were obtained and averaged. They are plotted in Fig. 5.17 vs. the OCDF, p_{corr} . A large error reflects the occasional case that one GB moved while the other one remained essentially sessile. The DF was usually imposed on the system in such a way that in the lower grain *A* a higher excess energy was installed than in the upper grain *B*, which led to the shrinkage and disappearance of grain *A*.

The GB mobility was determined from the slope of the GB velocity vs. OCDF plots (Fig. 5.17). An Arrhenius plot (Fig. 5.18) yielded the activation parameters of GB migration. The activation enthalpy found for the $\Sigma 5$ boundary was $Q = 0.64 \pm 0.04$ eV and the pre-exponential factor $m_0 = 4.2 \cdot 10^{-8} [\text{m}^4/\text{Js}]$.

It was already observed for MD simulations with imposed elastic stress [524] that for the $\Sigma 5$ (210) tilt GB during GB sliding and migration GB diffusion was necessary to reconstruct the GB structure. Hence, it does not come as a surprise that the $\Sigma 5$ (210) tilt GB can move by a diffusion-controlled or diffusion-assisted mechanism that is not coupled to GB sliding. If the h_{22} , h_{23} , h_{32} and h_{33} box variables remained adjustable this enforced GB sliding. For such a case Fig. 5.19 presents GB position vs. time profiles at 800 K and 1100 K whereas Fig. 5.20 shows the temporal evolution of the strain component ε_{YZ} for all simulations conducted. An analysis of the ε_{YZ} profiles proved that under the studied boundary conditions for the simulation box GB sliding and GB migration were coupled. The data show that the higher the temper-

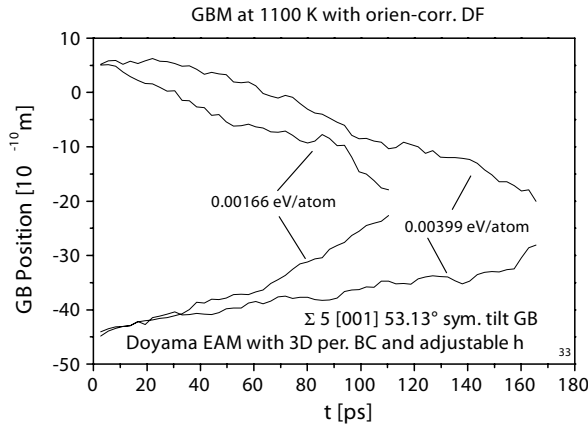


FIGURE 5.15

GB position profiles at 1100 K of the $\Sigma 5$ (210) symmetrical tilt GB with adjustable h_{33} box variable and OCDF.

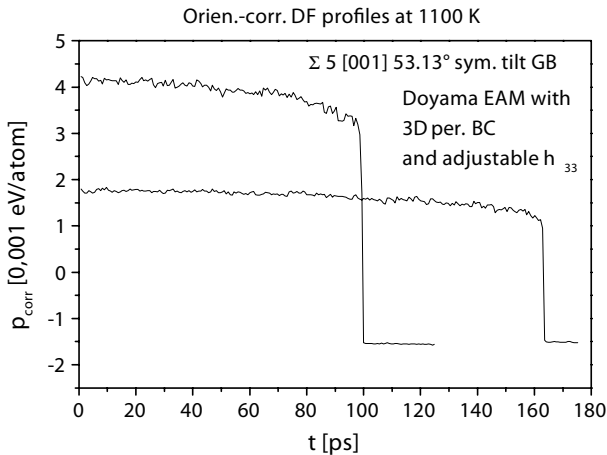


FIGURE 5.16

OCDF profiles at 1100 K of the data presented in Fig. 5.15. The observed decline of the DF occurs close to the annihilation of the two GBs in a system where 3D periodic BC are applied.

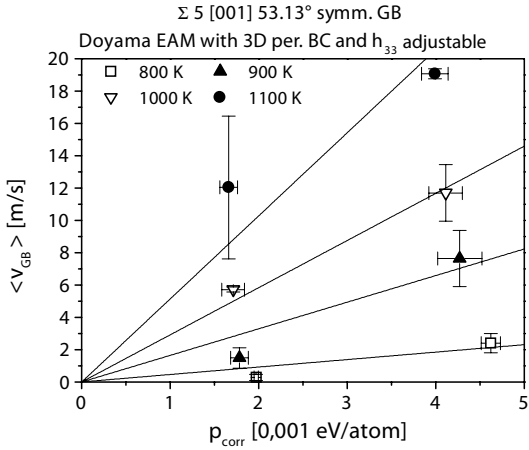


FIGURE 5.17
Average GB velocity vs. OCDF of the $\Sigma 5$ (210) symmetrical tilt GB with adjustable h_{33} box variable at 800 K to 1100 K.

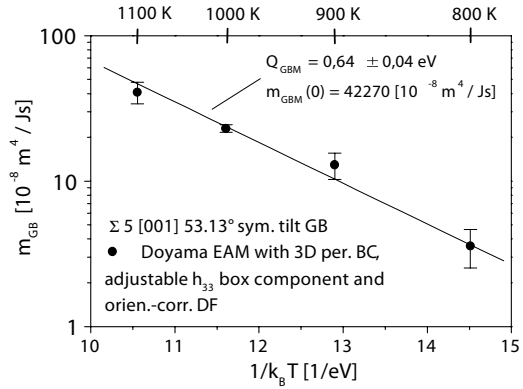
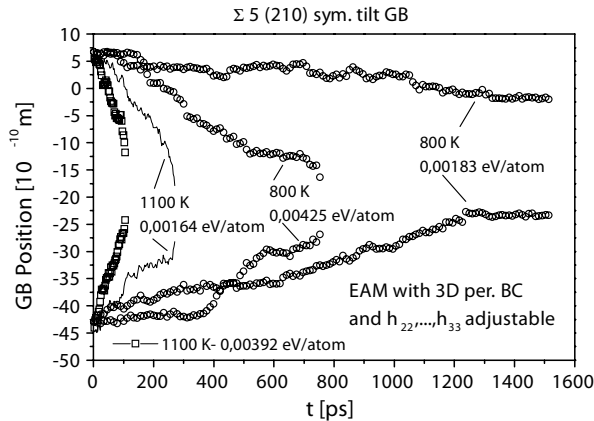


FIGURE 5.18
Arrhenius plot of GB mobility of the $\Sigma 5$ (210) symmetrical tilt GB with adjustable h_{33} box variable and OCDF.

**FIGURE 5.19**

GB position vs. time plots of the $\Sigma 5$ (210) symmetrical tilt GB with adjustable h_{22}, \dots, h_{33} box variables and OCDF at 800 K and 1100 K.

ature the lower the accumulated ε_{YZ} strain.

The 900 K data revealed that for different magnitudes of the OCDF at one temperature, the accumulated ε_{YZ} strain was still the same. This was not found for all temperatures. The decrease in ε_{YZ} with increasing temperature can be understood from a change in the mechanism from a coupled GB sliding and migration mechanism to a more diffusion-controlled GB motion mechanism. This underlines that with increasing temperature a change in GB character occurs for this GB. The average GB velocity vs. OCDF at different temperatures is shown in Fig. 5.21, and an Arrhenius plot of the temperature dependence of the GB mobility is given in Fig. 5.22.

The results appear slightly different from the results of the simulations with only an adjustable h_{33} box variable. First of all, the obtained GB velocities of GB₁ and GB₂ of a single simulation run agree much better as manifested by the relatively small error bars compared to Fig. 5.17. Second, the average GB velocity vs. OCDF plots were almost perfectly linear which was not observed to the same degree for the simulations with only an adjustable h_{33} box variable. This substantiates that GB migration of the $\Sigma 5$ (210) tilt GB proceeds by coupled GB sliding and migration. The data imply a change of GB mechanism with increasing temperature which is reflected by the two regime fit of the GB mobility data. Since the error bars of the GB mobility data are

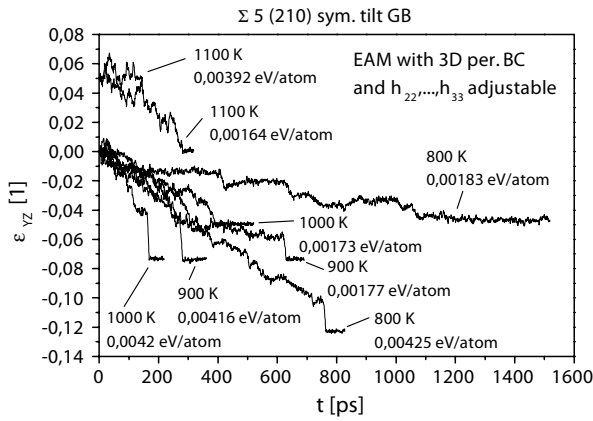


FIGURE 5.20
Temporal evolution of the strain component, ϵ_{YZ} , obtained by simulations of the $\Sigma 5$ (210) symmetrical tilt GB with adjustable h_{22}, \dots, h_{33} box variables and OCDF.

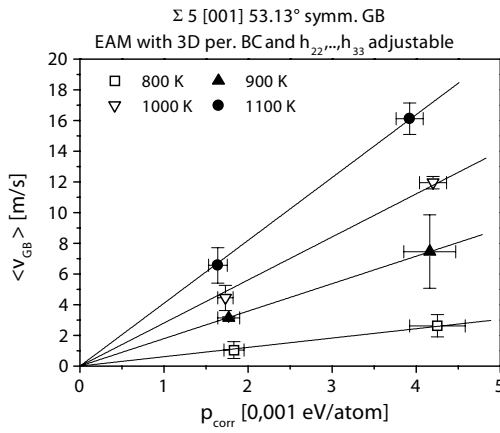
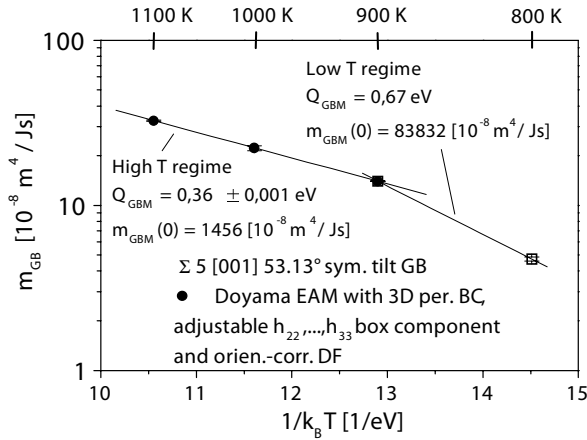


FIGURE 5.21
Average GB velocity vs. OCDF of the $\Sigma 5$ (210) symmetrical tilt GB with adjustable h_{22}, \dots, h_{33} box variables and OCDF from 800 K to 1100 K.

**FIGURE 5.22**

Arrhenius plot of GB mobility of the $\Sigma 5$ (210) symmetrical tilt GB with adjustable h_{22}, \dots, h_{33} box variables and OCDF.

very small, the data seem reproducible, and a true low temperature and high temperature regime for GB migration do exist.

Comparing the GB mobility data obtained by the simulations with only the adjustable h_{33} box variable and adjustable h_{22}, \dots, h_{33} box variables (Fig. 5.23) reveals very good data agreement between both data sets. It is interesting to note that out of all data points, the 800 K data points give the poorest match. This again supports the interpretation that due to different simulation box boundary conditions, ideal GB migration was hindered in the low temperature simulation runs with only one adjustable h_{33} box variable. To elucidate the thermally activated processes of the $\Sigma 5$ [001] 53.13° symmetrical tilt GB, the results of GB self-diffusion [524] (GBD) and GB migration of this GB are listed in Table 5.4. For the simulation results with only adjustable h_{33} and the low temperature regime of the simulations with adjustable h_{22} , h_{23} , h_{32} , and h_{33} , the GB migration enthalpy and the GB self-diffusion enthalpy are the same. For the simulation results with only adjustable h_{33} , this finding and the non-occurrence of GB sliding events demonstrate that under such simulation box constraints, this tilt GB can move by a mechanism not accompanied by GB sliding. At higher temperatures for the simulations with adjustable h_{22} , h_{23} , h_{32} and h_{33} , the GB migration mechanism changes according to the found GB migration activation parameters where the activation enthalpy of migration becomes about half of the activation enthalpy of GB self-diffusion. This ratio of approximately two between the enthalpy for GB self-diffusion and GB migration was found as well for the studied high-angle [001] twist GBs [524, 527]. For the simulations with adjustable h_{22} , h_{23} , h_{32} and h_{33} , GB migration and GB sliding are coupled although the grain boundary strength

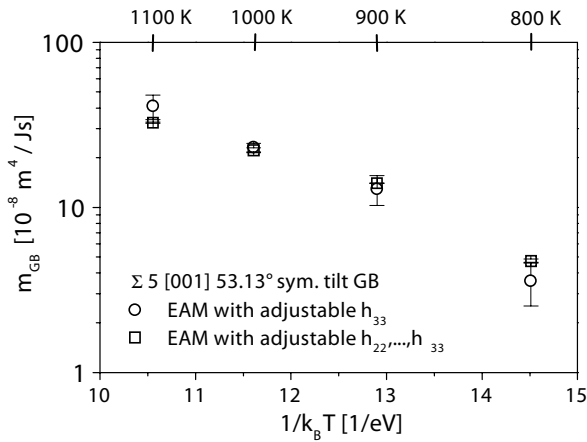


FIGURE 5.23
Arrhenius plots of GB mobility of the $\Sigma 5$ (210) symmetrical tilt GB for adjustable h_{33} box variable and adjustable h_{22}, \dots, h_{33} box variables.

TABLE 5.4
GB Migration and GB Self-Diffusion [524] Activation Parameters of the Studied $\Sigma 5$ [001] 53.13° Symmetrical Tilt GB Using EAM Potentials

GB ¹	Q_{GBM} [eV]	$m_{GBM}(0)$ [$10^{-8} \text{ m}^4/\text{Js}$]	Temp. regime	Q_{GBD} [eV]	$\frac{\delta \cdot D_{GB}(0)}{\Omega}$ [$\frac{1}{ps}$]
$\Sigma 5$ (210)	0.64 ± 0.04	42270	One	0.59 ± 0.05	11.477
$\Sigma 5$ (210)	0.67	83832	Low		
	0.36	1456	High		

Note: The listed GB migration activation parameters are associated with the orientation-correlated DF.
¹ GBM data obtained by simulations with adjustable h_{33} component.

decreases steadily with increasing temperature.

5.5 Compensation Effect

The obtained activation parameters of the studied [001] twist GBs were also analysed with respect to the compensation effect [389]. The standard compensation effect analysis [389] of the [001] twist GB data is given in Fig. 5.24 where the GB migration enthalpy is plotted vs. the logarithm of the pre-exponential factor of GB mobility yielding the compensation temperature T_c according to

$Q_{GBM} = \alpha + \beta \cdot \ln(m_o)$ with $\beta = k_B T_C$. Physically speaking the compensation temperature is considered to be the equilibrium temperature between ground state and activated state [389], here for the mechanism of GB migration.

Two data sets seem to exist that are associated with either low-angle or

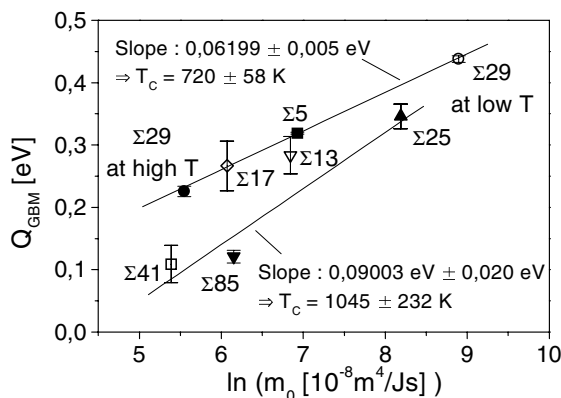


FIGURE 5.24

Compensation plot of the GB migration activation parameters of the studied [001] twist GBs.

high-angle [001] twist GBs. The compensation temperatures T_C found seem realistic. It is especially interesting that the low-angle twist GBs have a rather high T_C compared to the high-angle GBs, actually close to the melting temperature. The lower T_C for the high-angle twist GBs indicates structural transitions in the boundary as, for instance, observed for the $\Sigma 29$ twist GB.

5.6 Comparison with Experiments

Winning [521] studied the motion of planar [001] low- and high-angle tilt and twist GBs in Al driven by a Peach-Koehler driving force. Although the studied GBs were non-CSL GBs, the experimental data lend themselves to a comparison. It was observed experimentally that high-angle curved tilt GBs had a rather high GB migration enthalpy compared to the same planar tilt GBs. Furthermore, it was found that planar [001] tilt GBs had a higher activation enthalpy than [001] twist GBs. Finally the level of purity of a studied GB sys-

tem determined to some extent the magnitude of the GB migration activation enthalpy. A comparison of the data by Winning [521] and the computed data of this work reveals that the GB migration enthalpies of the high-angle GBs are in a comparable range. Knowing that the bulk self-diffusion enthalpy is 1.29eV in Al and 2.01eV in Cu, the expected experimental activation data of a Cu material would be about 35 percent higher than the Al data assuming a simple scaling behavior. In the low-angle regime, the data agreement is poor. The difference might be due to purity effects. The computed low-angle GB migration behavior represents the motion of a screw dislocation network in an absolutely pure material which may explain the extremely low activation enthalpies.

5.7 Grain Boundary Diffusion

5.7.1 Computational Procedure

The temporal evolution of the mean-square displacement (MSD) of atoms can be used to determine the diffusion coefficient D of various diffusive processes in atomistic systems.

The calculation scheme is based on the mean-square displacement (MSD) contribution of GB atoms arising from GB self-diffusion. Usually, rather restricted atomic systems have been used to study GB self-diffusion [531]–[533] to suppress GB sliding. It is a common experience that GB sliding occurs under 3D periodic boundary conditions. However, GB sliding, GB migration and GB self-diffusion are conceived always to occur simultaneously. Hence, in order to study real material behavior GB sliding should not a priori be suppressed.

Since GB sliding occurs during almost every conducted GB simulation, a refined analysis of atomic displacements is necessary to determine only the diffusive GB MSD. Usually, every 1000 time steps the position of each atom within the system is stored to be analyzed subsequently. Hence, the data analysis on atomic configurations is performed in time steps of usually 1.84 ps. The analysis procedure itself works in two steps. In step one at time t the common neighbor analysis (CNA) method is used to classify atoms either as true fcc atoms or not. Any true fcc atom is excluded from the GB MSD analysis at time t and its instantaneous position is kept as the reference position for the following analysis at $t + \delta t$. Non-fcc atoms are evaluated for calculating the diffusive GB MSD. In order to separate GB sliding displacements from GB self-diffusion data, a threshold displacement of $0.35a_o$ is used. Any GB atom having a displacement less than $0.35a_o$ between $t - \delta t$ and t is considered non-diffusive and does not enter the calculation of the diffusive GB MSD at time t . Its position at time t is kept as the reference position for the following

time step. Only displacements beyond the nearest-neighbor(NN)-distance are considered diffusive and used to calculate the GB diffusive MSD at time t . If considered diffusive the displacement of that atom is counted to the GB MSD, and the position at time t is kept as the new reference position for the following time step. Accordingly, only the diffusive MSD of GB atoms is determined. Apart from GB sliding, GB migration events occur during such simulations as well although no explicit DF has been introduced. Nevertheless, the analysis scheme presented is capable of separating atomic displacements due to GB migration and GB sliding from the diffusive GB displacement data.

Once the GB diffusive MSD data are determined, the GB self-diffusion coefficient, D_{GB} , is calculated from Eqs. 5.30 and 5.31

$$MSD(t, t_0) = \frac{SSD(t, t_0)}{N_{GB}} = \frac{1}{N_{GB}} \sum_{j=1}^{N_{GB}} (\mathbf{r}_j(t + t_0) - \mathbf{r}_j(t_0))^2 \quad (5.30)$$

$$D_{GB} = \lim_{t \rightarrow \infty} \left\langle \frac{MSD}{2 \cdot \dim \cdot t} \right\rangle_{t_0} \quad (5.31)$$

where SSD represents the summed-square displacement of all true GB atoms. The quantity \dim defines the spatial dimension of the diffusive process which is considered three dimensional because at high temperatures the diffusive jumps become three dimensional.

Eq. (5.30) implies that the diffusive GB MSD is normalized to the number of GB atoms, N_{GB} . Unfortunately, the definition of the GB region and its width as well as the number of GB atoms is not a simple and unambiguous task. In the following it will be shown that it is not necessary to normalize the GB MSD data directly to the number of GB atoms but rather to the GB area. Hence, Eq. (5.30) serves as the starting point to derive the final equation to determine the GB self-diffusion coefficient.

Quantifying N_{GB} is achieved by approximating N_{GB} through the GB area A_{GB} , the GB width δ and the atomic volume Ω_{fcc} . The number of GB atoms is given by

$$N_{GB} \approx \frac{A_{GB} \cdot \delta}{\Omega_{fcc}} \quad (5.32)$$

Furthermore, the temporal evolution of the GB diffusive MSD and SSD data is expected to be linear in time, and so in Eq. (5.31) the average over $\langle \dots \rangle_{t_0}$ becomes irrelevant for the calculation. Then, the equation for the GB self-diffusion coefficient, D_{GB} , is given by

$$\frac{\delta \cdot D_{GB}}{\Omega_{fcc}} = \lim_{t \rightarrow \infty} \frac{\sum_{j=1}^{N^{DGB}} (\mathbf{r}_j(t) - \mathbf{r}_j(t_0 = 0))^2}{A_{GB} \cdot 2 \cdot \dim \cdot t} = \lim_{t \rightarrow \infty} \frac{SSD}{A_{GB} \cdot 2 \cdot \dim \cdot t} \quad (5.33)$$

Here N^{DGB} represents only the diffusive GB atoms according to the selection scheme mentioned. Evidently, D_{GB} can not be obtained separately rather only

data on $\frac{\delta \cdot D_{GB}}{\Omega_{fcc}}$ can be determined. The expression $\frac{\delta \cdot D_{GB}}{\Omega_{fcc}}$ is obtained from a plot of SSD vs. time where the slope multiplied by the factor $\frac{1}{2 \cdot \dim \cdot A_{GB}}$ yields $\frac{\delta \cdot D_{GB}}{\Omega_{fcc}}$.

5.7.2 Activation Energies

From the temporal evolution of the diffusive SSD for each of the studied [001] twist GBs, the GB self-diffusion coefficients were determined. In Figs. 5.25 and 5.26 the diffusive GB SSD data were normalized to twice the GB area, $2 \cdot A_{GB}$, in order to be representative for the later on to determine GB self-diffusion coefficient D_{GB} . It is necessary to use the GB area twice since two [001] twist GBs are present in the simulation box because of the applied 3D periodic boundary conditions.

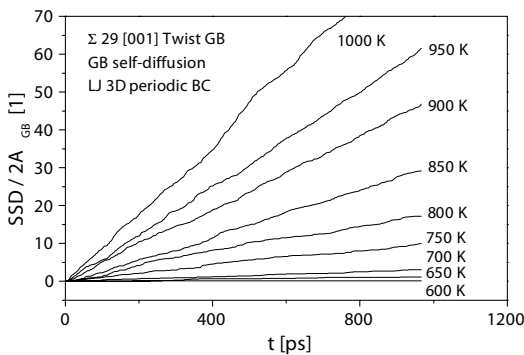


FIGURE 5.25

Total diffusive SSD per GB area of the $\Sigma 29$ [001] 43.60° twist GB at different temperatures.

At intermediate and high temperatures the diffusive jumps of atoms occurred no longer exclusively in-plane but very often out-of-plane. Also, the GB self-diffusion coefficient can only be determined as a product with the GB width δ which is temperature dependent [533].

Fig. 5.27 presents the GB self-diffusion data of the $\Sigma 29$ twist GB. The data are representative for high-angle twist GBs since they exhibit one important aspect. For the $\Sigma 29$ and $\Sigma 5$ twist GBs there is a low temperature and a high temperature regime for both GB self-diffusion and GB migration. This is best seen for the GB self-diffusion data of the $\Sigma 29$ twist GB in Fig. 5.27.

The determined temperature dependence of the GB diffusion coefficient D_{GB} is presented in an Arrhenius plot in Fig. 5.28. From a linear fit of the data the activation parameters for GB diffusion of these [001] twist GBs, namely

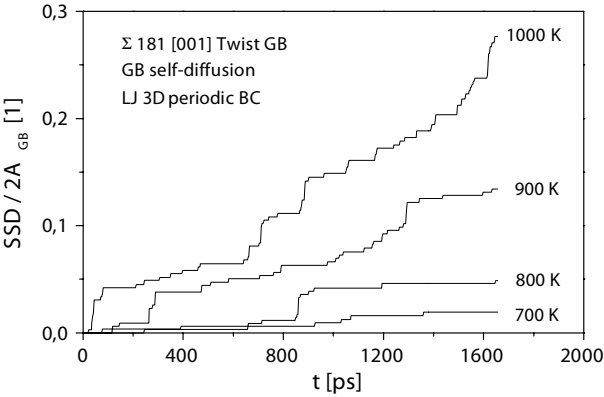


FIGURE 5.26
Total diffusive SSD per GB area of the $\Sigma 181$ [001] 6.03° twist GB at different temperatures.

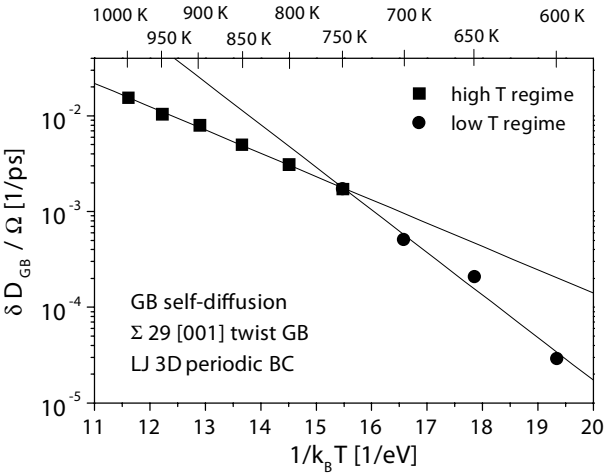
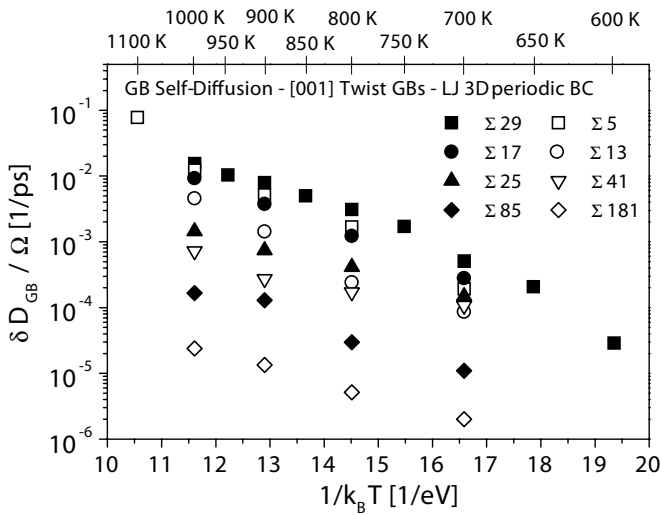


FIGURE 5.27
Arrhenius plot of the GB self-diffusion data of the $\Sigma 29$ [001] twist GB. Here the results of the temperature range 600 to 1000 K are given.

**FIGURE 5.28**

Arrhenius plot of the GB self-diffusion data of the [001] twist GBs. The simulations were done for the LJ potential with 3D periodic BC and in the presence of no DF.

the GB self-diffusion enthalpy and the GB self-diffusion pre-exponential factor, were determined (Table 5.5). A more detailed analysis demonstrates that for the low-angle twist GBs with lowest misorientation, namely $\Sigma 181$ and $\Sigma 85$, the activation enthalpies again increase with decreasing twist angle (Fig. 5.29). One may surmise that even for smaller twist angles the activation enthalpy will rise further or at least stay on a rather high level. In the limit of zero misorientation the volume self-diffusion activation enthalpy of 1.97 eV limit must be found, of course.

Interesting aspects are the low and high temperature GB self-diffusion regimes of the $\Sigma 29$ and $\Sigma 5$ twist GBs. The results with the EAM Doyama [534] and the LJ potential for the $\Sigma 5$ illustrate that the activation enthalpies derived from the LJ and EAM potentials do not differ substantially. A GB self-diffusion data analysis performed on moving GBs driven by explicit DFs proved that GB self-diffusion remained almost identical for stationary and moving GBs. This is confirmed by recent experimental work [535, 536] and hence adds further confidence in the data analysis used. The GB self-diffusion data of the $\Sigma 5$ [001] twist GB in the stationary and moving case is presented in Table 5.6 for 950 K and 1000 K. The data reveal that GB self-diffusion via vacancies remains the same for non-driven and driven GBs. No effect of the magnitude of the DF used on the GB self-diffusion data was found.

The computed grain boundary diffusivities comply with the compensation effect (Fig. 5.30). In principle all data can be fitted by a single compensation

TABLE 5.5
GB Self-Diffusion Activation Parameters of the Studied [001] Twist GBs for the LJ Potential Utilizing 3D Periodic BC

GB plane	θ	Σ	Q_{GBD} [eV]	$\ln(\frac{\delta \cdot D_{GB}^0}{\Omega} [\frac{1}{ps}])$
(001)	43.60°	29	1.023 ± 0.086	9.518
	43.60°	29	0.560 ± 0.014	2.342
(001)	36.87°	5	1.042	8.757
	36.87°	5	0.684 ± 0.007	3.560
(001)	28.07°	17	0.701 ± 0.030	3.464
(001)	22.62°	13	0.816 ± 0.097	3.949
(001)	16.26°	25	0.446 ± 0.020	-1.376
(001)	12.68°	41	0.252 ± 0.016	-4.979
(001)	8.80°	85	0.585 ± 0.081	-1.727
(001)	6.03°	181	0.507 ± 0.020	-4.735

Note: The data shown relate to MD finite temperature simulations without any DF.

line with a relatively low compensation temperature, though. If only the high angle boundaries are considered, the compensation temperature compares to the temperature where structural transitions of the $\Sigma 5$ and $\Sigma 29$ boundaries were found.

5.7.3 Temperature Effects

In order to assess how ordered or disordered the GBs remain at elevated temperatures the angular distribution of the GB diffusion displacement vectors can be analyzed. The data presented in Figs. 5.31–5.34 represent the normalized angular distribution of diffusional GB jumps of at least the next neighbor distance. To perform such an analysis, first the CNA method is applied to identify the GB atoms. Then the displacement vectors have to be analyzed. Since GB sliding might interfere with the analysis scheme, an updating scheme of the reference position of each GB atom has to ensure that only diffusive GB jumps are oriented for their angular distribution. Once a jump is identified, it can be examined with respect to its angular coordinate within the (002) plane. For this the jump vectors are projected onto the (002) plane, and the jump angle is determined. The reference coordinate system for this analysis is the $x - y$ simulation box coordinate system. For a complete MD run, all jump events and the sum of their angular distributions $\gamma(i)$ are represented in a histogram containing 72 classes of 5°. In order to normalize the angular histogram, the data of each class are normalized to $\Gamma(i) = \frac{72 \cdot \gamma(i)}{\sum_{i=1}^{72} \gamma(i)}$. According to this normalization, an isotropic uniform angular distribution would assume the value 1 for each of the 72 angular classes. Usually, at low temperatures the GBs will have some structural order which has to be reflected in the dif-

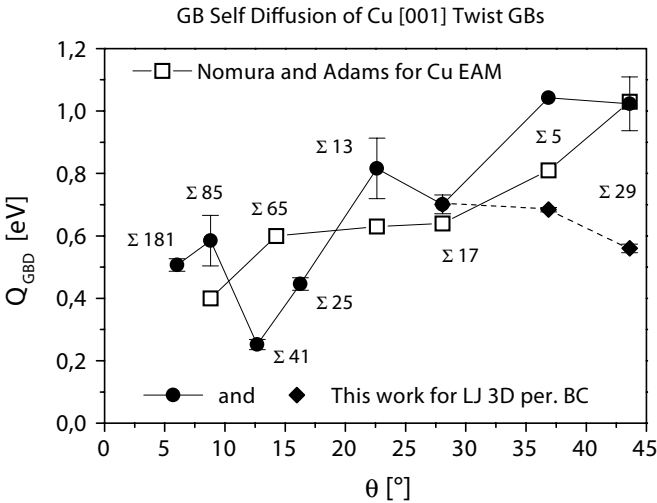


FIGURE 5.29 Misorientation dependence of the activation enthalpy of GB self-diffusion of the [001] twist GBs studied. The data shown represent the results of the LJ 3D periodic BC simulations of this work and the results by Nomura [532] as a reference.

TABLE 5.6
GB Self-Diffusion Coefficient Determined from GB Migration Simulations of the $\Sigma 5$ [001] Twist GB at 950 K and 1000 K

T [K]	p_{corr} [0,001 eV/atom]	$\delta D_{GB} / \Omega$ [1/ps]
950	0,00	0,0086368
950	3,20	0,0093457
950	6,38	0,0086679
1000	0,00	0,0143417
1000	3,15	0,0137255
1000	6,21	0,0137216

Note: Here the results of the LJ simulations in the presence of an OCDF, p_{corr} , are presented. For simulation runs at fixed temperature but different DFs, the GB diffusion coefficient remains the same. No systematic effect of the magnitude of the DF is observed on the GB diffusion coefficient.

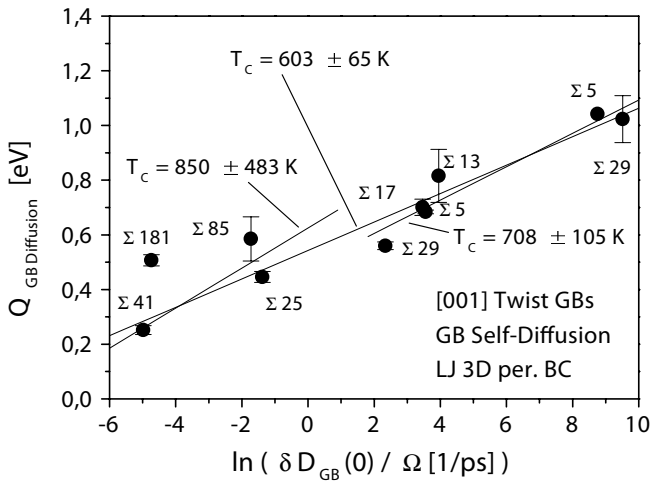


FIGURE 5.30

Compensation plot of the GB self-diffusion data for the [001] twist GBs studied. Three linear data fits were done. One data fit of the overall data yielded 605 K for the compensation temperature, a data fit of only the high-angle GB data yielded 708 K, and finally a fit of only the low-angle GB data yielded 850 K.

fusional data.

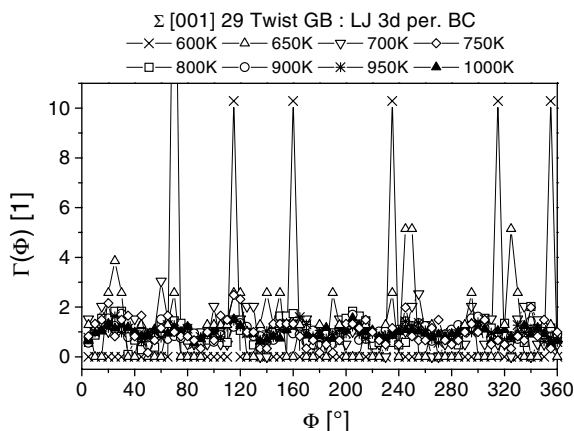


FIGURE 5.31

Angular distribution of the diffusion jump vectors of the $\Sigma 29$ [001] 43.60° twist GB at different temperatures.

The analysis relies on the fact that discrete single GB diffusional jumps can be identified within the system. Typically, only after every 1000 time steps the positions of all atoms in the system are stored. For high temperatures this means that not every single jump event can be identified, since numerous jump events may have occurred within the time range of 1000 time steps. Nevertheless, the approach is capable of identifying diffusional GB jump events and yields solid data on their angular distribution. From the angular distribution two main conclusions can be drawn:

- (1) All high-angle GBs, especially the $\Sigma 29$ and $\Sigma 5$, seem to undergo a structural transition far below the melting temperature.
- (2) Low-angle GBs seem to remain crystalline throughout the temperature range studied. The thermal weakening of the GB structure was less pronounced than in the case of high-angle [001] twist GBs.

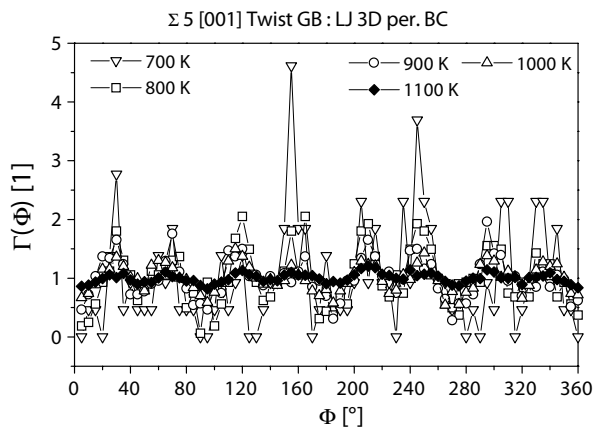


FIGURE 5.32
Angular distribution of the diffusion jump vectors of the $\Sigma 5$ [001] 38.87° twist GB at different temperatures.

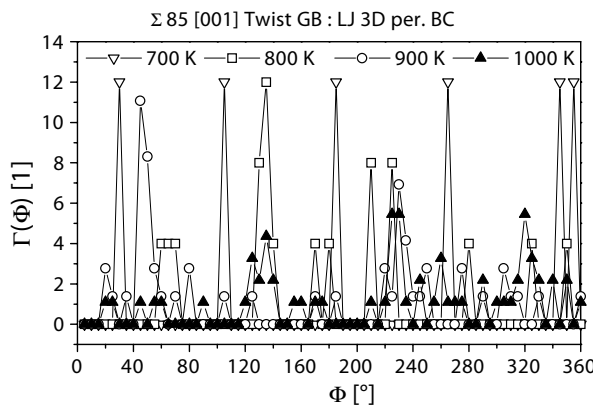
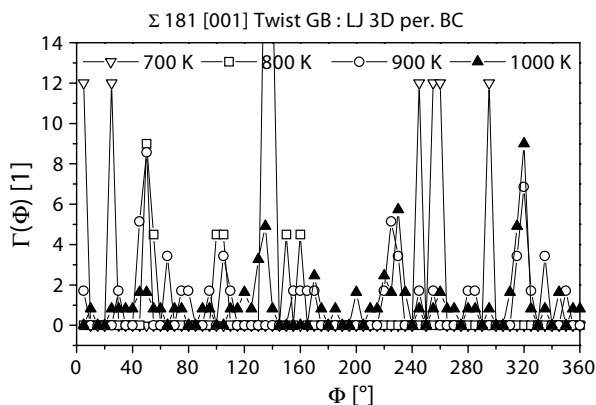


FIGURE 5.33
Angular distribution of the diffusion jump vectors of the $\Sigma 85$ [001] 8.80° twist GB at different temperatures.

**FIGURE 5.34**

Angular distribution of the diffusion jump vectors of the $\Sigma 181$ [001] 6.03° twist GB at different temperatures.

5.8 Atomic Mechanisms

5.8.1 GB Migration of [001] Twist Boundaries

The simulations revealed several GB migration mechanisms:

- (1) Collective shuffle mechanism of four atoms for the $\Sigma 29$, $\Sigma 5$ and $\Sigma 17$ GBs.
 - (2) Dislocation-based mechanism for the $\Sigma 41$, $\Sigma 85$ and $\Sigma 181$ GBs.
 - (3) Neither of the two mechanisms are hard to identify for $\Sigma 13$ and $\Sigma 25$ GBs.
- The $\Sigma 29$, $\Sigma 5$ and $\Sigma 17$ twist GBs moved by a collective shuffle mechanism at least at low and intermediate temperatures. The elementary act of the collective shuffle mechanism is a cooperative four atom movement. Majid and Bristowe [537] were the first to report a shuffle mechanism for the $\Sigma 5$ [001] twist GB.

The migration of the $\Sigma 41$, $\Sigma 85$ and $\Sigma 181$ twist GBs was found to be connected to the motion of their screw dislocation networks which can be characterized as follows :

- (a) The GB structure in the temperature range studied (700 K to 1000 K) consisted of a discrete network of screw dislocations. This network was even present at the highest applied temperatures.
- (b) Normally no jumps of atoms across the GB were observed during GB migration even at the highest temperatures studied. This shows that the GB migration mechanism was predominantly confined to each (002) plane. This behavior is quite different from high-angle twist GBs at elevated temperatures.
- (c) GB sliding increased with rising twist angle. The $\Sigma 41$ (12.7°) twist GB

still showed some tendency to GB sliding, but its magnitude was far less than for the $\Sigma 5$ (36.9°) twist GB.

(d) The final displacement field found in each (002) plane after a GB had swept the plane was dominated by in-plane displacements that were linked to the GB screw dislocation cores. The atoms moved in a cooperative manner. The largest displacement vectors were in the range of a next neighbor distance or less. Even at the highest temperatures the discrete screw dislocation network of the low-angle twist GBs prevailed, and even when the approaching GBs came very close, this situation did not change. This demonstrates that the low-angle twist GBs behaved exactly like a discrete screw dislocation network in fcc crystals. The activation enthalpies found for the low-angle twist GBs are very low, low even compared to the [001] high-angle twist GBs studied in this work and must be associated with the motion of the structural screw dislocations. It also explains the drop in activation enthalpy observed in the transition from high-angle [001] twist to low-angle twist GBs.

TABLE 5.7
Scaling Behavior of the Found GB Activation Enthalpies of the Studied [001] Twist GBs for the LJ Potential

GB plane	θ	Σ	Q_{GBD}/Q_{vac} [1]	Q_{GBM}/Q_{GBD} [1]	Q_{GBM}/Q_{fus} [1]
(001)	43.60°	29	0.519	0.428	3.4
	43.60°	29	0.284	0.404	1.7
(001)	36.87°	5	0.528	0.306	2.5
	36.87°	5	0.347	0.466	—
(001)	28.07°	17	0.355	0.381	2.1
(001)	22.62°	13	0.414	0.348	2.2
(001)	16.26°	25	0.226	0.776	2.7
(001)	12.68°	41	0.128	0.433	0.8
(001)	8.80°	85	0.297	0.207	0.9
(001)	6.03°	181	0.257	—	—

Note: Here the activation enthalpy of volume self-diffusion via mono-vacancies in an fcc system modeled by the LJ potential used in this work with 3D periodic BC is Q_{vac} =1.972 eV. Further Q_{GBD} represents the GB self-diffusion enthalpy as determined in this work for each GB and Q_{GBM} is the GB migration enthalpy. Finally Q_{fus} is the latent heat of fusion as determined in [539] and reads Q_{fus} =0.13 eV.

5.8.2 Grain Boundary Diffusion of [001] Twist Boundaries

Owing to a lack of reliable data on grain boundary mobility it is frequently assumed that GB migration and GB diffusion involve the same mechanisms so that the activation energies are essentially identical. The computed activation

enthalpies of GB self-diffusion of each GB and volume self-diffusion are listed in Table 5.7 namely, $r_{vac}^{GBD} = \frac{Q_{GBD}}{Q_{vac}}$ and $r_{GBD}^{GBM} = \frac{Q_{GBM}}{Q_{GBD}}$. These data yield the following information:

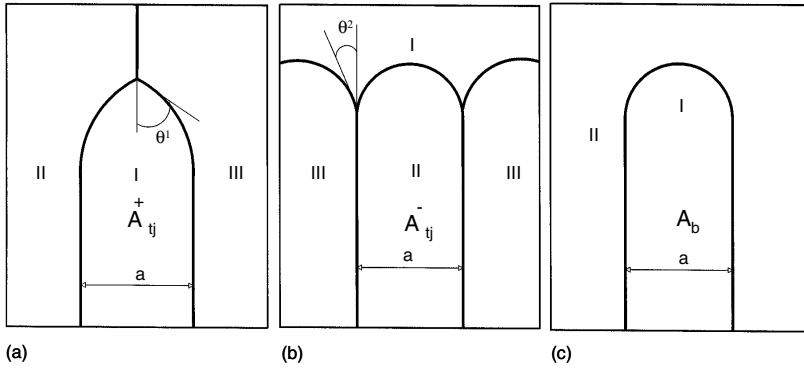
- (a) The computed GB self-diffusion activation enthalpy for the $\Sigma 29$ and $\Sigma 5$ twist GBs in the low temperature regime were about half the value for volume self-diffusion via mono-vacancies. The other listed data in Table 5.7 of r_{vac}^{GBD} range from 0.128 to 0.414 depending on the misorientation angle of the GB. Generally r_{vac}^{GBD} is assumed to be approximately 0.5.
- (b) The r_{GBD}^{GBM} values range from 0.207 to 0.776 depending on the misorientation angle of the GB. Roughly speaking, the ratio is one third to one half. This clearly demonstrates that GB migration and GB self-diffusion are distinctly different processes. This is supported by the results of the GB migration mechanisms; for instance, for high-angle [001] twist GBs a cooperative four atom shuffle mechanism was identified as the key element which was quite different from the GB diffusion mechanism.

This result is also supported by atomic resolution TEM experiments to observe in situ grain boundary motion [538]. A cooperative shuffle process as the dominant migration mechanism was reported.

5.9 Simulation of Triple Junction Motion

5.9.1 Theoretical Background

In the following we focus on the determination of the intrinsic triple junction mobilities in simulations where the migration is driven by grain boundary curvature. Two simulation geometries designed to achieve steady-state boundary and triple junction migration and from which the steady-state triple junction mobility may be extracted are shown in Fig. 5.35. In the geometry of Figs. 5.35(a) and (b), the boundary curvatures are such that the triple junction moves either into or away from grain *a* (referred to as the + and – directions, respectively). Three grains, I, II and III, separated by three grain boundaries with misorientations $\alpha I-II$, $\alpha I-III$ and $\alpha II-III = \alpha I-II + \alpha I-III$ meet at the triple junction. Since the grain boundaries are assumed to extend perpendicular to the plane of view, the geometry is quasi two-dimensional. The II-III grain boundary is assumed to be symmetric such that $\alpha I-II = \alpha I-III$ and the I-II and I-III boundaries are equivalent. The orientations of the constituent grains in the two geometries are chosen such that the triple junctions in Figs. 5.35(a) and (b) are structurally identical. The force balance associated with the grain boundary (surface) tensions (in the direction parallel to the II-III boundary) at the triple junction results in a thermodynamic driving

**FIGURE 5.35**

Schematic illustrations of the geometries employed in the simulations. The definition of the triple junction angle θ , half-loop grain width a and grain identities are shown. The orientations of the I, II and III grains are the same in all three geometries. The misorientation across the I-II and the I-III boundaries is $\pm\varphi$ and that across the II-III boundary is 2φ . The simulation geometries in (a) and (b), referred to as the “+” and “-” geometries because the II-III boundary increases or decreases, respectively, during curvature-driven boundary migration. The geometry in (c) represents the simulation cell used to study boundary migration in the absence of a triple junction; there is a bicrystal half-loop of width a and area A_b [440].

force, F_{tj} given by

$$F_{tj}^{\pm} = 2\gamma_{I-II}\cos\theta^{\pm} - \gamma_{II-III} = \mp 2\gamma_{I-II}(\cos\theta^{\pm} - \cos\theta^{eq}) \quad (5.34)$$

where the superscript \pm indicates that the variable applies to either the “+” or “-” configuration (Figs. 5.35(a) and (b), respectively), θ is one-half the dynamic included angle within grain, I and γ_{I-II} and γ_{II-III} are the grain boundary energies (if the boundary energy depends on boundary inclination, then the boundary energies must be replaced with $\gamma_{\eta\Psi}\partial^2\gamma_{\eta\Psi}/\partial\varphi^2$, where φ refers to the orientation of the grain boundary normal and η and Ψ represent either I or II. In static equilibrium, the net force on the triple junction is zero, $F_{tj} = 0$, such that the static value of θ is given by $2\gamma\cos\theta^{eq} = \gamma_{II-III}$ which is used in the second equality in Eq. 5.34 (γ_{ab} is denoted as γ for simplicity). Then the expression for the triple junction migration rate looks:

$$v_{tj} = m_{tj}^{\pm}F_{tj} = \mp 2\gamma m_{tj}^{\pm}(\cos\theta^{\pm} - \cos\theta^{eq}) \quad (5.35)$$

We can easily extract the triple junction migration rate in terms of a quantity which can be extracted from the simulations, i.e. the rate of change in area

\dot{A}_{tj}^{\pm} of the half-loop grain (grain I in Fig. 5.35(a) and grain II in Fig. 5.35(b)). Geometrically, \dot{A}_{tj}^{\pm} is simply the product of the width a of the half-loop grain and the triple junction velocity, $v_{tj} \cdot \dot{A}_{tj}^{\pm} = v_{tj}^{\pm} a = 2\gamma m_{tj}^{\pm} a |\cos \theta^{\pm} - \cos \theta^{eq}|$. In the simulations, we measure \dot{A}_{tj}^{\pm} , θ^{\pm} and θ^{eq} for each set of simulation conditions (simulation geometry, misorientation φ , width a and temperature T) and use the expression for \dot{A}_{tj}^{\pm} to extract the reduced mobility of the triple junction. The normalized triple junction mobility is directly obtainable from the simulations (\dot{A}_b^{+} , \dot{A}_b^{-} , θ^{\pm} and θ^{eq})

$$\Lambda_{\text{sim}}^{\pm} = \frac{m_{tj}^{\pm} a}{m_b} = \left(\frac{\pi}{2}\right) \left(\frac{\dot{A}_{tj}^{\pm}}{\dot{A}_b}\right) \frac{1}{|\cos \theta^{\pm} - \cos \theta^{eq}|} \quad (5.36)$$

The mobility ratio Λ_{an}^{\pm} can also be calculated directly from the analytical result for the triple junction migration given the static and dynamic angles θ^{eq} and θ^{\pm}

$$\Lambda_{an}^{+} = \frac{m_{tj}^{+}}{m_b} = \left| \frac{\theta^{+}}{\cos \theta^{+} - \cos \theta^{eq}} \right| \quad (5.37a)$$

$$\Lambda_{an}^{-} = \frac{m_{tj}^{-} a}{m_b} = \left| \frac{\ln(\sin \theta^{-})}{\cos \theta^{-} - \cos \theta^{eq}} \right| \quad (5.37b)$$

Equating the simulation and analytical expressions for the triple junction velocity gives the relationship between the rate of change in grain area and the triple junction angles

$$\theta^{+} = \left(\frac{\pi}{2}\right) \frac{\pi \dot{A}_{tj}^{+}}{\dot{A}_b} \quad (5.38a)$$

and

$$\theta^{-} = \sin^{-1} \left[\exp \left(\frac{\pi \dot{A}_{tj}^{-}}{2 \dot{A}_b} \right) \right] \quad (5.38b)$$

5.9.2 Simulation Method

Molecular dynamics was performed in the simulations to extract the triple junction mobility by measuring $\dot{A}_{tj} pm$ and the static and dynamic angles θ^q and θ^{\pm} [440]. These quantities were measured as a function of the orientations of the bounding grains and temperature. The simulations were performed using the simple, well-characterized Lennard-Jones pair potential. Because the simulation geometries in Fig. 5.35 are inherently two dimensional, the simulations were performed in two dimensions (i.e. the XY plane). Energies are reported in units of the Lennard-Jones potential well depth ε , distance in units of the equilibrium atom separation r_0 , area in units of the perfect crystal area per atom a_0 and time in units of $\tau = (M_{at} r_0 / \varepsilon)^{1/2}$, where M_{at} is the

atomic mass. For example, in the case of Al, $\varepsilon = 0.57$ eV and $r_0 = 2.86\text{\AA}$. The potential was cut off at $r_c = 2.1r_0$, which is midway between the second and third nearest neighbors in the zero temperature equilibrium triangular lattice. A velocity-resealing thermostating algorithm was used to set the temperature [440, 485]. Periodic boundary conditions were employed in the direction perpendicular to the straight boundaries in Fig. 5.35. In order to maintain the grain misorientations (especially at high temperature), the bottom three layers were frozen. Additionally, the X-coordinates of the atoms in the top three layers were fixed such that those atoms could move only in the Y-direction to accommodate the dilatational stresses generated due to the decrease in net boundary area during the simulation. Additional simulations were performed in the geometry of Figs. 5.35(a) and (c) with free surfaces on the top and sides to ensure that these boundary conditions did not significantly modify the results.

The initial atomic configurations were created by misorienting grains II and III with respect to grain I by $\pm\varphi$ and hence with respect to each other by 2φ , such that the grain boundary II-III is a symmetric boundary. This methodology enables the reduction of the description of the entire tri-crystallography in terms of a single misorientation variable φ . The simulation geometries were relaxed by performing molecular dynamics simulations at very low temperatures ($0.0100.025\varepsilon/k_B$) prior to the grain boundary migration study to enable the atoms at the grain boundaries to equilibrate. The entire system is then heated slowly to the desired temperature in a step-wise fashion. The migration rate \dot{A}_{tj}^\pm is deduced from the slope of the area of the half-loop grain A_{tj}^\pm vs. time t plot. \dot{A}_{tj}^\pm is simply the product of the number of atoms in the half-loop grain and the area per atom a_0 . This requires the assignment of each atom in the simulation cell to one of the grains at each time [202]. The dynamic triple junction angle θ^\pm was extracted by measuring the angle subtended between the tangent of the I-II grain boundary at the triple junction and the extension of the II-III boundary into grain I (i.e. $\theta_{I-II} + \theta_{I-III}$; see Figs. 5.35(a) and (b)). \dot{A}_{tj}^\pm and θ_{tj}^\pm measurements are only made during times for which the grain boundary(ies) enclosing the half-loop grain shrinks or grows in a steady-state, self-similar manner. The angles reported were averaged over several measurements during the course of each of three simulations performed for each set of conditions. The static equilibrium angles θ^{eq} were determined by performing larger scale simulations at high temperatures until the boundaries have stopped migrating (see [540]).

The dependence of triple junction mobility on grain boundary and triple junction crystallography is simulated in tri-crystals for a range of boundary misorientations. Special or singular boundaries (e.g. $\Sigma = 7$, $\theta = 38.2^\circ$ and $\Sigma = 13$, $\varphi = 32.21^\circ$, where Σ is, as usual, the inverse density of coincidence sites), vicinal or near-singular boundaries (near $\Sigma = 7$ and $\Sigma = 13$), and general boundaries were all simulated. It should be noted that in the present 2D triangular lattice simulations, where misorientations correspond

to tilts about the $\langle 111 \rangle$ axis in the related fcc lattice, an I-II and I-III misorientation φ corresponding to Σ_{I-II} produces a II-III boundary corresponding to $\Sigma_{II-III} = \Sigma_{I-II}^2$. All misorientations φ were within the range $30^\circ \leq \theta \leq 40^\circ$, where the entire range of unique boundary misorientations lies between $30^\circ \leq \theta \leq 60^\circ$ which are symmetry related to those with $30^\circ > \theta > 0^\circ$ in this lattice.

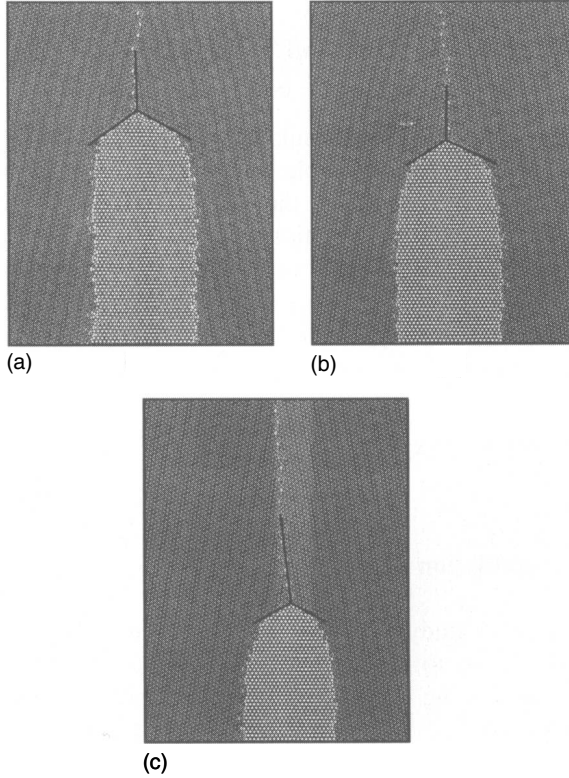
Triple junction kinetics were also investigated as a function of grain size (half-loop width) and temperature. These simulations were performed for tri-crystallographies for which significant triple junction drag was observed. The simulations were performed for $19r_0 < w < 50r_0$ and $0.075\varepsilon/k_B < T < 0.250\varepsilon/k_B$. Activation energies for migration were extracted from Arrhenius plots of the rate of change in half-loop area with temperature. Three runs were performed for each simulation condition and the simulation parameters.

5.9.3 Simulation Results

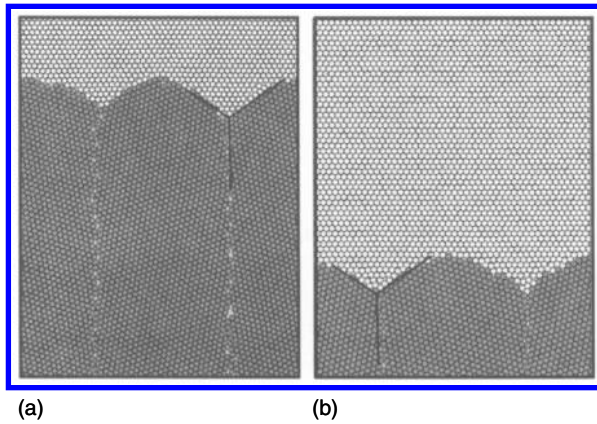
Fig. 5.36 shows the atomic configurations corresponding to three different times ($t = 550\tau$, 1245τ , and 1750τ), for a simulation performed for the “+” geometry at $T = 0.125\varepsilon/k_B$, half-loop width of $a = 25r_0$ and $\theta = 40^\circ$. Careful examination shows that apart from small fluctuations, the curvatures of the constituent grain boundaries at the triple junctions remain constant, implying that the triple junction migration is very nearly self-similar and, hence, steady state, and that the triple junction angle is preserved throughout the simulation. Fig. 5.37 shows the atomic configurations for the simulation geometry in Fig. 5.35(b) ($t = 2000\tau$ and $t = 14000\tau$) at the same temperature and half-loop width as in Fig. 5.36. Again, it is clear from the figure that the tri-crystal shape is self-similar during its migration.

The self-similarity of triple junction migration enables us to extract the triple junction migration rate in terms of the rate of change in the area of the half-loop grain \dot{A}_{tj}^\pm . The temporal evolution of the grain areas for the structures in Fig. 5.35 are shown in Fig. 5.38 for the same conditions as in Figs. 5.36 and 5.37. It is important to note that for the “−” simulation geometry, the total calculated area corresponds to the sum of the areas of grains I and II, which in turn is twice that of the half-loop area. The half-loop area decreases with time in a monotonic fashion, with some superimposed noise. At late times, the retracting half-loop is influenced by the frozen layer of atoms at the bottom of the simulation cell and, hence, no measurements can be made there. Some of the fluctuations seen in Fig. 5.38 at intermediate time are associated with thermal transients in the shape of the half-loop and triple junction angle during half-loop retraction.

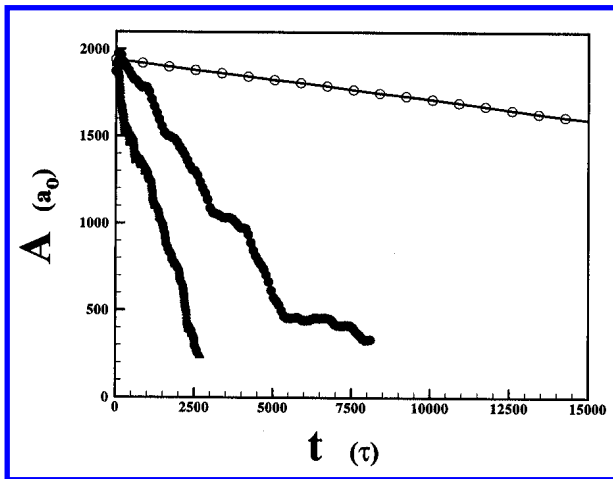
More detailed discussion of the nature of the fluctuations/transients in the \dot{A}_{tj}^\pm vs. t plots may be found elsewhere [202]. These transients are excluded from the determination of the steady-state slope. The regions of steady-state migration are characterized by constant θ^{pm} as well as a linear \dot{A}_{tj}^\pm vs. t plot. For the simulation conditions corresponding to Figs. 5.36 and 5.37, the ex-

**FIGURE 5.36**

The atomic configuration of a $\varphi = 33^\circ$ migrating triple junction ($T = 0.125\varepsilon/k_B$, $w = 25r_0$ for the “+” simulation geometry at three instants of time: (a) $t = 550\tau$, (b) $t = 1245\tau$ and (c) $t = 2550\tau$. The bold lines indicate the tangents to the half-loop boundary at the triple junction. The dynamic triple junction angle was $\theta^+ = 56^\circ$ in (a) $\theta^+ = 58^\circ$ in (b), and $\theta^+ = 58^\circ$ in (c) [440].

**FIGURE 5.37**

The atomic configuration of a $\varphi = 33^\circ$ migration triple junction ($T = 0.125\varphi/k_B$, $w = 25r_0$) for the “ $-$ ” simulation geometry. The atomic configurations correspond to instants of time: (a) $t = 2000\tau$ and (b) $t = 14000\tau$. The dynamic triple junction angle was $\theta^- = 61^\circ$ in (a) and $\theta^- = 62^\circ$ in (b) [440].

**FIGURE 5.38**

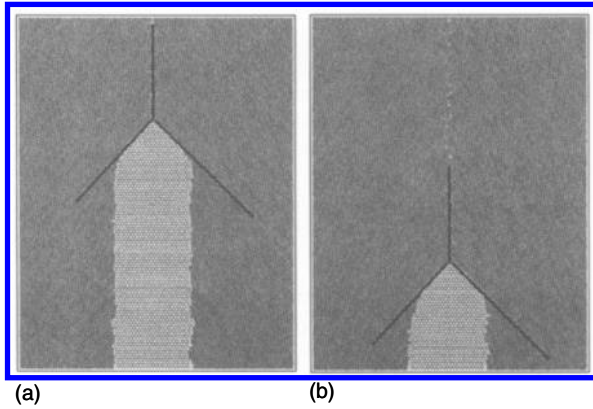
The rate of change in the area of the half-loop grain (grain I in Figs. 5.35(a) and (c), and grain II in Fig. 5.35(b) with and without triple junctions for the same conditions as in Fig. 5.35(c)). The filled and open circles indicate the “ $+$ ” and “ $-$ ” geometries, respectively, and the shaded triangles indicate the results of the bicrystal simulation [440].

tracted rates of change of the half-loop grain area are $\dot{A}_{tj}^+ = 0.33 \pm 0.06a_0/\tau$ and $\dot{A}_{tj}^- = 0.024 \pm 0.009a_0/\tau$. The difference between the two values of \dot{A}_{tj}^\pm is expected based upon the differences in geometry.

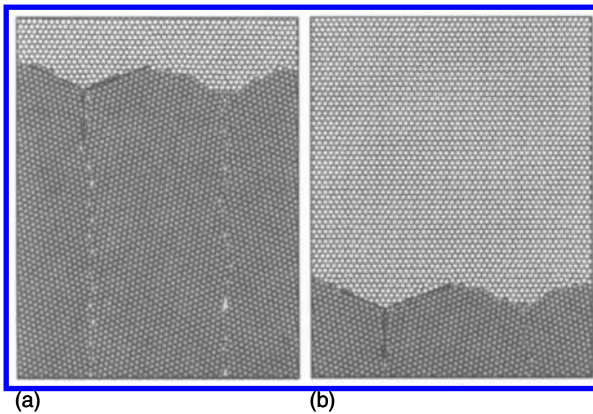
Fig. 5.39 also shows simulation data obtained from the bi-crystal half-loop (i.e., without a triple junction) simulations (see Fig. 5.35(c), A_b vs. t , for the same (I-II) misorientation, temperature and half-loop width as for the triple junction migration simulations. The slope of this curve is $\dot{A}_b = 0.54 \pm 0.03a_0/\tau$. Comparing \dot{A}_{tj}^\pm and \dot{A}_b , it is found that $\dot{A}_{tj}^- < \dot{A}_{tj}^+ < \dot{A}_b$. For the simulations shown in Figs. 5.36 and 5.37, the average dynamic triple junction angles are $\theta^+ = 59^\circ \pm 1^\circ$ and $\theta^- = 62^\circ \pm 1^\circ$. The static triple junction angle for this tricrystallography has been previously determined to be $\theta^{eq} = 61^\circ \pm 1^\circ$. Hence, for this tricrystal, the dynamic triple junction angle θ^\pm is approximately the same as θ^{eq} .

Figs. 5.40 and 5.41 show the atomic configurations during triple junction migration in both the “+” ($t = 450\tau$ and 2550τ) and “−” ($t = 3000\tau$ and 25000τ) directions, respectively, under the same conditions as Figs. 5.36 and 5.37, but for $\varphi = 38.2^\circ$. This angle corresponds to a high symmetry, low Σ (i.e., $\Sigma 7$) misorientation. Once again, it is clear that triple junction migration takes place in a nearly self-similar fashion, with constant β_{tj}^\pm . The temporal evolution of the areas of the half-loop grains for the tri-crystal simulations shown in Figs. 5.40 and 5.41 as well as the corresponding bicrystal simulations is shown in Fig. 5.42. Averaged over three different simulation runs, the steady-state slopes of the \dot{A}_{tj}^\pm vs. t plots for the “+” and “−” geometries are $\dot{A}_{tj}^+ = 0.64 \pm 0.05a_0/\tau$ and $\dot{A}_{tj}^- = 0.039 \pm 0.006a_0/\tau$. The rate of change of area for the bicrystal half-loops at $\varphi = 38.2^\circ$ is $\dot{A}_b = 1.32 \pm 0.08a_0/\tau$. The dynamic triple junction angles for the “+” and “−” geometry are measured to be $\theta^+ = 47^\circ \pm 1^\circ$ and $\theta^- = 72^\circ \pm 1^\circ$, respectively. For this tricrystallography, the static triple junction angle is $\theta^{eq} = 60 \pm 2^\circ$. Unlike in the low symmetry $\varphi = 40^\circ$ case, where the triple junction angles were nearly the same in the “+” and “−” geometries, in the $\varphi = 38.2^\circ$ case the triple junction angles are much different ($\Delta\varphi = 25^\circ \pm 2^\circ$), implying that in the $\varphi = 38.2^\circ$ case, triple junction drag may be substantial.

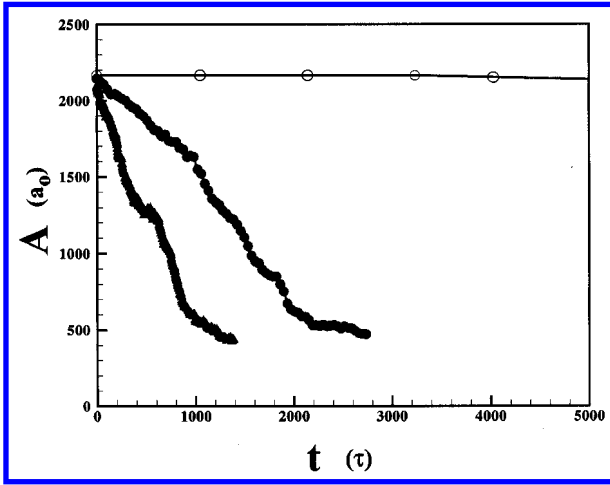
As mentioned before, one of the major advantages of the computer simulation approach is the ability to study the effect of grain boundary misorientation φ on triple junction motion. Triple junction migration simulations were performed for a total of 13 different grain boundary misorientations φ at fixed width ($w = 25r_0$) and temperature ($T = 0.125\varepsilon/k_B$). Depending on the misorientation, \dot{A}_{tj}^\pm and \dot{A}_b can be very similar or very different (by as much as a factor of two). This difference is largest for low Σ (singular) boundaries. On the other hand, \dot{A}_{tj}^- is always approximately an order of magnitude lower than \dot{A}_b for all misorientations. The static triple junction angles are nearly independent of misorientation in this two-dimensional Lennard-Jones system and are very close to the isotropic limit of $\theta = 60^\circ$. The dynamic triple junction angle θ^+ varies from a low of $44^\circ \pm 1^\circ$ to a high of $59^\circ \pm 1^\circ$, and from

**FIGURE 5.39**

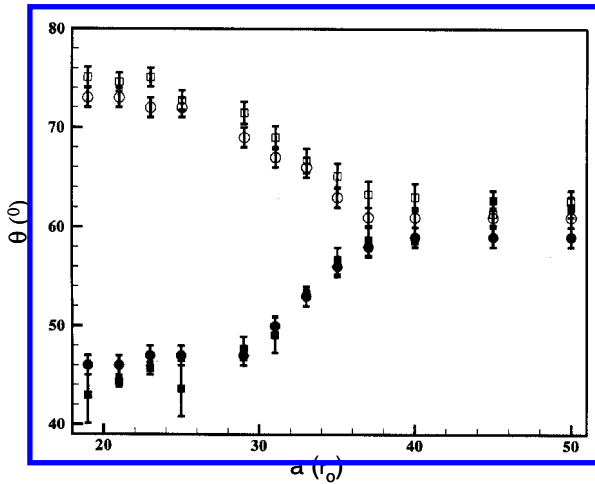
Atomic configurations during the migration of a $\varphi = 38.2^\circ (\Sigma = 7)$ “+” geometry triple junction ($T = 0.125\varepsilon/k_B$, $w = 25r_0$) at two instants of time: (a) $t = 450\tau$ and (b) $t = 2150\tau$. The dynamic triple junction angles were measured to be $\theta^+ = 47^\circ$ in (a) and $\theta^+ = 48^\circ$ in (b) [440].

**FIGURE 5.40**

Atomic configurations during the migration of a $\varphi = 38.2^\circ (\Sigma = 7)$ for the “-” geometry triple junction. The dynamic triple junction angles were measured to be $\theta^- = 72^\circ$ in (a) and $\theta^- = 71^\circ$ in (b) [440].

**FIGURE 5.41**

The rate of change in the area of the half-loop grain with and without triple junctions for the same conditions as in Fig. 5.39. The filled and open circles indicate the “+” and “-” geometries, respectively, and the shaded triangles indicate the results of the bi-crystal simulation [440].

**FIGURE 5.42**

The dynamic triple junction angle θ^\pm plotted as a function of the half-loop grain width a , for both the “+” (filled symbols) and “-” (open symbols) geometries and for simulation conditions $\varphi = 38.2^\circ$ and $T = 0.125\varepsilon/k_B$. The circles indicate the directly measured dynamic angles while the squares correspond to θ^- from Figs. 5.41(a) and (b) [440].

a low of $60^\circ \pm 1^\circ$ to a high of $74^\circ \pm 1^\circ$ for the “–” geometry. Of more importance than the absolute value of the dynamic triple junction angle is the deviation of this angle from its equilibrium value $|\theta^+ - \theta^{eq}|$. While little or no deviations (within the error bars) of the dynamic triple junction angles from the static value of 60° are common in the simulation performed, significant deviations do occur at or very near low Σ misorientations: $|\theta^+ - \theta^{eq}| = 16^\circ$ and $|\theta^- - \theta^{eq}| = 14^\circ$ for $\Sigma 13$ ($\varphi = 32.2^\circ$) and $|\theta^+ - \theta^{eq}| = 13^\circ$ and $|\theta^- - \theta^{eq}| = 1^\circ$ for $\Sigma 7$ ($\varphi = 38.2^\circ$). The observation of large deviations of the dynamic angle from their equilibrium values appears strongly correlated with large deviations of \dot{A}_{tj}^\pm from \dot{A}_b .

The variation of the dynamic angle θ^\pm (as measured from figures such as Figs. 5.36 and 5.37) with half-loop width is shown in Fig. 5.42. As the half-loop width increases, the deviation $\theta^\pm - \theta^{eq}$ decreases for both the “+” and “–” geometries. For widths above approximately $40r_0$, the dynamic angle θ^\pm is nearly indistinguishable from the static equilibrium value $\theta^{eq} = 60^\circ \pm 1^\circ$. These data suggest that at small half-loop width triple junction drag is significant.

Fig. 5.43 shows the variation of θ^\pm with temperature T , where θ^+ has been directly measured from images of the migrating triple junction and deduced from Figs. 5.39(a) and (b). Within the error bars of the determination of θ^+ , both methods yield the same values. As the temperature increases, the deviation of the dynamic angle from the static angle $|\theta^+ - \theta^{eq}|$ decreases. Similar trends are also observed for the “–” geometry of Fig. 5.40(b). Substantial deviations of θ^\pm from its equilibrium value θ^{eq} only occur for special misorientations, small grain size and relatively low temperature.

The results show that for low Σ misorientations and misorientations near these, the dynamic triple junction angles deviate significantly from their equilibrium values. This results in significantly slower boundary migration in the tri-crystal geometries, as indicated by the extracted values of the rates of change in area of the half-loop grain \dot{A}_{tj}^\pm .

The simulations confirm the experimental observations of non-equilibrium triple junction angles and substantial triple junction drag seen in recent experiments [183, 436]. One discrepancy between the experiments and simulations is the conditions under which triple junction drag is significant. In the simulations, triple junction drag was never found to substantially retard boundary migration at grain sizes above approximately fifty inter-atomic spacings. On the other hand, the experiments have demonstrated triple junction drag for grain sizes in excess of $10 \mu\text{m}$. This difference is likely attributable to the presence of impurities on the grain boundaries in the experiments, while the simulations model (intrinsic) migration in an ideally pure material. This suggests that impurity effects, even in extremely high purity materials, may substantially influence grain boundary and triple junction migration because of segregation effects. Such an explanation is meaningful since impurities affect the triple junction and grain boundary mobility differently. Nonetheless, it is

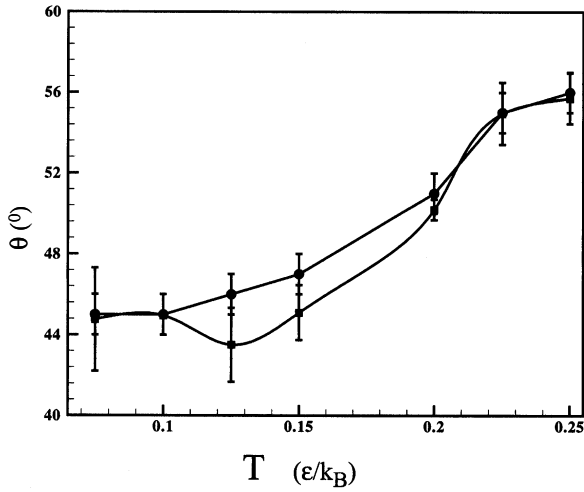


FIGURE 5.43

The dynamic triple junction angle β_d^+ vs. temperature T , for the “+” geometry and for simulation conditions $\varphi = 38.2^\circ$ and $T = 0.125\varepsilon/k_B$. The circles indicate the directly measured dynamic angles while the squares correspond to θ^+ from Figs. 5.41(a) and (b) [440].

emphasized that according to experimental results and computer simulation data that triple junction drag must always be considered for the thermal behavior of modern nano-structured materials.

“Pooh felt that he ought to say something helpful about it, but didn’t quite know what. So he decided to do something helpful instead.”

— *A.A. Milne*

6.1 Characterization of Microstructure and Texture

6.1.1 Introductory Remarks

Because of the complexity of microstructures in crystalline solids, it is virtually impossible to comprehensively characterize and, accordingly, represent microstructures. The microstructure of commercial materials like hardened steels or heavily deformed metals consists of complex morphological features, defect arrangements and phase distributions even under high magnification, i.e. on a nanoscale level.

For many applications only the macroscopic behavior of a material is of practical interest and, therefore, the common approach in the past was the correlation of macroscopic properties with average values of dominant microstructural features, usually features to be identified by optical microscopy, like grain size and macroscopic phase distribution besides overall chemistry. In crystalline solids the macroscopic properties are not necessarily isotropic, i.e. equal for all specimen directions. This is due to the fact that the individual crystals are non-random arrangements of atoms. On the contrary they consist of strictly aligned atoms on a long-range periodic pattern. Therefore, the physical properties of a crystal depend on the considered crystal direction, i.e. physical properties of crystallites are anisotropic, which requires their representation by a second rank tensor. A crystalline solid usually consists of many crystallites (typically $10^6/\text{mm}^3$). If the grains in a polycrystal are randomly arranged, then the anisotropic properties of the individual crystallites average out, and the polycrystal behaves isotropically. During the processing of a material to the final product, however, usually non-random distributions of crystallite orientations are generated, which cause an anisotropic behavior of

the macroscopic specimen. Therefore, in addition to the grain size and shape as well as the phase distribution and morphology, the orientation distribution is also of interest for macroscopic material behavior. The orientation distribution in crystalline solids is referred to as crystallographic texture, or simply texture¹.

The texture of a material is by definition a macroscopic average of the orientations in a polycrystalline aggregate (macrotexture). On a more local scale, the orientation distribution (microtexture) may be different from the macroscopic average, if orientation correlations exist, i.e. clustering of orientations or preferred next neighbors. Evidently, in deformed microstructures the orientation distribution in deformation inhomogeneities may be quite different from the homogeneously deformed matrix.

While the macrotexture determines the anisotropy of a material property, the microtexture provides information on the mechanisms of material behavior and microstructure evolution. More specifically, the microtexture encompasses the grain boundary character distribution so that all mechanisms involving grain boundary processes will be primarily affected by this microtextural characteristic.

In the framework of this text we will consider the effect of grain boundary motion on microstructure and texture development. Correspondingly, we shall confine microstructure characterization mainly to grain structures in single phase materials, i.e. characterized by grain size distribution and morphology as well as crystallographic texture, both on a macroscopic and microscopic level. The main features of both characterization groups, grain structure and texture, are textbook knowledge and thus will be only concisely reviewed in the following.

6.1.2 Microstructure

The grain size y of a crystalline solid is practically never uniform; rather, there is a grain size distribution Ψ (Fig. 6.1), which usually can be described by a log-normal distribution

$$\Psi(y)dy = \frac{1}{\sqrt{2\pi}\sigma} \exp \left(-\frac{1}{2} \left[\frac{\ln \left(\frac{y}{y_0} \right)}{\sigma} \right]^2 \right) d(\ln y) \quad (6.1)$$

¹We note at this point that the term texture is not understood unambiguously among the disciplines concerned with crystalline solid. While in the materials science community texture is synonymous with crystallographic texture, in mineralogy or geology the term texture stands for the morphological appearance of the usually complex minerals or rocks. Therefore, geologists choose the term “preferred orientation” rather than texture. Of course, there is also texture in textile fabrics, food and art with quite different meanings, but because we are so far removed from these disciplines there is no need to differentiate meanings. We shall refer to texture as crystallographic texture in the following.

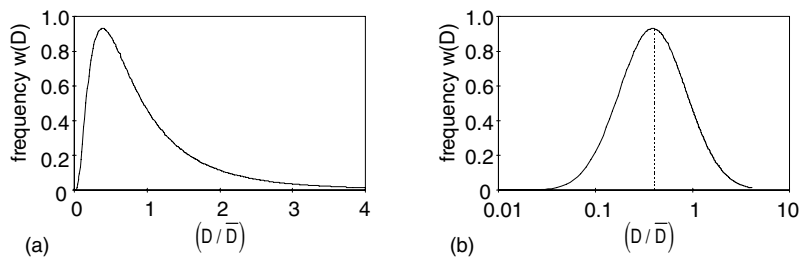


FIGURE 6.1
(a) Logarithmic normal distribution as given by Eq. (6.1) plotted linearly (normalized to mean grain size \bar{D}). The maximum is not at $D/\bar{D} = 1$. (b) Plot of the distribution in (a) over the logarithm of grain size. The distribution is symmetrical.

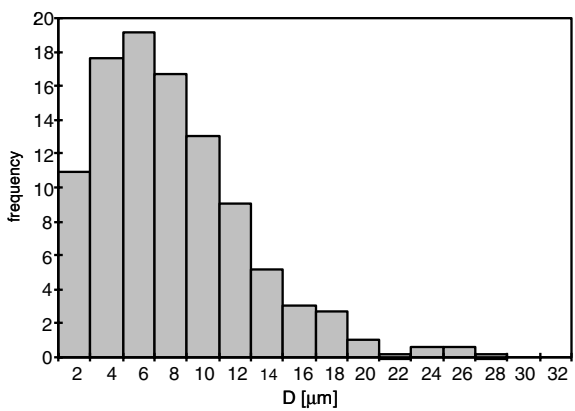


FIGURE 6.2
Histogram of grain size distribution in recrystallized Fe-17%Cr commercial sheet metal (70% rolled, annealed 250 min. at 1050°C).

Here, $\ln y_0$ is the mean value of $\ln y$ and σ is the width of the distribution and $\Psi(y^*)dy$ represents the frequency of grains of size y with $y^* \leq y \leq y^* + dy$. In a linear plot $\Psi(y)$ vs. y the distribution is asymmetrical (Fig. 6.2) and, therefore, the most frequent value y_0 (median) does not coincide with the average value (mean) \bar{y} . Rather, y_0 and \bar{y} are related by

$$y_0 = \exp(\ln \bar{y} - \sigma^2) \quad (6.2)$$

i.e. $y_0 < \bar{y}$. The log-normal distribution does not follow easily from fundamental considerations. On the contrary, from theoretical models of grain growth, the stationary grain size distribution, which would satisfy

$$\frac{d}{dt} \Psi \left(\ln \left[\frac{y}{y_0} \right] \right) = 0 \quad (6.3)$$

does not yield a log-normal distribution but a distribution, which is not observed in real grain structures. This contradiction is commonly reconciled by the assumption that the kinetic processes, which modify the grain structure toward a steady-state, cease to operate before a stationary distribution is attained, and the log-normal distribution represents an approximation of the non-stationary structure.

The mathematical grain size distribution as expressed in terms of Eq. (6.1) and displayed in Fig. 6.1 relates to an infinitely large assembly of grains. Despite the large number of grains in a polycrystal ($10^6/\text{mm}^3$) one would probably not find any grain with a precisely given grain size. Therefore, experimental grain size distributions are represented in terms of histograms, where the frequency of grains in a given size interval is plotted as a bar graph (Fig. 6.2).

Neither the average grain size nor the grain size distribution can provide a comprehensive description of polycrystalline aggregates. Grain morphology and topology are rarely accounted for, since stereology requires laborious specimen handling for a 3D image of the grain assembly. Grain shape — in terms of ellipticity — or distribution of the number of grain edges and corners can be determined to more adequately represent the grain structure. However, owing to the extraordinary efforts involved in gaining this information experimentally, it is only collected on particular need, e.g. if grain topology plays a role for the problem under consideration, as in a comprehensive treatment of grain growth. Nowadays, powerful image analysis systems, which allow digital storage of metallurgical micrographs, i.e. sections through grain assemblies, are now becoming available to facilitate stereological evaluation.

The quantitative evaluation of heterogeneous microstructures from 2D sections is the subject of textbooks on stereology and image analysis systems. In the context of grain boundaries in single phase materials areas of primary interest usually include grain size, grain shape and spatial orientation of grain boundary planes. There are two basic methods to determine the average grain size: lineal and areal analysis. An automated image analysis system will reveal

the boundaries in a planar section and determine the mean cross section \bar{A} of a grain, from which the mean grain size \bar{D} can be derived, assuming equiaxed grain shape

$$\bar{D} = \sqrt{\bar{A}} \quad (6.4)$$

For manual evaluation of micrographs from planar sections, it is most common to superimpose parallel lines to the microstructure such that any single grain is intersected only once by a line. Then the number N of intersections of grain boundaries with the total line length L is counted to yield the average grain size \bar{D}

$$\bar{D} = \frac{L}{N} \quad (6.5)$$

as a mean linear intercept. In the case of nonequiaxed microstructures the linear intercepts in three perpendicular directions \bar{D}_1 , \bar{D}_2 , \bar{D}_3 have to be determined, requiring two mutually perpendicular sections, to yield

$$\bar{D} = (\bar{D}_1 \cdot \bar{D}_2 \cdot \bar{D}_3)^{1/3} \quad (6.6)$$

The ratios \bar{D}_1/\bar{D}_2 , \bar{D}_2/\bar{D}_3 , \bar{D}_1/\bar{D}_3 denote the respective ellipticity or aspect ratio.

A quantity of particular interest with regard to grain boundaries is the surface area A_v per unit volume, which is found to be [565]

$$A_v = \frac{2}{\bar{D}} = 2 \cdot \frac{N}{L} \equiv 2N_L \quad (6.7)$$

In the case of non-equiaxed microstructures

$$A_v = 0.429 N_{L1} + 2.571 N_{L3} - N_{L2} \cong \left[0.429 \frac{\bar{D}_2}{\bar{D}_1} + 2.571 \frac{\bar{D}_2}{\bar{D}_3} - 1 \right] N_{L2} \quad (6.8)$$

where N_{Li} represents the respective inverse linear intercepts or boundary counts per unit length [566].

6.1.3 Crystallographic Texture

6.1.3.1 Definitions

Metallic materials are crystalline, i.e. within a crystallite the atoms are arranged in a strictly periodic pattern, which is represented by the crystallographic unit cell of the particular crystal structure. While all grains of a polycrystal have the same crystal structure, the orientation of the unit cell with respect to the macroscopic specimen coordinate system changes from grain to grain. This relationship between spatial orientation of the crystallographic unit cell as defined by its fundamental crystallographic axes and the macroscopic specimen system as defined by its characteristic directions is referred to as crystallographic orientation. The distribution of orientations in

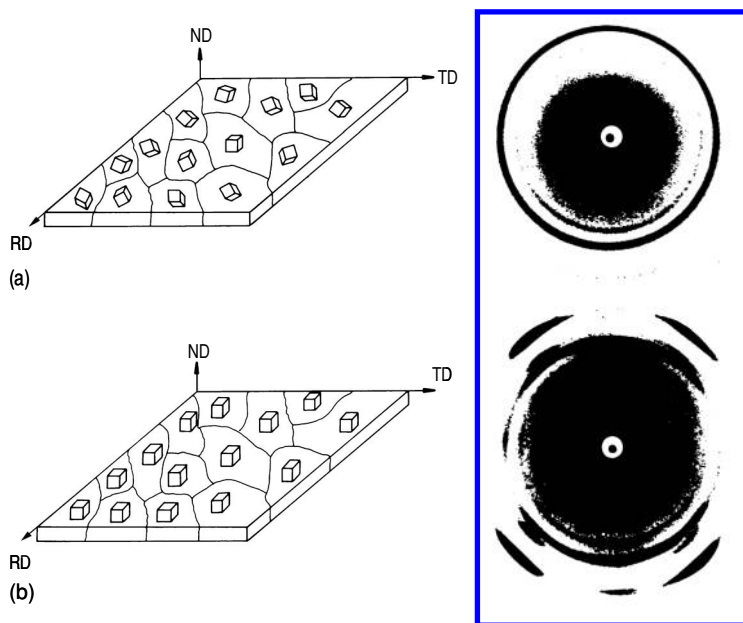


FIGURE 6.3

Schematic representation of the orientation distribution and the resulting Debye-Scherrer images in sheet metal with (a) random distribution; (b) when a preferred orientation exists (here: Cube texture).

a polycrystal is termed its crystallographic texture, or simply texture. Real textures comprise very different cases, from a random orientation distribution (random or gray texture) to a single component texture, the extreme of which would be a single crystal (Fig. 6.3).

Quantitatively, the texture is represented by the orientation distribution function (ODF) $f(g)$ [567, 568], where $f(g^*)dg$ is the specimen volume fraction dV/V with orientation g^* in the interval $g^* \leq g \leq g^* + dg$, i.e.

$$f(g)dg = \frac{dV}{V} \quad (6.9)$$

Since the orientation of a cubic crystal is defined as the relation between the (orthonormal) crystal axes and the (orthonormal) specimen axes, it is mathematically represented by the rotation that makes the specimen axes align with the crystal axes. There is an infinite number of ways to prescribe a procedure of rotations that makes two coordinate systems coincide. Irrespective of the procedure, however, the rotation is mathematically formulated in a unique way, namely by the rotation matrix \mathbf{g} , which is defined as

$$\mathbf{r}' = \mathbf{g}\mathbf{r} \quad (6.10)$$

where \mathbf{r} represents any vector of the unrotated system and \mathbf{r}' is the corresponding vector in the rotated system. By using the bases of the two systems to define the vector \mathbf{r} or \mathbf{r}' it is obvious that the columns of the (3×3) matrix \mathbf{g} correspond to the direction cosines of the base vectors of the rotated system with respect to the unrotated system.

Three quantities are necessary to describe a rotation in three dimensions, for example three angles of subsequent rotations around prescribed axes. Since there is an infinite set of three axes, there is an infinite number of ways to put up the rotation matrix. There are three ways which are most convenient and, therefore, most commonly used to describe an orientation relationship (Fig. 6.4c):

a) Axis and angle of rotation: $\omega[\text{HKL}]$ (Fig. 6.4a). It is easy to imagine and readily handled in stereographic projection. The notation is especially useful for the treatment of problems related to grain boundaries, as the type of grain boundary is commonly defined by the orientation of the boundary plane with respect to the axis of rotation² (see Chapter 2).

b) Miller indices (Fig. 6.4c): 2 crystallographic directions in coordinate system 1, which are parallel to the base vectors of coordinate system 2. For instance, for rolling geometry parallel to rolling plane normal: (hkl) and rolling direction: $[uvw]$. It is commonly used when the crystal lattice is to be related to the specimen coordinate system, e.g. in a tensile sample with respect to the tensile axis or for rolling geometry with respect to rolling plane and rolling direction.

c) The three Euler angles (Fig. 6.4b): $\varphi_1, \Phi, \varphi_2$. This is widely used for an analytical treatment of rotations. It is standard for the calculation and representation of textures in terms of the three-dimensional orientation distribution function (ODF).

The rotation matrix \mathbf{g} is only unique if there is no crystal symmetry [568]. In cubic crystals there is a 24-fold symmetry, i.e. there are 24 different rotations \mathbf{S}_i^c which do not change the position of lattice points. Each rotation \mathbf{g} may, therefore, be superimposed by any combination of \mathbf{S}_i^c to give an equivalent orientation of the rotated lattice. Any of the 24 different orientations of a vector \mathbf{r}_i in cubic lattices is, therefore, obtained by

$$\mathbf{r}'_i = \mathbf{S}_i^c \cdot \mathbf{g} \cdot \mathbf{r}_i \quad (6.11)$$

²This definition of the grain boundary character is not unambiguous in crystal structures of high symmetry, like the cubic lattice. Depending on the choice of the 24 possible symmetry elements in a cubic lattice, a grain boundary may be either tilt or twist boundary. An example gives the coherent twin plane in fcc crystals. Its Miller indices (plane normal) are $\{111\}$, in particular (111) . The twin orientation can be described by a $60^\circ[111]$ rotation. In this case the (111) boundary plane is a twist boundary. A symmetrically equivalent rotation is $70.6^\circ[1\bar{1}0]$. The coherent twin boundary is now a tilt boundary. Therefore, for uniqueness in highly symmetric lattices additional rules of selection have to be applied. Unambiguity is attained by selection of the smallest angle of rotation.

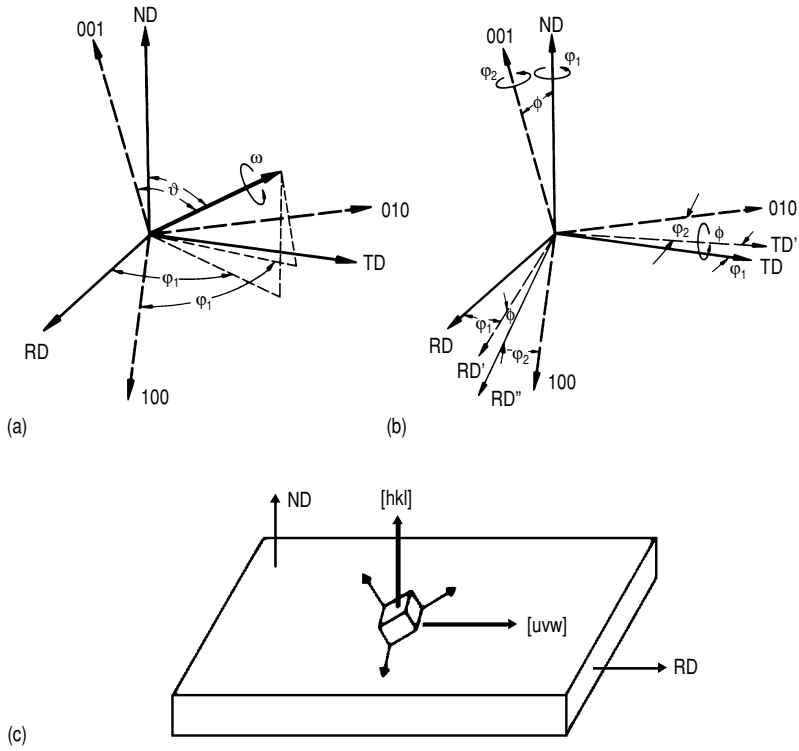


FIGURE 6.4

Different representation of an orientation relationship: (a) axis and angle of rotation; (b) Euler angles; (c) Miller indices.

($i = 1, 24$). \mathbf{S}_i^c is any of the 24 cubic symmetry matrices. In addition there may be a specimen symmetry, like the orthorhombic specimen symmetry of a rolled specimen. If the specimen symmetry matrices are denoted by \mathbf{S}_k^s ($k = 1, \max$), then

$$\mathbf{r}'_{ik} = [\mathbf{S}_i^c \cdot (\mathbf{S}_k^s)^{-1}] \mathbf{r} \quad (6.12)$$

6.1.3.2 The Rotation Matrix

Except for the symmetry relations given in Eq. (6.11) the rotation matrix is unique, irrespective of the way it is derived. It can be expressed in terms of Euler angles, Miller indices and axis-angle pair as given below. A calculation of the rotation matrix is given in Appendix B.

\mathbf{g} in terms of Euler angles $\mathbf{g}\{(\varphi_1, \Phi, \varphi_2)\}$ is defined as

$$\mathbf{g} = \begin{bmatrix} \cos \varphi_1 \cos \varphi_2 - \sin \varphi_1 \sin \varphi_2 \cos \phi & \sin \varphi_1 \cos \varphi_2 + \cos \varphi_1 \sin \varphi_2 \cos \phi & \sin \varphi_2 \sin \phi \\ -\cos \varphi_1 \sin \varphi_2 - \sin \varphi_1 \cos \varphi_2 \cos \phi & -\sin \varphi_1 \sin \varphi_2 + \cos \varphi_1 \cos \varphi_2 \cos \phi & \cos \varphi_2 \sin \phi \\ \sin \varphi_1 \sin \phi & -\cos \varphi_1 \sin \phi & \cos \phi \end{bmatrix} \quad (6.13)$$

\mathbf{g} in terms of Miller indices $\mathbf{g}\{(hkl)[uvw]\}$ is defined as

$$\mathbf{g} = \begin{bmatrix} \frac{u}{N_1} & \frac{v1-kw}{N_3} & \frac{h}{N_2} \\ \frac{v}{N_1} & \frac{hw-u1}{N_3} & \frac{k}{N_2} \\ \frac{w}{N_1} & \frac{uk-vh}{N_3} & \frac{l}{N_2} \end{bmatrix} \quad (6.14)$$

where $N_1 = \sqrt{u^2 + v^2 + w^2}$, $N_2 = \sqrt{h^2 + k^2 + l^2}$, and $N_3 = N_1 \cdot N_2$; \mathbf{g} in terms of axis and angle of rotation $\mathbf{g}\{\omega[a_1, a_2, a_3]\}$ is defined as

$$\mathbf{g} = \begin{bmatrix} (1-a_1^2) \cos \omega + a_1^2 & a_1 a_2 (1-\cos \omega) + a_3 \sin \omega & a_1 a_3 (1-\cos \omega) - a_2 \sin \omega \\ a_1 a_2 (1-\cos \omega) - a_3 \sin \omega & (1-a_2^2) \cos \omega + a_2^2 & a_2 a_3 (1-\cos \omega) + a_1 \sin \omega \\ a_1 a_3 (1-\cos \omega) + a_2 \sin \omega & a_2 a_3 (1-\cos \omega) - a_1 \sin \omega & (1-a_3^2) \cos \omega + a_3^2 \end{bmatrix} \quad (6.15)$$

Since the rotation matrix is unique and independent of its derivation, Euler angles, Miller indices and axis and angle of rotation can be extracted from a given rotation matrix with the relations given above.

6.1.3.3 Stereographic Projection, Pole Figure and Inverse Pole Figure

Orientations are most commonly represented by their pole figures in the stereographic projection (Fig. 6.5). The stereographic projection is a two-dimensional image of the three-dimensional orientation space. It is constructed by placing the origin of the coordinate system in the center of a sphere. A direction $[hkl]$ (or the normal of a plane (hkl)) centered in the origin will intersect a surrounding sphere at a point P . The connection of P with the south pole S of the sphere intersects the equatorial plane at P' . P' is called the pole of the direction $[hkl]$ (or plane (hkl)). The projection of different low

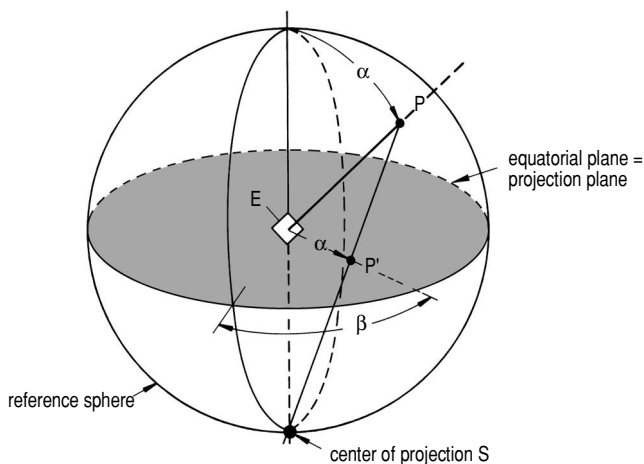
**FIGURE 6.5**

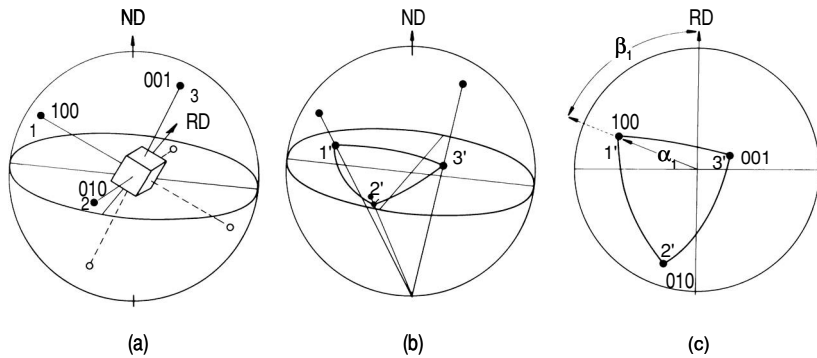
Illustration of the principle of stereographic projection: E — crystallographic plane, P' — pole of E in stereographic projection.

index directions with $[001]$ pointing to the north pole of the sphere — which becomes the center of the projection — is called the (001) or standard projection.

Limitation to only one set of crystallographically equivalent poles $\{hkl\}$ represents the $\{hkl\}$ pole figure in standard projection (Fig. 6.6). All other poles can be constructed by means of the known crystal symmetry. For the standard projection pole figures are trivial and superfluous. The reference coordinate system, however, is usually the specimen coordinate system $\{S\}$. The orientation of a crystallite with respect to $\{S\}$ is then denoted by the position of its poles within this reference system. This may be illustrated by an example.

A rolled sample has the distinguished specimen coordinate axes: rolling direction (RD) and rolling plane normal (ND). Consequently, the third orthogonal axis is the transverse direction (TD). The $\{hkl\}$ pole figure of a crystallite is then given by the position of the poles $\{hkl\}$ within this coordinate system. The orientation relationship between specimen coordinate system and crystal coordinate system is usually and easily described by the crystallographic direction parallel to the rolling plane normal (hkl) and the rolling direction $[uvw]$.

While in normal pole figures the crystal orientation is represented with respect to a given specimen coordinate system as a reference, in the inverse pole figure the specimen coordinate system is represented with respect to a given crystal coordinate system (standard position) as a reference (Fig. 6.7). This is most useful if only one specimen axis is distinguished, like the axis of a

**FIGURE 6.6**

Representation of an orientation in terms of the $\{100\}$ axes in stereographic projection. (a) Position of the crystal at the center of the orientation sphere; (b) stereographic projection of the cubic axes; (c) $\{100\}$ pole figure showing orientation and definition of the angles α_1 and β_1 associated with pole 1.

wire or a tensile specimen. In cubic crystals the representation can be reduced to only one characteristic stereographic triangle framed by, e.g. (001) – (011) – $(\bar{1}11)$, because of the crystal symmetry.

For more difficult specimen geometries the inverse pole figure can also be constructed, but it is less convenient to use, since the whole projection plane is needed to represent more than one axis in an inverse pole figure. Therefore, in such cases, a representation as a pole figure is more appropriate and easier to imagine.

6.1.3.4 Measurement and Analysis of Pole Figures

The importance of pole figures can be attributed to the fact that they can be experimentally determined with an X-ray texture goniometer. Its principle of operation is based on Bragg's law, i.e. the reflection of X-rays of wavelength λ is obtained from a set of planes $\{hkl\}$ if

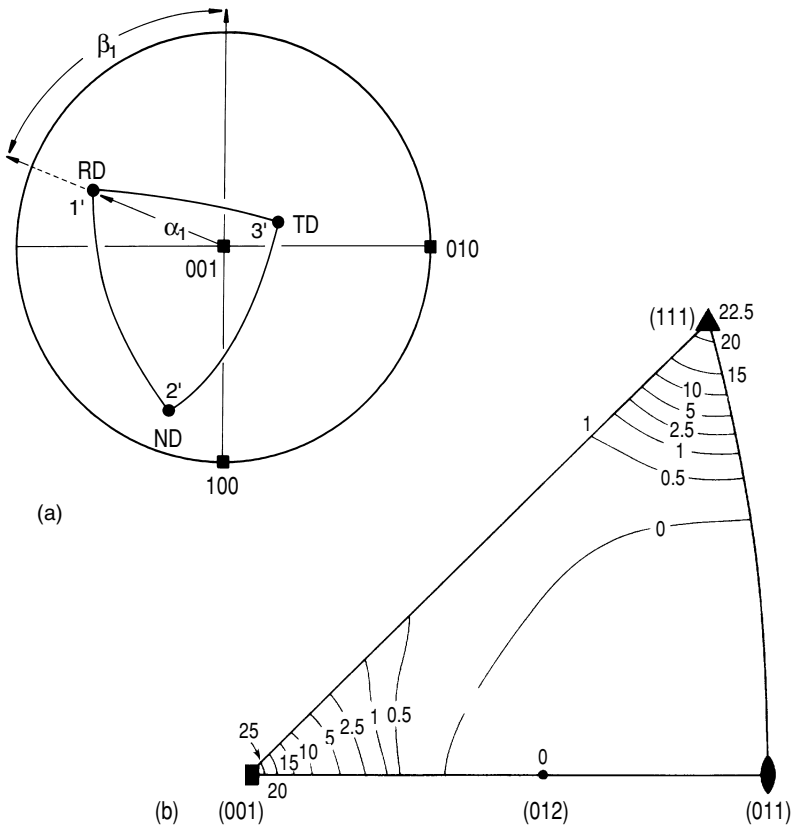
$$\lambda = 2d \cdot \sin \Theta \quad (6.16)$$

where Θ is the angle between incident X-ray beam and lattice plane normal $\{hkl\}$ (Fig. 6.8). The spacing d between adjacent planes $\{hkl\}$ in cubic crystals is given by

$$d = \frac{b}{\sqrt{h^2 + k^2 + l^2}} \quad (6.17)$$

where b denotes the lattice parameter.

The lattice plane normal $\{hkl\}$ bisects the incident and reflected beam at an angle Θ . For a given wave length λ and for a constant angle 2Θ between

**FIGURE 6.7**

(a) Diagrammatic illustration of the inverse pole figure of a sample of rolled material; (b) Inverse pole figure of extruded aluminum wire (sample orientation = wire axis). The lines indicate contours of equal measured intensity (after [569]).

X-ray source and counter a reflected signal is counted only if a plane $\{hkl\}$ is in reflection position. By rotating the specimen around two perpendicular specimen axes up to ideally 90° all possible positions of planes $\{hkl\}$ will be found. Since Bragg's law does not discriminate signs of $\{hkl\}$ all combinations of $\{\pm h, \pm k, \pm l\}$ will contribute, i.e. all equivalent poles will be recorded (Fig. 6.9).

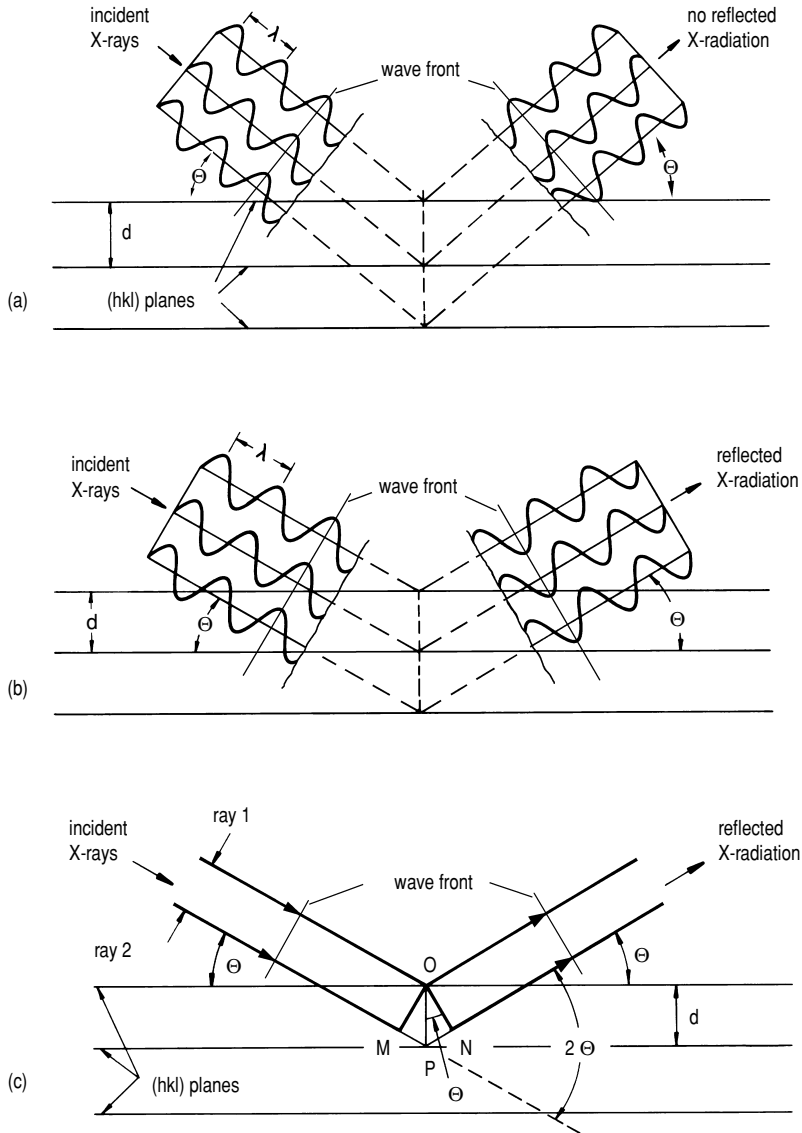
If the specimen is a polycrystal, all crystallites having a set $\{hkl\}$ in reflection position will contribute to the measured intensity for a given position (α, β) of the specimen. The result of such a measurement is the frequency of occurrence of a given pole $\{hkl\}$ in all illuminated crystals for any given position (α, β) of the specimen, i.e. the pole intensity distribution.

To keep evaluation simple, low index poles like $\{200\}$, $\{220\}$ and $\{111\}$ for fcc crystals are usually chosen³.

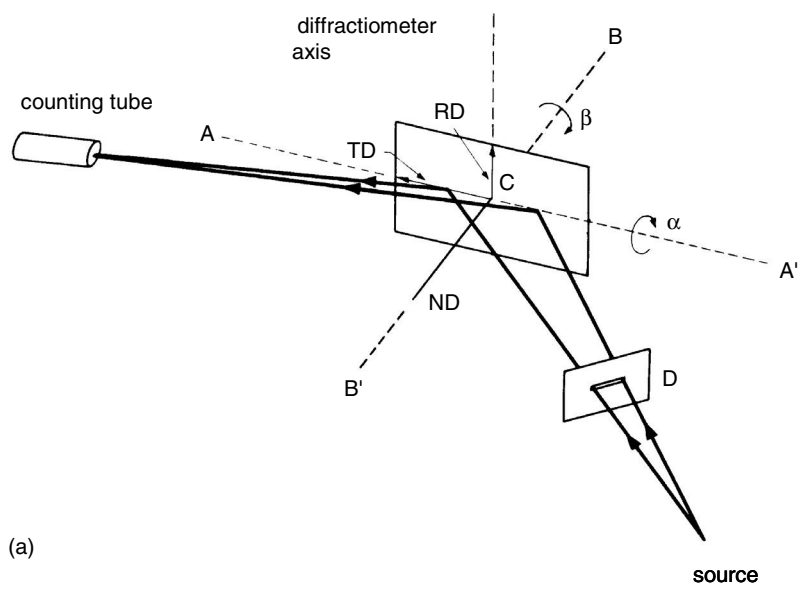
The pole figure represents the distribution of a specific family of lattice planes in the stereographic projection. Because of the known crystallography of the reflecting crystal lattice, it is possible to determine the orientation of an illuminated crystal. To begin with, all poles which belong to the same orientation, for instance, all four $\{111\}$ or all three $\{100\}$ poles have to be identified. Since the angles between these crystallographic directions (for instance 90° between any two $\{100\}$ poles) are known, the orientation can be calculated. A worked example is given in Appendix C.

In case of single crystals or very simple types of textures (for instance, the Cube texture) the evaluation of a single pole figure is sufficient to determine the orientation, since the poles belonging to the same orientation are easy to identify. However, if several orientations occur concurrently, it is possible that poles of different orientations overlap, which renders impossible an unambiguous association of poles to a defined orientation. In such a case it is necessary to utilize more than one pole figure to identify orientations. In experimental pole figures of polycrystals, however, an identification of all components is extremely difficult even when several pole figures are known. In particular, a quantitative analysis of weaker components is practically impossible. The fundamental reason for this deficiency of a texture analysis by means of pole figures is the fact that a pole figure is a two-dimensional projection (of the crystal axes) of a three-dimensional quantity (the orientation). This projection is accompanied by a loss of information, which would be necessary to identify the poles belonging to a common crystal orientation. However, in the past 20 years mathematical tools have been developed that use high-power computers to calculate the orientation distribution function (ODF) from a few measured pole figures [567]. The result of this computation is not unambiguous. In fact, it is impossible to determine the true ODF from experimental pole figures. This is due to the fact that Bragg's law does not differentiate between $\{hkl\}$

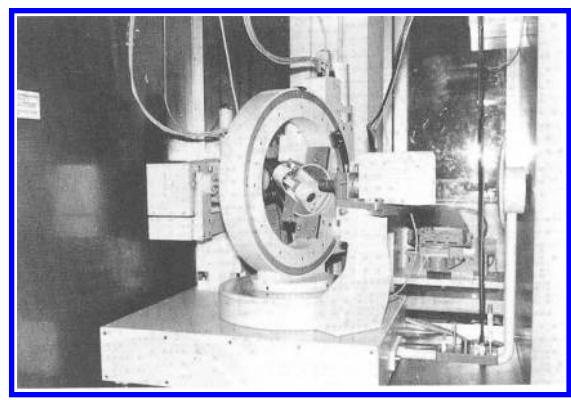
³Because of extinction, in fcc crystals only reflection occurs where the Miller indices are either all even or all odd, i.e. $\{111\}$, $\{200\}$, In bcc crystals, reflections only occur if the sum $h + k + l$ is even, i.e. $\{110\}$, $\{200\}$,

**FIGURE 6.8**

X-ray diffraction by a crystal lattice can be regarded as reflection from a semi-reflecting mirror. Only if rays diffracted by parallel planes are in phase (b) (equal phase in every plane perpendicular to the direction of propagation), they will not cancel each other out (like in (a)) and reflection will occur. Equal phase will result only if the path difference from successive planes (MPN in (c)) is an integral number of wave lengths. This condition leads to the Bragg equation.



(a)



(b)

FIGURE 6.9
(a) Beam geometry and sample rotation in an X-ray-texture goniometer (here: the Schulz reflection method); (b) X-ray-texture goniometer at the IMM.

and $\{\overline{hkl}\}$ poles so that from pole figures only the symmetrical components of the ODF can be determined. There are also a variety of methods to determine the asymmetrical components; however, such solutions are not unique. Usually the omission of the odd coefficients generates so-called ghosts, that is, falsely pretended intensities in the ODF, which can be corrected for, if the major components of the ODF are known. If, however, the true ODF of an unknown texture ought to be determined, it would be more reasonable to complement macroscopic pole figure measurements by single grain orientation measurements in terms of orientation imaging microscopy (OIM), from which the true ODF can be calculated, although the number of measured individual grains may be much smaller than the number of grains contributing to the intensity in the X-ray pole figure measurements [570, 571]. It has been demonstrated recently that, for reasonably defined textures, the true ODF of a polycrystalline specimen can be calculated with sufficient accuracy from about a thousand randomly sampled individual grain orientation measurements.

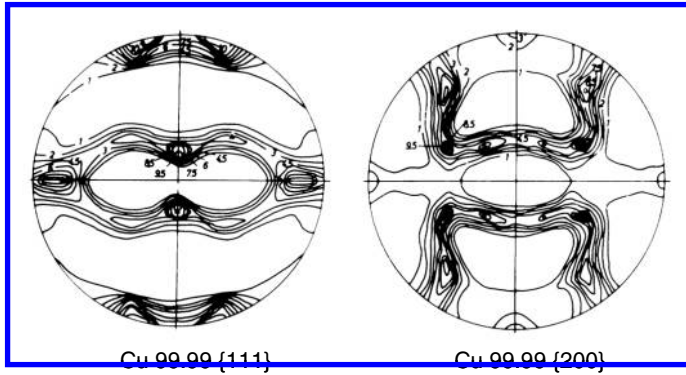
6.1.3.5 The Orientation Distribution Function (ODF)

The association of poles belonging to a particular orientation from the intensity distribution in a pole figure of a polycrystal is usually impossible to determine. The problem can be alleviated by measuring a second pole figure and identifying orientations which comply with both pole figures. This is very tedious but it often helps remove ambiguity or rule out the occurrence of a particular orientation.

A famous example for illustration of this problem is the cube orientation in the Cu-rolling texture. As will be shown below, a sharp cube texture is the recrystallization texture of the Cu-type rolling texture. For elucidation of the texture development it is most important to know whether the cube orientation is already present in the rolling texture. The $\{111\}$ pole figure of the rolling texture indicates (falsely) that this might be the case (Fig. 6.10). But the $\{200\}$ pole figure of the rolling texture reveals a definite absence of the cube orientation $(001)[100]$ in the deformed material, as evident from the missing intensity in the center of the $\{200\}$ pole figure.

In most cases even two pole figures are not sufficient for obtaining an unambiguous assignment, leaving alone the cumbersome task to compare the possible orientations. Modern texture analysis instead utilizes the three-dimensional orientation space. This is the space where any orientation is represented unambiguously by only one point. Orientation space is set up by the axes of a three-dimensional coordinate system, where each axis represents one of the three quantities that define a given rotation. Correspondingly, the origin (i.e. no rotation) is the standard orientation (or the orientation of any given external reference system).

Most common is the rectangular coordinate system with the three Euler

**FIGURE 6.10**

{111} and {200} pole figures of 95% rolled Cu.

angles $\varphi_1, \Phi, \varphi_2$ as axes. Any point $g^0 (\varphi_1^0, \Phi^0, \varphi_2^0)$ in orientation space is uniquely described by its Euler angles and, therefore, represents exactly the orientation which is obtained by rotating the standard position $(0, 0, 0)$ by the angles $\varphi_1^0, \Phi^0, \varphi_2^0$. This three-dimensional orientation space is also referred to as Euler space.

For cubic crystal symmetry and orthorhombic specimen symmetry (like in rolling) all orientations occur three times in the triple unit cell $0 \leq \varphi_1, \Phi, \varphi_2 \leq \pi/2$ [568]. The function $f(g)$ which describes the frequency of occurrence (intensity) of any particular orientation g in a crystalline aggregate is called the three-dimensional orientation distribution function (ODF). As pointed out in Section 5.1.3.1 the value of $f(g)$ for a given g represents the volume fraction dV/V of material that has an orientation within an infinitesimal volume around g in orientation space

$$f(g)dg = \frac{dV}{V} \quad (6.18)$$

which takes note of the normalization

$$\frac{1}{8\pi^2} \int f(g)dg = 1 \quad (6.19)$$

where integration is performed over a complete unit cell of the orientation space.

The measured $\{hkl\}$ pole figure P_{hkl} gives only the distribution of a particular crystal axis $[hkl]$. Every orientation that has an axis $[hkl]$ at a given point P^0 in the pole figure contributes to the intensity at P^0 . With a point in the $\{hkl\}$ pole figure given by its polar coordinates (α, β) the intensity P_{hkl} is given

$$P_{hkl}(\alpha, \beta) = \frac{1}{2\pi} \int_0^{2\pi} f(\alpha, \beta, \gamma) d\gamma \quad (6.20)$$

Since the rotation g is defined on a sphere, $f(g)$ can be readily expanded in terms of the generalized spherical harmonics $T_{\lambda}^{\mu\nu}$ (which are the known generalized Legendre polynomials)

$$f(g) = \sum_{\lambda=0}^{\infty} \sum_{\mu=-\lambda}^{\lambda} \sum_{\nu=-\lambda}^{\lambda} C_{\lambda}^{\mu\nu} T_{\lambda}^{\mu\nu}(g) \quad (6.21)$$

Expansion of $P_{\text{hkl}}(\alpha, \beta)$ in terms of the reduced spherical harmonics $k_{\lambda}^{\nu}(\alpha, \beta)$ yields

$$P_{\text{hkl}}(\alpha, \beta) = \sum_{\lambda=0}^{\infty} \sum_{\nu=-\lambda}^{\lambda} F_{\lambda}^{\nu}(\text{hkl}) k_{\lambda}^{\nu}(\alpha, \beta) \quad (6.22)$$

The correlation between Eq. (6.22) and Eq. (6.21) is given by the integral equation (5.20) which renders the relation of the coefficients F_{λ}^{ν} and $C_{\lambda}^{\mu\nu}$

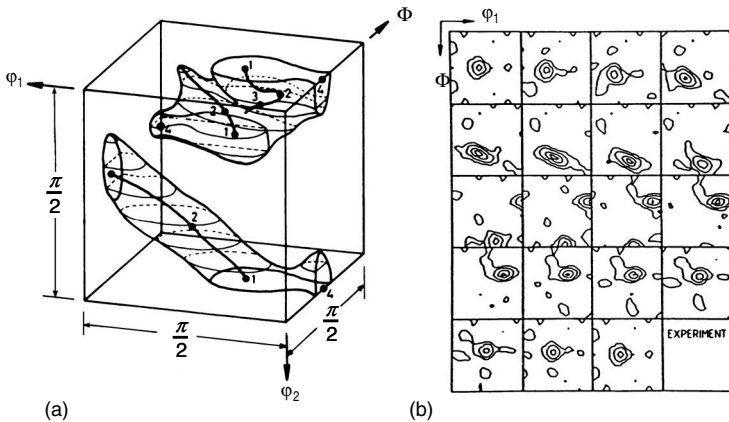
$$F_{\lambda}^{\nu}(\text{hkl}) = \frac{4\pi}{2\lambda+1} \sum_{\mu=-\lambda}^{\lambda} C_{\lambda}^{\mu\nu} k_{\lambda}^{\mu}(\alpha, \beta) \quad (6.23)$$

Since $T_{\lambda}^{\mu\nu}$ is known analytically, and $C_{\lambda}^{\mu\nu}$ can be calculated from P_{hkl} according to Eqs. (6.23) and (6.22) [567], $f(g)$ can be computed from Eq. (6.21). For practical purposes the expansion has to be limited to finite values of λ .

Current evaluation programs commonly truncate for $\lambda > 22$. Taking into account specimen and crystal symmetry simplifies the procedure for rolled cubic crystals considerably. In contrast, textures of materials with low crystal symmetry (most minerals) are not yet analyzed on a sophisticated level.

The computed result for the Cu-rolling texture is shown as an example in Fig. 6.11. The lines connect points of 1/2 maximum intensity. The texture resembles a tube in Euler space. The three-dimensional drawing of contour lines in orientation space is rather inconvenient. Instead, sections parallel to φ_2 in increments of $\Delta\varphi_2 = 5^\circ$ are usually presented in the literature.

It is noted again that in highly symmetric lattices like the cubic structure, the interpretation of the ODF in Euler space is complicated by the presence of three crystallographically equivalent orientations in the cell $0 \leq \varphi_1, \Phi, \varphi_2 \leq \pi/2$. The appropriate unit cell which accounts for specimen symmetry as well as crystal symmetry can be of rather complicated shape and, therefore, inconvenient to handle. Usually, the ODF is represented in $0 \leq \varphi_1, \Phi, \varphi_2 \leq \pi/2$ and the reader has to take note of the multiplicity of symmetric components. Owing to a long tradition of research on rolling textures in cubic crystals the most familiar notation of an orientation is still $\{\text{hkl}\}\langle uvw \rangle$. For practical purposes there are conversion tables from $\{\text{hkl}\}\langle uvw \rangle$ to $(\varphi_1, \Phi, \varphi_2)$ to facilitate evaluation.

**FIGURE 6.11**

(a) 3D representation of the orientation distribution of rolled high purity copper in Euler space. Unlike in the 2D pole figure, here an orientation is represented unambiguously in three coordinates (by three Euler angles); (b) Illustration of the orientation distribution by sections through Euler space perpendicular to the angle φ_2 at 5° intervals.

6.1.3.6 Quantitative Analysis in Terms of Scattered Ideal Orientations

The contour lines of the ODF are rather inconvenient for practical use. Real textured material contains, however, strong maxima as well as regions with virtually zero intensity. The maximum intensity can exceed the intensity of a random distribution (i.e. distribution of a powder specimen) by a factor of 100 and more. The common way of qualitative texture analysis is, therefore, the interpretation of pole figures and ODFs in terms of ideal orientations, which coincide with the dominant maxima in the intensity distribution [572]. When the intensity maxima are smeared out, there is a certain ambiguity on how many ideal orientations are necessary to represent the ODF, and what is their most adequate notation. The Cu-rolling texture is represented in the ODF in Fig. 6.11 and in the pole figure in Fig. 6.10. The intensity maxima are well represented by three ideal orientations which are known under the names: $\{011\}\langle 21\bar{1} \rangle$ brass orientation (main component in brass-rolling texture), $\{112\}\langle 11\bar{1} \rangle$ Cu-orientation (main component in Cu-rolling texture) and $\{123\}\langle 634 \rangle$ S-orientation (leads to S-shape of Cu-rolling texture).

For a quantitative texture analysis the scatter σ around the ideal orientation must be taken into account. For this purpose the ODF is fitted by Gauss-type

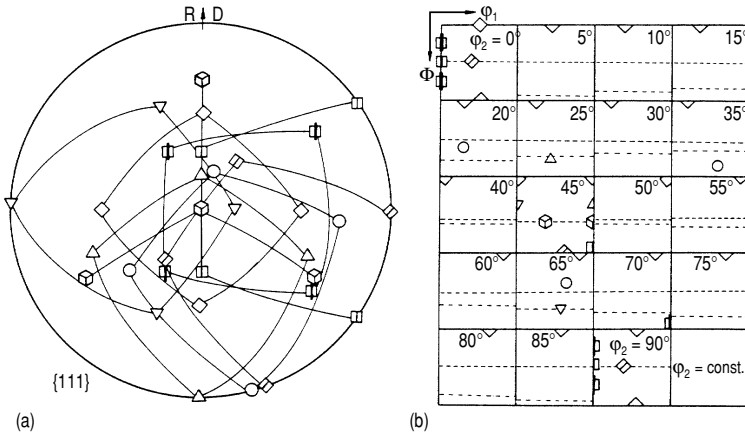


FIGURE 6.12

Main rolling texture components of cubic metals. (a) {111} pole figure; (b) in Euler space.

distributions around ideal orientations [573]:

$$S_i(g) = S_i(g_0) \exp \left[-\frac{(g - g_0)^2}{\sigma_i^2} \right] \quad (6.24)$$

$$f(g_0) = \sum_i S_i(g) \quad (6.25)$$

From the result the volume fraction M_i of each texture component can be derived by integration of Eq. (6.18) within the orientation regime of each component and taking note of Eq. (6.19).

$$M_i = \frac{1}{2\sqrt{\pi}} Z_i S_i(g_0) \sigma_i \left[1 - \exp \left(-\frac{\sigma_i^2}{4} \right) \right] \quad (6.26)$$

Tables 6.1 and 6.2 and Figs. 6.12 and 6.13 summarize the most important components of the rolling textures (Fig. 6.12) and recrystallization textures, (Fig. 6.13) of cubic metals and alloys.

6.1.3.7 Misorientation Distributions

While an orientation represents a rotation of the specimen coordinate system into the crystal coordinate system, a misorientation corresponds to the rotation that makes the two crystal orientations coincide. Therefore, a misorientation distribution can be represented like an orientation distribution, in

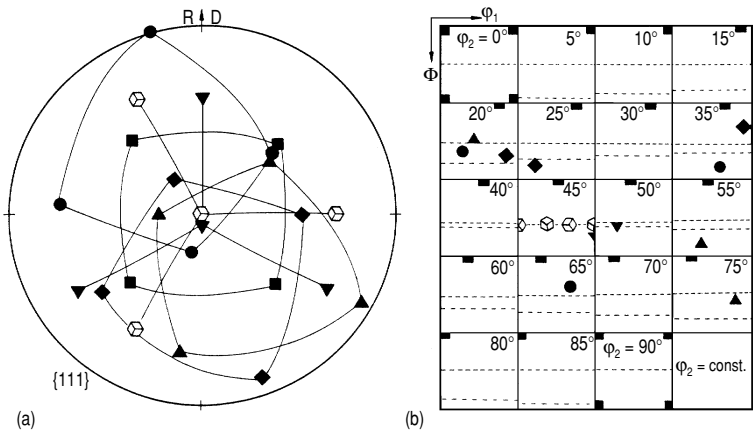


FIGURE 6.13
Main recrystallization texture components of cubic metals. (a) {111} pole figure; (b) in Euler space.

TABLE 6.1
Main Rolling Texture Components of Cubic Metals

Notation	{hkl}	$\langle uvw \rangle$	φ_1	Φ	φ_2	Symbol
C	{112}	$\langle 11\bar{1} \rangle$	90°	35°	45°	\triangle
S	{123}	$\langle 63\bar{4} \rangle$	59°	37°	63°	\circ
Bs	{011}	$\langle 21\bar{1} \rangle$	35°	45°	0°	\diamond
Goss	{011}	$\langle 100 \rangle$	0°	45°	0°	\boxplus
	{112}	$\langle 110 \rangle$	0°	35°	45°	∇
Rotated Cube	{001}	$\langle 110 \rangle$	45°	0°	0°	\diamond
	{111}	$\langle 11\bar{2} \rangle$	90°	55°	45°	\boxtimes
Cube _{RD}	{025}	$\langle 100 \rangle$	0°	22°	0°	\boxplus

principle. The most commonly used space to represent an orientation distribution is the Euler space, in particular for the reason that the Euler angles can be handled as independent and separate variables for the computation of the ODF. Despite its standard use, Euler space has major disadvantages owing to its severe distortions, in particular for rotations about the *z* (ND) direction.

A representation of misorientation more easy to imagine is the notation in terms of axis **n** and angle ω of rotation, which can be most conveniently represented by its Rodrigues vector [574, 575]

$$\mathbf{R} = \mathbf{n} \cdot \tan \frac{\omega}{2} \tag{6.27}$$

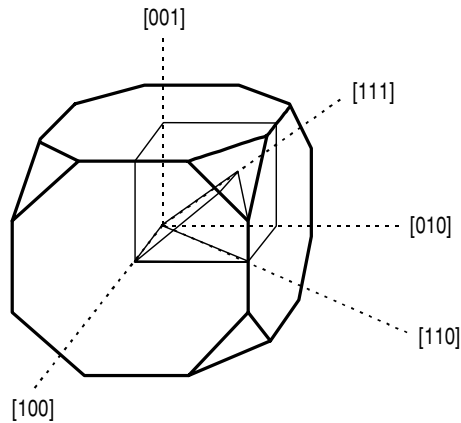
TABLE 6.2
Main Recrystallization Texture Components of Cubic Metals

Notation	{hkl}	⟨uvw⟩	φ_1	Φ	φ_2	Symbol
Cube	{001}	⟨100⟩	0°	0°	0°	■
R	{123}	⟨634⟩	59°	37°	63°	●
or also	{124}	⟨211̄⟩	57°	29°	63°	
bs/R	{236}	⟨385⟩	79°	31°	33°	◆
Intermediate	{258}	⟨121̄⟩	47°	34°	22°	▲
	{554}	⟨225̄⟩	90°	61°	45°	▼
	{111}	⟨112̄⟩	90°	55°	45°	⊞
	{111}	⟨110̄⟩	0°	5°	45°	⊗

in Rodrigues space. The coordinate system of Rodrigues space coincides with the crystal coordinate system, but its unit cell is determined by crystal symmetry. Any misorientation can be represented by its Rodrigues vector **R**, which is parallel to the rotation axis **n** (which, by definition, is common to both lattices), and the length of which is determined by $\tan\omega/2$. This choice of vector length results in minimal distortions of misorientation space, i.e. all volume elements are almost equally large, irrespective of their location. In the following the geometrical properties of Rodrigues space for cubic crystals will be addressed more closely.

Because of the high symmetry of cubic crystals their fundamental zone in Rodrigues space is relatively small and simple. Since there are $24 \cdot 24 = 576$ different ways to represent an orientation relationship in cubic crystals, but only one is needed, a selection is made with regard to the smallest angle of rotation to define the elementary Rodrigues vector. All possible elementary Rodrigues vectors define the fundamental zone of Rodrigues space for cubic crystals (Fig. 6.14). Rodrigues space consists of a cube with the corners cut off. The Rodrigues vector emerges from the center of the cube and is defined by its components with regard to the orthogonal axes, which are parallel to the cubic crystal axes. The maximum length of a Rodrigues vector along the $\langle 100 \rangle$ axes is $\sqrt{2} - 1$, corresponding to a 45° rotation. The vector of maximum length is obtained at the corner of a triangular face. The triangular face is perpendicular to the $\langle 111 \rangle$ axis and intersects the cube at an angle of 60° , i.e. the center of the triangular face is touched by the Rodrigues vector $1/3\langle 111 \rangle$. The corner of the triangular face corresponds to a $62.8^\circ\langle 1, 1, (\sqrt{2} - 1) \rangle$ rotation, which is crystallographically equivalent to a $90^\circ\langle 110 \rangle$ rotation. It may be helpful to remember

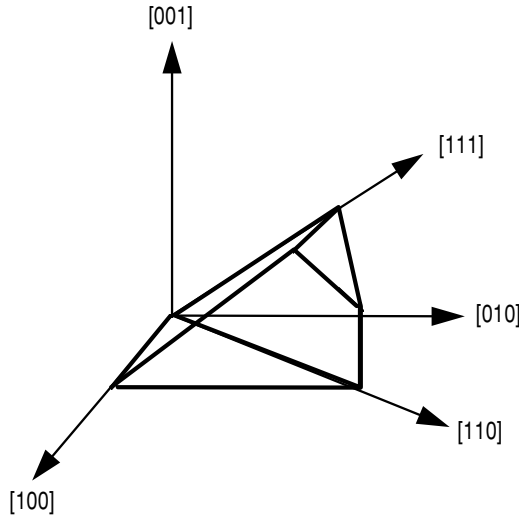
- small angle rotations are located close to the origin
- $\langle 100 \rangle$ rotations extend along the coordinate axes

**FIGURE 6.14**

Fundamental zone of Rodrigues space.

- $\langle 110 \rangle$ rotations extend along the cube face diagonals
- $\langle 111 \rangle$ rotations extend along the cube space diagonal
- twin rotations ($60^\circ \langle 111 \rangle$) are found in the center of the triangular faces

If positive and negative rotations about crystallographically equivalent axes are considered to be equivalent, then the fundamental zone of Rodrigues space can be reduced to $1/48$ of its size, which defines the so-called Mackenzie cell (Fig. 6.15). In the Mackenzie cell all equivalent rotations appear only once [576]. Its shape is odd, however, and therefore less attractive for representation, since the resemblance to cubic symmetry is less obvious. Therefore, we prefer to utilize one full eighth of the fundamental zone, which is a capped cube and thus easy to associate with cubic symmetry. This convenience is offset by the disadvantage that more than one equivalent rotation will occur in the chosen subspace. Since the orientation relationships in each square section have a mirror symmetry with regard to the diagonal of the square, each triangle contains three equivalent orientation relationships. This situation is akin to the representation of orientations in Euler space, where the threefold $\langle 111 \rangle$ symmetry also subdivides the cubic $0 \leq \varphi_1, \Phi, \varphi_2 \leq \pi/2$ space with a complicated geometry such that one accepts the inconvenience of orientation

**FIGURE 6.15**

Mackenzie cell.

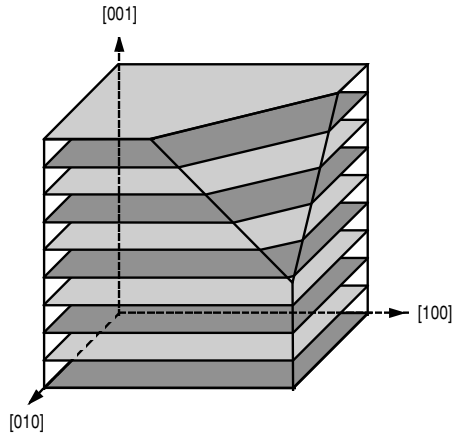
multiplicity to maintain the cubic shape of the represented zone.

For a two-dimensional representation equidistant 5° sections through Rodrigues space perpendicular to the $[001]$ axis will be used (Fig. 6.16). The sections also are plotted as complete squares to simplify graphical representation, although the $\langle 111 \rangle$ corner of Rodrigues space is capped. Instead, the line of intersection with the triangular plane is indicated in the section to denote the limit of the fundamental Rodrigues zone. To graphically represent the misorientation distribution function (MODF) f each measured misorientation Δg_i is associated with a Gauss-type scatter ξ

$$f_i(\Delta g_i) d(\Delta g) = \frac{1}{\xi \sqrt{2\pi}} \exp \left[-\frac{(\Delta g - \Delta g_i)^2}{2\xi^2} \right] d(\Delta g) \quad (6.28)$$

$$f(\Delta g) d\Delta g = \sum_i f_i(\Delta g_i) d(\Delta g) \quad (6.29)$$

and contour lines of equal intensity are plotted. This is entirely analogous to the representation of the ODF in terms of single grain orientations. For illustration, select misorientation distributions for uniform $\langle 100 \rangle$, $\langle 110 \rangle$, and $\langle 111 \rangle$ rotations are given in Fig. 6.17. We will neglect the (not trivial but not serious) problem that the scatter of a component can exceed the boundaries of the Mackenzie cell and, therefore, appears at some different location of the

**FIGURE 6.16**

Equidistant sections through Rodrigues space perpendicular to $[001]$.

cell. As a density function the MODF has to be normalized to unity

$$\int f(\Delta g) d(\Delta g) = 1 \quad (6.30)$$

For a particular microtexture, however, it is also important to relate the measured MODF to a reference MODF [577]. This reference may be either a random misorientation distribution, which can be calculated analytically according to Mackenzie, or which can be simulated from a set of random orientations by computing the frequency of occurrence of any misorientation from the set of misorientations, i.e. the misorientations of each orientation with all other orientations in the set. If the texture of the specimen is not random, then the orientation distribution can be discretized and the reference MODF can be computed analogously. The corresponding misorientation distribution is also referred to as orientation difference distribution function (ODDF). The necessity for this normalization is easy to realize. If a texture would consist of only two strong components, the probability to measure a misorientation relationship between adjacent grains close to the ideal misorientation of the two components is much higher than for a random texture. Any deviation from unity of a MODF/ODDF indicates a nonrandom misorientation distribution.

A random MODF computed for a random orientation set is given in Fig. 6.1. The MODF normalized by the ODDF is commonly termed orientation correlation function (OCF). For illustration, a microstructure with many small angle boundaries and first order twin boundaries is represented in terms of MODF, ODDF and OCF in Fig. 6.19.

Every grain boundary manifests a misorientation between adjacent grains,

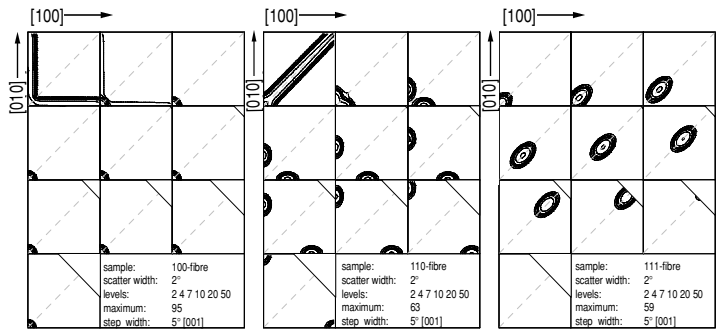


FIGURE 6.17
Representation of orientation relationships in $[001]$ sections of Rodrigues space: rotations about (a) $\langle 100 \rangle$; (b) $\langle 110 \rangle$; and (c) $\langle 111 \rangle$ axes.

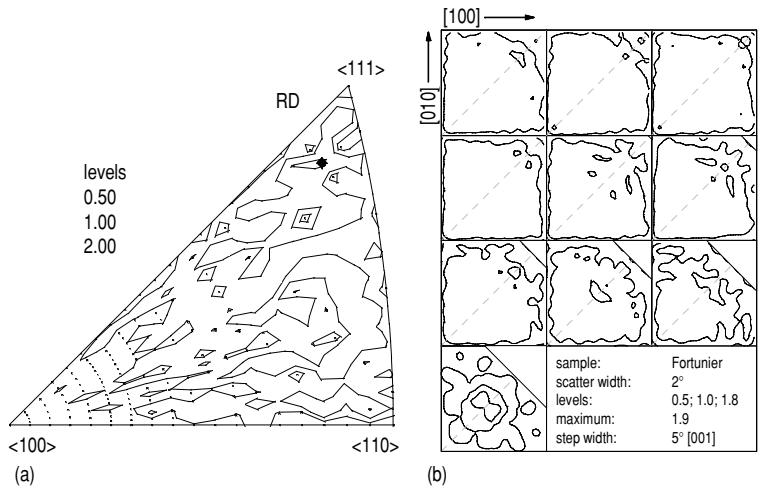
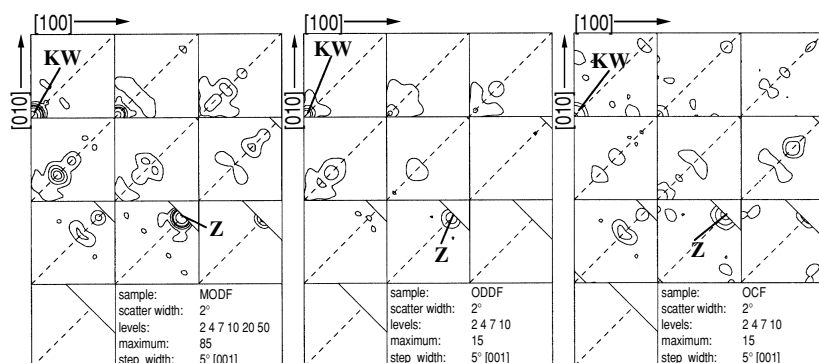


FIGURE 6.18
Random orientation distribution (a) in inverse pole figure; (b) in Rodrigues space.

**FIGURE 6.19**

Comparison of normalization principles (a) MODF; (b) ODDF; (c) OCF. Small angle relationships (KW), first order twin relationships (Z).

by definition. If the character of a grain boundary can be reduced to its misorientation, i.e. if the spatial orientation of the grain boundary plane can be neglected, then the distribution of grain boundary character is represented by the MODF. For a random distribution of all low Σ boundaries with $\Sigma < 29$, where each misorientation was allowed to have a scatter of 5° , the grain boundary character distribution is given in Fig. 6.20.

6.2 Recrystallization and Grain Growth

6.2.1 Phenomenology and Terminology of Recrystallization and Grain Growth

The capability of metals to substantially change their properties during a treatment have made metals and alloys the most versatile and most widely used structural materials. The macroscopic property changes are mainly due to either phase transformations or recrystallization and related phenomena. In this context we will focus on the latter, in particular on recrystallization and grain growth.

During plastic deformation of a metal due to cold or hot working, dislocations are generated and stored in the crystal. Dislocations are lattice defects, which do not occur in thermodynamic equilibrium, and, therefore, a deformed solid tends to remove these lattice defects. On the other hand, although thermodynamically unstable, the dislocation arrangement of a deformed crystal

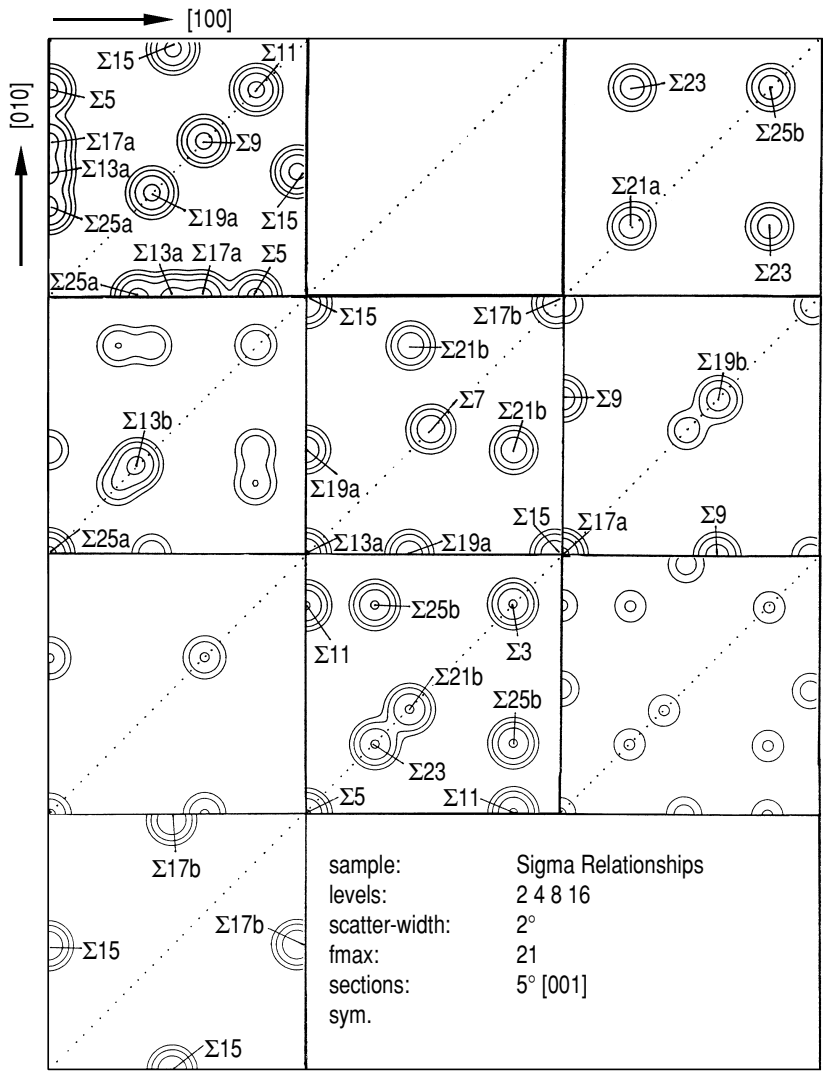


FIGURE 6.20
Location of low Σ orientation relationships in Rodrigues space.

is mechanically stable. By heat treatment sufficient thermal energy is introduced into the crystal to destabilize the dislocation arrangement. In principle, there are two ways to remove the dislocations, or at least to reduce the stored strain energy associated with the dislocations, namely recovery and recrystallization. While recovery comprises all processes, which result in an annihilation or rearrangement of dislocations in low energy dislocation structures, recrystallization proceeds by generation and motion of grain boundaries, which are capable of removing the swept-up dislocations. Therefore, while recovery will locally rearrange and reduce the dislocation density, recrystallization will completely destroy the dislocation structure and rebuild a new strain-free crystal arrangement. In the context of grain boundary migration, we shall focus on recrystallization phenomena in the following.

Usually recrystallization proceeds from an abundance of recrystallization nuclei and, therefore, the completely recrystallized material contains a high density of grain boundaries. Owing to insufficient configuration entropy, grain boundaries — like dislocations — also are not structural essentials of thermodynamic equilibrium and thus liable to be removed. As a consequence, fine-grained recrystallized microstructures undergo grain growth, driven by the increase in grain boundary energy. Grain growth can proceed in a continuous or discontinuous way. During continuous grain growth, some grains will shrink while others will grow, but the average grain size will grow while the grain size distribution remains self-similar, i.e. normalized with the average grain size the grain size distribution will not change upon continuous grain growth (Fig. 6.21a). In contrast, during discontinuous grain growth, few grains grow at the expense of the other non-growing grains. The microstructural evolution bears a resemblance to the process of recrystallization and, therefore, is referred to as secondary recrystallization. During discontinuous grain growth a bimodal grain size distribution will develop and, thus, the self-similarity of the grain size distribution is not maintained in this process (Fig. 6.21b).

There is a confusing variety of terms for the various microstructural changes during heat treatment of deformed materials. The typical recrystallization process during heat treatment of a cold worked metal is referred to as static primary recrystallization or short recrystallization. Sometimes it is also referred to as discontinuous recrystallization, since it proceeds locally and thus does not affect the entire volume concurrently. In contrast, continuous recrystallization is not a real recrystallization process, but rather describes the phenomena of very strong recovery, which also may result in the generation of large angle grain boundaries. The term static recrystallization is used to distinguish the two-step process, namely cold work and subsequent heat treatment, from the recrystallization phenomena occurring concurrently with deformation at elevated temperatures, which is referred to as dynamic recrystallization.

In contrast to the atomistic mechanisms of recrystallization the energetic causes of recrystallization are relatively well understood. There is always a driving force on a grain boundary, if — at a constant pressure and temperature — the displacement of the boundary reduces the Gibbs free energy G of

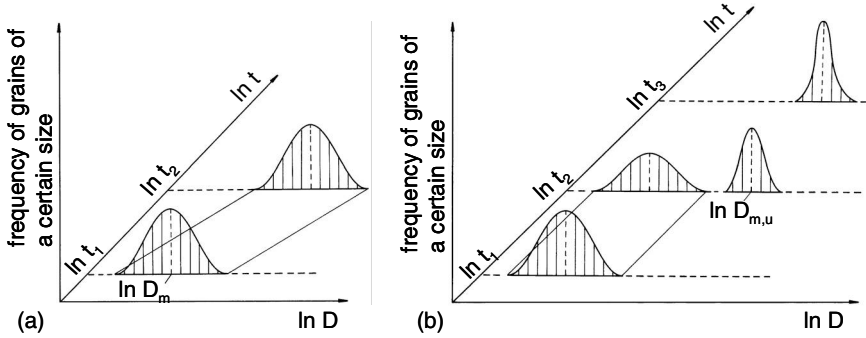


FIGURE 6.21

Time dependence of grain size distribution for normal (a) and abnormal (b) grain growth (schematic).

the solid. The reduction of Gibbs free energy by displacement of a boundary element of size $d\tilde{A}$ by the distance dx reads

$$dG = -Pd\tilde{A}dx = -PdV \quad (6.31)$$

where dV is the volume swept by the boundary during its migration. The quantity

$$P = -\frac{dG}{dV} \quad (6.32)$$

is referred to as driving force. It is a free energy gain per unit volume, which equivalently can be understood as a force per unit area of the boundary, i.e. as a pressure on the boundary. The driving force for primary recrystallization is the strain energy of stored dislocations. If these dislocations are consumed by the moving grain boundary, then the driving force is given by

$$P = \rho E_v = \frac{1}{2}\rho\mu b^2 \quad (6.33)$$

where E_v is the energy per unit length of a dislocation (μ — shear modulus, b — Burgers vector).

With a dislocation density $\rho = 10^{16}\text{m}^{-2}$, $\mu = 5 \cdot 10^4$ MPa, and $b = 2 \cdot 10^{-10}\text{m}$ the driving force amounts to about $P = 10$ MPa, which has been confirmed by calorimetric measurements of the stored energy of cold work.

The driving force for grain growth is provided by the energy of the grain boundaries. For discontinuous grain growth (secondary recrystallization) the driving force reads

$$P = \frac{3d^2\gamma}{d^3} = \frac{3\gamma}{d} \quad (6.34a)$$

where it is assumed that the recrystallized and thus consumed grains comprise cubes of size d and γ is the grain boundary energy per unit area. For a recrystallized grain size of $d = 10^{-4}\text{m}$ and a grain boundary energy $\gamma = 1\text{J/m}^2$ one obtains $P = 0.03\text{ MPa}$. Obviously, the driving force for secondary recrystallization is smaller by orders of magnitude than the driving force for primary recrystallization. Therefore, grain growth phenomena proceed much more slowly or at much higher temperatures compared to recrystallization. For continuous grain growth an element of a grain boundary feels the driving force for migration by the curvature of the boundary. This curvature is due to the fact that grain boundary triple junctions have to comply with the force equilibrium of surface tensions. For 3D crystal arrangements it is impossible to establish both planar grain boundaries and equilibrium conditions at the triple lines or quadruple junction where grain boundaries meet. Therefore, polycrystals are always liable to grain growth and particular measures have to be taken to suppress grain growth, for instance, to maintain a stationary microstructure in metallic parts during high temperature service, e.g. of turbine blades in jet engines. The driving force for continuous grain growth reads

$$P = \frac{2\gamma}{R} \quad (6.34b)$$

where R is the radius of curvature. Since the radius of curvature R usually exceeds the grain size by about an order of magnitude, the driving force for continuous grain growth is about an order of magnitude smaller than for secondary recrystallization.

Reference is sometimes made to a process termed tertiary recrystallization. This usually occurs in thin sheets, when grain growth has ceased due to grooving of the grain boundaries exposed to the sheet surface. In such a case, the difference in surface energy γ^s of the various grains acts as a driving force on the grain boundaries, and this driving force may exceed the driving force for grain growth, if the surface energy differentials $\Delta\gamma^s$ are large and the sheet thickness h is small, since the driving force reads (Fig. 6.22)

$$P = \frac{2\Delta\gamma^s}{h} \quad (6.35)$$

For instance, for $\Delta\gamma^s = 0.1\text{J/m}^2$ and a sheet thickness $h = 10^{-4}\text{m}$ the driving force $P = 2 \cdot 10^{-3}\text{ MPa}$. Since the surface energy can be modified by adsorption, the process of tertiary recrystallization depends on the atmosphere, and by changing atmospheres it is even possible to invert the direction of grain boundary motion.

6.2.2 Nucleation of Recrystallization

As previously mentioned, the deformed microstructure is mechanically stable. To destabilize the dislocation arrangement after deformation three criteria

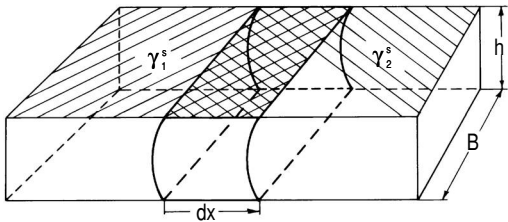


FIGURE 6.22
Illustration of the driving force of tertiary recrystallization for $\gamma_1^s < \gamma_2^s$.

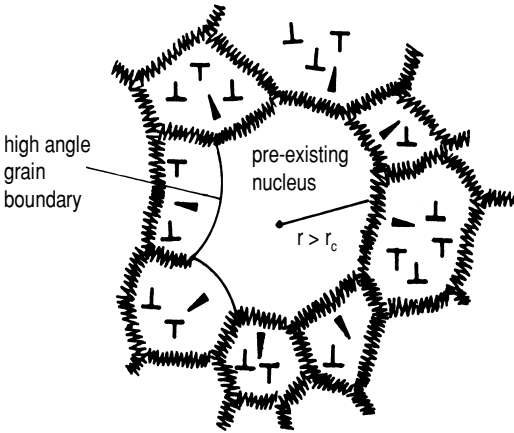


FIGURE 6.23
Schematic illustration of a recrystallization nucleus with growth potential in a deformed structure.

have to be met (instability criteria (Fig. 6.23)).

Thermodynamic Instability

A nucleus can only grow if the total free energy decreases during expansion of the nucleus. For this a critical nucleus size r_c has to be exceeded

$$r_c = \frac{2\gamma}{P} = \frac{4\gamma}{\rho\mu b^2} \quad (6.36)$$

Since the nucleation rate due to thermal fluctuations is much too small to set off recrystallization, a supercritical nucleus must already be present in the deformed microstructure. Usually, the deformation microstructure consists of cellular arrangements, like dislocation cell structures or subgrain structures. Thus, it is commonly assumed that there is a cell or subgrain of supercritical size present in the microstructure to act as a viable recrystallization nucleus.

Mechanical Instability

Since the nucleus is embedded in a cellular arrangement of similar structure, there is not necessarily a net driving force on its boundaries for nucleus growth; rather, it may also shrink or experience no net driving force at all on its surface. An instability of the microstructure for recrystallization, therefore, requires that there is a net driving force for growth on at least part of the surface of a nucleus. This can be achieved by an inhomogeneous dislocation density distribution or a broad subgrain size distribution, which also comprises large cells or subgrains. The latter can potentially be produced by recovery.

Kinetic Instability

The most stringent requirement is, however, that the surface of the nucleus must be a mobile grain boundary. As evident from Chapter 3, this requires a large angle grain boundary. The generation of a mobile large angle grain boundary in a deformed microstructure is the most difficult step for nucleation of recrystallization. Potential mechanisms may be nucleation at preexisting grain boundaries, discontinuous subgrain growth in orientation gradients, deformation inhomogeneities with large misorientations and generation of annealing twins, in particular annealing twin chains.

The requirement for concurrent compliance with all three instability criteria strongly prefers nucleation in certain locations of the deformed microstructure, in particular in deformation inhomogeneities (Fig. 6.24a) like shear bands or microbands, or at preexisting large angle grain boundaries (Fig. 6.24b). An exception is the formation of annealing twins, which by continued twinning and thus generation of a twin chain (twin family) may produce a mobile large angle grain boundary (Fig. 6.25). So far, observations have only confirmed that twinning proceeds from a moving grain boundary, and thus already requires the formation of a viable recrystallization nucleus.

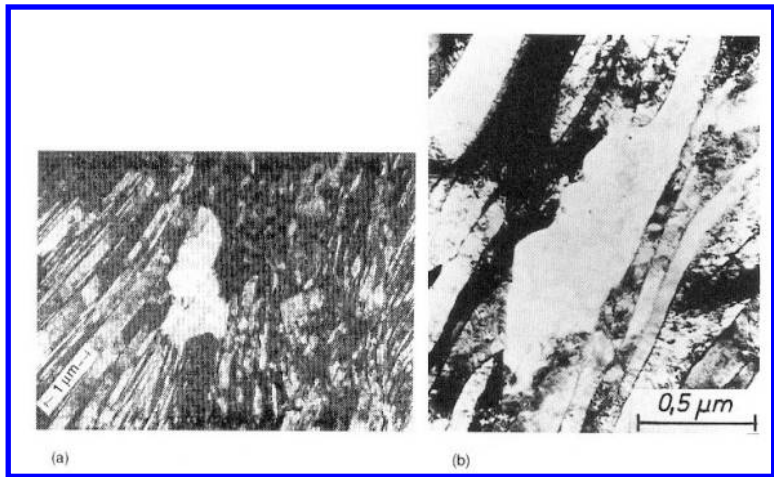


FIGURE 6.24
(a) TEM image of a recrystallized nucleus that developed near the edge of a shear band and is growing into the deformed structure; (b) nucleation at the grain edges of zone annealed aluminum.

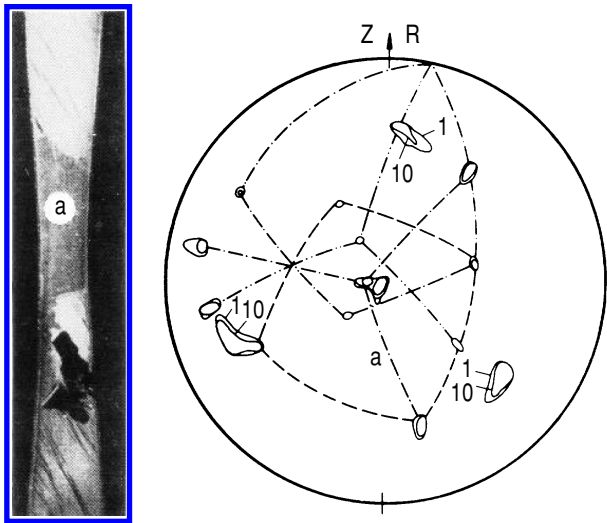
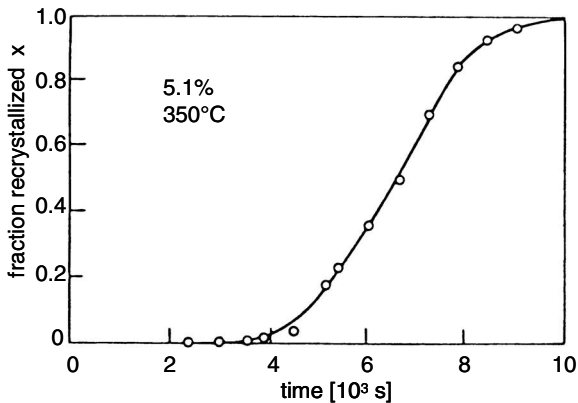


FIGURE 6.25
Micrograph and $\{111\}$ pole figure of a copper single-crystal after dynamic recrystallization during a tensile test at 1103 K. (--- first-; - · - second-; · · · third-generation twinning.)

**FIGURE 6.26**

Recrystallized volume fraction as a function of annealing time following 5.1% tensile deformation (after [581]).

6.2.3 Kinetics of Primary Recrystallization

The kinetics of recrystallization, i.e. the change of recrystallized volume fraction X with annealing time t (Fig. 6.26) is determined by thermal activation of the recrystallization mechanisms nucleation and nucleus growth. From numerous experimental investigations, it is evident that the recrystallization kinetics can be described by the Avrami-Johnson-Mehl-Kolmogorov equation [578]–[580]

$$X = 1 - \exp \left\{ - \left(\frac{t}{t_R} \right)^q \right\} \quad (6.37)$$

In this equation q is the Avrami exponent and t_R a characteristic time for recrystallization, i.e. when 63.2% of the volume is recrystallized. In the case of a constant and homogeneous nucleation rate \dot{N} and isotropic growth rate v the above equation can be derived as

$$X(t) = 1 - \exp \left(- \frac{\pi}{3} \dot{N} v^3 t^4 \right) \quad (6.38)$$

Comparing Eq. (6.38) with (6.37) the characteristic time for recrystallization t_R and the recrystallized grain size d

$$t_R = \left(\frac{\pi}{3} \dot{N} v^3 \right)^{-1/4} \quad (6.39)$$

$$d = 2vt_R \cong 2 \left(\frac{3}{\pi} \frac{v}{\dot{N}} \right)^{1/4} \quad (6.40)$$

Evidently, the recrystallized grain size is the result of a competition between growth rate and nucleation rate. In contrast, the recrystallization time is a joint effect of nucleation and growth, although very strongly dominated by the growth rate. Apparently, the grain boundary migration rate, and thus the grain boundary mobility, governs the kinetics of recrystallization and the characteristics of the recrystallized microstructure.

6.2.4 Recrystallization Texture

6.2.4.1 Origin of Textures

The dominant deformation mechanism in metals is crystallographic slip by dislocation glide. Crystallographic slip is a pure shear deformation and, therefore, accompanied by rigid body rotation, which is the cause for the development of deformation textures during cold work. Depending on material, temperature, strain rate and, of course, strain, a specific deformation texture will be formed, for instance, during rolling, which is the most common industrial forming process. Interestingly, for a given rolling texture a defined recrystallization texture develops upon annealing⁴. As an example, a conspicuously pronounced Cube texture is found upon recrystallization of rolled copper (Fig. 6.27a,b). The texture is very sharp, almost like a single crystal. Equivalently, the typical brass recrystallization texture develops from the brass rolling texture (Figs. 6.27c,d). The respective orientations and their volume fractions are listed in Table 6.3. There is also a specific texture development in bcc materials during annealing of rolled sheet, for instance in ferritic steels (Fig. 6.28).

Because of the importance of recrystallization textures for commercial applications, such as industrial forming processes or electrical steels, there have been considerable efforts to account for the formation of a recrystallization texture from a given deformation texture. Since the process of recrystallization comprises the stages nucleation and growth, theories were developed that either attributed the recrystallization texture to the preference of special orientations to be nucleated or the preference of special misorientations to grow, i.e. to high mobility grain boundaries [582]–[584]. Extensive investigations into this issue in the past 30 years have substantiated that there are many more nucleus orientations than recrystallization texture components and also that there is no growth competition among randomly disoriented grains. Rather, it is now common belief that recrystallization textures are formed by growth competition for a limited spectrum of nucleus orientations. Because of the extreme sensitivity of the recrystallization kinetics on the growth rate, as evident from Eq. (6.38), essentially only the maximum growth rate misorientation dominates the recrystallization texture development. Therefore, considerable

⁴For ideal orientations of rolling and recrystallization textures in cubic crystals see Figs. 6.12 and 6.13 and Tables 6.1 and 6.2.

efforts were dedicated to a determination of the maximum growth rate mis-orientation by so-called growth selection experiments [585].

TABLE 6.3
Pure Cu: Rolling Texture

φ_1	Φ	φ_1	$f(g_i)$	M_i	σ_i	{hkl}	$\langle uvw \rangle$	OR Name
Pure Cu: Rolling Texture								
35	45	0	15.1	29.5	7.9	011	211	Brass-Def
62	33.5	63	18.5	42.1	7.4	123	634	S
90	32	45	16.9	25.5	8.4	112	111	Cu
90	80	45	5.5	2.8	6.7	255	511	Twin to Cu
0	21	0	4.1	1.8	5.6	025	100	Tilted Cube
Pure Cu: Recrystallization Texture								
0	0	0	90.6	52.6	7.1	001	100	Cube
63	48	63	22.9	20.0	6.5	122	212	1 st Twin to Cube
16.5	26	10.0	6.8	9.5	8.7	148	841	2 nd Twin to Cube
76	29	74	6.6	9.5	9.3	148	747	2 nd Twin to Cube
90	35	0	11.5	2.7	7.8	035	053	Tilted Cube
45	37	45	6.0	3.9	6.9	447	184	2 nd Twin to Cube
Cu-22% Zn (Brass): Rolling Texture								
32	45	0	13.8	65.2	13.2	011	211	Brass-Def
0	45	0	5.5	17.3	14.8	011	100	Goss
90	66	45	3.4	10.5	12.4	233	311	{223}
0	51	45	2.7	7.0	10.6	111	110	{111}
Cu-22% Zn (Brass): Recrystallization Texture								
82	30	34	9.0	63.2	12.0	236	385	Brass Rex
90	33	0	4.4	8.9	10.4	035	053	Tilted Cube
0	20	0	2.7	8.1	11.6	025	100	Tilted Cube
45	38	68	2.5	18.5	12.1	134	132	–
0	0	0	1.2	0.3	7.8	001	100	Cube

Basic types of rolling and recrystallization textures in fcc metals:
 M_i — volume fraction; $f(g_i)$ — value of ODF at g_i ;
 σ_i — scattering amplitude; OR — name of orientation [590].

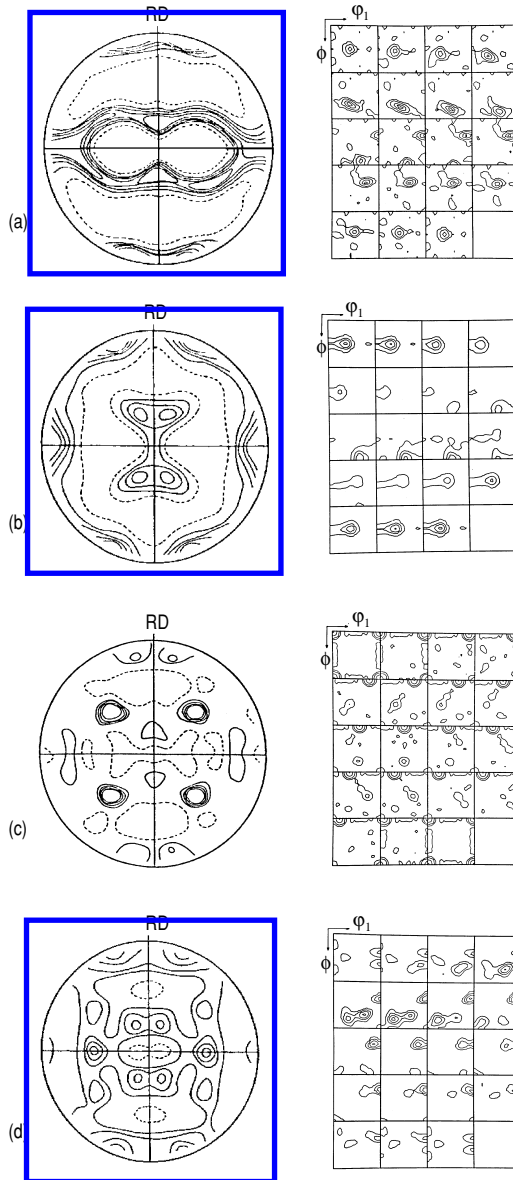


FIGURE 6.27

Rolling and recrystallization textures of Cube metals in $\{111\}$ pole figure and Euler space. (a) Cu-type rolling texture; (b) brass-type rolling texture; (c) Cube texture (Cu-recrystallization texture); (d) brass recrystallization texture.

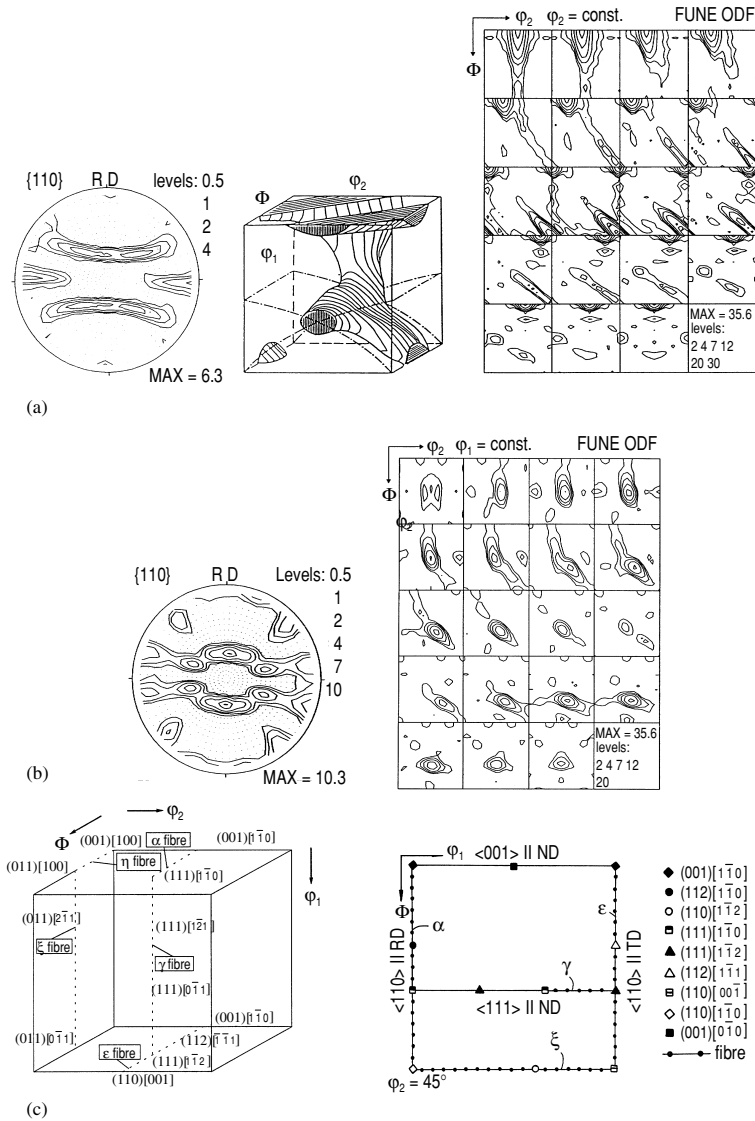


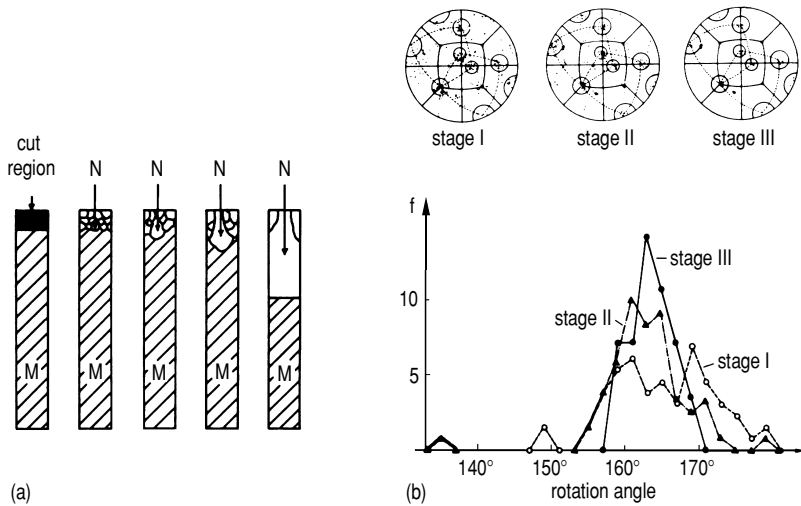
FIGURE 6.28

Rolling and recrystallization texture of bcc metals (ferritic steel). (a) $\{110\}$ pole figure, and ODF in 3D and sectional Euler space of rolling texture; (b) $\{110\}$ pole figure and ODF in Euler space; (c) location of fibers in Euler space that contain the main texture components. The $\varphi_2 = 45^\circ$ sections contain the most information.

6.2.4.2 Pure Metals: Growth Selection

In such experiments a single crystal is slightly deformed, for instance by rolling. If the orientation of the single crystal does not change or decompose during deformation, the deformed specimen still represents a single crystal but with a stored energy of cold work in terms of the elastic energy of the stored dislocations. After deformation, one face of the single crystal will be subjected to an additional strong deformation, e.g. by grinding, filing or sawing. Afterwards the sample is annealed in a strong temperature gradient, such that only a small volume of the sample is heated while the remaining deformed volume is kept at ambient temperature (Fig. 6.29). Annealing starts at the additionally deformed end, giving rise to a high nucleation density with virtually random orientation distribution. These nuclei grow upon displacement of the hot zone and compete with one another such that the fastest growing grains will cut off the path of the more slowly growing grains, and eventually a single grain will dominate and cover the entire cross section of the consumed single crystal. Obviously, this final surviving grain will be the fastest (maximum growth rate orientation), and the grain boundary between this grain and the deformed single crystal possesses the highest mobility among all competing grain boundaries. Of course, a single experiment might give incidental results. However, hundreds of experiments were conducted on high purity Al with the overwhelming result that grains with a $40^\circ\langle 111 \rangle$ orientation relationship to the deformed matrix evidently grew fastest. Naturally, there is a certain statistical distribution of fast-growing orientations. However, the further the competing grains proceed into the consumed deformed single crystal, the sharper the distribution of misorientation angles (Fig. 6.29).

According to such experiments, the maximum of the distribution is attained at an angle slightly above 40° about a $\langle 111 \rangle$ axis. In the past, the high mobility of $40^\circ\langle 111 \rangle$ boundaries was interpreted such that the $40^\circ\langle 111 \rangle$ boundary actually represented a $38.2^\circ\langle 111 \rangle \Sigma 7$ coincidence boundary [394, 587]. Owing to the high density of coincidence sites the boundary would segregate less solute atoms than other boundaries and thus be less affected by impurity drag. Less impurity drag is equivalent to a higher effective driving force and thus higher growth rate. In fact, the orientation dependence of grain boundary mobility measured for the individual grain boundaries proved that low Σ CSL boundaries (special boundaries) behaved in a more mobile way than random boundaries (non-special boundaries), and among all boundaries with low index rotation axes the $\Sigma 7$ boundary moved fastest (see Chapter 3). However, the maximum growth rate misorientation is distinctly different from the $\Sigma 7$ orientation relationship, and always larger by at least 2 degrees. Thus, the interpretation given above obviously is at variance with the results of growth selection experiments. A more detailed analysis reveals the reason for the discrepancy. The $\Sigma 7$ boundary indeed moves fastest at temperatures below 430°C (Fig. 6.30) while at higher temperatures the $40.5^\circ\langle 111 \rangle$ boundary exhibits the highest mobility. Given the fact that the temperature during growth selection

**FIGURE 6.29**

(a) Principle of growth selection; (b) $\{111\}$ pole figures and frequency distribution of the orientations still in contact with the deformed matrix for three consecutive stages of growth selection ([586]).

experiments is very high, typically above 600°C for Al, it is evident that such experiments are designed to reveal a $40^\circ \langle 111 \rangle$ misorientation as maximum growth rate (mis)orientation rather than the $\Sigma 7$ misorientation (Fig. 6.31).

The physical principle that creates this confusion is the compensation effect discussed at length in Chapter 3. At temperatures below the compensation temperature T_c the process with the lower activation enthalpy will dominate, while above T_c such mechanisms are favored that carry the largest pre-exponential factor (Fig. 6.32). It is noted that this result reveals a common misconception, namely that the process with the lower activation enthalpy will always be favored, tacitly assuming that the pre-exponential factor hardly varies, which is obviously wrong. The widely practiced habit to analyze thermally activated processes only with regard to the activation enthalpy is, therefore, liable to serious misinterpretation. This is particularly true for interfacial phenomena, where the activation enthalpy varies in a wide range. For instance, if only the activation enthalpy would differ for the mobility of dissimilar (large angle) boundaries, the mobilities would differ by many orders of magnitude, while in reality the mobility of grain boundaries varies only within a factor of ten or so.

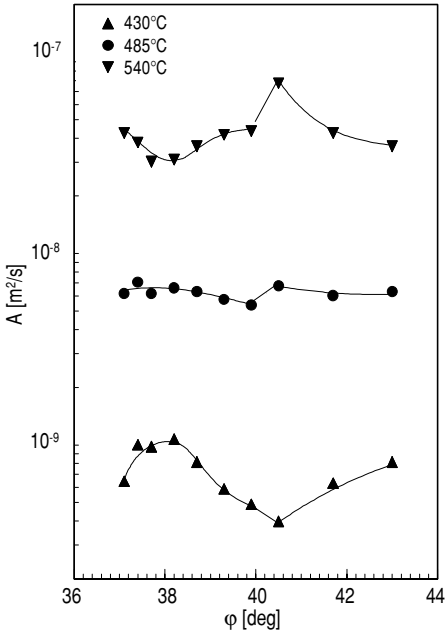


FIGURE 6.30
Dependence of the reduced mobility of $\langle 111 \rangle$ tilt grain boundaries on rotation angle in pure Al at different temperatures.

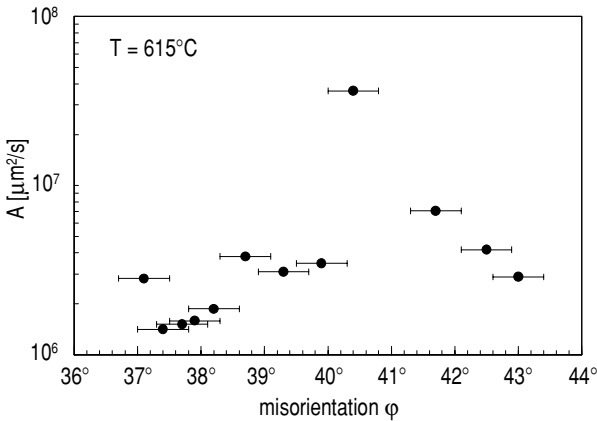
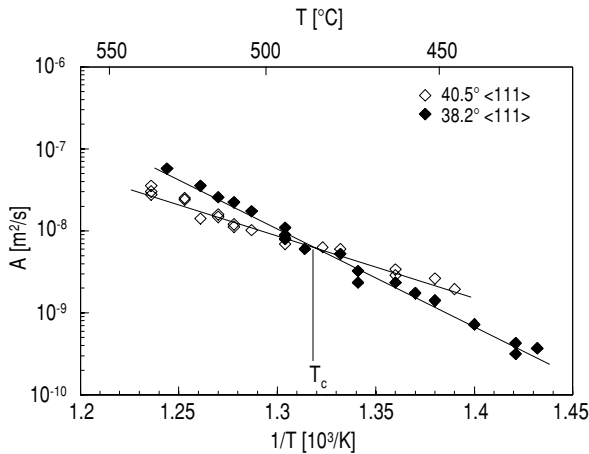


FIGURE 6.31
Reduced mobility of investigated $\langle 111 \rangle$ tilt grain boundaries in Al at 615°C (obtained by extrapolation of the measured temperature dependence to 615°C).

**FIGURE 6.32**

Temperature dependence of the reduced mobility A for 38.2° and $40.5^\circ\langle 111 \rangle$ tilt grain boundaries in pure Al.

6.2.4.3 Growth-Controlled Recrystallization Textures

Growth selection experiments on pure aluminum have clearly established the high growth rate of $40^\circ\langle 111 \rangle$ tilt boundaries in this material. Its importance for microstructure development, however, derives from the fact that the main components of the recrystallization textures of rolled Al (Cube texture) can be related to the major rolling texture components (S-orientation) by a $40^\circ\langle 111 \rangle$ orientation relationship (Fig. 6.33). This constitutes the basis of the so-called “theory of oriented growth” which contends that the recrystallization texture forms from (tacitly assumed) randomly oriented nuclei by growth selection in favor of maximum growth rate orientations, i.e. $40^\circ\langle 111 \rangle$. There have been refinements to this approach to account for obvious discrepancies from ideal $40^\circ\langle 111 \rangle$ rotations, in particular the compromise texture approach, which demands that a growing grain be able to grow quickly into more than a single component of the rolling texture (Fig. 6.33) [583]. More refined modeling approaches [588] and computer simulations [589] have confirmed that a growth preference of a $40^\circ\langle 111 \rangle$ rotation leads to the observed recrystallization textures. The influence of a growth advantage is so strong that other compromise $40^\circ\langle 111 \rangle$ rotations are completely suppressed even if their compromise fit is marginally less perfect. This would explain why other potential recrystallization texture components were never observed.

Other approaches also have been put forward recently to explain the dominance of the $40^\circ\langle 111 \rangle$ misorientation, even in the absence of an orientation-dependent growth rate. Besides the classical contention of oriented nucleation,

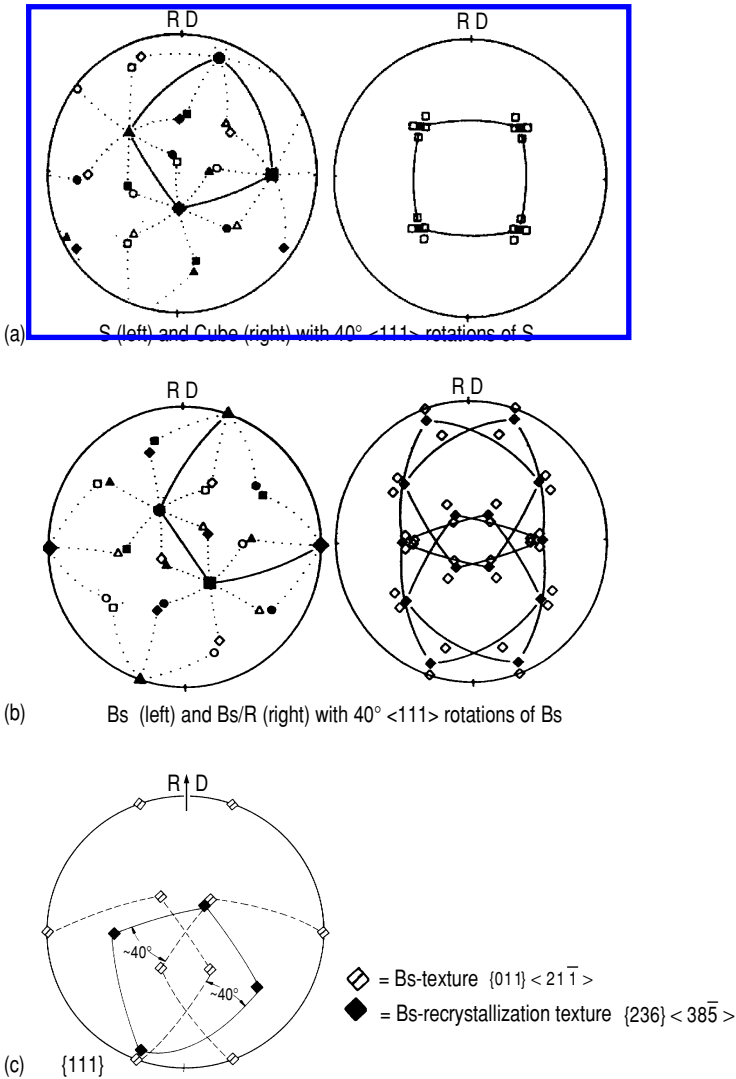


FIGURE 6.33

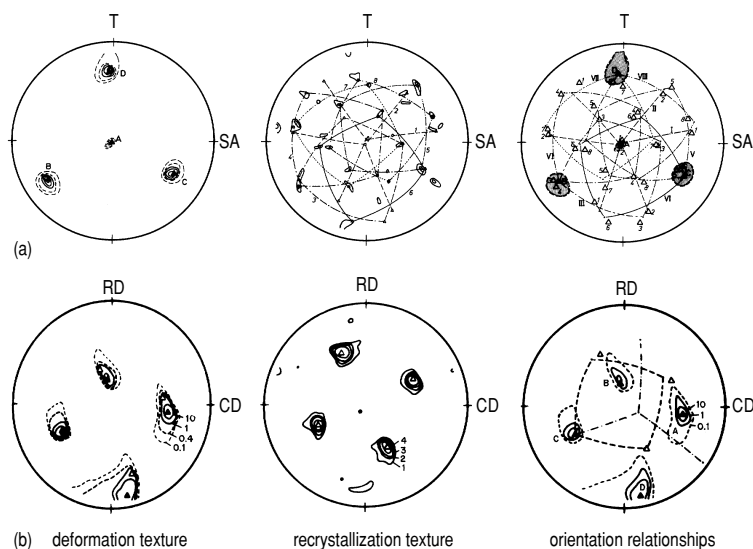
Orientation relationship between rolling and recrystallization texture components. (a) The Cube texture satisfies a best fit of a $40^\circ \langle 111 \rangle$ rotation of the S orientation; (b) the brass recrystallization texture is related to the brass rolling texture by a $40^\circ \langle 111 \rangle$ rotation; (c) illustration of the orientation relationship for one brass rolling and recrystallization component.

i.e. the preferential nucleation of major recrystallization texture components, e.g. the Cube texture in aluminum, an effect of orientation pinning recently was proposed [590]. Orientation pinning relates to the experimental observation that small angle boundaries (and coherent twin boundaries) have low mobility and can be considered as essentially sessile. While it is difficult to completely block a grain boundary in three dimensions this concept also cannot satisfactorily account for the observed recrystallization textures [591], although it amplifies selective growth and thus perhaps another reason for the observed sharp recrystallization textures in aluminum alloys.

A truly surprising phenomenon is that the selective growth, which was unambiguously evidenced in pure Al, can also account for recrystallization texture formation in other metals and alloys, even intermetallic compounds. For instance, the recrystallization texture of Cu-30%Zn (α -brass) can be successfully predicted by assuming a compromise texture of $40^\circ\langle 111 \rangle$ rotations (Fig. 6.33) [592]. This is remarkable, since the deformation structure and the recrystallized microstructure of brass are entirely different from the deformed and recrystallized state of Al, namely heavily twinned and shear banded after rolling as well as fine-grain sized and massively twinned after recrystallization. The major problem of relating the recrystallization texture to the rolling texture in brass is the fact that not all theoretically predicted compromise orientations appear in the experimental recrystallization texture. This problem can be mitigated by twin formation as an additional selective nucleation process [593].

For copper and silver a $30^\circ\langle 111 \rangle$ rotation seems to more appropriately describe the maximum growth rate orientation, as evident from recrystallization experiments on single crystals. Growth selection experiments are more difficult to conduct for these materials, since repeated annealing twin formation generates high-order twin families, which interfere with the growth process such that usually more than a single grain survives growth competition [594]. Nevertheless, the grains surviving growth selection can be associated with some scatter to a $30^\circ\langle 111 \rangle$ orientation relationship between growing grain and consumed deformed matrix. To reconcile the results on Al with observations on other fcc materials, reference usually is made to a $30^\circ - 40^\circ\langle 111 \rangle$ rotation. This is, however, incorrect, as shown by very detailed investigations on Al and can only be tolerated in view of the lack of reliable data on materials other than Al.

The dominance of $40^\circ\langle 111 \rangle$ rotations is truly remarkable. If an Al single crystal is deformed such that the spread of the orientation will slightly favor the occurrence of only a single variant of all possible eight $\pm 40^\circ\langle 111 \rangle$ rotations, then the recrystallization texture consists of only one component (Fig. 6.34), namely this variant, despite the fact that there are many other orientations present in the orientation spread of the deformed matrix [595, 596]. Even more surprising is the recrystallization texture of deformed single crystals with a stable orientation during rolling. The recrystallization texture comprises exactly all eight $\pm 40^\circ\langle 111 \rangle$ rotations of the rolled single crystal orientation,

**FIGURE 6.34**

$\{111\}$ pole figures of deformed and recrystallized Al single crystals (according to [596]). (a) $\langle 112 \rangle$ crystals, tensile deformed 50%; (b) $(2.1.10)[421]$ crystal, 80% rolled.

irrespective of whether it is aluminum, brass [593] or even the intermetallic compound Ni_3Al (Fig. 6.35) [597]. The latter case is particularly surprising, since rolled Ni_3Al polycrystals exhibit only a very weak recrystallization texture, and it is generally assumed that long-range order strongly reduces grain boundary mobility and thus eliminates a particular orientation dependence of grain boundary mobility.

Recently, Hutchinson [598] proposed attributing the observed frequency of $40^\circ \langle 111 \rangle$ rotations to a special property of a random misorientation distribution. When a random misorientation distribution is sorted into rotations about low index rotation axes, e.g. $\langle 111 \rangle$ rotation axes, allowing for a deviation of about 15° , the corresponding angular misorientation distribution is not random but peaks at an angle of about 30° , similar to growth selection experiments; however, this result has to be treated with caution. In growth selection experiments it is determined which orientation grows into a specific (single crystal) orientation. If this growth would be orientation independent then the distribution of successful grains ought to represent the orientation distribution itself and not the misorientation distribution. Besides, the computed angular misorientation distribution is distinctly different from growth selection results on Al, and the results of mobility measurements on individual grain boundaries in Al prove an orientation dependence of grain boundary

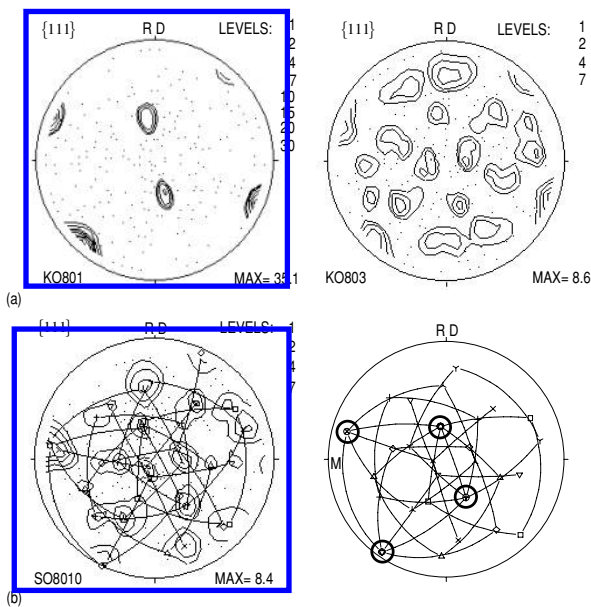


FIGURE 6.35
(a) {111} pole figure of rolling and recrystallization texture of a (617)⟨3.10.4̄⟩ single crystal of Ni₃Al; (b) the recrystallization texture comprises all eight ±35°⟨111⟩ rotations of the single crystal orientation.

mobility. Hutchinson has pointed out that the computed and measured angular misorientation distributions about $\langle 111 \rangle$ axes are not identical. However, the computation certainly demonstrates that caution has to be exercised when interpreting apparently non-random misorientation distributions.

6.2.4.4 Recrystallization in Single Phase Alloys

From innumerable experiments it is known that the addition of solute elements to a pure metal drastically affects its recrystallization behavior. The recrystallization kinetics slows down, the recrystallized grain size decreases and the recrystallization texture may change completely even with small contents of the alloying element.

Evidently, the effect of alloying elements on recrystallization kinetics, grain size and texture has to be attributed to a change in nucleation rate \dot{N} and/or growth rate v . The deformation microstructure and deformation texture is usually less dramatically influenced by minor additions of alloying elements; thus the nucleation rate ought to be less affected or at least not markedly increased by alloying. For instance, the addition of only 0.1% P to pure Cu hardly affects the rolling texture but leads to a very different recrystallization texture upon annealing (Fig. 6.36) [599]. Other prominent examples are the system Fe in Al or Nb in steel. Therefore, the delay of recrystallization kinetics and the grain refinement upon alloying have to be attributed to a decrease in the growth rate rather than to an increase in nucleation rate. The effect can be very drastic, however, e.g. the addition of 0.01%Fe to Al increases the recrystallization time by orders of magnitude (Fig. 6.37).

A qualitative explanation of these phenomena provides the impurity drag theory, as presented in Chapter 3. Much more difficult is a quantitative treatment of the impurity drag effect on recrystallization kinetics. This is due to the fact that impurity drag is a consequence of segregation in grain boundaries, and the understanding of segregation is still in its infancy. Only recently have atomistic calculations on segregation in select systems been provided [601] for a stationary grain boundary, but virtually nothing is known about dynamic segregation in a moving grain boundary.

Another shortcoming of the impurity drag theory is its phenomenological character, which does not make use of grain boundary structure. From the experimental data presented in Chapter 3, in particular the different behavior of pre-exponential factor and activation enthalpy, respectively, it is very likely that segregated elements not only exert an impurity drag on the boundary but also affect grain boundary structure and thus its mobility. An improvement of the traditional impurity drag theory by also accounting for solute-solute interaction in the boundary is a first attempt to tackle this problem (see Chapter 3). Also, it is not improbable that minute precipitates form in the boundary and move along with the boundary, which would strongly reduce the growth rate, as discussed in Chapter 3.

The effect of segregation on grain boundary structure is particularly dras-

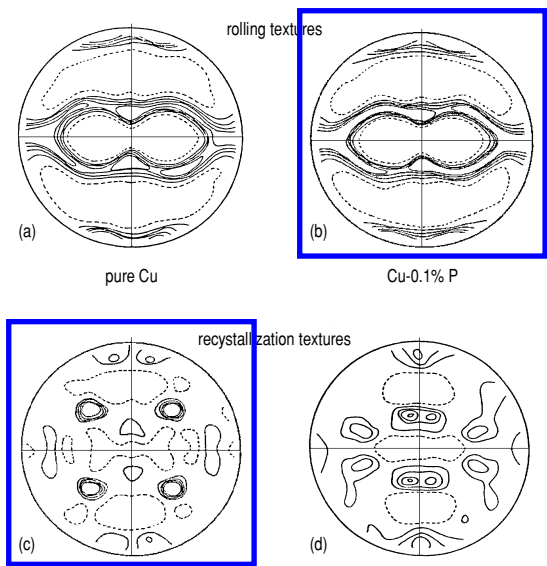


FIGURE 6.36
 $\{111\}$ Pole figures of rolling and recrystallization textures of pure Cu and Cu-0.1%P (degree of rolling: 95%).

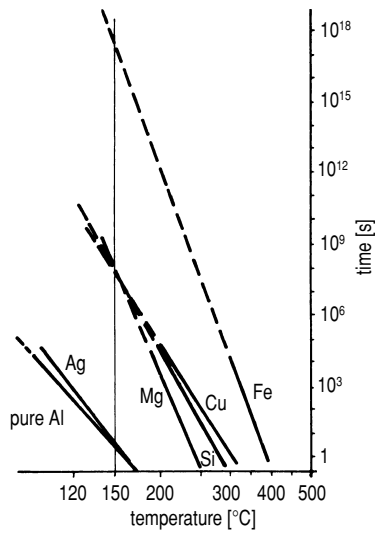
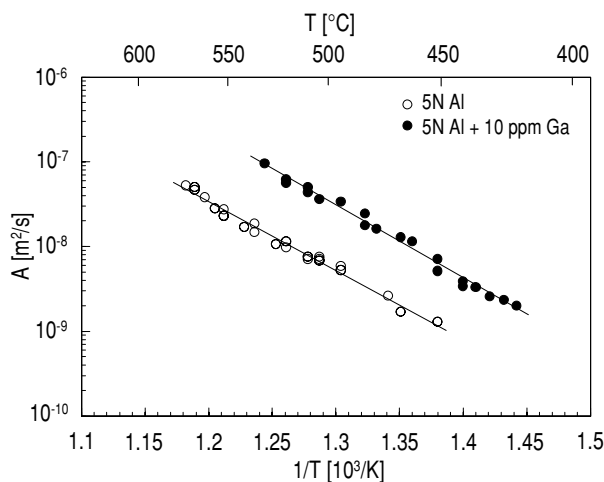


FIGURE 6.37
Temperature dependence of the recrystallization time of binary alloys of high purity aluminum and 1/100 atomic percent of a second metal (after [600]).

**FIGURE 6.38**

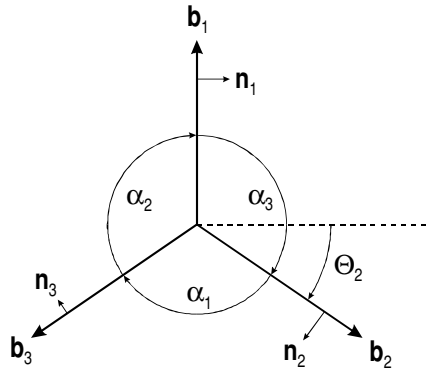
Arrhenius plot of the reduced mobility of a $38.2^\circ\langle 111 \rangle$ tilt grain boundary in pure Al and pure Al doped with 10 ppm Ga.

tic if the segregated solute promotes the tendency for a grain boundary phase transformation, e.g. in terms of a prewetting or a regular wetting transition, i.e. essentially the formation of a more or less continuous film of solute in the boundary. If this film becomes viscous it may drastically change grain boundary mobility. This is likely for immiscible elements as for the system Al-Ga. Contrary to expectations, grain boundaries in Al doped with 10 ppm Ga show a mobility far higher than grain boundaries in pure Al (Fig. 6.38). This behavior cannot be understood in terms of the impurity drag theory; rather, it provides unambiguous evidence for the effect of segregated solute atoms on grain boundary structure (see Chapter 3).

Of course, such behavior has a drastic influence on recrystallization kinetics and microstructure evolution, i.e. small amounts of Ga added to pure Al considerably speed up recrystallization kinetics and alter the recrystallized grain size. In fact, most commercial Al alloys contain some amount of Ga.

6.2.5 Grain Growth

After primary recrystallization, when the grains impinge with a random morphology, the grain boundary surface area can be reduced by arranging grain boundaries in planar positions. Grain growth is basically caused by the fact that it is impossible to reconcile a completely planar boundary arrangement and an equilibrium of surface tensions at grain boundary junctions. This is easy to visualize for a two-dimensional model. Equilibrium of surface tensions

**FIGURE 6.39**

Equilibrium of grain boundary surface tensions at a triple junction. α_i — contact angles; Φ_i — inclination; \mathbf{n}_i — boundary normal; \mathbf{b}_i — in plane direction.

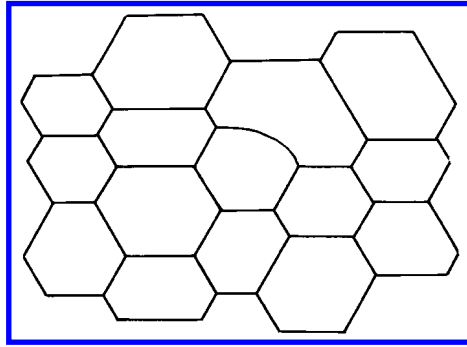
γ_i^s at a junction is obtained for the angles α_i according to the Herring equation [73] (Fig. 6.39)

$$\sum_{i=1}^3 \left[\gamma_i^s \mathbf{b}_i + \left(\frac{\partial \gamma_i^s}{\partial \Theta_i} \right) \mathbf{n}_i \right] = 0 \quad (6.41)$$

If the grain boundary energy does not depend on the spatial orientation of the grain boundary plane, then the torque terms $\partial \gamma / \partial \Theta$ vanish and

$$\frac{\gamma_1}{\sin \alpha_1} = \frac{\gamma_2}{\sin \alpha_2} = \frac{\gamma_3}{\sin \alpha_3} \quad (6.42)$$

In the absence of an orientation dependence of grain boundary energy $\alpha_1 = \alpha_2 = \alpha_3 \equiv \alpha = 120^\circ$. Both straight boundaries and $\alpha = 120^\circ$ can be achieved only for an exclusively hexagonal grain structure. A single five-sided grain has to bend at least one grain boundary to balance the force at all boundary junctions (Fig. 6.40). The curvature of this boundary, however, results in a driving force to straighten the boundary. The boundary will move toward the center of curvature and thus mistune the equilibrium angles at the junctions and cause repeated rearrangements. As a result, no equilibrium at all can be obtained. It follows that grains with fewer than six sides have convexly curved boundaries and thus shrink while grains with more than six sides have concavely curved boundaries and thus expand. Since large grains are in contact with many small grains, their boundaries are composed of a large number of concavely curved segments, even though their macroscopic appearance may suggest a convex shape (Fig. 6.41); consequently, they will expand. In three dimensions the situation is similar, although more complex in detail. The balance of surface

**FIGURE 6.40**

Two-dimensional equilibrium structure that, except for one defect, consists only of hexagons with 120° contact angles.

tensions requires in this case an angle of 120° at grain boundary junctions and a tetrahedral angle where four grains are in contact. The impossibility of reconciling these requirements with planar grain boundaries again causes an expansion of large grains, while small grains shrink.

The kinetics of normal grain growth can be readily obtained by assuming that the radius of curvature R is proportional to the average grain diameter D ($R = \alpha D$), and the grain diameter varies proportionally to the average growth rate ($v = \beta dD/dt$). Eqs. (6.34b) and (3.6) combine to form

$$\beta \frac{dD}{dt} = m_b \frac{2\gamma}{\alpha D} \quad (6.43)$$

which integrates for $D(t=0) = D_0$ to

$$D^2 - D_0^2 \left[\frac{2m_b\gamma}{(\alpha\beta)} \right] t = K_1 t \quad (6.44)$$

The kinetic constant K_1 has the temperature dependence of the grain boundary mobility m_b . For a small initial (primary) grain size D_0 , the grain diameter is expected to grow proportionally to the square root of annealing time, which is observed only for ultrapure materials. Normally, grain growth progresses less rapidly (Fig. 6.42), so that the results can be better approximated by the relation

$$D = K_2 t^n \quad (6.45)$$

where $n < 1/2$ and K_2 is a constant. Frequently, grain coarsening even ceases completely, which may be due to a variety of reasons.

If the grain size becomes comparable to the smallest specimen dimensions, grain growth is substantially reduced. This is immediately evident for a bamboo structure in wires. In sheets, a two-dimensional growth ought to proceed after a columnar grain structure perpendicular to the sheet surface has

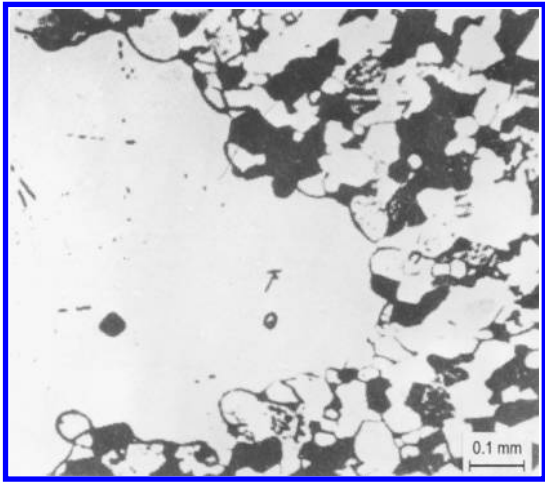


FIGURE 6.41
Abnormal grain growth in Zn. Note that grain boundary is macroscopically convex but microscopically concave [605].

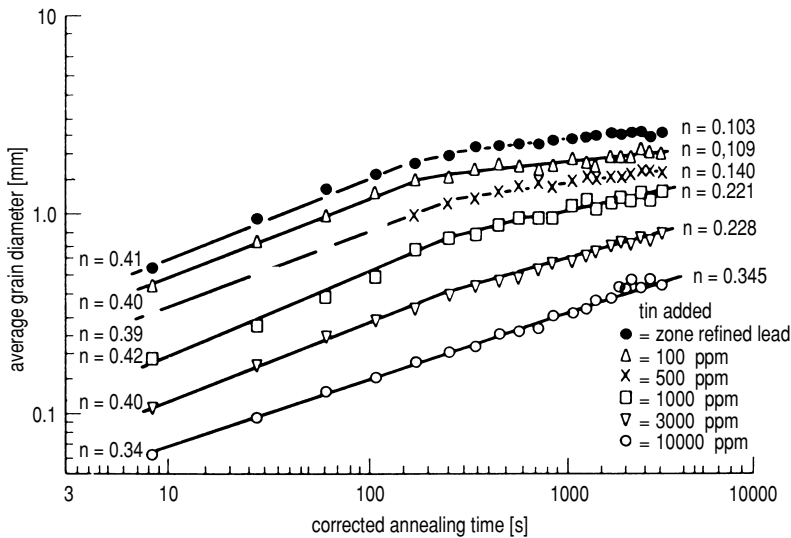


FIGURE 6.42
Grain growth in zone refined lead and lead with different tin contents. The deviation of the exponent from the ideal value of 0.5, and the increase of this deviation with increasing grain size are apparent (after [606]).

been established. This is, however, prevented by thermal grooving of grain boundaries at surfaces (see Chapter 3). The final grain size is usually well approximated by about twice the sheet thickness. For secondary recrystallization, however, the driving forces are generally sufficient to overcome grooving, and growth continues in two dimensions.

In the presence of inclusions of a second phase, grain boundary motion is hindered (see Chapter 3). Grain coarsening will cease, once the driving force (Eq. (6.34b)), which decreases with increasing grain size, is balanced by the Zener drag $P_R = 3f\gamma/2r_p$, where f and r_p represent volume fraction and average size of the particles. Assuming $R = \alpha D$, the final grain size D_f is

$$D_f = \frac{4r_p}{3\alpha f} \quad (6.46)$$

Even in solid solutions grain growth may tend to cease in the course of time. Because of the decrease in driving force with increasing grain size, the growth rate decreases and the boundary may change from a free to a loaded state (see Chapter 3). This can reduce the growth rate by several orders of magnitude.

Grain coarsening can be substantially restricted in strongly textured microstructures. Since the grain boundary migration rate is very small for small orientation differences, grain growth is absent, if the recrystallization texture consists of only one component such as the cube texture in fcc metals, but major texture changes can result if minor amounts of other orientations exist in a sharply textured microstructure.

Thus far we have considered only the effect of grain boundaries on the evolution of microstructure during recrystallization and grain growth. As evident from Chapter 4, however, triple junctions may play an essential role in the dynamics and kinetics of grain boundary assemblies. In this context the criterion

$$\Lambda = \frac{m_{tj} \cdot \lambda}{m_b} \quad (6.47)$$

plays a role, where λ is the characteristic length, i.e. the grain size D in polycrystals or the subgrain size d in cellular deformed structures. Owing to the almost complete neglect of triple junction properties on microstructure evolution there is little quantitative data on the behavior of boundary-junction systems. In Chapter 4 we already noted the influence of triple junctions on the Von Neumann-Mullins relation and its drag effect on grain boundary motion. According to Eq. (6.47) a large impact of triple junction mobility may be expected if the characteristic length λ is very small, i.e. for ultrafine microstructures or even nanocrystalline material. Owing to the experimental difficulties to properly characterize nanocrystalline microstructures and in particular to account for impurities, second-phase particles produced during consolidation, as well as a potentially altered grain boundary structure at large surface to volume ratios, it is not possible to accurately compare the grain growth dynamics of nano- and micro-sized grain structures.

However, there are indications that triple junctions substantially slow down

grain growth kinetics in ultrafine grain structures, and they may even give rise to the suppression of recrystallization and set off abnormal grain growth. One “suspicious” example is mechanically alloyed ODS superalloys, which are very fine grained ($D \sim 100\text{nm}$) after hot extrusion and exhibit conspicuous resistance to recrystallization and grain growth, which may be set off only at very high homologous temperatures ($T > 0.8T_m$). Although not yet beyond the state of speculation, this behavior may be due to triple junctions, since all hypotheses that try to account for the observed effect by second-phase particles, cannot yet be confirmed. It is in particular noteworthy that intermediate anneals at not so high temperature can set off abnormal grain growth at even more elevated temperatures, i.e. small changes in grain size may render the microstructure unstable [603, 604].

6.3 On Precipitation-Controlled Grain Size

It is textbook knowledge that second-phase particles slow down the process of grain growth (see Chapter 3). However, in [601, 602, 607] the question was risen whether the formation of a second phase always slows down grain growth in polycrystals, in particular in nanocrystals. The authors of [607] considered the grain boundary motion in an alloy with a miscibility gap. When the sample (polycrystal) is single phase, grain boundary motion or the rate of grain growth is described by the theories of impurity drag (see Chapter 3). However, if we lower the temperature by ΔT or change the concentration by Δc (Fig. 6.43) the systems changes to a two-phase field. This causes two changes, namely the formation of precipitates of a second phase and depletion of solute atoms in the bulk of a grain. Decreasing the temperature by ΔT will offset the system to the two-phase field and the mass W_p of the precipitates with respect to the solid solution $W_{\text{sol.sol.}}$ will be according to the lever rule (Fig. 6.43)

$$\frac{W_p}{W_{\text{sol.sol.}}} = \frac{c_0 - c_A}{c_B - c_0} \quad (6.48)$$

$$V(c'_0 = c_A, \text{ precipitates}) > V(c_0) \quad (6.49)$$

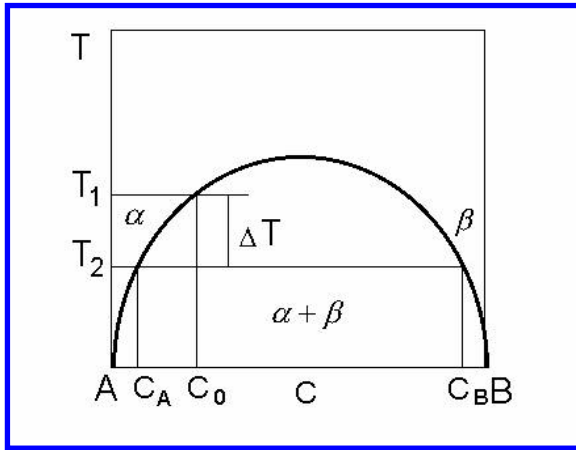
where V is the boundary migration rate.

Two situations have to be distinguished, namely, large immobile and small mobile precipitates.

For large immobile particles the grain growth rate can be represented as [607]

$$V = m_b [P - P_{\text{im}}^{tp}(V) - P_p] > m_b [P - P_{\text{im}}^{SS}(V)] \quad (6.50)$$

where $P = \frac{\alpha\gamma}{R}$ is the driving force for grain growth, γ is the grain boundary surface tension, P_{im}^{SS} and P^{tp} are dragging forces in the solid solution and

**FIGURE 6.43**

Binary phase diagram with miscibility gap (see text for details) [607].

the two-phase regime, respectively. P_p is the dragging force by immobile particles, and α is a geometrical parameter that correlates grain size and grain boundary curvature and will be taken to be $\alpha = 3$ in the following. To assess Eq. (6.50) the Zener- and the Lücke-Detert approximations for particle drag and impurity drag, respectively

$$P_{\text{drag}} = \frac{3\bar{c}\gamma}{2r} \quad (6.51)$$

$$P_{\text{im}} = \Gamma \frac{V}{D_{\text{im}}} kT \quad (6.52)$$

\bar{c} — the volume fraction of the particles, r — particle radius, Γ — adsorption at the grain boundary, D_{im} — bulk diffusion coefficient of the solute atoms.

The next inequality expresses the acceleration of grain growth caused by precipitation [607]

$$\frac{P - \frac{3\bar{c}\gamma}{2r}}{\Gamma(c'_0 = c_A)} > \frac{P}{\Gamma(c_0)} \quad (6.53)$$

Eq. (6.53) is valid under the assumption that the impurity diffusion coefficient is independent of concentration. With the driving force for grain growth $P \approx 3 \cdot \frac{\gamma}{R}$, and the Henry adsorption isotherm $\Gamma(c) = Bc$, Eq. (6.53) reads

$$\frac{\frac{1}{R} - \frac{\bar{c}}{2r}}{c_A} > \frac{1}{Rc_0} \quad (6.54)$$

It is pointed out that, strictly speaking, for solids the isotherms should be used which take into consideration the interaction between species (see Chapter 1).

The Henry isotherm was used in [607] for a rough estimate to establish the essential physical link between the parameters of the problem.

The next relation follows from Eqs. (6.48), (6.49) and (6.54) [607]

$$\frac{1 - \frac{c_0 - c_A}{c_B - c_A} \cdot \frac{\bar{R}}{r}}{c_a} > \frac{1}{c_0} \quad (6.55)$$

or, using evident relationships between c_A , c_0 , c_B

$$\frac{\bar{R}}{r} < \frac{c_B}{c_0} \quad (6.56)$$

Eqs. (6.55) and (6.56) determine the conditions under which precipitation accelerates grain growth in the alloy. Since the relations (6.55) and (6.56) are derived under the assumption that the second-phase particles are immobile, the larger r (particle radius) and the smaller \bar{R} (mean grain size), the better the approach. For $c_B \sim 1$, $c_0 \sim 10^{-3}$, $c_A \sim 10^{-4}$ Eq. (6.56) yields $\frac{\bar{R}}{r} < 10^3$.

However, the phenomenon discussed holds as well for particles moving together with the grain boundary, in other words, for small, mobile particles. The theory of grain boundary motion dragged by mobile particles was comprehensively considered in Chapter 3. In particular, it was shown that the velocity of joint motion of a grain boundary and the particles with a continuous size distribution $\bar{n}(r)$ can be expressed as

$$V = \frac{Pm_b}{1 + \int_0^\infty \frac{\bar{n}(r)m_b}{m_p(r)} dr} \quad (6.57)$$

where $m_p(r)$ is the mobility of a particle of size r . The total number of particles per unit area n is as follows:

$$n = \int_0^\infty \bar{n}(r) dr \quad (6.58)$$

The border between free grain boundary motion and the joint motion of the grain boundary with the particles is established by dimensionless criterion ρ :

$$\rho = \int_0^\infty \frac{\bar{n}(r)m_b}{m_p(r)} dr \quad (6.59)$$

If $\rho \ll 1$ then $V \cong m_b P$, and the grain boundary velocity is determined by the mobility of the boundary. If $\rho \gg 1$ grain boundary motion is determined by the mobility of the particles and their distribution function, which in the simple case of a uniform size distribution $r = r_0$ can be represented as

$$\begin{aligned} \bar{n}(r) &= n_0 \delta(r - r_0) \\ V &= \frac{Pm_p(r_0)}{n_0} \\ \rho &= \frac{n_0 m_b}{m_p(r_0)} \end{aligned} \quad (6.60)$$

where $n(r_0)$ is the number of particles of size r_0 per unit area.

As discussed in Chapter 3 (see Table 3.2), the particle mobility is determined by its size and the mass transport mechanism. If mass transport is conducted through the bulk of a particle $m_p(r) \sim \frac{1}{r^3}$; if it operates by interfacial diffusion $m_p(r) \sim \frac{1}{r^4}$.

In particular, for rather small particles which are moving by interfacial diffusion (D_S), their mobility can be derived as (Table 3.2)

$$m_p(r) = \frac{\Omega_a D_S \lambda}{\pi k T r^4} \quad (6.61)$$

where Ω_a , D_S , λ are the atomic volume, interfacial diffusion coefficient, and thickness of the interfacial layer in which the diffusion occurs, respectively.

Neglecting the change of grain boundary surface tension due to the depletion of concentration of the impurity atoms in the bulk of the grains, the condition for grain growth acceleration can be written (in the case of a uniform size distribution $r = r_0$) as [607]

$$r_0^2 < \Omega_a \lambda \cdot \Gamma(c_0) \frac{D_S}{D_m} \cdot \frac{c_B - c_A}{c_0 - c_A} \quad (6.62)$$

For $D_S \approx 10^{-10} \text{m}^2 \text{s}^{-1}$, $D_{im} \approx 10^{-14} \text{m}^2 \cdot \text{s}^{-1}$, $\Omega_a \cong 10^{-5} \text{m}^3 \cdot \text{mol}^{-1}$, $\Gamma(c_0) \approx 10^{-5} \text{mol} \cdot \text{m}^{-2}$, $\lambda \approx 10^{-9} \text{m}$, $c_b = 1$, $c_a \approx 10^{-4}$, $c_0 \cong 10^{-3}$, the particle size $r_0 < 10^{-6} \text{m}$.

Grain boundary motion together with the particles is bound to have a point of detachment. As shown in [607], the detachment condition can be represented as

$$f(r_0) m_p(r_0) < V(c_A) \quad (6.63)$$

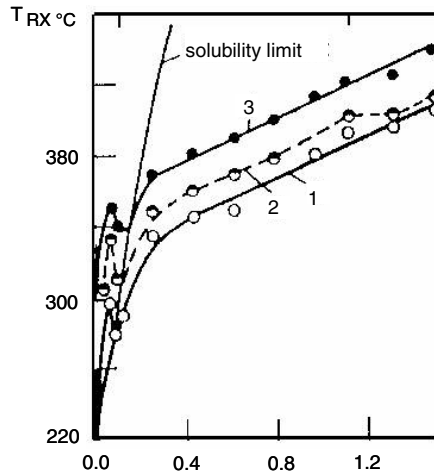
or

$$\frac{r_0^3}{\bar{R}} > \lambda \Omega_a \Gamma(c_A) \frac{D_S}{D_{im}} \quad (6.64)$$

For the values of the parameters given above Eq. (6.64) is followed for $\frac{r_0^3}{\bar{R}} > 10^{-15} \text{m}^2$, for instance, by $r_0 > 10^{-7} \text{m}$ and $\bar{R} < 10^{-6} \text{m}$.

Consequently, the predicted effect can actually occur in systems with mobile and immobile particles. From Eqs. (6.55) and (6.56) follows that the effect in samples with immobile particles is more pronounced in systems with low solute solubility (c_A and c_0 are small) and rather small mean grain size \bar{R} . By contrast, for mobile particles the only constraint is the size of the particles: they must be sufficiently small.

The only experimental data which can be connected with this effect [607] are the recrystallization of Al-Mn alloys [608] (Fig. 6.44). Fig. 6.44 shows the concentration dependence of recrystallization in Al-Mn alloys for the temperature of different stages of recrystallization — the early stage ($1 - t_r^e$), 50% recrystallized ($2 - t_r^{0.5}$) and the final stage of recrystallization ($3 - t_r^f$) [608] (Fig. 6.44). In the close vicinity of the solubility limit a sharp minimum can

**FIGURE 6.44**

Concentration dependence of recrystallization temperature $T_{\text{recr.}}$ of Al-Mn alloys with different Mn content: 1 — beginning of recrystallization; % recrystallized volume; 2 — 50% recrystallized volume; 3 — terminal recrystallization [608].

be observed for all t_r , indicating an acceleration of the process. It is stressed that the minimum mentioned is also evident for temperatures at the end of recrystallization, when the major contribution to the microstructure change is associated with grain growth, as assumed in the theoretical framework given above. From the analysis given above it is obvious that the necessary conditions for the effect of precipitation accelerated grain growth are not so tough, and certainly ought to be observed in nanocrystalline materials.

The approach put forward in [607] was developed in [609]. The main idea of the proposed approach can be easily understood from consideration of the simplest case: the behavior of a binary system with a solubility limit c_0 of solute atoms and with zero solubility of the solvent atoms in the pure solute. The second-phase particles in such a system are particles consisting of pure solute. For simplicity the density of the solid solution (matrix) and the second-phase particles is assumed to be equal. The grain boundary is immobile when the sum of the forces acting on it vanishes

$$P_{\text{gg}} - P_{\text{drag}} = 0 \quad (6.65)$$

where $P_{\text{gg}} = \frac{2\gamma}{R}$ is the driving force for grain growth, γ , R are grain boundary surface tension and radius of curvature, which is proportional to the grain size D : $R = \eta D$, where η is in the range of 5 to 10. P_{drag} is the drag force induced by immobile particles, Eq. (6.51). In [609] the situation was considered

when the solute atoms are partitioned among the particles, matrix, and grain boundaries. Both grain boundary adsorption (segregation) and solute drag are constant since the concentration in the bulk is equal to the solubility limit during grain growth. However, for rather small particles of radius r the equilibrium concentration of the second component (impurity) in the bulk should be different from the solubility limit in accordance with the Gibbs-Thomson relation

$$c'_0 = c_0 \exp\left(\frac{2\gamma\Omega}{rkT}\right) \quad (6.66)$$

$$c'_0\Omega + A\Omega\Gamma(c'_0) + \bar{c} = \text{const} \quad (6.67)$$

where c'_0 is the changed solubility limit, Ω is the atomic volume, $\Gamma(c'_0)$, $A = \frac{3}{D}$ are grain boundary adsorption (segregation) and the grain boundary area per unit volume of a polycrystal (all grains are supposed to be cuboidal). On the other hand, the average volume concentration of impurity atoms c , in other words, the number of the impurity atoms per unit volume of a polycrystal with mean grain size (radius) $D = D_0$, is equal to

$$c = c_0 + A \cdot \Gamma(c_0) = c_0 + \frac{3}{D_0}\Gamma(c_0) \quad (6.68)$$

Therefore

$$\bar{c} = c\Omega - c'\Omega - A\Omega\Gamma(c'_0) = c_0\Omega + \frac{3\Omega}{D_0}\Gamma(c_0) - c'_0\Omega - A\Omega\Gamma(c'_0) \quad (6.69)$$

Eqs. (6.65) and (6.69) yield the size of the particles which arrest grain growth in a polycrystal. Eqs. (6.65) and (6.67) allow us to find the relation between grain size and the size of the particles in the form of a differential equation [609]. Differentiation of Eq. (6.69) yields

$$\frac{4}{3}\frac{1}{\eta D} - \frac{4}{3}\frac{r}{\eta D^2}\frac{dD}{dr} = \frac{2\gamma\Omega^2c_0}{r^2kT}\exp\left(\frac{2\gamma\Omega}{rkT}\right) + \frac{3\Omega}{D^2}\Gamma(c'_0)\frac{dD}{dr} - \frac{3\Omega}{D}\frac{d\Gamma(c'_0)}{dD}\frac{dD}{dr} \quad (6.70)$$

where γ is the surface tension of the interface particle-matrix.

Eq. (6.70) predicts an extremum (minimum) of $D(r)$. The integration of Eq. (6.70) in the limits of D_0 and D gives the size of the particles which arrest grain growth in the polycrystal. The equations derived reflect the situation when the particles are located in the bulk of the grains and the grain boundaries interact with them in the course of grain growth. However, the conditions of particle formation suggest that there is a large probability for the scenario that the particles will nucleate directly at grain boundaries. Let us consider such a situation where all particles are located at grain boundaries. In the framework of the Zener approach the drag force of the particles at grain boundaries is equal to

$$P_{\text{drag}} = 2\pi r\gamma n \quad (6.71)$$

where n is the number of the particles per unit area at the grain boundary, γ is the grain boundary surface tension. The volume fraction of the particles can be expressed as

$$\bar{c} = A \cdot n \cdot \frac{4}{3}\pi r^3 = \frac{4\pi n}{D}r^3 \quad (6.72)$$

and

$$P_{\text{drag}} = \frac{1}{2} \frac{\bar{c}\gamma D}{r^2} \quad (6.73)$$

With Eqs.(6.65) and (6.73) we arrive at

$$\frac{2\gamma}{\eta D} = \frac{1}{2} \frac{\bar{c}\gamma D}{r^2} \quad (6.74)$$

Eqs. (6.69) and (6.74) yield the size of the particles which arrest grain growth in a polycrystal for the case when all particles are located at grain boundaries.

The differential equation, derived in [609], predicts an extremum of $D(r)$, in analogy to Eq. (6.70). The equations considered are somewhat simplified. In the vicinity of $c \approx c_0$ the grain boundaries can be considered as a saturated by impurity atoms and $\Gamma(c_0) = \text{const}$. For rather “large” particles we can neglect the Gibbs-Thomson relation. In this case Eq. (6.65) has the solution

$$r = \frac{9}{4}\Omega\Gamma(c_0)\eta\left(\frac{D-D_0}{D_0}\right) \quad (6.75)$$

where the initial grain size D_0 can be extracted from Eq. (6.68)

$$D_0 = \frac{3\Gamma(c_0)}{c - c_0} \quad (6.76)$$

When all rather “large” particles are located at the grain boundaries we get from Eqs. (6.69) and (6.74)

$$r^2 = \frac{3\Gamma(c_0)\Omega\left(\frac{1}{D_0} - \frac{1}{D}\right)D^2}{4} \quad (6.77)$$

The approach and the equations developed were applied to grain growth in the system Ni-P studied intensively in [610, 611]. For a polycrystal of Ni with mean grain size $D = 100$ nm doped with 3.6% of P the critical (i.e. the maximum) radius of the particles which arrests grain growth in such a system is given in Eq. (6.70): $r = \eta \cdot 2.25$ nm and in Eq. (6.77) $r = 1.6\eta$ nm. With $\eta \approx 5$ the critical particle radius is of the order of 10 nm. We would like to remind the readers that Eq. (6.70) is derived using the Gibbs-Thomson relation, whereas Eq. (6.77) does not take into account the capillary effect of small particles.

Up to this point the main goal was to find the radius of the particles which arrest grain growth in the system. This critical radius was treated as a function of the solute concentration, its limit of solubility, running grain size and

grain boundary adsorption. However, the particle pinning of grain boundaries results from two interdependent processes. On the one hand, solute atoms are liberated in the course of grain growth, owing to the decrease in grain boundary area. This gives rise to the nucleation and growth of precipitates. On the other hand, because particles nucleate and grow, grain growth is hindered and eventually ceases. It is virtually unfeasible to model accurately the interdependency between grain growth and precipitation. If the bulk solute concentration corresponds to the solubility limit, grain growth leads to the formation of precipitates owing to the reduction of grain boundary area. The concept of grain boundary adsorption in conjunction with particle drag in the Zener approximation makes it possible to determine both the volume fraction and the radius of the particles which arrest grain growth.

For a computational exercise an Al-Cu alloy will be considered in the following, with the nominal composition Al-1at%Cu. The initial grain size is set to $D_0 = 100$ nm. The copper adsorption at grain boundaries Γ_{Cu} is assumed to be saturated, i.e. $3.2 \cdot 10^{-5}$ mol/m². These conditions lead to an initial Cu concentration c_0 in the grain of $4.5 \cdot 10^1$ mol/m³ or $4.4 \cdot 10^{-2}$ at% which corresponds to the solubility limit of copper in aluminium at $T = 200^\circ\text{C}$ where tempering is performed. To simplify the calculations, it is also assumed that the precipitates which arrest grain growth are composed of pure copper and have a spherical shape.

At the beginning of the heat treatment, there are no particles in the system, the average grain size is D_0 , and the concentration in the matrix equals the solubility limit c_0 . This state is labeled *S* in Fig. 6.45. In the first stage of grain growth, all solute liberated from the grain boundaries enriches the matrix and the solute concentration in the matrix c^M rises to

$$c^M = c_0 + 3\Gamma(c^M) \left[\frac{1}{D_0} - \frac{1}{D} \right] \quad (6.78)$$

As c^M increases, the driving force for the phase transformation increases and the critical radius r_{crit} for nucleation shrinks rapidly (dotted line in Fig. 6.45, [609])

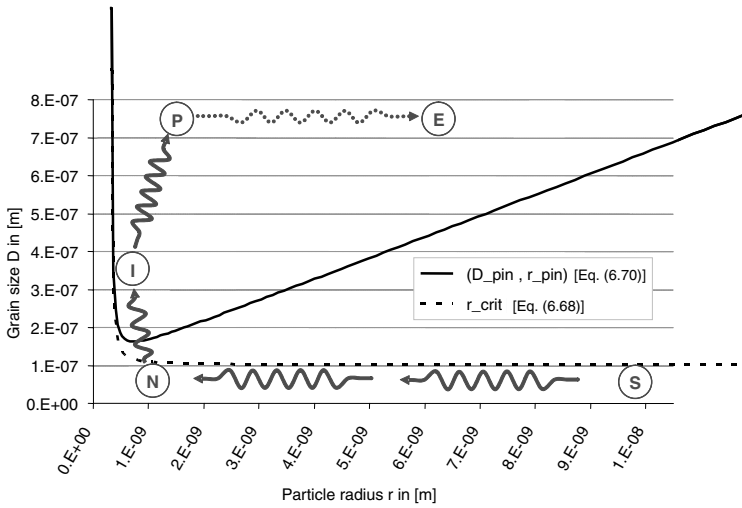
$$r_{\text{crit}} = \frac{2\gamma V_m}{R_g T \cdot \ln\left(\frac{c^M}{c_0}\right)} = \frac{2\gamma V_m}{R_g T \cdot \ln\left(1 + \frac{3\Gamma(c^M)}{c_0} \left[\frac{1}{D_0} - \frac{1}{D}\right]\right)} \quad (6.79)$$

where R_g is the gas constant.

Eventually a state (*N* in Fig. 6.45) is reached where nucleation can be thermally activated. Precipitates are not yet present. The process requires an incubation period τ_{nuc}

$$\tau_{\text{nuc}} = (2 \cdot Z^2 \cdot \beta^*)^{-1} \quad (6.80)$$

where Z is the Zeldovich factor and β^* the rate at which atoms are added to the critical nucleus. After incubation the system reaches position *I* in Fig. 6.45. At this point, grain boundary pinning can occur. The first condition for an

**FIGURE 6.45**

Pinning of grain boundaries by second-phase particles [609].

effective pinning is a state (D, r) above the limit $(D_{\text{pin}}, r_{\text{pin}})$. This limit can be obtained by integration of the differential equation (6.70), and is represented by a solid line in Fig. 6.45 [609]

$$D_{\text{pin}} = \frac{3\Gamma(c'_0) + \frac{4}{3V_m\eta}r_{\text{pin}}}{c_0 \left[1 - \exp\left(\frac{2\gamma V_m}{R_g T \cdot r_{\text{pin}}}\right) \right] + \frac{3\Gamma(c_0)}{D_0}} \quad (6.81)$$

The second necessary condition is the precipitation of a sufficiently large volume fraction. This is achieved at P in Fig. 6.45, where an efficient pinning occurs and grain growth ceases. However, grain growth does not become arrested because of particle coarsening, and it evolves slowly to a point E, the end of the heat treatment. In order to illustrate the above methodology, the points N-I-P were estimated by computer simulation using the precipitation kinetics model ClaNG. This model is based on the classical nucleation and growth theory for precipitation. It follows the Kampmann and Wagner methodology to determine the evolution of the precipitate size distributions. A detailed description of the simulation tool can be found elsewhere [610]. In order to simplify the calculation, the parabolic grain growth kinetics $D^2(t) - D_0^2 = A \cdot t$, A is kept constant and set to $5.0 \cdot 10^{-15} \text{m}^2/\text{s}^{-1}$ (see Chapter 3) are considered to remain constant with time, i.e. not influenced by solute content or precipitate volume fraction, until it finally ceases. Using the ClaNG model, it is found that the point N in Fig. 6.45 is obtained very quickly, in less than 1 s. The first precipitates appear after about 20 s when the grain size has reached $D \approx 300 \text{ nm}$. After 50 s ($D \approx 500 \text{ nm}$), which corresponds to the calculated

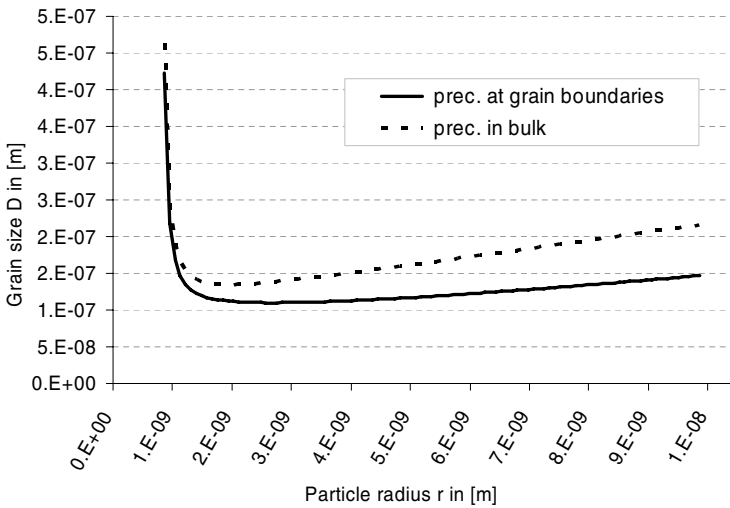


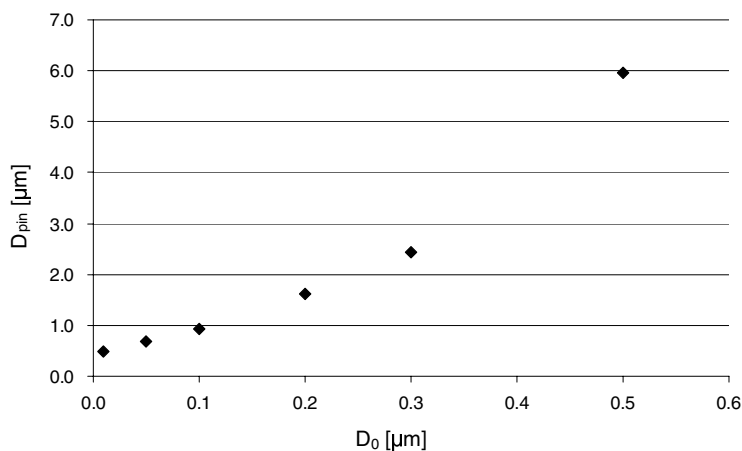
FIGURE 6.46

Pinning region (D_{pin} , r_{pin}) in case of preferred precipitation at grain boundary. The dotted line indicates the case of homogeneous nucleation in the bulk [609].

incubation period τ_{nucl} , a high density of particles, $10^{20}m^{-3}$ is present but the precipitated volume fraction $\bar{c} = 2.2 \cdot 10^{-7}$ is still too low to allow an efficient pinning of the grain boundaries. The critical condition $P_{drag} = P_{gg}$ is finally achieved after 150 s. At this time the precipitate density reached $4.3 \cdot 10^{23}m^{-3}$ for an average radius of 0.8 nm. The grains have grown to their final size $D_{crit} = 0.9 \mu m$ and are efficiently pinned by second-phase particles.

It is emphasized that the simulations are based on several strong assumptions (spherical shape, constant grain growth kinetic) and thus will not represent a real case, but they render important information on the interplay of the various concurrent atomistic processes. For instance, it can be learned that the incubation period τ_{nucl} plays an important role [609]. This also holds for a scenario where pinning originates from particles heterogeneously precipitated at grain boundaries. In such case the pinning region (D_{pin} , R_{pin}) is also larger (Fig. 6.46).

A sensitive parameter is, of course, the initial grain size since it controls both the amount of liberated solute and the driving force for grain growth (Fig. 6.47). The interaction of grain growth and precipitation is most effective for small grain sizes, in particular for nanocrystalline material. If the initial grain size is changed from $D_0 = 100 \text{ nm}$ to $D_0 = 50 \text{ nm}$ grain growth will cease after 43 s at a final grain size of $D_{pin} = 0.5 \mu m$ and a precipitate size of $r_{pin} = 1.4 \text{ nm}$ ($\bar{c} = 0.45\%$) compared to 150 s, $D_{pin} = 0.9 \mu m$, $r_{pin} = 0.8 \text{ nm}$,

**FIGURE 6.47**

Dependency of the pinned grain size D_{pin} on the initial grain sized D_0 [609].

$f = 0.1\%$. For $D_0 = 700$ nm grain growth would not be arrested even after 10 hours. Therefore, for conventional material with a typical grain size of $10\ \mu\text{m}$, a stagnation of grain growth will not be obtained by a redistribution of solute from boundaries to the bulk.

In spite of several strong assumptions made in the course of the calculations (spherical shape of the particles, constant grain growth kinetic, the neglecting of the change of the volume by vanishing grain boundaries: in the relations discussed the strict Gibbs approach was used, i.e. the volume of the grain boundaries is neglected; since the volume fraction S/V of grain boundaries changes in proportion to $1/D$ such approximation is reasonable when $D \geq 50$ nm because for cuboidal grain shape $S/V = \frac{3}{D}\delta$ which amounts to 6% for $D = 50$ nm and a boundary thickness of 1 nm) computer simulations reveal that the respective precipitation kinetics that eventually terminate grain growth sensitively depend on solute supersaturation and solute diffusivity.

6.4 Mechanisms on Retardation of Grain Growth

The design of materials with given requirements for microstructure stability is connected inseparably with an essential engineering problem: a comparison of the efficiency of the various drag effects on grain growth. Actually, to produce a fine-grained or nanocrystalline material is part of the problem only. It is of equal importance to slow down the process of grain growth since the small

grain size generates a large driving force for grain growth. In [612] an attempt is undertaken to assess the efficiency of drag effects by different structural elements of a polycrystal on grain growth. The rate of grain area change is chosen as a measure of stability of a grain structure and the inhibition of grain growth is pairwise evaluated among all drag effects considered. The rate of grain area change dS/dt is chosen as a measure for the stability of a 2D grain structure. The change of grain area characterizes grain growth to a greater extent than the change of grain size and both can be distinctly different even for the same grain. The consideration of the problem is restricted by 2D polycrystalline structures. The concepts of grain growth on the basis of boundary and junction migration best for 2D systems were elaborated. Since the issue considered is the relative efficiency for grain growth retardation a 2D approach is physically adequate. To define the relative efficiency of grain growth drag due to different drag effects the authors of [612] construct a hierarchy of pairwise dimensionless criteria $\lambda_{i,k}$

$$\lambda_{i,k} = \frac{\left(\frac{dS}{dt}\right)_i}{\left(\frac{dS}{dt}\right)_k} \quad (6.82)$$

which constitutes the ratio of the rate of grain area change for a pair of different drag mechanisms. When $\lambda_{i,k} < 1$ grain growth is controlled by mechanism (i), and the magnitude of $\lambda_{i,k} < 1$ denotes the drag efficiency.

The rate of grain area change $\frac{dS}{dt}$ is expressed by the Von Neumann-Mullins relation (4.55). The influence of impurities is reflected basically by the grain boundary mobility $m_b(c)$, where c is the concentration of the impurities. The criterion $\lambda_{\text{imp},0}$ in this case is equal to

$$\lambda_{\text{imp},0} = \frac{\left(\frac{dS}{dt}\right)_{\text{imp}}}{\left(\frac{dS}{dt}\right)_{c=0}} = \frac{\frac{m_b(c)\gamma\pi}{3}(n-6)}{\frac{m_b\gamma\pi}{3}(n-6)} = \frac{m_b(c)}{m_b} \quad (6.83)$$

where $\left(\frac{dS}{dt}\right)_{c=0}$ and $\left(\frac{dS}{dt}\right)_{\text{imp}}$ are the rate of grain area change in “pure” metal and in a metal with impurities, respectively. As the mobility depends strongly on the crystallographic parameters of a grain boundary the most correct way to define $\lambda_{\text{imp},0}$ is to use data for specific and defined grain boundaries with different amount of impurities. For a $\langle 111 \rangle$ tilt grain boundary (misorientation angle 38.2° ($\Sigma 7$)) in Al with total impurity content 0.4 ppm and 7.0 ppm, respectively, at 200°C , $\lambda_{\text{imp},0} = 5 \cdot 10^{-4}$. For a non-special $\langle 111 \rangle$ tilt grain boundary (misorientation angle 40.5°) at the same temperature $\lambda_{\text{imp},0} = 1.7 \cdot 10^{-4}$. The estimation made in [612] for random grain boundary in Al doped with Fe ($c \approx 10^{-5}$) at 200°C gives $\lambda_{\text{imp},0} \approx 3.6 \cdot 10^{-3}$.

The criterion λ for triple junction drag compares the rate of area change as affected by triple junction with the rate for free uniform boundary motion

[612]

$$\lambda_{tj,b} = \frac{-m_{tj}\gamma\bar{R}n\sin\left(\frac{2\pi}{n}\right)\left[2\sin\left(\frac{\pi}{n}\right)-1\right]}{\frac{m_b\gamma\pi}{3}(n-6)} =$$

$$\lambda_{tj,b} = \lim_{n \rightarrow \infty} \frac{\frac{d}{dn}\left(\frac{dS_{tj}}{dt}\right)}{\frac{d}{dn}\left(\frac{dS_b}{dt}\right)} = \frac{3}{4} \frac{m_{tj}\bar{R}}{m_b} = \frac{3}{4} \Lambda \quad (6.84)$$

where \bar{R} is the grain size, Λ is defined by this equation, n is a topological class of a grain. A distinctive property of Eq. (6.84) is the explicit dependency of $\lambda_{tj,b}$ on the grain size. The values of the criterion $\lambda_{tj,b}$ were evaluated in [612] on the basis of experimental data for a triple junction mobility in pure Al. It was shown that for Al polycrystal with the grain size $\bar{R} = 10^{-8}\text{m}$ at 200°C the criterion $\lambda_{tj,b}$ is in the range of $\lambda_{tj,b} \approx 10^{-12} - 10^{-11}$.

To define the criterion $\lambda_{qp,b}$, which describes the retardation of grain growth by quadruple junctions, the approach put forward in [619] can be utilized. As shown in [447, 619] the grain growth kinetics in polycrystals can be described by Eq. (4.96)

$$V = \frac{m_b\gamma\kappa}{1 + \frac{1}{\Lambda} + \frac{1}{\bar{\Lambda}_{qp}}}$$

where $\Lambda = \frac{m_{tj}\bar{R}}{m_b}$ and $\bar{\Lambda}_{qp} = \frac{m_{qp}\bar{R}^2}{m_b}$ are the criteria which determine the triple junction drag and the quadruple junction drag of grain growth, respectively. Then the desired criterion $\lambda_{qp,b}$ can be expressed as a ratio of grain growth kinetics where the influence of the junctions is neglected and the grain growth kinetics influenced by boundary junction(s)

$$\lambda_{\text{junctions},b} = \frac{V_{\text{junctions}}}{V_b} = \frac{1}{1 + \frac{1}{\Lambda} + \frac{1}{\bar{\Lambda}_{qp}}} \quad (6.85)$$

Using the value of the quadruple junction mobility in Al evaluated in [447] (at 600°C $m_{qp} \approx 2 \cdot 10^{-4}\text{s}^{-1}$) and the experimental data for grain boundary mobility presented in Chapter 3 for the criterion $\lambda_{qp,b}$ at 600°C we obtain $\lambda_{qp,b} \approx 10^{-13}$. The criterion $\lambda_{tj,b}$ at 600°C in Al for $\bar{R} \approx 10^{-8}\text{m}$ [436, 437] is equal to 10^{-8} . At first glance the results ($\lambda_{tj,b} \gg \lambda_{qp,b}$) contradict both computer simulation data (see Chapter 4) and our previous calculations. However, we would like to remind the reader that the latter ones were carried out for 200°C . To recalculate the criterion $\lambda_{qp,b}$ from 600°C to 200°C the quadruple junction mobility at 200°C should be known. Unfortunately, our knowledge of quadruple junction mobility is extremely poor. Nevertheless, it can be assumed that the enthalpy of activation of quadruple junction motion is rather small. It follows both on general grounds (a quadruple junction is a structural element of zero dimension, similar to a small particle) and the evaluation of quadruple junction mobility for nanocrystalline Pd at room temperature: $m_{qp} \approx 10^{-5}\text{s}^{-1}$, a value which is very akin to the quadruple junction mobility in nanocrystalline Al at 600°C , in spite of a huge difference in nature

of the metals and the temperature of motion. Let us estimate the dimensionless criterion $\lambda_{\text{junctions},b}$ using the particular value of quadruple junction mobility ($m_{qp} \approx 2 \cdot 10^{-4} \text{ s}^{-1}$) and grain boundary and triple junction mobility for Al (Table 4.4, $\langle 110 \rangle$ tilt grain boundary) at 200°C. One can see that for $\bar{R} = 10^{-8} \text{ m}$ and $\gamma = 0.5 \text{ J/m}^2$ the criteria are equal to

$$\begin{aligned}\Lambda_{tj} &= 10^{-13}; \\ \Lambda_{qp} &= 3 \cdot 10^{-6}\end{aligned}$$

and

$$\Lambda_{\text{junctions},b} = 10^{-13}$$

It is obvious that the main contribution to $\lambda_{\text{junctions},b}$ comes from triple junctions drag. It is stressed that the effects of the different grain boundary junctions are closely connected; indeed,

$$\Lambda_{qp} = \frac{m_{qp}\bar{R}}{m_{tj}}\Lambda_{tj} \quad (6.86)$$

At high temperatures where the mobility of the triple junctions due to their high activation enthalpy is large, the major drag of grain growth in nanocrystalline materials is exerted by quadruple junctions whereas at rather low temperature the retardation is affected by triple junctions

Owing to the loss of excess volume during grain growth, vacancies are generated to temporarily compensate the volume change. This leads to a drag effect during grain growth [12], [458]–[460] (see Chapter 4). The criterion $\lambda_{\text{vac},b}$ for this type of drag can be expressed as

$$\lambda_{\text{vac},b} = \frac{m_{\text{beff}}\gamma\pi(n-6)/3}{m_b\gamma\pi(n-6)/3} = \frac{D_{SD}}{A_b} \frac{1}{36} \frac{\bar{R}\gamma}{NkTZ(V^{\text{ex}})^2} \quad (6.87)$$

where $A_b = m_b\gamma$ is the reduced grain boundary mobility, N is the number of the atoms per unit volume, Z is the coordination number, D_{SD} is the bulk self-diffusion coefficient, V^{ex} is the grain boundary excess free volume. For pure Al at 300°C $\lambda_{\text{vac},b} \approx 10^3 \bar{R}$, and for $\bar{R} \approx 10^{-8} \text{ m}$ this yields $\lambda_{\text{vac},b} \approx 10^{-5}$.

In general two types of particle drag effects on grain growth should be considered: the drag by small mobile particles and by large immobile particles. However, the consideration in [612] is confined to nanocrystalline materials. The grain size in nanostructures is so small that it is difficult to imagine the existence of large immobile particles which are comparable in size with the grains. That is why only the drag by particles moving jointly with the grain boundaries was analyzed in [612]. The velocity of a grain boundary moving together with particles is given in Chapter 3 Eq. (3.71). The effective mobility of such a grain boundary can be expressed as

$$m_{\text{eff}} = \frac{m_p(r_0)}{n_0} \quad (6.88)$$

where $m_p(r_0)$ is the mobility of particles of radius r_0 , and n_0 is the number of particles per unit area of the boundary, respectively. For the second-phase particles considered in [612], the criterion $\lambda_{\text{part},b}$ can be represented as [607]

$$\lambda_{\text{part},b} = \frac{\left. \frac{dS}{dt} \right|_{\text{part}}}{\left. \frac{dS}{dt} \right|_b} = \frac{m_{\text{beff}}}{m_b} = \frac{m_p(r)}{n} \cdot \frac{1}{m_b} \quad (6.89)$$

where the number of second-phase particles n is determined by the phase diagram and the cooling interval. As shown in [612] for a system with rather small solubility the criterion $\lambda_{\text{part},b}$ can be expressed as $\lambda_{\text{part},b} \cong \frac{10^{-15} \text{m}^2}{r^2}$. In other words, only “sufficiently large” particles will exert an efficient drag on grain growth in nanocrystalline systems.

It is of interest to consider the relative efficiency of particles and triple junctions on retardation of grain growth. The relation which describes the relative efficiency of triple junction drag compared to mobile particle drag was derived in [612]:

$$\lambda_{tj,p} = \frac{3}{4} \frac{m_{tj} \bar{R}}{4m_{\text{beff}}} = \frac{3}{4} \frac{m_{tj}}{\pi m_p(r_0) r_0} \quad (6.90)$$

With the same values of the parameters used in the evaluations discussed above, relation (6.90) can be transformed to

$$\lambda_{tj,\text{part}} \approx 2 \cdot 10^{15} \text{m}^{-3} \cdot r^3 \quad (6.91)$$

Obviously, triple junction drag becomes comparable with particle drag only for $r \geq 10^{-5} \text{m}$, in other words for very large particles, $r > 10 \mu\text{m}$.

From this analysis it can be concluded that grain boundary junctions are most effective for microstructural stabilization of very fine-grained microstructures in the range of the used parameters.

6.5 Grain Boundary Junction Engineering

The concept of grain boundary engineering (GBE) has been embodied in the papers of the groups of Watanabe and Palumbo, respectively [614]–[618]. The practical realization of this idea was reduced to thermomechanical treatment, most often to the thermocycling. Such treatment results in an increase in the number of special grain boundaries, predominantly twin boundaries. While not questioning the prospects of such an approach the authors would like to call the reader’s attention to the fact that a deeper understanding of well-known processes or physical phenomena which permit us to create materials with given properties and (or) distribution of grain boundaries is

subsumed under GBE as well. Strictly speaking, all processes which transform the properties of materials due to a change in grain boundary properties and distribution, in other words, in grain microstructure — recovery, recrystallization and especially grain growth — fall in this category. This is our understanding of GBE. In particular, the essential difference between grain microstructure obtained during grain growth under different regimes — triple junction regime and grain boundary kinetics — indicates that there is a way to utilize this behavior to influence microstructural evolution, which will be referred to as grain boundary junction engineering, that utilizes junction properties for microstructure control [447]. Grain boundary junction engineering is a new branch of GBE. The consideration given in [619] is confined to grain growth. Grain growth affects the grain microstructure but its development depends on the internal parameters of the sample — chemical nature of the matrix, i.e. impurities, composition — and the characteristics of the process — temperature, pressure, time of annealing. To generate the desired grain microstructure is only half of the problem. It is equally important to stabilize the formed microstructure. This issue is of special importance for ultrafine-grained and nanocrystalline materials. To stabilize a small grain size usually drag forces by impurities or particles are introduced. However, both methods require a special phase and chemical composition of the material on the one hand, and change, as a consequence, its physical and mechanical properties (see Chapter 6). In [619] another approach is proposed, based on the essential difference in grain microstructures formed by junction kinetics and by boundary kinetics. The theoretical foundations of grain boundary junctions kinetics and the special features of grain growth affected by boundary junctions are considered comprehensively in Chapter 4. Here we would like to dwell on some aspects of the problem.

As shown in Chapter 4, in the course of grain growth influenced by triple junctions the grains with a number of sides n with $n_L^* < n < n_H^*$ become locked and can neither grow nor shrink. The influence of such a “layer” of locked grains on the stability of grain microstructure will be more severe for fine-grained and nanocrystalline materials.

It is emphasized repeatedly that a limited triple junction mobility always slows down the evolution of the grain microstructure of polycrystals, irrespective whether the topological class of the considered grain is smaller or larger than 6. However, the finite mobility of triple junctions not only slows down grain microstructure evolution, it changes the final distribution of the grains of different topological classes, as well. Actually, relation (4.74) provides a way of estimating the time dependence of the criterion Λ [447, 619]

$$\dot{S} = \frac{dS}{dR} \cdot \frac{dR}{d\Lambda} \cdot \frac{d\Lambda}{dt} = 2 \frac{\alpha_S}{\alpha_\Lambda} R \frac{m_b}{m_{tj}} \frac{d\Lambda}{dt} = \beta' \cdot \Lambda \cdot \frac{d\Lambda}{dt} \quad (6.92)$$

where $\beta' = 2 \frac{\alpha_S m_j^2}{\alpha_\Lambda m_{tj}^2}$, α_S and α_Λ are geometrical coefficients of the order of one. From (6.92) and (4.74) we arrive at

$$\frac{d\Lambda}{dt} = -\beta \cdot \frac{2\pi - n(\pi - 2\theta)}{\Lambda} \quad (6.93)$$

where $\beta = \frac{A_b}{\beta'}$.

The rate of change of the parameter Λ depends on the topological class n of a grain. A more specific relation for $\frac{d\Lambda}{dt}$ can be obtained in the vicinity of $\theta = \pi/3$ (see Chapter 4).

The temporal change of Λ during grain growth is given in Fig. 6.48. It can be seen from Fig. 6.48 and Eq. (6.93) that triple junction drag affects the growth of grains with different topological class n markedly different. Furthermore, Fig. 6.48 illustrates that the junction drag eliminates the unique border between growing and shrinking grains: for rather small Λ the derivative $\frac{d\Lambda}{dt}$ is positive for $n = 5$ and negative for $n = 7$. This issue is the key for understanding the influence of triple junctions on grain microstructure evolution. Moreover, this effect provides another explanation of abnormal grain growth in fine grained materials. Namely, a grain of rather large topological class will break free of triple junction drag and will start to grow at boundary kinetics much faster than the grains with small or not so large n . Evidently, such a strong acceleration of the growth of an individual grain is characteristic of abnormal grain growth. A possible way of junction kinetics treatment (JKT) is schematically depicted in Fig. 6.49, which illustrates a sequence of annealings. As shown in Chapter 4, the annealing at a relatively low temperature initiates grain growth at triple junction kinetics, and the grain microstructure resulting from this treatment is a typical “junction” microstructure, a system of polygonal grains which tends to assume an equilateral shape, etc. Fig. 6.49 presents the results of grain growth studied by computer simulations. Evidently, a subsequent annealing at boundary kinetics conditions (subsequent to junction kinetics) requires a much larger time to reach the same grain size. An increase in the effect of JKT as expressed by the grain area ratio after junction-controlled growth, S_t/S_0 , conspicuously delays regular grain growth under boundary kinetics. This phenomenon can be seen more clearly in Fig. 6.50, where the ratio of the growth rates with and without JKT is presented for different $W = \frac{d(S_t/S_0)/dt_{\text{after JKT}}}{d(S_t/S_0)/dt_{\text{bk}}}$. The numerator of W is the slope of the time dependency of the mean grain area change after JKT, while the denominator is the rate of mean grain area change at boundary kinetics. The value W^{-1} is a measure for the stabilization of the grain microstructure in the course of such a treatment.

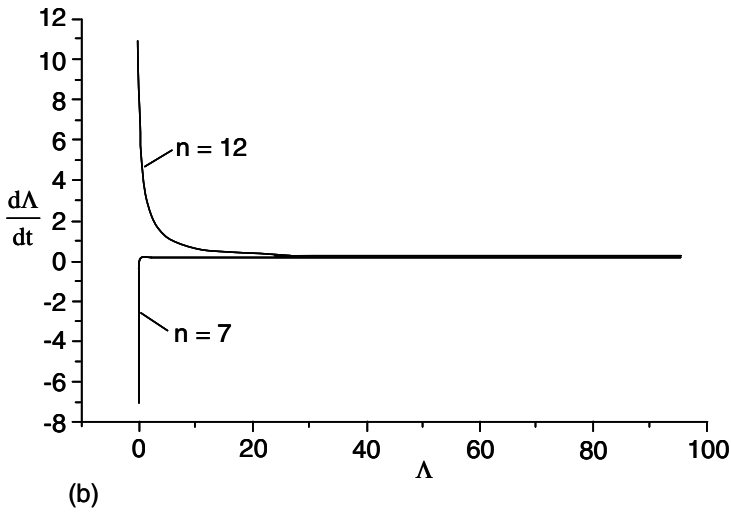
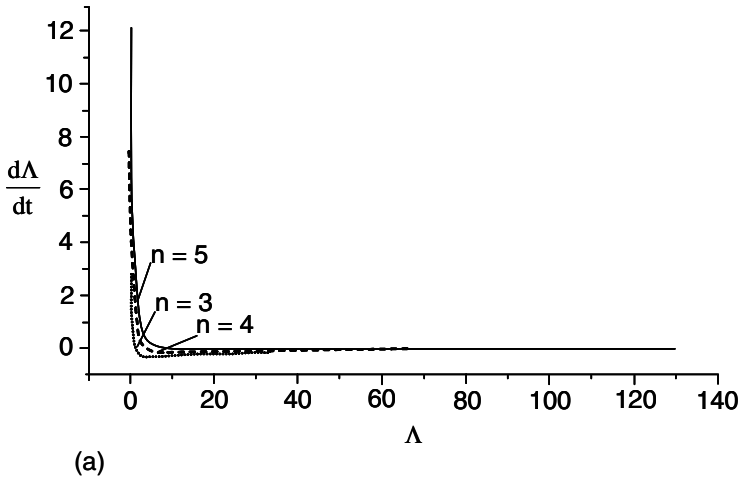


FIGURE 6.48

The dependence of $\frac{d\Lambda}{dt}$ on Λ for grains with (a) $n = 3, 4, 5$ and (b) $n = 7, 12$, respectively [447].

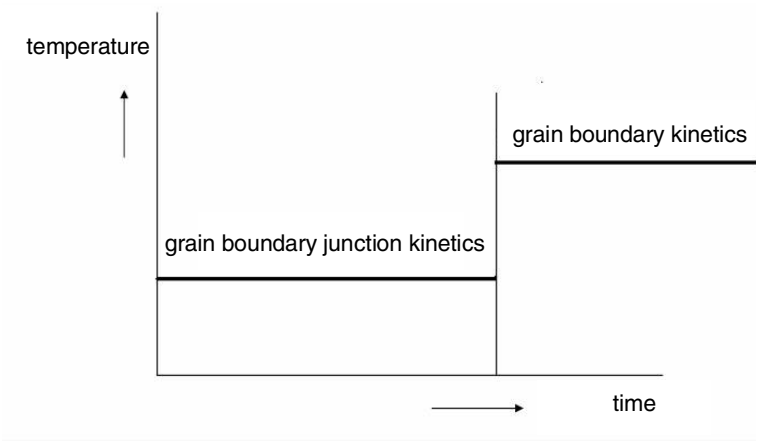


FIGURE 6.49 Procedure of junction kinetics heat treatment (JKT): two consecutive annealings: at junction and grain boundary kinetics, respectively [447].

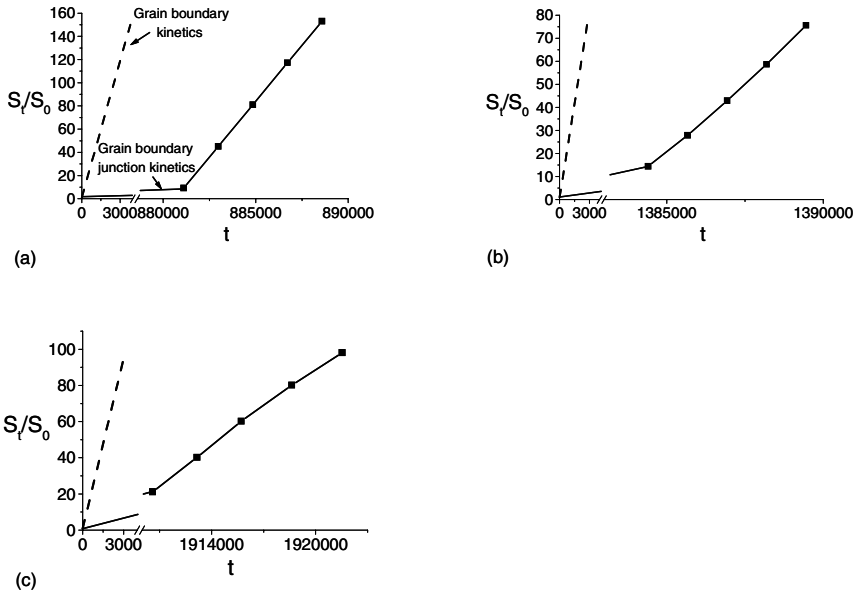


FIGURE 6.50

The kinetics of mean grain area change for JKT: boundary kinetics (dashed line) and junction kinetics (solid line), ■ — annealing at boundary kinetics after heat treatment at junction kinetics ($\Lambda = 10^{-4}$) for different starting ratio $\frac{S_t}{S_0}$: 10 (a); 15 (b); 20 (c) correspondingly; the time of annealing is given in arbitrary units [447].

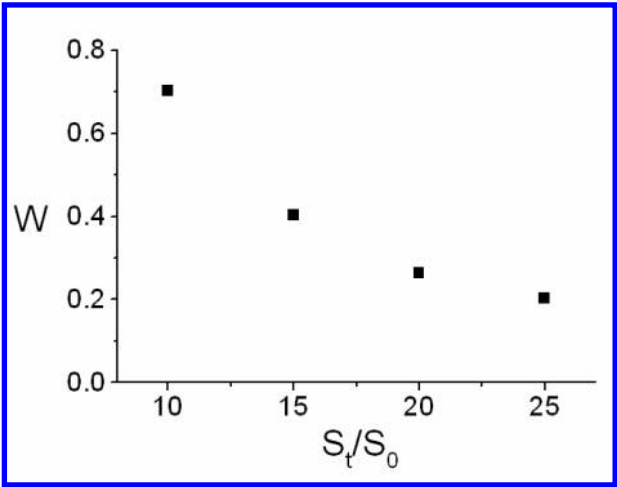


FIGURE 6.51
The dependence of $W = \frac{d(S_t/S_0)/dt_{\text{after } JkT}}{d(S_t/S_0)/dt_{\text{bk}}}$ on $\frac{S_t}{S_0}$ [447].

Appendices

7.1 Appendix A

7.1.1 Mass Transport in Solids in Terms of Osmotic Pressure

If the given mass, enclosed as before, is divided into two parts, each of which is homogeneous and fluid, by a diaphragm which is capable of supporting an excess of pressure on either side, and is permeable to some of the components and impermeable to others, we shall have the equations of conditions

$$\delta\eta' + \delta\eta'' = 0, \quad \delta\nu' = 0, \quad \delta\nu'' = 0$$

and for the components which cannot pass by the diaphragm

$$\delta m'_a = 0, \quad \delta m''_a = 0, \quad \delta m'_b = 0, \quad \delta m''_b = 0, \quad \text{etc.}$$

and for those which can

$$\delta m'_h + \delta m''_h = 0, \quad \delta m'_i + \delta m''_i = 0, \quad \text{etc.}$$

With these equations of condition, the general condition of equilibrium will give the following particular conditions:

$$t' = t''$$

and for the components which can pass the diaphragm, if actual components of both masses

$$\mu'_h = \mu''_h, \quad \mu'_i = \mu''_i, \quad \text{etc.}$$

but not

$$p' = p''$$

nor

$$\mu'_a = \mu''_a, \quad \mu'_b = \mu''_b, \quad \text{etc.}$$

([1]), where the signs ' and '' denote the values in two parts of the system accordingly; η is entropy, v and m are the volume of the parts of the system and the masses of the components, respectively, t and p are the absolute temperature and pressure, respectively.

The osmotic pressure is a thermodynamic effect in the sense that it arises as a result of tendency of the system to change in a manner such that the chemical potentials of the components become equal at all points of the system. Since the magnitude of the osmotic pressure depends on the difference between the chemical potentials (for the dilute solutions — on the difference between the concentrations) and drops down to zero when they are equal. However, the reason of the osmotic pressure is kinetic — the difference between the mobilities of atoms of different species. Traditionally the osmotic pressure was considered in the limiting case when the mobility of one of the component is equal to zero. The theory of osmotic pressure in solutions was developed for liquids, but the arguments can be transferred to solids. The situation when the atoms of components move with different velocities is most typical for the diffusion in metals. The Kirkendall effect in self-diffusion results from the difference between mobilities, so that the original interface is displaced (a marker placed at this interface is displaced).

In an analysis of self-diffusion, the driving force for the diffusive mixing is usually assumed to be gradients of the chemical potentials of the components, $\nabla\mu_i$, in which only the entropy term $RT\nabla\ln n_i$, (n_i is the density of particles in species i) was incorporated. This approach leads to the well-known Darken's results [620]. However, in the general case $\nabla\mu_i$ also contains a term proportional to the pressure gradient ($v_i\nabla p$, where v_i is a partial volume). This term is usually neglected, reasoning that $p = \text{const.}$ The situation changes where there is osmotic pressure [621]. To show the difference between the classical approach [620] and this one, which takes into consideration the osmotic pressure [621], let us briefly review Darken's analysis of self-diffusion. The component fluxes in the laboratory coordinate system can be expressed as

$$\begin{aligned} j_1^0 &= -D_1\nabla n_1 + Vn_1 \\ j_2^0 &= -D_2\nabla n_2 + Vn_2 \end{aligned} \quad (7.1)$$

where D_1 and D_2 are the partial diffusion coefficients of the components, and V is the interface velocity.

Assuming $n_1 + n_2 = n = \text{const.}$ and $j_1^0 + j_2^0 = 0$, we find

$$V = (D_1 - D_2)\nabla N_1 \quad (7.2)$$

where $N_1 = n_1/n$.

Since $j_1^0 = -\tilde{D}\nabla n_1$, we have

$$\tilde{D} = D_1N_2 + D_2N_1 \quad (7.3)$$

which determines the rate of mixing of the components and is obtained from the Boltzman-Mattano solution. \tilde{D} is often called the chemical diffusion coefficient.

Let us consider now the process taking into account in the expression for the driving force X_i the pressure gradient

$$X_i = -kT \ln n_i - v_i\nabla p_i \quad (7.4)$$

The expressions for the fluxes ($j_i = L_{ik}X_i$) can be written using the same restrictions used by Darken ($L_{11} = L_{22} = 0$, $\nabla n_1 = -\nabla n_2$, $v_1 = v_2 = \Omega_a$, the atomic volume)

$$\begin{aligned} j_1^0 &= -L_{11} \left(\frac{kT}{n_1} \nabla n_1 + \Omega_a \nabla p \right) \\ j_2^0 &= -L_{22} \left(-\frac{kT}{n_2} \nabla n_2 + \Omega_a \nabla p \right) \end{aligned} \quad (7.5)$$

It follows from the constancy of the volume that $j_1^0 + j_2^0 = 0$ so that

$$\nabla p = kT \frac{\frac{L_{22}}{n_2} - \frac{L_{11}}{n_1}}{\Omega_a (L_{11} + L_{22})} \nabla n_1 \quad (7.6)$$

Since $L_{ii} = D_{ii}n_i/(kT)$, then

$$\nabla p = \frac{kT}{\Omega_a} \frac{D_2 - D_1}{D_1 n_1 + D_2 n_2} \nabla n_1 \quad (7.7)$$

One can see from (7.7) that the resulting pressure gradient ∇p is proportional to the difference of the diffusion coefficients (mobilities) and disappears in the absence of a concentration gradient.

For the classical case (the mobility (diffusion coefficient) of one of the components is equal to zero) the expression (7.7) reduces to the van't Hoff equation.

As shown in [621], the inclusion of the osmotic pressure in the diffusion process leads to the same equation (7.2) for the interface (inert markers) velocity, whereas the expression for the chemical diffusion coefficient, obtained with a consideration of the osmotic pressure, is essentially different from Darken's equation

$$\frac{1}{\bar{D}} = \frac{N_1}{D_2} + \frac{N_2}{D_1} \quad (7.8)$$

Actually, Eqs. (7.3) and (7.8) show that under the condition $D_1 \gg D_2$ ($N_1 \cong N_2$) the velocity of mixing in Darken's theory is determined by the diffusion of the "fast" component ($\bar{D} \cong N_2 D_1$) whereas in the "osmotic" theory it is controlled by the diffusion of the "slow" component, which is more reasonable from a physical point of view. In some cases the relation (7.8) gives a better agreement with experiment than (7.3).

7.2 Appendix B

7.2.1 Calculation of the Rotation Matrix

(a) Euler angles: $\mathbf{g}(\varphi_1, \Phi, \varphi_2)$

If 2 coordinate systems $\{K_1\}$ and $\{K_2\}$ are given, the rotation of $\{K_1\}$ into $\{K_2\}$ can be described in terms of three successive rotations about base vectors of the coordinate systems according to Euler. This procedure defines the three Euler angles $\varphi_1, \Phi, \varphi_2$ (Fig. 7.1).

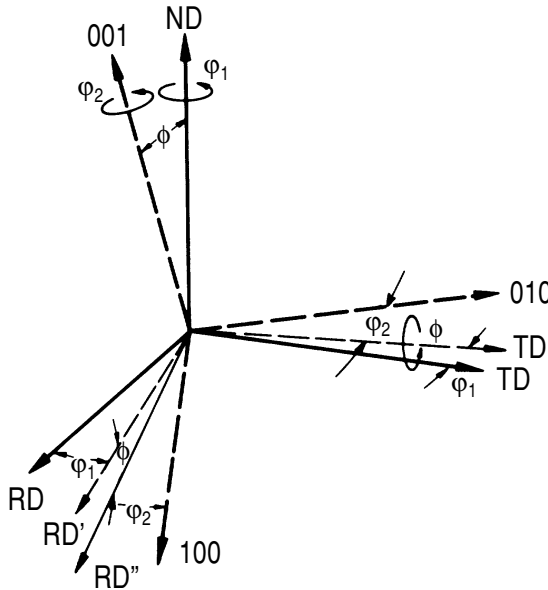
- φ_1 (rotation \mathbf{g}_1):
rotate $\{K_1\}$ about \mathbf{z}_1 by φ_1 , so that rotated \mathbf{x} (i.e. \mathbf{x}'_1) lies in plane $(\mathbf{x}_1, \mathbf{x}_2)$. The rotated system is termed $\{K'_1\} = \{\mathbf{x}'_1, \mathbf{y}'_1, \mathbf{z}'_1\}$ with $\mathbf{z}'_1 = \mathbf{z}_1$.
- Φ (rotation \mathbf{g}_2):
rotate $\{K'_1\}$ about \mathbf{x}'_1 by Φ so that the rotated \mathbf{z}'_1 (i.e. \mathbf{z}''_1) is parallel to \mathbf{z}_2 . The two times rotated system is termed $\{K''_1\} = \{\mathbf{x}''_1, \mathbf{y}''_1, \mathbf{z}''_1\}$ with $\mathbf{x}'_1 \equiv \mathbf{x}''_1$ and $\mathbf{z}''_1 \equiv \mathbf{z}_2$.
- φ_2 (rotation \mathbf{g}_3):
final rotation of $\{K''_1\}$ about $\mathbf{z}''_1 \equiv \mathbf{z}_2$ by φ_2 so that the rotated \mathbf{x}''_1 and \mathbf{y}''_1 (i.e. $\mathbf{x}'''_1, \mathbf{y}'''_1$) coincide with \mathbf{x}_2 and \mathbf{y}_2 , respectively.

Now all rotated base vectors of $\{K_1\}$ coincide with the base vectors of $\{K_2\}$ and the rotation is complete. In terms of the cube axes $\{[100], [010], [001]\}$ and for rolling geometry with rolling direction RD, rolling plane normal ND and transverse direction TD, the coordinate systems read:

$$\begin{aligned}\{K_1\} &= \{\text{RD}, \text{TD}, \text{ND}\} \\ \{K'_1\} &= \{\text{RD}', \text{TD}', \text{ND}\} \\ \{K''_1\} &= \{\text{RD}', \text{TD}', [001]\} \\ \{K_2\} &= \{[100], [010], [001]\}\end{aligned}$$

Making use of the rule that the rotation matrix for two subsequent rotations is given by the product of the matrices for each rotation, we obtain the rotation matrix for the Euler rotation $\mathbf{g}(\varphi_1, \Phi, \varphi_2)$

$$\mathbf{g} = \mathbf{g}_3 \cdot \mathbf{g}_2 \cdot \mathbf{g}_1 \quad (7.9)$$

**FIGURE 7.1**

Definition of Euler angles.

The rotation \mathbf{g}_1 is about base vectors ND and thus easy to put up (note: right-hand convention) with

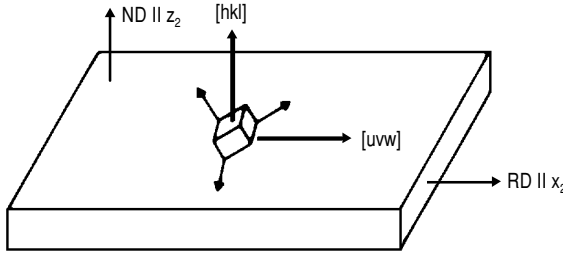
$$\mathbf{x}'_1 = \begin{pmatrix} \cos \varphi_1 \\ \sin \varphi_1 \\ 0 \end{pmatrix} \quad \mathbf{y}'_1 = \begin{pmatrix} -\sin \varphi_1 \\ \cos \varphi_1 \\ 0 \end{pmatrix} \quad \mathbf{z}'_1 = \begin{pmatrix} 0 \\ 0 \\ 1 \end{pmatrix} \quad (7.10)$$

$$\mathbf{g}_1 = \begin{pmatrix} \cos \varphi_1 & -\sin \varphi_1 & 0 \\ \sin \varphi_1 & \cos \varphi_1 & 0 \\ 0 & 0 & 1 \end{pmatrix} \quad (7.11)$$

Note that the column vectors of the rotation matrix are the base vectors of the rotated coordinate system with respect to the unrotated system. Since a rotation is an orthonormal transformation $\mathbf{g}^{-1} = \mathbf{g}'$. Hence the row vectors of the rotation matrix are the base vectors of the unrotated system with respect to the rotated system.

In analogy one obtains the rotation matrices \mathbf{g}_2 and \mathbf{g}_3

$$\mathbf{g}_2 = \begin{pmatrix} 1 & 0 & 0 \\ 0 & \cos \Phi & -\sin \Phi \\ 0 & \sin \Phi & \cos \Phi \end{pmatrix} \quad \mathbf{g}_3 = \begin{pmatrix} \cos \Phi_2 & -\sin \Phi_2 & 0 \\ \sin \Phi_2 & \cos \Phi_2 & 0 \\ 0 & 0 & 1 \end{pmatrix} \quad (7.12)$$



9

FIGURE 7.2

Definition of Miller indices.

which gives \mathbf{g} according to Eq. (7.12) as

$$\mathbf{g} = \begin{bmatrix} \cos \varphi_1 \cos \varphi_2 - \sin \varphi_1 \sin \varphi_2 \cos \phi & \sin \varphi_1 \cos \varphi_2 + \cos \varphi_1 \sin \varphi_2 \cos \phi & \sin \varphi_2 \sin \phi \\ -\cos \varphi_1 \sin \varphi_2 - \sin \varphi_1 \cos \varphi_2 \cos \phi & -\sin \varphi_1 \sin \varphi_2 + \cos \varphi_1 \cos \varphi_2 \cos \phi & \cos \varphi_2 \sin \phi \\ \sin \varphi_1 \sin \phi & -\cos \varphi_1 \sin \phi & \cos \phi \end{bmatrix} \quad (7.13)$$

This is the rotation matrix expressed in terms of the Euler angles.

The representation $(hkl)[uvw]$ and $\omega[hkl]$ are readily related to this rotation matrix.

(b) Miller Indices: $\mathbf{g}(hkl)[uvw]$

Let $[uvw]$ be a vector of $\{K_1\}$ that is parallel to \mathbf{x}_2 (of $\{K_2\}$) and $[hkl]$ a vector of $\{K_1\}$ parallel to \mathbf{z}_2 (of $\{K_2\}$). Since the column vectors of \mathbf{g} are identical with the rotated base vectors of $\{K_1\}$, the rotation matrix must read

$$\mathbf{g} = \begin{bmatrix} \frac{u}{N_1} & \frac{vl-kw}{N_3} & \frac{h}{N_2} \\ \frac{v}{N_1} & \frac{hw-ul}{N_3} & \frac{k}{N_2} \\ \frac{w}{N_1} & \frac{uk-vh}{N_3} & \frac{l}{N_2} \end{bmatrix} \quad (7.14)$$

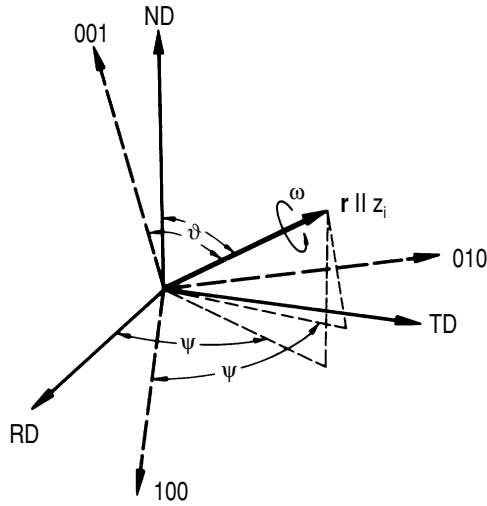
with

$$N_1 = \sqrt{u^2 + v^2 + w^2} \quad N_2 = \sqrt{h^2 + k^2 + l^2} \quad N_3 = N_1 \cdot N_2$$

By means of Eq. (7.14) $[uvw]$ and (hkl) can be determined from \mathbf{g} and vice versa. An example is the representation of an orientation in a rolled sample with respect to the rolling plane (hkl) and rolling direction $[uvw]$ (Fig. 7.2).

(c) Axis and angle of rotation: $\mathbf{g}(\omega[\text{HKL}])$

The most imaginative description of a rotation is the notation in terms of angle and axis of rotation. It can be derived by rotating $\{K_1\} = \{(100), (010), (001)\}$ and $\{K_2\} = \{\text{RD}, \text{TD}, \text{ND}\}$ into an intermediate coordinate system $\{K_i\}$ with the \mathbf{z}_i axis parallel to the rotation axis \mathbf{r} . The rotation is then completed by a rotation of $\{K_i\}$ about \mathbf{z}_i with angle ω (Fig. 7.3).

**FIGURE 7.3**

Definition of Miller indices.

The rotation axis is by definition common to both, the rotated and unrotated coordinate system. Thus, it has the same vector components with respect to both lattices. Defining the rotation axis in polar coordinates Ψ and ϑ we obtain a simple relation between axis and angle of rotation and to the Euler angles.

In order to rotate z_1 into \mathbf{r} around RD by ϑ , it must be

$$\varphi_1 = \psi + \frac{\pi}{2}, \quad \Phi = \vartheta \quad (7.15)$$

with respect to the Euler angles. Since in the intermediate system only the \mathbf{z} axis is defined to be parallel to \mathbf{r} , the \mathbf{x} and \mathbf{y} axes are arbitrary. For convenience they are chosen such that the rotation of the system $\{K_2\}$ coincides with the intermediate system after $(\varphi_1, \Phi, 0)$. Correspondingly the system $\{K_1\}$ has to be rotated by φ_1, Φ, ω . We obtain

$$\begin{aligned} \{K_i\} &= \mathbf{g}_1(\varphi_1, \Phi, \omega) \{K_1\} \\ \{K_i\} &= \mathbf{g}_2(\varphi_1, \Phi, 0) \{K_2\} \\ \{K_2\} &= \mathbf{g}_2^{-1}(\varphi_1, \Phi, 0) \cdot \mathbf{g}_1(\varphi_1, \Phi, \omega) \{K_1\} \end{aligned} \quad (7.16)$$

and the components of the rotation axis $\mathbf{r} = (a_1, a_2, a_3)$

$$a_1 = \sin \vartheta \cos \psi; \quad a_2 = \sin \vartheta \sin \psi; \quad a_3 = \cos \vartheta \quad (7.17)$$

The rotation matrix in terms of axis and angle of rotation reads:

$$\mathbf{g} = \mathbf{g}_2^{-1}(\varphi_1, \Phi, 0) \cdot \mathbf{g}_1(\varphi_1, \Phi, \omega) =$$

$$= \begin{bmatrix} (1-a_1^2) \cos \omega + a_1^2 & a_1 a_2 (1 - \cos \omega) + a_3 \sin \omega & a_1 a_3 (1 - \cos \omega) - a_2 \sin \omega \\ a_1 a_2 (1 - \cos \omega) - a_3 \sin \omega & (1-a_2^2) \cos \omega + a_2^2 & a_2 a_3 (1 - \cos \omega) + a_1 \sin \omega \\ a_1 a_3 (1 - \cos \omega) + a_2 \sin \omega & a_2 a_3 (1 - \cos \omega) - a_1 \sin \omega & (1-a_3^2) \cos \omega + a_3^2 \end{bmatrix} \quad (7.18)$$

With the notation

$$\mathbf{g} = \begin{bmatrix} g_{11} & g_{12} & g_{13} \\ g_{21} & g_{22} & g_{33} \\ g_{31} & g_{32} & g_{33} \end{bmatrix} \quad (7.19)$$

the following relations are obtained

$$a_1 \cdot 2 \sin \omega = g_{23} - g_{32} \quad (7.20a)$$

$$a_2 \cdot 2 \sin \omega = g_{31} - g_{13}$$

$$a_3 \cdot 2 \sin \omega = g_{12} - g_{21}$$

and

$$\omega = \arccos \left\{ \frac{1}{2} (a_{11} + a_{22} + a_{33} - 1) \right\} \quad (7.20b)$$

Since $a_1^2 + a_2^2 + a_3^2 = 1$, the rotation axis is known from \mathbf{g} according to Eq. (7.20a) with a constant multiplier $2\sin\omega$, which is eliminated by normalization.

7.3 Appendix C

7.3.1 Indexing of Pole Figures

We will demonstrate the procedure to determine the orientation from a pole figure for the orientation $(0\bar{1}1)[211]$ (brass orientation in an fcc lattice), which is supposed to be given in terms of its $\{111\}$ pole figure (Fig. 7.4). If the orientation of the crystal is determined, the rotation matrix is easily constructed as shown above. In this case

$$\begin{aligned} \{hkl\} &= (0\bar{1}1) \\ [uvw] &= (\bar{2}\bar{1}\bar{1}) \\ [qrs] &= (\bar{1}11) \end{aligned} \quad (7.21)$$

and according to Eq. (7.14)

$$\mathbf{g} = \begin{pmatrix} \frac{-2}{\sqrt{6}} & \frac{-1}{\sqrt{3}} & 0 \\ \frac{-1}{\sqrt{6}} & \frac{1}{\sqrt{3}} & \frac{-1}{\sqrt{2}} \\ \frac{-1}{\sqrt{6}} & \frac{1}{\sqrt{3}} & \frac{1}{\sqrt{2}} \end{pmatrix} \quad (7.22)$$

The Miller indices of the orientation can be found from the pole figure as follows. Let the specimen axes' rolling direction (RD), normal direction (ND), and transverse direction (TD) and the four $\{111\}$ poles be defined as

$$\begin{aligned} \mathbf{a} &= (a_1, a_2, a_3) = (111) \\ \mathbf{b} &= (b_1, b_2, b_3) = (\bar{1}11) \\ \mathbf{c} &= (c_1, c_2, c_3) = (\bar{1}\bar{1}1) \\ \mathbf{d} &= (d_1, d_2, d_3) = (1\bar{1}1) \\ \mathbf{x} &= (x_1, x_2, x_3) = RD \\ \mathbf{z} &= (z_1, z_2, z_3) = ND \end{aligned} \quad (7.23)$$

The orientations of the vectors \mathbf{a} , \mathbf{b} , \mathbf{c} and \mathbf{d} are denoted in the pole figure. Since the orientation is given by the vectors of the rolling direction $RD(=\mathbf{x})$ and the rolling plane normal $ND(=\mathbf{z})$ in terms of the Miller indices $\{hkl\}$ and $\langle uvw \rangle$ of the corresponding directions in the crystal lattice, we have to determine the vector components of \mathbf{x} and \mathbf{z} . For the vector \mathbf{z} of the rolling plane normal in the crystal coordinate system the dot products with the four $\{111\}$ poles yield

$$\begin{aligned} (\mathbf{z}, \mathbf{a}) &= |\mathbf{z}| \cdot |\mathbf{a}| \cos \alpha_z = z_1 a_1 + z_2 \cdot a_2 + z_3 \cdot a_3 \\ (\mathbf{z}, \mathbf{b}) &= |\mathbf{z}| \cdot |\mathbf{b}| \cos \beta_z = z_1 b_1 + z_2 \cdot b_2 + z_3 \cdot b_3 \\ (\mathbf{z}, \mathbf{c}) &= |\mathbf{z}| \cdot |\mathbf{c}| \cos \gamma_z = z_1 c_1 + z_2 \cdot c_2 + z_3 \cdot c_3 \\ (\mathbf{z}, \mathbf{d}) &= |\mathbf{z}| \cdot |\mathbf{d}| \cos \delta_z = z_1 d_1 + z_2 \cdot d_2 + z_3 \cdot d_3 \end{aligned} \quad (7.24)$$

The angles α_z through δ_z can be read from the pole figure by means of a Wulff's net. If we choose for simplicity the length of the vector \mathbf{z} to be $|\mathbf{z}| = 1/\sqrt{3}$, then we obtain from Eq. (7.24) with the vector components for \mathbf{a} , \mathbf{b} , \mathbf{c} and \mathbf{d} according to Eq. (7.23)

$$\begin{aligned} \cos \alpha_z &= +z_1 + z_2 + z_3 \\ \cos \beta_z &= -z_1 + z_2 + z_3 \\ \cos \gamma_z &= -z_1 - z_2 + z_3 \\ \cos \delta_z &= +z_1 - z_2 + z_3 \end{aligned} \quad (7.25)$$

The normalized vectors $[u^*, v^*, w^*] / \sqrt{u^{*2} + v^{*2} + w^{*2}}$ and $(h^*, k^*, l^*) / \sqrt{h^{*2} + k^{*2} + l^{*2}}$ are identical according to Eq. (7.14) with the first and third column vectors of the rotation matrix \mathbf{g} . The second column is given according to Eq. (7.14) by the cross product $(\mathbf{z} \times \mathbf{a})$. This completely determines the rotation matrix.

This procedure can be applied to any pole figure $\{hkl\}$ by associating the vectors \mathbf{a} , \mathbf{b} and so on with the respective poles $\{hkl\}$ and by determining the dot products of these vectors with \mathbf{x} and \mathbf{z} according to Eq. (7.25). Of course, especially simple is the calculation of the orientation from the $\{100\}$ pole figure, since the $\{100\}$ poles represent the projection of the base vectors of the crystal coordinate system. In this case we obtain

$$\begin{aligned} z_1 = h^* = \cos \alpha_z & \quad x_1 = u^* = \cos \alpha_x \\ z_2 = k^* = \cos \beta_z & \quad x_2 = u^* = \cos \beta_x \\ z_3 = l^* = \cos \gamma_z & \quad x_3 = u^* = \cos \gamma_x \end{aligned} \quad (7.28)$$

The Miller indices and the rotation matrix follow in analogy to the example of the $\{111\}$ pole figure given above.

Conversely, if the position of a pole in the stereographic projection is to be determined from a known rotation matrix, this is most conveniently obtained in terms of the angles α_i (tilt angle with regard to the rolling plane normal) and β_i (rotation in the rolling plane) as depicted in Fig. 7.4. These angles are related to the vectors of the lattice plane normals \mathbf{N}_i (for instance $(1\bar{1}1)$) by means of the rotation matrix

$$\begin{pmatrix} \sin \alpha_i & \cos \beta_i \\ \sin \alpha_i & \sin \beta_i \\ \cos \alpha_i \end{pmatrix} = \begin{pmatrix} g_{11} & g_{21} & g_{31} \\ g_{12} & g_{22} & g_{32} \\ g_{13} & g_{23} & g_{33} \end{pmatrix} \begin{pmatrix} x_i^* \\ y_i^* \\ z_i^* \end{pmatrix} = \mathbf{g}^{-1} \cdot \mathbf{N}_i^* \quad (7.29)$$

$\mathbf{N}_i^* = (\mathbf{x}_i^*, \mathbf{y}_i^*, \mathbf{z}_i^*)$ means the unit vector of $\mathbf{N}_i = (x_i, y_i, z_i)$, i.e. $\mathbf{x}_i^* = \mathbf{x}_i / \sqrt{x_i^2 + y_i^2 + z_i^2}$. Eq. (7.29) provides another way to determine the Miller indices of an orientation from the measured angles α_i and β_i .

When it is possible to evaluate pole figures according to the methods given above, it is very convenient to utilize tables in which the Miller indices (limited to values of 15 or less) are listed for all possible angles between related lattice plane normals and specimen directions [568].

Solutions

“You start a question, and it’s like starting a stone.”

— *Robert Louis Stevenson*

PROBLEM 1.1

It is well known that the principal result of Carnot’s cycle does not depend on the nature of the “working body” used in the cycle. Let us consider the elementary Carnot’s cycle which utilizes a grain boundary as a working body. Let us consider the diagram surface tension γ vs. area of the surface S (Mlodzeevski, 1939).

In the first stage, we increase the area at constant temperature from S_1 to S_2 . Due to the constant temperature the surface tension is constant as well. The formation of a new surface is accompanied by a cooling of the system, so to maintain a constant temperature the grain boundary should get an amount of the heat $Q = q\Delta S$ from the heater; q is the specific heat of grain boundary area formation.

In the second stage, from point B we increase the grain boundary area adiabatically. The temperature of the grain boundary drops by dT and the surface tension γ increases by $d\gamma$, respectively.

On the way C-D our grain boundary reduces the area S at constant temperature $T - dT$. In the course of this process the heat released arrives at the cooler. Finally, the boundary on the way D-A reduces its area adiabatically. The work of the cycle is the product

$$dW = (S_2 - S_1) d\gamma \quad (8.1)$$

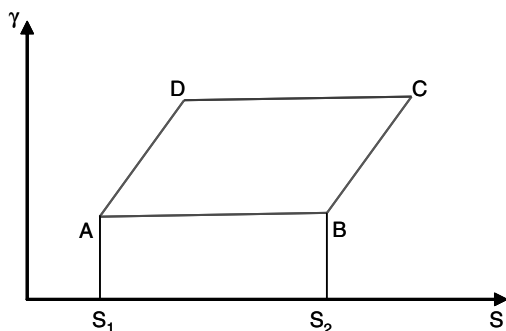
The efficiency of the cycle is equal to

$$\eta = -\frac{(S_2 - S_1) d\gamma}{Q} = \frac{dT}{T} \quad (8.2)$$

The “minus” sign indicates that the positive work of grain boundary reduction is accompanied by the emission of heat; on the other hand, a positive amount of heat from the heater is absorbed by the grain boundary when it is stretched by the external forces.

From Eq. (8.2) we arrive at

$$\frac{d\gamma}{dT} = -\frac{Q}{(S_2 - S_1)} \cdot \frac{1}{T} \quad (8.3)$$

**FIGURE 8.1**

Carnot's cycle for a thin film.

The ratio $\frac{Q}{\Delta S}$, as mentioned previously, is the specific heat to form a unit of area of the grain boundary.

Finally, the expression for the temperature coefficient of grain boundary surface tension reads

$$\frac{d\gamma}{dT} = -\frac{q}{T} \quad (8.4)$$

It is known from experiment that q is positive (it is absorbed by a surface), so $\frac{d\gamma}{dT}$ is negative.

At last we would like to emphasize one issue. It is clear that it is impossible to change the area of a grain boundary independently of the bulk of the grains. However, it should be intimated that the change in the area of a liquid film is connected with the interaction between the surface layer and the bulk of the liquid film as well; there is no surface in the uncombined state.

PROBLEM 1.2

The number of grain boundaries over the length ℓ of the rivet is equal to

$$n = \frac{\ell}{D_0} \quad (8.5)$$

Then the change of the length of the rivet in the course of annealing (due to grain growth) can be expressed as

$$\Delta\ell_{\text{gg}} = \ell \left(\frac{1}{D_0} - \frac{1}{D} \right) V^{\text{ex}} \quad (8.6)$$

The change of the length of the rivet due to thermal expansion of Al reads

$$\Delta\ell_{T\text{Al}} = \ell\alpha\Delta T \quad (8.7)$$

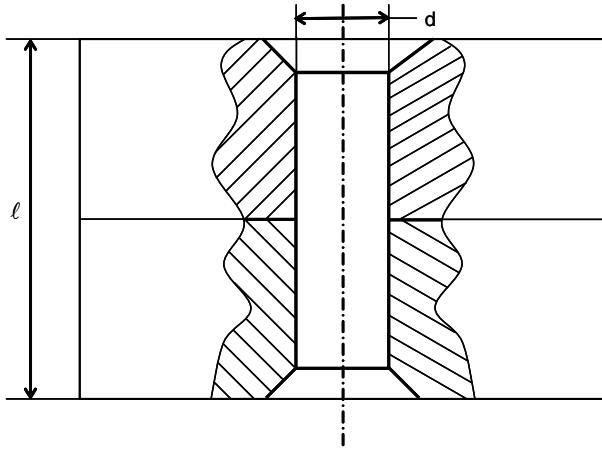
**FIGURE 8.2**

Diagram of two pieces of material connected by a rivet.

From Eqs. (8.6) and (8.7) we arrive at the expression for the resulting change in length of the rivet

$$\bar{\Delta}\ell = \Delta\ell_{\text{gg}} - \Delta\ell_{T\text{Al}} = \ell \left[\left(\frac{1}{D_0} - \frac{1}{D} \right) V^{\text{ex}} - \alpha\Delta T \right] \quad (8.8)$$

For the values of the parameters given in the problem we arrive at

$$\bar{\Delta}\ell = \ell \left[\left(\frac{1}{10^{-8}} - \frac{1}{10^{-7}} \right) \cdot 1.35 \cdot 10^{-10} - 2 \cdot 10^{-5} \cdot 200 \right] = 8 \cdot 10^{-3} \ell \quad (8.9)$$

One can see that the total shortening of the rivet is rather large, in the range of 1% of the length. The stresses which occur in the rivet depend on the thermal expansion of the connected materials as well

$$\bar{\Delta}\ell = \Delta\ell_{\text{gg}} - \Delta\ell_{T\text{Al}} - (\Delta\ell_{T\text{Al}} - \Delta\ell_{T\text{con}}) \quad (8.10)$$

where the term $\Delta\ell_{T\text{con}}$ describes the thermal expansion of the connected materials. For the simplest case (the last term on the right-hand side of Eq. (8.10) is zero) we obtain

$$\sigma = E \frac{\bar{\Delta}\ell}{\ell} = 8 \cdot 10^{-3} E \quad (8.11)$$

We stress that the major peculiarity of the construction proposed is the possibility of controlling the value of the stresses matching the initial and final mean grain size.

PROBLEM 1.3

1. Using the Henry isotherm for adsorption of vacancies at the grain boundary we arrive at

$$zBc_v^{eq} = V^{ex} \quad (8.12)$$

where z is the adsorption capacity of the grain boundary, $B = B_0 \exp\left(\frac{Q}{kT}\right)$ is the adsorption constant, c_v^{eq} is the equilibrium concentration of the vacancies.

Considering the width of the grain boundary equal to three atomic layers, the adsorption capacity can be defined as

$$z = \frac{3}{(2.86 \cdot 10^{-10})^2} = 3.6 \cdot 10^{19} \text{ at/m}^2 = 6 \cdot 10^{-5} \text{ mol/m}^2 \quad (8.13)$$

The adsorption constant B can be defined as

$$B = \frac{V^{ex}}{zc_v^{eq}} = \frac{V^{ex}}{z} (c_v^{eq})^{-1} \quad (8.14)$$

One can see that the adsorption heat Q is equal to the enthalpy of vacancy formation in the bulk H_f . For Al $H_f = 0.76$ eV, $S_f = 0.7$ K. For a $40^\circ\langle 111 \rangle$ grain boundary in Al $V^{ex} = 6.4 \cdot 10^{-6} \text{ mol/m}^2$. Then at the melting temperature $B = 6.2 \cdot 10^2$.

2. The enrichment coefficient β is equal to

$$\beta = \frac{\Gamma}{zc_v^{eq}} = B \quad (8.15)$$

Let us plot this value against the volume solubility of the vacancies (c_v^{eq}) on the Seah-Hondros diagram (Fig. 1.3) for the melting temperature. Evidently, the agreement is poor.

3. All our calculations were carried out in the framework of the simplest adsorptional isotherm — the Henry isotherm. Let us extract the value B from the Zhuchovitskii-McLean isotherm (1.144). Then

$$\frac{zBc_v^{eq}}{1 - c_v^{eq} + Bc_v^{eq}} = V^{ex} \quad (8.16)$$

and

$$B = \frac{V^{ex} (1 - c_v^{eq}) (c_v^{eq})^{-1}}{z - V^{ex}} \quad (8.17)$$

For $T = T_m$ we obtain $B = 712$. Comparing this result with the previous one, which was derived in the framework of the Henry isotherm, one can see that the difference is in the range of $\sim 10\%$.

PROBLEM 1.4

1. The excess grain boundary free volume V^{ex} for a $40^\circ\langle 111 \rangle$ tilt boundary can be expressed as $V^{ex} = -\Gamma_0\Omega_0 = 6.4 \cdot 10^{-11} \text{ m}^3/\text{m}^2$. In other words, every grain boundary increases the size of a polycrystal by $\Delta\delta = 6.4 \cdot 10^{-11} \text{ m}$. Let

us consider a cubic sample with the side of the cube equal to L . Under the assumption that the grains are uniform and cubic as well with the grain size a we arrive at

$$\begin{aligned} V &= L^3; \\ L &= L_0 + \frac{L}{a} \Delta\delta \end{aligned}$$

and

$$L = \frac{L_0}{1 - \frac{\Delta\delta}{a}} \cong L_0 \left(1 + \frac{\Delta\delta}{a} \right) \quad (8.18)$$

where L_0 is the size of a side of the corresponding single crystal.

2. The free energy of polycrystals can be expressed as

$$G = G^s + G^{grav} \quad (8.19)$$

where G^s is the surface (grain boundary) part of the free energy, G^{grav} is the gravitational part of the free energy.

The total number of grains in the polycrystal can be represented as

$$N = \frac{L_0^3 \left(1 + \frac{\Delta\delta}{a} \right)^3}{a^3} \quad (8.20)$$

($N \gg 1$).

The total grain boundary area is equal to

$$S = \frac{1}{2} 6Na^2 = \frac{3}{a} L_0^3 \left(1 + \frac{\Delta\delta}{a} \right)^3 \quad (8.21)$$

and, respectively, the “grain boundary” part of the free energy is equal to

$$G^s = \frac{3}{a} \gamma L_0^3 \left(1 + \frac{\Delta\delta}{a} \right)^3 \quad (8.22)$$

γ is the grain boundary surface tension.

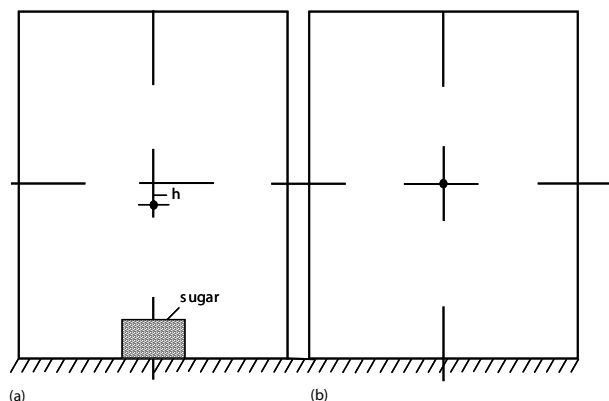
The gravitational part of the free energy of the polycrystal can be represented as follows: for a polycrystal which rests on a support

$$G_I^{grav} = \frac{1}{2} L_0 \left(1 + \frac{\Delta\delta}{a} \right) V_0 \rho g \quad (8.23)$$

for the suspended polycrystal

$$G_{II}^{grav} = \left[H_0 - \frac{1}{2} L_0 \left(1 + \frac{\Delta\delta}{a} \right) \right] V_0 \rho g \quad (8.24)$$

where V_0 is a volume of the corresponding single crystal, ρ is the density of the perfect crystal, g is the gravity acceleration.

**FIGURE 8.3**

Two glasses with water and sugar: (a) a piece of sugar in water; (b) sugar is dissolved in water.

The expression for the free energy of the polycrystal can be written correspondingly as

$$G_I = \frac{3}{a} \gamma L_0^3 \left(1 + \frac{\Delta\delta}{a}\right)^3 + \frac{1}{2} L_0 \left(1 + \frac{\Delta\delta}{a}\right) V_0 \rho g \quad (8.25)$$

$$G_{II} = \frac{3}{a} L_0^3 \gamma \left(1 + \frac{\Delta\delta}{a}\right)^3 + \left[H_0 - \frac{1}{2} L_0 \left(1 + \frac{\Delta\delta}{a}\right) \right] V_0 \rho g \quad (8.26)$$

One can see that for the polycrystal which rests on the support (Eq. (8.25)) there is no equilibrium grain size, the minimum of the free energy is achieved at $a \rightarrow \infty$.

The relation for the equilibrium grain size for the suspended polycrystal reads

$$a^* = \frac{L_0^3 \gamma \Delta\delta}{L_0 \Delta\delta V_0 \rho g - 3 L_0^3 \gamma} \cong \frac{\gamma \Delta\delta}{L_0 \Delta\delta \rho g - 3 \gamma} \quad (8.27)$$

A positive value of a^* can be obtained only for $L_0 \geq 10^6$ m.

3. In the examples considered the system includes the polycrystal and the earth. The position of the center of masses of this system — the polycrystal + the earth — remains unchanged. To better understand the core of the problem let us consider a cylindrical glass with tea and a piece of sugar (Fig. 8.3). The center of gravity of the glass with the undissolved piece of sugar is situated a little bit below the geometrical center of the glass due to the larger density of sugar in comparison to water.

When the sugar dissolves in water the center of the gravity rises by the distance h . However, the position of the system the earth + the glass remains

unchanged. In cosmic space during dissolution the glass will change its position with respect to the coordinates connected with the earth, the sun or the stars. The energy of this motion is the reduction of the free energy of the system due to the formation of the dissolution of sugar in water.

The situation with a polycrystal is in perfect analogy with the considered one. The annealing of the homogeneous polycrystal will lead to a single crystal with the same coordinates of the center of masses, whereas the polycrystal with grains distributed along the length will change the position of the center of the masses in the course of grain growth.

PROBLEM 1.5

1. The change of the melting temperature can be evaluated by Eq. (1.203)

$$\Delta T \cong \frac{\gamma \cdot T_m}{q D} \quad (8.28)$$

where q is the specific heat of melting. For Al $q = 10^9 \text{ J/m}^3$, $\gamma = 0.45 \text{ J/m}^2$ and for $D = 10 \text{ nm}$ ΔT is equal to $\cong 0.05 T_m$. The melting temperature for the nanocrystalline sample considered is $0.05 T_m$ lower than that for a single crystal of Al.

2. To derive the Clausius-Clapeyron equation for a nanocrystalline material we do not have to consider an equal chemical potential of the two phases — solid and liquid — but the free energy of the polycrystal and of the relevant amount of liquid. If N is the number of atoms in the polycrystal, we arrive at

$$N \mu_s + A \gamma = N \mu_\ell \quad (8.29)$$

where μ_s and μ_ℓ are the chemical potentials of the atoms in the solid and liquid, respectively. A is the total grain boundary area of the polycrystal. We neglect hereby the surface energy of the nanocrystalline specimen in the liquid state.

Then

$$\begin{aligned} N \left(\frac{\partial \mu_s}{\partial T} \right)_p dT + N \left(\frac{\partial \mu_s}{\partial P} \right)_T dP + A \left(\frac{\partial \gamma}{\partial T} \right)_p dT + A \left(\frac{\partial \gamma}{\partial T} \right)_T dP \\ = N \left(\frac{d\mu_\ell}{dT} \right)_p + N \left(\frac{d\mu_\ell}{dp} \right) dp \end{aligned} \quad (8.30)$$

Taking into account that $-\left(\frac{\partial \gamma}{\partial T}\right)_p = S_b$ is the grain boundary entropy and $\left(\frac{\partial \gamma}{\partial p}\right) = V^{\text{ex}}$ is the excess volume,¹ relation (8.30) can be expressed as

$$[N \Delta S_{L-S} - A S_b] dt = [N \Omega_{L-S} - A V^{\text{ex}}] dP \quad (8.31)$$

¹We would like to remind the reader that the grain boundary excess free volume (Chapter 1) is equal to $V^{\text{ex}} = -\Gamma_0 \Omega_s [\text{m}^3/\text{m}^2]$ where Γ_0 is the autoadsorption.

The Clausius-Clapeyron equation for the nanocrystalline sample then reads

$$\frac{dP}{dT} = \frac{\frac{q}{T} - \frac{A}{N} S_b}{\Delta\Omega - \frac{A}{N} V^{\text{ex}}} \quad (8.32)$$

The grain boundary entropy is on the order of $\sim -10^{-3} \text{ J/m}^2\text{K}$.

The ratio $\frac{A}{N}$ can be extracted from the following considerations. If spherical (or cuboidal) grains are assumed, the total grain boundary area of a sample with volume V is equal to

$$A = \frac{3V}{D} \quad (8.33)$$

and the total number of atoms N can be expressed as

$$N = \frac{V \left[1 - \frac{3}{D} V^{\text{ex}}\right]}{\Omega_s} \quad (8.34)$$

and the ratio $\frac{A}{N}$ reads

$$\frac{A}{N} = \frac{3\Omega_s}{D \left[1 - \frac{3}{D} V^{\text{ex}}\right]} \quad (8.35)$$

Finally, the Clausius-Clapeyron relation for nanocrystals can be expressed as

$$\frac{dP}{dT} = \frac{\frac{q}{T} + \frac{3\Omega_s}{D \left[1 - \frac{3}{D} V^{\text{ex}}\right]} \cdot \left(\frac{\partial \gamma}{\partial T}\right)_p}{\Delta\Omega - \frac{3\Omega_s}{D \left[1 - \frac{3}{D} V^{\text{ex}}\right]} V^{\text{ex}}} \quad (8.36)$$

One can see that the impact of grain boundaries can change qualitatively the behavior of the system at the melting point. This is evident from the influence of the denominator of Eq. (8.36). Actually, the grain boundary excess free volume decreases, and “compensates” the change of the atomic volume during melting of “normal” metals, where $\Delta\Omega_{L-S} > 0$ and promotes the “abnormal” behavior in cases that $\Delta\Omega_{L-S} < 0$ (Bi, Ga).

3. Let us consider Eq. (8.36) for nanocrystalline Al. As can be seen the effect connected with the grain boundary excess free volume does not change essentially the numerator of (8.36), so the expression (8.36) can be rewritten as

$$\frac{dT}{dP} = \frac{\frac{\Delta\Omega}{\Omega_s} - \frac{3V^{\text{ex}}}{D - 3V^{\text{ex}}}}{\frac{q}{\Omega_s}} \cdot T \quad (8.37)$$

For $D = 7 \text{ nm}$

$$\frac{dT}{dP} \cong 4.5 \cdot 10^{-3} \frac{\Omega_s}{q}$$

and for $D = 25 \text{ nm}$

$$\frac{dT}{dP} \cong 0.05 \frac{\Omega_s}{q} T$$

For $D = 5$ nm the melting temperature decreases with increasing pressure, like for water, Ga, Bi; for $D = 7$ nm the melting temperature is nearly independent of pressure, and for $D = 25$ nm the polycrystal qualitatively behaves like a coarse-grained Al polycrystal.

PROBLEM 2.1

In order to determine the surface tension of the low-angle tilt grain boundary let us invoke the Read-Shockley relation (2.3) in a form which is convenient for calculation

$$\gamma = \gamma_0 \varphi (A_0 - \ln \varphi) \quad (8.38)$$

where

$$\gamma_0 = \frac{\mu b}{2\pi(1-\nu)}, \quad A_0 = 0.5$$

For $\langle 112 \rangle$ tilt grain boundaries the Burgers vector $b = \frac{a}{2}\langle 110 \rangle$, where $a = 4.5 \cdot 10^{-10}$ m is the lattice constant; $b = \frac{a\sqrt{2}}{2} = 2.86 \cdot 10^{-10}$ m

$$\mu = 26.46 \text{ Pa}$$

Then for $\varphi = 0.5^\circ$ we obtain $\gamma = 0.082 \text{ J/m}^2$, for $\varphi = 3^\circ$ $\gamma = 0.323 \text{ J/m}^2$, for $\varphi = 5^\circ$ $\gamma = 0.46 \text{ J/m}^2$, for $\varphi = 8^\circ$ $\gamma = 0.62 \text{ J/m}^2$.

PROBLEM 2.2

For mechanical equilibrium at a triple junction, given that the grain boundary surface tension does not depend on the orientation of the boundaries, the surface tensions should satisfy Young's theorem (1.162)

$$\frac{\gamma_1}{\sin \alpha_1} = \frac{\gamma_2}{\sin \alpha_2} = \frac{\gamma_3}{\sin \alpha_3}$$

Then, the desired angles should satisfy the system of equations

$$\begin{aligned} \alpha_1 + \alpha_2 + \alpha_3 &= 2\pi \\ \frac{\gamma_1}{\sin \alpha_1} &= \frac{\gamma_3}{\sin(2\pi - \alpha_1 - \alpha_3)} \\ \frac{\gamma_1}{\sin \alpha_1} &= \frac{\gamma_3}{\sin \alpha_3} \end{aligned}$$

For the given values of grain boundary surface tension

$$\alpha_1 = 150^\circ$$

$$\alpha_2 = 103^\circ$$

$$\alpha_3 = 107^\circ$$

PROBLEM 2.3

As stressed in Sec. 1.4.1 grains in a polycrystal play the role of a source of pressure to confine a boundary in the deformed state. It was mentioned as well that since the material in a grain boundary is stretched the pressure p_0 applied to a grain boundary should be negative: $p_0 < 0$. Thus, our problem is reduced to a quantitative evaluation of the pressure which is necessary to confine a liquid layer at a temperature which is much lower than the melting point.

The Clausius-Clapeyron equation in our case reads

$$\frac{dP}{dT} = \frac{\Delta H^{L \rightarrow S}}{T \Delta \ell^{L-S}} \quad (8.39)$$

where $\Delta H^{L \rightarrow S}$ is the change in enthalpy of the two phases at the melting point

$$\Delta H = H^{solid} - H^{liquid} \quad (8.40)$$

$$\frac{\Delta H^{L-S}}{T} = \Delta S^{L-S} \quad (8.41)$$

The enthalpy change is identical to the specific heat of melting, $\Delta \Omega$ is the change in the atomic volume at the melting point.

To study Eq. (8.39) in a rather wide temperature range the dependencies $\Delta H^{L-S}(T)$ and $\Delta V^{L-S}(T)$ should be known

$$dH^{L-S} = \Delta C_p dT + \Delta [\Omega (1 - T\alpha)] dp \quad (8.42)$$

where

$$\Delta c_p = c_p^{sol} - c_p^{liq} \quad (8.43)$$

is the difference of the specific heat for the liquid and solid phase, respectively,

$$\Delta V(1 - T\alpha) = [\Omega^{solid} (1 - T\alpha^{solid})] - [\Omega^{liquid} (1 - T\alpha^{liquid})] \quad (8.44)$$

However, for our purpose — the evaluation of the pressure — we will ignore the change in the enthalpy and atomic volume with temperature.

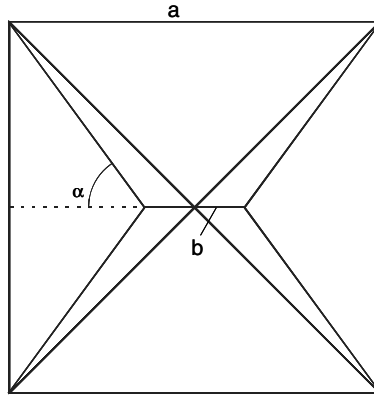
Then, from Eq. (8.39) we arrive at

$$\Delta P = P - P_0 = \frac{q}{\Delta \Omega} \ln \frac{T}{T_0} \quad (8.45)$$

where q is the specific heat of melting, P_0 is the atmospheric pressure (1 atm).

Using the reference values for the parameters of (8.45) we obtain

$$\begin{aligned} Al : \Delta P &= -5.4 \cdot 10^4 \text{ atm} \cong -5.4 \text{ GPa} \\ Pb : \Delta P &= -2.2 \cdot 10^3 \text{ atm} \cong -0.22 \text{ GPa} \\ Au : \Delta P &= -9.4 \cdot 10^5 \text{ atm} \cong -9.46 \text{ GPa} \end{aligned} \quad (8.46)$$

**FIGURE 8.4**

Configuration of a 2D quadruple junction (bold lines) and an energetically more favorable configuration (thin lines).

Such negative pressure should act from the bulk on the grain boundary to confine it as a liquid.

PROBLEM 2.4

Let us consider a quadruple junction in a 2D square (Fig. 8.4). The length of the sides is a .

The total length of the grain boundaries which form the quadruple junction (bold lines) is equal to $L_0 = 2a\sqrt{2}$.

However, the same grains can be connected in another way, namely as shown in Fig. 8.4. In this case the total length of grain boundaries, which border the grains, is equal to

$$L = 2a \frac{1}{\sin \alpha} + a - \frac{a}{\tan \alpha} \quad (8.47)$$

This length reaches the minimal value at $\alpha = 60^\circ$. Indeed:

$$\frac{dL}{d\alpha} = -\frac{2\cos\alpha}{\sin^2\alpha} + \frac{1}{\sin^2\alpha} = 0 \quad (8.48)$$

The new length of the grains is equal to

$$L = \frac{4a}{\sqrt{3}} + a - \frac{a}{\sqrt{3}} = (\sqrt{3} + 1)a \cong 2.73a \quad (8.49)$$

while the initial length is equal to $L_0 \cong 2.83a$. In other words, the new configuration is energetically more acceptable.

We would like to draw the attention of the reader to the point that the difference between the initial and energetically favorable length is rather small.

That is why the quadruple junction configurations which are observed in 2D microstructures might be of kinetic origin.

PROBLEM 2.5

(a) Let us consider a grain boundary system which is formed by grain boundaries with the surface tensions γ_1 and γ_2 , respectively (Fig. 2.20). The total free energy of the grain boundaries can be described as

$$G = \frac{2a}{\sin \alpha} \gamma_1 + \left(a - a \frac{1}{\tan \alpha} \right) \gamma_2 \quad (8.50)$$

The minimum of the Eq. (8.50) is achieved at

$$\cos \alpha = \frac{1}{2} \frac{\gamma_2}{\gamma_1} \quad (8.51)$$

On the other hand, we are looking for the condition when the length ℓ of the cross-piece is equal to zero

$$\ell = a - \frac{a}{\tan \alpha} = 0 \quad (8.52)$$

or $\tan \alpha = 1$

$$\alpha = 45^\circ \quad (8.53)$$

The desired solution is

$$\begin{aligned} \cos 45^\circ &= \frac{1}{2} \frac{\gamma_2}{\gamma_1} \\ \gamma_2 &= \sqrt{2} \gamma_1 \end{aligned} \quad (8.54)$$

(b) In accordance with Eq. (8.54) we arrive at the equation

$$\gamma_2 (A - \ln \gamma_2) = \sqrt{2} \gamma_1 (A - \ln \gamma_1) \quad (8.55)$$

The solution of Eq. (8.55) is

$$\gamma_2 \cong 0.155 \text{ rad} \quad \text{or} \quad \gamma_2 \cong 9.86^\circ \quad (8.56)$$

(c) The calculation in the frame work of the Read-Shockley equation gives

$$\gamma_2 \cong 17^\circ \quad (8.57)$$

Strictly speaking, this value is outside the regime of low-angle boundaries. In other words, we are unable to find a misorientation of the grain boundary with known surface tension. However, the deviation is rather small, and, for the first approximation, we can accept this value.

PROBLEM 2.6

(a) Let us consider the merger of two grain boundaries with misorientation

angle φ_n .

The surface tension of a low-angle boundary with misorientation φ_n is given by the Read-Shockley relation (2.3)

$$\gamma_n = \frac{\mu b}{4\pi(1-\nu)} \varphi_n [A - \ln \varphi_n] \quad (8.58)$$

After combination instead of two grain boundaries with the energy (surface tension) given by Eq. (8.58), we will have one grain boundary with misorientation angle $2\varphi_n$ with the energy

$$\gamma_{2n} = \frac{\mu b}{4\pi(1-\nu)} 2\varphi_n [A - \ln 2\varphi_n] \quad (8.59)$$

The energy gain is equal to

$$\gamma_{2n} - 2\gamma_n = -\frac{2\mu b}{4\pi(1-\nu)} 2\varphi_n \ln 2 < 0 \quad (8.60)$$

which is the required result.

(b) The driving force for grain growth can be found from the formal expression

$$P = -\frac{\Delta G}{\Delta V} \quad (8.61)$$

where ΔG is the infinitesimal change of the free energy of the system when the grain boundary sweeps a small volume ΔV . If we displace the grain boundary by the distance Δx_n , we obtain

$$\Delta G = (\gamma_{2n} - 2\gamma_n) a\delta = \left[-\frac{2\mu b}{4\pi(1-\nu)} \varphi_n \ln 2 \right] a\delta \quad (8.62)$$

$$\Delta V = a\delta \Delta x_n \quad (8.63)$$

Then the driving force P reads

$$P = \frac{\frac{2\mu b}{4\pi(1-\nu)} \varphi_n \ln 2}{\Delta x_n} \quad (8.64)$$

(c) The unification of neighboring grain boundaries will be energetically favorable because this process decreases the stress field of the dislocations. For angles larger than 15° the dislocation model fails, because the dislocation cores tend to overlap (see Sec. 2.2.2), and the grain boundary energy remains essentially constant.

So, with the critical angle taken as 15° we arrive at

$$\varphi_{crit} = 15^\circ = 0.262 \text{ rad} \quad (8.65)$$

On the other hand, the angle φ_n can be defined as

$$\varphi_n = 2^n \varphi_0 \quad (8.66)$$

where φ_0 is the initial angle of misorientation of two adjacent grains, n is the number of the step of unification.

The number n can be found from the relation

$$\varphi_n = 2^n \varphi_0 = \varphi_{crit} \quad (8.67)$$

and

$$n = \frac{\ln \varphi_{crit} - \ln \varphi_0}{\ln 2} \quad (8.68)$$

For example, if $\varphi_0 \cong 0.001(0.06^\circ)$ then the number n is equal to

$$n = \frac{\ln 0.262 - \ln 0.001}{\ln 2} = 8 \quad (8.69)$$

(d) The grain size Δx_n at the moment when grain growth will be arrested can be found from the simple expression

$$\Delta x_n = 2^n \Delta x_0 \quad (8.70)$$

If $\varphi_0 = 0.001$ rad and $\Delta x_0 = 10^{-7}$ m

$$\Delta x_0 = 2^8 \cdot 10^{-7} \text{ m} = 2.5 \cdot 10^{-5} \text{ m} \quad (8.71)$$

PROBLEM 2.7

The idea of the solution is that we should compare the energy of a twist grain boundary with a misorientation angle $\Delta\varphi$ with the elastic energy of a pipe with a length x_0 , which is twisted by the same angle $\Delta\varphi$.

The twist angle can be expressed as

$$\Delta\varphi = \frac{M_k x}{\mu J_p} \quad (8.72)$$

where M_k is the torque, μ is the shear modulus, J_p is the moment of inertia. For a thin-wall pipe (Fig. 2.22)

$$J_p = 0.5\pi R^3 \delta$$

The elastic energy of a twisted pipe is equal to

$$U_{el} = \frac{M_k^2 x}{2GJ_p} = \frac{\Delta\varphi^2 \mu J_p}{2x} \quad (8.73)$$

On the other hand, the energy of a low-angle twist grain boundary with misorientation angle $\Delta\varphi$ reads

$$\gamma = \frac{2\mu b}{4\pi} \Delta\varphi (A - \ln \Delta\varphi) \quad (8.74)$$

where $b = 2.86 \cdot 10^{-10} \text{m}$ (for Al) is the Burgers vector, $A = 0.5$ reflects the energy of the dislocation core.

Since

$$2\pi R\delta\gamma = U_{el} \quad (8.75)$$

we arrive at

$$x_0 = \frac{0.5\pi R^2 \Delta\varphi}{b(A - \ln\Delta\varphi)} \quad (8.76)$$

For $\Delta\varphi = 0.01 (\sim 0.5^\circ)$ we arrive at the surprising result: $x = 270 \text{m}$! The rather strong dependence of x_0 on the radius of the pipe makes the situation more reasonable for a small pipe diameter. For instance, if $R = 5 \cdot 10^{-6} \text{m}$ (5 microns) the length x_0 is equal to $\sim 2.7 \text{ mm}$.

PROBLEM 2.8

The bending stress of a grain boundary as a beam is equal to (Fig. 2.23a)

$$\tau(y) = E \frac{y}{\rho} \quad (8.77)$$

where ρ is the radius of curvature, E is Young's modulus

$$\frac{1}{\rho} = \frac{M}{EJ_z} \quad (8.78)$$

M is the bending moment, I_z is the moment of inertia of the beam (boundary) (Fig. 2.23b).

The bending angle φ is

$$d\varphi = \frac{M dx}{EJ_z} \quad (8.79)$$

The free energy of the elastically deformed beam is equal to

$$G_{el} = \int_{-\ell}^{\ell} \frac{M^2}{2EJ_z} dx = \int_{-\ell}^{\ell} \frac{M^2}{2EJ_z} dx = \int_{-\ell}^{\ell} \frac{EJ_z}{2} \left(\frac{1}{\rho}\right)^2 dx \quad (8.80)$$

The free energy of the system reads

$$G = \int_{-\ell}^{\ell} \left[2\Delta\gamma^s y + \frac{EJ_z}{2} \frac{1}{\rho^2} \right] dx \quad (8.81)$$

The equilibrium shape of the boundary can be extracted from Eq. (8.81), taking into account that

$$\frac{1}{\rho} = \frac{y''}{(1 + y'^2)^{3/2}} \quad (8.82)$$

where $y(x)$ is the equation of the shape of the grain boundary.

The functional of the shape of the grain boundary considered as a beam is

$$G = \int_{-\ell}^{\ell} \left[2\Delta\gamma^s y + \frac{EJ_z}{2} \cdot \left(\frac{y''^2}{(1 + y'^2)^3} \right) \right] dx \quad (8.83)$$

For small deformation Eq. (8.83) can be transformed to

$$G_{el} = \int_{-\ell}^{\ell} \left[2\Delta\gamma^s y + \frac{EJ_z}{2} y''^2 \right] dx \quad (8.84)$$

with the boundary conditions: $y(-\ell) = 0$; $y(\ell) = 0$; $y'(-\ell) = -\tan \theta$; $y'(\ell) = \tan \theta$.

For the sake of simplicity assume that $\tan \theta = 0$. The Euler-Poisson equation, in this case

$$2\Delta\gamma^s + \frac{d^2}{dx^2} \left(\frac{EJ_z}{2} y''^2 \right) = 0 \quad (8.85)$$

or

$$y'''' = -\frac{2\Delta\gamma^s}{EJ_z} \quad (8.86)$$

Then we arrive at

$$y = -\frac{\Delta\gamma^s}{12 EJ_z} (x^4 - 2\ell^2 x^2 + \ell^4) = -\frac{\Delta\gamma^s}{12 EJ_z} (x^2 - \ell^2)^2 \quad (8.87)$$

At $x = 0$ $y = -\frac{\Delta\gamma^s}{12 EJ_z} \ell^4$.

On the other hand, the grain boundary is curved due to the well-known balance between the difference of surface tensions of the two grains and the capillary pressure created by the curved boundary (Fig. 2.23)

$$\frac{2\Delta\gamma^s}{\delta} = \frac{\gamma}{R} \quad (8.88)$$

In this case the displacement $y(0)$ can be expressed as (Fig. 2.23)

$$y(0) = R \left(1 - \sqrt{1 - \left(\frac{\ell}{R} \right)^2} \right) \quad (8.89)$$

Eqs. (8.87) and (8.89) define the desired value E as

$$E = -\frac{\Delta\gamma^s \ell^4}{12J_z R \left(1 - \sqrt{1 - \left(\frac{\ell}{R} \right)^2} \right)} \quad (8.90)$$

where the radius R is defined by Eq. (8.88).

It is noted that the shape of the boundary which is considered as an elastically deformed beam (Eq. (8.87)) and a curved grain boundary (Eq. (8.88)) are different, strictly speaking. However, for our purposes — rough estimation — such neglect is acceptable. Moreover, as can be seen from Eq. (8.87), for small x the shape of the loaded beam is a circle.

For $\Delta\gamma^s = 0.05 \text{ J/m}^2$, $\gamma = 0.5 \text{ J/m}^2$, $\ell = 0.1 \text{ cm}$; $R = 0.5 \text{ cm}$, $J = \frac{\lambda\delta^3}{12}$, where δ is the thickness of the sample ($\delta \cong 10^{-2} \text{ m}$), λ is the width of the grain

boundary ($\lambda \cong 10^{-9}\text{m}$), $E \cong 0.5 \cdot 10^6\text{Pa}$. It should be noted that the elastic modulus obtained is relevant not only for the grain boundary structure, but also for the system.

PROBLEM 3.1

Let us consider the behavior of a polycrystal under a hydrostatic pressure during grain growth. The reduction of the grain boundary area in the course of grain growth decreases the volume of the specimen and, correspondingly, decreases the free energy of the system by the value

$$\frac{3pV^{\text{ex}}}{\langle D \rangle} \quad (8.91)$$

where $\frac{3}{\langle D \rangle}$ is the grain boundary area per unit volume, $\langle D \rangle$ is the mean grain diameter, V^{ex} is the grain boundary excess free volume and p is the pressure.

Relation (8.92) can be derived from formal considerations: the pressure part of grain boundary surface tension is pV^{ex} , thus the driving force of grain growth in a system with mean grain diameter $\langle D \rangle$ can be expressed as

$$P = \frac{3\gamma}{\langle D \rangle} + \frac{3pV^{\text{ex}}}{\langle D \rangle} \quad (8.92)$$

PROBLEM 3.2

First let us calculate the grain boundary mobility under a hydrostatic pressure

$$m_b = m_{0b} e^{-\frac{pV^{\text{ex}}}{kT}} \quad (8.93)$$

where m_0 is the grain boundary mobility at the temperature T and the pressure $p = 0$.

Substituting the parameters given in the problem into Eq. (8.93) we get: $m = 1.5 \cdot 10^{-14}\text{m}^4/\text{Js}$.

The kinetic equation of grain growth in this case reads

$$\frac{d\langle D \rangle}{dt} = \frac{2m_b}{\langle D \rangle} (\gamma + pV^{\text{ex}}) \quad (8.94)$$

We are interested in the time when grain II disappears, i.e., when grain boundary GB₁ will “meet” grain boundary GB₂.

From Eq. (8.94) we arrive at

$$\langle D_0 \rangle^2 - \langle D \rangle^2 = 4m_b (\gamma + pV^{\text{ex}}) t \quad (8.95)$$

and, finally

$$t = \frac{\langle D_0 \rangle_1^2 - \langle D_0 \rangle_2^2}{4m_b [V_1^{\text{ex}} - V_2^{\text{ex}}]} \quad (8.96)$$

Final result: the time when grain II disappears and the sample will be transformed from a tricrystal to a bicrystal is equal to $t = 1333$ s.

PROBLEM 3.3

For the motion of spherical boundaries Eq. (8.94) should be changed to

$$\frac{d \langle D \rangle}{dt} = \frac{4m}{\langle D \rangle} (\gamma + pV^{\text{ex}}) \quad (8.97)$$

and Eq. (8.96) will be transformed correspondingly to

$$t = \frac{\langle D_0 \rangle_1^2 - \langle D_0^2 \rangle_2}{8m_b [V_1^{\text{ex}} - V_2^{\text{ex}}]} \quad (8.98)$$

The time t , which defines the disappearance of grain II, will be equal in this case to

$$t = 666 \text{ s}$$

PROBLEM 3.4

The conditions of thermodynamic equilibrium of a physical body in an external field are [5]

$$T = \text{const.} \quad (8.99)$$

$$\mu = \text{const.} \quad (8.100)$$

Contrary to the temperature and chemical potential the pressure will be different in the different points of the body. In particular, in a gravity field the potential energy of a molecule u is a function of the coordinates x, y, z of its center of gravity and does not depend on the disposition of the atoms inside the molecule

$$\mu = \mu_0 + \mu(x, y, z) = \text{const.} \quad (8.101)$$

where $\mu_0(P, T)$ is the chemical potential in the absence of the field.

The conditions of thermal equilibrium of a body by angular motion can be obtained by substituting the centrifugal energy as the energy of the external field $u(x, y, z)$ into Eq. (8.101)

$$\mu_0(P, T) - \frac{m\omega^2 r^2}{2} = \text{const.} \quad (8.102)$$

where μ_0 is the chemical potential of the stationary body, m is the mass of the molecule, r is the distance to the rotation axis.

If we consider the solid or part of the solid so small that it can be described by the mass M and the radius of angular motion R , then we get

$$G = G_0 - \Sigma \frac{m\omega^2 r^2}{2} = G_0 - \frac{M\Omega^2 r^2}{2} \quad (8.103)$$

where G_0 is Gibbs' free energy for a stationary solid.

The density of the grain boundary differs from the density of the bulk of a grain. Then the driving force of grain boundary motion can be derived from (8.103) as the difference between the free energy of angular motion of a unit area of the boundary and the bulk of the same width

$$\Delta G = P = \frac{\rho_{\text{bulk}}\omega^2 R^2}{2} - \frac{\rho_{\text{bound}}\omega^2 R^2}{2} \quad (8.104)$$

where ρ_{bulk} and ρ_{bound} are the densities of the material in the bulk of the grain and at the grain boundary, respectively. If Γ_0 is the negative autoadsorption, δ the grain boundary width, and Ω_a the atomic volume, the desired difference of the densities in the numerator of (8.104) can be expressed as

$$\rho_{\text{bulk}} - \rho_{\text{bound}} = -\frac{\Gamma_0\Omega_0}{\delta}\rho_{\text{bulk}} \quad (8.105)$$

Taking $\Gamma_0 = -6.4 \cdot 10^{-11} \text{ mol/m}^2$ (see Chapter 1 “Grain boundary excess free volume”), $\delta \cong 10^{-9} \text{ m}$, and the other parameters which are characteristic for Al, $R = 0.1 \text{ m}$ and $\omega \sim 2 \cdot 10^3 \text{ rad} \cdot \text{s}^{-1}$ we arrive at

$$P = \frac{\Gamma_0\Omega_0}{\delta}\rho_{\text{bulk}} \cdot (2 \cdot 10^3\pi)^2 \cdot R^2 \quad (8.106)$$

As can be seen the driving force is in the range of $700 \text{ J/m}^3 = 7 \cdot 10^{-3} \text{ MPa}$, which is comparable to the capillary driving force of grain boundary motion in bicrystals. It does no harm that under such driving force the grain boundary will move to the rotation axis.

PROBLEM 3.5

Let us compare the time necessary to reduce the surface area by the same value.

For a circle let us determine the time during which the circle disappears, for the half-loop the time to shorten the area by $2\pi R$.

The solution for the circle is

$$\begin{aligned} V &= m_b P = \frac{m_b \gamma}{R} \\ \frac{dR}{dt} &= \frac{m_b \gamma}{R} \end{aligned} \quad (8.107)$$

$$\begin{aligned} \frac{1}{2}R^2 &= m_b \gamma t \\ t &= \frac{R^2}{2m_b \gamma} \end{aligned} \quad (8.108)$$

For the half-loop the expression for the grain boundary velocity reads

$$V = \frac{\pi \gamma m_b}{R} \quad (8.109)$$

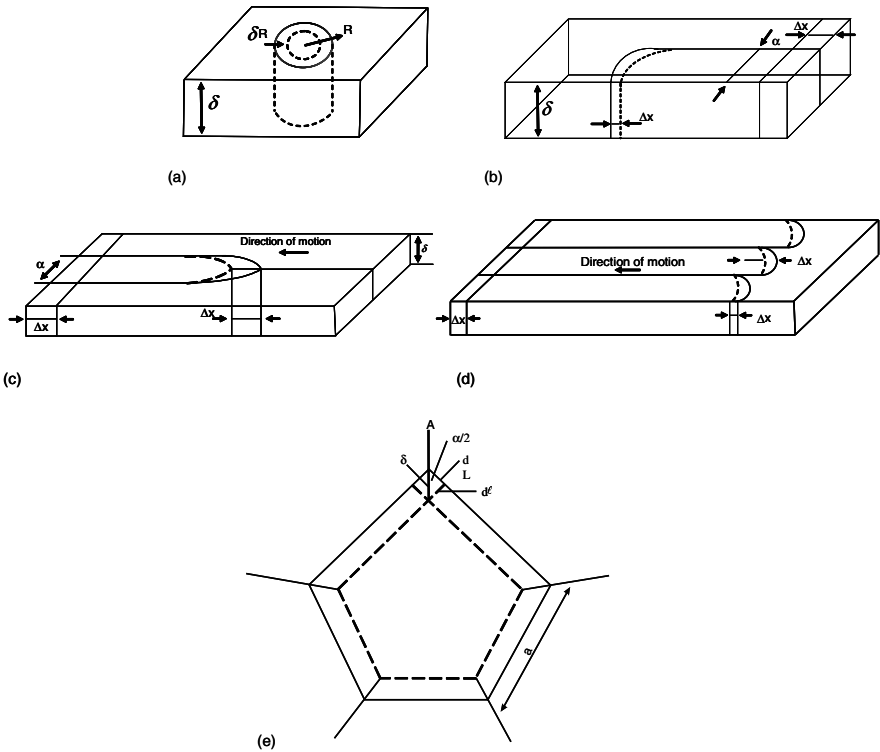


FIGURE 8.5

The diagram shows how to determine the driving force of grain boundary motion in the “weighted mean curvature” approach for: (a) circular cylinder; (b) grain boundary quarter-loop; (c) grain boundary system with a triple junction ($n < 6$); (d) grain boundary system with triple junctions ($n > 6$); and (e) grain growth of a regular pentagonal grain.

$$\begin{aligned}
 Vt &= 2\pi R = \frac{\pi\gamma m_b}{R}t \\
 t &= \frac{2\pi R^2}{\pi\gamma m_b} = \frac{2R^2}{\gamma m_b}
 \end{aligned}
 \tag{8.110}$$

PROBLEM 3.6

The so-called “weighted mean curvature”-approach (WMC) was introduced by Herring and Taylor (see Chapter 3). The weighted mean curvature is defined by the reduction of the total interfacial energy (with the sign “-”) in the course of an infinitesimal displacement divided by the volume swept by this

displacement.

1. The driving force for grain boundary motion in a quasi-2D configuration with circular cylinder can be defined as follows (Fig. 8.5a)

(a) The reduction of the interfacial energy as the result of an infinitesimal displacement of the grain boundary:

$$\Delta V = d(2\pi R\delta\gamma) = 2\pi\delta\gamma dR \quad (8.111)$$

(b) The volume swept by the moving grain boundary:

$$\Delta V = 2\pi R\delta dR \quad (8.112)$$

For the driving force we arrive at:

$$P = \frac{\Delta G}{\Delta V} = \frac{\gamma}{R} \quad (8.113)$$

2. The driving force for a sphere can be determined in the same way:

$$P = \frac{\Delta G}{\Delta V} = \frac{8\pi R\gamma dR}{4\pi R^2 dR} = \frac{2\gamma}{R} \quad (8.114)$$

3. For the grain boundary quarter-loop (Fig. 8.5b) the change of the interfacial energy is equal to

$$\Delta G = \delta\Delta x\gamma \quad (8.115)$$

while the swept volume is equal to

$$\Delta V = \delta a\Delta x \quad (8.116)$$

Then the driving force P is equal to

$$P = \frac{\gamma}{a} \quad (8.117)$$

4. 2D uniform ($\gamma_1 = \gamma_2 = \gamma$) grain boundary system with triple junctions

(1) $n < 6$ (Fig. 8.5c)

(2) $n > 6$ (Fig. 8.5d)

(for the number of the sections $N \gg 1$).

(1) The reduction of the interfacial energy as a result of an infinitesimal displacement of the grain boundary (Fig. 8.5c) for configuration (c)

$$\Delta G = 2\gamma\Delta x - \gamma\Delta x = \gamma\Delta x \quad (8.118)$$

the swept volume is

$$\Delta V = a\Delta x\delta \quad (8.119)$$

The driving force is

$$P = \frac{\gamma}{a} \quad (8.120)$$

(2) The reduction of the interfacial energy in the course of a displacement (Fig. 8.5d):

$$\Delta G = N\Delta x\delta\gamma \quad (8.121)$$

N is the number of the sections; in Fig. 8.5d three sections are shown.

The swept volume

$$\Delta V = N\Delta x\delta a\gamma \quad (8.122)$$

The driving force is equal to

$$P = \frac{\gamma}{a} \quad (8.123)$$

5. As shown in Chapter 4, in the course of 2D grain growth controlled by triple junction kinetics a grain of arbitrary shape is bound to transform itself into an equilateral polygon, and any deviation from an equilateral polygon will generate a force to restore the equilibrium shape.

Let us consider the evolution of the area and the length of the perimeter of the n -sided regular polygon in the course of the grain growth at junction kinetics in accordance with the “weighted mean curvature” concept. The driving force P can be expressed as

$$P = \frac{\gamma \left[-2nd\ell \left(\tan \frac{\alpha}{2} \right)^{-1} + nd\ell \left(\sin \frac{\alpha}{2} \right)^{-1} \right]}{n \cdot ad\ell} \quad (8.124)$$

where $d\ell$ is an elementary normal displacement of a grain side, α is the internal angle of the polygon. The second term in the brackets of the numerator of (8.124) appears since, in accordance with the WMC, we should take into account all changes in the course of a small displacement of a facet (side), including the change of the length of the boundary A in a triple junction (Fig. 8.5e). The expression (8.124) can be converted to

$$P = \frac{\gamma}{a} \left[\frac{1 - 2\sin(\pi/n)}{\cos(\pi/n)} \right] \quad (8.125)$$

One can see that P varies inversely with the length of the grain side a : for $n < 6$ the driving force $P < 0$, in other words, such a grain will vanish during grain growth. For $n > 6$ $P > 0$, such grain will grow, and for $n = 6$, $P = 0$. It is of interest to know how the driving force P changes with topological class n . The answer is given by the derivative $\frac{dP}{dn}$

$$\frac{dP}{dn} = \frac{\gamma}{an^2} \left[\frac{2 - \sin(\pi/n)}{\cos^2(\pi/n)} \right] \quad (8.126)$$

According to Eq. (8.126) the driving force P increases with topological class, however, the rate of increase slows down with increasing topological class.

PROBLEM 3.7

The derivation of the Lücke-Detert relation for grain boundary motion in a

system with impurities of positive adsorption is given in Chapter 3.

Let us consider the motion of a flat grain boundary which moves under the action of a constant driving force P in a system with impurities. The distinctive property of this impurity is its negative adsorption at the grain boundary, in other words, the concentration of the impurities at the grain boundary is smaller than in the bulk of the grain. The velocity of grain boundary motion can be described as

$$V = P_{eff} m_b \quad (8.127)$$

The effective driving force P_{eff} can be expressed as

$$P_{eff} = P - f\Gamma \quad (8.128)$$

where f is a repulsive force between grain boundary and impurity atom, Γ is the adsorption

$$f = \frac{V}{D_{im}} \quad (8.129)$$

where D is the diffusion coefficient of the impurity.

From Eqs. (8.127)–(8.129) we arrive at

$$V = \frac{P m_b}{1 + \Gamma \frac{m_b}{D_{im}/kT}} \quad (8.130)$$

At $\Gamma \frac{m_b}{D/kT} \gg 1$ we arrive at the Lücke-Detert relation

$$V = \frac{P D_{im}}{\Gamma kT} \quad (8.131)$$

We note that the adsorption isotherm in the Lücke-Detert relation is the Henry isotherm: $\Gamma = zBc$, where z is the number of active sites at the grain boundary, B is the adsorption isotherm.

Let us consider grain growth in a polycrystal with mean grain size $\langle \bar{D} \rangle$. The total grain boundary area and the driving force P of grain growth are equal to

$$S = \frac{3}{\langle \bar{D} \rangle} \quad (8.132a)$$

and

$$P = \frac{\gamma}{\langle \bar{D} \rangle} \quad (8.132b)$$

(The grains are represented by spheres or cubes with diameter or side equal to $\langle \bar{D} \rangle$, respectively.)

Then the rate of change of the free energy of the system reads

$$\frac{dG}{dt} = \frac{d}{dt} \left(\frac{3\gamma}{\langle \bar{D} \rangle} \right) = -\frac{3\gamma}{\langle \bar{D} \rangle^2} \frac{d\langle \bar{D} \rangle}{dt} = -\frac{3\gamma}{\langle \bar{D} \rangle^2} \cdot V \quad (8.133)$$

From (8.130) and (8.133) we arrive at

$$\frac{dG}{dt} - \frac{3\gamma}{<\bar{D}>^2} \cdot \frac{P D_{\text{im}}}{\Gamma RT} \quad (8.134)$$

Taking into account that $\gamma = \gamma_0 + \Gamma kT$ (we note that Γ is negative), the condition of the extremum reads

$$\frac{d}{d\Gamma} \left(\frac{dG}{dt} \right) = \frac{d}{d\Gamma} \left(-\frac{3}{<\bar{D}>^3} \cdot \frac{(\gamma_0 - \Gamma kT)^2 D_{\text{im}}}{\Gamma kT} \right) = 0 \quad (8.135)$$

and

$$-\Gamma^* = \frac{\gamma_0}{kT} \quad (8.136)$$

As obvious from (8.135) at the point Γ^* the derivative $\frac{dG}{dt}$ attains a maximum.

Relation (8.136) gives us the adsorption Γ^* at which the grain growth in the system with impurities complies with the maximal rate of free energy reduction.

PROBLEM 3.8

The theoretical basis of our current understanding of solute drag is given in Sec. 3.3.

Here, we give an example of how to apply the theoretical concept to real experimental data. In our description we will follow the scheme of calculation proposed by Lücke and Stüwe (Chapter 3 [194]) and utilized in [194, 297, 301, 613]

As the authors of [194] mentioned, they “reformulated and extended the impurity drag theory in order to simplify the evaluation of measurements.” That is why we first give a concise approximative approach of the Lücke-Stüwe theory. In our description we adhere to the designations given in [194], which will alleviate the utilization of this technique in the future.

The solute drag $P_F(v)$ exerted on the boundary is equal to

$$P_F(v) = N \int_{-\infty}^{\infty} c(x, v) \frac{dU}{dx} dx \quad (8.137)$$

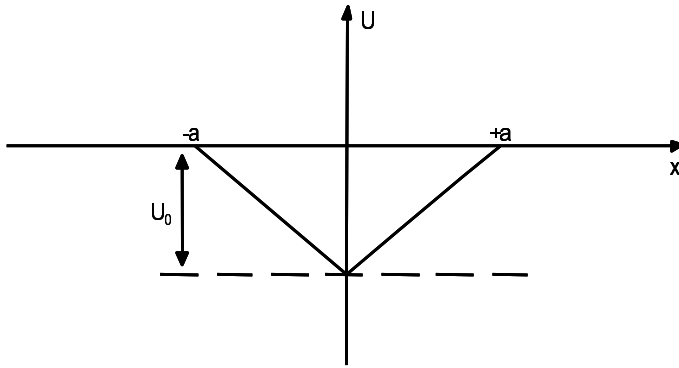
where N is the atomic density, $c(x, v)$ is the impurity concentration as a function of the distance from the grain boundary and the boundary velocity v ,

$$v = m_b [P - P_F(v)] \quad (8.138)$$

$-\frac{dU}{dx}$ is the force exerted by the boundary on a foreign atom. We assume as the simplest case a triangular potential $U(x)$ of width $2a$ and depth U_0 ; U_0 is the binding energy between boundary and impurity atom (Fig. 8.6).

For this potential Eq. (8.137) reduces to

$$P_F(v) = N \frac{U_0}{a} \left\{ \int_{-a}^0 c dx - \int_0^a c dx \right\} = N U_0 c_{\text{eff}} \quad (8.139)$$

**FIGURE 8.6**

One-atomic boundary. Energy level of an impurity atom in the bulk and in the boundary.

For quantitative calculations Eq. (8.138) is replaced in [194] by the approximation

$$P_F(v) = N U c_{eff} = \frac{rv}{1 + sv^2} \quad (8.140)$$

The parameters r and s which do not depend on v are obtained by equating Eqs. (8.138) and (8.139) for very large and very small v . Then, for $D(x) = D = \text{const}$ and inserting Eq. (8.139) into (8.137) we arrive at the cubic equation (see Sec. 3.3)

$$y^3 - y^2 + \frac{1 - \rho}{\sigma^2} y - \frac{1}{\sigma^2} = 0 \quad (8.141)$$

where

$$y = \frac{v}{A_b P} = \frac{v}{v_F} \quad (8.142)$$

v_F is the velocity of a free boundary

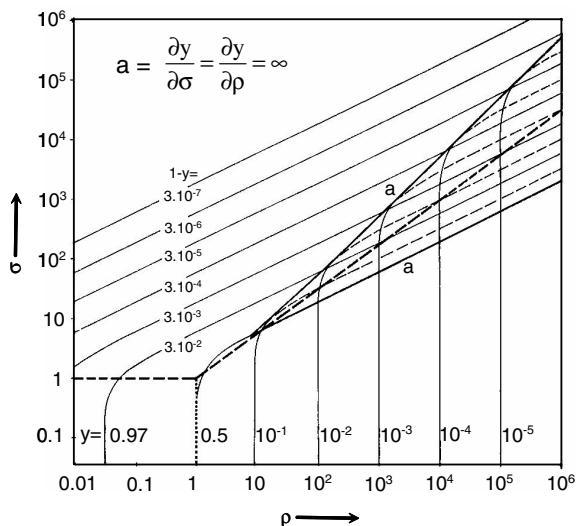
$$v_F = m_b P = b^2 P D_m / kT \quad (8.143)$$

$$\rho = 2\alpha K^2 \frac{D_m}{D} c \quad (8.144)$$

is the reduced concentration,

$$\sigma = \alpha K \frac{D_m}{D} \cdot \frac{b^3 P}{U_0} \quad (8.145)$$

is the reduced driving force, b is the lattice constant, $D = D_0 \exp(-Q/kT)$ is the diffusion coefficient for atoms lagging behind the grain boundary and $D_m = D_{m0} \exp(-Q_m/kT)$ is the diffusion coefficient for matrix atoms crossing the boundary, $\alpha = \frac{a}{\delta}$ is half of the thickness of the grain boundary, K is

**FIGURE 8.7**

Contour-line representation of the function $y = y(\sigma, \rho)$, resulting from Eq. (8.141) [194].

given by

$$K = \left\{ \frac{kT}{U_0} \left[\exp\left(\frac{U_0}{kT}\right) - \exp\left(-\frac{U_0}{kT}\right) - 2\frac{U_0}{kT} \right] \right\}^{1/2} \quad (8.146)$$

The coefficients in Eq. (8.141) are calculated in the following manner:

1. For the lower part of the curve (Fig. 3.70) it may be assumed that $V \ll V_F$ and

$$y = \frac{V}{V_F} \ll 1$$

Then

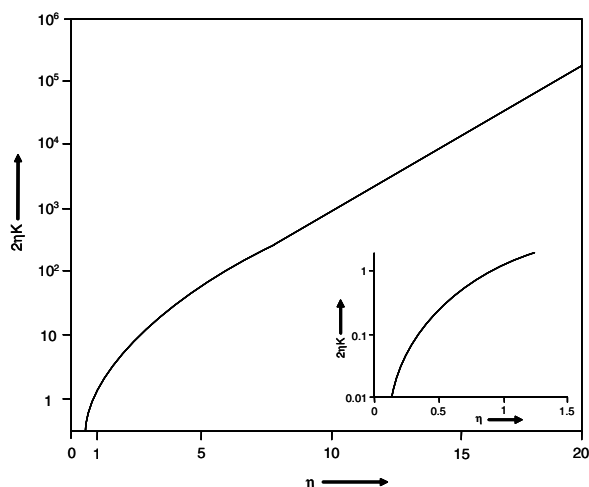
$$\rho \cong \frac{1}{y} \quad (8.147)$$

From the experimental curve (Fig. 3.70) the ratio of the velocities (mobilities) of “free” and loaded grain boundaries at the temperature of detachment for curve II we get $\rho = 25$.

2. Using the results of a numerical solution of Eq. (8.141) [194] (Fig. 8.7) we obtain $\sigma = 12$.

3. From Eqs. (8.144) and (8.145) we arrive at

$$2\eta K = \frac{Pb^3}{ckT} \cdot \frac{\rho}{\sigma} \quad (8.148)$$

**FIGURE 8.8**

The function $2\eta K$ (from Eq. (8.146) [194]).

Then, using the dependence $2\eta K$ on η (Fig. 8.8. [194]) and the value of $2\eta K$ known from Eq. (8.148) we obtain the corresponding value of η

$$\eta = \frac{U_0}{kT_0} \quad (8.149)$$

where T_0 is the temperature of detachment.

The determination of $2\eta K$ requires knowledge of the impurities, which are lost in the course of detachment. As a first approximation let us assume that this is the impurity with the highest concentration for sample II; this concentration is equal to $3 \cdot 10^{-7}$. $2\eta K = 8.6$, $\eta = 2.5$, $U_0 = 0.15$ eV, $K = 1.75$.

4. Since the upper branch of the curve (Fig. 3.70, II) characterizes the motion of a “free” (in the framework of the Cahn-Lücke-Stüwe theory) grain boundary, the parameters of this branch determine the diffusion coefficient of the matrix atoms in the vicinity of the boundary

$$D_m = \frac{V_F k T_0}{P \cdot b^2} = 1.7 \cdot 10^{-9} \text{ m}^2/\text{s} \quad (8.150)$$

The diffusion activation enthalpy of a matrix atom in the vicinity of the boundary [194] can be defined by the grain boundary migration activation enthalpy E_F after detachment

$$E_F = \frac{\partial \ln V_F}{\partial (1/kT)} = Q_m - kT_0 \quad (8.151)$$

$$Q_m = 0.5 \text{ eV} \quad (8.152)$$

The pre-exponential factor of the matrix diffusion coefficient

$$D_{m_0} = D_m \exp\left(\frac{Q_m}{kT}\right) = 9.2 \cdot 10^{-6} \text{m}^2/\text{s} \quad (8.153)$$

The diffusion coefficient for the impurity atoms can be extracted from Eq. (8.144)

$$D = \frac{2\alpha K^2 D_m}{\rho} c \quad (8.154)$$

where $\alpha = \frac{a}{b}$ is half of the grain boundary width. For $\alpha = 1$ $D = 1.2 \cdot 10^{-16} \text{m}^2/\text{s}$, the activation enthalpy of the impurity atoms is equal to

$$Q = E_L + U_0 - 2kT_0 \cong 0.7 \text{eV} \quad (8.155)$$

and the pre-exponential factor D_0 is equal to

$$D_0 \cong 10^{-11} \text{m}^2/\text{s}$$

Such characteristics of diffusion in an Al matrix are also typical for Fe, Co, Ni, Mo and Cr. In accordance with the results of the chemical analysis we can conclude that the most active impurity in our case is iron.

Actually, the diffusion parameters of Fe in Al are $D_0 = 4 \cdot 10^{-13} \text{m}^2/\text{s}$, $Q = 0.6 \text{eV}$ [622] while the other impurities in Al differ markedly from the measured values. For instance, for diffusion of Cu in Al $D_0 = 1.5 \cdot 10^{-5} \text{m}^2/\text{s}$, $Q = 1.3 \text{eV}$, for diffusion of Zn along a $38^\circ \langle 111 \rangle$ tilt grain boundary in Al $D_0 = 1.5 \cdot 10^{-3} \text{m}^2/\text{s}$, $Q = 0.83 \text{eV}$ [280].

The results obtained cause us to reconsider the previous calculation in the light of the new concentration of the active impurity — the iron atoms: $c = 10^{-7}$. Then $2\eta K = 26$; $\eta = 4.0$; $U_0 = 0.25 \text{eV}$, $K = 3, 25$; $D = 1.4 \cdot 10^{-16} \text{m}^2/\text{s}$; $D_0 = 2.5 \cdot 10^{-12} \text{m}^2/\text{s}$.

6. The concentration of the active impurity in the moving grain boundary can be found from the numerical solution of the differential equation (8.138) as a function of the reduced velocity: $\Phi = \frac{V\alpha b}{D} = 0.53$.

$$\frac{c_{eff}}{c} = 2.5$$

The value of $\frac{c_{eff}}{c}$ makes it possible to determine the drag force P_F

$$P_F = N U_0 c_{eff} = 5.8 \text{ J/m}^2 \quad (8.156)$$

In the framework of the Cahn-Lücke-Stüwe theories it is assumed that the grain boundary is homogeneous, in other words, all lattice points in the grain boundary are potential sites for adsorption of the foreign atoms. However, it is more likely that the adsorption of impurity atoms occurs on specific active centers in the grain boundary. The number of such centers can be found

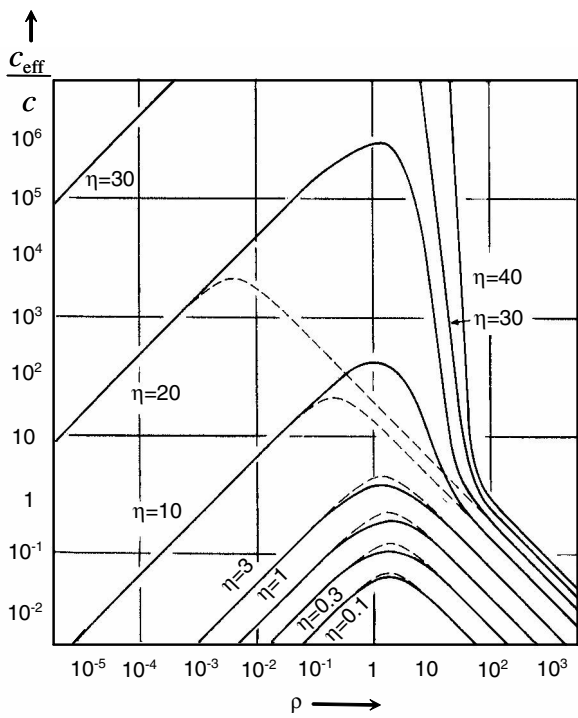


FIGURE 8.9
Effective concentration in the grain boundary as a function of boundary velocity according to continuum theory. Solid lines — Eq. (8.138), dashed lines — approximation by Eq. (8.139) [194].

from the adsorption isotherm: $\Gamma = \frac{zbc}{1-c+bc}$ (see Chapter 1). For rather small concentrations the adsorption isotherm can be transformed into $\Gamma = ze^{U_0/kT}c$

$$\frac{\Gamma}{c} = \frac{\delta N}{\Omega} \cdot \frac{c_{eff}}{c} = z \cdot e^{U_0/kT} \quad (8.157)$$

where δ is the width of the grain boundary (in [194] δ is assumed to be $2b$), Ω is the atomic volume. Then the number of adsorptionally active sites is equal to $z \cong 0.8 \cdot 10^{18} \text{m}^{-2}$. The adsorption Γ is equal to $\Gamma \cong 5 \cdot 10^{12} \text{at/m}^2$.

It is useful to compare the results obtained in the framework the Cahn-Lücke-Stüwe model with the values which can be extracted from the Lücke-Detert approach. In this case the velocity of grain boundary motion is equal to (Chapter 3)

$$V = \frac{P}{\Gamma \frac{kT}{D}} \quad (8.158)$$

At the detachment of the moving grain boundary from the impurities the denominator of expression (8.158) can be written as $\Gamma \cdot \frac{f_0}{V_0}$, $f_0 = \frac{U_0}{b}$, where V_0 is the grain boundary velocity at the detachment point. Eq. (8.158) reads

$$V_0 = \frac{P}{\Gamma \frac{U_0}{bV_0}} \quad (8.159)$$

or

$$z e^{\frac{U_0}{kT_0}} \cdot c = \frac{Pb}{U_0} \quad (8.160)$$

Expression (8.160) is an equation with two unknowns: the energy of interaction between impurity atom and grain boundary U_0 and the number of active sites z . In Fig. 3.70 the results of three independent experiments are presented, which allows us to determine the desired parameters. The energy of interaction U_0 , defined in the framework of the Lücke-Detert mode, is $U_0 \cong 0.5 \text{eV}$; the number of adsorption sites in the grain boundary $z \cong 10^{14} - 10^{15} \text{at/m}^2$.

The difference between the results obtained in the framework of the Cahn-Lücke-Stüwe model and the Lücke-Detert model becomes apparent if we recollect the assumptions made in the Lücke-Detert approach: all impurity atoms at the grain boundary interact with the grain boundary with the same force and, what is important, the grain boundary breaks away simultaneously from all adsorbed atoms.

PROBLEM 3.9

If the moving grain boundary sweeps all particles in the course of grain growth, the infinitesimal change of the number n of the particles per unit grain boundary area can be expressed as:

$$dn = \frac{c}{4/3\pi r^3} 4\pi R^2 dR \cdot \frac{1}{4\pi R^2} \quad (8.161)$$

where R is the radius of the growing grain.

For the dependence $n(R)$ we arrive at:

$$\int_{n_0}^n dn = \int_{R_0}^R \frac{R}{4/3\pi r^3} dR = n - n_0 = \frac{c}{4/3\pi r^3} (R - R_0) \quad n = n_0 + \frac{c}{4/3\pi r^3} (R - R_0) \quad (8.162)$$

Using the equation for the velocity of grain boundary motion with mobile particles (Eq. (3.71)), we come to the expression for grain growth kinetics:

$$\frac{dR}{dt} = \frac{2m_p\gamma}{Rn} = \frac{2\gamma m_p}{R \left(n_0 + \frac{c(R-R_0)}{4/3\pi r^3} \right)} \quad (8.163)$$

Integrating expression (8.163) with regard to (8.162) gives us the desired time dependency of the radius of the growing grain

$$2m_p\gamma t = \int_{R_0}^R R \left(n_0 + \frac{c(R-R_0)}{4/3\pi r^3} \right) dR \quad (8.164)$$

$$2m_p\gamma t = \frac{1}{3} (R^3 - R_0^3) \frac{c}{4/3\pi r^3} + \frac{1}{2} (R^2 - R_0^2) n_0 - \frac{1}{2} (R^2 R_0 - R_0^3) \frac{c}{4/3\pi r^3}$$

Novikov [623] studied the influence of mobile particles, located at a grain boundary during grain growth. In particular, he discovered that the kinetics of grain growth, affected by mobile particles can be approximated by the law $R^3 - R_0^3 \sim t$.

PROBLEM 3.10

As shown in Chapter 6 the criterion $\lambda_{\text{part,b}}$, which describes the efficiency of retardation of grain boundary motion by mobile particles reads (see Chapter 3, Eq. (3.71))

$$\lambda_{\text{part,b}} = \frac{m_p(r)}{n} \cdot \frac{1}{m_b} \quad (8.165)$$

In Eq. (8.165) the simplest case of particle distribution — a single size distribution — was utilized (see Chapter 3, Eq. (3.71)). The mobility of the particles $m_p(r)$ depends on the mechanism of mass transfer during particle motion and the radius of the particles. n is the number of the particles per unit of grain boundary area. Let us assume that all particles are located at the grain boundaries. The number n can be evaluated as the total number of the particles ($c/4/3\pi r^3$) divided by the total area of the grain boundaries per unit volume ($\frac{3}{\langle D \rangle}$, $\langle D \rangle$ is the mean diameter of the grains)

$$n = \frac{c \langle D \rangle}{4\pi r^3} \quad (8.166)$$

The criterion $\lambda_{\text{part,b}}$ can be expressed as

$$\lambda_{\text{part,b}} = \frac{m_p(r) \cdot 4\pi r^3}{c \langle D \rangle} \cdot \frac{1}{m_b} \quad (8.167)$$

If the particles are rather small then their motion should be controlled by interface diffusion (see Sec. 3.5), and the particle mobility can be expressed as

$$m_p(r) = \frac{\delta}{\pi r^4} \frac{D_s \Omega}{kT} \quad (8.168)$$

where δ is the effective thickness of the surface layer, $\delta \cong 10^{-9}\text{m}$, D_s is an interface diffusion coefficient ($D_s \cong 10^{-11} \text{ m}^2/\text{s}$), Ω is an atomic volume ($\Omega = 10^{-5} \text{ m}^3/\text{mol}$). Finally, the expression for the criterion $\lambda_{\text{part,b}}$ reads

$$\lambda_{\text{part,b}} = \frac{4\delta D_s \Omega}{r k T c < D > m_b} \quad (8.169)$$

Taking $< D >$ for the initial grain microstructure equal to $< D > \cong 3 \cdot 10^{-5}\text{m}$, we obtain

$$\lambda_{\text{part,b}} \cong 0.2 \quad (8.170)$$

The results of the computer simulation of grain growth in Al at the same values of the parameters [623] are expressed in the time dependency of the mean grain size $< D >$. Basically the criterion λ is the ratio of the rate of grain growth under the action of a drag factor and free grain growth. In other words, we should find the ratio of $\frac{d<D>}{dt}$ for the grain growth with the mobile particles and in the case of a pure grain boundary. The results for different $< D >$ are given in Table 8.1. One can see that the agreement between the evaluation given by Eq. (8.169) and the experiment is reasonable.

TABLE 8.1

Efficiency of Grain Growth Inhibition by Second-Phase Particles

$< D >$	$\lambda_{\text{part,b}}$ from Eq. (8.169)	$\lambda_{\text{part,b}}$ from computer simulation [623]
$7 \cdot 10^{-5}\text{m}$	0.1	0.36
$5 \cdot 10^{-5}\text{m}$	0.14	0.16

PROBLEM 3.11

Let us consider the grain growth inhibited by second-phase particles. If the particles are rather small there are two ways of inhibiting grain growth: Zener drag, where the interaction between particles and grain boundary reduces the driving force of grain growth, and the joint motion of particles and grain boundary.

For the sake of simplicity we consider the single size distribution. Using relation (3.61) (see Chapter 3) the grain growth kinetics for Zener dragging can be expressed as

$$\frac{d<D>}{dt} = m_b \left(\frac{\gamma}{<D>} - \frac{3c\gamma}{r} \right) \quad (8.171)$$

where $\langle D \rangle$ is the mean grain diameter of the polycrystal.

The grain growth kinetics for the joint motion of grain boundary and particles is given by Eq. (3.71) (see Chapter 3)

$$V = \frac{\gamma m_p(r_0)}{\langle D \rangle n_0} \quad (8.172)$$

n_0 is the number of the particles per unit area of the boundary. The criterion λ , which determines the relative efficiency of these two ways of dragging (see Chapter 6) can be constructed as

$$\lambda_{\text{Zener, part}} = \frac{m_b \left(\frac{\gamma}{\langle D \rangle} - \frac{3c\gamma}{r_0} \right) n_0}{m_p(r_0) \frac{\gamma}{\langle D \rangle}} \quad (8.173)$$

or

$$\lambda_{\text{Zener, part}} = \frac{m_b \left(\frac{1}{\langle D \rangle} - \frac{3c}{r_0} \right) n_0 \langle D \rangle}{m_p(r_0)} \quad (8.174)$$

The number of particles per unit area of the boundary $n_0 = \frac{3c}{2\pi r^2}$. For rather small particles the dominant mechanism of the mass transfer is interfacial diffusion; that is why the particle mobility is inversely proportional to r^4 (Chapter 3, Eq. (3.35))

$$m_p = \frac{m_{p0}}{\pi r_0^4} \quad (8.175)$$

The expression for $\lambda_{\text{Zener, part}}$ can be transformed into

$$\lambda_{\text{Zener, part}} = M (r_0^2 - 3cr_0 \langle D \rangle) \quad (8.176)$$

where $M = \frac{m_b}{m_{p0}} c$.

Relation (8.176) has a minimum at

$$r_0 = \frac{3}{2} c \langle D \rangle \quad (8.177)$$

Such radius of second-phase particles in a single size distribution complies with the maximal relative efficiency of Zener drag.

PROBLEM 3.12

1. The slope of the line $H/k - \ln A_0$ can be determined by analytical geometry — the straight line which passes through two points

$$T_c = \frac{\frac{H_i}{k} - \frac{H_j}{k}}{\ln A_{0i} - \ln A_{0j}} = \frac{\frac{\Delta H_{ij}}{k}}{\ln \frac{A_{0i}}{A_{0j}}} \quad (8.178)$$

where H_i , H_j , A_{0i} , A_{0j} are the activation enthalpies and the pre-exponential factors of the two considered grain boundaries, respectively.

For grain boundaries I and II we arrive at

$$T_c = \frac{\Delta H_{ij}}{k \ln \frac{A_{0i}}{A_{0j}}} = 672 \text{ K } (399^\circ \text{C}) \quad (8.179)$$

for grain boundaries I and III the compensation temperature is equal to 681 K (408°C) and for the pair II-III boundaries $T_c = 667$ K (394°C).

1. Let us now find the compensation temperature as the point of intersection of two (or more) kinetic dependencies in coordinates $\ln \frac{A_b}{A_0} - \frac{H}{kT}$, namely

$$\begin{aligned} A_1x + B_1y + C_1 &= 0 \\ A_2x + B_2y + C_2 &= 0 \end{aligned} \quad (8.180)$$

$$H_i \frac{1}{T} + \ln A_{bi} - \ln A_{0i} = 0 \quad (8.181)$$

Solution by matrix algebra yields

$$\frac{1}{T_c} = \frac{\begin{vmatrix} B_1 & C_1 \\ B_2 & C_2 \end{vmatrix}}{\begin{vmatrix} A_1 & B_1 \\ A_2 & B_2 \end{vmatrix}}, \quad \ln A_{bc} = \frac{\begin{vmatrix} C_1 & A_1 \\ C_2 & A_2 \end{vmatrix}}{\begin{vmatrix} A_1 & B_1 \\ A_2 & B_2 \end{vmatrix}} \quad (8.182)$$

or for the pair GBI-GBIII we arrive at

$$\begin{aligned} \frac{1}{T_c} &= \frac{\begin{vmatrix} 1 & -4.6 \\ 1 & -9.2 \end{vmatrix}}{\begin{vmatrix} 1.62 \cdot 10^4 & 1 \\ 1.92 \cdot 10^4 & 1 \end{vmatrix}}, \quad \ln A_{bc} = \frac{\begin{vmatrix} -4.6 & 1.62 \cdot 10^4 \\ -9.2 & 1.92 \cdot 10^4 \end{vmatrix}}{\begin{vmatrix} 1.62 \cdot 10^4 & 1 \\ 1.92 \cdot 10^4 & 1 \end{vmatrix}} \\ \frac{1}{T_c} &= \frac{-9.2 + 4.6}{1.62 \cdot 10^4 - 1.93 \cdot 10^4} = 1.48 \cdot 10^{-3} \text{K}^{-1} \end{aligned} \quad (8.183)$$

$T_c = 674$ K (401°C); $A_{bc} = 4 \cdot 10^{-9} \text{m}^2/\text{s}$.

For the grain boundaries II-III and I-II we get, respectively,

$$\begin{aligned} T_c &= 667 \text{ K (394°C); } A_{bc} = 2 \cdot 10^{-9} \text{m}^2/\text{s} \\ T_c &= 676 \text{ K (403°C); } A_{bc} = 3 \cdot 10^{-9} \text{m}^2/\text{s} \end{aligned}$$

2. The condition that three grain boundaries intersect in one point is

$$\begin{vmatrix} A_1 & B_1 & C_1 \\ A_2 & B_2 & C_2 \\ A_3 & B_3 & C_3 \end{vmatrix} = 0 \quad (8.184)$$

or

$$A_1 B_2 C_3 - B_1 C_2 A_3 - C_1 A_2 B_3 - C_1 B_2 A_3 - A_1 C_2 B_3 - B_1 A_2 C_3 = 0 \quad (8.185)$$

The sum in Eq. (8.185) is equal to ~ 592 .

Eq. (8.185) gives an assessment of the deviation of the pair intersection points from the virtual triple point. It is noteworthy that the magnitude of every term in (8.185) is in the range of 10^5 . So the intersection points are very

close to each other.

3. The mobilities of the grain boundaries at 320°C are equal, respectively:

$$\text{GBI} : A_b = 1.3 \cdot 10^{-10} \text{m}^2/\text{s}$$

$$\text{GBII} : A_b = 2.0 \cdot 10^{-11} \text{m}^2/\text{s}$$

$$\text{GBIII} : A_b = 2.4 \cdot 10^{-7} \text{m}^2/\text{s}$$

The mobilities of these grain boundaries at 520°C are

$$\text{GBI} A_b = 1 \cdot 10^{-7} \text{m}^2/\text{s}$$

$$\text{GBII} A_b = 1.0 \cdot 10^{-6} \text{m}^2/\text{s}$$

$$\text{GBIII} A_b = 2.4 \cdot 10^{-7} \text{m}^2/\text{s}$$

At a temperature lower than T_c the boundaries with low energy of activation are most mobile, whereas at temperatures higher than T_c grain boundaries with a high energy of activation are the fastest ones.

PROBLEM 3.13

From Eq. (3.234) we arrive at

$$m = m_0(1 - \alpha V) \quad (8.186)$$

where m_0 is the grain boundary mobility without magnetic field $\alpha = \frac{\sigma \ell}{c^2}$.

From Eq. (8.186) we obtain the relation for the grain boundary mobility in a magnetic field in the case that the driving force of grain boundary motion is a capillary driving force

$$m = m_0 [1 - \alpha (m\gamma\kappa)] \quad (8.187)$$

where κ is the curvature.

Then the kinetic equation for grain growth in a polycrystal in a magnetic field reads

$$\frac{dR}{dt} = \frac{m_0\gamma}{\left(1 + \frac{\alpha m_0\gamma}{R}\right) R} \quad (8.188)$$

and the time dependency for the mean grain radius R can be expressed as

$$\frac{1}{2} (R^2 - R_0^2) + \alpha m_0\gamma (R - R_0) = m_0\gamma t \quad (8.189)$$

where R_0 is the mean grain radius at $t = 0$. (The mean grain size (twice the radius R) and the radius of the curvature of the moving grain boundary are not identical. Here we do not make a distinction between these parameters since we are looking for a qualitative result.)

It should be stressed that, as described in Chapter 3, there are several contributions to the total drag force, some of which can be characterized by a strong dependency of the mobility change on the grain boundary migration rate. Eq. (8.186) represents the simplest one.

PROBLEM 4.1

(a) The volume fraction c of the particles is equal to

$$c = \frac{4}{3}\pi r^3 N \cong 4 \cdot 10^{-3}$$

Then the maximum pinning force

$$f_1 = \frac{3c\gamma}{r} = 6 \cdot 10^5 \text{ J/m}^3$$

(b)

$$c = \frac{4}{3}\pi r^3 N = 5 \cdot 10^{-3}$$

$$f_1 = \frac{3c\gamma}{r} = \frac{3 \cdot 10^{-3} \cdot 0.5}{5 \cdot 10^{-9}} = 1.4 \cdot 10^6 \text{ J/m}^3 \quad (8.190)$$

PROBLEM 4.2

(a) If a spherical particle with radius r intersects a triple line the total reduction of grain boundary energy and the line energy of the triple junction can be expressed as

$$\Delta G = \gamma \left(1 - \frac{3}{2}\pi r^2 \right) - 2r\gamma^\ell \quad (8.191)$$

where γ^ℓ is the line tension of the triple junction.

Correspondingly, the maximum attraction force f^* is

$$f^* = 3\pi r\gamma + 2\gamma^\ell \quad (8.192)$$

The particles in contact with the triple junction are confined to a volume $\frac{\pi(2r)^2}{4} \cdot 1\text{m} = \pi r^2$, i.e. the number of particles per 1m of triple junction length is equal to

$$\bar{n} = \pi r^2 \cdot N = \frac{3c}{4r} \quad (8.193)$$

Thus, the maximum pinning force f_{max}^*

$$f_{max}^* = \bar{n}f^* \cdot \bar{L} \quad (8.194)$$

where \bar{L} is the length of the triple junction per 1 m² of a grain boundary.

The number of a triple junctions N_{tr} in a polycrystal per unit volume is equal to [551]

$$N_{tj} \approx 12n \quad (8.195)$$

where n is the number of grains per unit volume.

Let us consider the grains as spheres with diameter $< D >$. Then the

number of grains per unit volume is equal to $\frac{6}{\pi \langle D \rangle^3}$ and the total area of the grain boundaries is

$$\frac{1}{2} \frac{6}{\pi \langle D \rangle^3} \cdot \pi \langle D \rangle^2 = \frac{3}{\langle D \rangle} \quad (8.196)$$

The coefficient 1/2 is introduced due to the fact that one boundary belongs to two grains.

Then N_{tj} can be expressed as

$$N_{tj} = 12n = \frac{72}{\pi \langle D \rangle^3} \quad (8.197)$$

The total length of the triple junctions per unit volume can be evaluated as

$$\bar{L}_{tj} \cong \frac{1}{2} \langle D \rangle N_{tj} = \frac{36}{\pi \langle D \rangle^2} \quad (8.198)$$

The desired ratio of the length of the triple junctions to grain boundary area \bar{L} reads

$$\bar{L} = \frac{\bar{L}_{tj}}{3 \langle D \rangle} = \frac{12}{\pi \langle D \rangle} \quad (8.199)$$

Finally, the maximal pinning force by particles on triple junctions can be expressed as

$$f_2 = \frac{3c}{4r} \cdot f^* \cdot \bar{L} = \frac{3c}{4r} \cdot (3\pi r \gamma + 2\gamma^\ell) \cdot \frac{12}{\pi \langle D \rangle} \cong 25 \frac{\gamma c}{\langle D \rangle} + 6 \cdot \frac{\gamma^\ell c}{r \langle D \rangle} \quad (8.200)$$

$$P_2 \cong 50 \cdot 10^3 \text{ J/m}^3 + 25 \cdot 10^2 \text{ J/m}^3 \cong 5.3 \cdot 10^4 \text{ J/m}^3 \quad (8.201)$$

As can be seen for the given parameters, the pinning force of the particles on the triple junctions is at least an order of magnitude smaller than the pinning force from the particles on the grain boundary. The general pinning force is equal to the sum of these pinning forces. The force f_2 is the pinning force when the particles are located exactly on the triple line.

(b) The pinning force is equal to (see Eq. (8.201) in the previous problem):

$$f_2 = 25 \frac{\gamma c}{\langle D \rangle} + 6 \frac{\gamma^\ell c}{r \langle D \rangle}$$

$$c = \frac{4}{3} \pi r^4 N \cong 5 \cdot 10^{-3}$$

$$f_2 \cong 9 \cdot 10^5 \text{ J/m}^3$$

PROBLEM 4.3

(a) If a spherical particle with radius r is located at a quadruple point the total reduction of the grain boundary energy can be expressed as

$$\Delta G = \gamma (1 - 2\pi r^2) \quad (8.202)$$

Since nothing is known about the energy of a quadruple junction we assume that we can neglect the effect of this parameter on the energetics of the system.

From (8.202) we obtain the maximum attraction force f_3^*

$$f_3^* = 4\pi r \gamma \quad (8.203)$$

If we assume that a quadruple junction can be occupied by only one particle, then the maximum pinning force f_3 will be equal to

$$f_3 = 4\pi r \gamma c \cdot \bar{N}_{\text{quad}} \quad (8.204)$$

where \bar{N}_{quad} is the number of quadruple junctions per unit grain boundary area.

The number of quadruple junctions in a polycrystal with n grains per unit volume is equal to [551]

$$N_{\text{quad}} \cong 6n \quad (8.205)$$

Since $n = \frac{6}{\pi \langle D \rangle^3}$, where $\langle D \rangle$ is the diameter and $3/\langle D \rangle$ is the total grain boundary area per unit volume

$$N_{\text{quad}} = \frac{36}{\pi \langle D \rangle^3} \quad (8.206)$$

and

$$\bar{N}_{\text{quad}} = \frac{36 \langle D \rangle}{\pi \langle D \rangle^3 \cdot 3} = \frac{12}{\pi \langle D \rangle^2} \quad (8.207)$$

Then for the maximum pinning force f_3 we arrive at

$$f_3 = 4\pi r \gamma c \bar{N} = \frac{64\pi r^4 \gamma N}{\langle D \rangle^2} \quad (8.208)$$

Substituting the parameters given in the problem we come to

$$f_3 \cong 10^3 \text{ J/m}^3 \quad (8.209)$$

Note that the force f_3 depends very strongly on the size of the second-phase particles.

(b) Substituting the parameters of the problem into Eq. (8.208) yields

$$f_3 = 10^7 \text{ J/m}^3$$

PROBLEM 4.4

The total grain boundary area of a sample with the mean grain size $\langle D \rangle$ is equal to

$$S = \frac{3}{\langle D \rangle} \quad (8.210)$$

On the other hand, the rate of grain boundary motion is equal to

$$\dot{R} = \frac{m\gamma}{R} \quad (8.211)$$

where R is the radius of the curvature of the moving boundary; $R \sim \langle D \rangle$.

Then

$$\frac{dS}{dt} = -\frac{3}{\langle D \rangle^2} \frac{d\langle D \rangle}{dt} \sim -\frac{3m\gamma}{\langle D \rangle^3} \sim -\frac{1}{9}m\gamma S^3 \quad (8.212)$$

PROBLEM 4.5

The rate of grain area change is given by the Von Neumann-Mullins relation

$$\frac{dS}{dt} = -A_b [2\pi - n(\pi - 2\theta)] \quad (8.213)$$

As shown in Chapter 4 for a system with triple junctions of finite mobility the angle θ is a function of the dimensionless parameter Λ ($\Lambda = \frac{m_{tj}a}{m_b}$). The equilibrium value $\theta = \pi/3$ is obtained for $\Lambda \rightarrow \infty$

$$\frac{dS}{dt} = \frac{\pi}{3}m_b\gamma(n-6) \quad (8.214)$$

To find the dependence of the grain area change rate for $\Lambda \neq \infty$ a consideration of the relation (8.213) in the vicinity of “equilibrium” ($\theta = \pi/3$) can be invoked (Eqs. (4.82) and (4.85)). The diagram of $\frac{dS}{dt}$ for different Λ is given in Fig. 8.10.

For $\Lambda \cong 10$ and grains with $n < 6$ the topological class which meets the condition $\frac{dS}{dt} = 0$ is equal to 5 instead of 6 as for $\Lambda \rightarrow \infty$. A similar phenomenon can be observed qualitatively for grains with $n > 6$, however, quantitatively it manifests itself as less pronounced. For example, the line $\frac{dS}{dt}(n)$ for $n > 6$ intersects the axis n in the point $n = 7$ at $\Lambda = 1.11$. For rather large Λ both the lines — for $n < 6$ and $n > 6$ — merge, as can be seen for $\Lambda = 10^3$.

PROBLEM 4.6

As shown in Chapter 3 for the steady-state motion of a grain boundary half-loop the following relations for the grain boundary velocity and the velocity of the facet hold:

$$V = \frac{m_b\gamma(\theta - \varphi)}{a/2 - \ell \sin \theta} \quad (8.215)$$

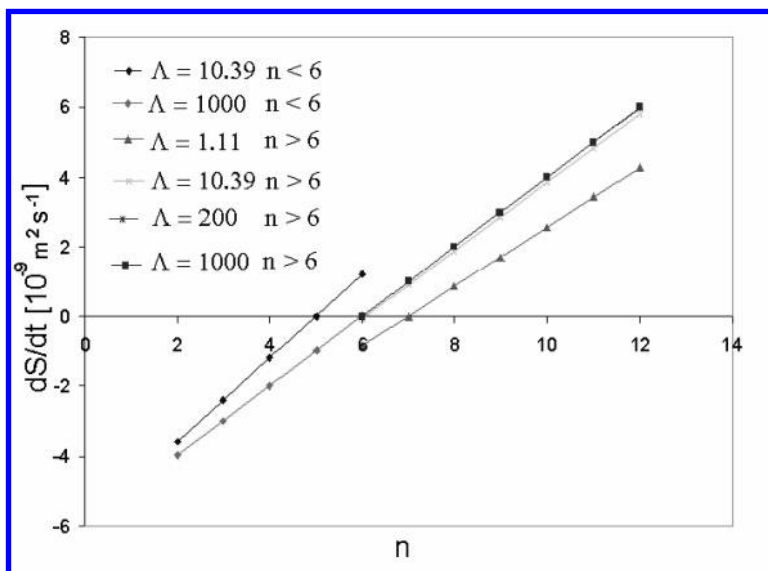
**FIGURE 8.10**

Diagram “grain area change vs. topological class” for different values of the criterion Λ .

$$V = \frac{m_f \gamma \sin \varphi \sin \theta}{\ell} \quad (8.216)$$

In the case that the grain boundary system includes a triple junction (Fig. 8.11) the velocity of the triple junction can be expressed as

$$V = m_{tj} (2\gamma \cos \varphi \cos \theta - \gamma) \quad (8.217)$$

It is stressed that for a steady-state motion the faceted and the curved segments of the half-loop along with the triple junction have to move with the same velocity.

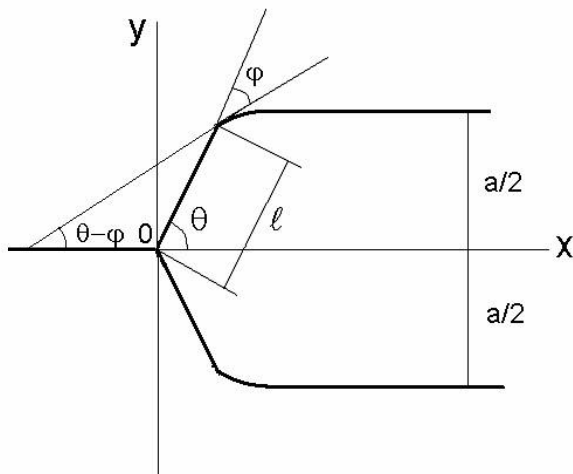
Combining Eqs. (8.215) and (8.216) yields the length of a moving facet

$$\ell = \frac{a/2}{\sin \theta + \frac{m_b(\theta - \varphi)}{m_f \sin \varphi \sin \theta}} \quad (8.218)$$

From Eqs. (8.215) and (8.217) we arrive at

$$\frac{m_{tj} \left(\frac{a}{2} - \ell \sin \theta \right)}{m_b} = \frac{\theta - \varphi}{2 \cos \varphi \cos \theta - 1} \quad (8.219)$$

One can see that the left hand-side of Eq. (8.219) constitutes the criterion Λ for a grain boundary system with triple junction and a facet. However,

**FIGURE 8.11**

Grain boundary system with facets and triple junction.

contrary to the criterion Λ considered in Chapter 4, there is one distinctive property of the criterion analyzed here. Namely, since the right-hand side of Eq. (8.219) is a constant value, by definition, the changes in grain boundary and triple junction mobility have to be compensated by a variation of the facet length ℓ .

If the ratio $\frac{m_{tj}}{m_b}$ increases ℓ tends to its maximal value $\ell = \frac{a}{2 \sin \theta}$. By contrast, when the decrease of the ratio $\frac{m_{tj}}{m_b}$ causes the disappearance of the facet $\ell = 0$, the grain boundary system transforms into the well-known grain boundary configuration with a triple junction (Fig. 4.2). Indeed, in this case $\varphi = 0$ and Eq. (8.219) converts to

$$\frac{m_{tj}a}{m_b} = \frac{2\theta}{2 \cos \theta - 1} \quad (8.220)$$

Combining Eqs. (8.216) and (8.217) we arrive at

$$\frac{m_{tj}\ell}{m_f} = \frac{\sin \varphi \sin \theta}{2 \cos \varphi \cos \theta - 1} \quad (8.221)$$

Again, as discussed above, the left-hand side of relation (8.221) is a criterion Λ for a grain boundary half-loop with facet and triple junction; this criterion is expressed in terms of triple junction and facet mobility. Contrary to the criterion (8.219), an increase in the ratio $\frac{m_{tj}}{m_f}$ in (8.221) leads to a reduction of ℓ . One can see that at $\ell = 0$ the right-hand side tends to zero as well: at $\ell = 0$ the angle $\varphi = 0$.

PROBLEM 4.7

The major ideas of a dimensional analysis were put forward by Newton, Fourier, Buckingham, Rayleigh, Tolman, Bridgman, and Huntley. In particular, Fourier's contribution should be distinguished because he introduced important concepts. The first is the description of the so-called "dimension formula," while the second is a clear understanding of the dimensional homogeneity of physical expressions [624].

The "dimensional formula" reflects the requirement that physical relations have to be independent of the units used. The second Fourier concept expresses the dimensional homogeneity of the physical relations; the relation must be "dimensionally homogeneous." "For each physical quantity there is one, and only one, dimension formulated. Conversely, corresponding to each dimensional formula there is one, and only one, physical quantity" [625]. There are some exceptions, which we will not discuss here. Another presentation of this principle is given in the so-called " π -theorem" (Buckingham theorem): The physical equations can be expressed as a relationship between dimensionless complexes. In accordance with the π -theorem the number of independent dimensionless complexes is equal to the number of quantities considered minus the number of elementary dimensions used. The meaning of the approaches mentioned will be discussed in the following for specific examples ("fundamental quantities").

- (a) The first step is to define the quantities which determine the motion of a grain boundary, the time t which is necessary to obtain the given mean grain size $\langle D \rangle$. Obviously, t is a function of grain boundary mobility m_b , grain boundary surface tension γ and mean grain size $\langle D \rangle$; in other words,

$$t = f(m_b, \gamma, \langle D \rangle) \quad (8.222)$$

In accordance with the principle of dimensional homogeneity we arrive at

$$T = m_b^a \gamma^b \langle D \rangle^c \quad (8.223)$$

Since the dimension of m_b is $\left[\frac{L^4}{E \cdot T}\right] = [L^2 M^{-1} T]$, γ is $\left[\frac{E}{L^2}\right] = [MT^{-2}]$, $\langle D \rangle [L]$, where E is the dimension of the energy, L of the length, T of the time, M of the mass, we have:

— exponent of T : $1 = a - 2b$

— exponent of L : $2a + c = 0$

— exponent of M : $-a + b = 0$

The solution is $a = -1$; $b = -1$; $c = 2$.

Then the expression for the desired dependence can be presented as

$$\langle D \rangle^2 = C m_b \gamma t \quad (8.224)$$

where C is a numerical coefficient.

It can be seen that presenting the surface tension as $\gamma \left[\frac{E}{L^2}\right]$ and the

grain boundary mobility as $m_b \left[\frac{L^4}{ET} \right]$ we can arrive at the result (8.224) even faster. We accept as an axiom that, in the framework of a system of fundamental quantities, the dimension formula of a physical variable can be expressed in a unique way. However, the choice of the “fundamental” quantities to a certain extent is a question of convenience [626]. Moreover, this can be achieved by practice only, and the shortest way at the first stage is to use a standard set of fundamental quantities. In the framework of the concept of the π -theorem, the result (8.224) manifests that there is only one dimensionless complex which can be formed from the quantities m_b , γ , $\langle D \rangle$, and time t .

- (b) The primary aim of the second problem is to find the dimensionless complexes which determine the motion of connected grain boundaries. The first step is to decide what physical and structural quantities are involved in this process. We chose the following physical parameters of the problem:

- grain boundary velocity $V \left[\frac{L}{T} \right]$
- distance between the junctions $a[L]$
- grain boundary mobility $m_b \left[\frac{L^2 T}{M} \right]$
- triple junction mobility $m_{tj} \left[\frac{L T}{M} \right]$
- quadruple junction mobility $m_{qp} \left[\frac{T}{M} \right]$
- driving force of grain boundary motion $P \left[\frac{M}{T^2 L} \right]$

As can be seen the number of independent dimensionless complexes is equal to the number of quantities considered minus the number of fundamental quantities: $6 - 3 = 3$.

Then

$$V^a a^b m_b^c m_{tj}^d m_{qp}^e P^f = K \quad (8.225)$$

- exponent of L : $a + b + 2c + d - f = 0$
- exponent of T : $-a + c + d + e - 2f = 0$
- exponent of M : $-c - d - e + f = 0$

Finally

- $c = -a - \frac{b}{2} - \frac{d}{2}$
- $e = \frac{b}{2} - \frac{d}{2}$
- $f = -a$

The complexes obtained look like this:

$$\left(\frac{V}{P m_b} \right) - I; \left(\frac{a m_{qp}^{1/2}}{m_b^{1/2}} \right) - II; \left(\frac{m_{tj}}{m_b^{1/2} \cdot m_{qp}^{1/2}} \right) - III \quad (8.226)$$

It is easy to see that we get the main dimensionless criteria which were derived analytically from microscopic considerations. Indeed:

$$\Lambda_{tj} = \frac{m_{tj} a}{m_b} = (II) \cdot (III); \quad \Lambda_{gp} = \frac{m_{gp} a^2}{m_b} = (II)^2 \quad (8.227)$$

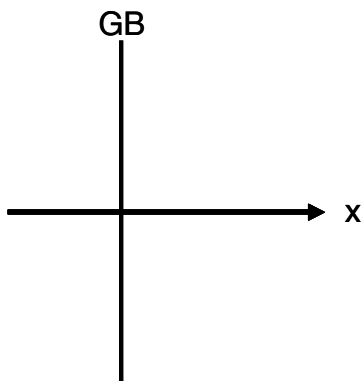
**FIGURE 8.12**

Diagram of a grain boundary (GB) which moves in the direction x .

- (c) The problem “3” is closely connected with the approach put forward by W. Williams (1892), Noon and Spencer (1949) and analyzed in Huntley [624].

As can be seen from the given examples, a solution to a problem can be found by dimensional analysis when the number of independent quantities exceeds the number of the fundamental quantities $L, M, T \dots$) by one. The principal idea of the approach described is that, if it is necessary to increase the number of fundamental quantities, considering components of the length in three mutually perpendicular directions. In this case the fundamental quantities are $[L_x], [L_y], [L_z]$. This simple change, at first glance, makes many dimensional expressions more informative. This is particularly true for the velocity; the difference between LT^{-1} and $L_x T^{-1}$ is evident.

Let us apply this approach to a problem: to find a relation for the velocity of a flat grain boundary which moves into the direction x under the action of a constant driving force in the system with the concentration c of dissolved impurities (Fig. 8.12).

The major physical quantities which define the problem are the velocity of grain boundary motion, driving force for motion, grain boundary mobility, concentration of the impurities. In accordance with the approach described and Fig. 8.12 we get

$$V \left[\frac{L_x}{T} \right], P \left[\frac{ML_x}{T^2 L_y L_z} \right], m_b \left[\frac{L_x^2 T}{M} \right], c \left[\frac{1}{L_x L_y L_z} \right] \quad (8.228)$$

Then

$$\left(\frac{L_x}{T}\right) = K \left(\frac{ML_x}{T^2 L_y L_x}\right)^a \left(\frac{L_x^2 T}{M}\right)^b \cdot \left(\frac{1}{L_x L_y L_z}\right)^e \quad (8.229)$$

$$L_x : 1 = a + 2b - e$$

$$L_y : 0 = -a - e$$

$$L_z : 0 = -a - e$$

$$T : -1 = -2a + b$$

$$M : a - b = 0$$

This yields:

$$b = 1; \quad a = 1; \quad c = -1$$

Finally we obtain:

$$V = K \frac{P m_b}{c} \quad (8.230)$$

where K is a numerical coefficient.

Expression (8.230) was derived by Lücke and Detert in 1957 from macroscopic considerations. The model put forward by Lücke and Detert is convincing and physically clear.

Finally, we would like to cite Rayleigh; this equation is relevant to all problems considered in this paragraph.

"I have often been impressed by the scanty attention paid even by original workers in physica to the great principle of similitude. It happens not infrequently that results in the form of 'laws' are put forward as novelties on the basis of elaborate experiments which might have predicted a priori after a few minutes' consideration."

PROBLEM 4.8

- (1) The criterion $\Lambda_{gp} = \frac{m_{gp} x_0}{m_{tj}} = \frac{9 \cdot 10^{-5} \cdot 10^{-8}}{4 \cdot 10^{-12}} \cong 1.1$.
The tetrahedral angle Θ is equal to $\sim 108.5^\circ$.

- (2) The criterion Λ for a 2D configuration $n < 6$ $\Lambda = \frac{m_{tj} \langle R \rangle}{m_b} = \frac{4 \cdot 10^{-12} \cdot 5 \cdot 10^{-8}}{2 \cdot 10^{-14}} = 10^{-5}$.

The angle Θ can be found from the relation

$$\Lambda = \frac{2\Theta}{2 \cos \Theta - 1}$$

$$\Theta = 10^{-5}.$$

For the configuration $n > 6$

$$\Lambda = -\frac{\ln \sin \Theta}{1 - 2 \cos \Theta}$$

The angle Θ for $\Lambda = 10^{-5}$ is equal to $\cong 89.8^\circ$.

PROBLEM 4.9

(a) The rate of change of \dot{S} for pure grain boundary kinetics (triple junction mobility, or, more correctly, the criterion $\Lambda \rightarrow \infty$) can be found using Eq. (4.71)

$$\frac{d\dot{S}}{dn} = \frac{m_b\gamma\pi}{3} \quad (8.231)$$

It can be seen from Eq. (8.231) that the rate of change of \dot{S} with n is constant; when $n \rightarrow \infty$, \dot{S} tends to infinity as well.

(b) In the intermediate case, when the effect of the triple junctions is large, and grain growth kinetics can be viewed as grain boundary motion, the generalized Von Neumann-Mullins relation can be expressed by relation (4.82) for $n < 6$ and relation (4.85) for $n > 6$.

The rate of change of \dot{S} with topological class can be represented as

$$\frac{d\dot{S}}{dn} = \frac{m_b\gamma\pi}{3} \cdot \frac{6 + \sqrt{3}\Lambda}{2 + \sqrt{3}\Lambda} \quad (8.232)$$

$$\frac{d\dot{S}}{dn} = \frac{m_b\gamma\pi}{3} \cdot \left(1 - \frac{6}{\pi\Lambda B}\right) \quad (8.233)$$

One can see that the rate $\frac{d\dot{S}}{dn}$ is positive; however, it depends on the criterion Λ . For $\Lambda \rightarrow \infty$ the rate $\frac{d\dot{S}}{dn}$ tends to the constant value $\frac{m_b\gamma\pi}{3}$, characteristic of pure grain boundary kinetics. The effect of Λ on the parameter $\frac{d\dot{S}}{dn}$ is qualitatively different for $n < 6$ and $n > 6$. Namely, for $n < 6$

$$\frac{d}{d\Lambda} \left(\frac{d\dot{S}}{dn} \right) = -\frac{4\sqrt{3}m_b\gamma\pi}{3(2 + \sqrt{3}\Lambda)^2} < 0 \quad (8.234)$$

and for $n > 6$

$$\frac{d}{d\Lambda} \left(\frac{d\dot{S}}{dn} \right) = \frac{2m_b\gamma}{\Lambda^2 B} > 0 \quad (8.235)$$

For both branches the rate of change of $\frac{d\dot{S}}{dn}$ with Λ tends to zero as Λ increases.

(c) As shown in Chapter 4, under triple junction kinetics, the rate of grain area change \dot{S} is expressed by Eq. (4.89).

Contrary to the relations for \dot{S} for grain boundary kinetics and for intermediate kinetics, for pure triple junction kinetics at $n \rightarrow \infty$ the function \dot{S} tends to a product $\infty \cdot 0$.

To remove this uncertainty the L'Hôpital's rule can be utilized: if we are looking for the limit of the fraction $\frac{f(x)}{g(x)}$ and the $\lim_{x \rightarrow \infty} \frac{f'(x)}{g'(x)} = A$ the limit of the fraction $\frac{f(x)}{g(x)}$, $\lim_{x \rightarrow \infty} \frac{f(x)}{g(x)} = A$ as well.

Let us represent our junction \dot{S} as²

$$\dot{S} = \frac{-m_{tj}\gamma n \bar{R} \sin\left(\frac{2\pi}{n}\right) \left[2\sin\left(\frac{\pi}{n}\right) - 1\right]}{1/n} \quad (8.236)$$

As easy to see the expression $\left(\frac{d\dot{S}}{dn}\right)_{n \rightarrow \infty}$ is equal to

$$\begin{aligned} \left(\frac{d\dot{S}}{dn}\right)_{n \rightarrow \infty} &= \lim_{n \rightarrow \infty} \left\{ -m_{tj}\gamma \tilde{R} \frac{\frac{2\pi}{n^2} \cos\left(\frac{2\pi}{n}\right) \left[2\sin\left(\frac{\pi}{n}\right) - 1\right] + \frac{2\pi}{n^2} \sin\left(\frac{2\pi}{n}\right) \cos\left(\frac{\pi}{n}\right)}{1/n^2} \right\} = \\ &= 2\pi m_{tj}\gamma \tilde{R} \end{aligned} \quad (8.237)$$

Computer simulations of 2D grain growth under triple junction kinetics [441, 442] Chapter 4, Fig. 4.44, confirm the results found in (8.237).

²In our calculations we restrict ourselves to the expression with exterior radius \bar{R} . We leave to the reader the possibility of finding the limit for the expression with the interior radius \bar{r} .

References

- [1] Gibbs JW. In *The Collected Works Two Volumes*, Longmans, Green, New York, 1928.
- [2] Marchenko VI. *JETP*, 52:129, 1980.
- [3] Andreev AF. *JETP*, 80:2042, 1980.
- [4] Marchenko VI. *JETP Letters*, 33:397, 1981.
- [5] Landau LD and Lifshits EM. *Ser. Theoretical Physics*, Vol. 5, 1977.
- [6] Fradkov VE and Shvindlerman LS. *Phys. Chem. Mech. Surfaces*, 9:2505, 1982.
- [7] Hart EW. In Hu H. editor, *The Nature and Behaviour of Grain Boundaries*, pp. 155, Plenum Press, New York, 1982.
- [8] Guggenheim EA and Adam NK. *Proc. Roy. Soc.*, A139:216, 1933.
- [9] Fradkov VE and Shvindlerman LS. *Fiz. Metall. Metalloved.*, 48:297, 1979.
- [10] Spetnak JW and Speiser R. *Trans. ASM*, 43:734, 1951.
- [11] Estrin Y, Gottstein G, Shvindlerman LS. *Scripta Mater.*, 41:385, 1999.
- [12] Estrin Y, Gottstein G, Rabkin EJ, Shvindlerman LS. *Scripta Mater.*, 43:141, 2000.
- [13] Chaudhari P. *Vac. Sci. Techn.*, 9:520, 1972.
- [14] Thompson CV, Carel R. *J. Mech. Phys. Sol.*, 44:657, 1996.
- [15] Knizhnik GS. *Povernost: Fizika, Shimia, Mehanika (in Russian)*, 5:50, 1981.
- [16] Meiser H, Gleiter H. *Scripta Metall.*, 14:1980, 1980.
- [17] Merkle KL, Csencits R, Rynes KL, Withrow JP, Stadelmann PA. *J. of Microscopy* 190:204, 1998
- [18] Ivanov VA, Molodov DA, Shvindlerman LS, Gottstein G, Kolesnikov D, Lojkowski W. *Mat. Sci. Forum*, 519-521:1557, 2006.

- [19] Read WT, Shockley W. *Phys. Review*, 28:275, 1950.
- [20] Molodov DA, Shvindlerman LS. *IJMR*, 4:461, 2009.
- [21] Stout F. *Acta Metall.*, 1:753, 1953.
- [22] Cahn JW and Hillard JE. *Acta Metall.*, 7:219, 1959.
- [23] McLean D. *Grain Boundaries in Metals*, Clarendon Press, Oxford, 1957.
- [24] Bokstein BS, Klinger LM, Nikol'skii GS, Fradkov VE, Shvindlerman LS. *Fiz. Metallov i Metallovedenie*, 48(6):1212, 1979.
- [25] Zhuchovitskii AA. *Zn. Fiz. Khimii*, 18:214, 1944.
- [26] Shvindlerman LS, Gottstein G, Molodov DA. *Phys. Stat. Sol. (a)*, 160:419, 1997.
- [27] Bokstein BS and Shvindlerman LS. In *Theoretical Fundamentals of Materials Science*, Moscow, 'Nauka,' 115, 1981.
- [28] Hill TL. *J. Chem. Phys.*, 14:263, 1946.
- [29] Guggenheim EA. In *Applications of Statistical Mechanics*, Clarendon Press, Oxford, 1966.
- [30] Guttmann M. *Metall. Trans.*, 8A:1383, 1977.
- [31] Hondros ED and Seah MP. In Cahn RW and Haasen P, editors, *Physical Metallurgy*, North Holland, Amsterdam, pp. 855, 1983.
- [32] Seidman DN. *Mat. Sci. and Eng.*, A137:57, 1991.
- [33] Cabane J and Cabane F. In Nowotny J., editor, *Interface Segregation and Related Processes in Materials*, Trans. Techn. Publications, Zürich, 1, 1991.
- [34] Lejcek P and Hofmann S. *Critical Reviews in Solid State and Materials Sciences*, 20(1):1, 1995.
- [35] Sutton AP and Balluffi RW. *Interfaces in Crystalline Materials*, Oxford, U.K., Oxford University Press, 1995.
- [36] Seah MP and Hondros ED. *Proc. R. Soc. London, Ser. A*, 335:191, 1973.
- [37] Chang L-S, Straumal BB, Rabkin EJ, Gust W, Sommer FJ. *Phase Equilibria*, 18:128, 1997.
- [38] Sutton AP and Vitek V. *Acta Metall.*, 30:2011, 1982.
- [39] Thomas WR and Chalmers B. *Acta Metall.*, 3:17, 1955.
- [40] Lejcek P, Adamek J, Hofmann S. *Surf. Sci.*, 246:449, 1992.

- [41] Hu JG and Seidman DN. *Scripta Metall. Mater.*, 27:693, 1992.
- [42] Hu JG and Seidman DN. *Phys. Rev. Lett.*, 65:1615, 1990.
- [43] Seidman DN. *Mater. Sci. Eng.*, A137:57, 1991.
- [44] Balluffi RW. In Johnson WC and Blakely SM, editors, *Interfacial Segregation*, American Society of Metals, Metals Park, OH, p. 193, 1979.
- [45] Menghard M, Jan M, Vitek V. *Acta Metall. Mater.*, 42:783, 1994.
- [46] Udler D and Seidman DN. *Phys. Stat. Sol. B*, 172:267, 1992.
- [47] Udler D and Seidman DN. *Acta Metall. Mater.*, 42:1959, 1994.
- [48] Udler D and Seidman DN. *Mater. Sci. Forum*, 126-128:165, 1993.
- [49] Watanabe T, Kitamura S, Karashima S. *Acta Metall.*, 28:455, 1980.
- [50] Lejcek P and Hofmann S. *Met. Sci. Forum*, 126-128:157, 1993.
- [51] Luzzi DE. *Phil. Mag. Lett.*, 63:281, 1991.
- [52] Jan M, Sob M, Luzzi DE., Vitek V, Ackland GJ., Methfessel M, Rodriguez CO. *Phys. Rev.*, B47:5571, 1993.
- [53] Lejcek P and Hofmann S. *Acta Metall. Mater.*, 39:2469, 1991.
- [54] Masuda-Jindo K. *Phys. Stat. Sol. B*, 134:545, 1986.
- [55] Hashimoto M, Ishida J, Jamamoto R, Doyama M. In Ishida, J, editor, *Grain Boundaries Structure and Related Phenomena Proc. 4th Jpn. Inst. Met. Int. Symp.*, Trans. Jpn. Inst. Met., Suppl. 27:229, 1986.
- [56] Lejcek P and Hofmann S. *Mater. Sci. Eng.*, A185:109, 1994.
- [57] Lundberg M. *Phys. Rev.*, B36:4692, 1987.
- [58] Najafabadi R, Srolovitz, DJ, LeSar R. *J. Mater. Res.*, 6:999, 1991.
- [59] Najafabadi R, Wang HY, R, Srolovitz DJ, LeSar R. *Acta Metall. Mater.*, 39:3071, 1991.
- [60] Mehl RF. *Trans. Amer. Soc. Metals*, 29:28, 1941.
- [61] Arharov VJ. *Trudu the Ural Filial of the Academy of Sciences of the USSR*, 16:7, 1955.
- [62] Hondros ED. *Proc. R. Soc. London Ser.*, A.286:479, 1965.
- [63] Hondros ED and Seah MP. *Scripta Metall.*, 6:1007, 1972.
- [64] Erhart H and Grabke HJ. *Met. Sci.*, 15:401, 1981.

- [65] Muschik T, Hofmann S, Gust W, Predel B. *Appl. Surf. Sci.*, 37:439, 1989.
- [66] Hondros ED and Seah MP. *Met. Trans. A*, 8A:1363, 1977.
- [67] Brunauer S, Emmet PH, Teller E. *J. Amer. Chem. Soc.*, 60:309, 1938.
- [68] Seah MP and Hondros ED. *Scripta Metall.*, 7:735, 1973.
- [69] Gas P, Guttman M, Bernardini J. *Acta Metall.*, 30:1309, 1982.
- [70] Bokstein BS, Kopetskii ChV, Shvindlerman LS. *Thermodynamics and Kinetics of Grain Boundaries in Metals*, Metallurgia, Moscow, p. 224, 1986.
- [71] Smith CS. *Trans. AIME*, 175:15, 1948.
- [72] Chalmers B. *Proc. Roy. Soc.*, A196:64, 1949.
- [73] Herring C. In Kingston WE, editor, *Physics of Powder Metallurgy*, McGraw-Hill, New York, 1951.
- [74] Fullman RL. *J. Appl. Phys.*, 22:456, 1951.
- [75] Friedel J, Cullity B, Crussard C. *Acta Metall.*, 1:79, 1953.
- [76] Maksimova EL, Shvindlerman LS, Straumal BB. *Acta Metall.*, 36, 1573, 1988.
- [77] Wilson TL and Shewmon PG. *Trans. AIME*, 236:48, 1966.
- [78] Herrmann G, Gleiter H, Bäro G. *Acta Metall.*, 24:353, 1976.
- [79] Mori T, Miura H, Tokita T, Haji J, Kato M. *Phil. Mag. Letters*, 58:11, 1988.
- [80] Chan SW and Balluffi RW. *Acta Metall.*, 33:1113, 1985.
- [81] Herrmann G, Gleiter H, Bäro G. In Walter JL, Westbrook JH, Woodford DA, editors, *4th Bolton Landing Conf. Grain Boundaries in Engineering Materials*, p. 43, Baton Rouge Claitors, 1974.
- [82] Udin H, Shaler AJ, Wulff J. *Trans. AIME*, 185:186, 1949.
- [83] Jones H. *Scripta Met.*, 6:423, 1972.
- [84] Jones H. *Mater. Sci. Eng.*, 4:106, 1969.
- [85] Murr LE, Wong, GI, Honglew RJ. *Acta Metall.*, 21:595, 1973.
- [86] Mullins WW. *Acta Metall.*, 4:421, 1956.
- [87] Molodov DA, Gottstein G, Heringhaus F, Shvindlerman LS. *Acta Metall.*, 46:5627, 1998.

- [88] Ashavskii BS, Bokstein BS, Nikolskii GS. *Poverhrost*, (in Russian) 11:28, 1982.
- [89] Brongersma HH and Sparnaay MJ. *Surf. Sci.*, 71:657, 1978.
- [90] Hillard JE, Cohen M, Auerbach BL. *Acta Metall.*, 8:26, 1960.
- [91] Ashavskii BS, Bokstein BS, Nikolskii GS, Holodov SN. *Poverhrost* 8:107, 1984.
- [92] Hultgren R, Desai PD, Hawkins DT, Gleiter M, Kelley KK. In *Selected Values of the Thermodynamic Properties of Binary Alloys*, AMS, Metals Park, OH, 1973.
- [93] Hultgren R, Desai PD, Hawkins DT, Gleiter M, Kelley KK, Wagman DD. In *Selected Values of the Thermodynamic Properties of Binary Alloys*, AMS, Metals Park, OH, 1973.
- [94] Aleksandrovich VL, Fradkov VE, Shvindlerman LS. *Phys. Met. Metall.* 54:136, 1982.
- [95] Hondros ED. In *Energetics of Solid – Solid Interfaces*, Symposium of Interfaces, p. 77, Melbourne, Australia, 1969.
- [96] Bokstein BS and Shvindlerman LS. *Sov. Phys. Solid State*, 19:542, 1977.
- [97] Shvindlerman LS and Faulkner RG. *Interface Sci.*, 6:213, 1998.
- [98] Cahn JW. *J. Phys. Colloq.*, C6 43:199, 1982.
- [99] Rottmann E. *J. Phys. Colloq.*, C5 49:313, 1988.
- [100] Rabkin EJ, Shvindlerman LS, Straumal BB. *Int. J. of Modern Physics B*, 5:2989, 1991.
- [101] Shewmon PG. *Acta Metall.*, 5:335, 1957.
- [102] Li JCM. *J. Appl. Phys.*, 32:525, 1961.
- [103] Bokstein BS, Klinger LM, Shvindlerman LS. *J. of Chem. Phys.*, (in Russian) XLVIII(6):1527, 1974.
- [104] Glicksman ME and Vold CL. in *Solidification*, American Society of Metals, Metals Park, OH, 1971.
- [105] Rottman C. *Scripta Metall.*, 19:43, 1985.
- [106] Hsieh TE and Balluffi RW. *Acta Metall.*, 37:1637, 1989.
- [107] Ciccotti G, Guillope M, Pontikis V. *Phys. Rev.*, B27:5576, 1983.
- [108] Broughton JQ, Gilner GH. *Phys. Rev. Lett.*, 56:2692, 1986.
- [109] Lutsko JF and Wolf D, *Scripta Metall.*, 22:1923, 1988.

- [110] Kikuchi R and Cahn JW. *Phys. Rev.*, B21:1893, 1980.
- [111] Kikuchi R and Cahn JW. *Phys. Rev.*, B36:418, 1987.
- [112] Derrida B and Schick M. *J. Phys.* A19:1439, 1986.
- [113] Passerone A and Sangiorgi R. *Acta Metall.*, 33:771, 1985.
- [114] Ikeuye KK and Smith CS. *Trans. AIME*, 185:762, 1949.
- [115] Passerone A, Sangiorgi R, Eustathopoulos N. *Scripta Met.*, 16:547, 1982.
- [116] Cahn JW. *J. Chem. Phys.*, 66:3667, 1977.
- [117] Hammond C. *Phys. Technol.*, 14:263, 1983.
- [118] Valiev RU, Gertsman VYu and Kaibystev OA. *Phys. Stat. Sol.*, 97A:11, 1986.
- [119] Rabkin EJ, Shvindlerman LS, Straumal BB. *J. Less - Common Met.*, 158:23, 1990.
- [120] Rabkin EJ, Shvindlerman LS, Straumal BB. *J. Less - Common Met.*, 159:43, 1990.
- [121] Rabkin EJ, Semenov VN, Shvindlerman LS, Straumal BB. *Acta Metall. Mater.*, 39:627, 1991.
- [122] Noskovich OI, Rabkin EJ, Semenov VN, Shvindlerman LS, Straumal BB. *Acta Metall. Mater.*, 39:3091, 1991.
- [123] Noskovich OI, Rabkin EJ, Semenov VN, Straumal BB. *Scripta Met.*, 25:1441, 1991.
- [124] Rabkin EJ, Shvindlerman LS, Straumal BB, Noskovich OI. *Surface Sci.*, 251:674, 1991.
- [125] Straumal BB, Noskovich OI, Semenov VN, Shvindlerman LS, Gust W, Predel B. *Acta Metall. Mater.*, 40:795, 1992.
- [126] Massalski TB, Okamoto H, Subramanian PR, Kacprzak L, editors, *Binary Alloy Phase Diagrams*, ASM International, Materials Park, OH, 1990.
- [127] Nishizawa T, Hasebe M, Ko M. *Acta Metall.*, 27:817, 1979.
- [128] Rabkin EJ, Shvindlerman LS, Straumal BB, Gust W. *Mat. Sci. Forum*, 126-128:305, 1993.
- [129] Rabkin EJ, Shvindlerman LS, Straumal BB. *J. Physique*, 51:C5-99, 1990.
- [130] Shvindlerman LS, Lojkowski W, Rabkin EJ, Straumal BB. *J. Phys. Colloq.*, C151:629, 1990.

- [131] Dietrich S. In Domb C and Lebowitz JH, editors, *Phase Transitions and Critical Phenomena*, Vol.12, page 2, Academic, London, 1988.
- [132] Gennes G de. *Rev. Mod. Phys.*, 57:827, 1985.
- [133] Kellay H, Bonn D and Meunier J. *Phys. Rev. Lett.*, 71:2607, 1993.
- [134] Schmidt JW and Moldover MR. *J. Chem. Phys.*, 79:379, 1983.
- [135] Straumal BB, Muschik T, Gust W, Predel B. *Acta Metall. Mater.*, 40:939, 1992.
- [136] Straumal BB, Gust W, Molodov DA. *Interface Science*, 3:127, 1995.
- [137] Straumal BB, Rabkin EJ, Lojkowski W, Gust W, Shvindlerman LS. *Acta Mater.*, 45:1931, 1997.
- [138] Sickafus KF and Sass SL. *Acta Metall.*, 35:69, 1987.
- [139] Lin CH and Sass SL. *Scripta Metall.*, 22:735, 1988.
- [140] Lin CH and Sass SL. *Scripta Metall.*, 22:1569, 1988.
- [141] Hsieh TE and Balluffi RW. *Acta Metall.*, 37:2133, 1989.
- [142] Ference TG and Balluffi RW. *Scripta Metall.*, 22:1929, 1988.
- [143] Watanabe T, Kimura SI, Karasima S. *Phil. Mag.*, A49:845, 1984.
- [144] Maksimova EL, Shvindlerman LS, Straumal BB. *Acta Metall.*, 36:1573, 1988.
- [145] Maksimova EL, Rabkin EJ, Shvindlerman LS, Straumal BB. *Acta Metall.*, 37:1995, 1989.
- [146] Gleiter H. *Scripta Metall.*, 11:305, 1977.
- [147] Maksimova EL, Rabkin EJ, Shvindlerman LS, Straumal BB. *Defect and Diffusion Forum* 66-69:869, 1990.
- [148] Farkas D and Sang H. *Scripta Metall.*, 22:1431, 1988.
- [149] Aleshin AN, Prokofjew SI, Shvindlerman LS. *Scripta Metall.*, 19:35, 1985.
- [150] Shvindlerman LS and Straumal BB. *Acta Metall.*, 33:35, 1985.
- [151] Zisman AA and Rybin VV. *Phys. Chem. Mech. Surfaces*, 7:87, 1982.
- [152] Grimmer H, Bollmann W, Warrington DH. *Acta Cryst.*, A30:197, 1974.
- [153] Warrington DH and Grimmer H. *Phil. Mag.*, 30:461, 1974.

- [154] Leibfried G. In *Encyclopedia of Physics*, Vol.7, Springer-Verlag, Berlin, 1955.
- [155] Landau LD. In *To the 70th Anniversary of A.F. Ioffe*, p. 44, Academy of Sciences of the USSR, Moscow, 1950.
- [156] Erenfest P. *Ann. der Physik* 48:360, 1915.
- [157] Mullins WW. *J. Appl. Phys.* 30:77, 1957; *Acta Metall.* 6:414, 1958.
- [158] Fradkov VE and Shvindlerman LS. *Phys. Chem. Mech. Surfaces*, 1:3253, 1984.
- [159] Marchenko VJ, Parshin AJ. *JETP* 79:257, 1980.
- [160] Kocevic VM, Baisuldin BM. *Fiz. Metall. Metalloved.*, 48, 443, 1973.
- [161] Read WT, Shockley W. *Phys. Rev.* 78:275, 1950.
- [162] Mott NF. *Proc. Roy. Soc.*, 60:391, 1948.
- [163] Gifkins, R.C. *Mat. Sci. Eng.*, 2:181, 1967.
- [164] Burke, J.E., Turnbull, D. *Progr. Met. Phys.*, 3:220, 1953.
- [165] Bollmann W. In Bollmann W, editor, *Crystals Defects and Crystalline Interfaces*, Springer-Verlag, Berlin, 1970.
- [166] Pond RC, Smith DA. *Int. Met. Rev.* 21:61, 1976.
- [167] Sutton AP, Finnis MW, Pettifor DG, Ohta Y. *J. Phys. C Sol. Stat. Phys.*, 21:35, 1988.
- [168] Vitek V, Sutton AP, Smith DA, Pond RC. In Balluffi RW, editor, *Grain Boundary Structure and Kinetics*, page 115, ASM, Materials Park, OH, 1980.
- [169] Wolf D. *Acta Metall.* 32:245, 1984.
- [170] Ashby MF, Spaepen F. *Scripta Metall.* 12:193, 1978.
- [171] Sutton AP, Vitek V. *Phil. Trans. Roy. Soc. London* A309:37, 1985.
- [172] Krakow W. *Acta Metall. Mater.* 40:977, 1992.
- [173] Hu W, Schönfelder B, Gottstein G. unpublished results.
- [174] Hasson G et al. In Hu H, editor, *The Nature and Behaviour of Grain Boundaries*, p. 3, TMS-AIME, 1972.
- [175] Clark WAT, Smith DA. *Phil. Mag.* 38A:367, 1978.
- [176] Gladstone S, Leider K, Eyring H *The Theory of Rate Processes*, McGraw-Hill, 1941.
- [177] Gleiter H. *Acta Metall.* 17:853, 1969.

- [178] Haessner F, Hofmann S. *Z. Metallk.* 62:807, 1971.
- [179] Cahn RW, Haasen P. *Physical Metallurgy*, North-Holland, 1996.
- [180] Aust KT, Rutter JW. *Trans. AIME*, 215:119, 1959.
- [181] Aust KT, Rutter JW. *Trans. AIME*, 215:820, 1959.
- [182] Aust KT, Rutter JW. *Acta Metall.* 12:181, 1965.
- [183] Czubayko U, Sursaeva VG, Gottstein G, Shvindlerman LS. *Acta Metall.* 46:5863, 1998.
- [184] Hasson G, Goux C. *Scripta Metall.* 5:889, 1971.
- [185] Mullins WW. *Acta Metall.* 4:421, 1956.
- [186] Goetz A, Focke A. *Phys. Rev.* 45:170, 1934.
- [187] Kapitza, P. *Proc. Roy. Soc.*, A131:224, 1931.
- [188] Kapitza, P. *Proc. Roy. Soc.*, A135:556, 1932.
- [189] Molodov DA, Gottstein G, Heringhaus F, Shvindlerman LS. *Scripta Mater.*, 37:1207, 1997.
- [190] Molodov DA, Czubayko U, Gottstein G, Shvindlerman LS. *Scripta Mater.*, 32:529, 1995.
- [191] Gottstein G, Molodov DA, Shvindlerman LS. *Interface Science* 6:7, 1998.
- [192] Molodov DA, Gottstein G, Heringhaus F, Shvindlerman LS. In 1997 *NHMFL Annual Report*, p. 165, 1998.
- [193] Lücke K, Detert K. *Acta Metall.* 5:628, 1957.
- [194] Lücke K, Stüwe HP. *Acta Metall.* 19:1087, 1971.
- [195] Cahn JW. *Acta Metall.* 10:789, 1962.
- [196] Westbrook JH. *Metallurgical Rev.* V.II:129, 1966.
- [197] Molodov DA, Czubayko U, Gottstein G, Shvindlerman LS. *Acta Mater.* 46:553, 1998
- [198] Lücke K, Gottstein G. *Acta Metall.*, 29:779, 1981.
- [199] Estrin Y., Lücke K. *Acta Metall.*, 29:791, 1981.
- [200] Gleiter H. *Acta Metall.*, 27:187, 1979.
- [201] Upmanyu M, Srolovitz DJ, Shvindlerman LS, Gottstein G. *Interface Science*, 6:289, 1998.
- [202] Upmanyu M, Smith RW, Srolovitz DJ. *Interface Science*, 6:41, 1998.

- [203] Smith CS. *Trans. AIME*, 175:15, 1948.
- [204] Gladman T. *Proc. Roy. Soc.*, 294ff:298, 1966.
- [205] Ashby MF. In Hansen N, Jones AR, Leffers T., editors, *Proc 1st RISØ Int Symp. on Metallurgy and Materials Science*, p. 32, RISØ Nat. Lab., 1980.
- [206] Ashby MF, Harper J, Lewis L. *Trans. AIME*, 245:413, 1969.
- [207] Geguzin YaE, Krivoglaz MA. In *Migration of Macroscopic Inclusions in Solids*, Consultants Bureau, New York, 1979.
- [208] Gottstein G, Shvindlerman LS. *Acta Metall. Mater.*, 41:3267, 1993.
- [209] Kokhanchik GJ, Serebryakov AV, Shiyanov YuA. *Physica Status Solidi (a)*, 23:99, 1974.
- [210] Aristov VYu, Fradkov VE, Shvindlerman LS. *Phys. Met. Metall.*, 45:83, 1979.
- [211] Shewmon PG. *Trans. AIME*, 230:1134, 1964.
- [212] Gruber EE. *J. Appl. Phys.*, 38:243, 1967.
- [213] Balandin BN, Sokolov BK, Gubernatorov VV. *Fiz. Metal. Metalloved.*, 49:590, 1980.
- [214] Goldstein VYa, Bobkova OP, Nitskaya SG. *Fiz. Metal. Metalloved.*, 54:512, 1982.
- [215] Mullins WW. *J. Appl. Phys.*, 28:333, 1957.
- [216] Mullins WW. *Acta Metall.*, 6:414, 1958.
- [217] Mullins WW. *J. Appl. Phys.*, 1:77, 1959.
- [218] Mullins WW. *Trans. AIME*, 218:354, 1960.
- [219] Vilenkin AJ, Brokman A. *J. Cryst. Growth*, 123:261, 1992; 129:67, 1993; 131:239, 1993.
- [220] Brokman A, Kris R, Mullins WW. *Scripta Metall. Mater.*, 32:1341, 1995.
- [221] Cho J, Thompson CV. *J. Appl. Phys. Letters*, 54:2577, 1989.
- [222] Sanchez JE, Artz E. *Scripta Metall. Mater.*, 26:1325, 1992.
- [223] Schmidt PF. *Ph.D. Thesis*, Universität Münster, 1977.
- [224] Babcock SE, Balluffi RW. *Acta Metall.* 37:2357, and 37:2367, 1989.
- [225] Gottstein G, Shvindlerman LS. *Scripta Metall. Mater.*, 27:1521, 1992.

- [226] Oding JA, Lozinskii MG, Fedotov SG. *Dokl. Akad. Nauk SSSR*, 1:91, 1953.
- [227] Fridman EM, Kopetskii ChV, Shvindlerman LS, Aristov VYu. *Z. Metallk.*, 64:458, 1973.
- [228] Antonov AV, Kopetskii ChV, Shindlerman LS, Sursaeva VG. *Sov. Phys. Dokl.*, 18:736, 1974.
- [229] Masteller MS, Bauer CL. In Haessner F., editor, *Recrystallization of Metallic Materials*, Dr. Riederer Verlag GmbH, Stuttgart, 1978.
- [230] Rath BB, Hu H. *Met. Trans.*, 245:1577, 1969.
- [231] Rath BB, Hu H. In Hu H., editor, *The Nature and Behaviour of Grain Boundaries*, Plenum Press, New York, 1972.
- [232] Rath BB, Hu H. *Trans. TMS – AIME*, 245:1243, 1969.
- [233] Rath BB, Hu H. *Trans. TMS – AIME*, 236:1193, 1966.
- [234] Sun RC, Bauer CL. *Acta Metall.*, 18:635, 1970.
- [235] Sun RC, Bauer CL. *Acta Metall.*, 18:639, 1970.
- [236] Antonov AV, Kopetskii ChV, Shvindlerman LS, Mukovskii YaM. *Phys. Stat. Sol. (a)*, 9:45, 1972.
- [237] Grey EA, Higgins GT. *Scripta Metall.*, 6:253, 1972.
- [238] Grey EA, Higgins GT. *Acta Metall.*, 21:309, 1973.
- [239] Sursaeva VG, Andreeva AV, Kopetskii ChV, Shvindlerman LS. *Phys. Met. Metall.*, 41:98, 1976.
- [240] Furtkamp M, Gottstein G, Molodov DA, Semenov VN, Shvindlerman LS. *Acta Mater.*, 46:4103, 1998.
- [241] Furtkamp M, Gottstein G, Shvindlerman LS. *Interface Science*, 6:279, 1998.
- [242] Mullins WW. *J. Appl. Phys.*, 27:900, 1956.
- [243] Aristov VYu, Fradkov VE, Shvindlerman LS. *Sov. Phys. Solid State*, 22:1055, 1980.
- [244] Verhasselt JCh, Gottstein G, Molodov DA, Shvindlerman LS. *Acta Mater.*, 47:887, 1999.
- [245] Aristov VYu, Fridman EM, Shvindlerman LS. *Fiz. Met. Metalloved.*, 35:859, 1973.
- [246] Dunn CG, Daniels PW, Bolton NY. *Trans. AIME*, 185:770, 1949.

- [247] Straumal BB, Sursaeva VG, Shvindlerman LS. *Phys. Met. Metalloved.*, 49:102, 1980.
- [248] Kopetskii ChV, Musikhin LA, Shvindlerman LS. *Phys. Met. Metalloved.*, 13:620, 1971.
- [249] Gastaldi J, Jourdan C. *Phys. Stat. Sol. (a)*, 49:529, 1978.
- [250] Gastaldi J, Jourdan C, Grange G. *Mater. Sci. Forum*, 94-96:17, 1992.
- [251] Aristov VYu, Kopetskii ChV, Shvindlerman LS. *Authors Certificate of Invention*, 64:2638 G01N23/20, 1979 (in Russian).
- [252] Aristov VYu, Kopetskii ChV, Molodov DA, Shvindlerman LS. *Sov. Phys. Solid State*, 22:1900, 1980.
- [253] Czubayko U, Molodov DA, Petersen BC, Gottstein G, Shvindlerman LS. *Meas. Sci. Technol.*, 6:947, 1995.
- [254] Huang Y, Humphreys FJ. In *Proc. of the Third Intern. Conf. on Grain Growth*, Carnegie Mellon University, Pittsburgh, PA, 1998.
- [255] Shvindlerman LS, Gottstein G, Molodov DA. *Phys. Stat. Sol. (a)*, 160:419, 1997.
- [256] Fradkov VE, Shvindlerman LS. *Phys. Chem. Mech. Surface*, 1:180, 1982.
- [257] Landau LD. In *The Collected Works in Two Volumes*, Moscow, Nauka, 1969.
- [258] Antonov AV, Kopetskii ChV, Mukovskii YaM, Shvindlerman LS. *Sov. Phys. Solid State*, 13:2533, 1972.
- [259] Antonov AV, Shvindlerman LS. *Sov. Phys. Solid State*, 15:1083, 1973.
- [260] Ziegler M. *Some Extremum Principle in Irreversible Thermodynamics with Application to Continuum Mechanics*, North Holland, Amsterdam, 1963.
- [261] Antonov AV, Boglaev YuP, Kopetskii ChV, Shvindlerman LS. *Soviet Physics Doklady*, 17:260, 1972.
- [262] Vandermeer RA. *Trans. AIME*, 233:266, 1965.
- [263] Swalin RA. *Thermodynamics of Solids*, John Wiley & Sons, New York, 1962.
- [264] Liebman B, Lücke K, Masing G. *Z. Metallk.*, 47:57, 1956.
- [265] Yoshida M, Liebman B, Lücke K. *Acta Metall.*, 7:51, 1959.

- [266] Mattissen D, Molodov DA, Gottstein G, Shvindlerman LS. In Gottstein G, Molodov DA., editors, *Recrystallization and Grain Growth*, p. 421, Springer, New York, 1962.
- [267] Kirch DM, Ziemons A, Burlet T, Lischewski X, Molodova X, Molodov DA, Gottstein G. *Re. Sci. Instrum.*, 79:043902, 2008.
- [268] Ivanov VA, Molodov DA, Shvindlerman LS, Gottstein G. *Acta Metall.*, 52:969, 2004.
- [269] Gottstein G, Murmann MC, Renner G, Simpson C, Lücke K. In Gottstein G, Lücke K, editors, *Textures of Materials*, p. 521, Springer-Verlag, Berlin, 1978.
- [270] Deminczuk DM, Aust KT. *Acta Metall.*, 21:1149, 1975.
- [271] Viswanathan R, Bauer CL *Acta Metall.*, 21:1099, 1973.
- [272] Masteller MS, Bauer CL. *Scripta Metall.*, 10:1033, 1976.
- [273] Fridman EM, Kopetskii ChV, Shvindlerman LS. *Z. Metallk.*, 66:533, 1975.
- [274] Aristov VYu, Kopetskii ChV, Shvindlerman LS. In *Theoretical Fundamentals of Materials Science*, p. 84, Moscow, Nauka, 1981.
- [275] Aristov VYu, Mirochnik VL, Shvindlerman LS. *Sov. Phys. Solid State*, 18:137, 1976.
- [276] Kopetskii ChV, Sursaeva VG, Shvindlerman LS. *Mobility of High – Angle Grain Boundaries in Zn*, (in Russian), Chernokolovka, 1979.
- [277] Rutter JW, Aust KT. *Trans. AIME*, 218:682, 1960.
- [278] Gottstein G, Shvindlerman LS, Molodov DA, Czubayko U. In Duxburg PM, Pence TJ, editors, *Dynamics of Crystal Surfaces and Interfaces*, p. 109, Plenum Press, New York, 1997.
- [279] Gottstein G, Shvindlerman LS. *Scripta Metall. Mater.*, 27:1515, 1992.
- [280] Aleshin AN, Aristov, VYu, Bokstein BS, Shvindlerman LS. *Phys. Stat. Sol. (a)*, 45:359, 1978.
- [281] Aleshin AN, Bokstein BS, Shvindlerman LS. *Sov. Phys. Solid State*, 19:2051, 1977.
- [282] Kaur J, Mishin Yu, Gust W. In *Fundamentals of Grain and Interphase Boundary Diffusion*, John Wiley & Sons, New York, 1995.
- [283] Budke E, Herzig Chr, Prokofjew SI, Shvindlerman LS. *Mat. Sci. Forum*, 207-209:465, 1996.

- [284] Gottstein G, Molodov DA, Czubayko U, Shvindlerman LS. *J. Physique IV*, 5:C3-89, 1995.
- [285] Udler D, Seidman DN. *Interface Science*, 3:41, 1995.
- [286] Udler D, Seidman D. *Scripta metall. mater.*, 26:449, 1992.
- [287] Westengen H, Ryum N. *Phil. Mag. A*, 38A:3279, 1978.
- [288] Frois C, Dimitrov O. *Ann. Chim., Paris*, 1.113, 1966.
- [289] Dimitrov O, Fromageau R, Dimitrov C. In Himmel L, editor, *Recovery and Recrystallization of Metals*, Wiley, New York, Interscience, 1963.
- [290] Gordon P, Vandermeer RA. *Trans. AIME*, 24:917, 1962.
- [291] Gordon P, Vandermeer RA. In Margolin H, editor, *Recrystallization, Grain Growth and Texture*, p. 205, ASM, Materials Park, OH, 1966.
- [292] Shvindlerman LS. *Mat. Sci. Forum*, 94-96:169, 1992.
- [293] Aristov VYu, Kopetskii ChV, Sursaeva VG, Shvindlerman LS. *Sov. Phys. Dokl.*, 20:842, 1975.
- [294] Molodov DA, Kopetskii ChV, Shvindlerman LS. *Sov. Phys. Solid State*, 23:1718, 1981.
- [295] Molodov DA, Fradkov VE, Shvindlerman LS, Kaplan GJ. *Sov. Phys. Solid State*, 26:284, 1984.
- [296] Grünwald W, Haessner F. *Acta Metall.*, 18:217, 1970.
- [297] Aristov VYu, Kopetskii ChV, Molodov DA, Shvindlerman LS. *Sov. Phys. Solid State*, 22:11, 1980.
- [298] Kopetskii ChV, Sursaeva VG, Shvindlerman LS. *Scripta Metall.*, 12:953, 1978.
- [299] Kopetskii ChV., Sursaeva VG, Shvindlerman LS. *Sov. Phys. Dokl.*, 23:137, 1978.
- [300] Tsurekawa T, Ueda T, Ichikawa K, Nakashima H, Yoshitomi Y, Yoshinada H. *Mat. Sci. Forum*, 204-206:221, 1990.
- [301] Aristov VYu, Kopetskii ChV., Shvindlerman LS. *Scripta Metall.*, 11:109, 1977.
- [302] Molodov DA, Straumal BB, Shvindlerman LS. *Scripta Metall.*, 18:207, 1984.
- [303] Molodov DA, Straumal BB, Shvindlerman LS. *Sov. Phys. Solid State*, 26:629, 1984.

- [304] Molodov DA, Swiderski J, Gottstein G, Lojkowski W, Shvindlerman LS. *Acta Metall. Mater.*, 42:3397, 1994.
- [305] Hahn M, Gleiter H. *Scripta Metall.*, 14:3, 1979.
- [306] Lojkowski W. *J. Physiq. Coll.*, C5:673, 1987.
- [307] Molodov DA. *Ph.D. Thesis*, Chernogolovka, Moscow district, 1984.
- [308] Jhan RJ, Bristowe PD. *Scripta Metall.*, 24:1313, 1990.
- [309] Schönfelder B, Wolf D, Phillpot SR, Furtkamp M. *Interface Science*, 5:245, 1997.
- [310] Gottstein G. *Physical Foundations of Materials Science*, Springer-Verlag, Berlin, 2004.
- [311] Ivanov VA, Molodov DA, Shvindlerman LS, Gottstein G. *Mat. Sci. Forum*, 467-470:617, 2004.
- [312] Watson GM, Gibbs D, Song S, Sandy AR, Mochril SGJ, Zener GM. *Phys. Rev.*, 52:12329, 1995.
- [313] Lee SB, Yoon NY, Henry MB. *Acta Mater.*, 48:3071, 2000.
- [314] Koo JB, Yoon DY. *Metall. Trans. Mater.*, 32:469, 2001.
- [315] Karzaryan A, Wang Y, Dregia SA, Patton BR. *Acta Mater.*, 50:2491, 2002.
- [316] Straumal BB, Rabkin EJ, Sursaeva VG, Gornakova AS. *Z. Metallk.*, 96:2, 2005.
- [317] Rabkin EJ. *J. Mater. Sci.*, 40:875, 2005.
- [318] Carter WC, Roosen AR, Cahn JW, Taylor JE. *Acta metall. mater.*, 43:4309, 1995.
- [319] Taylor JE.. *Acta Mat.*, 40:1475, 1992.
- [320] Sursaeva VG, Straumal BB, Gornakova AS, Shvindlerman LS, Gottstein G. *Acta Mater.*, 56:2728, 2008.
- [321] Gottstein G, Shvindlerman LS, Sursaeva VG. *IJMR*, 5:491, 2008.
- [322] Wolf U, Ernst F, Muschik T, Finnis MW, Fischmeister HF. *Phil. Mag.*, A66:1991, 1992.
- [323] Bruggeman GA, Bishop GH, Hart WH. In Hu H, editor, *The Nature and Behaviour of Grain Boundaries*, New York, Plenum, 1972.
- [324] Kirch GM, Zhao B, Molodov DA, Gottstein G. *Scripta Mat.*, 56:939, 2007.
- [325] Yoon DY, Cho YK. *J. Mat. Sci.*, 40:861, 2005.

- [326] Goetz A. *Phys. Rev.*, 35:193, 1950.
- [327] Fraser MJ, Gold RE, Mullins WW. *Acta Metall.*, 9:960, 1961.
- [328] Molodov DA, Gottstein G, Heringhaus F, Shvindlerman LS. *Acta Mater.*, 46:5627, 1998.
- [329] Maksimova EL, Shvindlerman LS, Straumal BB. *Acta Metall.*, 36:1573, 1988.
- [330] Molodov DA, Czubyko U, Gottstein G, Shvindlerman LS, Gust W, Straumal BB. *Phil. Mag. Lett.*, 7:361, 1995.
- [331] Molodov DA, Gottstein G, Czubyko U, Shvindlerman LS. *Fiz. Metall. Metalloved.*, 83:115, 1997; *Defect and Diffusion Forum*, 143-147:1493, 1997.
- [332] Molodov DA. *Habilitation*, Shaker-Verlag, Aachen, 1999.
- [333] Straumal BB. *private communication*.
- [334] Cahn JW. *J. Chem. Phys.*, 66:3667, 1977.
- [335] Rabkin EJ, Shvindlerman LS, Straumal BB. *Int. J. Modern Physics*, B5:2089, 1991.
- [336] Dienes GJ. *J. Appl. Phys.*, 21:1950, 1989.
- [337] Kisilishin GJ. *Metals*, 1:230, 1976 (in Russian).
- [338] Surmava GM, Tavavse FN. *Solid State Physics*, 10:910, 1968.
- [339] Aleshin AN, Bokstein BS, Shvindlerman LS. *Soviet Phys. Chem. Mech. Surfaces*, 6:1, 1982.
- [340] Gottstein G, Molodov DA, Rabkin EJJ, Shvindlerman LS, Snapiro J. *Interface Sci.*, 10:279, 2002.
- [341] Winning M, Gottstein G, Shvindlerman LS. *Mat. Sci. Eng.*, A317:17, 2001.
- [342] Winning M, Gottstein G, Shvindlerman LS. *Acta. Mat.*, 49:211, 2001.
- [343] Winning M, Gottstein G, Shvindlerman LS. *Acta. Mat.*, 50:353, 2002.
- [344] Winning M. In Gottstein G, Molodov DA. editors, *Recrystallization and Grain Growth*, p.193, Springer-Verlag, 2001.
- [345] Gottstein G, Molodov DA, Shvindlerman LS, Winning M. *Ann. Chim. Sci. Mat.*, 27:33, 2002.

- [346] Gottstein G, Molodov DA, Winning M, Shvindlerman LS. *Interface. Sci.*, 9:297, 2001.
- [347] Winning M. In Kramer B. editor, *Solid State Physics*, Vol. 43 p.563, Springer-Verlag, New York, 2003.
- [348] Winning M, Eisenlohr P, Blum W. *Phys. Stat. Sol. (a)*, 200:339, 2003.
- [349] Winning M. *Z. f. Metallk.*, 95:233, 2004.
- [350] Winning M. *Physik Journal*, 3:77, 2004.
- [351] Winning M. *Phys. Stat. Sol. (a)*, 201:2867, 2004.
- [352] Winning M. *Mat. Sci. Forum*, 495-497:1279, 2005.
- [353] Winning M. *Z. f. Metallk.*, 96:465, 2005.
- [354] Winning M. *Scripta Mat.*, 54:987, 2006.
- [355] Molodov DA, Ivanov VA, Gottstein G. *Acta Mat.*, 55:1843, 2007.
- [356] Winning M. *Mat. Sci. Forum*, 558-559:927, 2007.
- [357] Gorkaya T, Molodov DA, Gottstein G. In Hirsch J, Skrotzki B, Gottstein G., editors, *Aluminium Alloys — Their Physical and Mechanical Properties*, Vol. 1 p.1071, New York, Wiley-VCH (DGM), 2008.
- [358] Winning M. *Acta. Mater.*, 54:4953, 2006.
- [359] Straumal BB, Bokstein BS, Klinger LM, Shvindlerman LS. *Scripta Metall.*, 15:1197, 1981; *Sov. Phys. Solid State*, 24:748, 1982.
- [360] Gottstein G, Shvindlerman LS. *Z. f. Metallk.*, 95:219, 2004.
- [361] Gottstein G, Shvindlerman LS. *Scripta Mater.*, 52:863, 2005
- [362] Cahn JW, van Vleck ES. *Acta. mater.*, 47:4627, 1928.
- [363] Swygenhoven Van H, Farkas D, Caro A. *Phys Rev.*, B62:831, 2000.
- [364] Srinivasan SG, Cahn JW, Jónsson, Kalonji G. *Acta. Mater.*, 47:2821, 1999.
- [365] Caro A, Van Swygenhoven H. *Phys. Rev. B*, 63:134101, 2001.
- [366] Zhao B, Verhasselt JCh, Shvindlerman LS, Gottstein G. *Acta. Mater.*, in press, 2009.
- [367] Straumal BB, Klinger LM, Shvindlerman LS. *Acta Metall.*, 32:1355, 1984.

- [368] Lojkowski W, Kwecinski J, Wyrzkowski J. In *Proceedings of the Intern. Conf. of Light Metals*, Japan Inst. of Metals, Tokyo, 1991.
- [369] Constable F. *Proc. R. Soc., Serv.*, A108:355, 1923.
- [370] Sukharukov BJ, Lichtenstein GJ. *Biofizika*, 10:935, 1965.
- [371] Barnes R, Vogel H, Gordon J. *Proc. US Nat. Acad. Sci.*, 62:263, 1969.
- [372] Leffler JE. *J. Organic. Chem.*, 20:1202, 1955.
- [373] Kang HC, Sachinowski TA, Weinberg WH. *J. Chem. Phys.*, 93:1418, 1950.
- [374] Fichthorn KA, Weinberg WH. *Langmuir*, 7:2539, 1991.
- [375] Sommer E, Kreuzer MJ. *Phys. Rev. Lett.*, 49:61, 1982.
- [376] Hirth JP, Pond RC, Lothar J. *Acta Mater.*, 54:237, 2006.
- [377] Johansson PX. *J Chem. Physics Letters*, 65:366, 1979.
- [378] Peacock-Lopez E, Suhl M. *Phys. Rev. B*, 26:3874, 1982.
- [379] Fridman EM, Kopetskii ChV, Shvindlerman LS. *Sov. Phys. Solid State*, 16:1152, 1974.
- [380] Kopetskii ChV, Sursaeva VG., Shvindlerman LS. *Sov. Phys. Solid State*, 21:238, 1979.
- [381] Aleshin AN, Bokstein BS, Petelin AL, Shvindlerman LS. *Metallofizika*, 2:83, 1980 (in Russian).
- [382] Maksimova EL, Straumal BB, Fradkov VE, Shvindlerman LS. *Phys. Met. Metall.*, 56:133, 1983.
- [383] Kirkadly JS, Purdy GR. *Scripta Metall.*, 25:901, 1991.
- [384] Bokstein BS, Bokstein SZ, Zuhovitskii AA. *Thermodynamics and Kinetics of Diffusion in Solids*, p. 280, Moscow, Metallurgia, 1974.
- [385] Finkelstein BN, Mait YuL. *Dokl. Akad. of Sciences of USSR*, 144:85, 1962.
- [386] Aleshin AN, Bokstein BS. *Phys. Met. Metall.*, 48:887, 1979.
- [387] Klinger LM. *Metallofizika*, 6:11, 1984 (in Russian).
- [388] Brown AM, Ashby MF. *Acta Metall.*, 28:1085, 1980.
- [389] Gottstein G, Shvindlerman LS. *Interface Science*, 6:267, 1998.
- [390] Lücke K. *Can. Met. Quart.*, 14:261, 1974.
- [391] Lücke K, Masing G, Nölting P. *Z. Metallk.*, 47:64, 1956.

- [392] Zener C. *J. Appl. Phys.*, 22:372, 1951.
- [393] Gottstein G, Czubayko U, Molodov DA, Shvindlerman LS, Wunderlich W. *Mater. Sci. Forum*, 204-206:96, 1996.
- [394] Kronberg ML, Wilson FH. *Trans. AIME*, 185:501, 1949.
- [395] Pond RC, Smith DA. *Phil. Mag. A* 36:353, 1977.
- [396] Janssens GK, Olmsted D, Holms, EA, Foiles SM, Derlet PM. *Nature Materials*, 5:124, 2006.
- [397] Gottstein G. In *Habilitation Thesis*, p. 119, RWTH Aachen, 1979.
- [398] Gottstein G, Karduck P. In Smith DA., editor, *Interface Migration and Control of Microstructure*, p. 131, ASM, Metals Park, OH, 1986.
- [399] Smith DA, Rae CMF, Grovenor CRM. In Balluffi, R.W., editor, *Grain Boundary Structure and Kinetics*, p. 131, ASM, Metals Park, OH, 1980.
- [400] Gottstein G, Molodov DA, Shvindlerman LS. *J. Mater. Sci.*, 41:7730, 20006.
- [401] Fradkov VE, Shvindlerman LS. In *Structure and Properties of Interfaces in Metals*, p. 213, Moscow, 'Nauka', 1988.
- [402] King AH. In Pond RC, Clark WAT, King AH, Williams DB., editors, *Boundaries and Interfaces in Materials : The David A. Smith Symposium*, TMS, Warrendale, PA, 151, 1998.
- [403] Galina AV, Fradkov VE, Shvindlerman LS. *Phys. Met. Metall.*, 63:165, 1987.
- [404] Gottstein G, Shvindlerman LS Crumbach M. *Mat. Sci. Forum*, 558-559:3-12, 20007.
- [405] Srinivasan SG, Cahn JW, Jonsson H, Kalonji G. In *Proc. 3rd Int. Conference on Grain Growth*, Pittsburgh, PA, 1998.
- [406] Fortier P, Palumbo, Bruce GD, Miller WA, Aust KT. *Scripta Metall.*, 25:177, 1991.
- [407] Nishimura G. *M.A. Sc. Thesis*, University of Toronto, 1973.
- [408] Fortes MA. In *Metal Interfaces*, p. 179. AM Soc. Metals, Cleveland, 1952.
- [409] Soares A, Ferro AC, Fortes MA. *Scripta Metall.*, 19:1491, 1985.
- [410] Gottstein G, Molodov DA, Shvindlerman LS. *Interface Science*, 6:7, 1998.

- [411] Czubyayko U, Sursaeva VG, Gottstein G, Shvindlerman LS. In Weiland H, Adams BL, Rollett AD, editors, *Grain Growth in Polycrystalline Materials*, The Mineral, Metals & Materials Society, 1998.
- [412] Andrievski RA. *J. Mater. Sci.*, 38:1367, 2003.
- [413] Gottstein G, Molodov DA, Shvindlerman LS. *J. Mater. Sci.*, 41:7730, 2006.
- [414] Shvindlerman LS, Gottstein G, Czubyayko U, Sursaeva VG. In Terry R, editor, *Recrystallization and Related Phenomena*, p.255, Mc-Nelley, Monterey, 1997.
- [415] Sursaeva VG. *Mater. Sci. Forum*, 62-64:807, 1990.
- [416] Fradkov VE, Shvindlerman LS. In Bokstein BS, editor, *Structure and Properties of Grain Boundaries in Metals*, Moscow, Metallurgy, 1990.
- [417] Fradkov VE, Udler DG. *Advances in Physics*, 4/16:739, 1994.
- [418] Novikov V. In *Grain Growth and Control of Microstructure and Texture in Polycrystalline Metals*, CRC Press, Boca Raton, FL, 1994.
- [419] Williams RE, Smith SC. *Metals*, 194:755, 1952.
- [420] Sursaeva VG, Protasova SG. *Mat Sci. Forum*, 294-296:513, 1988.
- [421] Galina AV, Fradkov VE, Shvindlerman LS. *Phys. Chem. Mech. Surf.*, 1:100, 1988.
- [422] Demirel MC, Kuprat AP, George DC, Rollet AD. *Phys. Rev. Lett.*, 90:016106, 2003.
- [423] Lejcek P, Adamek J. *J. Phys. IV*, C3:107, 1995.
- [424] Czubyayko U. *Ph.D. Thesis*, RWTH Aachen, 1998.
- [425] Rabkin EJ. *Scripta Mater.*, 39:1631, 1998.
- [426] Czubyayko U, Sursaeva VG, Gottstein G, Shvindlerman LS. In *Proc. Third Intern. Conf. on Grain Growth*, p, 423, Carnegie Mellon Univ. Pittsbvurg, USA, 1998.
- [427] Gottstein G, Shvindlerman LS. *Scripta Mater.*, 38:1542, 1998, 39:1489, 1998.
- [428] Gottstein G, King AH, Shvindlerman LS. *Acta Mater.*, 48:397, 2000.
- [429] Mattissen D, Molodov DA, Shvindlerman LS, Gottstein G. *Acta Mater.*, 53:2049, 2005.

- [430] Mattissen D, Waero A, Molodov DA, Shvindlerman LS, Gottstein G. *J. of Microscopy*, 213:257, 2004.
- [431] Mattissen D, Kirch D, Molodov DA, Shvindlerman LS, Gottstein G. *Mat. Sci. Forum*, 467-470:777, 2004.
- [432] Mattissen D. *Ph.D. Thesis*, RWTH Aachen, 2004.
- [433] Ivanov V. *Ph.D. Thesis*, RWTH Aachen, 2006.
- [434] Sursaeva VG, Gottstein G, Shvindlerman LS. In Gottstein G, Molodov SA, editors, *Recrystallization and Grain Growth*, p.455, Springer-Verlag, New York, Vol. 1, 2001.
- [435] Gottstein G, Molodov DA, Czubayko U, Shvindlerman LS. *J. Physique VI*, C3, 5:89, 1995.
- [436] Protasova SG, Gottstein G, Molodov DA, Sursaeva VG, Shvindlerman LS. *Acta Mater.*, 49:2519, 2001.
- [437] Protasova SG, Sursaeva VG. *Mat. Sci. Forum*, 467-479:795, 2004.
- [438] Kirch D. *Ph.D. Thesis*, RWTH Aachen, Vuvillier Verlag, Göttingen, 2008.
- [439] Upmanyu M, Srolovitz DJ, Shvindlerman LS, Gottstein G. *Interface Sci.*, 7:2307, 1999.
- [440] Upmanyu M, Srolovitz DJ, Shvindlerman LS, Gottstein G. *Acta Mater.*, 50:1405, 2002.
- [441] Gottstein G, Shvindlerman LS. *Acta Mater.*, 50:703, 2002.
- [442] Gottstein G, Ma Y, Shvindlerman LS. *Acta Mater.*, 53:1535, 2005.
- [443] Kawasaki K, Nagai T, Nakashima K. *Phil. Mag.*, 60:399, 1989.
- [444] Weygand D, Brechet Y. *Phil. Mag. B*, 78:329, 1998.
- [445] Novikov VYu. *Mat. Sci. Forum*, 467-470:1093, 2004.
- [446] Novikov VYu. *Scripta Mater.*, 52:857, 2005; *Zt. Metallk.* 96:1112, 2005.
- [447] Gottstein G, Shvindlerman LS. *Scripta Mater.*, 54:1065, 2006.
- [448] Fradkov VE, Kravchenko AS, Shvindlerman LS. *Scripta Mater.*, 19:1291, 1985.
- [449] Sursaeva VG, Protasova SG. in Gottstein G, Molodov DA, editors, *Recrystallization and Grain Growth*, Vol. I, p. 327, Springer-Verlag, 2001.
- [450] Molodov DA. in Gottstein G, Moldovo DA, editors, *Recrystallization and Grain Growth*, Vol. I, p. 17, Springer-Verlag, 2001

- [451] Krill CE, Helfen L, Michels D, Natter H, Fitch A, Masson O, Birringer R. *Phys. Rev. Lett.*, 86:842, 2001.
- [452] Krill CE, Birringer R. In Gottstein G, Molodov DA, editors, *Recrystallization and Grain Growth*, Springer-Verlag, Berlin, p. 2005, 2001.
- [453] Claudio L, deCastro, Mitchell BS. *Mater. Sci. Eng.*, A396:124, 2005.
- [454] Ames M, Markmann J, Karos R, Michels A, Tschöpe A, Birringer R. *Acta Mater.*, 56:4255, 2008.
- [455] Geguzin YaE. In *Physik des Sinterns*, Deutscher Verlag für Grundstoffindustrie, Leipzig, 1973.
- [456] Wolf W, Merkel KL. In Wolf D and Yip S, editors, *Material Interfaces*, Chapman & Hall, London, p. 87, 1992.
- [457] Upmanyu M, Srolovitz DJ, Gottstein G, Shvindlerman LS. *Interface Science*, 6:289, 1998.
- [458] Estrin Y, Gottstein G, Shvindlerman LS. *Scripta Mater.*, 41:415, 1999.
- [459] Estrin Y, Gottstein G, Shvindlerman LS. *Acta Mater.*, 47:3541, 1999.
- [460] Estrin Y, Gottstein G, Rabkin EJ, Shvindlerman LS. *Acta Mat.*, 49:673, 2001.
- [461] Shvindlerman LS, Gottstein G. *J. Mater. Sci.*, 40:819, 2005.
- [462] Gust W. *D.Sc. Thesis*, University of Stuttgart, 1980.
- [463] King AH. *Int. Mater. Rev.*, 32:173, 1987.
- [464] Semenov V, Rabkin EJ, Bischoff E., Gust W. *Acta Mater.*, 46:2289, 1998.
- [465] Mullins WW. *Acta. Metall.*, 6:414, 1958.
- [466] Genin FY. *J. Appl. Phys.*, 77:5130, 1995.
- [467] Chaudhari P. *J. Res. Develop.*, 13:197, 1969.
- [468] Carel R, Thompson CV, Frost HJ. *Acta Mater.*, 44:6,2479, 1996.
- [469] Thompson CV. *J. Mater. Res.*, 8:237, 1993.
- [470] Kanel J, Novick-Cohen A, Vilenkin A. *Acta Mater.*, 51:1981, 2003.
- [471] Lücke K, Heckelmann I, Abbruzzese G. *Acta Metall. Mater.*, 40:533, 1992.

- [472] Anderson MP, Srolovitz DJ, Grest GS, Sahni P. *Acta Metall.*, 32:783 1984.
- [473] Fradkov VE, Shvindlerman LS, Udler DG. *Scripta Metall.*, 19:1285, 1985.
- [474] Gottstein G, Shvindlerman LS. *Scripta Mater.*, 38:1541, 1998.
- [475] Kanel J, Novick-Cohen A, Vilenkin A. *Acta. Mat.*, 53:227, 2005.
- [476] Von Neumann J. in *Metal Interfaces*, p. 108, Cleveland, 1952.
- [477] Gusak AM, Tu KN. *Acta Mater.*, 51:3895, 2003.
- [478] Hunderi O, Ryum N. *Scripta Mater.*, 53:719, 2005.
- [479] Gottstein G, Rollett AD, Shvindlerman LS. *Scripta Mater.*, 51:611, 2004.
- [480] Rickman JM, Phillpot SR, Wolf D, Woodraska DL, Yip S. *J. Mat. Res.*, 6:2291, 1991.
- [481] Gottstein G, Sursaeva V, Shvindlerman LS. *Interface Sci.*, 7:273, 1999.
- [482] Srolovitz DJ, Mendelev MI, Upmanyu M, Molodov DM, Gottstein G, Shvindlerman LS. in Hansen N. et al. (editors), *Proc. of the 21st. RISO Symp. on Materials Science : Recrystallization – Fundamental Aspects and Relations to Deformation Microstructure*, page 157, RISO Nat. Lab.. Roskilde, Denmark, 2000.
- [483] Gottstein G, Molodov DM, Shvindlerman LS, Srolovitz DJ, Winning M. *Current Opinion in Solid State & Mat. Sci.*, 5:9, 2001.
- [484] Mendelev NI, Srolovitz DJ, Shvindlerman LS, Gottstein G. *J. Mater. Sci.*, 17:234, 2002.
- [485] Zhang H, Srolovitz DJ, Warren J, Douglas JF. *Phys. Rev.*, B74:115404, 2006.
- [486] Zhang H, Upmanyu M, Srolovitz DJ. *Acta Mater.*, 53:79, 2005.
- [487] Zhang H, Mendelev MI, Srolovitz DJ. *Scripta Mater.*, 52:1193, 2005.
- [488] Zhang H, Srolovitz DJ. *Acta Mater.*, 54:623, 2006.
- [489] Mishin Y, Asta M, Li J. *Acta Mater.*, in press, 2009.
- [490] Olmsted DL, Holm EA, Foiles SM. *Acta Mater.*, in press, 2009.
- [491] Allen MP and Tildesley DJ. In *Computer Simulation of Liquids*, Clarendon Press, Oxford, 1989.

- [492] Adler BJ and Wainwright TE. *J. Chem. Phys.*, 31:459, 1959.
- [493] Nose S. *Molec. Phys.*, 52:255-268, 1984.
- [494] Nose S. *J. Chem. Phys.*, 81:511-519, 1984.
- [495] Daw MS and Baskes MI. *Phys. Rev. B*, 29:6443-6453, 1984.
- [496] Ercolessi F and Adams JB. *Europhys. Lett.*, 26:583-588, 1994.
- [497] Nose S. *Molec. Phys.*, 57:187-191, 1986.
- [498] Hoover WG. *Phys. Rev. A*, 31:1695-1697, 1985.
- [499] Finnis MW and Sinclair JE. *Phil. Mag. A*, 50:45-55, 1984.
- [500] Andersen HC. *J. Chem. Phys.*, 72:2384-2393, 1980.
- [501] Parrinello M and Rahman A. *J. Appl. Phys.*, 52:7182-7190, 1981.
- [502] Teichler H. In Klimanek P and Pantleon W, editors, *Freiberger Forschungshefte B279 ueber Simulationstechniken in der Materialwissenschaft, Vortrag: Grundelemente der MD Modellierungen*, pages 215-234, 1996.
- [503] Wolf D. in Wolf D and Yip S, editors, *Materials Interfaces : Atomic – Level Structure and Properties*, Chapter 3, Chapman & Hall, London 1992.
- [504] Wolf D. *Acta Metall.*, 37:1983-1993, 1989.
- [505] Ray JR and Rahman A. *J. Chem. Phys.*, 80:4423-4428, 1984.
- [506] Goldstein H. In *Klassische Mechanik*, 8th ed., AULA Verlag Wiesbaden, 1985.
- [507] Lutsko JF, Wolf D, Yip S, Phillpot V. Nguyen T. *Phys. Rev. B*, 38:11572-11581, 1988.
- [508] Furtkamp M. *Internal report titled “MD simulation of GB migration in fcc Metals”*, unpublished, 1993.
- [509] Nye JF. *Physical Properties of Crystals*, Oxford at Clarendon Press, Oxford, 1957.
- [510] Gottstein G. *Physikalische Grundlagen der Materialkunde*, 2nd edition, Springer-Verlag Berlin, 2001.
- [511] Washburn J and Parker ER. *J. of Metals*, 4:1076-1078, 1952.
- [512] Winning M. *Ph.D. Thesis*, RWTH Aachen, Shaker Verlag, Aachen 1999.
- [513] Phillpot SR, Lutsko JF, Wolf D, Yip S. *Phys. Rev. B*, 40:2831-2840, 1989.

- [514] Fan W, Yizhen He Gong XG. *Phil. Mag. A*, 79:1321-1333, 1999.
- [515] Keglinski P, Wolf D, Phillpot SR, Gleiter H. *Phil. Mag. A*, 79:2735-2761, 1999.
- [516] Clarke AS and Jonsson H. *Phys. Rev. E*, 47:1993, 3975.
- [517] Faken D and Jonsson H. *Comp. Mater. Science*, 2:279, 1994.
- [518] Plimpton SJ and Wolf ED. *Phys. Rev. B*, 41:2712-2721, 1990.
- [519] Nomura M and Adams JB. *J. Mater. Res.*, 7:3202-3212, 1992.
- [520] Schönfelder B, Keglinski P, Wolf D, Phillpot SR. in *Proceedings of the International Conference on Intergranular and Interphase Boundaries in Materials*, p. 9-16, Prague, 1999.
- [521] Winning M. *Z. Metallkd.*, 95:233-238, 2004.
- [522] Babcock SE and Balluffi RW. *Acta Metall.*, 37:2367-2376, 1989.
- [523] Majid I and P.D.Bristowe PD. *Scripta Metall.*, 21:1153-1157, 1987.
- [524] Schönfelder B. *Doctoral Thesis*, Institut für Metallkunde und Metallphysik, RWTH Aachen, 2004.
- [525] Bishop Jr. GH, Harrison RJ, Kwok T, Yip S. *J. Appl. Phys.*, 53:5596-5608, 1982.
- [526] Bishop Jr. GH, Harrison RJ, Kwok R, Yip S. *J. Appl. Phys.*, 53:5609-5616, 1982.
- [527] Schönfelder B, Gottstein G, Shvindlerman LS. *Acta Mater.*, 53:1597-1609, 2005.
- [528] Sursaeva VG, Protasova SG, Straumal BB. *Def. Diff. Forum*, 192-193:15-26, 2001.
- [529] Wolf D. *Acta Metall. Mater.*, 37:1983-1993, 1989.
- [530] Goßmann R. *Diploma Thesis*, Institut für Metallkunde und Metallphysik, RWTH Aachen, May 2000.
- [531] Plimpton SJ and Wolf ED. *Phy. Rev. B*, 41:2712-2721, 1990.
- [532] Nomura N and Adams JB. *J. Mater. Res.*, 7:3202-3212, 1992.
- [533] Keglinski P, Wolf D, Phillpot SR, Gleiter H. *Phil. Mag. A*, 79:2735-2761, 1999.
- [534] Doyama M and Kogure Y. *Comp. Mat. Sci.*, 14:80-83, 1999.
- [535] Zieba P and Gust W. *Interface Sci.*, 10:27-30, 2002.
- [536] Zieba P. *Interface Sci.*, 11:51-58, 2003.
- [537] Majid I and Bristowe PD. *Scripta Metall.*, 21:1153, 1990.

- [538] Merkle KL and Thompson LJ. *Interface Sci.*, 12:277-292, 2004.
- [539] Schönfelder B, Wolf D, Phillpot SR Furtkamp M. *Interface Sci.*, 5:45-262, 1997.
- [540] Srolovitz DJ, Upmanyu M. *Ceramic Trans.*, 118:89, 2000.
- [541] Barrales-Mora LA, Shvindlerman LS, Mohles. V, Gottstein G. *Mat. Sci. Forum*, 558:1051, 2007.
- [542] Barrales-Mora LA, Mohles V, Shvindlerman LS, Gottstein G. *Acta Mater.*, 56:1151, 2008.
- [543] Brechet Y, Militzer M. *Scripta Mat.*, 52:1299, 2005.
- [544] Levine D, Acron JE, Brokman A. *Mater. Sci. Forum*, 94-96:281 1992.
- [545] Hilgenfeldt S, Kryn timer AM, Koehler SS, Stome HA. *Phys. Rev. Letter*, 86:2685, 2001.
- [546] Mullins WW. *Acta Metall.*, 37:2979, 1998.
- [547] Glicksman ME. *Phil. Mag.*, 85:3, 2005.
- [548] Rios PR, Glicksman ME. *Acta Mater.*, 55:1565, 2007.
- [549] Rios PR, Glicksman ME. *Acta Mater.*, 54:5313, 2006.
- [550] Rios PR, Glicksman ME. *Acta Mater.*, 56:1165, 2008.
- [551] Glicksman ME, Rios PR. *Intern. Journal of Materials Research*, 10:1099, 2005.
- [552] MacPherson RD, Srolovitz DJ. *Nature*, 446:1053, 2007.
- [553] Cahn JM. *Trans. Met, Soc. AIME*, 239:610, 1967.
- [554] Barrales-Mora L, Gottstein G, Shvindlerman LS. *Acta. Mater.*, 56:5915, 2008.
- [555] Wakai F, Enomoto N, Ogawa H. *Acta. Mater.*, 48:1297, 2008.
- [556] Weygand D, Brechet Y, Lepinoux J, Gust W. *Phil. Mag. B*, 79:703, 1999.
- [557] Kim, SG, Kim DI, Kim WT, Park YB. *Phys. Rev. E* , 74:061605, 2006.
- [558] Nabarro FR. *Report on a Conference on the Strength of Metals*, Phys. Soc. London, 1948.
- [559] Herring C. *J. Appl. Phys.*, 21:437, 1950.
- [560] Coble RL. *J. Appl. Phys.*, 34:1679, 1963.

- [561] Estrin Y, Gottstein G, Shvindlerman LS. *Mat. Sci. Forum*, 467-470:1283, 2004.
- [562] Kim HS, Estrin Y, Bush MB. *Mat. Sci. Eng*, 316:195, 2001.
- [563] Yamakov V, Wolt D, Phillpot SR, Gleiter H. *Acta Mater*, 60:6, 2002.
- [564] Gorkaya T, Ivanov V. *private communication*.
- [565] Underwood, E. E. In Dehoff RT, Rhines FN, editors, *Quantitative Microscopy*, McGraw-Hill, New York, 77, 1968.
- [566] Orsetti Rossi P, Sellars CM. *Acta Mater*. 24:137, 1997.
- [567] Bunge HJ. In Bunge HJ, editor, *Mathematische Methoden der Texturanalyse*, Akademie-Verlag, 1969.
- [568] Hansen PJ, Pospiech J, Lücke K. In Bunge HJ, editor, *Tables for Texture Analysis of Cubic Crystals*, Springer-Verlag, Berlin, 1978.
- [569] McHargue CJ, Jetter LK, Ogle JC. In Barrett C, Massalski TB, editors, *Structure of Metals*, p. 546, 1980.
- [570] Engler O, Gottstein G, Jura J. *Mat. Sci. Forum*, 157-162:259, 1994.
- [571] Pospiech J, Jura J, Gottstein G. *Mat. Sci. Forum* 157-162:407, 1994.
- [572] Wassermann G, Grewen J. In Wassermann G, Grewen J, editors, *Texturen Metallischer Werkstoffe*, Springer-Verlag, Berlin, 1962.
- [573] Virnich KH, Pospiech J, Lücke K. In Gottstein G, Lücke K, editors, *Textures of Materials*, p. 129, Springer-Verlag, Berlin, 1978.
- [574] Gottstein G. In Kallend J, Gottstein G, editors, *Proc. ICOTOM 8*, p. 1195, TMS, Warrendale, PA, 1988.
- [575] Rodrigues O. *J. de Mathématiques Pures et Appliquées*, 5:380, 1840.
- [576] Mackenzie JK. *Biometrika*, 45:229, 1958.
- [577] Pospiech J, Lücke K, Sztwiertnia K. *Acta Metall. Mater.*, 41:305, 1993.
- [578] Avrami MJ. *J. Chem. Phys.*, 7:1103, 1939.
- [579] Kolmogorov AN. *1st Akad. Nauk SSR, Ser. Fiz.*, 3:355, 1937.
- [580] Johnson WA. *Trans. AIME*, 135:416, 1939.

- [581] Anderson WA, Mehl RF. *Trans. AIME*, 161:140, 1945.
- [582] Gottstein G. In Gottstein G, Lücke K, editors, *Textures of Materials*, p. 93, Springer-Verlag, Berlin, 1978.
- [583] Pospiech J, Lücke K. *Acta Metall.*, 23:997, 1975.
- [584] Dillamore IL, Katoh H. *Metal Sci.*, 8:73, 1974.
- [585] Ibe G, Lücke K. In Margolin H, editor, *Recrystallization, Grain Growth and Texture*, p. 434, ASM, Metals Park, OH, 1966.
- [586] Ibe G, Dietz W, Fraker AC, Lücke K. *Z. Metallk.*, 61:498, 1970.
- [587] Randle V and Engler O. *Introduction to Texture Analysis*, CRC Press, Boca Raton, FL, 2000.
- [588] Köhler U, Bunge HJ. In Liang Z, Zuo L, Chu Y, editors, *Textures of Materials*, p. 497, Int. Academie Publishers, Beijing, 1996.
- [589] Marx V, Raabe D, Gottstein G. In *Proc. of the 4th Europ. Conf. on Advanced Materials*, Vol. F, p. 331, 1995.
- [590] Juul Jensen D. *Acta Metall. Mater.*, 43:4117, 1995.
- [591] Engler O. *Acta Mater.*, 46:1555, 1998.
- [592] Lücke K, Rixen R, Rosenbaum FW. In Hu H, editor, *The Nature and Behavior of Grain Boundaries*, p. 245, Plenum Press, New York, 1972.
- [593] Virnich KH. *Doctoral Thesis*, RWTH Aachen, 1979.
- [594] Möhlmann U. *Doctoral Thesis*, RWTH Aachen, 1966.
- [595] Lücke K, Rixen R, Senna M. *Acta Metall.*, 24:103, 1976.
- [596] Senna M, Lücke K. *Z. Metallk.*, 67:752, 1976.
- [597] Escher C, Neves S, Gottstein G. In Terry R, editor, *Third Intern. Conf. on Recrystallization and Related Phenomena*, p.645, Mc-Nelley, Monterey, 1997.
- [598] Hutchinson WB, Ryde L, Bate PS, Bacroix B. *Scripta Mat.*, 35:570, 1996.
- [599] Virnich, K. H., Hirsch, J., Lücke, K. In Nagashima S, editor, *Proc. ICOTOM 6*, p.550, Japan Iron and Steel Institute, Tokyo, 1981.
- [600] Detert K, Lücke K. *Report No. AFOSR – TN – 56 – 103 AD – 82016*, Brown Univ. 1956.
- [601] Udler D, Seidman DN. *Acta Metall. Mater.*, 42:1959, 1994.

- [602] Straumal BB. *Phase Transitions at Grain Boundaries*, (in russian) Moscow Science, 2003.
- [603] Liebeherr M, Gottstein G. In Mughrabi et al., editors, *Microstructure and Properties of Metallic High-Temperature Materials*, p.479, Wiley-VCH, Weinheim, Germany, , 1999.
- [604] Bhadeshia MKHD. *Mat. Sci. Eng.*, A223:64, 1997.
- [605] Burke J. In *Grain Control in Industrial Metallurgy*, p. 1, ASM, Metals Park, OH, 1949.
- [606] Grey EA, Higgins GT. *Acta Metall.*, 21:309, 1973.
- [607] Shvindlerman LS, Gottstein G. *Scripta Metall.*, 50:1051, 2004.
- [608] Gorelik SS. *Recrystallization in Metals and Alloys*, Metallurgica [in Russian], 1978.
- [609] Shvindlerman LS, Jannot E, Gottstein G. *Acta Metall.*, 55:3397, 2007.
- [610] Fäber B, Cadel E, Menand A, Schmitz G, Kirchheim R. *Acta Metall.*, 48:789, 2000.
- [611] Hentschel Th, Isheim D, Kirchheim R, Müller F, Kreve H. *Acta Metall.*, 48:933, 2000.
- [612] Shvindlerman LS, Gottstein G. *Z. f. Metallk.*, 95:239, 2004.
- [613] Aristov V. *Ph.D. Thesis*, Moscow, 1978.
- [614] Watanabe T, Fujii H, Oikawa H, Arai KI. *Acta Mat.*, 37:47, 1989.
- [615] Watanabe T, Tsurekawa S. *Acta Mat.*, 47:4171, 1999.
- [616] Watanabe T. In Gottstein G, Molodov DA, editors, *Recrystallization and Grain Growth*, Vol.I, p. 11-20, Springer-Verlag, 2001.
- [617] Aust KT, Erb U, Palumbo G. *Mat. Sci. Eng.*, A176:329, 1994.
- [618] Lenockey EM, Palumbo G, Lin P, Brennenstuhl A. *Metall. Mater. Trans.*, A29:387, 1998.
- [619] Shvindlerman LS, Gottstein G. *Scripta Mat.*, 54:1065, 2006.
- [620] Darken L. *AIIME*, 174:184, 1948.
- [621] Bokstein BS, Shvindlerman LS. *Sov. Phys. Solid State*, 16:1547, 1975.
- [622] Hirano K, Agarwalo RP, Cohen M. *Acta Met.*, 10:857, 1962.
- [623] Novikov Yu. *Scripta Mat.*, 55:243, 2006.

- [624] Huntley HE. In *Dimensional Analysis*, Dover, New York, 1967.
- [625] Fourier JBJ. In *La Theorie Analytique de la Chaleur*, Ch. 3, sec. 9, 1822.
- [626] Rayleigh JW, Riabouchinsky D. *Nature*, 95:591, 1915.